Current Opinion in Solid State and Materials Science 26 (2022) 100974

Contents lists available at ScienceDirect

Current Opinion in Solid State & Materials Science

journal homepage: www.elsevier.com/locate/cossms

Defects and anomalies in powder bed fusion metal additive manufacturing

Amir Mostafaei [a,*], Cang Zhao [b,c,*], Yining He [d], Seyed Reza Ghiaasiaan [e,f], Bo Shi [b,c], Shuai Shao [e,f], Nima Shamsaei [e,f], Ziheng Wu [d], Nadia Kouraytem [g], Tao Sun [h], Joseph Pauza [d], Jerard V. Gordon [i], Bryan Webler [d], Niranjan D. Parab [j], Mohammadreza Asherloo [a], Qilin Guo [k], Lianyi Chen [k], Anthony D. Rollett [d,l,*]

[a] Department of Mechanical, Materials and Aerospace Engineering, Illinois Institute of Technology, 10 W 32nd Street, Chicago, IL 60616, USA
[b] Department of Mechanical Engineering, Tsinghua University, Beijing 100084, China
[c] Key Laboratory for Advanced Materials Processing Technology, Ministry of Education, Beijing 100084, China
[d] Department of Materials Science and Engineering, Carnegie Mellon University, Pittsburgh, PA 15213, USA
[e] Department of Mechanical Engineering, Auburn University, Auburn, AL 36849, USA
[f] National Center for Additive Manufacturing Excellence (NCAME), Auburn University, Auburn, AL 36849, USA
[g] Department of Mechanical and Aerospace Engineering, Utah State University, Logan, UT 84322, USA
[h] Department of Materials Science and Engineering, University of Virginia, Charlottesville, VA 22904, USA
[i] Department of Mechanical Engineering, University of Michigan, Ann Arbor, MI 48109, USA
[j] X-ray Science Division, Argonne National Laboratory, Lemont, IL 60439, USA
[k] Department of Mechanical Engineering, University of Wisconsin-Madison, Madison, WI 53706, USA
[l] NextManufacturing Center, Carnegie Mellon University, Pittsburgh, PA 15213, USA

ARTICLE INFO

Keywords:
Additive manufacturing
Powder-related defects
Processing-related defects
Post-processing-related defects
Defect mitigation
Process-structure–property relationship

ABSTRACT

Metal additive manufacturing is a disruptive technology that is revolutionizing the manufacturing industry. Despite its unrivaled capability for directly fabricating metal parts with complex geometries, the wide realization of the technology is currently limited by microstructural defects and anomalies, which could significantly degrade the structural integrity and service performance of the product. Accurate detection, characterization, and prediction of these defects and anomalies have an important and immediate impact in manufacturing fully-dense and defect-free builds. This review seeks to elucidate common defects/anomalies and their formation mechanisms in powder bed fusion additive manufacturing processes. They could arise from raw materials, processing conditions, and post-processing. While defects/anomalies in laser welding have been studied extensively, their formation and evolution remain unclear. Additionally, the existence of powder in powder bed fusion techniques may generate new types of defects, e.g., porosity transferring from powder to builds. Practical strategies to mitigate defects are also addressed through fundamental understanding of their formation. Such explorations enable the validation and calibration of models and ease the process qualification without costly trial-and-error experimentation.

1. Introduction and background

1.1. Metal additive manufacturing

Metal additive manufacturing (AM, also known as 3D printing) is a family of technologies consisting of three main production processes, i.e., powder bed, powder feed, and wire feed. These processes differ in their manner of spreading or layering the material as well as the way to fuse or bond the feedstock. Compared to conventional manufacturing, metal AM possesses many superior capacities, including shortened design-to-market cycle, lower energy consumption, and the ability to consolidate components into unitary parts with complex geometries. There is also the capability to fabricate non-standard microstructures, with the potential to tailor local properties [1,2].

In fusion-based AM (e.g., laser powder bed fusion), a heat source (e.g., a laser) is used to fuse the material, and the fundamental knowledge

* Corresponding authors at: Department of Mechanical, Materials and Aerospace Engineering, Illinois Institute of Technology, 10 W 32nd Street, Chicago, IL 60616, USA (A. Mostafaei), Department of Mechanical Engineering, Tsinghua University, Beijing 100084, China (C. Zhao), Department of Materials Science and Engineering, Carnegie Mellon University, Pittsburgh, PA 15213, USA (A.D. Rollett).
E-mail addresses: mostafaei@iit.edu (A. Mostafaei), cangzhao@tsinghua.edu.cn (C. Zhao), rollett@andrew.cmu.edu (A.D. Rollett).

https://doi.org/10.1016/j.cossms.2021.100974
Received 6 June 2021; Received in revised form 2 December 2021; Accepted 9 December 2021
Available online 21 January 2022

behind the process is about melting and solidification. In comparison, welding metallurgy using high-energy–density beams such as lasers has been extensively studied for decades. So an intuitive idea is to learn from this existing body of knowledge and apply it when understanding the formation and evolution of the microstructures and defects in metal AM. Regardless of their similarities, it is noted that some weldable alloys (e.g., AA6061) are not easy to process by fusion-based AM processes because of cracking from a combination of shrinkage stress and large solidification range during AM processing [3,4]; therefore technical solutions such as high-temperature preheating are needed [5].

There has been a remarkable growth in adoption of metal AM technologies in different industry sectors for manufacturing high-quality, defect-free parts. Recently, Snow *et al.* [6] and Sanaei *et al.* [7] published review articles on the formation and influence of defects on mechanical properties. Moreover, several research groups have focused on defect detection in large-scale AM processes [8,9], *in situ* monitoring [10,11], computational modeling [12,13], and machine learning [14-16]. Significant progress in metal powder bed fusion AM requires the linking of multiple variables (e.g., process settings, starting materials, and post-processing) to resultant properties (e.g., physical, mechanical, and corrosion properties). But so far, the process-structure–property relationships and appropriate post-treatment "recipes" in metal AM have not been as extensively characterized as for conventional materials. Issues including macro-, micro-, and nano-scale defects, repeatability, inspection, and certification are crucial impediments to the wide implementation of AM parts.

The goal of this review is to provide a detailed summary of the characterizations of metal powder bed fusion AM defects and mitigation techniques to limit their occurrences. The metals here include nickel-, titanium-, aluminum-, and iron-based alloys. Sequentially, we describe powder bed fusion AM processes, characterization tools (*in situ* and *ex-situ*), powder-related, process-related, and post-process-related defects, mitigation techniques, possible prediction criteria, and mechanical and corrosion properties. Our aim for this review was to identify the gaps in the published literature and the research needs, thereby improving our understanding of metals AM processes and guiding the operation of AM machines.

1.2. Classification of powder bed fusion AM techniques

Powder bed fusion (PBF) techniques currently offer the best reproducibility and dimensional accuracy within metal AM production and, therefore, have been well-researched in both industry and academia. In general, PBF techniques utilize the following steps to fabricate a part: (1) a layer of metal powder of specified thickness is spread onto the build plate of the machine; (2) the desired area within the layer of powder is selectively melted together using a laser or electron beam heat source; (3) the build plate moves down, and a new layer of powder is spread onto the build plate; (4) this process is repeated layer-by-layer until the part is completed. PBF processes have been used in various industries for numerous applications such as medical (customized orthopedic components and implants from bio-materials of titanium, stainless steels, and cobalt-chrome alloys), aerospace and defense (fuel nozzles, brackets, turbine blades, engine components, and structural member), and energy (heat exchangers and turbine airfoils) [17].

As specified in the ISO/ASTM52900 standard [18], PBF is defined as an additive manufacturing process in which thermal energy selectively fuses regions of a powder bed. Processes that fall under this category include electron beam melting (EBM), selective laser melting/sintering (SLM/SLS), which are described more recently as direct metal laser melting (DMLM) or direct metal laser sintering (DMLS). ASTM has defined the following terminologies for AM technologies:

- For direct laser deposition → Laser beam directed energy deposition (L-DED);
- For selective laser melting, laser powder bed fusion, etc. → Laser beam powder bed fusion (L-PBF);
- For electron beam technologies such as powder feed or powder bed → E-DED and E-PBF, respectively.

1.2.1. Laser beam powder bed fusion

L-PBF (a.k.a. selective laser melting) uses a laser as the primary tool to manufacture a part in a layer-by-layer fashion. It is capable of producing parts in a range of metal alloys, including aluminum, titanium, iron, and nickel-based superalloys. There are different manufacturers for this type of metal AM [19].

A step-by-step process methodology for L-PBF AM is summarized in Fig. 1. Once the full part has been printed, the excess powder is removed (and often recycled) and then the build plate is unloaded from the build chamber. Since the printed part is fused to the build plate, mechanical removal is required. Before removal, the parts are typically left on the build plate and given a stress-relief heat treatment to minimize residual stresses, eliminate warping, and maintain dimensional accuracy.

The L-PBF technique fills niches in industries where either rapid prototyping or low-volume production is needed. The inherently additive nature of the process allows printing of complex lattice structures (Fig. 2a) [20] and parts with intricate internal geometries like the GE fuel nozzle (Fig. 2b) [21]. Moreover, it allows for part consolidation and ~~the~~ geometrical optimization for lighter weight such as the seat brackets (Fig. 2c) [22].

L-PBF of metal parts has largely developed in recent years. Besides the increasing number of commercially available machines, significant effort has gone into research to improve the technique. One of the major challenges, especially in applications where fatigue is a concern, is the defects that form inside a build. Understanding the building process and defect formation is the key to building high-quality parts.

There are many studies on the effect of process parameters on microstructure, porosity level, and defect formation. Influential process parameters are (1) laser-related parameters (e.g., laser power, spot size, pulse duration, and pulse frequency), (2) scan-related parameters (e.g., scan speed or velocity, scan spacing or hatch, scan rotation, and scan pattern), (3) powder related parameters (e.g., powder morphology, particle size and distribution, layer thickness, dosing, and materials properties), and (4) macroscopic parameters (e.g., powder bed temperature and its uniformity, gas flow, gas type, spreader bar type) [23]. Computational modeling has been applied to the L-PBF process to predict laser-powder interaction, melt pool geometry, and potential defect formation based on the input processing parameters [13]. The formation of defects in L-PBF has several causes. High speed x-ray visualization [10,24] has shown that, at sufficiently high laser power, the vapor cavities *aka* "keyholes" that form above a characteristic threshold in power density [25] are very likely to be unstable and generate keyhole porosity [24-26]. At a constant laser power, increasing the scanning speed elongates the keyhole and makes it shallower. In general, there is an optimal combination of power, velocity, hatch spacing and layer depth for printing [27], i.e., a process window. Nevertheless, transfer of porosity from the powder to the build can occur via capillary forces [28]. At high power and speed, bead-up or humping [29] leads to instabilities in melt pool shape that can also cause porosity. Finally, increasing the scan speed at constant power results in the lack-of-fusion (LOF) case where insufficient melt pool overlap results in unfused regions in the form of porosity and/or inclusion of unmelted particles [30]. The potential defects are shown, e.g., Fig. 7) as regions in the laser power-scanning speed "processing window" or region where full density can be expected. The point is that defect morphologies in PBF metal AM follow predictable trends within power-velocity-hatch-layer (*P-V-H-L*) processing parameter space [29,31]. In addition to the P-V-H-L processing combination, scan strategy (Fig. 3) plays an essential role in defect formation in PBF processes. Scan strategy influences heat transfer, melt formation from powder, and solidification rate, affecting the

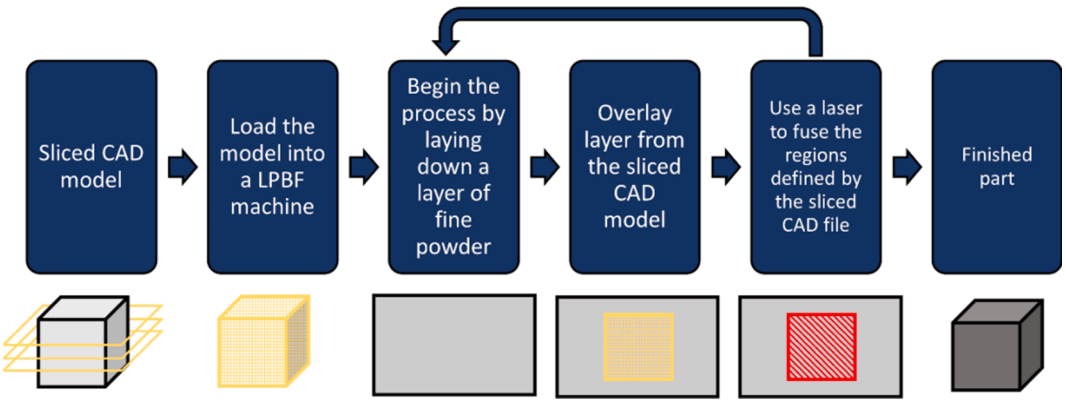

Fig. 1. General build methodology for an L-PBF machine. Rectangular grey drawings represent a bed of powder during the L-PBF process.

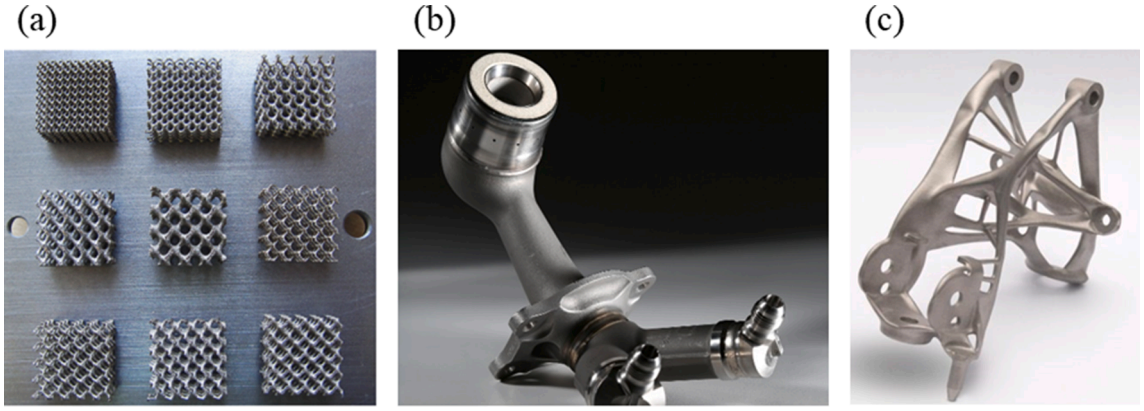

Fig. 2. Examples of AM geometries. (a) Complex lattice structures. Reprinted with permission from Ref. [20]. (b) Fuel nozzle printed by GE. Reprinted with permission from Ref. [21]. (c) Lightweight seat bracket produced by GM. Reprinted with permission from Ref. [22].

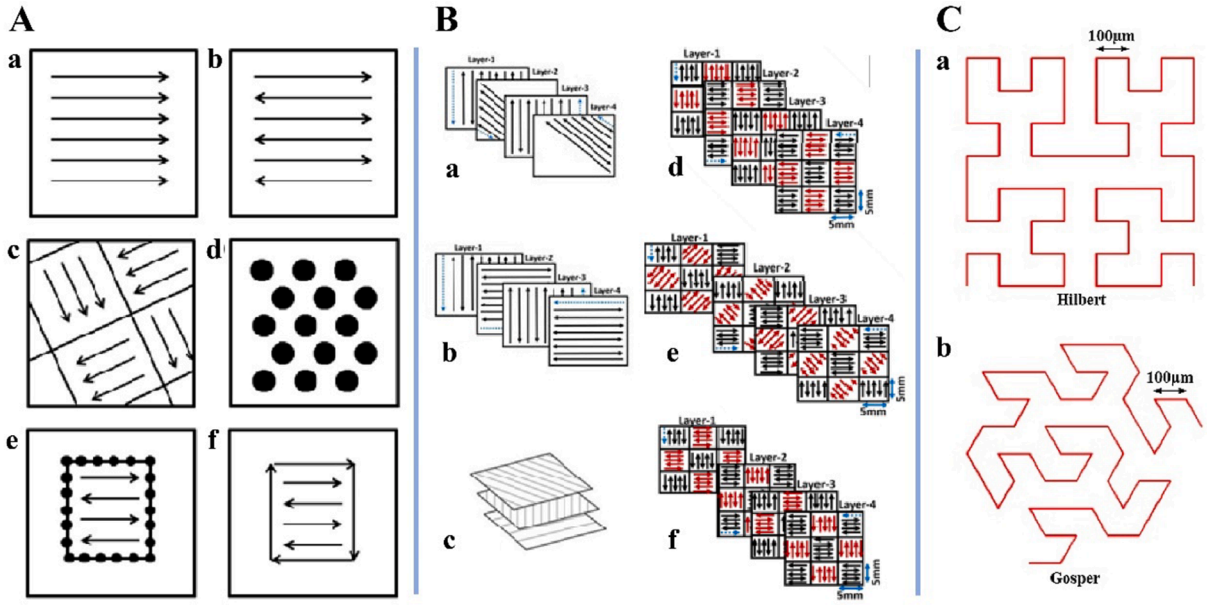

Fig. 3. (A) Different scan strategies used in the L-PBF process. (a) unidirectional or concurrent fill, (b) bi-directional, snaking, or countercurrent fill, (c) island scanning, (d) spot melting, (e) spot melting contours with snaking fill, and (f) line melting contours with snaking fill. Reprinted with permission from Ref. [32]. (B) Schematics illustrating scan patterns of (a) 45° alternating, (b) 90° alternating, (c) 67° alternating, (d) chessboard scanning, and chessboard scanning with adjacent chessboard block scanned in (e) 45° and (f) 90° rotated direction. Reprinted with permission from Ref. [40]. (C) Examples of fractal scan strategies of (a) Hilbert and (b) Gosper. Reprinted with permission from Ref. [41].

type of defects, location, and distribution as well as grain morphology [32-39]. Thus, it is crucial to optimize process parameters, heat source power, and scan speed and strategy for minimizing process-induced porosity.

During the laser powder bed fusion process and following powder spreading which is governed by many powder characteristics (Section 3.1), a laser selectively scans the surface of the powder layer to melt and fuse the metal powder following the STL input file in the respective layer. The complex laser-matter interaction leads to many phenomena that may result in defects in the final part [42]. Common defects include balling/bead-up, lack of fusion, keyhole porosity, the ejection of spatters of molten metal or powder particles, denudation of the surrounding substrate, or microstructural defects. Numerous studies focused on the experimental approach to visualize and analyze such anomalies. However, an important aspect that plays a major role in their formation is the laser-matter interaction.

This is defined as the interaction of the laser with the powder particles, molten pool, and vapors [43]. On a sub-millimeter scale, as soon as the laser hits the surface of the powder, a complex interaction between the laser and the powder occurs. Part of the laser's incident energy is absorbed by the powders and the rest of it is reflected within the powder layer. One inaccurate assumption is that the incident laser undergoes many reflections before it transitions into the melt pool which in turn absorbs energy by Fresnel absorption [44]. The number of reflections of the laser beam is dependent on local material properties, particle size, and packing density. Recent *in situ* observations or the full-physics simulations from, e.g., Lawrence Livermore National Laboratory [25,45,46], show that the laser interacts primarily with the liquid metal. Powder particles are either melted into the pool at the front end or swept away in the rapidly heated cover gas. There is plenty of evidence that the presence/absence of powder makes little difference to the net absorption of the incoming laser energy. It is also important to note that under the common occurrence of a keyhole, the laser light may be reflected from the wall of the cavity several times which substantially increases the effective absorptivity as indeed acknowledged in the following paragraph, e.g. [47,48].

A main parameter of interest to the community during laser-powder interaction is absorptivity; this is investigated either experimentally or using mathematical models. Bertoli *et al.* [49] performed *in situ* experimental measurement of the absorption of gas atomized and water atomized powders coupled with a COMSOL model to predict the cooling rates in the melt pool. Trapp *et al.* [50] used direct calorimetry to measure the effective absorptivity of continuous-wave 1070 nm laser light for bare and metal powder-coated discs of 316L stainless steel as well as for aluminum alloy 1100 and tungsten. The effective absorptivity was shown to increase markedly with increasing incident laser power from 30 up to ≈540 W for scanning speeds of 100, 500, and 1500 mm/s. The change in surface morphology that was observed in the high-speed images was correlated with a change in the effective absorptivity from 30 W until the onset of the formation of a recoil pressure-induced surface depression, i.e., keyhole. The possibility of multiple reflections and absorption steps inside a keyhole is the primary reason for enhanced absorptivity at high power densities [51]. Beyond the onset of keyhole mode, the value of the effective absorptivity showed a plateau for discs and powder-coated disks. For a powder layer of 100 μm thick, the effective absorptivity was two times that of a polished plate (surely this was only for the conduction mode, not for keyhole where the absorptivity is already ≈0.8). Tolochko *et al.* [52] experimentally assessed the absorptance of a number of powders of interest to sintering, including metals and oxides, under two different laser wavelengths of 1.06 μm and 10.6 μm obtained by using different laser types, namely Nd-YAG and CO_2 respectively. The absorptivity of metal powders was shown to decrease with increasing wavelength [50,53-56]; whereas it was shown to increase with increasing wavelength for oxides [57]. Fischer *et al.* [58] presented a mathematical model that compares the absorptivity of bulk solid and powder of pure Titanium metal. In the first step, the energy is absorbed in a narrow layer of individual particles determined by the bulk properties of the material, leading to a high temperature of particle surfaces during the interaction. After thermalization of the energy, heat flows mainly towards the center of the particles until a local steady state of the temperature within the powder is obtained. Finally, the surrounding powder properties are responsible for further thermal development.

The investigation of laser-powder interaction has been the topic of many experimental studies using high-speed optical imaging [59], x-ray imaging [24-26,48,60], and Schlieren imaging [61] aiming at the investigation of defects. However, due to the complexity of the laser-matter interaction, experimental investigations have historically driven numerical analyses. However, recent advances in numerical models allow the elucidation of the laser-matter interaction; this will be discussed in detail throughout the subsequent sections (e.g., [47,62-67]).

1.2.2. *Electron beam powder bed fusion*

E-PBF uses an electron beam as the heat source to selectively sinter/melt the powder. The process is capable of fabricating near-fully dense metallic parts that have mechanical properties comparable to conventionally manufactured parts, e.g., castings or forming. Thus, E-PBF parts can serve as load-bearing structures in many applications. The operation of commercialized E-PBF systems is optimized to minimize defects, just as in L-PBF. However, those systems offer less freedom for process modification and lack direct control over, e.g., power and scan speed. Many locally-built E-PBF systems [68-70] have been reported in the literature as being used for research purposes to study fundamentals, e.g., transient physical effects and interactions between the electron beam and powder.

An E-PBF system has three major components – electron delivery, powder spreading system, and build chamber. As suggested by the name, the major difference between E-PBF and L-PBF is with the heat source. The E-PBF process uses an electron gun as the heat source which is located directly above the powder bed shown in (Fig. 5). Electrons are generated through heating a filament, which can be a tungsten filament (printers such as S12, A2, A2X) or lanthanum hexaboride LaB_6 (printers such as Arcam Q10, Q20) cathode. The electrons are then accelerated by the applied voltage, focused and steered by a series of electromagnetic lenses. Compared with laser optics, the electromagnetic lenses in an E-PBF process can move the electron beam free of inertia. As a result, the peak scanning speed of an electron beam can reach 10^2 m/s which is significantly faster than the speed of a laser which is limited by the scan optics to a few m/s [71].

Using an electron beam as the heat source also introduces a unique problem known as "smoking", of which the outcome is similar to the powder spattering in the L-PBF process but in a much more chaotic manner. As the electrons decelerate on contact with the powder bed, their kinetic energy is converted into thermal energy which is what is needed to sinter/melt the feedstock; however, some of the energy can go into ejecting particles from the powder bed [70]. For the same energy level, electrons have a much larger momentum compared to a photons because of the finite mass of the electron (The incoming momentum may be larger than for photons but that would merely compact the powder bed, not disassemble it). Additionally, thanks to imperfect electrical conduction in the powder bed, electrons can accumulate which results in repulsion between negatively charged powder particles and consequent additional powder ejection during the scanning process [70,72]. Sigl *et al.* [70] have shown that the repulsive force between two adjacent powder particles is on the order of 10^{-6}N while the weight of a powder particle is on the order of 10^{-9}N assuming that an electron beam irradiates a specific region with 100 W power for 1 s. Clearly, "smoking" can be highly detrimental to the quality of each powder layer, which in turn introduces processing defects into the as-built parts and potentially leads to the termination of the build. Therefore, a conductive and fully grounded powder bed is essential to avoid charge accumulation, which

also explains why only metal feedstock can be used in the E-PBF process.

Many aspects of the build chamber are designed to mitigate the "smoking" issue including the high pre-heating and the vacuum environment. To maintain them, the build chamber needs to be airtight and thermally well insulated. The vacuum of E-PBF systems normally pumps down to 10^{-4}–10^{-5} mbar to minimize collisions between air molecules and electrons; it is also important for reducing the reaction between residual oxygen and the powder feedstock at high pre-heat [70,73]. To further mitigate "smoking", recent systems apply a "controlled vacuum", meaning a vacuum with a small partial pressure of helium during fabrication. Better electrical conductivity and thermal conductivity associated with the introduction of helium helps to minimize electrostatic charge accumulation in the powder bed and assist the cooling process [74].

Pre-heating is designed to reduce thermal gradients during fabrication and is another countermeasure against "smoking" [75,76]. The pre-heating step uses a defocused electron beam with low power density to sweep over the powder bed and raise the surface temperature. The elevated temperature promotes sintering of the particles which raises electrical conductivity to avoid charge accumulation and provides mechanical strength to make particle ejection less common [77]. However, pre-sintering also leads to difficulty with de-powdering, especially for complex part geometries with internal passages. Typically the pre-heat temperature varies from 300 °C [78] for pure copper to 1100 °C [79] for intermetallic compounds or nickel alloys.

The E-PBF process usually has two melting modes after the pre-heating steps as shown in Fig. 4. Hatching is the melting mode that fills the bulk area and uses the beam to scan back and forth along parallel scanning paths, separated by the pre-defined hatch spacing distance; afterwards, contouring outlines the edge of each cross-section and improves the surface finish. Some common parameters that can be changed include beam current, focus offset (which controls the spot size) hatch spacing distance, etc.

Another critical module in the E-PBF machine is the powder spreading system of which the essential goal is to deliver powder from the reservoir onto the build plate in a uniform layer before the melting step. In Arcam E-PBF systems, two hoppers and a rake are coordinated to complete the aforementioned task. The standard E-PBF particle size range is 45–106 μm, which is coarser than the feedstock used in L-PBF [80]. The coarser powder reduces smoking because of the larger particle mass, meaning that more kinetic energy is required to eject any given particle. Moreover, using finer powders is not necessary since the process resolution, i.e., melt pool size, is generally coarser in the E-PBF process. Certainly, using coarser powder is more cost-efficient because standard atomization technologies produce a wider range of particle size than can be used in AM. Sigl *et al.* [70] suggested that water atomized powder is preferable to gas atomized powder for stabilizing the process as the irregular morphology increases the surface contact between powder particles resulting in better grounding of the powder bed.

Similarly, a support structure is required for overhangs just as in the L-PBF process but serves different purposes. Unlike the latter process, little residual stress is likely to be stored for the high pre-heats used in E-PBF. There is always, however, the possibility of heat accumulation in overhangs surrounded by unmelted powder with lower thermal conductivity. Local overheating leads to excessive melt pool size and deviations from the intended build conditions (and dimensions). Support structures in E-PBF serve to provide solid channels for heat extraction from the overhangs.

Being able to fabricate nearly defect-free parts is important for safety–critical applications since the embedded defects can be sites of stress concentration which in turn can initiate, e.g., fatigue cracks. Besides hot cracking that limits the weldability and printability of many alloys, porosity is the most in need of optimization. Porosity can be simply categorized into raw material porosity and processing porosity based on the origin of porosity formation. Studies have shown that the amount of entrapped gas in powder strongly correlates with the concentration of the final in-part porosity under constant processing parameters [81]. The morphology of gas porosity is spherical; yet, they can expand and result in larger pores in the final parts than their original sizes in powder particles. Similar to other AM processes, lack-of-fusion porosity can exist in E-PBF parts. As discussed elsewhere, this occurs whenever inadequate melt pool overlap results in regions that were never melted. Unmelted/partially melted powder can often be observed within lack-of-fusion pores which typically have elongated shapes [82,83].

Despite the high-power levels available in E-PBF, key-hole porosity is

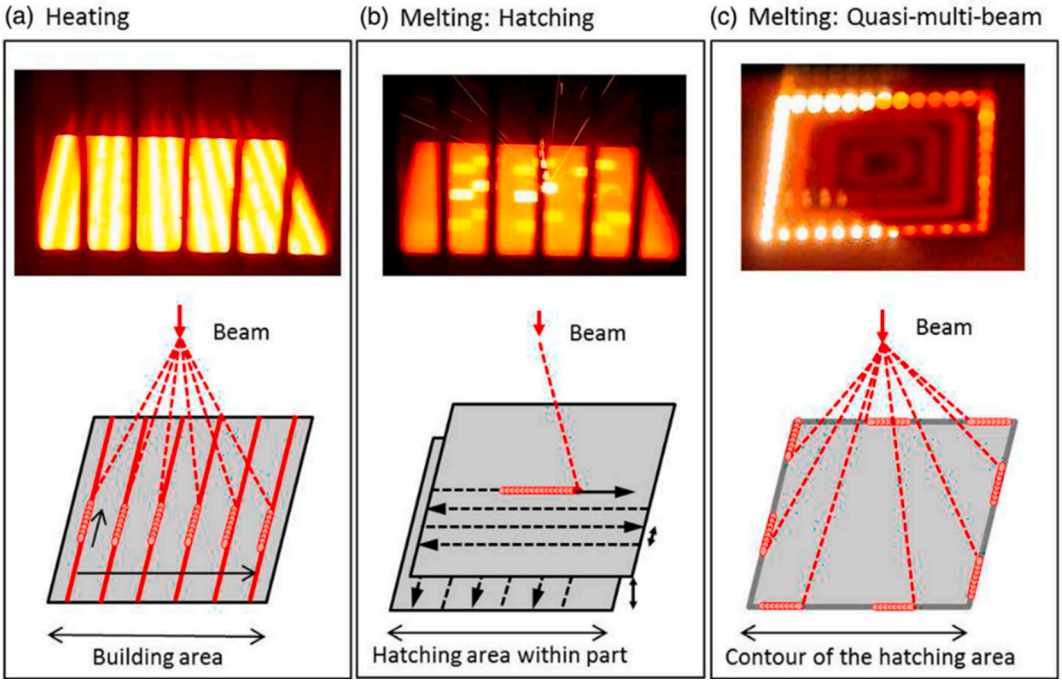

Fig. 4. Actual images and schematics of the three melting modes in the E-PBF process. Reprinted with permission from Ref. [71].

not a type of processing defect that is commonly observed in E-PBF. The primary reason is that the beam power and speed are automatically controlled by the software to avoid excessive energy input based on the given max beam current and speed function index [84]. Francis [85] showed that keyhole melting can be generated in the single-track experiment where beam power and velocity and focus offset are explicitly specified. In the electron beam and laser-based AM process, conduction mode and key-holing mode are the two standard melting modes. The power density on the surface of the molten metal surface determines which melting mode takes place where the threshold is of order 1 MW/cm^2 [25]. Finally, for post-processing, hot isostatic pressing (HIP) has repeatedly been shown to eliminate closed porosity in E-PBF parts [81]; however, subsequent heat treatment of HIPed parts at high temperature increases the diffusivity of inert and insoluble gas (e.g., Argon from the powder atomization) in the bulk and leads to the regrowth of the gas pores.

1.3. Melting modes

Powder-based additive manufacturing (AM) utilizes a moving energy source (e.g., Electron beam or laser) to selectively melt the metal powder in a layer-by-layer manner to build desired 3-Dimensional (3D) structures, as detailed in the previous section. As the source of energy scans across the metal, two different modes can be distinguished depending on the resultant molten pool shape. First is the conduction mode which occurs when a relatively low laser power intensity is used, and a semi-circular melt pool is created. Second is the keyhole mode which occurs when a relatively high laser power intensity is used which creates a deep and slender vapor depression cavity, i.e., the keyhole, in the melt pool, as discussed above. The keyhole mode has been found in laser-based AM to cause defect generation in AM parts when the depth-to-width ratio becomes too large [86,87]. Hence, the understanding and control of keyhole dynamics under various processing parameters is important for optimizing the process to obtain defect-free AM metal parts. The printing modes defined in this section are legacy terms from the welding community that cluster melt pool behavior into two separate categories. However, these terms help simplify and generalize communication of weld morphology as well as some fundamental aspects of the weld.

The difference between the two printing modes is substantial. A comparison between the laser energy absorptions in conduction and keyhole modes, for an assumed Gaussian laser beam, is shown in Fig. 5. Except for pure conduction mode, the laser interacts with the liquid metal and the powder melts into the liquid at the front of the melt pool. Additionally, defocus (in L-PBF) [88-90] or focus offset (in E-PBF) [91] can affect printing mode and porosity formation, i.e., spreading out the laser light reduces the power density which can help avoid unstable keyholes and pore formation [24].

1.3.1. Conduction mode

Conduction mode is typically associated with melt pools where the vapor cavity and its associated effects are negligible. Conduction mode generally produces semi-circular melt pools or melt pools with small aspect ratios, as illustrated in Fig. 5. The energy density in the substrate is low enough that the substrate temperature does not increase above the boiling point hence a vapor cavity does not form. The assumption of conduction-only heat transfer mode was used by Bag *et al.* [94] who successfully modeled spot welds using an adaptive volumetric source. In their study, the melt pools all showed the characteristic, approximately semi-circular shape associated with conduction mode welding. In a different approach, Russo *et al.* [95] described conduction mode welding as being where melt pool motion or an extended (de-focused) heat source does not disturb the thermal distribution.

As laser powder bed fusion additive manufacturing gained interest, it was clear that the printing process is analogous to micro-welding processes and these terms have been adopted in the AM community. Similar to traditional welding, conduction mode in laser powder bed fusion is used to refer to regular, semi-circular melt pools. It has been shown that, much like welding, L-PBF melt pools exhibit a transition from conduction mode to keyhole mode as the power increases for constant scan speed [96,97]. Fig. 5 illustrates the penetration caused by vaporization, which is discussed in more detail in the following section, as well as the increased re-melting into the previously melted layers. Throughout this work, when the term conduction mode is used it will be referring to melt pools that possess a negligible vapor cavity and small aspect ratio on the order of 0.5 (depth/width).

Ideally, conduction mode should result in fully-dense printed parts provided that there is sufficient melt pool overlap to avoid LOF porosity [98]. With increasing power and decreasing scan speeds, the transition of melt pools from conduction to keyhole mode was observed *in situ* [25] and post-solidification [93,99]. The keyhole mode has been of interest in the AM community mainly because of the tendency for unstable vapor cavities to generate keyhole porosity which may deteriorate properties such as fatigue strength and corrosion resistance. The keyhole mode is

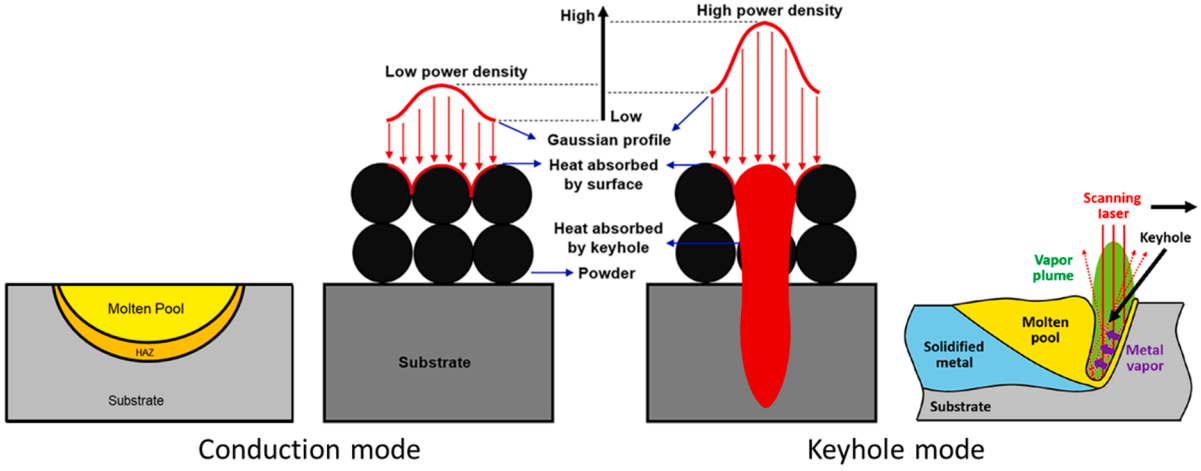

Fig. 5. Schematic of laser energy absorption in the conduction mode and the keyhole mode at the initial moment. The laser is assumed to have a Gaussian distribution. Laser energy is absorbed by the upper surface in the conduction mode, whereas it is mostly absorbed on the inner surface of the vapor cavity in keyhole mode. Reprinted with permission from Ref. [92]. (Bottom left) Schematic of the conduction mode showing the melt pool and heat-affected zone in the substrate. (bottom right) Schematic of the laser-induced keyhole. Reprinted with permission from Ref. [47]. The schematics illustrate heat history during (middle left) conduction and (middle right) keyhole modes. Reprinted with permission from Ref. [93].

discussed in more detail as follows.

1.3.2. Keyhole mode

As the laser power intensity increases above about 1 MW/cm^2, keyhole mode is achieved, as illustrated in Fig. 5 and described next. Laser light impinging on the surface of the material raises the temperature, leading to melting. As the temperature increases further and reaches the boiling point, the formation of metallic vapor generates a recoil pressure. The recoil pressure pushes down the molten metal resulting in the formation of a long and slender gas cavity known as the keyhole. After entering the keyhole, the laser light experiences multiple reflections from both the front and rear keyhole walls before it is absorbed (or partially reflected out). The observation and characterization of the keyhole phenomenon have been achieved through both experiments and simulations that we review in the following paragraphs. As indicated in Fig. 5, the already solidified part will experience more thermal cycles of re-melting and cooling during the PBF process compared with conduction mode [100].

Experimentally, observations of keyholes were initially limited to optical imaging looking down onto the top of the keyhole [101,102] because of the opacity of the substrate. Using high-speed imaging, the opening of the keyhole, and in some cases, some portion of the keyhole wall, was studied, however, and the underlying keyhole dynamics were deduced. In a different approach, a side view of the keyhole phenomenon was obtained using the "sandwich" method [103-105] where a thin metal plate is clamped between two thin glass plates. A laser scans along the length of the metal plate and the keyhole is observed from a side view at the interface of the metal and the transparent glass plate. However, the use of a confining glass plate may create wall effects and affect the keyhole behavior. More recently, advanced x-ray imaging techniques provided unprecedented spatial and temporal resolutions for the imaging of keyhole dynamics [24-26,48]. The use of x-ray imaging allowed the *in situ* observation and characterization of the keyhole formation to reveal detailed features of the keyhole shape and its fluctuations [26]. X-ray imaging has also been combined with high-speed imaging to study the effects of shielding gases [106], processing parameters [107], melt pool dynamics [108], and laser absorption [109] on keyhole dynamics and porosity formation. Details such as the keyhole dynamics, the resulting gas pore formation/suppression [110,111], and other defects will be further discussed in Section 4.

Complex physical phenomena affect keyhole formation and dynamics. The laser-matter interaction, multi-phase thermo-fluid flow, and phase change thermodynamics are challenging to measure experimentally. Therefore, the analysis and understanding of keyhole formation and dynamics leading to defect generation mechanisms require the use of multi-physics numerical modeling of the keyhole phenomena to complement experimental observations [47].

Numerical modeling efforts of the keyhole phenomena were first limited to simplified systems and isolated studies, e.g., multiple absorptions and reflections of the laser by the keyhole [112,113], and the front keyhole wall evolution [114,115]. Recent modeling efforts have primarily focused on the development of multi-physics models to simulate laser-induced keyholes with higher fidelity. The keyhole dynamics are dependent on the multiple reflections of the laser beam, which can be modeled using a ray-tracing model [112,113,116-119]. At this level of detail, the predicted keyhole morphology and laser absorption distribution agrees well with experimental observations. Recently, the ray-tracing model was coupled with thermo-fluid models and surface tracking [63,120-126]. Surface tracking is usually achieved using either Volume-of-Fluid (VOF) [120,123,126,127] or Level-Set (LS) [112,121,122,128] methods. By combining the multi-phase and multi-physics numerical modeling, it has been shown that laser reflections are dependent on the keyhole morphology which in turn is coupled with the non-uniform laser absorption distribution leading to the fluctuation of the laser-induced keyholes. Clearly, numerical modeling will be increasingly important for the prediction of defects during the keyhole phenomenon, further discussed in Section 7.

1.4. Classification of defects

1.4.1. General microstructural defects and anomalies

In general, defects can be created or transferred to the finished part in three specific ways, mainly through: (1) transfer from the feedstock powder *aka* powder related defects (Section 3), (2) the laser-powder-metal interaction during melting also known as processing-related defects (Section 4), and (3) post-processing-related defects due to heat treatments (Section 5) [81,84,129-134] (Fig. 6). Moreover, equipment, build preparation and part design can also affect defect formation in the AM parts. Commonly observed types of defects in metal additive manufacturing include various types of porosity such as lack-of-fusion, keyhole, balling, and trapped gas. Other defect types include surface roughness, residual stress, and distortion (warping) due to the rapid solidification of metal AM processes. In order to limit defect generation within metal AM, the mechanisms of defect formation and transfer must be considered and controlled through appropriate selection of material, process, and post-processing settings. The following sections provide more information on the sources of defects, in particular the specific characteristics of multiple different starting materials that lead to defect formation.

Powder-related defects. Typically, powder characteristics such as morphology, flowability, mean size and particle size distribution, surface contamination affect the quality and performance of the final product. In the fusion-based AM processes, powder characteristics are directly affected by the powder production technique such as water and gas atomization, plasma atomization, plasma rotating electrode process, etc. Higher apparent density, higher packing density, better powder flowability, and smooth surface finish are attained using spherical powders, however, the cost of powder production is high for spherical powder production. When too high fraction of fine (<5 μm) powders are used in PBF, powder agglomeration may occur, thus, negatively affecting the powder packing density, powder flowability, and final part density. The typical particle size range used in L-PBF is 15–45 μm while coarse powder particle of 45–110 μm is used in E-PBF. Layer thickness during printing depends on the powder's mean size and distribution. Feedstock powder may contain moisture, organic contamination on the surface, and/or trapped gasses, therefore, it has a detrimental effect on the final part quality. Powder porosity can carry over into the printed part but that has little to do with the actual beam-powder interaction; it probably happens when particles are drawn into (sucking in) the melt pool along the sides of the latter. Further information about the induced defects from powder particles is presented in Section 3.

Processing-related defects. Numerous studies [129,130,133-137] have investigated the effects of processing parameters such as power, scan speed, layer thickness, hatch spacing, and scan strategy on the formation of different defects mainly pores and voids. In more detail, the lack-of-fusion porosity boundary can be determined by whether there is sufficient overlap between melt pools to ensure that all points are melted at least once [98]. In contrast, the keyhole porosity boundary corresponds to instabilities in deep keyholes leading to pinch-off of pores [25]. A third boundary (known as the "beading-up" boundary) is determined by a combination of fluid flow patterns and capillary instability of the melt pool and is a limiting factor for increasing production rates while maintaining precision (e.g., increasing velocity and power simultaneously) in L-PBF AM systems [138,139]. Overall LOF, keyhole, and bead-up porosity boundaries define an effective process window for the production of parts with nominally full density. Full density can be quantified as samples possessing > 99.9% volumetric density, although it should be noted that large defects are still possible within the processing window (Fig. 7).

Other defects such as cracking, distortion, and super-elevated edges are affected by thermal history during printing and printing patterns which can be controlled by selecting a proper scan strategy and part

Classification and Sources of Defects

Powder-related defects	• Powder characteristics • Surface contamination and oxidation • Trapped Gas
Processing-related defects	• Powder spreading dynamics and anomalies • Balling or bead-up • Lack of Fusion Porosity • Keyhole Porosity • Microstructural Inhomogeneities and Impurities • Formation of Columnar Grains • Loss of Alloying Elements • Spattering • Turnarounds and End of Track Porosity • Residual Stresses, Cracking and Delamination • Geometric Defects and Dimensional Accuracy • Surface Finish and Roughness
Post-processing-related defects	• Thermally induced porosity

Fig. 6. Defect/anomaly formation mechanisms in powder bed fusion additive manufacturing fall into three broad categories: (1) powder-related defects, (2) processing-related defects, and (3) post-processing-related defects.

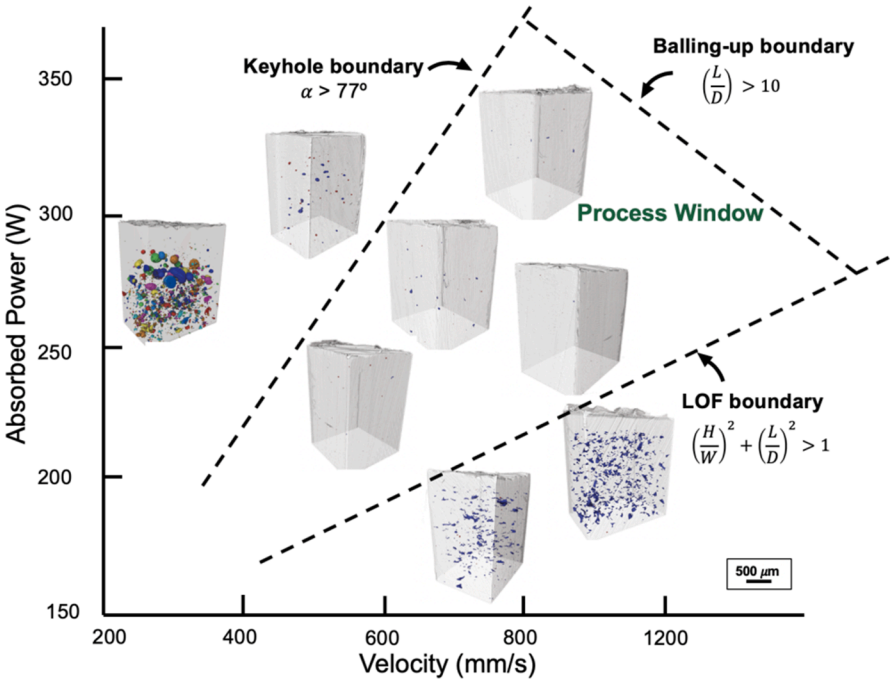

Fig. 7. Defect morphologies in L-PBF metal AM follow predictable trends within the power-velocity (P-V) processing parameter space. Common defects can be avoided by proper selection of process variables. Synchrotron x-ray micro-computed tomography (μSXCT) reconstructions show that by altering process settings, LOF and keyhole defect morphologies may be avoided. The LOF boundary is determined by whether there is sufficient overlap between melt pools to ensure that all points are melted at least once (Section 4.3). The keyhole porosity boundary corresponds to instabilities in deep keyholes leading to pinch-off of pores (Section 4.4). The beading-up boundary is determined by a combination of fluid flow patterns and capillary instability of the melt pool (Section 4.2). Note: standard (recommended) nominal process settings may also result in keyhole or LOF porosities; therefore, proper selection of processing parameters is vital to avoid laser-powder interaction defects in as-built metal AM parts. Reprinted with permission from Ref. [19].

design [35,140-142]. Mukherjee *et al.* [143] showed that the thermal strain could be controlled by low heat input (low laser power, high scan speed, and small layer thickness). Further, it was concluded that alloys with lower heat capacity and higher thermal diffusivity are susceptible to higher peak temperature, larger pool volume, and higher thermal strain. Among three common alloys of nickel superalloy 718, Ti-6Al-4V, and stainless steel 316, the thermal strain is relatively higher for alloy 718 and Ti-6Al-4V than stainless steel 316 [143].

Another source of defect known as spatters is caused by ejected particles from the powder bed or liquid metal from the melt pool (Section 4.6) [26,48,144-148]. There are two main possible reasons for the solid/liquid metal ejections in PBF systems including (1) a convective transport of liquid or vaporized metal out of the melt pool, also known as droplet spatters, and (2) solid powder particles blown away as a result of the heated cover gas that moves the powder out of the way [61], also known as powder or sideway spatters. Also, electrostatic repulsion of powder particles may occur in E-PBF systems causing solid powder particle ejection.

When the spatter powder forms and falls onto the bed of powder, two different types of issues appear. Typically, the spattered powder is coarse, therefore, if the laser/electron beam passes over the spattered powder, it may prevent complete melting leading to pore formation.

Further, if the spattered particle is displaced by the recoating blade, an uneven and irregular powder bed is produced which causes a discontinuity in the dispensed materials (Section 4.1). Generally, laser power profile and pulse shaping can reduce spatter particles in L-PBF. In E-PBF, the interactions between electrons and powder particles transmit both energy and electrical charge. In this situation, powder ejection is probable when repulsive electrostatic forces overwhelm the forces holding particles to the powder bed [149]. Finally, plasma formation due to ionization of the metallic vapor and surrounding gas has been reported in [150-153]. Plume formation can occur due to vapor formation and increased temperature of the surrounding gas, which shows chemical composition, temperature, and pressure difference from the surrounding atmosphere (Section 4.6). This phenomenon may alter the optical properties of the laser/electron beam path, affecting beam profile and energy density at the focal point on the powder bed surface. In other words, the formation of plasma or metal vapor plume can vary the power absorptivity along with melt pool depth and fluctuating melt pool shape during printing. As discussed elsewhere, Trapp *et al.* [50] show a transition from about 0.3 in conduction to about 0.8 in keyhole mode. The plume is far stronger in the latter, see [61], and yet it does not get in the way of the laser light. One may speculate that the plume is the reason that the absorptivity does not reach 100%.

Post-processing Related Defects. Because of the propensity for defects in AM parts, a hot-isostatic press (HIP) treatment is frequently applied to reduce the number and severity of internal defects. HIPing involves the application of high pressure and temperature in an inert environment, which acts to shrink the size of internal defects through the reduction of surface energy and unbalanced internal and external pressure [154]. The process needs to occur at a sufficiently high temperature and pressure to allow the material to deform and collapse the pores, and if the gas is soluble, allow it to diffuse out of the pores. Many studies have shown the effectiveness of HIPing to reduce porosity in AM components [155] and the subsequent improvement on elongation and fatigue life [7,156,157]. However, the extended time at a high temperature can cause considerable microstructural coarsening, resulting in reduced strength and unfavorable microstructures.

The problem arises when pores containing inert gas such as argon are HIPed and then subsequently exposed to a high temperature. Argon pores have been observed to regrow following high-temperature heat treatments after HIPing in a process known as thermally-induced porosity (TIP) and be significant enough to often cause degradation in mechanical properties [7,156,157]. This process is the result of heating the now pressurized pore from the HIP process to temperatures that allow the surrounding material to deform via creep. The question is not whether or not this will occur with AM metals, but whether or not AM defects contain sufficient inert gas to regrow to appreciable sizes at temperatures relevant to heat treatments. To date, this has not been investigated for processing flaws in AM such as keyholes or lack of fusion, but in the case of L-PBF, both could feasibly contain inert gas from the atmosphere, as shielding gas was detected in keyhole pores laser welding, and lack of fusion porosity was open to the atmosphere before being closed off by subsequent layers. Post-processing related defects are discussed in detail in Section 5.

In terms of defect generation in AM parts, there might be other resources such as equipment, powder handling and dispensing, and build preparation which could also contribute to defect generation. In the following, each of them is elaborated.

Equipment. Defects may form due to improper performance of the used AM machines due to setting and calibration problems. Additionally, different PBF machines have their own specifications in terms of print resolution, laser power, scan speed, powder layer thickness, powder dispensing method, laser spot size, etc. Amongst these differences, there are four main concerns related to the possible sources for defect formation associated with the equipment such as (1) defects caused by the electron/laser beam scanning or deflection system, (2) defects caused by the build chamber that requires better environmental control, (3) defects caused by the powder handling and dispensing system, (4) defects caused by baseplate [131].

Typically, porosity (keyhole and LOF) and geometric defects (distortion and low dimensional accuracy) can be related to the electron/laser beam scanning or deflection system [141]. Moylan *et al.* [158] reported the role of the optical system alignment quality, mirror quality, and the beam profile in the PBF AM process. Foster *el at.* [159] showed that an incorrectly calibrated system can lead to geometrical inaccuracy. Additionally, the shape of the beam (laser or electron source) can be affected by exposure location, i.e., there is an elliptical (defocusing) distortion close to the edges of the baseplate because of high scanner deflection angle. Based on the location of the build part, this issue may result in LOF defects or poor geometric accuracies although this is considered to be a second order effect.

It is probable that any contamination from the gaseous byproducts and reflected energy from the bed of powder impacts the local beam spatial energy distribution, causing poor geometrical accuracy. Sames *et al.* [32] suggested that the chamber environment can cause defective part production. Typically, an inert gas is directed over the build surface during the L-PBF process and the gas flow rate and the consequent deposition path for particles and spatter back onto the powder bed influences defect formation (porosity, spattered powder, poor dimensional accuracy, surface roughness) during the printing step [160,161]. An example of defect generation due to redeposition of spattered particles close to the gas outlet is shown in Fig. 8 [162].

Anwar and Pham investigated spattered powder during the L-PBF process [146]. They showed that increasing the gas flow velocity resulted in increasing the powder bed contamination due to powder transport by the inert gas flow and a higher chance for spatter particle formation and ejection from the melt pool. Another important concern related to the print environment is the oxygen content which is lower in E-PBF compared to L-PBF because of the vacuum used for the former. High oxygen content in the chamber promotes balling or bead-up initiation [163].

Powder handling and dispensing. These are other sources for defect formation in PBF processes. Kleszczynski *et al.* [164], Foster *et al.* [159] and Scime *et al.* [165] showed that the recoating system may affect powder bed density and smoothness of the spread layer, causing an inhomogeneous powder bed formation. In addition, if there is any spattered powder on the solidified area, the blade may hit the surface and deform the printed part. In other words, defects from spattered powder can cause an anomaly in the new spread layer of powder due to the linear motion of the recoating system over the build area. Furthermore, the uneven layer of powder has a detrimental effect on powder packing density and the laser-powder interaction leading to inconsistent processing conditions and potentially porosity formation. It is possible to replace the blade with a brush or rubber re-coater to reduce wear and friction between the dispensing system and the bed of powder. It also prevents collisions with the part being printed when the dispensing system goes over the build area. However, brush or rubber re-coaters are more easily damaged and typically need to be replaced frequently [166].

During fusion AM processes, printing occurs on a baseplate, thus, thickness affects heat dissipation. Defects such as warping, deformation, layer delamination, and cracking are all affected by the baseplate (as well as print strategy and laser power or energy density) [167]. Zeng [168] showed that heat dissipation and thermal stresses caused by solidification are both influenced by baseplate thickness. During E-PBF, preheating of powder bed is part of the AM process, while L-PBF does not have this option. Preheating can lower thermal gradient, residual stress, and deformation and enhance final part density [169-173].

Build preparation. Some defects are caused during the build design step for additive manufacturing including (1) part/build orientation with respect to the build plate and the printing direction and (2) support structure design and sacrificial components.

Build direction affects microstructure (texture and grain orientation) as well as potential porosity formation in the AM part [174].

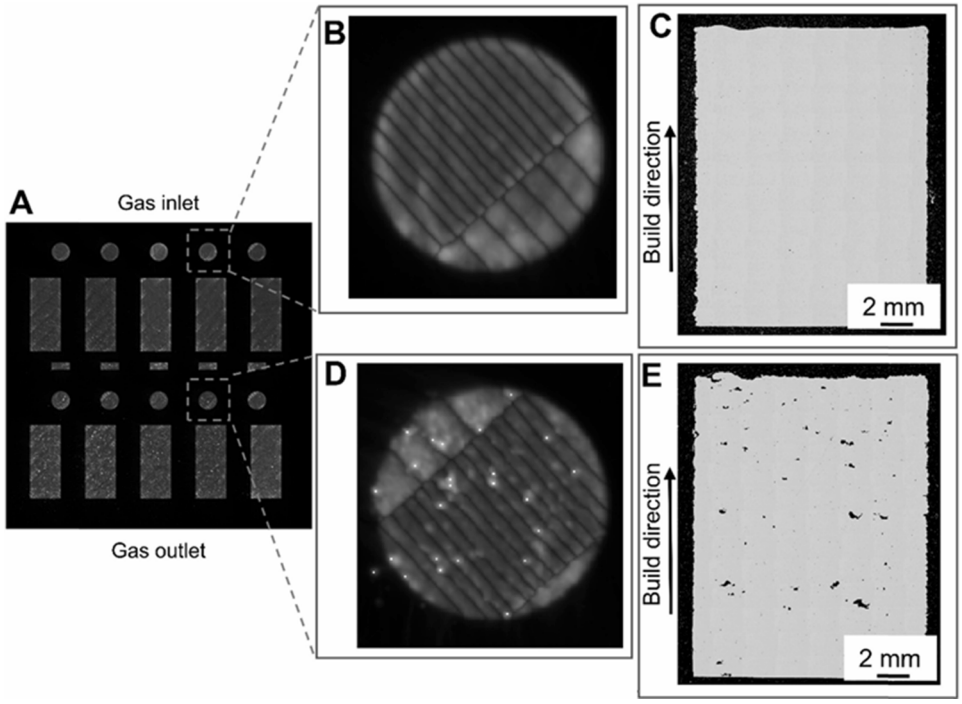

Fig. 8. (A) Build layout of specimens during LPBF in which parts close to the gas inlet had minimum internal defects while the LPBF printed parts close to the gas outlet showed significant spatted particles on the top surface and optical micrographs indicated lack of fusion pores. Reprinted with permission from Ref. [162].

Additionally, dimensional accuracy and surface finish are two other criteria affected by build direction [175]. Anisotropic behaviors such as mechanical properties and corrosion rates can be strongly affected by build direction [176-180]. Jamshidinia and Kovacevic [181] showed that the spacing between parts on the build plate affects heat accumulation leading to different surface quality. When parts are close to each other, heat distribution and dissipation are governed by the spacing between walls such that partial melting of the powder particles increases and they adhere together on the solidified surfaces, leading to increased surface roughness.

Selection and design of support structures are crucial steps of the build design, affecting final part quality and performance. After printing, the support structure needs to be removed to finish the AM part. For complex parts, support structures are required due to (1) avoiding the collapse of AM parts with overhang structures, (2) controlling thermal gradient and heat sink from the AM part to the build plate, and (3) reducing warping and distortion caused by residual stresses [159,168,182-185]. Fig. 9 illustrates examples of support structures and defects.

Detailed explanations for the processing-related defects are presented in Section 4 and possible mitigation techniques are proposed in Section 6.

1.4.2. Other defects

In this review, we focus on the general microstructural defects in powder bed fusion AM that are common on the macroscale and microscale. Usually, these defects tend to degrade the properties of the builds. When stepping down the length scale, there is a smaller body of research on defects at the atomic/nano-scale. Here, we summarize the key results reported in the recent literature papers in PBFed metallic parts to facilitate further exploration and discovery on this topic.

At nanoscale, defects can be classified by dimensions: (a) zero-dimensional defects (vacancies); (b) one-dimensional defects (dislocations); (c) two-dimensional defects (grain boundaries); and (d) three-dimensional defects (voids).

Vacancies are empty lattice sites, which tend to accumulate during the cyclic heating/cooling process in additive manufacturing. Mechanical, thermoelectric, and electrochemical properties in additive manufactured alloys can all be subject to the influence of vacancies. In the Fe-Al iron aluminide alloy system [187], the vacancy concentration was found to have a positive correlation with fracture strength and hardness, while negatively affecting elongation and ductility. Mirzade and Islamov [188] used phase-field modeling to suggest that vacancy migration also influences the stress field in the grains and vice versa. On the other hand, vacancies play an important role in thermoelectric materials (e.g., semiconductors) made by PBF. For PBF processing of the Bi_2Te_3 alloy system [189], thermally induced high concentration tellurium vacancies act as electron donors and the predominant active point defects, which can shift the original p-type material to n-type. Similar behavior was observed in Ti-6Al-4V [190] where oxygen vacancies form a n-type semiconductor in the oxide layer, increasing its affinity for aggressive ions such as chloride ions and thus weakening the corrosion resistance.

High dislocation densities are a normal feature in as-built PBF parts [191], primarily due to cyclic thermal expansion/shrinkage in a constrained medium [192]. Although identified as a crystallographic defect, dislocations are beneficial to AM parts in the following aspects:

(1) Dislocations help maintain the part integrity in two forms: (a) During dendritic growth, the cell boundaries have higher dislocation density to accommodate the mismatch between each dendrite branch [193]. (b) Geometrically necessary dislocations (GND) form to accommodate the deformation gradients that come from non-homogeneous deformation among different phases/grains/particles and the small, but non-negligible plastic strain that accompanies thermal shrinkage [194-198].
(2) Dislocations contribute greatly to the mechanical properties of parts. Dislocation can actively interact with other defects in the material, such as particles, twin/grain boundaries, and even segregated elements [196,199,200]. Such interactions create a progressive work-hardening mechanism. Dislocation networks in stainless steels, especially 316 L stainless steel, were recently identified and deemed as a critical contributor to the excellent strength and ductility of as-built 316 L stainless steel

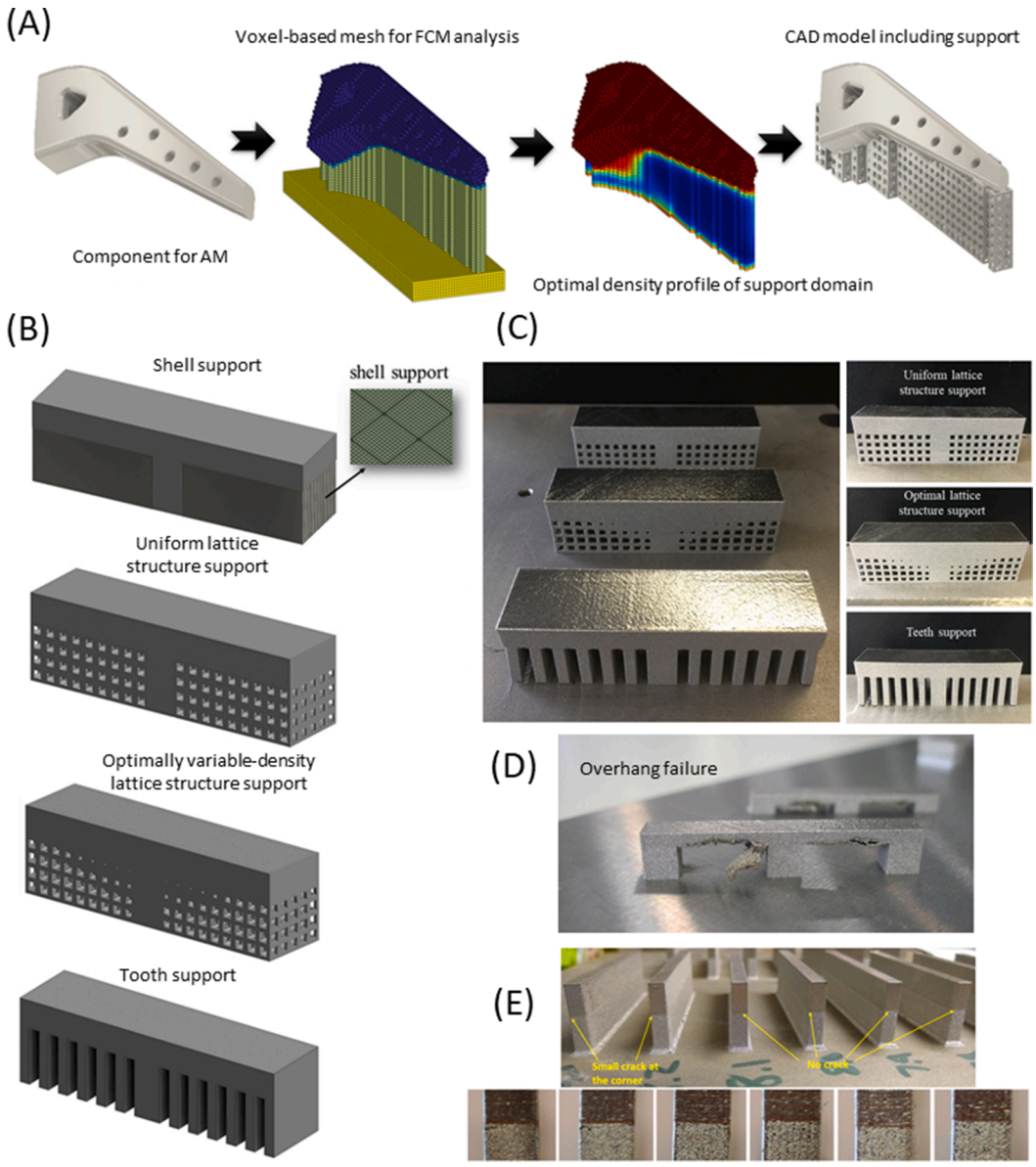

Fig. 9. (A) Reconstruction process for a practical component showing how the support structure is added to the AM part, (B) various support structure designs for double cantilever beam, (C) example of AM parts with different support structure indicating no crack was formed at the interface between the support structure and the build plate. Small cracks were observed in the teeth support design but it had no warping effect on the AM part. Reprinted with permission from Ref. [184]. (D) Overhang failure in PBF AM part. Reprinted with permission from Ref. [168]. (E) Examples indicating crack formation was dependent on the sample's height, in which all higher specimens from 8.2 mm and above cracked at the corners of their interfaces and shorter specimens from 8.1 mm did not crack at their ends. Reprinted with permission from Ref. [186].

[196,201,202]. The dislocation network can not only strengthen the material by hindering (not fully stopping) the dislocation movement but also improve the ductility by guaranteeing a continuous plastic flow by allowing dislocations from transmitting and therein breaking the strength-ductility trade-off.

Grain boundaries appear to be densely populated and highly anisotropic in as-built PBF parts, thanks to grain refinement and epitaxial grain growth. As a result, grain boundaries play an important role in determining the mechanical properties [203-206], electrochemical properties [207,208], and even magnetic properties [209,210] in the parts. Weak grain boundaries containing low melting phases at partially melted zone were found to initiate liquation cracking, as elucidated in Section 4.7. The cracking behavior under tensile loading is also subject to the relative direction of the loads and the direction of columnar grain boundaries. Besides, the fatigue crack path deflection is strongly influenced by the grain boundary structure. Depending on the orientation angle between neighboring grains, high-angle grain boundaries can block transgranular cracks if no available slip systems are oriented for easy slip transfer [211,212]. The corrosion behavior of PBF parts, which is surely dominated by porosity, is reviewed in Section 8.2, while the opinions on the effect of grain boundaries on corrosion resistance are quite divergent among different researchers. On one hand, grain boundaries can be the preferred sites for corrosion due to the irregular arrangement of atoms and the non-uniform distribution of elements breaks the passive film [208]. On the other hand, improved corrosion resistance has been found to closely relate to grain refinement, because of the formation of a passive film in the presence of a high density of grain boundaries [207]. Such divergence in observations may not be so contradictory. Recent research [213] suggests that the corrosion resistance–grain boundary density relationship depends on the actual corrosion rate: when the corrosion rate $< 10\ \mu A/cm^2$, high grain

boundary density will lead to high corrosion resistance; when the corrosion rate $\geq$ 10 μA/cm^2, the grain boundary density will have a negative influence on corrosion resistance. Therefore, further studies should consider such an effect on a case-by-case basis. Even within the same material system, the process differs on the degree of chemical segregation, stress concentration, texture development, etc. In the end, grain boundaries also influence the physical properties of PBF materials, such as magnetic properties. *In situ* or post infiltration with PBF manufactured magnets is practiced to enhance the coercivity by modifying the grain boundaries [209,210]. For example [209], the enrichment of Tb (introduced by infiltration) at the surface of $Nd_2Fe_{14}B$ hindered the nucleation of reversed domains, thus leading to increased coercivity in PBF NdFeB magnets.

A void can be viewed as a nanoscale cluster of lattice vacancies. The equilibrium vacancy concentration increases with temperature [214] and can be partially preserved by rapid cooling. A small density of small voids (<1 vol%, < 1 μm) does not usually pose a risk for material failure [215] under tensile or cyclic loading. However, it should be noted that a pair/group of voids can work together to initiate fracture owing to the increased stress and temperature by local significant plastic slip between the voids [216]. In addition, voids may influence the material behavior at elevated temperatures (but less than the recrystallization temperature) during their interaction with other nanoscale features (vacancies, dislocations, impurity elements, etc.) [214]. Large voids, however, are well known to act as fatigue crack initiation sites, as discussed elsewhere.

2. Defect characterization methods

Defect measurement is typically pursued using bulk methods such as Archimedean density, ultrasonic inspection, or cross-sectioning to compare pore volume to total bulk volume [133]. While these methods are generally fast and inexpensive, they only offer a first-level approximation on the defect structures seen in metal AM and are not able to generate information such as the three-dimensional (3D) spatial distribution and morphology of defects [81,84,134]. For the desired outcome of fractional density >99%, the frequency with which a cross-section intersects a pore is low enough that large areas must be characterized to obtain reasonable statistics. Alternatively, more time-consuming techniques such as laboratory scale and synchrotron-based x-ray computed tomography (XCT) have proven very useful in analyzing defect structures in welding [135,136], laser welding [137], and recently in metal AM [84,132,134,217,218]. XCT provides 3D information on internal defects by the reconstruction of a series of radiographs taken as the sample rotates over 180° or 360° [132,219-221]. Each scan typically requires several hours of data acquisition. Comparatively, synchrotron-based XCT methods enable fast data recording and collection times of a few minutes, improved spatial contrast and resolution to μXCT methods, and sub-micron voxel resolution. However, important challenges currently exist within the research community to make synchrotron-based XCT commonly accessible and to meet the high demands for beam time [222].

Other recently developed x-ray imaging techniques allow the *in situ* observation of the laser-material interaction at high speeds (>100 kHz) and visualization of defect formation mechanisms in real-time using the so called pioneering "dynamic x-ray radiography" techniques [24-26,48]. Cutting-edge *in situ* x-ray technologies have been used generate important insights into defect formation for powder and keyholing porosity [24,26,81] and have the potential for greatly enhanced understanding of melt pool dynamics, powder ejection, rapid solidification, and phase transformations within metal powder bed AM builds with unprecedented spatial and temporal resolutions [26]. In addition to imaging, the x-ray diffraction technique probes the atomistic information of the AM materials, such as residual stress, crystal structures of the precipitates or other secondary phases, and dislocation density, while small-angle x-ray scattering (SAXS) techniques probe the morphological information of sub-micron precipitates. A more detailed description of the use of x-ray imaging and scattering applied to metal additive manufacturing is provided in the following section. In particular, in-process monitoring image data can assist researchers to develop computer vision algorithms to automatically detect and classify defects using machine learning [24,26,48,131,223-230]. This area of research and development on PBF AM machines will also be presented briefly in this section and a few examples will be detailed in other sections.

2.1. Ex-situ monitoring

2.1.1. Optical microscopy

Optical microscopy is a widely available characterization technique that is used to observe the powder feedstock, microstructure, surface profiles, and defects in AM samples. Low-resolution optical microscopy is commonly used to obtain the particle size distributions of the powder feedstock before printing. For characterizing AM parts, the sample surfaces are typically polished using a series of fine grit sandpapers and other grinding solutions such as diamond slurry. To visualize the microstructure, the samples are normally etched using an appropriate etchant to show the microstructural details. Typically, a bench-top compound microscope in conjunction with a digital camera is used to record the images.

Optical microscopy has been used to visualize the melt-pool shapes and sizes (for example [231,232]), defect morphology (mainly voids and cracks [233-235]), and grain structure of the printed parts (for example [232]). Fig. 10 shows an example of optical microscopy characterization of FeCrCoMnNi high-entropy alloy samples built using L-DED with different laser powers. Note that the distinction between "Pore" and "Micro-void" are arbitrary in the sense that in essentially all reports that include statistical distributions show a continuous variation in size with no evidence of bi-modality required to sustain the distinction. The pores, micro-voids, and cracks can be readily revealed by optical imaging. The main advantage of optical microscopy is easy to access; it also suffers from less distortion than electron microscopy because of, e.g., variable accumulation of charge. Both microscopes are limited to the surface information for one location in the sample. Although reasonably high spatial resolution (~μm) at a given location, acquisition of 3D information requires lengthy serial sectioning [236]. To overcome the single surface limitation, some researchers have also used confocal optical microscopy to characterize the surface defects [237]. Optical microscopy is also limited to post-mortem analysis and is a destructive technique. Optical microscopy provides quantitative assessments of defects and grain structure provided that the micron resolution limit is appropriate and more advanced techniques such as XCT must be used to obtain 3D defect information.

2.1.2. Electron microscopy

Scanning electron microscopy (SEM) and TEM (including scanning TEM or STEM) are among the most widely adopted techniques for characterizing the microstructures of AM materials. Compared with optical techniques, SEM and TEM are available to essentially all researchers. Many other widely adopted techniques cannot rival the spatial resolution of electron microscopies, particularly TEM that can achieve atomic resolution. Beyond structure defects, AM materials exhibit drastically different microstructures than the same materials processed using casting or forging. Some of those unique structure attributes are favorable which help improve the properties of AM materials, while others are detrimental. Wang *et al.* comprehensively characterized the microstructures of L-PBF 316L stainless steel samples and elucidated how the unique features of AM materials affect their mechanical properties [196]. The capabilities of electron microscopy for multiscale multimodal structure characterization are convincingly demonstrated in Wang's work, as well as many other cases present in this contribution. Electron Backscatter Diffraction (EBSD) images commonly collected in a SEM maps crystallographic orientation from

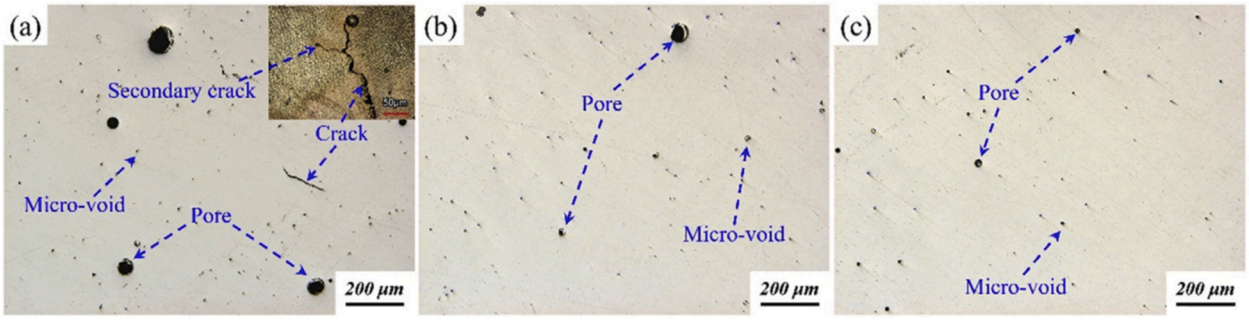

Fig. 10. Optical micrographs of cross-sections perpendicular to the build direction of FeCrCoMnNi high-entropy alloy samples built using L-DED process under different laser power, (a) 600 W, (b) 800 W, (c) 1000 W. The scan speed of the three samples is all 800 mm/min. Reprinted with permission from Ref. [238].

which grain morphology and orientation can be derived. The cellular structure and complex dislocation network in AM materials are well visualized by TEM bright-field and dark-field imaging. The chemical composition of different structural features can be measured using energy or wavelength dispersive x-ray spectroscopies (EDS or WDS) provided by a SEM or TEM. In addition, the phase of the precipitates can be identified using selected area diffraction (SAD) [239], and the elemental species and bonding state of a feature can be revealed by electron energy loss spectroscopy [240]. Both are commons tools afforded by a TEM.

Because of the vacuum environment, limited chamber space, and special sample requirement, electron microscopy is used more frequently for *ex-situ* microstructure characterization than *in situ*. It worth noting here the dynamic transmission electron microscopy (DTEM) technique is capable of studying laser melting and rapid solidification behavior of metals under conditions relevant to AM. The temporal resolution of DTEM is comparable to what the high-speed synchrotron x-ray imaging [24,26,48] affords (i.e., MHz frame rate, ns exposure time), yet its spatial resolution is far higher, approaching standard TEM [241]. Fig. 11 shows the DTEM study of the laser melting and rapid solidification of hypo-eutectic Al-11at.%Cu alloy. [242] DTEM allows the quantitative measurement of solidification interface velocity with nanoscale spatiotemporal resolution. Coupled with the following *ex-situ* TEM characterization of different microstructure zones, particularly secondary phases and their distribution, the unique non-equilibrium solute partitioning behavior could be understood.

An emerging electron microscopy technique that is worth noting here is the TriBeam tomography, i.e. a dual-beam SEM system equipped with an additional femtosecond laser for precisely and rapidly removing material with minimal damage [243]. The TriBeam system was developed by FEI and Prof. Tresa Pollock's team at the University of California - Santa Barbara, and have been used by the team for collecting 3D crystallographic, chemical, and structural information from AM samples [244,245]. Polonsky *et al.* found that sharp discontinuities in the grain morphology extended several build layers beyond the layer where the lack-of-fusion defect originated. As shown in Fig. 12, equiaxed grains present right above the lack-of-fusion porosity, and the columnar grain growth resumed within the next two build layers [244]. The 3D EBSD characterization by the TriBeam system is self-evidently destructive, so it cannot be used for *in situ* experiments as, for example, with the HEDM technique.

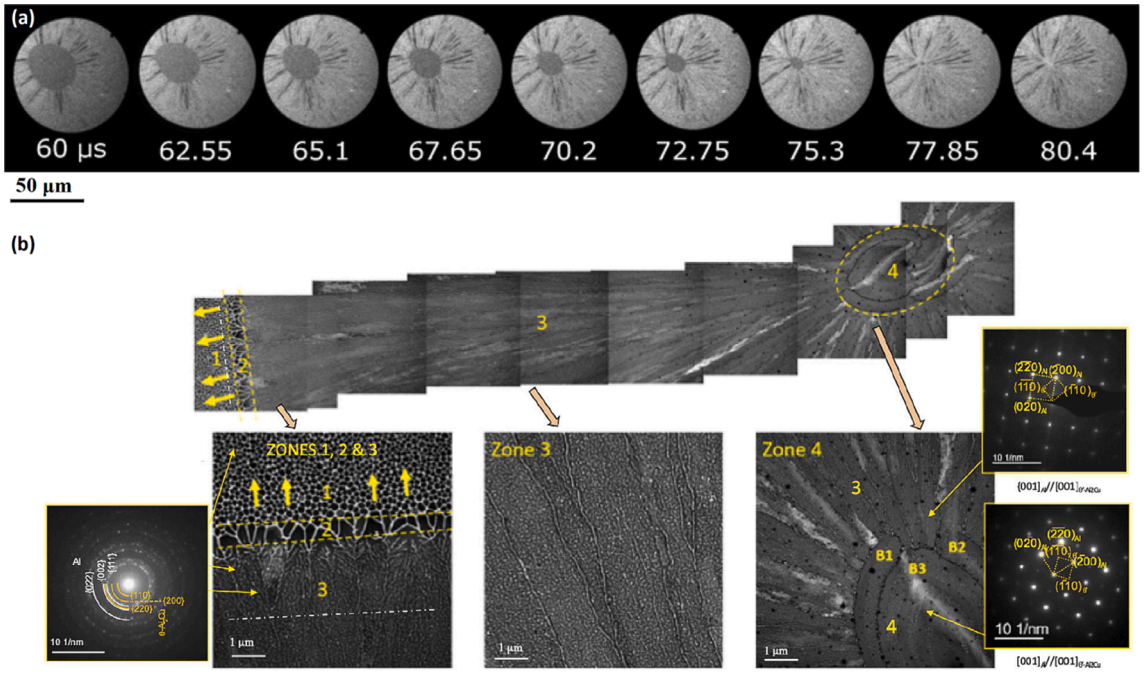

Fig. 11. (a) *In situ* DTEM movie mode bright-field image series showing the solidification of Al-11at.%Cu alloy. Numbers in the images are the time delays (in μs) between the peak of the Gaussian laser pulse that melted the film and the 50-ns electron pulse used to form the image. (b) *Ex-situ* TEM characterization of the solidified sample. The top row of HAADF STEM images showing the morphology of the solidification microstructure in the distinct zones of the heat-affected zone (label 1), the transition region/zone (label 2), the columnar growth zone (label 3), and the banded morphology zone (label 4). Enlarged details of the microstructures in these zones, as well as the SAD patterns of main and secondary phases, are shown below. Reprinted with permission from Ref. [242].

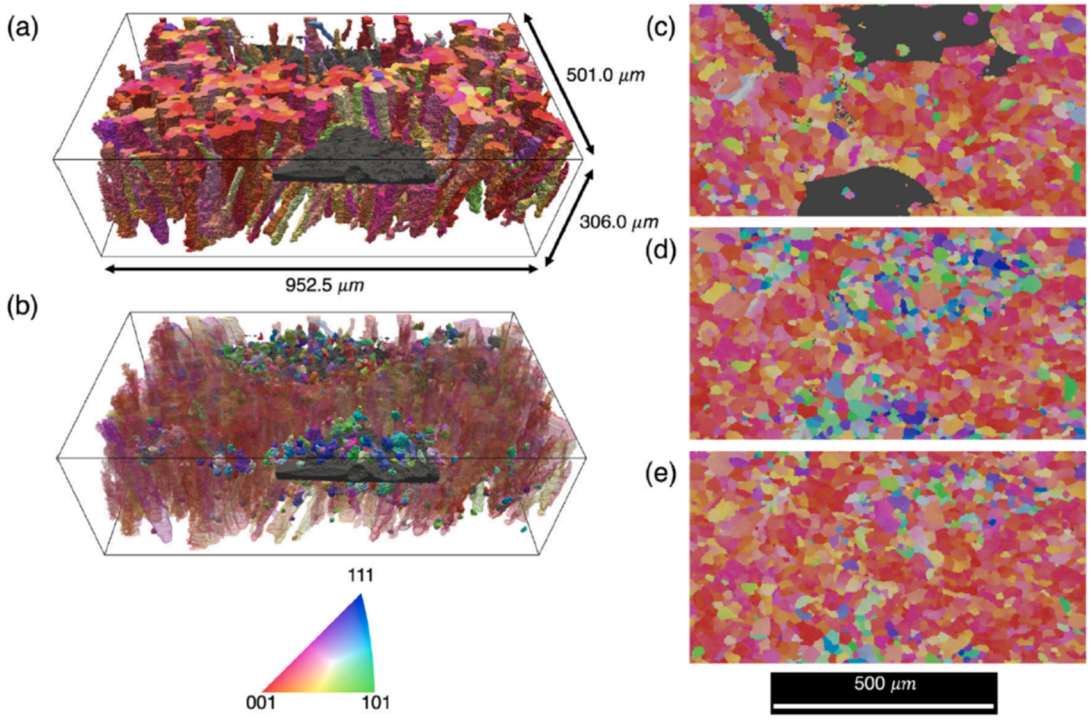

Fig. 12. 3D EBSD data of an alloy 718 sample fabricated using electron beam melting additive manufacturing technique. (a) Columnar grains surround the lack-of-fusion defects. (b) Equiaxed grains with non–[0 0 1] orientations fill the area immediately above lack-of-fusion defects. (c-e) 2D slices from the full 3D volume perpendicular to the build direction (c) within, (d) 40 μm above, and (e) 80 μm above the defects. Reprinted with permission from Ref. [244].

2.1.3. Synchrotron x-ray imaging and scattering

Synchrotron x-ray imaging and scattering are among the most versatile and effective techniques for characterizing materials microstructures as well as their evolution in response to different external stimuli. Compared with electrons and neutrons, x-ray photons strike a good balance between the interaction volume and resolutions, which makes them practical for studying bulk materials under real conditions. A variety of synchrotron x-ray techniques are used for studying AM materials to understand their unique microstructures and defects, including, but not limited to, high-resolution diffraction [246] and pole figures [232] for measuring residual stress and texture, computed tomography [28] for characterizing porosity in three dimensions (3D), Laue microscopy [247] and high-energy diffraction microscopy [248] for grain morphology and strain.

Owing to the large thermal gradient, rapid cooling rate, and complex part geometry in laser or e-beam AM, substantial residual stress can develop during the build process, which may lead to part distortion, cracking, or even delamination. X-ray diffraction (XRD), particularly high-energy synchrotron XRD, is one of the most frequently used techniques for measuring residual stress in AM materials. In order to measure all six stress tensor components, the sample is typically mounted on a four-axis diffractometer to gain freedom of translational and rotational motions. As shown in Fig. 13, Phan *et al.* mapped out the residual stress in an alloy Alloy 625 bridge structure built by L-PBF [249]. The spatial resolution in this particular measurement is ~100 μm and the strain sensitivity is 10^{-4}. XRD and neutron diffraction have a similar resolution in the reciprocal space (i.e., lattice displacement), whereas the x-ray technique affords higher resolution in real space but has far less penetration power than neutrons.

Precipitates are an essential component of most engineering alloy systems processed using a laser or e-beam AM, given the extreme thermal conditions involved. Transmission electron microscopes (TEM), including imaging, diffraction, and spectroscopy techniques afforded by a TEM, are particularly suitable for characterizing the chemical composition and phase of the precipitates, as will be elaborated in the next section. If the volume fraction of the precipitates is sufficiently large, SAXS is an effective tool for acquiring statistical information on their size and morphology. As shown in Fig. 14(a-b), Zhang *et al.* collected *in situ* SAXS data during isothermal heating treatment of AM alloy 625, and quantitatively measured the growth of deleterious δ phase precipitates[250], which is confirmed by the *in situ* XRD data (Fig. 14c). These *in situ* synchrotron x-ray experiments revealed that elemental segregation unique to AM processes is the root cause for the unusual precipitation behavior in alloy 625 during the stress-relief heat treatment, i.e., heavy elements such as Nb and Mo segregate to the interdendritic regions during solidification, regardless of the high cooling rate.

Synchrotron-based high energy diffraction microscopy (HEDM) is an emerging technique for 3D characterizing the grain morphology, phase, orientation, and strain in polycrystalline materials. Since HEDM is non-destructive, it has become a powerful technique for *in situ* probing the response of each individual grains to various external stimuli. Sangid *et al.* performed the HEDM characterization of alloy 718 (a.k.a. Alloy 718) in the high cycle fatigue experiment (Fig. 15) [248]. The result from the first part of experiment (cycle 1–20) provided a base structure model to inform the crystal plasticity finite element (CPFE) simulation, while the second part of experiment (cycle 21–59 k) measured grain-average stress evolution and were used for validating the model. By integrating HEDM, x-ray computed tomography (XCT), and CPFE simulation, this work identified the fatigue crack initiation site (i.e. surface-connected pore) and evaluated three CPFE models with and without the probabilistic insertion of twins.

The HEDM technique is still progressing and evolving [252]. X-ray sources, detectors, and data processing algorithms are all advancing rapidly to allow detection and reconstruction of a larger number of grains in a much shorter time. Given its irreplaceable capability and ever-increasing practicality, HEDM will become a powerful tool for studying the unique microstructures and properties of AM materials.

XCT uses the projection x-ray images of the sample from multiple angles to reconstruct the 3D model and obtain the through-the-thickness

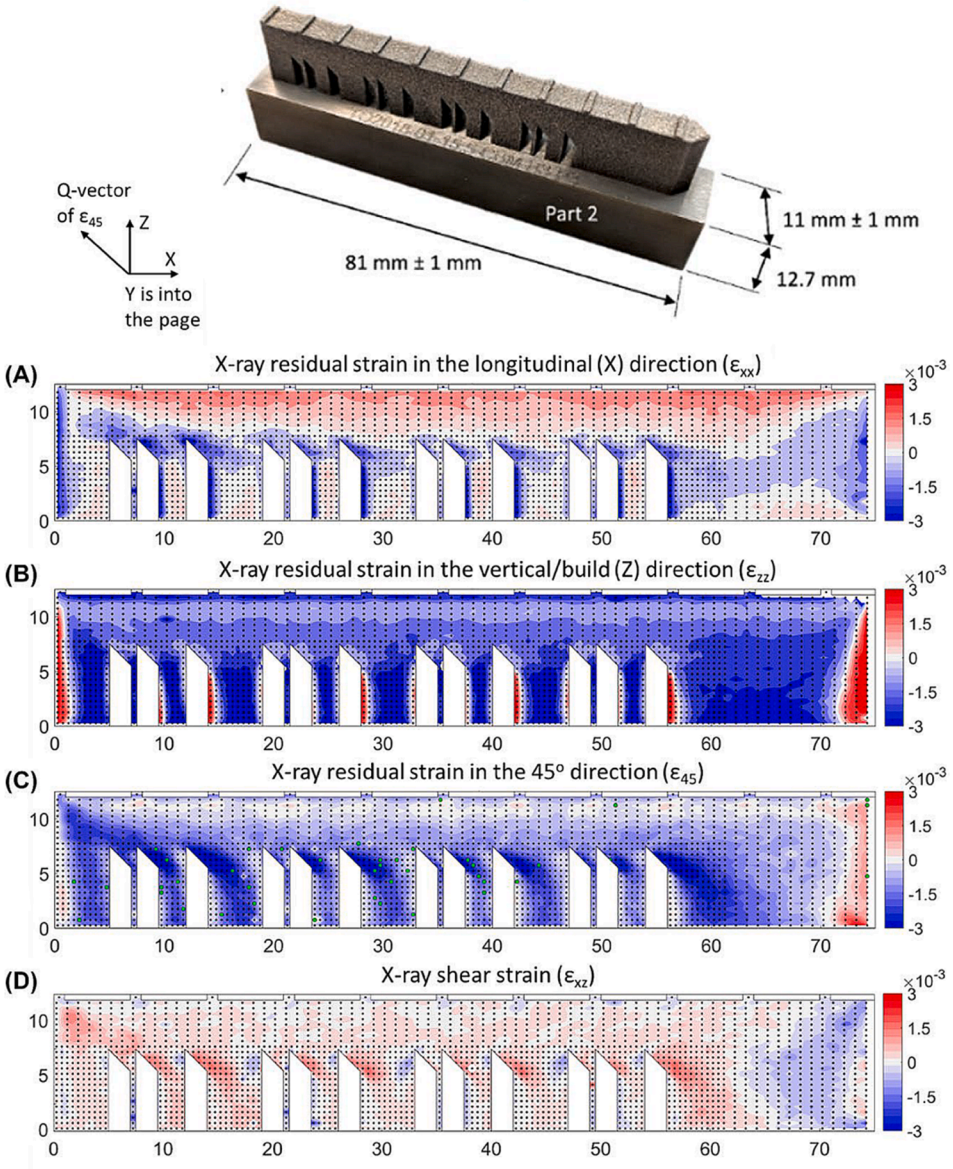

Fig. 13. Residual strain maps of the as-built AM alloy 625 bridge structure (sample photo is on top of the figure) measured using synchrotron XRD. Strain measurements were made in the middle cross section of the sample (Y = 2.5 mm) of the (A) longitudinal (X) strain, (B) the vertical/build (Z) strain, (C) the strain at 45°, and (D) calculated shear strain (ε_{xz}). Reprinted with permission from Ref. [249].

information [253]. Over time, three main methods of XCT have been used with increasing data collection rates. The three methods use the point, line, and plane source of x-ray radiation respectively [217]. The projection image of the sample is collected by translating the x-ray beam and the detector as needed for the point and line sources. Once the projection at a particular angle is collected, the sample or the source-detector pair is rotated by a small angle and the collection process is repeated. After the projections are recorded for all angles (180° or 360°), computational algorithms are used to reconstruct the 3D volume. A critical review of the use of XCT for studying AM parts is provided in [217,254].

XCT is mainly used to study two major flaws in AM parts: porosity and dimensional accuracy. XCT offers many advantages over traditional metrology and inspection techniques including serial sectioning and Archimedes measurements. XCT is a non-destructive measurement technique. It can be used to probe the sub-surface porosity and features that may be inaccessible through other techniques. It also provides information about the individual pore sizes and shapes in 3D, along with the bulk porosity values.

Two different types of XCT setups are currently used to study the AM parts and materials. One is the laboratory-based XCT setup where an x-ray tube is used to generate the x-rays [34,98,255-265]. The other is the synchrotron-based setup where synchrotron x-rays are used [231,266,267]. In both techniques, careful analysis of the competing experimental parameters must be performed to obtain good quality XCT data and reconstructions. The main data quality factors for the XCT setups are the resolution and the contrast of the images. Both of these must be sufficiently high resolution to detect the small pores and features that are typically present in the AM parts. Since the technique depends on the x-ray penetration through the object, an increase in the size of the object typically demands increasing exposure times and reduction in the resolution of the images. Higher density materials are also more difficult to measure because of limited x-ray penetration. Hence, the object sizes are also limited by the material density to achieve requisite contrast. In many cases, a small piece can be cut out of the part and scanned in lieu of the whole object. Although the scan quality can be improved in this manner the results may not be representative of the real object because of, e.g., location-dependent porosity.

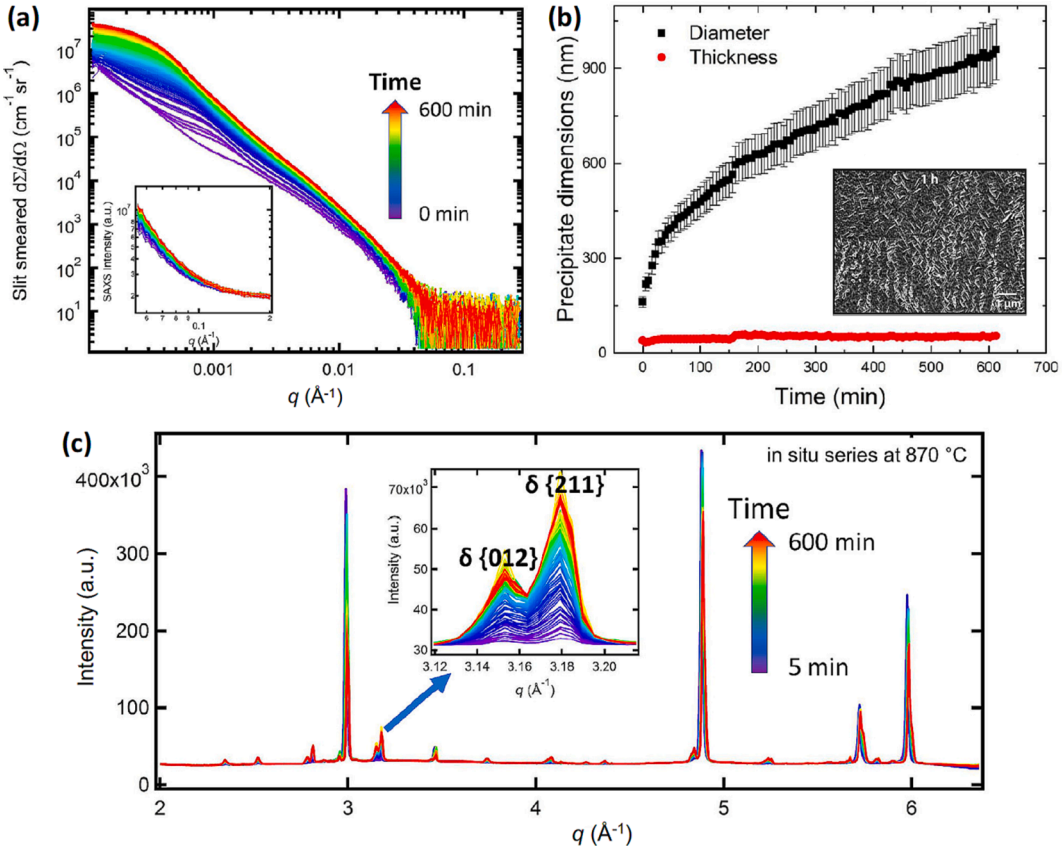

Fig. 14. *In situ* synchrotron x-ray study of the growth of deleterious δ phase precipitates in AM alloy 625 during stress-relief heat treatment. (a) A complete set of *in situ* SAXS data acquired from the alloy 625 sample during isothermal heat treatment at 870 ℃ for 613 min. The main plot shows the USAXS data, and the inset shows the SAXS data. (b) Time-dependent evolution of average diameter and thickness of the δ phase. The SEM image of the alloy 625 sample after 1 h is shown in the inset, which reveals the formation of δ phase precipitates. (c) *In situ* XRD results during the isothermal heat treatment show the growth of δ phase. Reprinted with permission from Ref. [250].

XCT has been used extensively to study the porosity in the parts built using the L-PBF [283–294]. An example of visualization of porosity in AM Al-10Si-Mg sample is presented in Fig. 16(a). XCT analysis was used to correlate the process parameters used during the print to the generated porosity in parts in several studies [34,255,257,281,282]. The effect on the residual porosity of post-processing heat treatments and HIP has also been studied [263]. Along with the pore-size distributions present in the parts, XCT is also used to correlate the porosity present in the part to the subsequent mechanical performance of the part [231,258,260,264–279]. XCT has also been used to characterize the size, shape, and porosity present in the feedstock powder particles (Fig. 16 (b)). Another important application of the XCT is the metrology of the printed parts for determining dimensional accuracy [34,256,283]. Lastly, XCT can be used to analyze surface roughness (Fig. 16 (c)) [269]. Over time, XCT has been implemented as a technique to study AM parts, particularly the porosity and dimensional accuracy of the parts. Although XCT provides accurate information about the flaws present in the parts, the origin of the observed flaws must be inferred from, e.g., their shape.

2.2. *In situ* process monitoring

It is no doubt that the PBF processes discussed herein are revolutionizing metal manufacturing with advantages such as lower material waste, consolidation of parts, etc. However, it is also clear that the qualification of AM parts is problematic in that some defects present in a printed part originate from the additive layer-by-layer process. Hence, *in situ* monitoring of these processes, even though limited [284,285], provides valuable insight into the defect formation process, which enables mitigation of defects in printed parts by controlling the process parameters *in situ*.

Real-time monitoring (aka *in situ* or in-process monitoring) will bring capabilities of observing defects formation in real time. Recently, Grasso and Colosimo published a literature review in the area of process defects and *in situ* monitoring [131]. Other applications of in-process monitoring in powder bed fusion AM processes include powder dispensing (e.g., defective spread powder layer, uneven powder bed due to part distortion, incomplete spreading, re-coater hopping, re-coater streaking, etc.) [286-288], laser-powder interaction (e.g., spatter formation, debris, super elevation and part failure) [26,48,131,152,164,224,225,289-291], melt pool (e.g. size, shape, temperature intensity and profile) [152,153,284,286,291-300], scan path (e.g., track geometry, ejected materials, and temperature profile) [223,225,290,301], and slice (surface pattern, geometry, thickness profile, temperature profile) [8,76,225,228,229,290,302]. Powder spreading monitoring is mostly focused on *operando* anomaly detection and porosity formation. Some efforts are focused on the use of optical imaging to monitor metal powder melting and consolidation, in which the powder layer is monitored using two-color pyrometry to investigate the metal powder consolidation process. Others are coupling the acquired data with data-driven techniques (e.g., convolutional neural networks, computer vision) to identify and classify defect formation using data from optical imaging or IR images [165,286,303-306]. There are also reports on the *in situ* monitoring of defect detection and their correlation with properties [9,15,287,307-309]. In each case, an *in situ* process monitoring technique could be employed to detect potential defect formation.

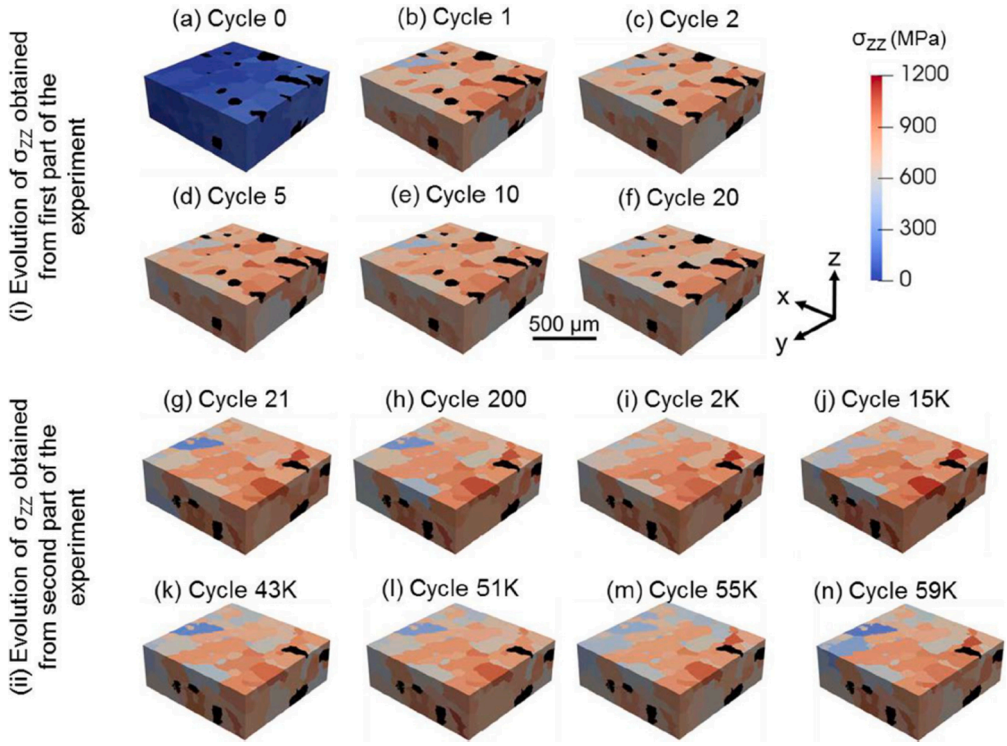

Fig. 15. *In situ* high-energy x-ray diffraction microscopy of post-processed alloy 718 built by laser powder bed fusion during high cycle fatigue experiment. The grain morphologies is reconstructed based on near-field diffraction data; while the grain-average stress values are measured based on far-field diffraction data. Reprinted with permission from Ref. [251].

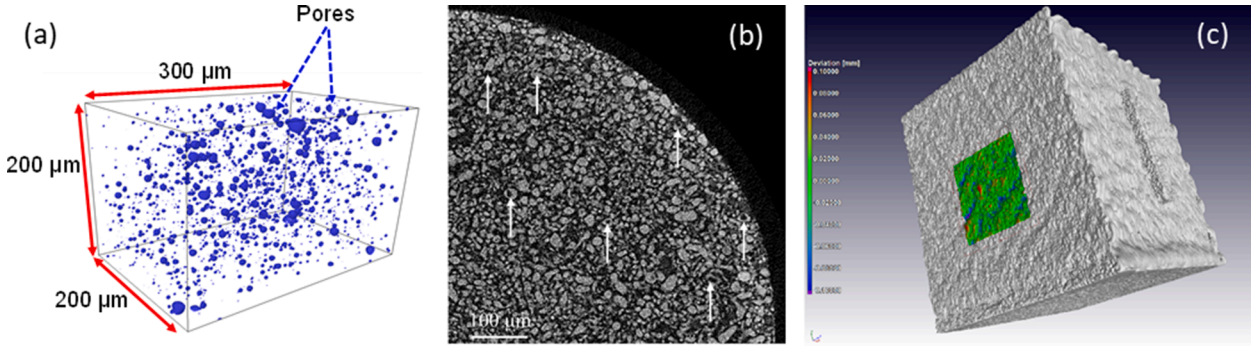

Fig. 16. Visualization of porosity in Al-10Si-Mg AM sample using XCT. setup at the APS. The pixel size in the dataset is 0.69 µm. Even the small pores can be visualized. Reprinted with permission from Ref. [267]. (b) powder porosity measurement using XCT. Reprinted with permission from Ref. [268]. (c) Surface roughness analysis using XCT. Reprinted with permission from Ref. [269].

2.2.1. *Visible-light high-speed imaging*

Quality and reproducibility are opportunities for improvement in additive manufacturing and manufacturers prefer to utilize inexpensive, practical monitoring tools on AM systems. High-speed imaging using visible light has been attracted interest in fusion AM processes to correlate in-process defect generation with those observed *ex situ* [218]. Cameras operating with visible-light and wavelength of 380–800 nm are an example of an *in situ* monitoring method [11]. Systems imaging at high scanning velocities with a high resolution require an external illumination source. Several studies use cameras to characterize laser-powder interaction which provides valuable information on spatter [11,49,310,311], melt pool signature [286], surface quality [300], and powder bed anomaly [288]. Lough *et al.* [294] proposed using optical emission spectroscopy in L-PBF to measure the spectral content of light emitted and gain insight into the chemistry and relative intensities of excited species vaporized. They found that the optical emission is largely affected by the build chamber pressure and gas species. Higher pressure and oxidizing gas environment create stronger optical emission signals. Kleszczynski *et al.* [312] utilized high-speed imaging to detect some types of process errors in the L-PBF process including process stability (e.g., insufficient powder supply, support connection, super elevations) and part quality (e.g., re-coater damage, poor compounds, dimensional accuracy). One main benefit of using high-resolution imaging is that it is feasible to integrate computer vision and machine learning approaches to minimize in-process defects.

2.2.2. *IR and near-IR high-speed imaging*

The use of pyrometry (describing sensor devices utilizing principles of pyrometry to measure temperature) and imaging, including infrared (IR) monitoring, emphasizes part process dependencies on thermal conditions [285,293,313]. In PBF technologies, many studies have focused on the monitoring of the temperature fields in order to predict anomalies and underlying microstructures [314-316]. The first efforts in monitoring focused on the process variables, mainly the melt pool

temperature [284,291]. Researchers have used *in situ* IR measurements to monitor the geometry of the melt pool and corresponding temperature during fusion AM processes. Any anomalies in the melt pool would be considered as possible defect formation in part. Nevertheless, tracking melt pool temperature and potential fluctuation requires a high-rate data acquisition (10 kHz) capability which is costly and considerably adds complexity in machine laser optics to the cost of the machine. As an alternative, full-field imaging can be employed with a lower frame rate as well as lesser data storage requirements. Boone *et al.* [317] suggested that using near-IR (e.g., silicon focal plane) could decrease the effect of emissivity on the measurements; therefore, resulted in lower measurement uncertainty (see Fig. 17)). It is worth noting that absolute temperature measurement needs a calibration of material emissivity and background temperature [261,318]. IR imaging was used in E-PBF to observe temperature distribution and potential defect generation [319]. Bartlett *et al.* [291] used full-field IR thermography of entire layers to identify material defects (e.g., keyhole and lack-of-fusion pores) and correlated results with ex-situ observations in L-PBF. Recently, McNeil *et al.* [320] found that the spatial and temporal variations in IR signatures were associated with thermomechanical drivers of defects (e.g., cracking) within the build.

Pyrometry and imaging present advantages and setbacks. Temperature measurements are performed without the need for physical contact which could disturb the process, and the operating temperature range of digital cameras fits within the expected melt pool temperatures. However, the size of the imaging setups might not be practical for *in situ* observation because of the limitation on the size of the printer's chamber as well as the associated cost of the setup. Moreover, the calibration of digital imaging setups is complicated. Specifically, pyrometry is based on the measurement of emitted radiation of the body compared to a black body; hence the emissivity of the body must be known a priori to achieve accurate measurements. Emissivity measurements are complicated due to the complexity of the phase transformation(s) that occur during the printing process.

2.2.3. *High-speed x-ray imaging and diffraction*

In addition to post-build characterizations, synchrotron x-ray imaging and diffraction techniques have also been used for *operando* study of the AM processes. The results provided remarkable insights into the mechanisms that are responsible for various structural defects in the builds.

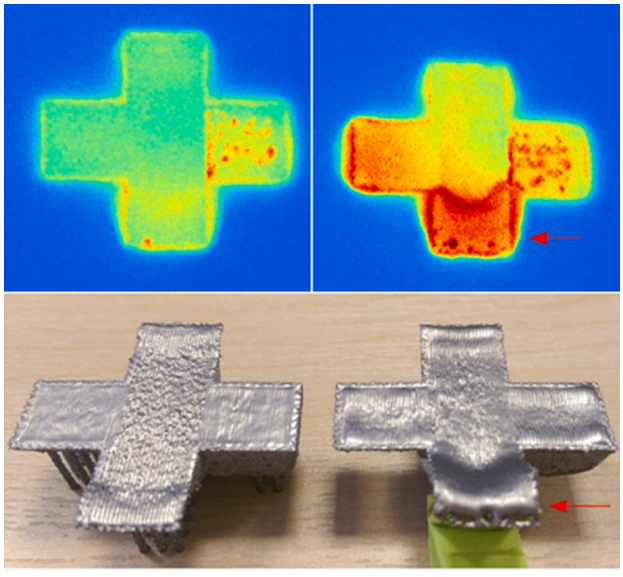

Fig. 17. Examples showing lack of fusion (small localized hot spots) and swelling (indicated by the red arrow). Reprinted with permission from Ref. [317].

Prior to synchrotron x-rays, laboratory x-rays were used in the 1990s by research groups such as the Seiji Katayama group at Osaka University to monitor the deep penetration of laser in keyhole-mode welding [111]. However, because a tube x-ray source was used in their works, the limited flux generated images with relatively low contrast and resolution. Therefore, information on the fine structure of front keyhole wall and melt pool morphology were lacking in their reports. Fig. 18 shows the visualization of keyhole porosity using the in-house x-ray imaging technique.

In 2016, Zhao and Sun *et al.* built a laser powder bed fusion simulator and integrated it with the high-speed synchrotron x-ray imaging and diffraction techniques at the Advanced Photon Source (APS) of Argonne National Laboratory. In 2017, they demonstrated the power of the platform and published the results in Scientific Reports [26]. This was the first time that synchrotron x-rays were used to monitor the laser melting process of metals. The experimental schematic is shown in Fig. 19. As demonstrated, many important phenomena in metal additive manufacturing could be examined with micrometer spatial and sub-nanosecond temporal resolutions, such as keyhole dynamics, melt pool dynamics, powder ejections, rapid solidification, and highly non-equilibrium phase transformation [26,321]. For example, Fig. 20 shows the details of the formation process of a keyhole pore and the growth process of columnar grains [26]. With the fastest cameras, the imaging frame rate can be as high as 10 MHz. Later, the platform was extended to study other AM processes such as directed energy deposition and binder jetting [322,323]. Note that the x-rays are not imaged directly and a scintillator is always used to convert x-rays to visible light for acquisition by high-speed cameras.

Currently, many teams across the world are using high-speed synchrotron x-ray imaging to study the defect formation in AM processes. At the Advanced Photon Source (APS), teams from academia, national labs, and industry have been researching different modes of defect generation in AM. Cunningham and Zhao *et al.* reported the keyhole morphology evolution during laser melting and rigorously defined the conduction, transition, and keyhole zones in the laser power-velocity space [25]. Zhao *et al.* discovered a new mechanism for the fast spatter formation, where the bulk explosion of a tongue-like protrusion on the front keyhole wall is the key [48]. Guo and Zhao *et al.* investigated the influence of ambient pressure on the powder motion and elaborated the critical roles of metal vapor plume and argon gas flow in the spattering phenomenon [325]. Hojjatzadeh *et al.* calculated the major forces that the micro pores experienced inside the melt pool and found that in the melt pool region close to the vapor depression, the thermocapillary force induced by the large thermal gradient dominates [267]. Most recently, Zhao *et al.* found that the keyhole porosity boundary in the laser power-velocity space is sharp and smooth and that, around the porosity boundary, there exists a dominant keyhole porosity mechanism [24]. The critical keyhole instability emits an acoustic (shock) wave directly into the liquid below. The wave then drives the pore near the keyhole tip to accelerate rapidly away from the keyhole. When the pore is captured by the solidification front, it becomes a detrimental structural defect in the build.

Besides, at the Stanford Synchrotron Radiation Light Source (SSRL), a collaborative team with researchers from Lawrence Livermore National Laboratory, SLAC National Laboratory, and Ames Laboratory have performed fast imaging experiments [326-329]. This team focused on the keyhole dynamics and studied the porosity generation caused by unstable keyhole and laser beam turning. Defect mitigation strategies were proposed in these studies to guide the practice. At the Diamond Light Source, Leung *et al.* used a high-energy monochromatic beam for fast imaging experiments [43,330]. They observed porosity generation and spattering during laser interaction with freely packed powder samples and also found that the oxygen content of aged/used powders can change the surface tension of the molten metal and thereby alter the Marangoni flow in the melt pool. Another interesting *operando* system

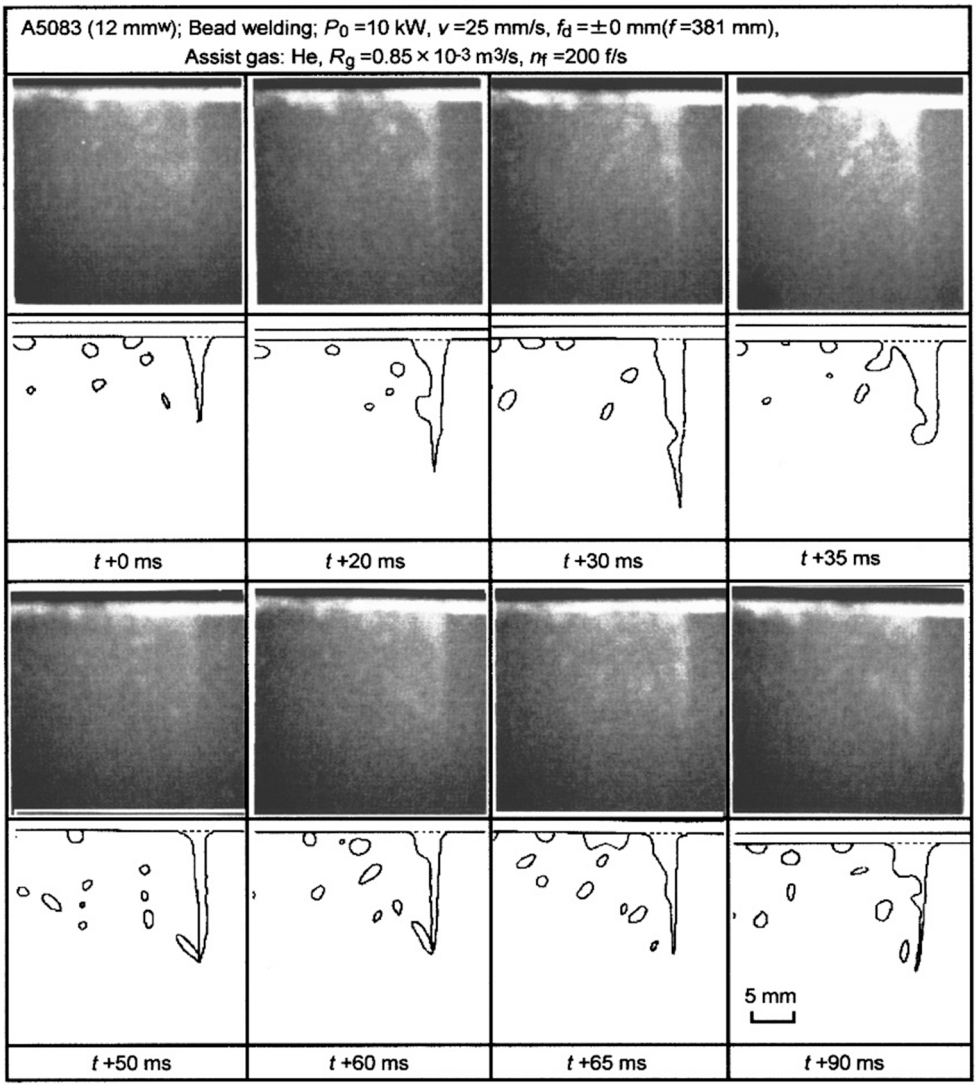

Fig. 18. Laboratory x-ray imaging of keyhole porosity in laser welding. Reprinted with permission from Ref. [111].

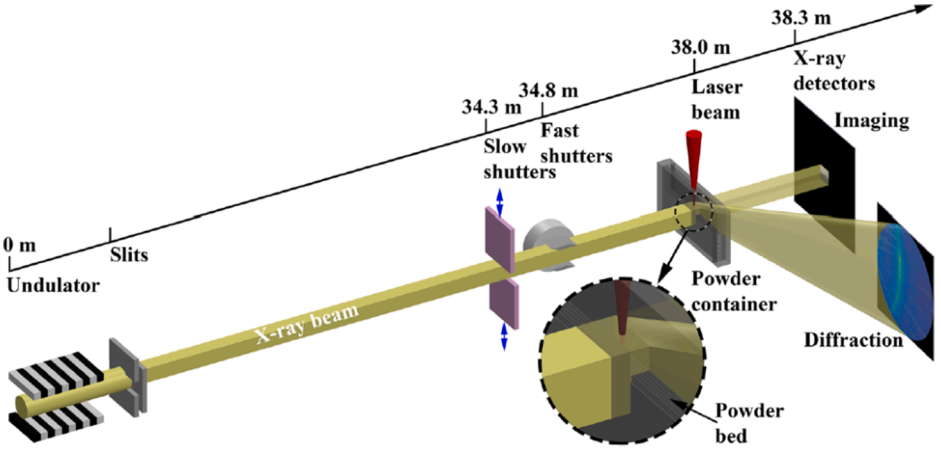

Fig. 19. Schematic of high-speed synchrotron x-ray imaging and diffraction experiments on laser powder bed fusion at the Advanced Photon Source of Argonne National Laboratory. Reprinted with permission from Ref. [26]. Besides the two detectors shown here, visible-light and infrared detectors can be added to collect complementary sample information simultaneously [324].

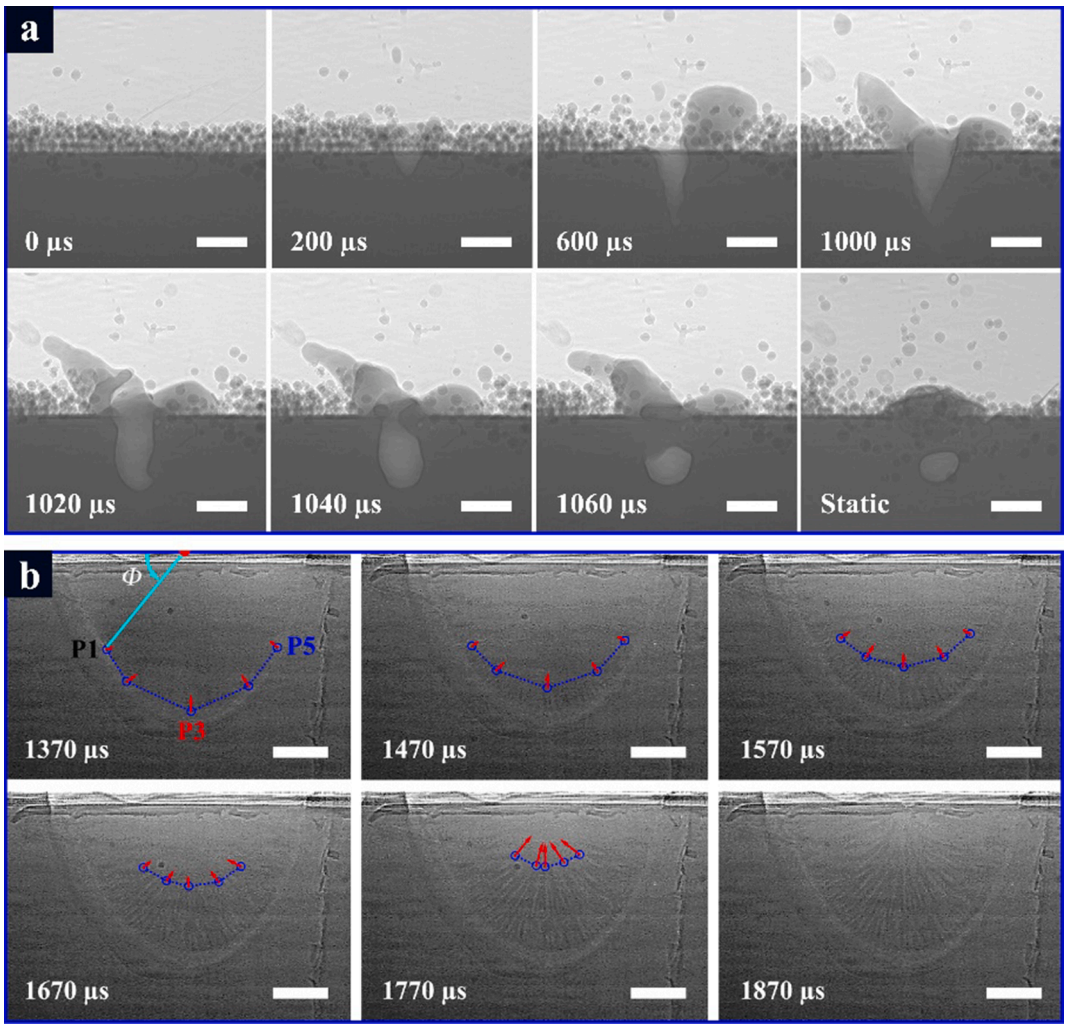

Fig. 20. High-speed synchrotron x-ray imaging of Ti-6Al-4V in laser melting and solidification. (a) Formation of a keyhole pore. (b) Growth of columnar grains. Reprinted with permission from Ref. [26].

developed by Lhuissier *et al.* enabled *in situ* 3D x-ray microtomography study of the L-PBF process [331]. In contrast to the full-field high-speed imaging experiments, these *in situ* tomography measurements were performed between build layers. The packing configuration of feedstock powder as well as the morphology of defects, e.g., porosity, can be characterized in 3D.

Except for imaging, high-speed synchrotron x-ray diffraction has been applied by several teams across the world to study material phase evolution during the solidification process relevant to AM [26,332-334]. In 2017, Zhao *et al.* observed the appearance of strong diffraction spots from the high temperature bcc phase during the initial solidification of Ti-6Al-4V and their replacement by the hexagonal phase as the sample continues to cool down, as shown in Fig. 21 [26]. Through the transformation times, they estimated the cooling rate and the solid phase transformation rate. Quantitative measurement of the stress development during the cooling process yet remains challenging, due to three major factors. First, owing to the rapid cooling rate in AM processes, sample rotation and translation is impossible, which makes the characterization of complete strain tensor extremely difficult. Second, the thermal effect also alters the lattice spacings of the material as stress does. The development of an effective approach to isolate these two effects holds the key for accurate stress measurement. Third, the geometry of *operando* diffraction is generally limited by the experiment setup, so a diffraction pattern contains signals from the entire illuminated volume, except for the reflection-mode diffraction experiment [335]. Given the large thermal gradient involved in laser or e-beam AM, a high-resolution stress measurement requires major assumptions and numerical modeling. Brown *et al.* estimated the stress development during wire arc AM of 308L stainless steel [334]. More effort is certainly needed for *operando* stress measurement associated with other AM processes with larger thermal gradient, faster cooling rate, and more complex sample environment, such as L-PBF.

Since the work of Zhao *et al.* [26], more and more teams have started to adopt the high-speed synchrotron x-ray techniques in their research to unravel the physics underlying the formation of different types of defects in AM processes. With further advances of synchrotron techniques (i.e., major source upgrades, x-ray technique development, and beamline instrument improvement), finer details of the energy-matter interaction involved in AM processes will be revealed, creating opportunities for building defect-free products.

2.2.4. *Other techniques*

Except for visible-light imaging, thermal imaging, x-ray imaging and diffraction techniques, integrating sphere radiometry (ISR) and acoustic testing (AT) are also used to monitor the additive manufacturing process of metals. Here, we introduce the general experimental principles and methods. Because of the difficulties in signal interpretation, these techniques are often combined with other techniques.

2.2.4.1. *Integrating sphere radiometry.* ***Experimental principles and***

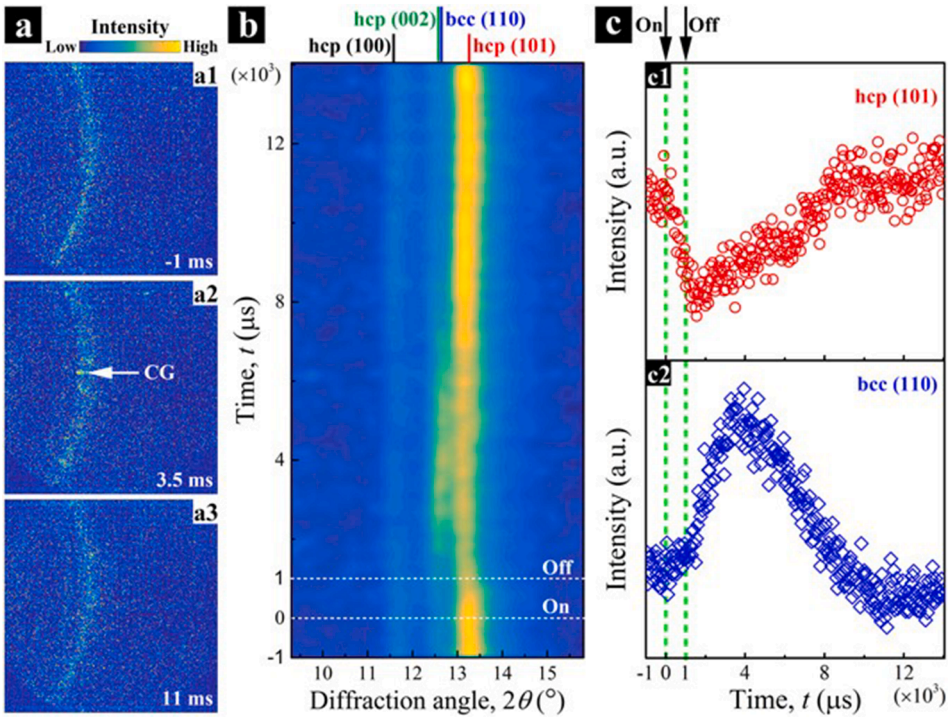

Fig. 21. High-speed synchrotron x-ray diffraction of Ti-6Al-4V in laser melting and solidification. Reprinted with permission from Ref. [26].

methods. An integrating sphere was used by J. T. Norris *et al.* at Sandia National Laboratories in 2008 to temporally evaluate the laser absorption during a laser welding process [336]. As shown in Fig. 22A, there are two spheres, one primary sphere and one secondary sphere. The primary sphere is positioned beneath the laser head. The weld sample locates inside the sphere and at the focal plane of the laser beam. Depending on the melting mode (conduction vs keyhole), the reflected laser light from the weld surface is either captured by the sphere or escapes from the top opening of the sphere. The former is detected by a near-infrared (NIR) photodiode, assisted by a narrow bandpass filter. The latter is captured by the secondary sphere and detected by a second NIR photodiode. The laser energy absorbed is estimated as, $E_W = E_0 - E_{S1} - E_{S2}$, where E_0 is the energy enters the primary sphere, E_{S1} is the integrated energy from the primary sphere, and E_{S2} is the integrated energy from the secondary sphere. Prior to Norris *et al.*, Fabbro *et al.* at LALP (CNRS)/GIP GERAILP implemented the technique in 2005 (Fig. 22B) to measure the laser energy transmitted through the keyhole during a full penetration laser welding process [102]. The temporal resolution of the photodiode was a few microseconds. Its signal was linearly related to the laser power entering the sphere. In 2018, Simonds *et al.* at the National Institute of Standards and Technology used the technique (Fig. 22C) to investigate the dynamic laser absorption during the melt and keyhole formation processes [337]. The temporal resolution was <1 microsecond. In their contribution, the inner surface is coated with $BaSO_4$, and a baffle design is adopted to avoid the direct detection of laser energy from the weld pool or the vapor plume.

Integrating ISR with other monitoring techniques. In 2020, Simonds *et al.* combined this technique and the inline coherent imaging or high-speed x-ray imaging, and correlated the laser absorption with the keyhole evolution (e.g., keyhole depth), as shown in Fig. 23 [51,338]. The inline coherent imaging system is capable of extracting the sample surface depth as a rate of 200 kHz and the spatial resolution is 15 μm. The main results are shown in Fig. 23C. At low incident laser power, the laser absorption continues to increase from 0.30 to 0.51, and the simultaneous depth measurements were attributed to thermal expansion of the sample as well as surface tension pressure and fluid flow in the melt pool. At high incident laser power, the laser absorption rapidly increases and largely fluctuates around 0.60, which agrees well with the change of sample surface depth over time. The measured depth fluctuation was attributed to the keyhole wall collapses and material ejections. At intermediate incident laser power, both laser absorption and sample depth oscillate rapidly, and occasionally, the sample surface depth can suddenly, but temporarily, increase with a simultaneous increase in laser absorption [25,48].

2.2.4.2. Acoustic testing. ***Experimental principles and methods.*** Acoustic testing has been used to monitor the laser melting process because of its fast data acquisition and processing [339-341]. The basic concept is that the amplitude of the scattered waveform is related to the elastic properties and mass density of the melt pool and build plate. With the melting of a metal, the shear modulus vanishes, and the compressional modulus and mass density largely reduce. As a result, there exists a large acoustic impendence difference at the boundary of the melt pool. This causes the strong scattering of the incident shear wave from the melt pool. Besides, the shear wave is more sensitive compared to the longitudinal wave because of its shorter wavelength.

Integrating AT with other monitoring techniques. Kube *et al.* used ultrasound and a few spherically focused immersion transducers to measure various shear scattering from the melt pool as it evolves [339]. As shown in Fig. 24, they found that the scattering of ultrasound is very sensitive to the melt pool depth. The melt pool depths were obtained from the post-mortem cross-sections after the laser welding. Also, as the melt pool evolves, the arrival time of the initial pulse increases because the shear wave velocity decreases. The link between the acoustic signals and the part quality is not straightforward. To address this challenge, Shevchik *et al.* at the Swiss Federal Laboratories for Materials Science and Technology proposed a method for detection of process instabilities that cause defects in real time [340,341]. Firstly, as shown in Fig. 25A, they used three techniques to monitor the laser melting process: high-speed x-ray imaging, laser back reflection, and acoustic emission. X-ray images are used for the ground truth of the part quality. Secondly, they applied a deep artificial neural network (Fig. 25B) to reveal the signatures of those events causing defects in wavelet spectrograms from the laser back reflection and acoustic emission signals (Fig. 25(C-E)). It

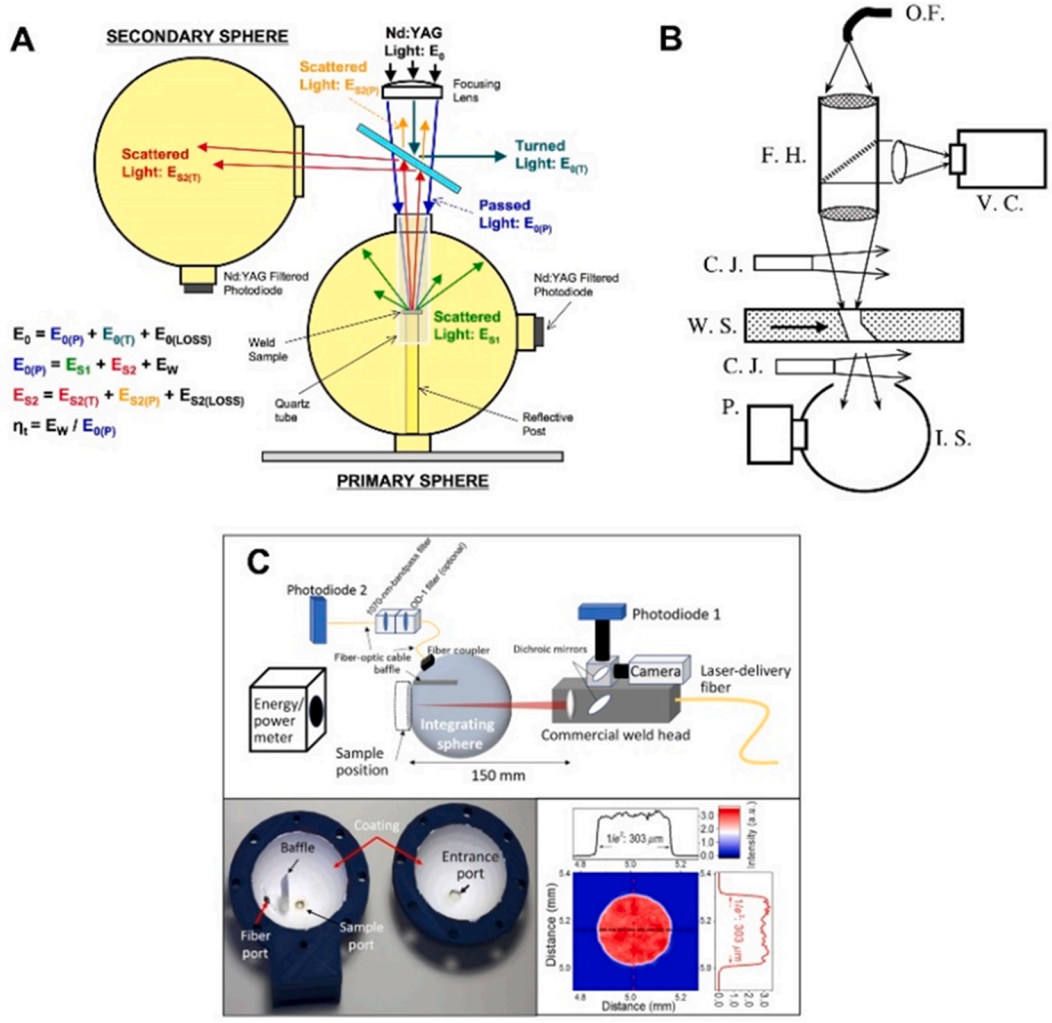

Fig. 22. Experimental setups using integrating sphere radiometry. (A) By J. T. Norris *et al.* at Sandia National Laboratories. Reprinted with permission from Ref. [336]. (B) By R. Fabbro *et al.* at LALP (CNRS)/GIP GERAILP. Reprinted with permission from Ref. [102]. (C) By B. J. Simonds *et al.* at the National Institute of Standards and Technology. Reprinted with permission from Ref. [337].

is claimed that the classification accuracy could be higher than 70%, for the conduction, stable keyhole, and unstable keyhole melting and the formations of spatters and pores. When combining the two signals, even higher accuracy could be achieved. Besides, the temporal resolution could be down to 2 ms.

3. Powder-related defects

There are different powder characteristics such as morphology, mean size, particle size distribution, powder flow, packing density, powder porosity, and surface contamination that affect the quality of the final AM parts. Powders with spherical morphology are preferred for AM processes since higher powder packing density with better powder flow can be attained. Low packing density will result in internal voids in the AM parts. Depending on the AM process, mean size and size distribution of the powder may vary. Typically, internal voids in feedstock powder can be transferred to the AM parts and it is difficult to remove them during printing (post processing such as hot isostatic press is needed to compress residual pores). Furthermore, powder composition, impurities, and inclusions with feedstock materials can be transferred to the final part and deteriorate mechanical properties and corrosion resistance. Therefore, it is essential to evaluate potential powder-related defects and remedies to improve build quality [9,342-346].

3.1. Powder production and characteristics

A critical component of the powder bed fusion machines is metal powder feedstock. It is produced by one or multiple techniques including gas atomization (GA), centrifugal methods, plasma rotating electrode processed (PREP), hydride-dehydride (HDH), wire atomization, and plasma atomization (PA) [347]. The most commonly used methods will be discussed herein. For more information about other powder production techniques, the reader is referred to the extensive review by Dawes *et al.* [348].

Atomization is a typical powder production process. The setup consists of a vacuum chamber that contains molten metal that is heated using an induction coil at the top. Vacuum is especially crucial to metal that is susceptible to oxidation. The molten metal is poured through the nozzle with a concentric high-pressure gas flowing which results in the breakup of the stream of melt, and surface tension results in the formation of spherical microdroplets of powder metal. The resulting powdered metal is collected in the lower chamber that is commonly filled with Argon gas or even water to collect some types of non-reactive metals. Many high-speed videos of the atomization process are presented by Kouraytem *et al.* [349] in their supplementary data. Even though water atomized powders are used in PBF, gas atomized powders are usually preferred due to their higher sphericity resulting from the lower heat capacity and slower quenching rates during atomization. A

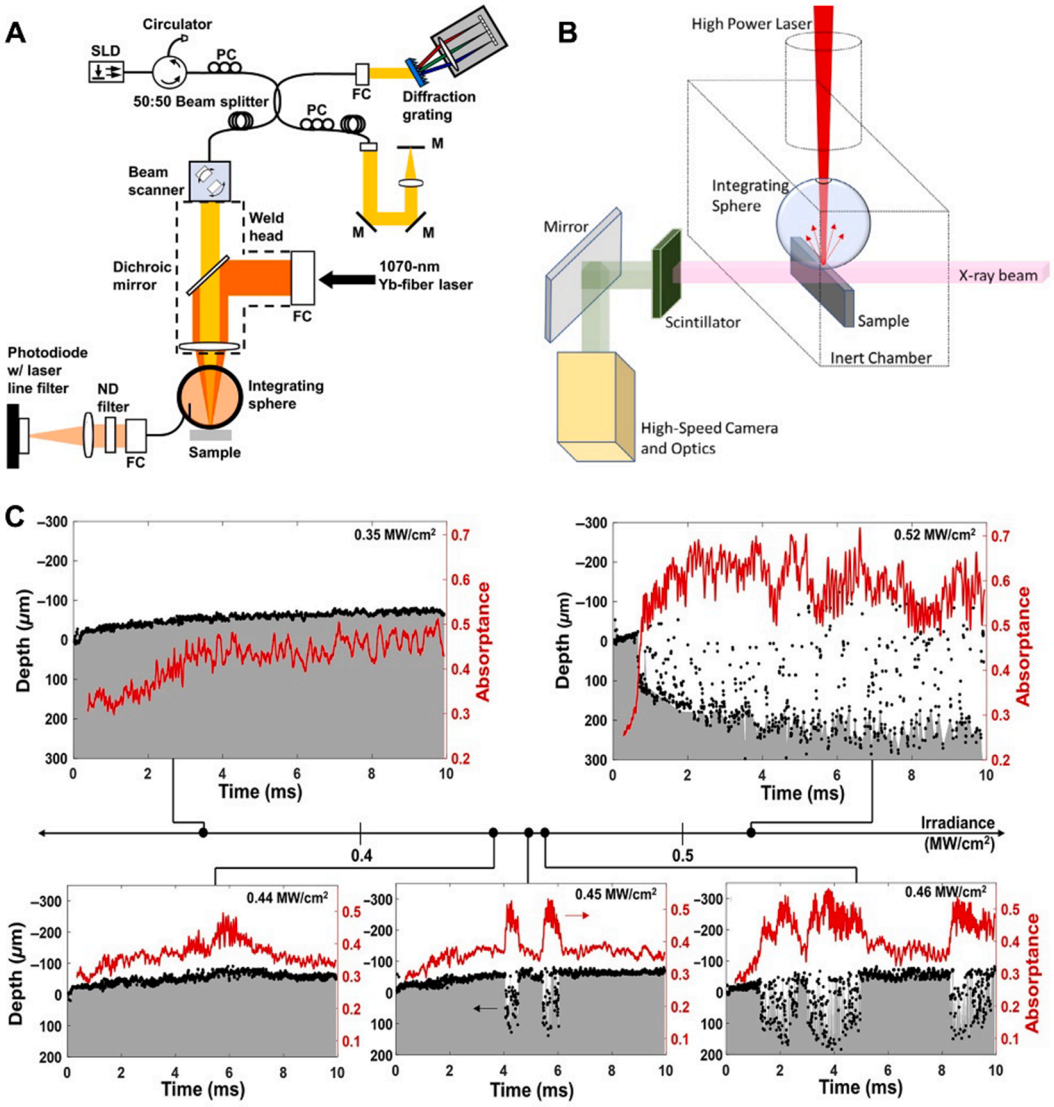

Fig. 23. Correlation laser absorption and sample surface depth. Sample surface depth measured from (A) inline coherent imaging and (B) high-speed x-ray imaging. (C) Time-resolved keyhole depth and laser absorption from conduction to transition to keyhole mode. Conduction mode: 0.35 MW/cm^2. Transition mode: 0.44–0.46 MW/cm^2. Keyhole mode: 0.52 MW/cm^2. Reprinted with permission from Refs. [51,338].

number of variations for GA have been introduced, notably vacuum induction melting with gas atomization (VIGA) and electrode induction melting gas atomization (EIGA). The variations mostly differ in the type of melt pool release mechanism or release of the melt through the nozzle. The EIGA technology is notable for eliminating contact between the feedstock and any crucible because the melting occurs via non-contact induction heating.

The PA method consists of a vacuum chamber containing electrodes across which an arc is induced to generate a plasma. The material of interest is in the form of a wire that is fed into the chamber and heated rapidly by the plasma. At that stage, other features of the system (that are not disclosed publicly) lead to the rapid breakup of the powder particles and then collected in the lower chamber. Another variant of PA is PREP, in which two electrodes are used to maintain an arc. On one side, an electrode (non-consumable) is fixed whereas the other one is the material to be atomized (consumable). By rotating the electrode, the liquid metal pinches off in the form of powdered metal. The size of the powder is related to the rotating speed of the electrode [350].

Rabin *et al.* [351] analyzed a variety of rapidly solidified powder particles produced using different atomization techniques including vacuum gas atomization, centrifugal atomization, ultrasonic gas atomization, and inert gas atomization. The materials analyzed included: type 304 stainless steel, Fe-16wt.%Ni-Cr, Fe-40wt.%Ni, Ni_3Al, Fe-9wt.%Cr-1wt.%Mo, Cu-2 wt%Zr, type 4340 steel, pure Al, and Al-alloy 2124 Al. They showed that both gas concentration and porosity increased with increasing particle size owing to the presence of gas bubbles within the powder particles. This was due to a mechanism for gas bubble entrapment during liquid droplet formation and solidification during the atomization process. Importantly it was found that much of the observed gas was accounted for as macroscopic gas porosity. In general, it was also deduced that gas content and porosity increased with increasing particle size because a greater fraction of larger particles contained gas pores.

Besides atomization, a completely different approach is hydride-dehydride (HDH) that works with hexagonal (also Nb and Ta) metals, commonly used to produce Titanium. In this method, hydrogen is added to titanium to form a hydride (TiH_2) which is very brittle and easily milled into fine albeit rough powders. Given that hydride is thermally unstable, the hydride powder is oxidized back to metal by driving off the hydrogen content using heating. The final titanium powder remains in similar size to the prior hydride, namely rough which makes it less interesting for use in AM. For AM, these powders are usually

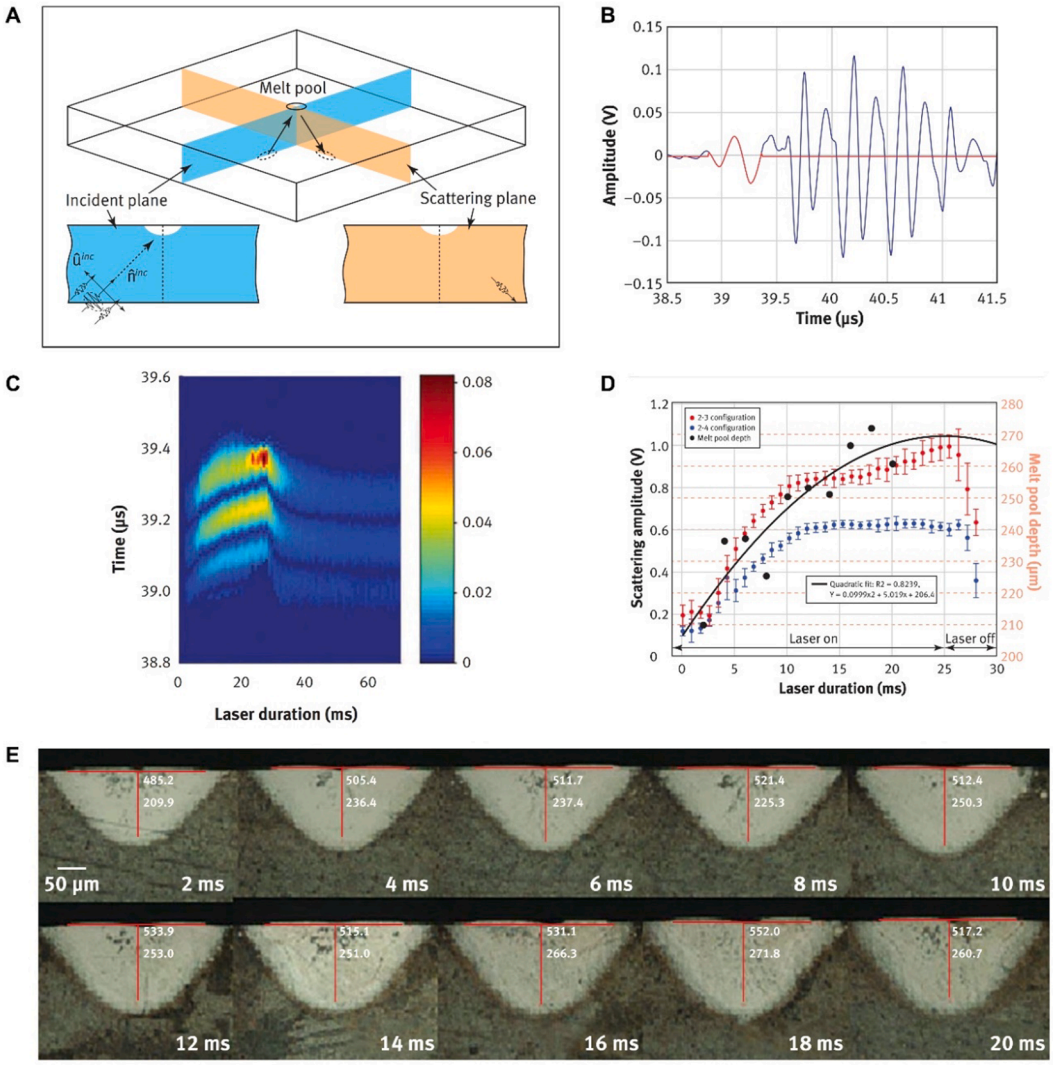

Fig. 24. Understanding of ultrasound testing of laser-induced melt pool. (A) Schematic of pitch-catch configuration. (B) Ultrasonic waveform during the formation of melt pool. (C) B-scan image over time. (D) Measured scattering amplitudes and melt pool depths. (E) Fused melt pools at various laser durations. Reprinted with permission from Ref. [339].

spheroidized by plasma treatment [352], although success in using the as-dehydrided powder has recently been demonstrated [353,354].

Resulting powders are characterized by several quantifiable properties that would affect the resulting part quality and performance in PBF processes [344], including geometric properties (e.g., particle size and distribution, mean size, shape, surface roughness, circularity, aspect ratio), chemical properties (e.g., bulk and surface compositions), microstructural properties (e.g., internal porosity, crystal structure, grain size, oxide layer thickness), bulk properties (e.g., thermal stability, tap density, flowability), etc. [355]. Depending on the powder production process, different powder characteristics are expected. For instance, powder production techniques that involve gas are generally prone to porosity entrapment in the powders [356], which is discussed in later sections as a potential source for the transferability of defects. More details will be presented on powder-related defects (Section 3), and powder spreading dynamics and anomalies (Section 4). The resulting size distribution of powders produced using different powder production methods are highly spread. For powder bed fusion applications, the average particle size of interest is mainly <100 μm. However, in a conventional freefall gas atomization system, only about 10% of the powders produced are generally <120 μm and may be of interest to powder bed fusion processes. Consequently, these powders present a higher cost of production knowing that only a very small fraction of the powder is useful for AM. From a point of view of cost efficiency for powder production, it makes GA techniques less interesting for AM. However, Fritsching *et al.* [357] suggested controlling the flow of the system, resulting in powder particles being shifted to smaller sizes. As a result, >40% of the produced powder may be used in powder bed fusion processes.

It is important to understand the flow properties of the powder. Usually, a flow rheometer is used to test the rheological behavior. A cup is filled with powder, and a rotating propeller blade is driven into and out of the powder to measure the torque to rotate it. Two types of measurements are possible using this technique, namely the confined and unconfined flow. In the first type, bulk flow energy (BFE) is measured during the entry of the propeller blade and is analogous to the stress encountered under the spreader in a powder bed fusion machine. In the second type, specific energy (SE) is measured during the pullout of the propeller, analogous to the stress in front of the spreader or a system where the powder is dropped out of a hopper. If either of these values is small, the powder is considered to be free-flowing under that condition.

Powders have been classified for their suitability to be used in AM depending on parameters such as the flowability. The flowability of powders is a function of the internal friction of the powders, i.e., Van der

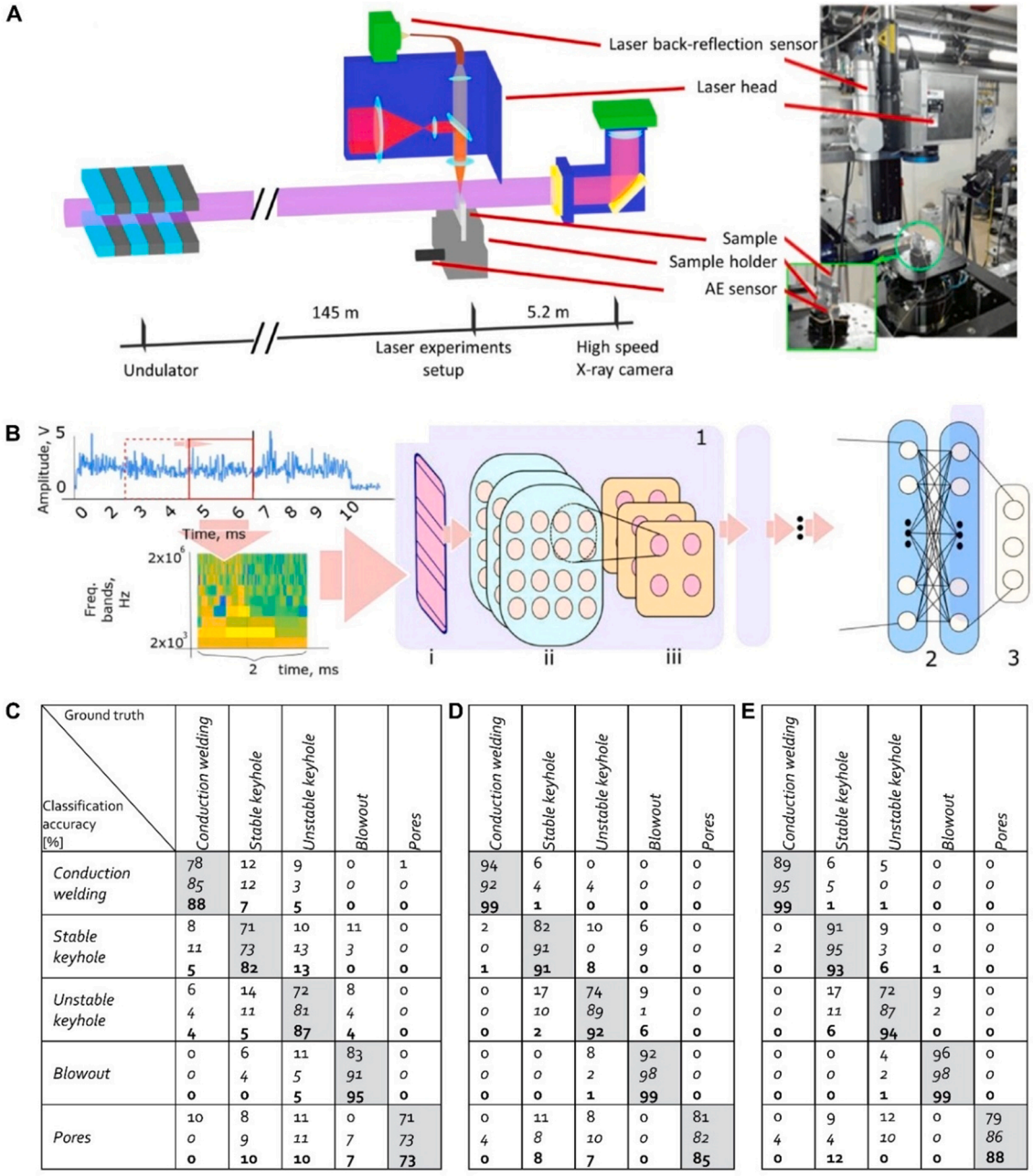

C	Conduction welding	Stable keyhole	Unstable keyhole	Blowout	Pores
Conduction welding	78 85 **88**	12 12 **7**	9 3 **5**	0 0 **0**	1 0 **0**
Stable keyhole	8 11 **5**	71 73 **82**	10 13 **13**	11 3 **0**	0 0 **0**
Unstable keyhole	6 4 **4**	14 11 **5**	72 81 **87**	8 4 **4**	0 0 **0**
Blowout	0 0 **0**	6 4 **0**	11 5 **5**	83 91 **95**	0 0 **0**
Pores	10 0 **0**	8 9 **10**	11 11 **10**	0 7 **7**	71 73 **73**

D	Conduction welding	Stable keyhole	Unstable keyhole	Blowout	Pores
Conduction welding	94 92 **99**	6 4 **1**	0 4 **0**	0 0 **0**	0 0 **0**
Stable keyhole	2 0 **1**	82 91 **91**	10 0 **8**	6 9 **0**	0 0 **0**
Unstable keyhole	0 0 **0**	17 10 **2**	74 89 **92**	9 1 **6**	0 0 **0**
Blowout	0 0 **0**	0 0 **0**	8 2 **1**	92 98 **99**	0 0 **0**
Pores	0 4 **0**	11 8 **8**	8 10 **7**	0 0 **0**	81 82 **85**

E	Conduction welding	Stable keyhole	Unstable keyhole	Blowout	Pores
Conduction welding	89 95 **99**	6 5 **1**	5 0 **1**	0 0 **0**	0 0 **0**
Stable keyhole	0 2 **0**	91 95 **93**	9 3 **6**	0 0 **1**	0 0 **0**
Unstable keyhole	0 0 **0**	17 11 **6**	72 87 **94**	9 2 **0**	0 0 **0**
Blowout	0 0 **0**	0 0 **0**	4 2 **1**	96 98 **99**	0 0 **0**
Pores	0 4 **0**	9 4 **12**	12 10 **0**	0 0 **0**	79 86 **88**

Fig. 25. Deep learning for quality monitoring of laser melting. (A) Experiment setups. Three techniques are used: high-speed x-ray imaging, laser back reflection, and acoustic emission. (B) A deep artificial neural network for signatures of events in laser back reflection and acoustic emission signals. Classification results for (B) the laser back reflection signal, (C) the acoustic emission signal, and (D) the combination of the two signals. The numbers in each cell are conventional CNN, cross residual CNN, and temporal CNN, respectively. Reprinted with permission from Ref. [341].

Waals, electrostatic and capillary forces. Typically, powders with lower internal friction (such as aluminum and stainless steels) show better flowability, while powders such as titanium exhibit worse flowability [358].

In addition to the conventional funnel test for testing the repose angle of powders, the rotating drum instrument has been presented to measure the dynamic properties of powders [359]. The method consists of a cylinder with a transparent wall that gets filled with a sample of powder. The drum is turned while systematically changing the rotating speed and the dynamic angle of repose is computed from the average interface position while the dynamic cohesive index is measured from the fluctuation of the interface. The instrument is based on an automated powder flowability test based on the rotating drum principle hence lower values of flowing angle usually correspond to better flowability.

As important as optimizing the process parameters for desired part properties, understanding powder characteristics is imperative in powder bed fusion. While many defects are generally correlated to the processing window or the inclusion of gas in powders, some defects may result from the characteristics of the powders used in the feedstock. During subsequent layer printing, powders are spread using either a roller that rotates to stir up the powder as it spreads it out or a blade spread that scrapes the powder into a layer [360]. Hence, good spreadability and flowability of powders are two important measures. Powders are characterized using various methods such as the bed expansion ratio, the angle of repose, ring shear cell, bulk/tap density, and the avalanche angle as well as by many quantifiable properties. Furthermore, reuse of the powders may lead to alteration in the feedstock behavior and resulting part properties.

Spherical powders are typically used with maximum powder size less than ~55 μm in diameter, hence <10% fraction of the powders generated using gas atomization [361]. Gas-atomized powders generally display a log-normal size distribution, with sudden changes due to sieving that will be discussed shortly [362]. Hence, powders are expected to achieve a random packing density that is lower than the theoretical close packing density. However, the addition of powder batches with large and small powders allows the small size particles to fill the voids between the large ones and increase the packing density [363]. In applications for AM, Zhu *et al.* [364] presented a theoretical model of bi-modal and tri-modal powder packing to achieve high apparent density. Although theoretically, a bimodal distribution with at least a 7:1 particle size ratio yields a packing factor of 0.868, actual packing density can be much lower due to inhomogeneity and other factors [365]. Karapatis *et al.* [366] adopted the bimodal approach with the ratio of 10:1 to enhance the packing density of direct metal laser sintered nickel powders. McGeary [367] suggested that a mixture of fine and coarse powder with a ratio of 10:1 can lead to a maximum packing fraction of ~82%. In L-PBF, the maximum particle size is ~55 μm, so a 10:1 size ratio means 5 μm particles but having a substantial fraction of such small particles will make the powder very 'sticky' i.e., very poor flowability. Such bi-modal powders would be also very expensive, thus seems impractical. When tested using L-PBF, the part produced using the tri-modal powder achieved a final density within the apparent density values, whereas the part produced using the bi-modal powder exhibited a lower final density. Other techniques to add smaller particles consist of wet [368] or dry coating [369] of powder particles with nanoparticles which is implemented for oxide strengthening of the material or improving the density of the powder, respectively. In the first method, nanoparticles are suspended in water then mixed with the metal powder, and finally dried in a furnace. Such a technique may be challenging to avoid oxidation of the metal powders. However, Karg *et al.* [369] established a wider powder size distribution by dry coating aluminum–silicon powders with silica nanoparticles to increase the density of the powders. During the printing process, about 20–30% of the powder in a layer is used, resulting in a used batch of powder that may be reused.

After the use of metallic powders during the powder bed fusion additive manufacturing techniques, powders may be reused. It is important to understand the life-cycle of different powders as a function of degradation during AM processes, chemical composition variation (e.g., interstitial pick-up), powder flowability, surface contamination, apparent density, powder morphology, sphericity, and size distribution [370,371]. Moreover, the surface roughness of the fusion-based AM processed parts is negatively affected by powder recycling. Typically, powder properties change after each time of use, thus, it is challenging to identify which alteration is influencing the component properties. Further, different materials do not age in the same way, and the same material will age differently when subject to different AM process parameters. Industries such as the aerospace, military, and medical sectors have highly specific requirements for the components produced, thus composition differences in the powder can affect performance. Therefore, precise prediction of powder degradation is hard and thus troublesome to determine the point at which metal powders are no longer acceptable for use within AM.

After the first use of a virgin powder, sieving should be performed to separate the smaller particles from the larger ones. To perform the sieving operation, the used powder is passed through various stacked mesh sizes, depending on the ultimate desired powder size where the mesh size is linked to equivalent particle size. During reuse, powders are expected to alter in size distribution and composition, specifically due to the reheating of the alloys which ultimately affects the mechanical properties of a printed part. To investigate the effect of recycling powders, Ardila *et al.* [372] studied the mechanical properties of L-PBF alloy 718 printed using a powder that was recycled up to 14 times. The authors established a methodology of consecutive sieving and drying iterations to recover the powder's initial properties. The powder distribution and powder composition were nominally maintained. The mechanical properties of the build parts tested using a Charpy impact test also exhibited similar results. A similar approach was also followed by Asgari *et al.* [373] to print L-PBF parts using recycled AlSi10Mg powder with the platform preheated to 200 °C. Results of this study unveiled comparable powder characteristics, microstructures, and mechanical properties (hardness and tensile properties). Cordova *et al.* [374] compared powder characteristics for the virgin and used metal powders (e.g., alloy 718, Ti-6Al-4V, AlSi10Mg, and Scalmalloy). It was shown that powder morphology, size distribution, powder flow, circularity, chemistry, and microstructure were affected after using powders for L-PBF (Fig. 26). Rafieazad *et al.* [375] showed that the virgin powder of AlSi10Mg had a mean particle size of 8.8 ± 7 μm, while it increased to 13.7 ± 9 μm after five-time recycling of L-PBF processed powders. It was also shown that the part porosity increased, the area fraction of Al-Si eutectic increased, and cracks were formed between eutectic arms. In other words, a higher density of internal defects such as porosity, microsegregation, and cracks appeared for L-PBF processed with the recycled powder. Since the mean size of the recycled powder was larger with irregular morphology, thermal conductivity was reduced thereby leading to a lower cooling rate of the melt pool and coarsening of Si at the melt pool boundaries. This issue caused crack susceptibility and lower corrosion resistance. It was shown in [144,376-378] that fine spattered particles that were not removed by sieving would cause porosity formation in the build by disrupting powder spreading, in turn influencing the packing density and leading to the formation of pores.

One of the risks of using sieving is that powders that are needle-shaped, with high aspect ratios thus undesirable in the printing process, may pass through the sieves. The availability of such powders within the batch may lead to defects such as issues in the spreading of the powder layer and the inaccuracy in the final shape of the printed layer. Powder sizes may be characterized depending on the powder sizes using microscopy, sieving, light scattering, etc. [379]. More efficient ways to characterize powder morphology include image-based computer vision and machine learning techniques that were applied to classify powder geometry into many categories [380,381]. Other efforts by Scime and Beuth [303] implemented a Convolutional Neural Network (CNN) to detect and classify defects in the spreading of powders during the laser powder bed fusion process.

Powder characteristics may affect the printed part surface quality, density/porosity, and mechanical properties [364,382,383]. Powders may also include defects within the powder particles as presented by Morrow *et al.* [382]. The authors studied the effect of defects in the feedstock on the microstructure and quasi-static response of Stainless steel parts. They showed sub-micron particles visible on surface defects of certain powders resolvable using TEM. Those sub-micron particles also showed up in the microstructure and fractography images along the cracked surfaces and exhibited a chemical composition that deviates from that of the virgin powder.

The characteristics of powders produced using different manufacturing techniques have also been shown to affect the mechanical properties of printed parts [384]. To test this effect, Irrinki *et al.* [384] used a gas-atomized (mostly spherical, bimodal distribution) and a water-atomized (irregular morphology, monomodal distribution) 17-4PH stainless steels powders with two median particles sizes of each type. Testing the effect of energy density while varying the values of the power and speed, results show an effect of the powder characteristics on the density and ultimate tensile strength. At low energy density, parts printed using the water-atomized powders exhibited lower density and ultimate tensile strength. With the increase of the energy density, those effects faded in the case of the part density, and ultimate strength. However, at higher energy densities the ultimate strength decreased overall. Hence, low-cost water-atomized powders may be used to produce AM parts with good mechanical properties when the processing parameter are adjusted.

The enhancements of powder characteristics are one of the ways to

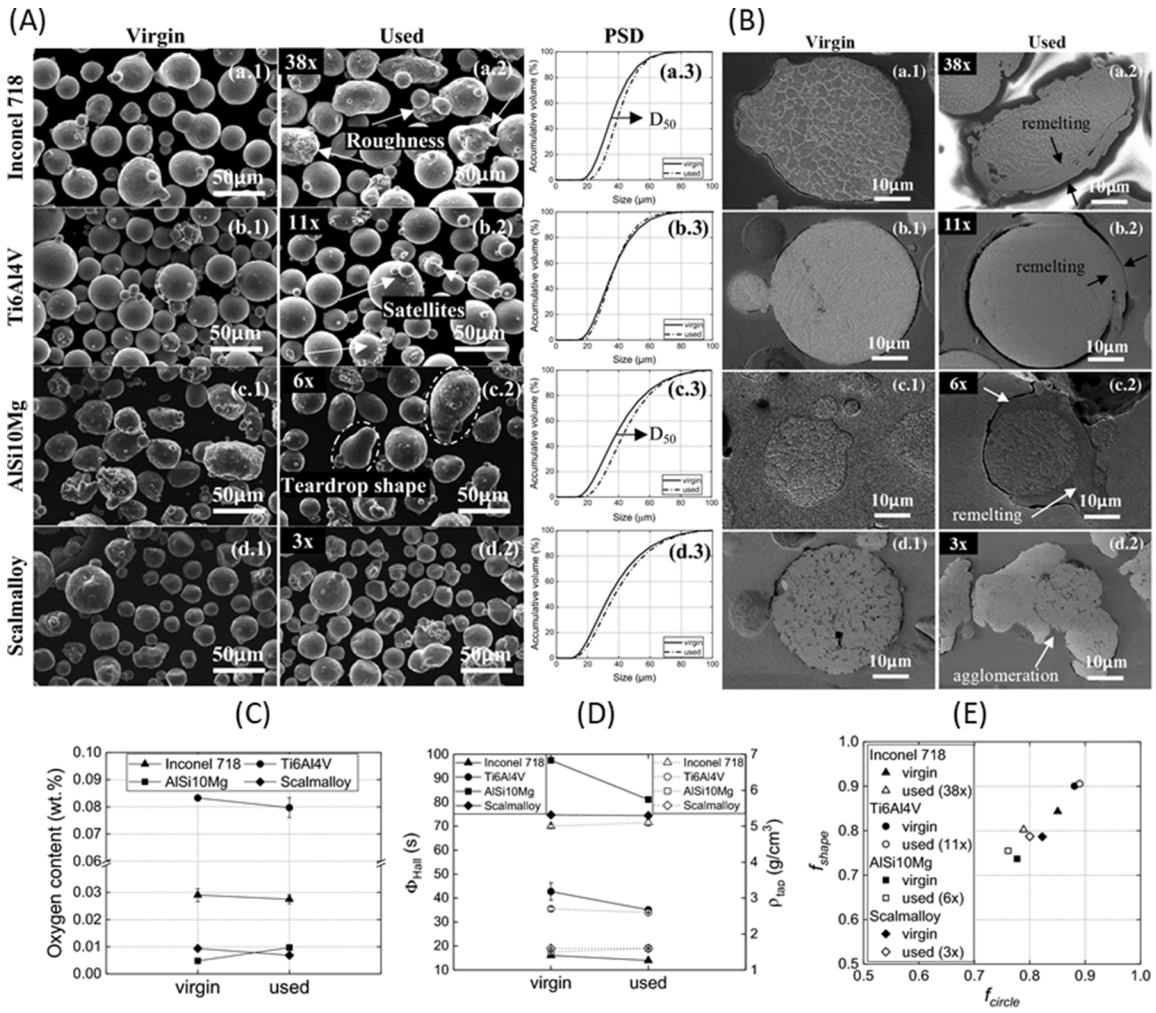

Fig. 26. Comparison between various characteristics of the virgin and used powders in L-PBF, (A) scanning electron micrographs and powder size distribution results, (B) cross-sectional SEM micrographs showing the effect of re-melting and agglomeration zones in used powders, (C) oxygen content measurement for the virgin and used powders, (D) comparison of the flow rate, tap density, true density, Hausner ratio and Carr index for the virgin and used powder, (E) particle shape vs. circularity parameters of powders. Reprinted with permission from Ref. [374].

improve the design and production of AM parts with improved surface quality and mechanical properties with many recommendations offered by Anderson *et al.* [385]. As mentioned earlier, spherical powders are usually preferred for their better flowability, layer spreading, and loose powder packing. However, powder characteristics such as size distribution, porosity, and argon content have been shown to vary depending on the powder manufacturing technique in spherical powders as well [350]. These characteristics and their effect on the transferability of pores from the powder to the printed part will be further discussed in a subsequent Section 3.4 with the presentation of some relevant investigations.

3.2. Common metals and defects

Additive manufacturing of metal powder is rapidly growing in different industries such as aerospace, automotive, and biomedical. It is necessary to evaluate the types of metal powder that can be effectively used in fusion-based AM machines. Although fusion-based AM technologies have the potential for the efficient production of complex, precisely dimensioned components, there are limitations in terms of composition for being used in AM machines. The main reason is related to the processability and weldability of metallic materials during the AM process to fabricate defect-free parts. Elemental evaporation, oxidation, segregation, cracking, and pore formation are the main concerns limiting materials selection for fusion AM processes.

Amongst all feedstock pre-alloys, nickel superalloys (mainly alloy 718 and 625), titanium alloys (mostly Ti-6Al-4V), aluminum alloy (mainly AlSi10Mg and AlSi12 and uncommon ones such as 7075, 6061, and Al-Cu-Mg), steels (stainless steels such as 316, 420, 17–4 PH and tool steel mostly H13) and a few other alloys such as magnetic materials [386,387], Co-Cr [388,389] and W [390-392] have been used for powder bed fusion AM. Although using pre-alloyed feedstock is the most common option in AM, there is an interest to use pre-mixed powder from available compounds and perform *in situ* alloying in PBF processes. *In situ* alloying from elemental powders opens up a wide range of composition adjustment possibilities to any alloy whose powder is difficult to obtain. There have been a number of reports of using elemental powder blends to fabricate parts in PBF AM such as Al + Si in L-PBF [393], Al + Cr + Mo + Nb + Ta in E-PBF [394], Al + Sc + Zr in L-PBF [395], Al + Mn in E-PBF [396], stainless steel 316 + Fe-Cr-Ni-B in E-PBF [397], Ti + Nb in L-PBF [398], and Ti + Al + V in L-DED [399]. All these studies pointed out the possibility of AM part production using pre-mixed powders that can compete with pre-alloyed powdered materials and effectively add a 4th dimension to 3D printing of metals. However, there remains the obvious challenge of achieving homogeneous microstructures from AM of pre-mixed alloys. Energy density plays an important role in the formation of the desired composition from pre-mixed powder. Evaporation of alloying elements such as Mn and Al during fusion AM processes

requires a higher fraction of these elements in the premixed powders [396,399]. It is also possible that new intermetallic compounds and phases form during the PBF of pre-mixed alloys [393]. Besides, Clayton [400] found that although fusion AM processed stainless steel 316 from pre-mixed and pre-alloyed powders showed similar microstructure and mechanical properties, stainless steel 430 showed a fully ferritic structure for pre-mixed powder and ferritic martensitic structures in pre-alloyed powders. He also found that the microstructure of Ti-6Al-4V was dependent on feedstock such that pre-alloyed powder showed the formation of basket-weave alpha along with regions of a martensitic alpha prime within prior beta grains; pre-mixed powder, by contrast, exhibited a larger alpha lath width because of slower cooling rates. In E-PBF, preheat temperature is needed before printing, thus, the pre-mixed powder containing low temperature melting materials may increase concerns for local melt formation and powder agglomeration (In Ti-6Al-4V or Al-Si pre-mixed powder). Indeed, some groups have suggested that local orientation gradients from incompletely mixed powders may have advantages [401]. Here, four main pre-alloys feedstock used for industrial application are presented.

3.2.1. *Titanium alloys*

In powder-based additive manufacturing (AM), titanium alloy normally refers to a particular composition, Ti-6Al-4V, which is the workhorse alloy in AM production. Ti-6Al-4V is widely applied in the aerospace industry [402] due to the outstanding mechanical properties (high strength to weight ratio) and corrosion resistance; it is also used in the biomedical industry, mostly for body prostheses and orthopedic implants, because of its well-studied biocompatibility [403]. Besides, many reports discuss the development and testing of novel titanium alloys for AM application, such as burn resistant BuRTi [404], damage tolerant TC2 [405], higher strength and lower density Ti-5553 [406], and biocompatible Ti-2448 [407].

Similar to other alloys, as shown in Fig. 27 pre-alloyed spherical Ti-6Al-4V powder can be produced through methods like gas atomization (GA) [408,409], electron induction melting – gas atomization (EIGA) [410], plasma rotating electrode process (PREP) [411,412], and induction plasma spheroidization (IPS) [413]. GA is a cost-efficient and the most popular powder production process as of today; however, it is inevitable to introduce entrapped gas [28,82,134] which can potentially become a source of defects in as-built AM parts. Water atomization [414], fluidized bed [144], and hydride-dehydride (HDH) [415] are processes that can produce non-spherical titanium powder. As discussed above, the HDH process involves both chemical and mechanical processes in which the titanium alloy is hydrogenated and transformed to an embrittled intermediate stage so that the feedstock can be effectively milled to fine powder; later, dehydriding can be completed by simply elevating the temperature. Although entrapped gas is not a concern for these irregularly shaped powders, the powder morphology can make the sieving process and the control of powder size substantially more difficult. Other novel powder production methods include the Metalysis or FFC® process [416], electrolytic methods, and metallothermic processes [417].

Ti-6Al-4V is a standard alloy for both laser and electron beam AM processes which have the applicable powder size from 20 to 45 μm and from 45 to 106 μm, respectively. This potentially increases the cost of AM powder. The remaining coarse powder is normally recycled or used for conventional powder metallurgy, e.g., hot isostatic pressing. Note that titanium alloy is highly reactive to oxygen, especially at elevated temperatures. Oxygen can be picked up during storage, fabrication, and powder recycling [419]. Thus, it is preferable to store, handle, and build titanium powder in a vacuum/inert gas environment. Oxygen content in titanium powder has always been a major concern especially building with recycled powder. A standard solution [420] is to add the virgin powder to regulate the oxygen content meanwhile balance the size distribution and compensate the alloy elements which are selectively evaporated during melting. Interestingly, Simonelli *et al.* [421] mentioned that the alloying elements reduce the volatility of titanium as no formation of the oxide layer or elemental segregation on the of Ti-6Al-4V spattered particles in the L-PBF process were observed. Oxygen concentration must be limited to <0.2% to avoid ductility problems. It is, however, a potent strengthening addition. Tang *et al.* [422] measured the oxygen content of the virgin and reused Ti-6Al-4V powder and it was

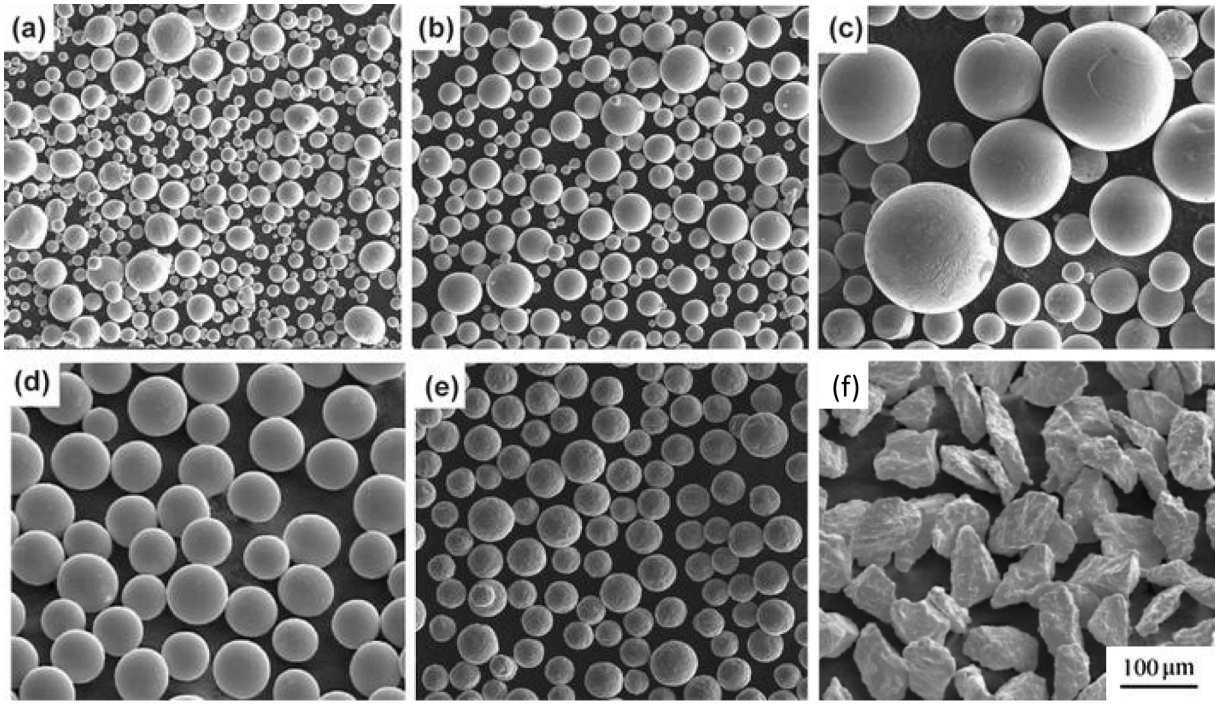

Fig. 27. Scanning electron micrographs of Ti-6Al-4V powder manufactured by (a) gas atomization, (b) plasma atomization, (c) plasma rotating electrode process, (d) plasma spheroidization from – 140 + 200 mesh HDH powder, (e) granulation-deoxygenation, and (f) HDH process (-140 + 200 mesh). Reprinted with permission from Ref. [418].

found that the oxygen level increased from 0.08 wt% (virgin) to 0.19 wt %. In addition, powder particles became less spherical, rougher, and coarser after 21 times of recycling, similar to [419] in which spherical powders were replaced by deformed and irregular powders. Composition variation in recycled powder was also reported. Surprisingly, powder flowability was improved with increasing the reuse time and the printed specimens showed highly consistent tensile properties [144].

In the fabrication of Ti-6Al-4V alloy, the evaporation of the aluminum alloying element is a major concern since it affects the properties of the as-built components. Fig. 28 reveals the inhomogeneity of aluminum in the cross-sections of as-built Ti-6Al-4V fabricated by selective electron beam melting. The loss of aluminum is positively correlated with the energy input [423] and the number of reuses. Many studies [424,425] attempted to use a modeling approach to understand the evaporation phenomenon in additively manufactured titanium alloy.

The common phases in titanium alloys include α, β, ω and martensite (α′ and α′′). In Ti-6Al-4V, the addition of vanadium stabilizes a small fraction of the β phase which makes Ti-6Al-4V a α + β alloy at room temperature [426,427]. The as-built microstructure of Ti-6Al-4V depends on the cooling rate of the building process [428-430]. Fast cooling suppresses the phase transformation from β to α and maximizes the residual strain into the as-built part (noted that the part attached to the base plate more directly causes strain to develop during thermal shrinkage); it leads to the formation of martensite through a diffusionless transformation in laser-based AM processes [235,431-433]. In contrast, the E-PBF process has a much lower cooling rate and smaller thermal gradient due to the high pre-heat. The matrix of as-built E-PBF microstructure is primarily α + β meaning the as-built E-PBF part exhibits lower strength but higher ductility compared with parts from laser-based AM processes [431,432,434,435]. An important feature in AM Ti-6Al-4V microstructure is the coarse columnar prior β grain which means that the microstructure of AM Ti-6Al-4V can be easily differentiated from conventionally manufactured material. In AM processes, epitaxial growth is the dominant solidification mode meaning the β grain preferentially grows along one of the variants of the ⟨100⟩ crystal orientation that closely aligns with the largest thermal gradient [433,436]. Thijs *et al.* [235] and Narra *et al.* [437] have demonstrated the capability of varying the directional grain growth and the local grain size in different AM processes by controlling the scanning strategy.

3.2.2. Nickel-based superalloys

Nickel-based superalloys are a class of precipitation strengthened alloys that perform well in high-temperature environments [438-440]. The excellent high-temperature properties of nickel-based superalloys have resulted in the implementation of this class of alloys into many aerospace applications [441,442]. The inherent interest of the aerospace industry in powder bed fusion additive manufacturing technologies has driven research in the ability to print these material systems.

The fine precipitates that form within the face-centered cubic matrix, known as γ, are what provide the Ni-based superalloys with their improved high-temperature properties. The two major strengthening precipitates are the γ' phase and the γ'' phase. The γ' phase is also a face-centered cubic structure possessing the composition Ni_3(Al, Ti) [443444]. The γ'' phase is a body-centered tetragonal phase and possesses the composition Ni_3(Nb, V) [445,446]. Different Ni-based superalloys possess different fractions of the γ' and γ''precipitates depending on the alloy composition and processing. MC carbide phases are also often found in Ni-based superalloy microstructures, with the majority of the MC carbides being TiC [443]. Additionally, the Laves phase is observed in some Nickel-based superalloys, including the popular alloy 718 [443]. σ-phase also appears in Ni-based superalloys that are exposed to high temperatures for long periods [443]. Large amounts of the σ-phase can be embrittling.

Nickel-based superalloys have been traditionally produced using powder metallurgy manufacturing techniques due to the improved homogeneity over the cast Ni-based superalloys [447]. Ni-based superalloy powders for powder metallurgy applications have been produced using a wide range of techniques including gas atomization [448,449], electrode induction melting gas atomization [450], and, more classically, hydrogen reduction to powder from an aqueous solution [451]. Gas atomization, plasma-rotating electrode process, water atomization, and electrode induction melting gas atomization are all popular techniques in the modern era for the production of powders for powder bed AM manufacturing techniques [268,452-454]. Many Ni-based superalloy powders are available commercially.

A wide range of Nickel-based superalloys have been developed for a variety of applications. The alloy 718 alloy system is considered one of the most weldable of the Ni-based superalloys [455]. As a result, parts of this alloy have been frequently fabricated using E-PBF and E-PBF manufacturing methods [456-459]. Other Nickel-based superalloys have also been used in the fabrication of parts using powder bed machines including alloy 625 [460,461], alloy 738 [462], Rene 142 [463], Hastelloy X [464,465], CMSX-4 [453], and Haynes 230 [466].

Ni-based superalloys are prone to cracking during welding [467,468]. Both hot cracking and strain-age cracking are observed in Ni-

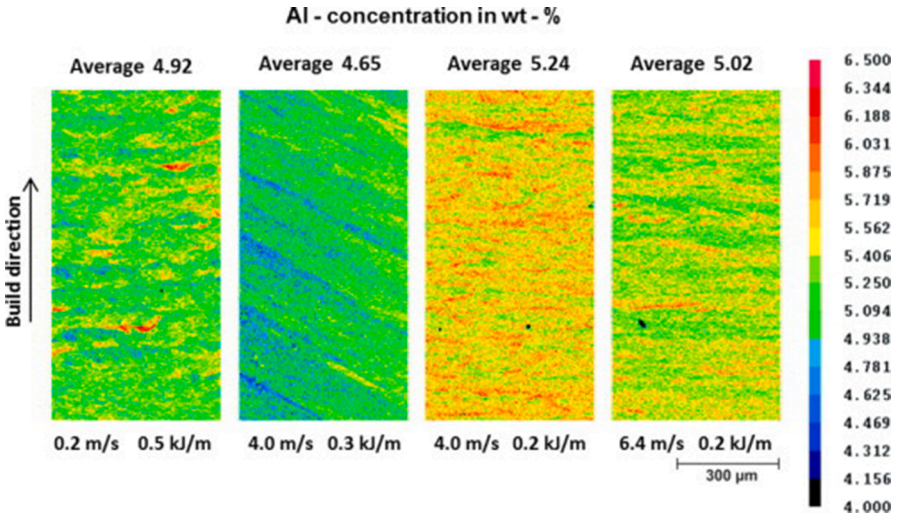

Fig. 28. Aluminum concentration of samples built with different scanning speeds and line energies in an E-PBF by electron probe microanalysis. Reprinted with permission from Ref. [423].

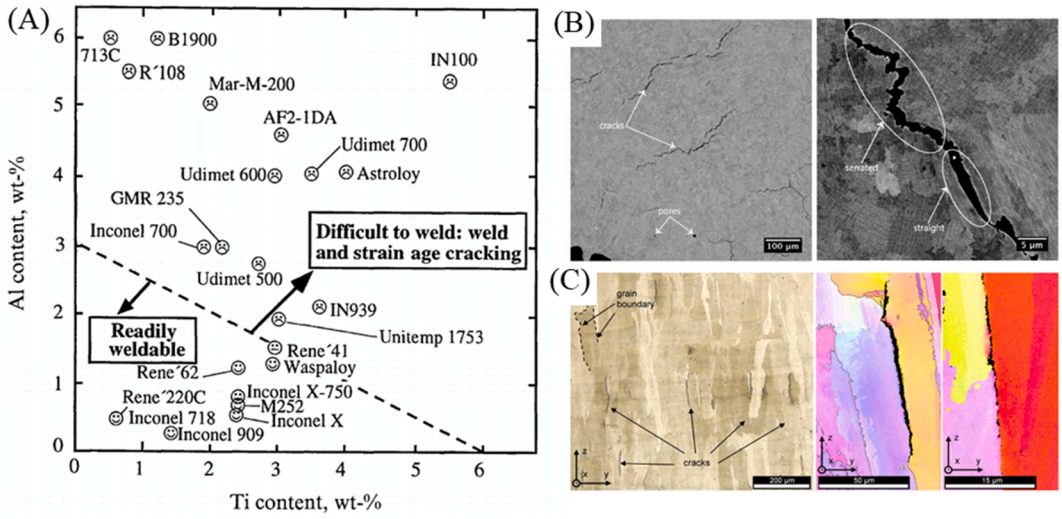

Fig. 29. (A) Plot of aluminum vs. titanium content in Ni-Based superalloys. The dotted line separates regions of good and poor weldability (reprinted with permission from Ref. [471]), (B, C) Microscopy images showing cracks present in L-PBF of nickel superalloys (B) CM247LC (reprinted with permission from Ref. [475]) and (C) IN738LC (reprinted with permission from Ref. [476]).

based superalloy welds [468]. This cracking behavior extends to AM applications as well [203,469,470]. The extent to which cracking is a concern varies from alloy to alloy due to the composition variations between the different Ni-based superalloys. Fig. 29(A) illustrates how weldability is affected by differing amounts of aluminum and titanium content in different Ni-based superalloys [471]. Cracking during L-PBF of Ni superalloys are shown in Fig. 29(B, C) and it is seen that cracks mostly form along with the build direction at the brain boundaries. Additionally, oxidation is a potential threat to Ni-based superalloy components. The wide variety of alloying elements found in Ni-based superalloys present the possibility of forming many oxidation products [472]. These oxidation products can negatively impact the performance of nickel-based superalloy parts [473]. Additive manufacturing processes are susceptible to exposing the alloys to environments where oxides can form [144,474].

Spattered particles and oxide layer formation on powder surface continuously form in the PBF process and will change powder characteristics such as morphology, mean size and particle size distribution, surface features, and flowability. Additionally, melt pool shape and behavior are influenced by them. In nickel alloy 718, alloying elements

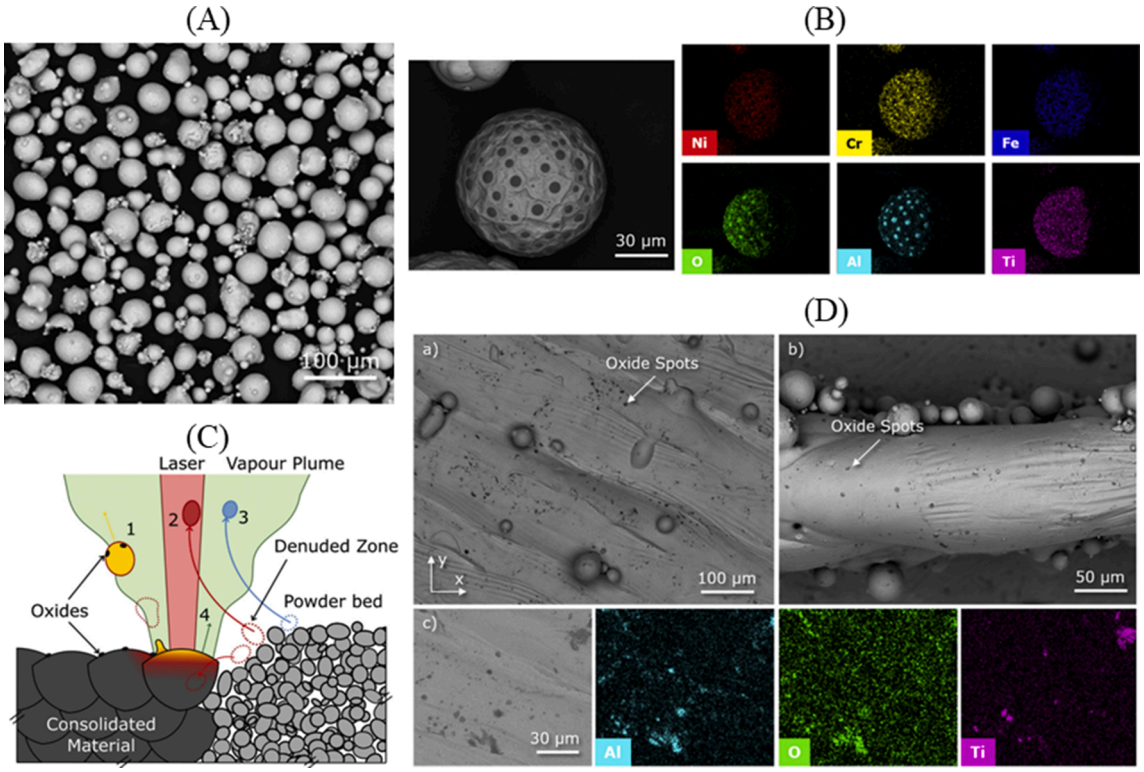

Fig. 30. (A) SEM micrograph of nickel alloy 718. Backscattered electron SEM micrograph and EDS elemental may analysis from (B) a spattered nickel alloy 718 particle, and (D) surface of the L-PBF process alloys 718 where oxide spots are detected, (C) Schematic illustrating laser-powder interaction and how spattered particles form during PBF process. Reprinted with permission from Ref. [144].

of Al and Ti have high oxygen reactivity and form nanoscale TiO_2 and Al_2O_3 layers on the powder particle surfaces (on spattered powders, Fig. 30(B)) or sub-micron oxide particles (as inclusions) in the microstructure or top surface of the AM parts (Fig. 30(D)). Gasper *et al.* proposed the spatter formation mechanisms as (1) melt-ejection spatter, (2) hot-entrained spatter, (3) cold-ejection spatter, and (4) metal vapor ejection and vapor plume [144]. It was shown that the spatter particles had sizes ranging 1–273 μm, negatively affecting size distribution of recycled powder and coarse spattered particles could land on the powder bed or print area, resulting in defective build production. As noted above, however, the mechanism illustrated in Fig. 31B is too simplistic as Zhao *et al.* [477] have shown that spatter is directly related to unstable fluid flow in deep keyholes.

3.2.3. Aluminum alloys

Aluminum alloys are increasingly used in automotive, aerospace, and heat exchanger applications [478,479] because of their high strength to weight ratio, superior recyclability, corrosion resistance, and thermal conductivity. Gas atomization [480,481] is the dominant powder production method for aluminum powders as of today. Additional powder production techniques [482-484] for aluminum alloy include centrifugal atomization, water atomization, and crushing/grinding, etc. Similar to other alloys, the vast majority of aluminum alloys cannot be built in powder-based AM processes mainly due to the formation of the undesired columnar microstructure and the hot cracking problem [99,485,486] caused by the directional rapid cooling. Additional challenges for AM aluminum components comes from their high reflectivity [487,488] of photon and reactivity with oxygen [489,490] making it rather difficult to obtain a stable melt pool in laser-based AM processes or to prevent the formation of oxide during fabrication. AlSi10Mg is the most reliable and frequently used aluminum alloy in AM processes due to its near-eutectic composition with a small solidification range. Extensive studies [23,491-494] have been performed on the microstructure and mechanical properties of AlSi10Mg alloy. Other studies have tested non-standard aluminum alloys [395], e.g., AlSi12 [495], Al7075 [485,486], Al7050 [99], Al-Cu-Mg [496], and 6061 [478,490,497] in different AM processes revealed valuable information about how to mitigate cracking at different levels of severity. Crack susceptibility as a function of alloying elements during L-PBF of Al alloys is shown in Fig. 31.

In addition to powder-based AM processes, hot cracking is a well-documented problem in many welding literature papers [499,500] despite welding possessing lower cooling rates compared with AM processes. Many aluminum alloys have a large solidification range and low solidus temperature, meaning that they could be increasingly susceptible to hot cracking. This is currently the primary roadblock for the application of aluminum alloys in AM. The addition of silicon can decrease the eutectic temperature, improve the fluidity and reduce the solidification range and the thermal expansion coefficient [485,501]; as a result, the cracking can be moderated which explains why the more reliable AM aluminum alloys have high silicon content. In laser-based AM processes, a higher operating temperature and a lower cooling rate can effectively mitigate the cracking problem [99,496]. Zhang *et al.* [496] successfully fabricated crack-free AM parts similar to high-strength wrought aluminum alloy by using a high energy density. Higher melt pool temperature is beneficial to the wettability of aluminum alloy, as it can decrease the surface tension of molten aluminum; meanwhile, a longer solidification time is more kinetically favorable for the molten aluminum to reach the smaller equilibrium contact angle [502]. Additionally, cracks originated from the isolated interdendritic liquid pools can be reduced by backfilling [496,500]. Martin *et al.* [503] had remarkable success by coating high-strength aluminum powders with nanoparticles. They provide nucleation sites for the formation of equiaxed grains which effectively accommodate strain and mitigate cracking.

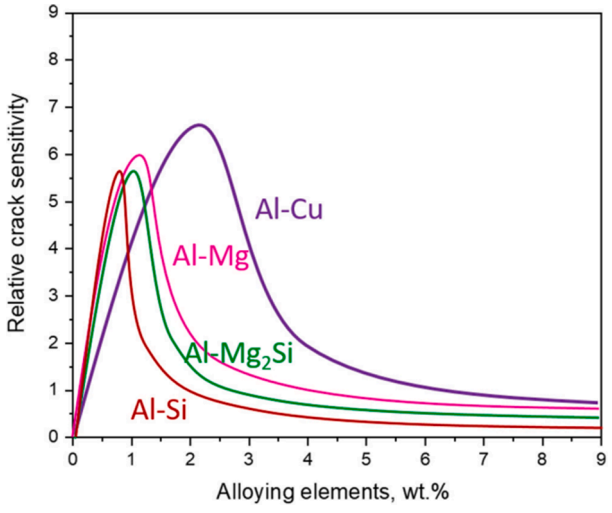

Fig. 31. The influence of chemical composition of crack susceptibility of welded (or fusion AM processed) aluminum alloys. Reprinted with permission from Ref. [498].

Oxide formation is a major concern for AM built aluminum alloys since the oxide is a potential site for the formation of defects [489,490,494]. Numerous literature papers [502,504,505] have reported that oxide formation increases the surface tension of the molten aluminum which promotes the balling effect [506] and suppresses wetting. Additionally, the oxide introduces extra difficulty for laser penetration, which in turn affects the densification process and leads to defect formation. As shown in Fig. 32 and Fig. 33, oxide layers are commonly found on the melt pool boundary and between layers. Owing to the low solubility limit and equilibrium partial pressure of oxygen (10^{-52} pO_2 at 600 °C) [490,507] in the oxidation reaction of aluminum, avoiding the formation of oxide is impossible in the current AM systems. Thus, the more practical way to mitigate its effects is to disrupt instead of avoid the oxide. Louvis *et al.* [490] attempted to control the Marangoni flow by adjusting the laser parameters; in this study it was believed that the flow pattern is responsible for the disruption of the oxide which effectively improves the wettability between layers, Fig. 33.

Similar to other alloys, processing related porosity [23,494,508,509] is common in as-built AM aluminum parts including keyhole and lack-of-fusion porosity. Residual hydrogen content from the aluminum production process can also induce the formation of hydrogen porosity in selective laser melting AlSi10Mg parts. Weingarten *et al.* [510] reported that the hydrogen porosity can be controlled by adjusting process parameters and drying the powder. Damon *et al.* [255] successfully used shot peening to reduce surface porosity by 15%–30%. Extensive studies [492-496,508] have been conducted to understand how in-part defects affect the mechanical performance of AM aluminum parts, which is addressed in Section 8.1.

3.2.4. Iron-based alloys

Iron-based alloy considered for additive manufacturing processing mostly lies in stainless steel (grade: 316L, 304L, 17–4, etc.), tooling steel (grade: M2, H13, P20, etc.) and Maraging steel (grade: 18Ni-300) and metal composites with these steel or pure Fe as matrix [511]. They are widely adopted for medical, automotive, aerospace, and tooling industries for applications including dental crafts, knee and hip joints, heat exchangers, tooling drill, casting and extrusion dies [512-514]. These applications usually require complex and customized part geometry design. Traditional processing routes (hot forming, cold forming) usually fabricate these components by dividing them into several smaller parts, which is time-consuming and material wasting. Additive manufacturing technology, due to its unique freedom of part geometry design, allows fabrication of these geometrically complex parts as a single unit. This draws great interest from the industry to develop AM to

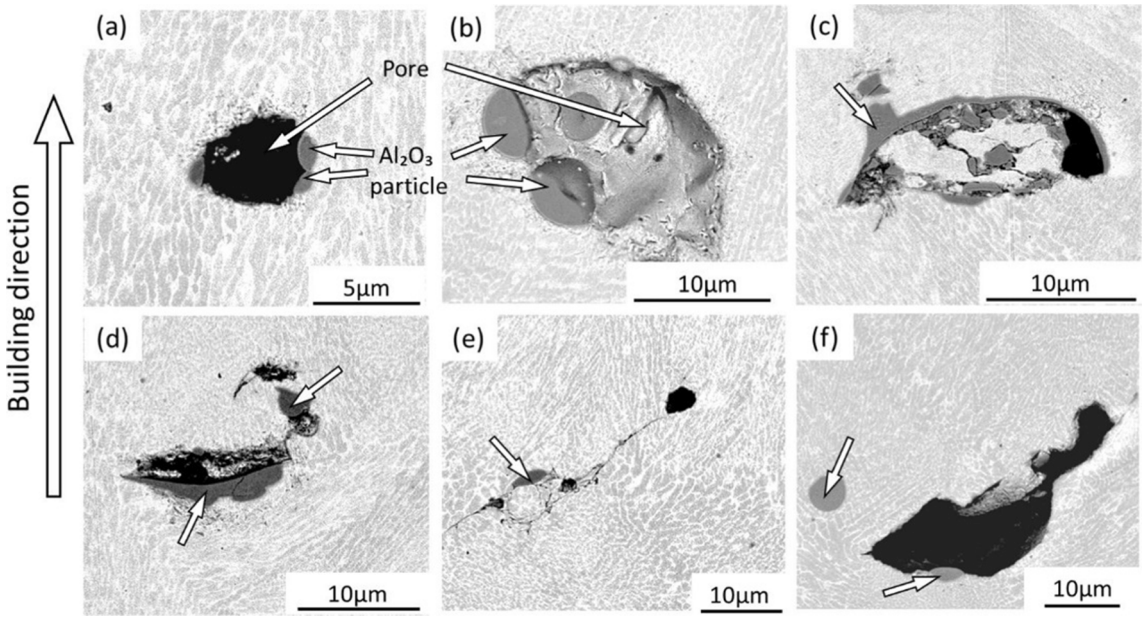

Fig. 32. Defects associated with oxide formation in AlSi10Mg part fabricated using laser powder bed fusion process. Reprinted with permission from Ref. [494].

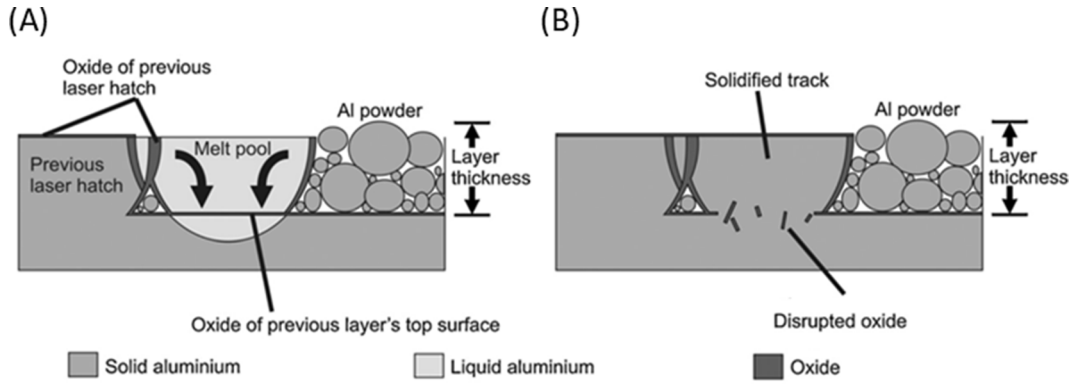

Fig. 33. Schematics of oxide formation in melt pools of aluminum alloy. Reprinted with permission from Ref. [490].

fabricate ferrous alloy components for the above applications.

Simonelli *et al.* [515] compared the microstructure of feedstock stainless steel 316L and laser spatter particle. Both particles showed austenitic phase structure, however, grains were finer with irregular morphology in the feedstock powder compared to that of the spatter particle with coarse, equiaxed grains. Besides, some extent of grain boundary segregation of Cr, Mo, and Mn elements were observed. Further, elemental analysis taken from the surface of the spattered powder confirmed oxide formation (mostly enriched in Mn, Si, and O elements).

For iron-based alloy processing, laser-based additive manufacturing is commonly selected, while much less effort has been made to explore the qualification of electron-beam additive manufacturing [516]. For ferrous alloy, its phase transition under AM processing conditions usually deviates from that under conventional processing conditions, resulting in significant microstructural differences between AM-processed ferrous alloy and their conventionally processed counterparts. Yu *et al.* [177] showed that for L-PBF -processed 304 stainless steel, high-temperature ferrite to austenite phase transition was partially suppressed due to the high cooling rate of L-PBF solidification. As a result, the high-temperature (delta) ferrite phase was retained in an austenite matrix in the as-built microstructure. Yu *et al.* [177] also reported the strengthening effect of the retained high-temperature ferrite phase. Here, the repeated heating cycle of AM processing conditions results in heterogeneous microstructure unexpected from that of conventionally processed ones. Chen *et al.* [517] showed that for L-PBF processed H13 tool steel, the martensitic microstructure was observed with different size scales and morphologies at the top, center, and bottom regions of each melt pool. This heterogeneous microstructure led to inferior ductility for the L-PBF-processed H13 tool steel compared to conventional-processed ones.

The influence of AM process parameters on microstructures and properties of Fe-based alloy have been investigated by abundant research, particularly in the effects of process parameters including laser power [517], scan speed [518], preheat temperature [519,520], build orientation [521], laser scan pattern [522] and hatch spacing [519]. Miranda *et al.* [523] developed six models to predict the hardness and shear strength of 316L stainless steel produced by L-PBF-AM with different laser power, scan speed, and hatch spacing. The models were developed by ANOVA statistical analysis to determine the main factors and the relationship between input (AM process parameter) and output (steel properties), which could be utilized as a design tool for AM process optimization with ferrous alloy. Besides, composition modifications by nano carbide and oxide addition have been observed to enhance properties of AM-processed Fe-based alloy [57,521,524,525]. Different property enhancement mechanisms were reported for ferrous alloy

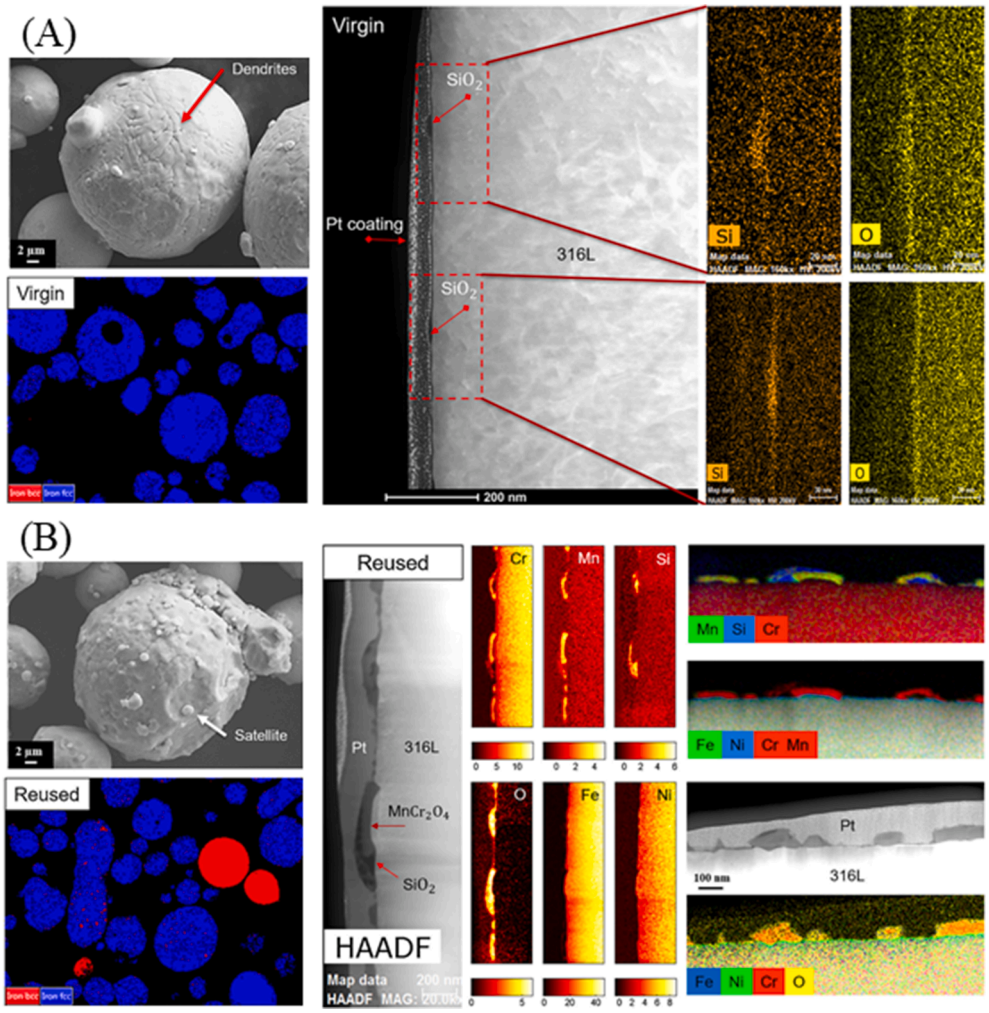

Fig. 34. A comparison between (A) virgin and (B) recycled or reused stainless steel 316L powder. Scanning electron micrograph (SEM), electron backscattered phase map (EBSD), and transmission electron microscopy images including elemental analysis results were presented for each powder type. Reprinted with permission from Ref. [355].

modified by different types of nano-particles, including laser absorptivity enhancement, grain refinement, grain boundary strengthening, and solid solution strengthening.

AM process not only affects the microstructure of the AM part but also changes powder characteristics. Heiden *et al.* [355] carried out a detailed analysis of the virgin and recycled 316L stainless steel powder (Fig. 34). It was shown that the virgin powder had dendritic morphology on the powder surface while it disappeared in the recycled particle in which submicron satellites (due to spatter powder or fused particles) stick to the coarse powder. In addition, the oxygen content was increased in the recycled powder and a mixture of SiO_2 and $MnCr_2O_4$ was formed for recycled particles. Since various cooling rates occur during the AM processes, new phases such as ferrite or martensite may form in recycled steel powder. Galicki *et al.* [526] showed that the L-PBF of stainless steel 316 picked up 0.1 wt% oxygen compared to that of the virgin powder with 0.033 wt% oxygen content.

3.3. Surface contamination and oxidation

Generally, oxide formation on the powder particles may affect AM processes since the melting and melt pool stability are affected by the presence of surface oxide layer in powders. Since the oxygen concentration is higher in L-PBF compared to that of the E-PBF, the high local temperature at the fusion area will likely trigger the formation of an oxide layer on powder surfaces. When the formed oxide layer is thin (in the nanometer size range in titanium and stainless steel), it has an insignificant impact on the melt pool formation. It is associated with laser-powder interaction and Marangoni flow in which the thin oxide layer is disrupted and stirred in the melt pool [515,527]. In contrast, a thick oxide layer cannot be disrupted during the PBF process and any oxide residue deteriorates the melting and stability of the melt pool. In other words, oxide residues lower the wettability between melt and substrate, thus induce balling, or bead-up occurs, leading to a rough surface of the as-built AM parts. Higher oxygen and sulfur in water atomized powder compared to the gas atomized powder was reported to negatively affect the melt pool dynamics [528]. Those impurities would alter the surface tension and the Marangoni flow in the melt pool, leading to a higher amount of oxygen in the water atomized powder could result in frequent spatter ejection.

Recently, Leung *et al.* [330] conducted an *in situ* x-ray imaging to understand the influence of powder oxidation on defect formation in the L-PBF AM process. Laser-powder interaction and melt pool evolution were compared for virgin and oxidized powders (Fig. 35). No gas porosity was evident in the single-track melt pool. At the same time, spattered powders (spherical morphology, Fig. 35C) ejected from the same direction as the gas flow and scan direction [43,330,529]. If any pores form in the melt pool, they may burst during solidification via pore coalescence and pore migration [43]. In contrast, different laser-powder interaction was seen when oxidized powders were used. A few gas pores (with counterclockwise rotation in melt pool and size <250 μm) and

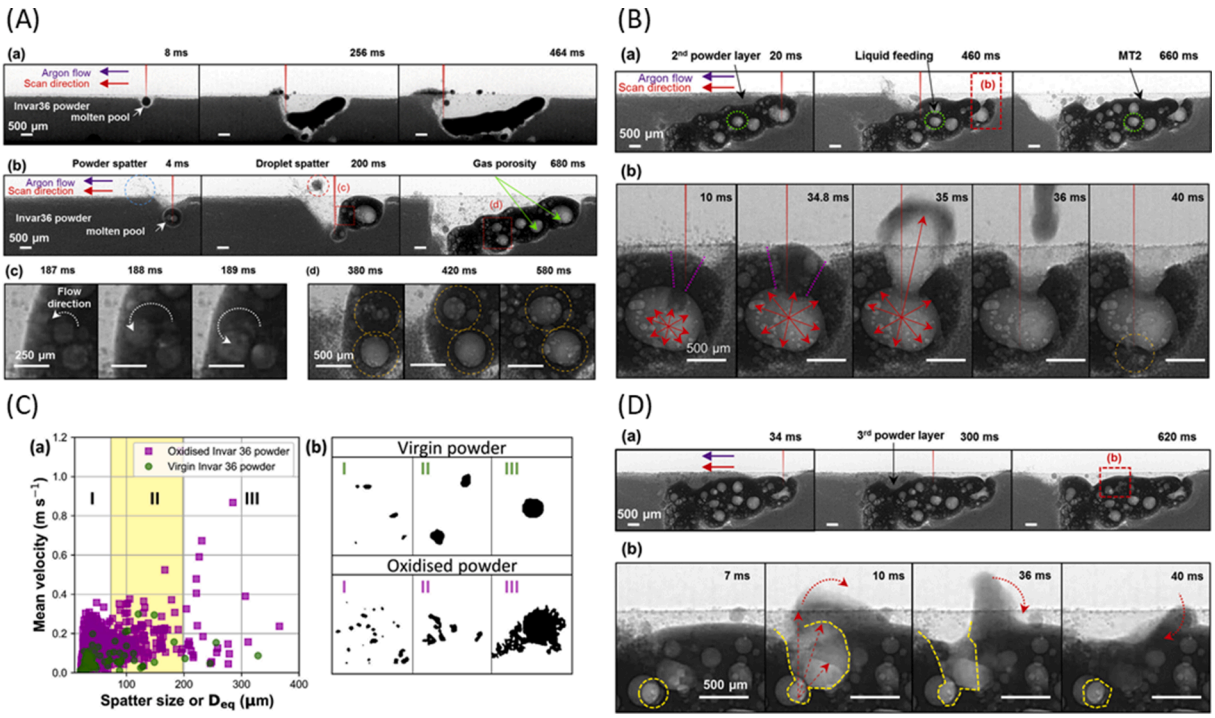

Fig. 35. Time-series radiographs results: (A) deposition of the first layer from virgin and oxide powders revealing defect-free and porous melt pool formation in which pore coarsening was visible during melt pool formation from oxide powder, (B) analysis illustrating size vs. velocity of the spattered particles and their morphology, (C) deposition of the second layer showing the formation of an open pore, and (D) deposition of the third layer revealing a pore healing mechanism due to the high surface tension of the molten pool causing the ejected spatter falls back to melt pool and heal the pore. A detailed explanation can be found in. Reprinted with permission from Ref. [330].

pores surrounded by oxide layers (with size ranges from 50 μm to 500 μm) were generated in the first printed layer. Typically, large pores (the later ones) grow by consuming gas pores with a final size of >350 μm. Also, droplet spatters (irregular shaped and formed from agglomerated powder or droplet spatter covered by agglomerated powder (Fig. 35C) were formed ahead of the laser beam. A negative temperature coefficient of surface tension was reported for liquid metals [530]. Centrifugal Marangoni convection occurs in the melt pool, while it is affected when oxygen concentration is above 50 ppm. In other words, the temperature coefficient of surface tension is changed from negative to positive (for the oxidized powder with 3430 ppm oxygen), leading to altering the Marangoni convection from centrifugal to centripetal [531] and the oxide might act as nucleation sites for pore formation. During printing the next layers, it is possible that laser re-melting of the previously deposited layer occurs, disrupting the oxide layers within the prior melt tracks and enabling entrapped gases to escape into the atmosphere via keyholing. Additionally, the size of pre-existing pores might be reduced, or they are partially filled by liquid feeding, which may result in irregularly shaped pore formation (Fig. 35B, D).

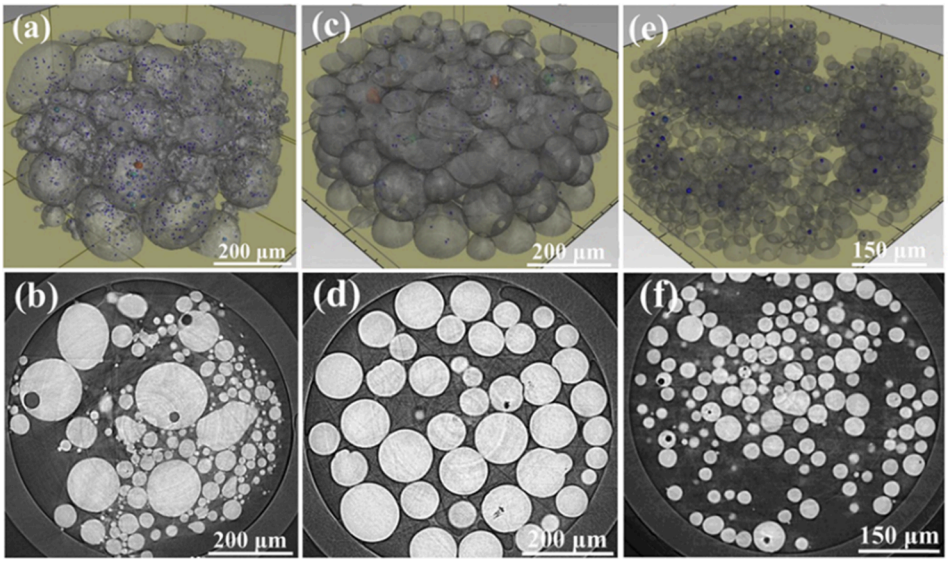

Fig. 36. 3D μCT reconstructions and cross-sectional micrographs of Ti-6Al-4V powders of: (a,b) gas atomized (GA) powder, (c,d) plasma rotating electrode process (PREP) powder, and (e,f) plasma atomized (PA) powder. Reprinted with permission from Ref. [350].

3.4. Gas pore transfer

Trapped gas from powder feedstock. Rapidly solidified powders produced in inert gas (e.g., argon or nitrogen) environments generally contain entrapped inert gas at levels on the order of several atomic parts per million [351,385,532,533]. Powder production techniques were experimentally shown to affect the amount and characteristics of the entrapped gas using x-ray imaging techniques. The majority of the powder feedstock used in powder-based fusion AM processes are produced via gas atomization (see Section 3.1), however, other methods such as plasma rotating electrode process (PREP) and plasma atomization (PA) have been also used. Using XCT, Chen *et al.* [350] compared three types of spherical Ti-6Al-4V powders: gas atomization (GA), plasma rotating electrode processed (PREP), and plasma atomization (PA), Fig. 36. Porosity and argon gas content, in particular, were analyzed for the three separate powder manufacturing methods. Overall, it was found that the powder particle size plays a crucial role in the amount of entrapped gas porosity and argon gas content within the atomized powders. The experimental results showed that argon content and porosity within the atomized powders increased with increasing particle size for each type of powders. Consequently, the pore population, size, and overall porosity values within the powders increased with the increasing particle size. Powders manufactured using GA and PA exhibit relatively higher pore sphericity than that of powders manufactured using PREP due to different gas pressures inside of powders. Notably, powders manufactured using PREP that are below 150 μm in size achieved the lowest porosity and argon content, while the powders manufactured using GA yielded the highest values. The reveal of the existence of trapped gas in metal powder stock is crucial to the study of the generation of pores in AM parts. Cunningham *et al.* [28] found that pore size in L-PBF of Ti-6Al-4V was similar to that of the gas pore in the feedstock. Anderson *et al.* [385] also compared different types of materials and powder production methods. In general, gas atomized powders offer the widest range of materials (Ni, Co, Fe, Ti, Al); however other methods such as PA or PREP may result in lower porosity but are only presently available for select alloys, e.g., Ti.

Tammas-Williams *et al.* [134] investigated powder porosity transfer during E-PBF of Ti-6Al-4V XCT. Using standard build parameters sets, the vast majority of discovered defects were small, spherical pores that were identified both in the powder and as-built samples and attributed to initial powder (gas) porosity. The pores were believed to predominately originate from argon contamination in the powder with smaller gas bubbles trapped in powder particles expanding and coalescing in the melt pool due to the reduced pressure in the build chamber [134,534]. They showed that larger melt pools gave the gas pores more opportunity to escape; therefore, minor changes in melt strategy or processing parameter selection could result in significant reductions in pore population (<0.2%). Gas pores were not randomly distributed and strong links between pore size distributions and laser beam scanning/control strategies were determined. Specifically, the mean equivalent diameter for porosity in the center (hatch) sections was about 1.4 times the mean equivalent diameter of pores in the edge (contour) sections, and 1.6 times the pore size measured in the powder. As in [174], gas pores were found to have their largest axis strongly orientated in the x–y plane, with no preferential alignment in the z-plane (orthogonal) direction.

In other material systems, less work has investigated trapped gas transferability in an effort toward suppressing internal porosity. Aboulkhair *et al.* [23] analyzed trapped gas porosity in L-PBF AlSi10Mg

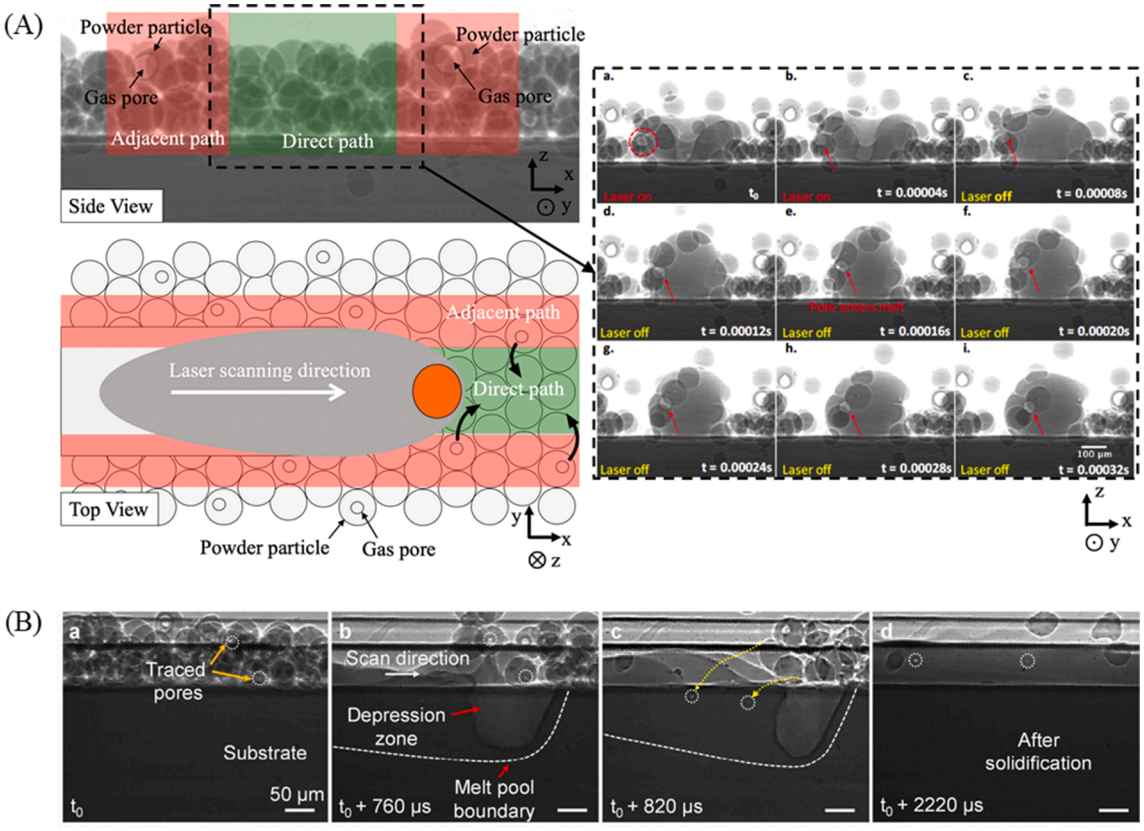

Fig. 37. (A) Schematic (left) and time sequence (a-i) showing the transfer of entrapped gas porosity from powder particles adjacent to the laser scan path into the melt pool. Reprinted with permission from Ref. [132]. (a) A powder particle containing a gas bubble (circled in red) located adjacent to the laser beam is pulled into the melt pool (b-c). (d) Once inside, the entrapped gas bubble may exit or remain within the melt pool, depending on the action of the laser beam (e-i). Reprinted with permission from Ref. [19]. (B) Pore formation from feedstock Ti-6Al-4V powders. Reprinted with permission from Ref. [537]. DXR images illustrating the transfer of pores from the powder bed into the melt pool, then, residing in the solidified track during the L-PBF process.

in which noticeable porosity was discovered within individual powder particles. The entrapped gas porosity was described as "metallurgical pores", namely small, spherical, hydrogen pores that are <100 μm in size. It was shown that a portion of porosity within the test cubes was generated at slow scanning speeds from gases trapped within the melt pool or evolved from the powder during consolidation. However, the specific powder production methods utilized in this study were not provided; thus, it is unclear how the pores were generated during powder production, and the specific mechanisms enabling their entrance into the melt pool.

Recent reports have focused on investigating the mechanisms of transfer for trapped gas porosity from powders to the as-built materials using x-ray techniques, in particular for Ti-6Al-4V materials [81,98,134,154,535,536]. Fig. 37 shows the mechanism of gas pore transfer to the melt pool during the laser powder interaction captured via ultrafast DXR scanning of Ti-6Al-4V utilizing a stationary laser [132]. In Fig. 37(A, a), a powder particle containing a gas bubble (circled in red) is located adjacent to the laser beam and pulled into the melt pool Fig. 37(A, b-c). Once inside, the entrapped gas bubble may exit or remain within the melt pool due to the competition between Marangoni convection and buoyancy forces Fig. 37(A, d-i). For the Ti-6Al-4V test blocks within the process window, it is deduced that the small-scale defects present within the μSXCT are indeed gas porosity.

Trapped gases during Solidification. Gas porosity is dependent on both processing parameters and melt pool dynamics. Typically, the floatation of gas bubbles (pores) within the melt pool is governed by buoyancy forces and Marangoni-driven flow. The Marangoni force (the spatial gradient of the surface tension resulting in a downward or upward force [538]) is determined to be approximately five times greater than the buoyancy forces (floatation of the air bubble), thereby driving bubbles to the bottom of the melt pool and resulting in porosity after solidification takes place [539]. These pores are known as keyhole induced pores which are discussed in Section 4.4). For metal AM powders, in particular, Anderson *et al.* [385] provide a detailed review of powders produced using atomization methods. Herein, multiple studies showed that large, internal porosities (pore diameter > 10–90% of powder diameter) resultant from trapped atomization gas were the most prevalent in larger sized powders (diameter > 70 μm); this behavior confirms the observations made by Rabin *et al.* [351]. Anderson *et al.* [385] noted that "micro porosity" (pore diameter ≪ 5% of powder diameter) may also be commonly present in metal AM parts due to trapped interdendritic solidification and are strongly related to the alloy's "mushy" zone range (the zone where both liquid and solid coexist). These are more apparent in coarser powders due to the slower solidification but do not typically present a problem in build microstructures.

When rapid solidification occurs, it was observed that new gas pores appeared in the weldments. In some alloys such as steel, aluminum, and titanium, the solubility of gases such as hydrogen varies with temperature [23,510,540-543]. Therefore, soluble gases in liquid metal start nucleating gas bubbles at the solid–liquid interface. This hydrogen gas may act as a source of hydroxide formation on metal powder particles (during atomization) or inclusions in the AM parts, as observed by Weingarten *et al.* in L-PBF of Al-10Si-0.5 Mg [510]. An inverse trend was reported in titanium alloys in which hydrogen solubility increases with temperature reduction [544,545]. This will matter when post-heat treatment such as hot isostatic pressing is applied to heal pores (as discussed in Section 5) [546].

4. Process-related defects and anomalies

Process-induced defects are associated with the formation of defects during the printing step. There are three main groups including (1) powder spreading dynamics and anomalies, (2) steady-state conditions for defect generation, and (3) location-specific conditions for defect formation in PBF additive manufacturing processes. The first issues occur during the powder dispensing step, where defects form on the bed of powder and bed quality such as uniformity and powder packing density, are affected. Powder characteristics play an important role in the formation of defects and voids in the bed of powder. The second and third types of defects form during laser-powder interaction. If a steady-state behavior of the vapor depression is considered in the melt pool area, three main defects may be generated such as balling, LOF, and keyhole pores which all mostly depended on the laser power and scan speed. However, the PBF AM processes necessarily contain many areas where these conditions are no longer true. Thus, other defects and issues may form under non-steady-state conditions such as powder spattering, turnaround and end of track pores, residual stress, cracking and delamination, geometrical defects, and dimensional inaccuracy, surface roughness, microstructural inhomogeneities, impurity and inclusion formation, and loss of alloying elements. In the following, the mechanism(s) of defect formation for each of these issues are explained.

4.1. Powder spreading dynamics and anomalies

Powder spreading is a critical first step in the additive manufacturing process. The powder spreading process is closely linked to the quality of the printed parts. The defects in the powder bed often translate into the defects in the printed parts due to the detrimental effects on the physical interaction between the laser beam and the powder bed [131,159]. The density of the powder bed also affects the quality of the printing layer with denser layers making fusion steadier and more continuous [547]. Further, sparse and discontinuous powder bed was observed to lead to defects including balling, shrinking, and porosity [547,548]. Further, irregularly shaped particles led to increased porosity in the printed parts [549]. The defects in laying of powder bed can be differentiated into five categories: (1) re-coater hopping (repeated vertical lines perpendicular to recoating direction), (2) re-coater streaking (horizontal lines parallel to the recoating direction), (3) debris, (4) super-elevation of printed parts, and (5) incomplete spreading [165]. Examples of defects are presented in Fig. 38. The powder particle shape, size, and material along with the recoating parameters such as recoating speed and the thickness of powder layer were observed to influence the density and continuity of the powder bed [547,550-552].

The mass flow rate in front of the recoater blade was observed to decrease with increasing recoating speed [550,552] which leads to better quality powder beds with lower recoating speeds [553,554]. Further, the roller type recoating mechanism was observed to perform better than the blade type recoater [554]. The mass flow rate also decreased with decreasing layer thickness [550]. Most of the particles were pushed out of the powder bed if the layer thickness was smaller than the mean particle size resulting in large empty patches [555,556]. The empty patches were caused by the jamming of the particles in front of the recoater blade [556]. Further, for larger layer thicknesses, short feed defects were observed in the powder layer [91]. For optimal layer quality, the nominal layer thickness of two to three times the maximum powder particle diameter is recommended [557].

There are a few experimental observations of the powder spreading process and subsequent quality of the powder bed. Chen *et al.* measured the packing density in the spread powder bed to verify their numerical model [547]. Escano *et al.* [558] used a high-speed x-ray imaging technique to observe the spreading process in a miniaturized machine. The schematic of the experiment is presented in Fig. 39(A). A representative x-ray image sequence from the spreading experiment is presented in Fig. 39(B). The *in situ* observation showed that the larger particles tend to move faster into the powder bed and smaller particles tend to agglomerate to form clusters that hinder the spreading process. Although the spreading process is a critical first step in ensuring the quality of the AM parts, more investigation of the process dynamics and optimization is required.

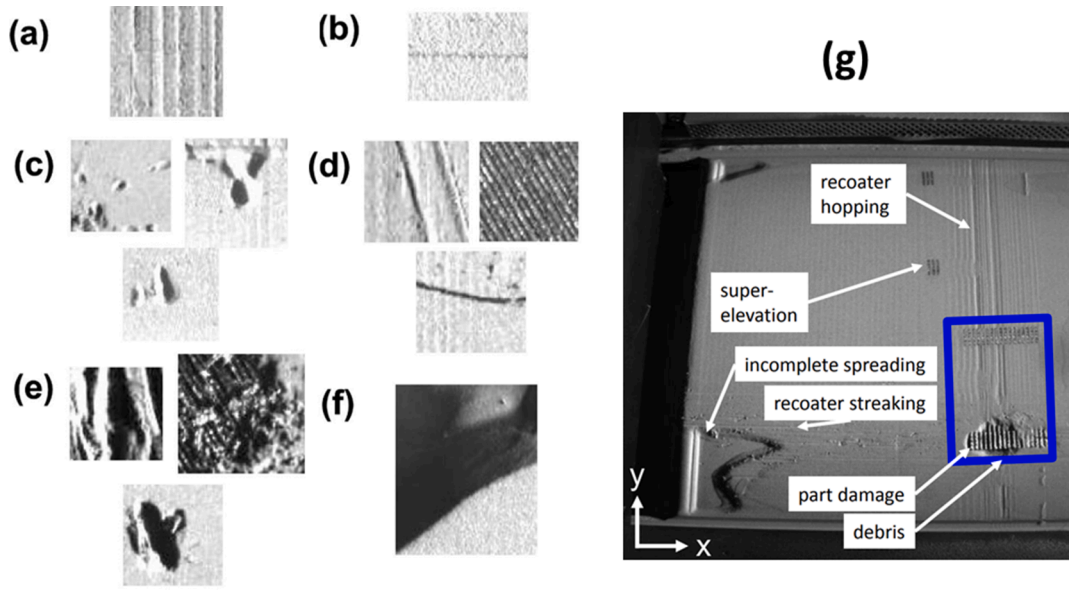

Fig. 38. Representative examples of the six different powder bed anomaly classes: (a) Recoater hopping, (b) Recoater streaking, (c) Debris, (d), Super elevation, (e) Part failure, (f) Incomplete spreading, and (g) example of powder anomalies manually annotated. Reprinted with permission from Ref. [165].

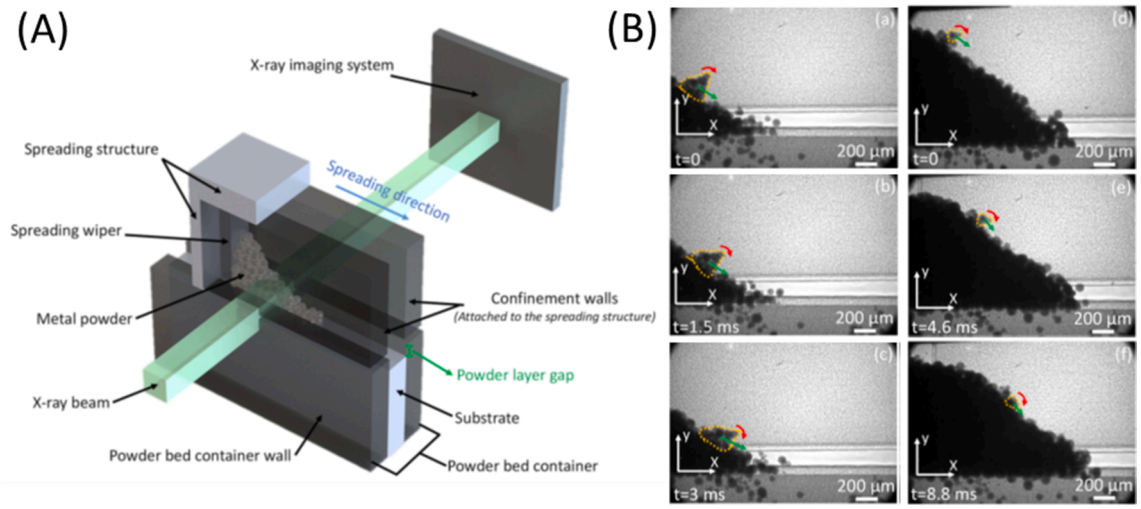

Fig. 39. (A) Schematic of the high-speed x-ray imaging setup used to observe the powder spreading process *in situ*. (B) Representative x-ray image sequence from the spreading experiment for coarse (left) and fine (right) powders. The image sequence clearly shows the formation and subsequent movement of the particle clusters formed for small particles. These clusters tend to tumble down the powder front as the bed is deposited. Reprinted with permission from Ref. [558].

4.2. Balling or bead-up

The balling phenomenon, also referred to as bead-up, is characterized by variations in height along the length of a melted track. The melt pool area (specifically the area of re-melted metal) also varies along the track length. Example images of balling melt pools are shown in Fig. 40. The undercut is also typically observed at the edges of the melt pool. This section reviews observations of balling, its proposed mechanisms of balling, and its impacts. Nearly all of the studies of balling in AM have focused on L-PBF processing. Balling is generally considered a phenomenon to be avoided because it can be a source of porosity in PBF parts. Since it tends to occur at high beam powers and travel speeds, it is a limitation on build rates in PBF.

Balling of melt pools has frequently been observed over many different L-PBF machines and process variable combinations [559-562] as well as in modeling studies [563,564]. An example of some observations for 316L stainless steel is shown in Fig. 41. Balling has been observed in multiple materials systems: 316L stainless steel [563-566], 904L stainless steel [567], AlSi10Mg [568], Al-Cu-Mg [569], Ti-6Al-4V [83], Ti-6Al-4V plus B [570]. Based on the variety of ranges indicated in Fig. 41, defining balling by beam power and velocity limits alone may not be possible. Other process variables like beam spot size, and material-dependent parameters like absorptivity, are relevant. This was demonstrated by Francis [85], who used spot size adjustments to modify the beam power and velocity combinations at which balling was observed in Ti-6Al-4V and 17–4 PH stainless steel. Other AM-related parameters that influence balling occurrence include hatch spacing [569], powder layer thickness [562], laser pulse frequency [142], powder particle size [571]. A beneficial effect of adding a deoxidizer to the powder has also been observed [562].

Many mechanisms have been advanced to explain the occurrence of balling and some of the aforementioned dependencies on process variables. At lower powers or higher layer thickness, complete melting does not occur. Instead, the melt pool is a solid–liquid mixture with high

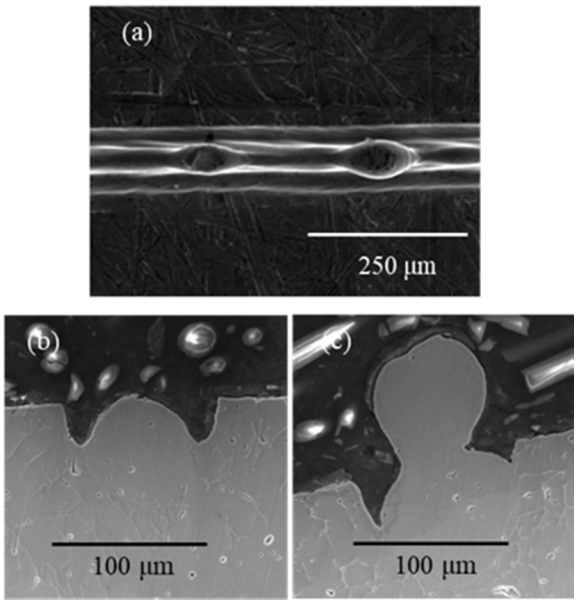

Fig. 40. Melt pool geometry variations when balling occurs (a) top view of laser track, (b) and (c) are two melt pool cross sections showing variability in height at different locations along the track length Melt pools were made melting one layer of 316L powder.

viscosity and poor wettability. As the laser beam moves, the solid–liquid mixtures formed at each irradiation zone tend to aggregate into a string of unconnected balls with a diameter similar to the laser beam diameter along the laser scan direction [562,572].

If the melt pool is fully molten, then the most common proposed mechanism for balling is the Plateau-Rayleigh (P-R) instability. The P-R instability occurs because a cylindrical column of liquid is an unstable shape due to its surface tension [573]. The surface tension drives the break-up of the column into droplets whose total surface area is lower than that of the column. Analysis of a small perturbation to the column shows that any axisymmetric perturbation will become stable if the perturbation wavelength is greater than the circumference of the cylinder. Mathematically, a perturbation is stable if $\lambda/2R > \pi$ (λ is the perturbation wavelength, R is the column radius).

In AM contexts, the P-R instability criterion is treated as a limit for the onset of melt pool balling, i.e. balling occurs when $L/W > \pi$ (melt pool length L is considered equal to the perturbation wavelength and melt pool width $W = 2R$). The P-R instability could explain the occurrence of balling at high power and velocity. Assuming only heat transfer by conduction (i.e., the Rosenthal solution describes heat transfer away from the melt pool), melt pool $L/W \propto \sqrt{QV}$, where Q is absorbed power and V is scan velocity. As power and velocity increase, melt pool L/W ratio increases and eventually balling occurs.

Applying the P-R criterion for L/W to L-PBF melt pools requires that one treats the liquid metal pool as a cylindrical column of fluid, ignoring any contact between the liquid pool and the underlying substrate. Yadroitsev *et al.* [560] attempted to account for this contact with a modified P-R stability criterion for a supported cylinder. Their supported cylinder criterion depends on the area of contact between the melt pool and the underlying substrate. If the worst case is assumed (there is only a line of contact between the circular melt pool and substrate), the criterion for balling would be $L/W > \pi\sqrt{3/2}$. This criterion then predicts the onset of balling at higher L/W values than the cylindrical column P-R criterion. Yadroitsev *et al.* [560] presented several results from steels and a CoCr that supported their criterion. However, for all of their build parameters except one, no balling was predicted, and it was not clear if balling occurred in the one exception. Additional work is needed to more fully test the stability criteria to assess if they are truly predictive of the onset of balling.

When balling occurs, the amount of solidified metal within a scan track varies along the track length. At some points, the solidified material is elevated above the surface of the bulk part. These two aspects of balling can lead to increased surface roughness [575] and porosity [23,85,574,576,577]. Balling-induced porosity and its formation mechanism are shown in Fig. 42, as observed by Li *et al.* [574] for 316L

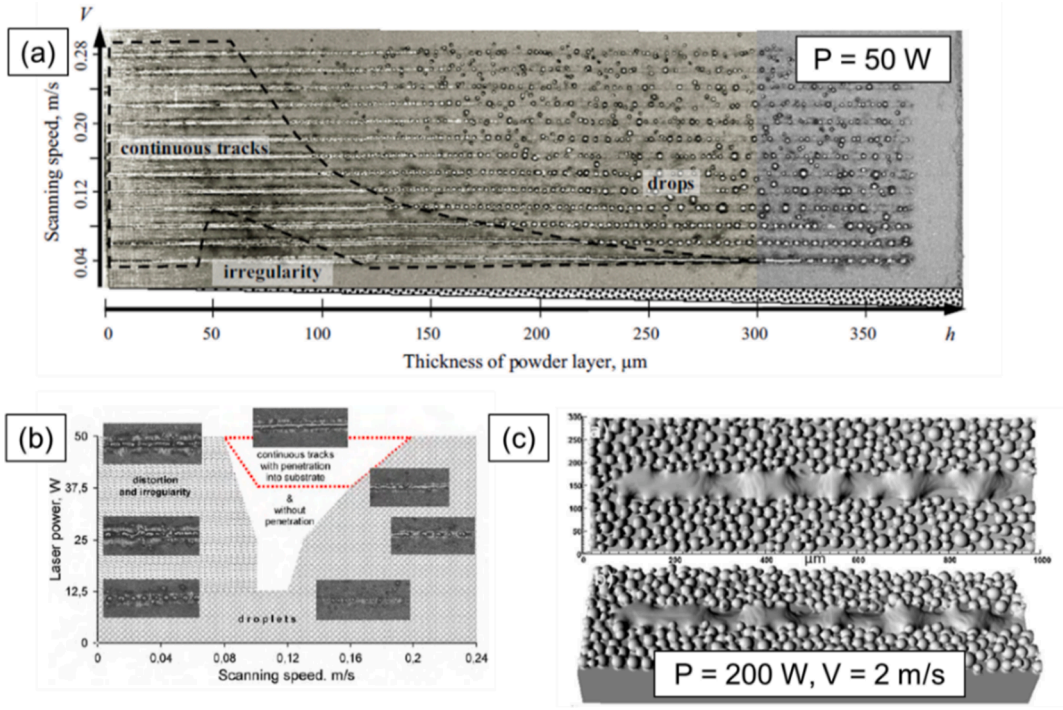

Fig. 41. Observations of balling in 316L stainless steel. (a) Effects of scanning speed and powder layer thickness. Reprinted with permission from Ref. [565]. (b) Effects of laser power and scanning speed. Reprinted with permission from Ref. [565]. (c) Multi-physics modeling results. Reprinted with permission from Ref. [564].

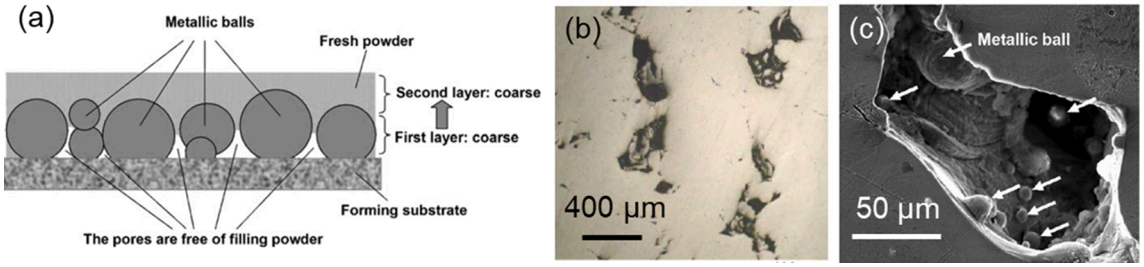

Fig. 42. (a) Schematic showing the mechanism for porosity induced by balling. Influence of balling phenomenon on part porosity where 316L stainless steel samples were built with (b) 190 W, 0.3 mm/s (balling), and (c) is a high magnification micrograph of the pore. Reprinted with permission from Ref. [574].

stainless steel.

Given it can be a source of porosity, the occurrence of balling represents a limit to building rates. This is because the spatial resolution of features is determined by the melt pool area. Assuming again only conduction heat transfer as an approximation, $A \propto Q/V$. Increasing build rates requires increasing velocity, but power must also increase to ensure constant melt pool areas and spatial resolution. However as noted above, balling occurs at high values of Q and V. There is much more work to be performed to describe the fundamentals of balling and to explore potential mitigation strategies.

The balling phenomenon in AM is similar to a phenomenon called "humping" in the welding literature. Observations of the humping defect during automatic gas tungsten arc welding (GTAW) were first made by Bradstreet in 1968 [578]. That work suggested the cylindrical P-R instability criterion. It also identified that oxygen in the shield gas or oxide on the plate surface promotes the occurrence of humping. There have been numerous theories advanced to explain the humping phenomenon in arc welding, including the cylindrical P-R instability [578], a supported cylinder P-R instability [31,579], Marangoni flow [580], arc pressure, and the forces on the fluid in the melt pool [29,581-583], and a Kelvin-Helmholtz fluid flow instability [584].

Humping has also been observed in electron beam welding [585], and laser welding [31]. Particularly in laser welding, the effect of the keyhole vapor cavity and fluid flow around this vapor cavity has been a common focus [586-591]. Recent dynamic x-ray radiography and modeling results have shown the effect of keyhole vapor cavities on AM melt pool fluid flow [25]. The radiography results also revealed vapor cavities are present even when build parameters are not in the keyholing regime. The potential influence of these vapor cavities and the effect of melt pool fluid flow on balling requires further investigation.

4.3. Lack of fusion

As one of the most common microstructural defects in laser powder bed fusion additive manufacturing, LOF porosity could act as cracking initiation points and greatly reduce the fatigue life of the printed part [32,47,592]. As shown in Fig. 43, unlike the gas entrapped pores which are often spherical, they are rather large, irregular, or elongated, and may have some un-melted particles inside [23,32,98,593]. Fundamentally, the LOF porosity formation is caused by insufficient penetration of the melt pool of an upper layer into the previously deposited layer or of a single track into the neighboring track on the same layer [23,98,594]. According to the dominant factors, lack of fusion porosity could be classified into laser processing induced porosity, unfavorable powder induced porosity, etc.

Insufficient overlap between melt pools. The formation of LOF porosity can fundamentally be attributed to the insufficient overlap of the melt pools and, thus, is closely related to the geometry of the melt pool [23,98,594]. In laser powder bed fusion additive manufacturing, the melt pool shape is influenced by both laser processing conditions and powder characteristics. For simplicity here, the melt pool shape is considered to be invariant although the variability of melt pool size [595] will locally decrease overlap. As shown in Fig. 44, W is the melt pool width, D is the total depth after the melting, H is the hatch spacing, and L is the layer thickness of metal powder [98]. When the hatch spacing or the layer thickness is relatively large, lack-of-fusion pores may form because of the insufficient overlap of the melt pool structure.

Based on the geometric relationships of the melt pool structure, Mukherjee *et al.* proposed a non-dimensional lack of fusion index, $LF = L/D$ [594]. When the index is larger than a threshold, LOF pores may form inside the sample. For Ti-6Al-4V, the threshold is 1.15 [594], and for CoCrMo alloy, it is ~1.5, as shown in Fig. 45(a) [596]. This lack of fusion index, however, does not account for the influence of hatch spacing. Tang *et al.* later introduced a second index to include this factor, $(H/W)^2 + (L/D)^2$, such that when the index is >1, lack of fusion pores are predicted [98]. Compared to the threshold based on the *LF* index, the Tang model is more conservative. Tang *et al.* claimed that their model can be applied to various materials such as Ti-6Al-4V, Al10SiMg, and stainless steel because it is purely geometrical, as shown in Fig. 45(b)

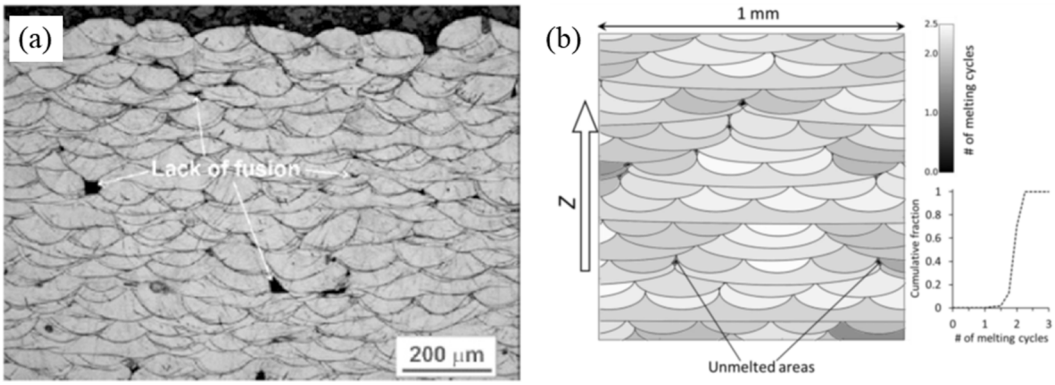

Fig. 43. Lack of fusion porosity inside the postmortem cross-section of the melt pool structure shown by an optical image after etching (reprinted with permission from Ref. [593]) and by a schematic (reprinted with permission from Ref. [98]).

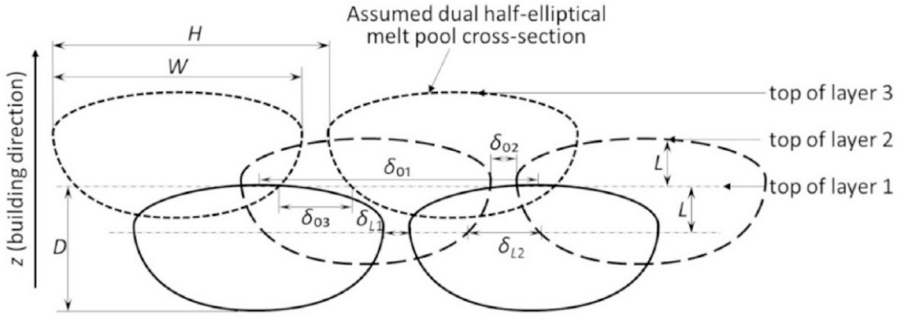

Fig. 44. Geometric relationships of the melt pool structure for lack of fusion porosity. Reprinted with permission from Ref. [98].

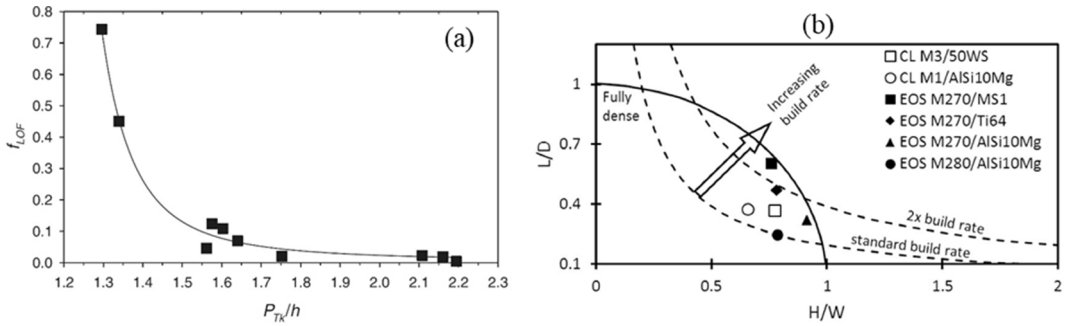

Fig. 45. (a) LOF porosity of CoCrMo alloy estimated from the optical images as a function of the ratio of penetration depth to layer thickness. Reprinted with permission from Ref. [596]. (b) Processing map of hatch spacing and layer thickness relative to melt pool dimensions. Reprinted with permission from Ref. [98].

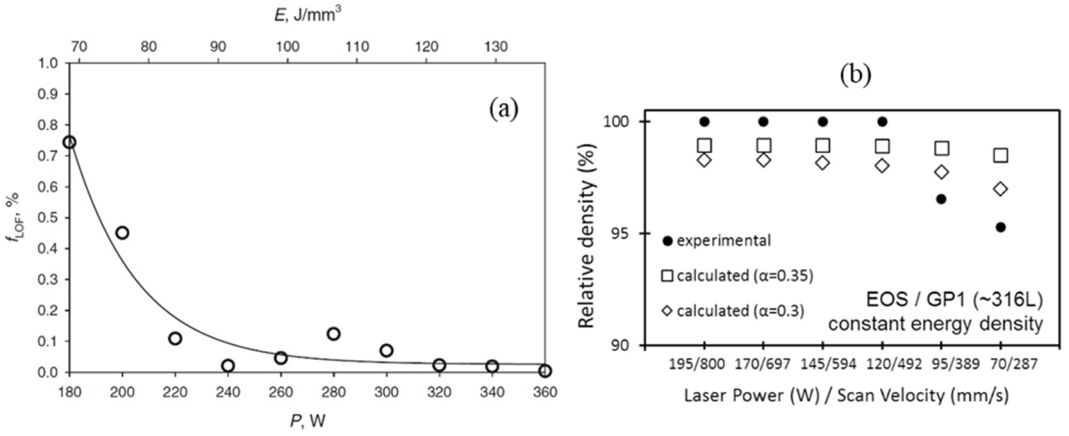

Fig. 46. (a) Lack of fusion porosity of CoCrMo alloy estimated from the optical images as a function of the laser power. Reprinted with permission from Ref. [596]. (b) Relative density of stainless steel under the same laser energy density but different laser power and scanning speed combinations. Reprinted with permission from Refs. [98,599].

[98].

Laser processing induced porosity. The melt pool structure could be changed dramatically through the laser processing conditions, e.g. laser power and scanning speed [25,26,321,597]. For example, the increase in laser power tends to result in a larger melt pool and a higher overlapping melt pool structure. As demonstrated in Fig. 46(a), the higher the laser power, the lower the fraction of lack of fusion porosity [596]. Many authors correlate the porosity of a printed part with the volumetric energy density $P/(V{\bullet}H{\bullet}L)$ [84,596,598]. However, because of the keyhole and the melt pool dynamics [25,48], even under the same volumetric energy density, the melt pool shape and dimensions vary substantially, which affects the LOF porosity, as shown in Fig. 46(b) [98,599]. Besides, for a given set of laser conditions (spot size, laser power, and scanning speed), the melt pool, as well as the keyhole inside, tends to fluctuate around a certain shape [25,26,321,595]. Cunningham *et al.* point out that these fluctuations may cause the formation of LOF porosity even in cases where the overlaps are theoretically sufficient [28]. Recently, Tenbrock *et al.* [600] showed that the laser-plume interactions may attenuate the laser absorption and cause the LOF porosity formation.

Unfavorable powder induced porosity. Unfavorable powder particles, either from the raw feedstock or from the spattering process, could be another source for LOF porosity [48,330,421,601]. For example, when the laser scans over the powder bed, some larger and irregular clusters can be generated [26,48,325,602], as shown in Fig. 47. These particles tend to have different compositions, microstructures, and morphologies from the raw feedstock [330,421,601]. When they fall back onto the powder bed, after another layer of powder spreading,

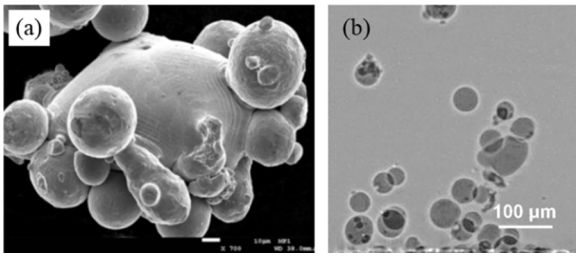

Fig. 47. Large and irregular particles under (a) a scanning electron microscope. Reprinted with permission from Ref. [601] and (b) a synchrotron x-ray imaging detector. Reprinted with permission from Ref. [48].

there might be some gaps around these unfavorable particles. When the laser melting finishes, these gaps could become LOF pores and remain inside the part. Unlike the LOF porosity induced by the laser processing conditions, the pores here are mainly dominated by the unfavorable characteristics of the powder, and thus, could be referred to powder induced LOF porosity.

4.4. Keyhole porosity

Keyhole porosity results from both stationary and scanning lasers. In the latter case, pores have been shown to form in the straight-line scan cases and more so when a laser is changing direction, hence going through a point of zero velocity. The latter case of turnaround and end-of-track porosity will be discussed in Section 4.5. In this section, the efforts to characterize pores resulting from deep keyholing will be discussed.

During the keyhole-mode melting, the material vaporizes rapidly, leading to a cavity called a vapor depression zone or a keyhole [111,539,603]. Depending on the local melt pool dynamics and solidification behavior, gas bubbles pinching-off from the keyhole may either escape or remain inside the build as entrapped keyhole porosity after solidification. It is important to note that not all keyhole mode melting activities result in keyhole porosity. Thus, the specific mechanisms behind the formation of keyhole porosity are important to illuminate (Fig. 48).

Keyhole porosity has been extensively characterized in laser welding, such as in the review article by DebRoy and David [539]. Notably, the work of Matsunawa *et al.* [111] where the authors conducted systematic studies on pulsed and continuous-wave laser welding of an Al (A5083) and 304 stainless steel alloy to reveal the mechanism of keyhole porosity formation using high-speed optical and x-ray transmission methods. X-ray transmission images taken by a high-speed video camera during CO_2 laser welding of the Al alloy in a He shield showed that the depth and shape of the keyhole fluctuated violently and large bubbles (keyhole pores) were intermittently formed mainly at the bottom of the keyhole. These keyhole pores were trapped within the melt track and frozen in the substrate as keyhole porosity. Gas analysis and SEM imaging revealed that the porosity was composed of both metal vapor and shielding gas. Interestingly, the depth and shape of the keyhole within the melt pool was also shown to change drastically with time for a constant set of processing parameters. They also described potential mitigation methods for keyhole porosity through the stabilization of the keyhole. For pulsed laser spot welding, the addition of a proper tailing pulse was very effective in suppressing the porosity formation due to the gradual decrease of the keyhole depth and the avoidance of a sudden keyhole collapse.

For metal powder bed AM, earlier studies on keyhole porosity also point to violent fluctuations of the keyhole resulting in the formation of large bubbles as observed in laser welding [26,96,604]. Much of the work in metal powder AM has focused on Ti-6Al-4V, such as work by Zhao *et al.* [26], Gong *et al.*[84], Panwisawas *et al.* [65], and Cunningham and Zhao *et al.* [25]. Zhao *et al.* [26] revealed the formation of keyhole porosity in the case of stationary laser melting as shown in Fig. 49. They presented high-speed synchrotron x-ray imaging and diffraction techniques that could be used to characterize the laser powder bed fusion process *in situ* and in real-time. Specifically, these techniques could be used to monitor pore formation, phase transformation, powder ejection with unprecedented spatial and temporal resolutions. For example, they found the time needed for the formation of a keyhole pore was <50 μs. Gong *et al.* [84] noticed that keyhole defects were directly correlated with excess energy input. Herein, near-spherical defects were discovered in the "over melting" (i.e., high power, low velocity) region of power-velocity space. The gas bubbles were formed far beneath the surface at the bottom of the melt pool. They hypothesized that the high solidification rate of the melt pool does not give the gas bubbles enough time to rise and escape from the surface, and thus, gas bubbles are trapped in the lower regions of the melt pool resulting in defect inclusion in the Ti–6Al–4 V samples. Panwisawas *et al.* [65] developed a computational fluid dynamics model based on melt flow dynamics to capture the morphological development of pores formed under different processing conditions in L-PBF. Here, process-induced porosity was determined to be dependent upon three parameters: plate thickness, laser power, and traveling speed. Porosity was found to be exacerbated by increasing plate thickness and decreasing scanning speed. Cunningham and Zhao *et al.* [25] pointed out that keyhole widely exists in L-PBF utilizing the high-speed synchrotron x-

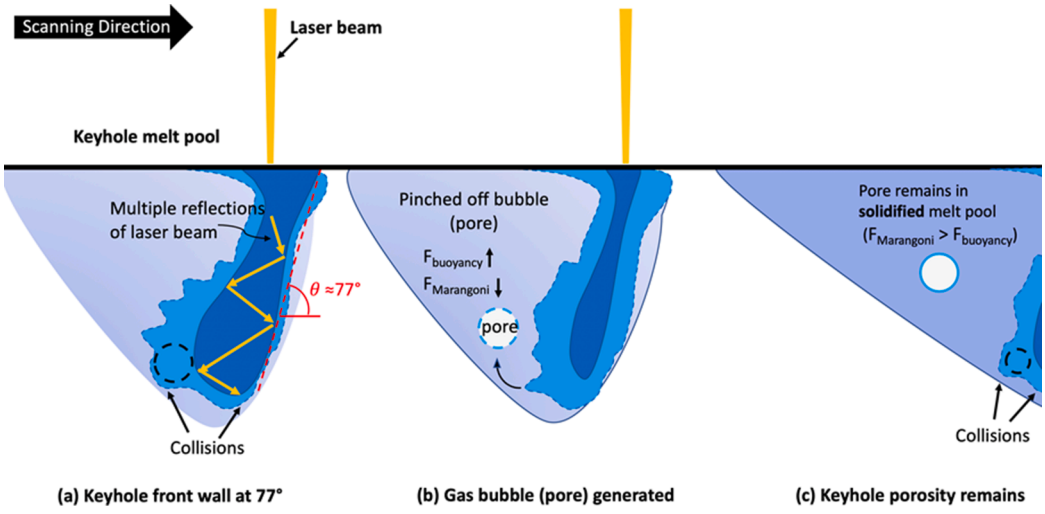

Fig. 48. A schematic showing the keyhole porosity formation mechanism in laser melting. Reprinted with permission from Ref. [19].

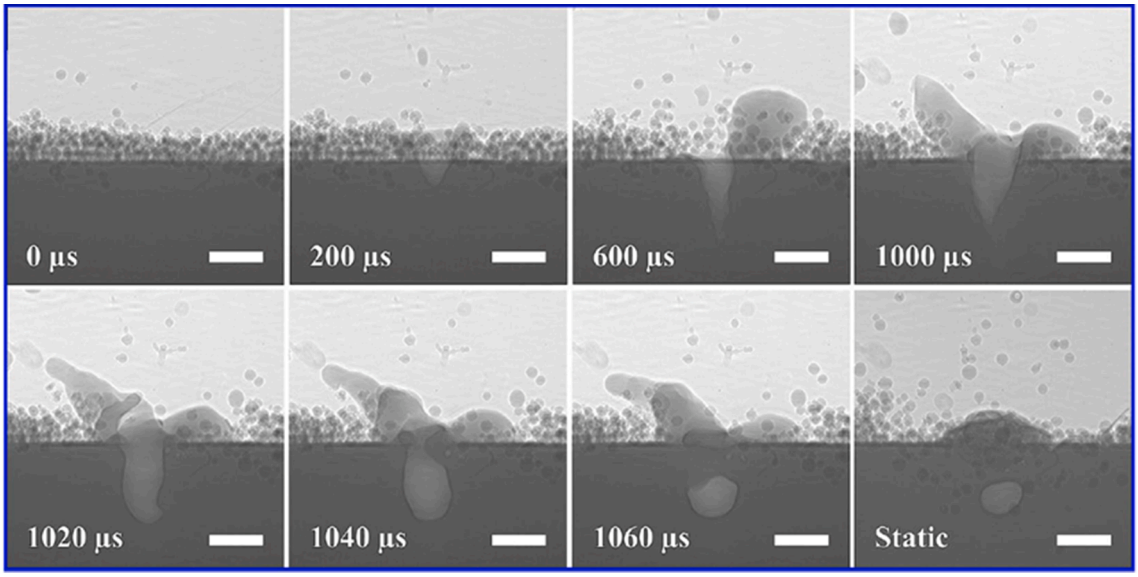

Fig. 49. Dynamic x-ray images of keyhole porosity formation in laser powder bed fusion processes of Ti-6Al-4V under a stationary laser beam. The laser is turned ON at t = 0 and continues to heat the sample till t = 1000 µs. The raw data were taken with a frame rate of 50 kHz. The exposure time for each image is 350 ns. Reprinted with permission from Ref. [26].

ray imaging technique and emphasized the importance of power density, as opposed to the various formulations of energy density. They confirmed that the collisions of the front and rear keyhole walls indeed generated pinched-off gas bubbles and that, once formed, the bubbles (likely a combination of atmospheric shielding gas and vaporized alloying elements) are ejected backward, driven by the competition between Marangoni flow and buoyancy forces.

Recently, Zhao *et al.* studied in detail the keyhole porosity problem in laser melting of Ti-6Al-4V [24]. They found that, as shown in Fig. 50, the keyhole porosity boundary in the laser power-scan velocity space is smooth and sharp, varying only slightly between bare plate and powder bed. Around the porosity boundary, they discovered a dominant mechanism for the formation of small and often spherical pores in the build, as described in Fig. 51. The formation of a keyhole pore starts from the emergence of a mini keyhole on top of a protrusion on the front keyhole rim (Fig. 51(A, E)). With the collapse of the keyhole, a pore and a microjet form (Fig. 51(B, C)). The high-speed microjet then drives the asymmetric collapse, chaotic splitting, and rapid rebound of the pore (Fig. 51(D, F)). With the help of the acoustic wave released from the pore collapse and rebound and the local recoil pressure drop as a result of the protrusion structure at the bottom of the front keyhole wall, the keyhole tip is reshaped into a narrow needle-like keyhole bottom (Fig. 51(H)). This needle-shaped bottom is unstable and undergoes rapid drilling and expansion, generating an acoustic (shock) wave in the melt pool. The wave then provides an additional yet vital driving force for the pores near the keyhole tip to rapidly migrate away from the large thermal gradient field around the keyhole (Fig. 51(I)). When the pores are captured by the advancing solidification front, they become trapped as defects in the build. Without sufficient kinetic energy from the acoustic wave, the pore remains around the keyhole and its motion is dominated by the competition between the thermocapillary and viscous drag forces. In the end, the thermocapillary force could draw the pore violently into the keyhole (Fig. 51(G)). In addition to this dominant mechanism, there exists a secondary mechanism at low power levels. The large keyhole fluctuation could create sufficient waiting time for the pore to be pinned by the solidification front. During this time window, drag forces may pull the pore away from the retracting keyhole. The work of Zhao *et al.* provides not only an in-depth understanding of keyhole pore formation under conditions relevant to additive manufacturing, but also guides AM users for optimizing process windows and building pore-free parts.

Keyhole porosity has also been investigated in other alloys such as AlSi10Mg by Aboulkhair *et al.* [23] and Thijs *et al.* [605], and 316L stainless steel by King *et al.* [96]. Aboulkhair *et al.* [23] discovered two types of porosity within the characteristic high-power, low-velocity regions of process space, namely “metallurgical” and “keyhole” pores. Metallurgical pores were described as small and spherical whereas keyhole pores were irregularly shaped and large in size (above 100 µm) and arose from unstable keyholing. Metallurgical pores are analogous to trapped gas porosity covered in earlier sections of this review article (Section 3.4). They believed that remelting (i.e., scanning each layer multiple times) was effective in reducing the keyhole pores. However, the excessive energy input during overlapping scans was shown to lead to extensive formation of gas pores at slower speeds, i.e., the elimination of keyhole pores was at the expense of introducing gas porosity [606]. Thijs *et al.* [605] characterized keyhole porosity in L-PBF AlSi10Mg at the start and end of melt tracks. It is believed to be the result of heat accumulation at those areas leading to keyhole mode melting. King *et al.* [96] investigated keyhole mode melting as a function of processing variables in single-track 316L experiments. Here, melt pool depth was observed as a function of power, laser speed, and spot size, respectively. Experimental observations using optical microscopy and XCT analysis indicated that a trail of voids in the wake of the laser beam were responsible for keyhole porosity. This was described as being due to the incomplete collapse of the vapor cavity leaving voids in the wake of the laser beam, which is consistent with the direct observations of Zhao *et al.* [24].

By determining a theoretical threshold for keyhole porosity, regions of optimum processing variables (i.e. power, speed, and beam size) can be determined to enable rapid, high-quality additively manufactured materials without keyhole porosity. In general, the two most common methods for determining such a threshold are as follows: (1) Enthalpy-based methods and (2) keyhole morphology methods.

Enthalpy-based methods. Previous investigations on the keyhole transition in laser welding involves the competing forces of surface tension acting to keep the liquid melt pool surface flat and the recoil pressure generated by the localized vaporization of the liquid metal under the laser beam when the material reaches its boiling point [115,607-610]. When the recoil pressure exceeds the surface tension then the liquid is repelled and a depression forms [611]. Studies by Hann *et al.* [607] (laser welding), King *et al.* [96] (based on the model by

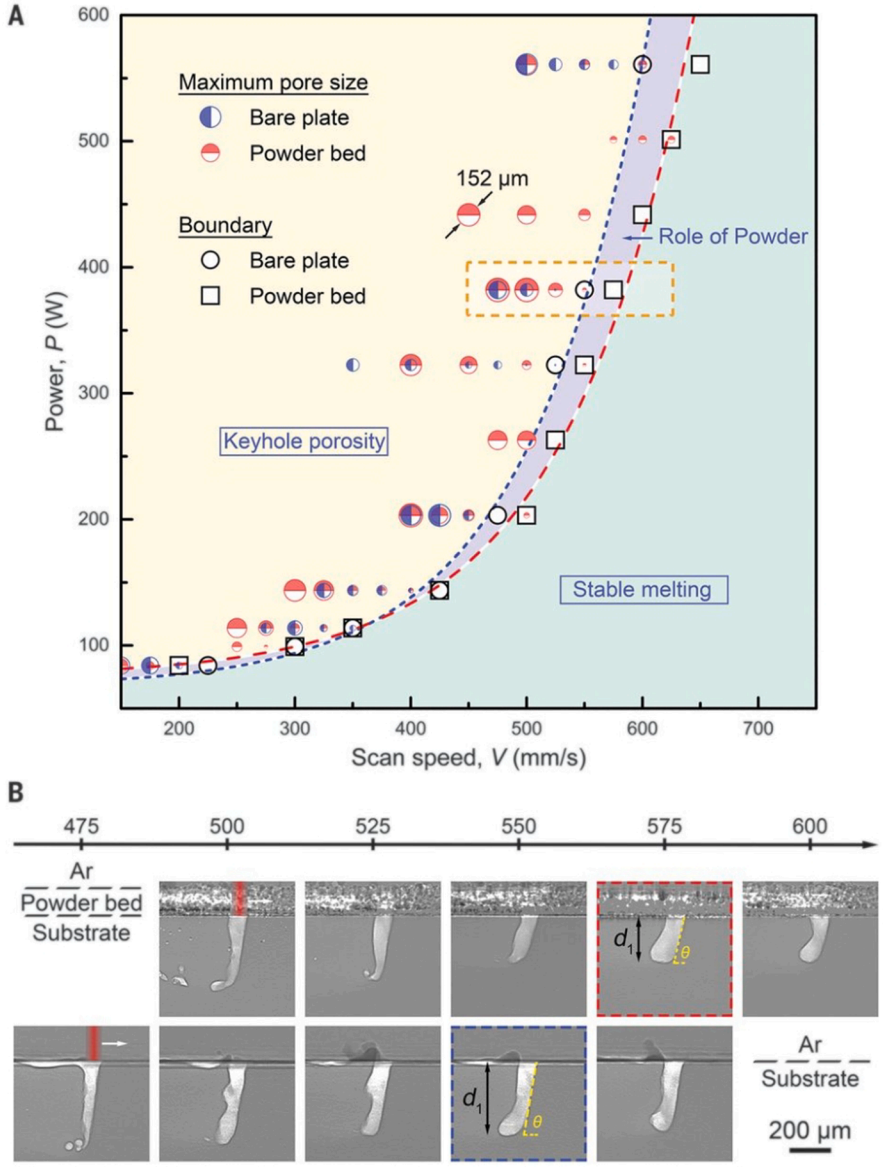

Fig. 50. Keyhole porosity boundary and role of powder in laser melting of Ti-6Al-4V. (A) Laser power-scan velocity space. The light yellow area shows the keyhole porosity regime, the light green area shows the stable melting regime, and the light purple area shows the role of powder in laser powder bed fusion additive manufacturing. Adding powder increases the instability and widens the porosity regime. (B) Representative x-ray images at a constant laser power of 382 W and varying scan speed across the porosity boundary. (Top) Powder bed samples. (Bottom) Bare plate samples. The red and blue dashed framed images correspond to the respective boundaries in scan speed. Reprinted with permission from Ref. [24].

Verhaeghe in [604]), and Kiss *et al.* [606] have predicted that the transition from conduction to keyhole occurs when the normalized enthalpy exceeds a certain value (between ~6–30) for Vanadium, 304 stainless steel, and Ti-6Al-4V. The conditions required for transition were identified as the ratio of deposited energy density (ΔH) to the enthalpy at melting (h_s). The simplified estimate for the criteria is given by King in equation (1) [96,376]:

$$\frac{\Delta H}{h_s} > \frac{T_b}{\pi T_m} \tag{1}$$

where T_b is the boiling temperature, and T_m is the melting temperature. For 316L, a theoretical normalized enthalpy ($\Delta H/h_s$) value of approximately 6–10 was estimated. However, the experimentally observed keyhole transition criterion was approximately 5 times larger ($\Delta H/h_s = 30$). The discrepancy was attributed to the fact that the keyhole mode threshold is expected to depend on powder layer thickness. Comparatively, a similar enthalpy-based model utilized by Kiss *et al.* determined the onset of void formation occurred at approximately 17 ± 8 (Fig. 52). This agreed well with the previous experimental estimate in King *et al.* using two different beam sizes, strengthening the proposition that normalized enthalpy is indeed a useful metric to compare selective laser melting under varying laser conditions and even across different materials. However, while Kiss *et al.* found that the average vapor depression depth and average void depth scale linearly with normalized enthalpy, the likelihood of void formation did not. The benefits of using enthalpy-based models are that keyhole transition behavior can be adequately estimated using material parameters and processing variables. However, these models cannot yet robustly determine the likelihood of porosity formation. This may be partly due to the complexity of melt pool dynamics such as melt pool currents, bubble splitting before solidification into clusters of smaller voids, and bubbles being formed from and then recaptured by the vapor depression leaving no voids in the final part [606]. Furthermore, these models do not account for the increasing absorptivity once a keyhole is formed, as shown for powder bed fusion 316L in Trapp *et al.* [50]. Such events complicate attempts to identify defect formation using surface sensitive process monitoring and simplified modeling tools [606].

Keyhole morphology methods. Another type of model that has shown some success in the prediction of keyhole void formation is based on keyhole morphology. This model was initially developed by Fabbro and Chouf [612] to generalize the concept of keyhole formation in laser welding. Keyhole front wall angle (θ) was determined as a function of

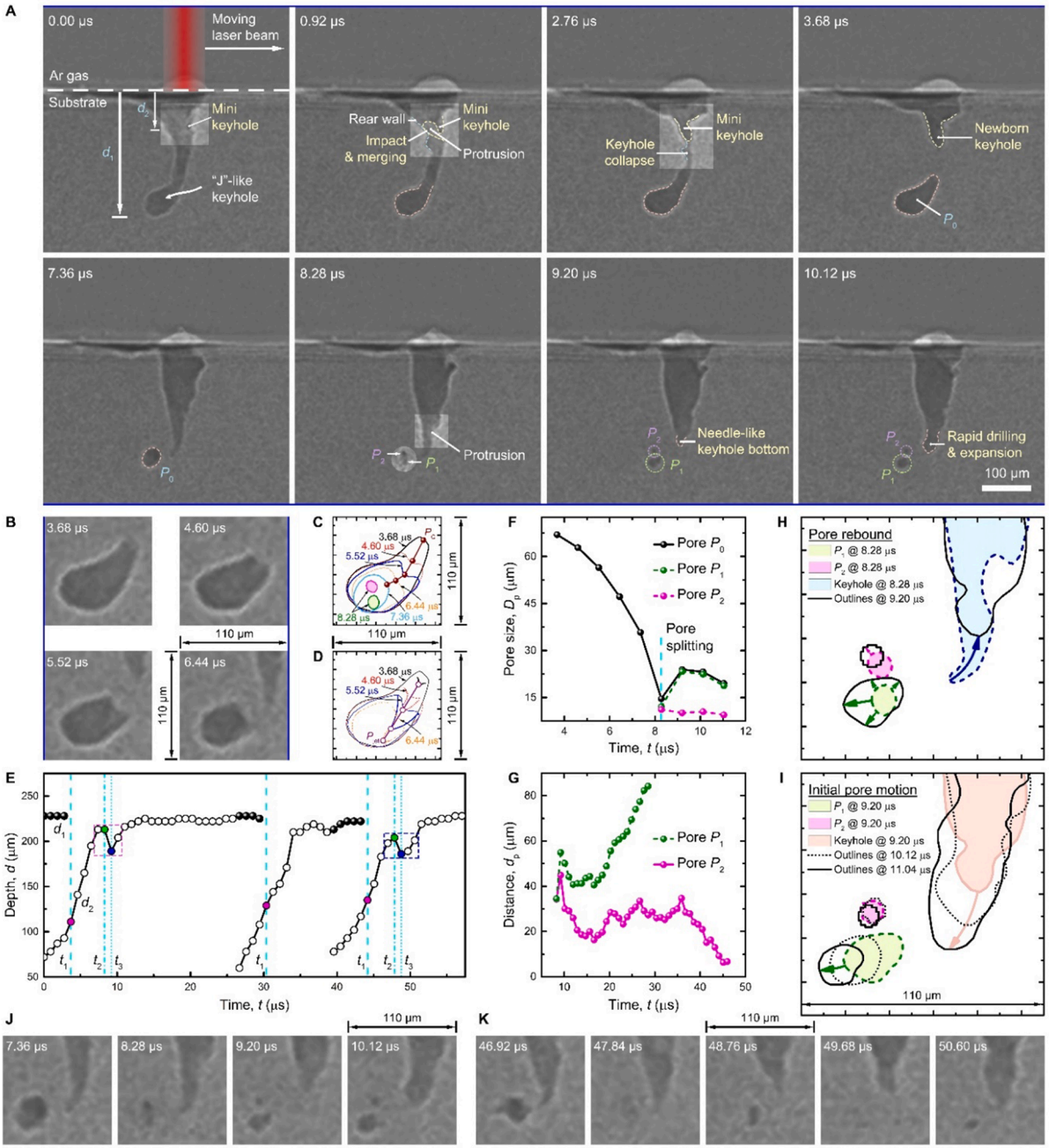

Fig. 51. Keyhole pore formation and motion driven by acoustic waves from keyhole instability. (A) MHz x-ray images of a keyhole pore formation process. (B) X-ray images showing the non-uniform collapse of pore P_0, driven by a microjet. (C and D) Contours of the pore P_0 and microjet morphologies. (E) Keyhole depths, d_1 and d_2. (F) Equivalent pore diameter, D_p. (G) Distances of pores away from the nearest keyhole wall. (H) Formation of a needle-like keyhole bottom. (I) Initial pore motions caused by the acoustic wave emitted from the needle-like keyhole bottom. L-V in (H and I) means the liquid–vapor interface of a keyhole or a pore. (J and K) X-ray images of keyhole pore collapse, rebound, and motion, corresponding to the two events highlighted by the magenta and blue dashed rectangles in (E), respectively. Reprinted with permission from Ref. [24].

both welding velocity (V_w) and drilling speed (V_d):

$$tan(\theta) = \frac{V_w}{V_d} \tag{2}$$

Furthermore, the penetration depth, d, was then used to classify melt pool morphology via:

$$d = \frac{D}{tan(\theta)} \tag{3}$$

where D is the effective laser spot size [85]. By using these equations, the relevant processing variable affecting keyhole behavior can be determined. This model was reasonably well for analyzing 304 stainless steel laser welds of different welding velocities at a laser power of 7 kW. Cunningham and Zhao *et al.* [25] investigated the keyhole morphology evolution in laser melting of Ti-6Al-4V using high-speed synchrotron x-ray imaging. They tested both bare plate and powder bed samples. Fig. 53 shows some measurement results of the keyhole morphology at various laser conditions. One of the contributions of their work is that, in stable keyholing, laser welding and powder bed fusion can be synergistically connected through the linear relationship between keyhole depth and tangent of front keyhole wall angle. Roughly speaking, when the front keyhole wall angle is >77°, keyhole porosity tends to be

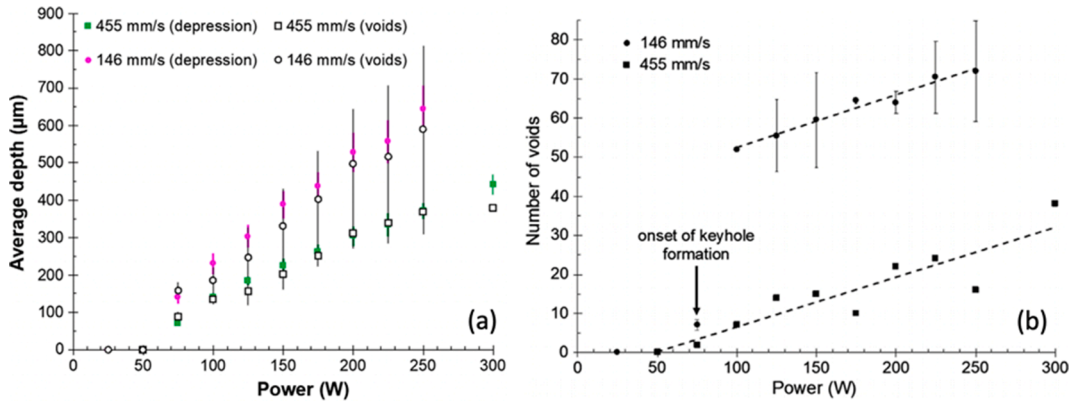

Fig. 52. Enthalpy-based models for the keyhole transition and porosity formation utilized in. (a) The average depth of the voids shows a linear trend with increasing laser power and the average vapor-depression depth. (b) Linear dependence of keyhole formation and the formation of voids with an arrow indicating the approximate location of the transition to the keyhole regime. Reprinted with permission from Ref. [606].

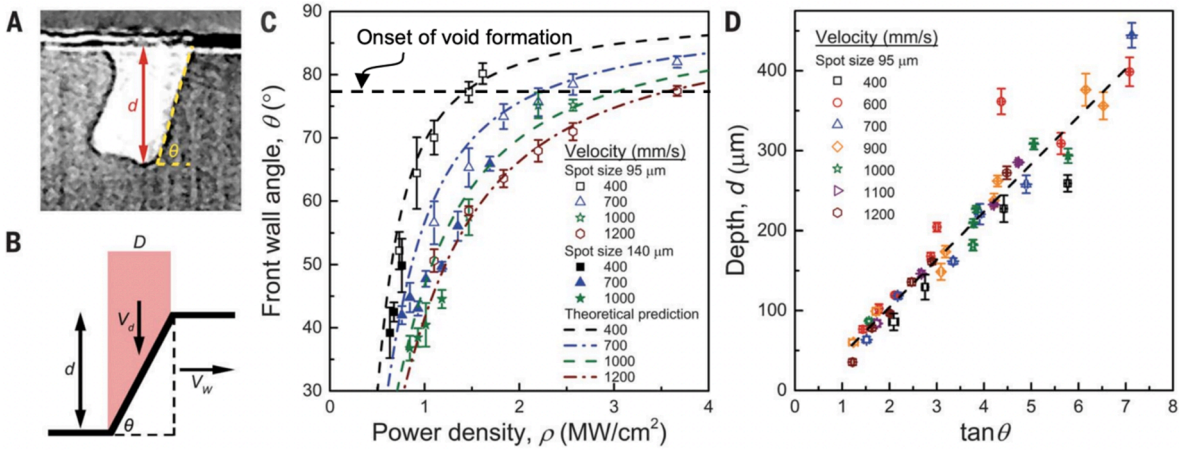

Fig. 53. Relationship between keyhole depth, front wall angle, and laser power density. Reprinted with permission from Ref. [25].

trapped inside the material.

Multiple studies from the laser melting community describe that the major part of the beam energy during keyhole-mode melting is distributed at the front wall [126,613-615]. Zhao *et al.* [126] described the action of the front wall as crucial in the formation of keyhole porosity as follows: (1) As the keyhole starts to shrink, the keyhole width becomes smaller and there is a protuberance of the keyhole wall. (2) The keyhole wall then collapses and a bubble forms at the bottom. (3) The depth of the keyhole diminishes suddenly at this point. (4) The liquid flow makes the bubble shrink and traps it in the molten pool. (5) If the bubble fails to escape from the molten pool, porosity is formed. Thus, it is sensible that a keyhole porosity criterion can be determined from melt pool morphology. The results of Cunningham and Zhao *et al.* [25] confirm that keyhole morphology plays an important role in the development of keyhole porosity. Zhao *et al.* [24] found a dominant mechanism for the keyhole porosity formation and it started from the behavior of the font keyhole wall. These results are promising. But more measurements and analyses such as the temperature distribution on the keyhole walls are needed to fully understand the keyhole porosity formation in laser melting of metals like powder bed fusion AM. This requires further advances of the monitoring techniques like the upgrade of synchrotron x-ray sources and the R&D of imaging detectors.

4.5. Turnaround and end-of-track porosity

Metal powder bed AM processes unavoidably contain areas where beam velocity and thermal conditions are no longer constant; this can result in defects via non-steady-state conditions [327,535,605,616]. The most common non-steady-state defects include: “End of track”, “End of process”, or “Turnaround” porosity. These porosities are crucial and influential when using elaborate scan strategies such as checkerboard and fractal. Below, a brief description of these porosity formation mechanisms in metal powder bed AM processes are presented.

End of track porosity. It occurs at the start or end points of the scan tracks and involves the partial re-melting of previously deposited layers formed. End of track porosity may occur both on different layers and near the edge of the part, leading to high-aspect-ratio (i.e. “high-risk”) melt pools morphologies for keyholing (and potentially LOF) porosity [327,605]. This is believed to be a result of the accumulated heat (e.g. high power) at these points resulting in a keyholing. Since the temperature profile at the start and end points of a scan track is transient, keyhole equilibrium may easily become very unstable and collapse, resulting in porosity as shown in 4.4. Higher temperatures have been observed within the raster when the laser beam is turned around at the end of a track in Groeber *et al.* [616]. Thijs *et al.* [605] were one of the first to experimentally characterize the end of track porosity in L-PBF AlSi10Mg. Here, steep and deep melt pools were observed to form at the start/end points of the scan tracks. It was believed that heat was accumulated at these points of the scan paths and a keyhole melt pool is created. Since the keyhole equilibrium is very sensitive and the transient character of the temperature evolution is at the start/end points, the keyhole easily becomes unstable and collapses, thereby creating large pores. Sinclair *et al.* [617] hypothesized that the formation of end of track pores could be augmented by soluble gas, partitioned into the melt

pool and swept to track ends, supersaturating during the end-of-track solidification and diffusing into pores increasing their size.

End of process porosity. It can occur during the rapid start-up or shut down of the laser beam (i.e. switching either on or off). Khairallah *et al.* [535] showed that the sudden shutdown of the laser beam was an opportunity for keyholing pores to arise upon switching off the laser. Khairallah modeled the results of King *et al.* [96] for 316L, namely end of process porosity resultant from switching off the laser during scanning. In the snapshots taken, after the laser is turned off at 585 μs, a large ellipsoidal pore getting trapped beneath the surface due to a fast laser ramp down (1 μs). Similarly, two other small spherical pores were formed. The importance of investigating the end of track defects is their potential to be a major source of porosity even if the main pass is free of pores [616].

Turn-around porosity. It is formed during changes in laser scan velocity at laser turn points via the rapid collapse of the vapor depression at the surface and subsequent trapping of argon by liquid metal flowing into the void [327]. Recently, Martin *et al.* [327] investigated turnaround porosity in L-PBF Ti-6Al-4V using subsurface *in situ* x-ray scanning. Overall, overheating at laser turn points leads to increased evaporation of metal from the surface causing a deep keyhole depression to form [327]. Thereafter, pores were then revealed to form due to the rapid formation then collapse of deep keyhole depressions in the surface which traps inert shielding gas in the solidifying metal. An example of turnaround porosity is shown in Fig. 54. Fig. 54(a-c) describes graphically the laser scanning track, while images Fig. 54(d-f) show the *in situ* x-ray time sequence images. Initially, the laser follows a prescribed trajectory (dotted black line) during laser melting (Fig. 54(a)). A slight keyhole melt pool can be observed during laser scanning condition in Fig. 54(d). The point at which the laser reaches the end of a track, decelerates, shifts a prescribed hatch spacing, and then changes scan direction by 180° this designated the "turnaround point", or where keyhole porosity is generated (Fig. 54(b)). It can be readily observed through x-ray imaging that a deep keyhole melt pool is generated at this turn-around point in Fig. 54(e). After the laser scan track accelerates along a new track parallel (Fig. 54(c)) and adjacent to the previous track, clear keyhole porosity can be observed in Fig. 54(f). Notably, the maximum depth of pores formed at the turn point was found to increases as a function of laser power, and this trend is independent of steady state scan speed. Furthermore, the majority of pores (87%) were primarily formed within 200 μm of the turn point under all investigated processing conditions. Pores closer to the turn point were found to be generally deeper in the material than pores formed farther from the turn-around point [327].

4.6. Spattering and denudation

Metal spattering is another highly undesirable phenomenon in laser powder bed fusion additive manufacturing [32,597,618,619]. When the laser beam scans across the powder bed, some molten metal droplets may get ejected directly from the melt pool. When they collide with each other or with the cold raw powder particles, larger and irregular clusters can then generate via coalescence or sintering [48,325,602]. On the microscopic scale, metal spattering could refer in particular to ejections of those molten metal droplets from the melt pool [48,602]; on the macroscopic scale, it is hard to distinguish such molten metal droplets from the numerous powder particles and clusters, so metal spattering could generally refer to ejections of any particle along the laser's path [26,325]. These ejected particles tend to be different from the original feedstock with respect to their compositions, microstructures, and morphologies [330,421,601], creating problems for powder recoating and recycling. For example, as shown in Fig. 55 when the large and irregular particles fall back onto the powder bed, because of their rough surface and bad flowability, after a second layer of powder spreading, locally and around these particles, the powder bed will not be uniform and there may be some gaps. After the printing, these gaps may become lack-of-fusion porosity and greatly reduce the fatigue life of the printed part [48,162,503,620].

Spattering mechanisms on the microscopic scale. As discussed in part in Section 1, during the past few years, much effort has been devoted to expanding our understanding of metal spattering formation mechanisms on the microscale [48,145,602]. Here, only the spatters ejected directly from the melt pool are the focus. Therefore, compared to laser powder bed fusion and laser cladding, laser heating of a metal plate is much simpler and has become an ideal model for experimental and theoretical studies [25,48].

Typically, under a stationary laser beam [25,127], the metal surface is first heated up by the laser and melted. When the temperature reaches the boiling point, local boiling happens, which generates a recoil on the liquid below. The liquid is then pushed out, forming a vapor depression zone or a keyhole. When the laser beam scans, most of the incident beam impinges on the front keyhole wall [613]. The laser heating is very powerful, so the temperature on the keyhole walls could be higher than the boiling point [48].

Many spatters are emitted from the keyhole rim, particularly from the front side [618]. In 2017, Ly *et al.* presented ultra-high-speed visible-light imaging and finite element modeling of metal spattering for a bare SS316L plate [602]. As illustrated in Fig. 56(a), under a scanning continuous-wave laser beam, the temperature on the front keyhole wall is higher. The higher the temperature, the stronger the evaporation, the higher the recoil pressure and the faster the molten liquid is pushed out

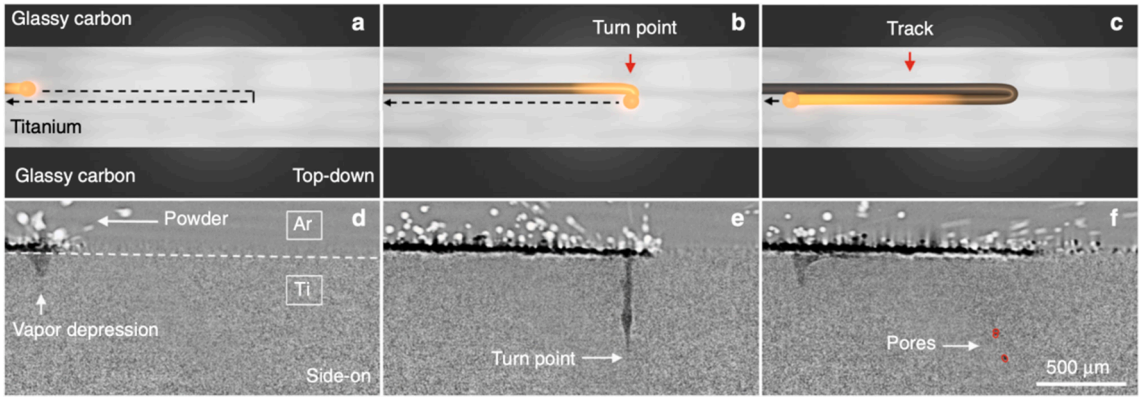

Fig. 54. An example of non-steady-state defects can be seen in the formation of porosity during changes in laser velocity at the end of scan tracks in Martin *et al.*. (a-c) Schematic of the laser scan path. (d-f) Corresponding x-ray images of subsurface melt pool morphology during laser scan experiments. Note: initial (slight) keyhole morphology in (d) results in full keyhole morphology in (e) after laser turn-around. Turn-around (keyhole) pores are seen in (f). Reprinted with permission from Ref. [327].

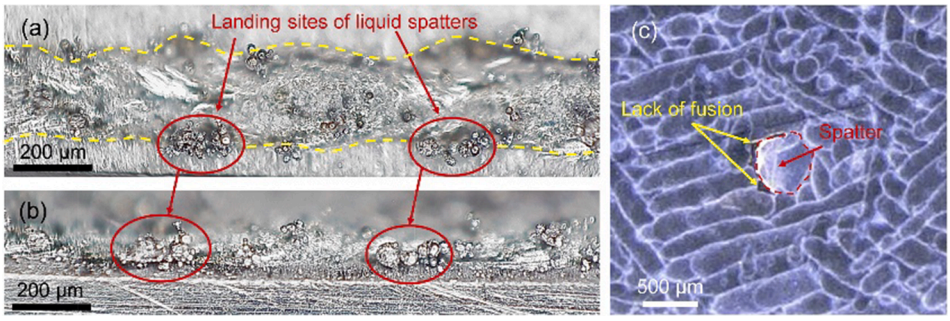

Fig. 55. Negative effects of metal spattering: (a) Top-view and (b) side-view taken from a single track indicating the solidified liquid spatters being sintered on the track. (c) Optical micrograph of L-PBF processed AlSi10Mg showing lack-of-fusion pores caused by spatters. Reprinted with permission from Ref. [325].

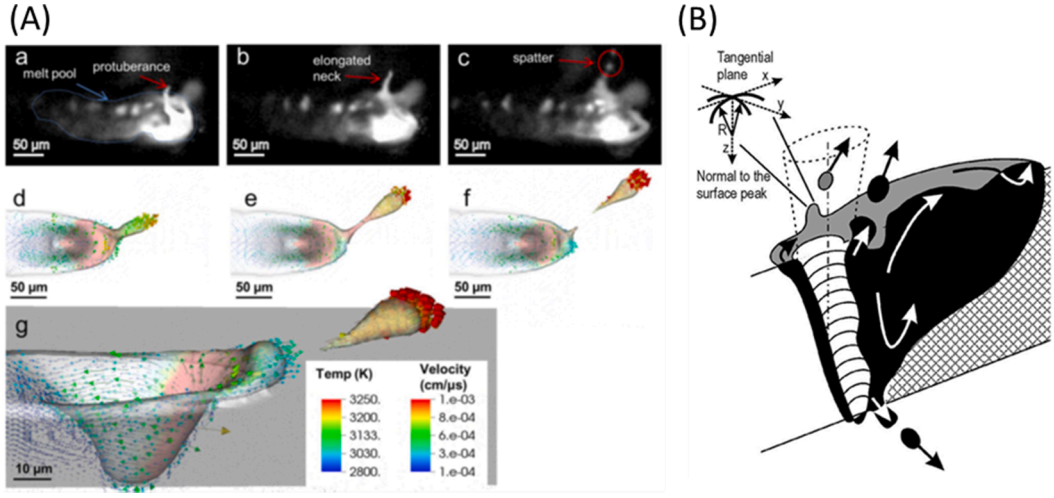

Fig. 56. (A) Intense evaporation induced metal spattering on the front keyhole rim for a bare SS316L plate. (a-c) Three experimental snapshots recorded using ultra-high-speed visible-light imaging. (d-g) Simulation of the three snapshots. Reprinted with permission from Ref. [602]. (B) Illustration of metal spattering on the rear keyhole rim. Reprinted with permission from Ref. [621].

and accelerated. Ly *et al.* called this molten liquid a protuberance. When its kinetic pressure or dynamic pressure is higher than the surface tension pressure, the protuberance will try to escape through necking. In the end, when it is separated from the melt pool, a spatter is formed. This theory sufficiently explains the formation of some spatters ejected from the front keyhole rim, and the spatter ejection speed is determined by the overheating on the front keyhole wall. It is reported that the spatter speed in SS316L ranges from ~6 m/s to ~20 m/s.

Under a scanning continuous-wave laser beam, some spatters are emitted from the rear keyhole rim [621,622]. As depicted in Fig. 56(b), when the local melt on the rear keyhole rim attains enough momentum, higher than a certain threshold, spatters can break free of the melt pool [621]. The momentum here mainly comes from two sources: the vertical component of the flow inside the melt pool and the vertical drag force of the vapor jet from the front keyhole wall. The threshold is mainly established by the surface tension, which can be greatly affected by the local temperature and surface oxidation and impurities. The ejection speed of such spatters from the rear keyhole rim in 304 stainless steel is reported to be 0.2–11 m/s [622].

As discussed above, the formation of the spatters from the front keyhole rim is closely related to the average temperature on the front keyhole wall, and that from the rear keyhole rim is dominated by the melt flow near the rear keyhole wall and the vapor jet ejected from the front keyhole wall. These two mechanisms are independent yet share some similarities: (1) the keyhole wall temperatures are the key to the spatter formations; (2) the keyhole wall temperature limits the spatter speed; (3) spatters are ejected along one keyhole rim.

In 2019, Zhao *et al.* unraveled a new mechanism for metal spattering under a scanning continuous-wave laser beam – the bulk explosion of a tongue-like protrusion on the front keyhole wall results in the formation of ligaments of molten metal at the keyhole rim and subsequent spattering [48]. This discovery was based on the ultra-high-speed synchrotron x-ray imaging technique at the Advanced Photon Source at Argonne National Laboratory, which was employed to monitor the metal additive manufacturing process for the first time in 2017 [26]. Compared to high-speed visible light and thermal imaging, the synchrotron x-ray imaging, because of the high penetration power of hard x-rays as well as super spatial and temporal resolutions [25,26,48,321], enables bridging the above-surface spattering behavior with the sub-surface keyhole and melt pool dynamics.

As shown in Fig. 57, at the time of t_2, a tongue-like protrusion (P) forms around the horizontal center of the keyhole, and on its top surface, there is a mini-keyhole. A necessary condition for the formation of such a unique protrusion structure is the keyhole morphology transformation from the typical "J"-like shape to a reverse-triangle-like shape (RTS), which creates directional vapor plume collisions towards the front keyhole rim and supports the growth of the small protrusion structure on the front wall from its bottom. This tongue-like protrusion then collapses within about a micro-second, like a bulk explosion. Combining direct experimental observations, quantitative image analysis, and numerical simulations, Zhao *et al.* attribute this unusual phenomenon to the rapid and intense laser heating of the protrusion's upper surface region as well as the large and irregular thermal fluctuation inside the protrusion. In triggering the explosion, the mini-keyhole on the top surface plays a

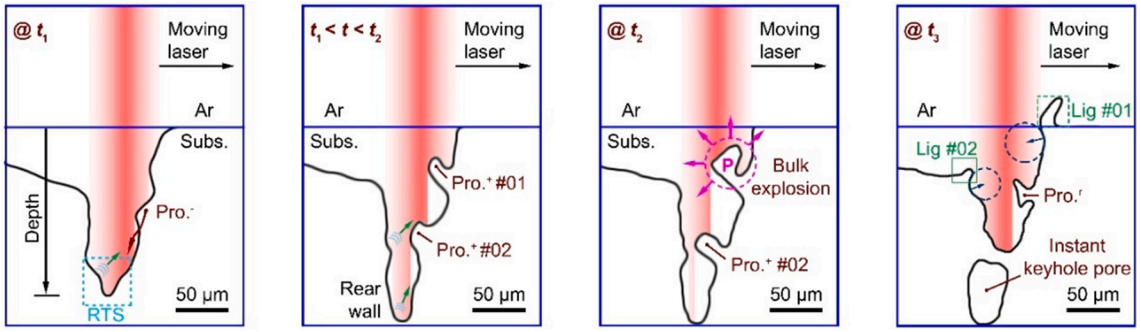

Fig. 57. Illustrations of bulk-explosion-induced metal spattering under a scanning continuous-wave laser beam. At t_1, a keyhole of reverse-triangle-like shape (RTS) forms. At t_2, a tongue-like protrusion (P) forms around the horizontal center of the keyhole, with a mini keyhole on its top surface. At t_3, thin melt ligaments (Lig) appear. Reprinted with permission from Ref. [48].

crucial role – focusing the laser intensity at the mini-keyhole bottom and producing intensive evaporation and a strong recoil on the side surface of the tongue-like protrusion. The explosion shatters the protrusion into a mixture of vapor and fine droplets. When they arrive at the keyhole rims, thin melt ligaments form, rise, neck, and eventually break up into spatters. This bulk explosion concept explains well the occurrence of those extremely fast spatters, e.g. 40 m/s in Ti-6Al-4V.

Unlike the two formation mechanisms for metal spattering mentioned at the beginning, the bulk explosion concept mainly differs in few ways: (1) rather than the keyhole wall temperature, the formation of the tongue-like protrusion structure is the key to the spatter formations; (2) the spatter speed is not limited by the keyhole wall temperature but is determined by the momentum released by the explosion of the protrusion, so it could be extremely high; (3) spatters are ejected along both the front and the rear keyhole rims.

Spattering mechanisms on the macroscopic scale. On the macroscopic scale, with the existence of powder, the spatter ejections are mainly dominated by the vapor plume from the keyhole and the environmental gas flow [48,61,66,325,602].

The keyhole shape is dominated by the laser heating conditions, and when the local keyhole wall temperature is higher than the boiling point, a metal vapor plume is emitted normal to the local boiling keyhole surface [25,602,622]. As shown in Fig. 58 [602], under high laser heating, the keyhole is deep and narrow, and the vapor plume emission is restricted by the walls mostly in the vertical direction, which results in spatters rising nearly vertically when powder particles present; while under low laser heating, the keyhole may still exist but is not that deep, and the vapor plume mainly faces backward, which causes spatters to fly at a similar direction with the existence of powder. In addition, the emergence of a protrusion structure at the front keyhole rim could produce an intense vapor plume [48]. As shown by the x-ray images in Fig. 59, at the time of ~152 μs, a protrusion forms at the front keyhole rim. The formation of this protrusion structure can considerably increase the local laser absorption. Hence, the stronger evaporation from its upper surface creates a more intense vapor plume and thus a stronger vapor pressure field, driving the spatters within it (as well as the powder particles if exist) to accelerate.

In addition to the metal vapor plume emitted from the keyhole walls, the environmental gas flow is the other crucial factor for metal spattering [66,325]. As illustrated in Fig. 60, at high pressures, the metal vapor jet and Bernoulli effect-driven gas flow tend to result in inward particle motion and fewer particle ejections; while at low pressures, the denudation is more pronounced, and more particles are ejected.

Therefore, the formation of spatters (powder spatters and/or droplet spatters) during PBF processes not only affects the microstructures but also influences the part quality and properties. Spatters generally

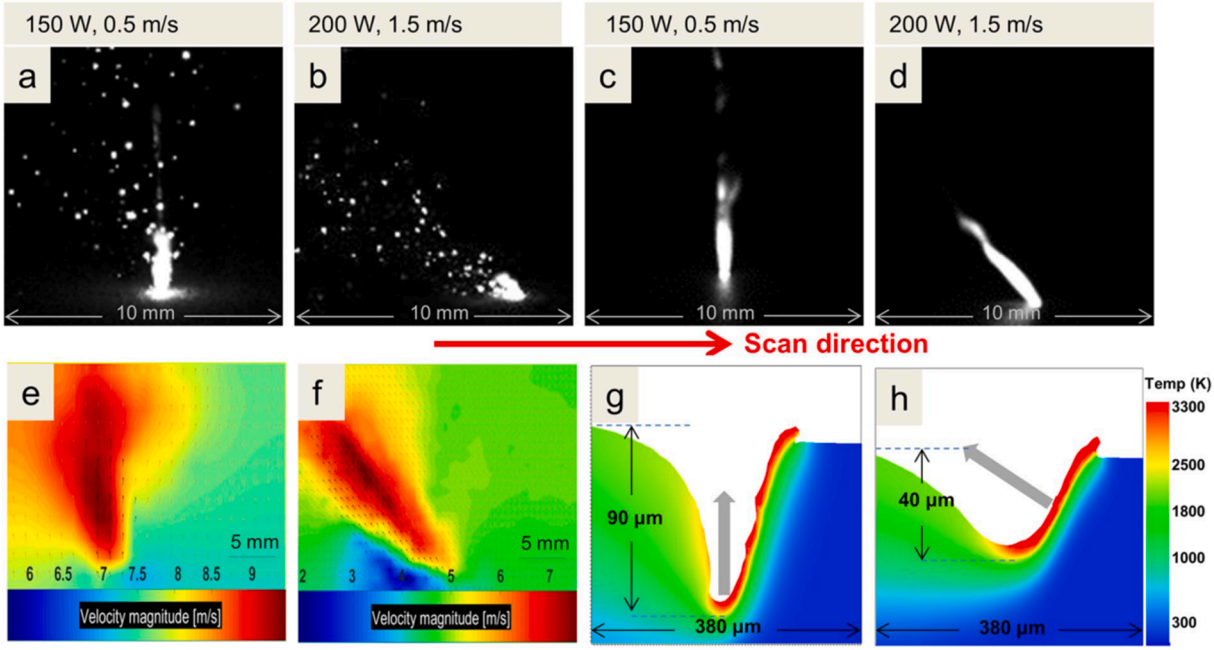

Fig. 58. Vapor plume driven metal spattering with the existence of powder. Reprinted with permission from Ref. [602].

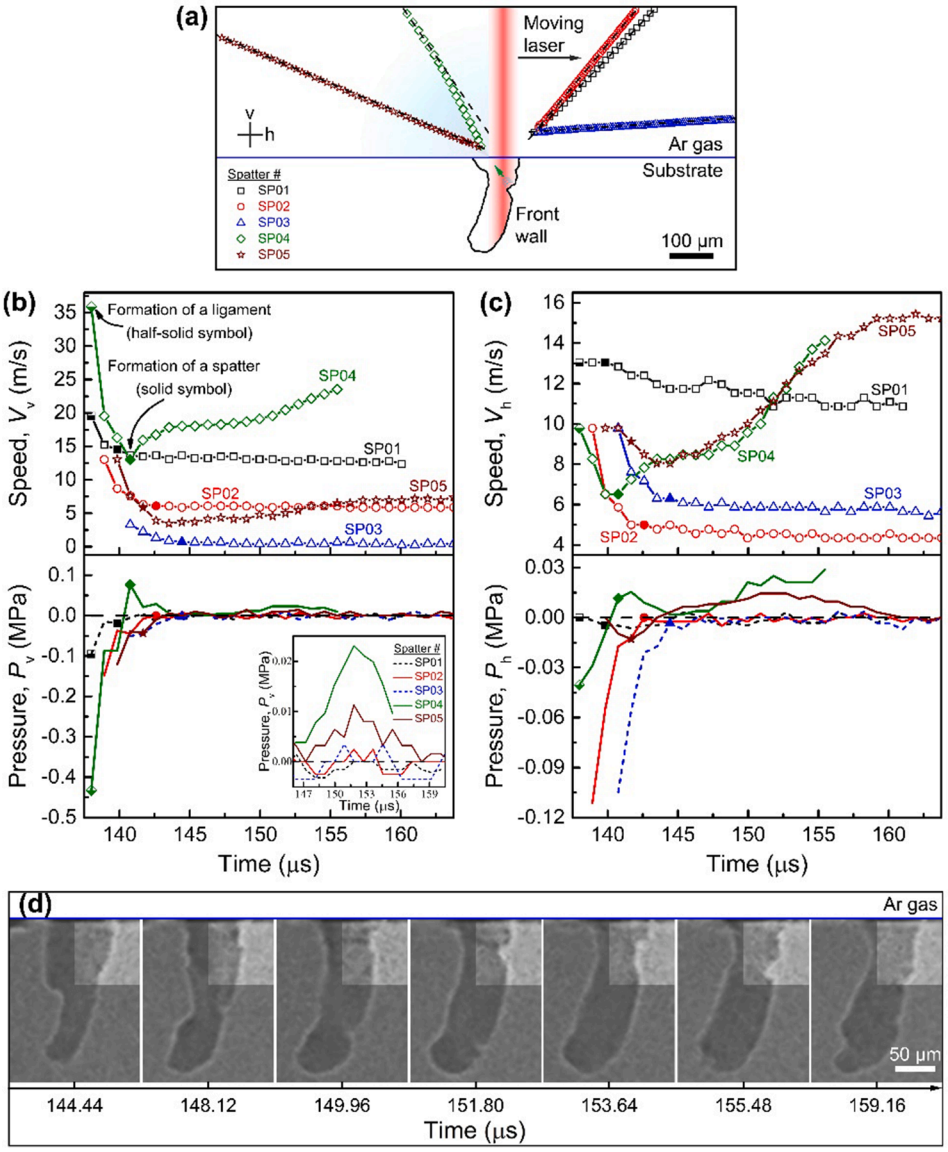

Fig. 59. Influence of an emerging protrusion structure at the front keyhole rim on the vapor plume ejection. Reprinted with permission from Ref. [48].

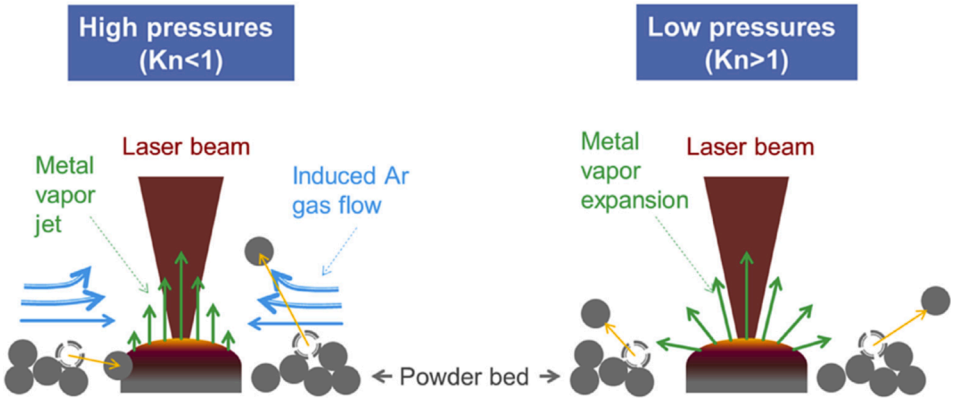

Fig. 60. Influence of environmental gas pressure on the powder ejection. Reprinted with permission from Ref. [66].

increase D_{90} and size distribution compared to virgin powder, showing different surface characteristics and chemistry [623,624]. Additionally, they increase the surface roughness of the AM parts which has a detrimental impact on mechanical properties like fatigue and tensile strength [625]. Thus, it is crucial to analyze recycled powder and assure the microstructures and resultant properties.

4.7. Residual stresses, cracking, and delamination

Lack-of-fusion porosity, keyhole porosity, and balling can be avoided with an appropriate selection of process parameters. Regardless of process parameter selection, residual stress will always develop in the AM-built component as a result of inherent AM processing characteristics, including the melting of small volumes, the high thermal gradients, and the repeated cycles of heating and cooling. Predicting and managing residual stress development during the part build is essential for AM part design since inappropriate part build setup could produce high levels of residual stresses which can cause excessive cracking and delamination in AM parts. Hence, it is crucial to understand the mechanisms and influencing factors leading to residual stress development and its relation to cracking and delamination in AM parts. In addition to the magnitude of the residual stress, metallurgical and microstructural factors also play important roles in part cracking and delamination susceptibility, both of which are also summarized in this section.

Residual stress. It can occur on both microscopic and macroscopic scales during the AM part build. Residual stress on the microscale could be induced directly by material volume change accompanied by some phase transition (e.g., martensitic transition) or be caused indirectly by the thermal effect of exothermic or endothermic phase transition. This was observed by Cottam *et al.* [626] for DMD processing with H13 steel. The occurrence of macroscopic residual stress in the AM part could be explained by thermal gradient mechanism (TGM) (Fig. 61(a,b)) from Mercelis and Kruth [627] or described by the three-bar frame model (Fig. 61(c,d)) originally developed for fusion welding [628].

The Thermal Gradient Mechanism (TGM) states that as the laser beam heats a local spot, it creates a steep thermal gradient in the solid-state material surrounding the melt pool, which leads to thermal expansion of this heated solid-state material. This material expansion tends to be restricted by the unaffected cold matrix material underlying the heated material, and in turn, creates compressive stress in the heated material. Meanwhile, the yield strength of the heated material might be greatly reduced due to the temperature rise, suggesting the possibility of plastic compressive strain as the compressive stress in the heated material might exceed its yield strength. As the laser beam moves away, the previously heated material tends to go through material shrinkage due to fast cooling. In this case, material shrinkage is restricted by plastic strain formed during the heating stage, and thus creates tensile residual stress in the previously heated zone of the additively manufactured part.

The Three-bar frame model is shown schematically in Fig. 61(c,d) in which three bars of equal length with only the middle bar going through a rapid heat-cool cycle and two rigid blocks at the two ends to force the three bars connected during the heat-cool cycle. In AM, the as-deposited track and the adjacent material are analogous to the middle bar, and the cold substrate far away from the deposition location is analogous to the two rigid side bars. (Eq. (4)) describes the stress of the middle bar as temperature changes [630,631], assuming stress on each of the side bars is equal to half the stress of middle bar.

$$\sigma_m = -\alpha \Delta T \frac{2E}{1+2E/E_t} \tag{4}$$

The stress–temperature profile of the middle bar is schematically depicted in Fig. 61(b). Here, heating and cooling correspond to the curves denoted by ABC and CDE, respectively. Stress evolution during heating is composed of two (2) stages. At the beginning of heating (AB), only elastic compression occurs. As the temperature keeps increasing, compressive stress is limited by the yield strength at each corresponding temperature, creating both elastic and plastic strain in the middle bar. Similarly, stress evolution during cooling is also composed of two (2) stages, with only elastic tensile action at the beginning (CD) and then both elastic and plastic action as temperature further decreases (DE). Finally, tensile residual stress develops in the middle bar, as represented by the arrow connecting points A and E in Fig. 61(b).

Both the TGM and three bar-frame models are reasonable but rather simplified models for AM residual stress prediction. They provide guidelines to understand the general trend of AM residual stress evolution. However, for accurate prediction, more comprehensive modeling is required. By far, abundant studies have developed a series of numerical thermal-stress coupling models to predict residual stress for various AM systems and alloys, with a detailed list summarized in several review papers [592,632,633]. The coupling of 3D transient heat transfer modeling with FEM mechanical modeling is predominantly adopted for AM residual stress simulation. Common FEM codes adapted to AM

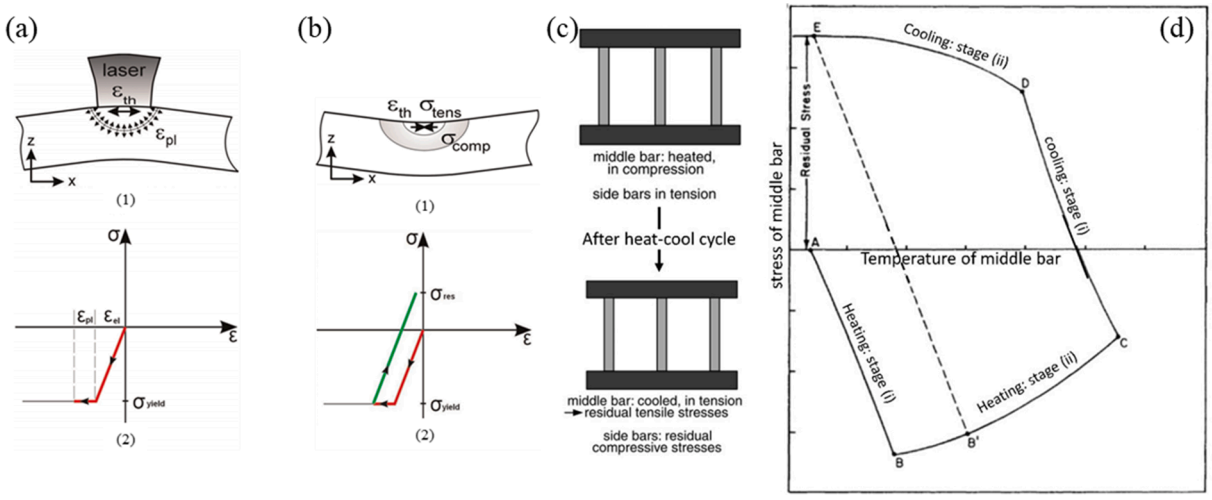

Fig. 61. Thermal Gradient Mechanism (TGM) for AM residual stress evolution: (a) Induced stresses and deformation (strain) during laser beam heating and (b) occurring stresses and deformation (strain) when the part cools down. Simplified representation of the formation of thermal stress and strains in the irradiated zone. Reprinted with permission from Ref. [629]. Three-bar frame model for AM residual stress evolution: (c) model schematic. Note that only the middle bar is going through heat-cool cycle; (d) schematic of the temperature-stress curve: ABC: heating; CDE: cooling; residual stress: represented by a dashed line. Reprinted with permission from Refs. [630,631].

modeling include Ansys, Abaqus, Cubic, MRC, and 3DSim. Common material (powder or wire) addition method include: "element birth", "quiet element", and "hybrid activation" [634]. "Element birth" method is usually adopted for powder/wire feed AM modeling. While for powder bed AM, selecting the appropriate material addition method is of more significance, as additional simulation treatment is required to allow thermal and mechanical properties different from the consolidated solid metal to be assigned to the preplaced powder bed.

There are four major challenges for AM residual stress modeling:

(1) First is the inclusion of all the relevant AM physical phenomena in the modeling scheme. Based on the simulation dimension scale, AM modeling could be categorized into micro-scale, particle-scale, *meso*-scale, and macro-scale [32]. AM residual stress simulation is usually in *meso*-scale and macro-scale, in which the particle layer is treated as a continuum with uniform property to reduce computational cost. However, this prevents the direct simulation of some important physical phenomena during melt pool evolution, including laser spattering, vaporization, or even keyhole formation. Besides, as mentioned earlier, the majority of AM residual stress simulations are thermal-stress coupled models while fluid flow modeling is often neglected, which in turn excludes the physical phenomena related to the melt pool fluid dynamics such as Marangoni flow. These phenomena might influence residual stress development by altering the melt pool temperature gradient distribution, e.g., by making the temperature in the melt pool more uniform than suggested by consideration of heat flow alone. Thus, naïve simplification of these physical phenomena could impair the simulation accuracy especially for modeling of thin-wall structures, in which case each layer is usually comprised of only one track.

(2) Second is the great difference in spatial-time scale between the localized and the global domain. AM residual stress modeling needs to address resolution in the order of laser spot size and melt pool solidification duration within a large global domain in the AM part scale and the whole build process. Therefore, to reach a reasonable trade-off between model resolution and productivity, careful consideration is required for mesh setup. In general, a refined mesh is required for the scanning and HAZ region with respect to the unaffected surrounding volume. Selecting a suitable mesh refinement technique and analysis for the unaffected volume boundary is of significance to ensure a balance between model accuracy and efficiency. On the other hand, many macro-scale modeling is constructed by thermal/structural scaling of *meso*-scale modeling. In this case, additional consideration needs to be put on the scaling method setup. A large error might be aroused if the scaling method does not appropriately address some melt pool scale issues, such as melt pool remelting by successive layers, which might cause a rather complex stress–strain field.

(3) Third is handling the non-linear effects of thermal phenomena and temperature dependence of material properties. Criael *et al.* [635] conducted a sensitivity analysis for material properties on FEA thermal modeling of L-PBF process, which shows the simulation result presenting a high degree of sensitivity to variation of reflectivity, thermal conductivity, density, and specific heat yet minimal sensitivity to latent heat, emissivity and heat transfer coefficient. This indicates the significance of adopting an accurate temperature-dependent value for the high-sensitivity properties in the AM residual stress model since a poorly approximated constant input for those properties was likely to largely affect the simulation accuracy. On the other hand, for properties with low sensitivity, adopting a constant value might be acceptable since even if the temporal change results in large variation for these properties, the related influence on simulation results is still negligible.

(4) Last is the time-consuming thermal and stress experimental validation. Thermal measurements were often conducted via thermocouples or thermographic cameras, which were reported with the problem of moderate measurement accuracy. Neutron diffraction and hole drilling are commonly used for residual stress measurements. The former could provide comprehensive stress characterization but requires a complicated experimental setup. The latter is a much simpler experimental approach but it only captures a localized stress profile.

Cracking and delamination. As mentioned earlier, residual stress in AM parts is a governing factor for part cracking and delamination susceptibility. There are three types of weld cracking, namely solidification cracking, liquation cracking, and strain-aging cracking [470,631]. Due to the analogy of AM and welding, this categorization could be adopted to distinguish cracking in AM. These three types of cracks are associated with different cracking mechanisms and could be distinguished by certain microstructure evidence as shown in Fig. 62.

First, *solidification cracking* occurs towards the end of melt pool solidification, propagating along intergranular regions within the melt pool. As solidification is about to terminate, the remaining liquid is distributed at the interdendritic or intergranular regions. In the meanwhile, tensile residual stress develops in the melt pool due to the contraction of the solidifying material that is restrained by the previously deposited substrate, as explained earlier by TGM and three-bar frame mechanisms. Subsequently, solidification cracking will form if all of the following conditions are fulfilled: (1) the final solidifying microstructure presents an interlocking solid network with the remaining liquid distributed as continuous liquid film among adjacent grains; (2) the amount of final liquid is not enough to provide "healing" by backfilling the incipient cracks; (3) the magnitude of the tensile residual stress exceeds the yield strength of the solidifying metal. Solidification cracking could be distinguished from the other two types of cracking by microstructure evidence of dendritic crack morphologies and dendritic fracture surface as seen in Fig. 62(a).

Second, unlike solidification cracking, *liquation cracking* occurs outside of the melt pool. Instead, it is located in the partially melted zone (PMZ) adjacent to the melt pool fusion line. In the PMZ, although the peak temperature never reaches the alloy solidus temperature during the part build, certain types of precipitates at the grain boundary have lower melting points than the matrix. This localization of melting, which can also occur via micro-segregation, allows the residual stress to generate cracks. This phenomenon is commonly referred to as grain boundary liquation (GB-liquation), which could be induced by four different mechanisms [630]. These GB-liquation precipitates provide potential cracking initiation location. As explained earlier in the TGM mechanism, tensile stress could also develop in the PMZ during cooling, creating adequate conditions for liquation cracking to propagate. As shown in Fig. 62(b), microstructure evidence for liquation cracking could be found by the existence of GB-liquation precipitates at the initiation point of cracking. Precipitates are usually intermetallic, eutectic products, or contamination by interstitial elements that segregate, any of which can locally lower the melting point [630,636-639].

Third, *strain-age cracking* is associated with the AM thermal characteristic of the repeated heat-cool cycle after deposition. The concept of strain-aging crack for welding arises from the observation that for precipitate-hardened alloy weldments, cracking often occurred in post-weld heat treatment at the aging temperature range [640]. Its mechanism lies in that reheating the weldments could lead to two competing stress evolution actions: one is the expected residual stress relaxation, the other is stress formation due to further precipitation at the aging temperature. If the latter is much faster than the former, strain-aging crack occurs. As a result, this type of cracking almost always nucleates at grain boundaries in the heat-affected zone. For AM part build, the repeated heating cycle induced by the deposition of each successive layer might create a thermal condition similar to post-weld aging heat

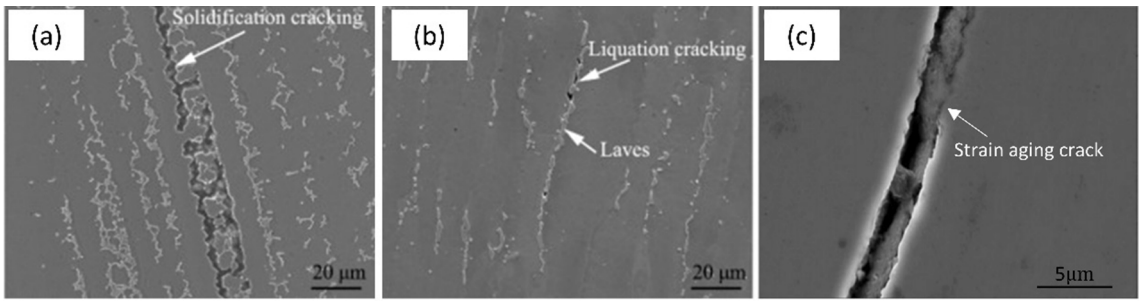

Fig. 62. Typical microstructure details for AM part delamination and different types of AM cracking: (a) solidification cracking; (b) liquation cracking; (c) strain aging cracking. Examples provided are for alloy 718 part built using L-DED ((a), (b), reprinted with permission from Ref. [644]) and for CM247LC super alloy part built using L-PBF((c), reprinted with permission from Ref. [470]).

treatment. Then the residual stress from direct layer deposition, combined with the newly developed stress due to successive layer deposition, gives the possibility for strain-age cracking to occur in as-built parts.

As aforementioned, the occurrence of the three types of AM cracking is determined by residual stress at different locations and stages during the AM part build: solidification cracking and liquation cracking are mainly induced by residual stress within the solidifying melt pool and within the PAZ region during deposition respectively, while strain-age cracking is mainly induced by residual stress within the HAZ post-deposition. Therefore, understanding residual stress evolution at each stage of AM part build is of great significance for predicting and mitigating part cracking susceptibility. Lastly, if residual stress is developed at layer interface, with its magnitude higher than alloy yield strength, cracking might propagate through the whole deposition layer, leading to delamination defect. As mentioned earlier, most of the residual stress modeling work (

Table 4) presents a general trend of higher residual stress at near-top and near-bottom layers of the part, which agrees with the location for part delamination experimentally observed in several studies [170,641-643].

Recently, Hojjatzadeh *et al.* [537] observed pore formation from a crack inside a previously built layer during laser melting of Al6061 substrate. It was observed from DXR images when the melt pool encountered the crack, pores nucleated from the crack, grew, and released multiple spherical pores. The inert gas in the chamber was considered as the main source of the gas in the crack. As the laser scans, the melt pool encompassed a larger area of the crack, and pores were gradually detached with spherical (pore) morphology into the melt pool (Fig. 63).

Besides residual stress, some metallurgical and microstructural factors also play a significant role in part cracking and delamination susceptibility. For the three types of AM cracking mentioned earlier, their associated mechanisms suggest that solidification cracking is fundamentally determined by the amount and distribution of final liquid at end of solidification, which is in turn determined by alloy solidification temperature range, solidification grain morphology, and dendrite spacing [645,646]. For liquation cracking, its occurrence essentially depends on the existence of GB-liquation precipitates, such as γ' phase in alloy alloy [636]. The relevant microstructure feature, including γ' precipitate morphology, distribution, and dimension are all important factors to consider for liquation cracking susceptibility. Similarly, strain-aging cracking essentially relies on solid-state precipitation, and thus the metallurgical factor relevant to solid-state precipitation kinetics has a profound influence on strain-aging crack susceptibility.

4.8. Surface finish and roughness

An important challenge in metal powder bed AM is the reduction of surface defects including surface roughness, porosity, and surface finish leading to reduced reliability in service, as well as undesirable surface finish conditions [156,575,647,648]. Although rough surfaces may be beneficial in certain biomedical applications [649], multiple studies have pointed to how rough surfaces result in stress concentrations at the free surface and premature failure in as-built metal AM parts [625,649-652]. Particularly detrimental to part performance are deep valleys on the surface which act as preferential sites for mechanical damage during cyclic loading and corrosion [157,653-655]. As with bulk defects, starting material characteristics, processing variables, and post-processing treatments (particularly affecting the contour regions) of AM parts can all significantly impact the as-built part surfaces.

In general, rough surfaces in metal powder AM parts are determined to be the result of (1) the adherence of partially or non-melted powder, and (2) the formation of menisci (e.g. "surface waviness") on free surfaces [657]. This is shown in Fig. 64 (see insert) for E-PBF Alloy 718 [656]. It can be readily observed that the contour regions undergo complex relationships of spattering, balling, condensate formation, and melt pool behavior during metal AM processing. This leads to partially sintered particles, satellite particles, and micro notches which result in rough surface characteristics [656,658,659]. The contour regions also serve as potential areas for non-steady-state defect formation (e.g. end of track, end of process, and turnaround porosities, see Section 4.5) namely keyhole porosity due to the complex thermal histories within these areas [24,327,535,605,616]. Thus, surface defects in powder bed metal AM

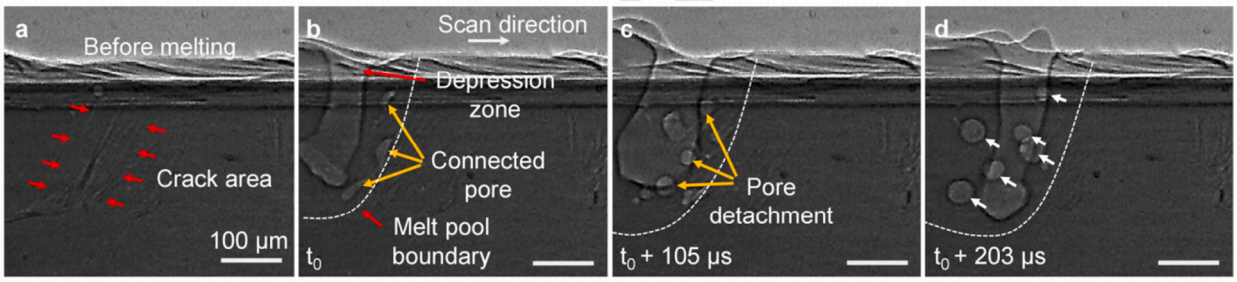

Fig. 63. Pore formation from a crack during laser melting of Al6061 substrate. Reprinted with permission from Ref. [537].

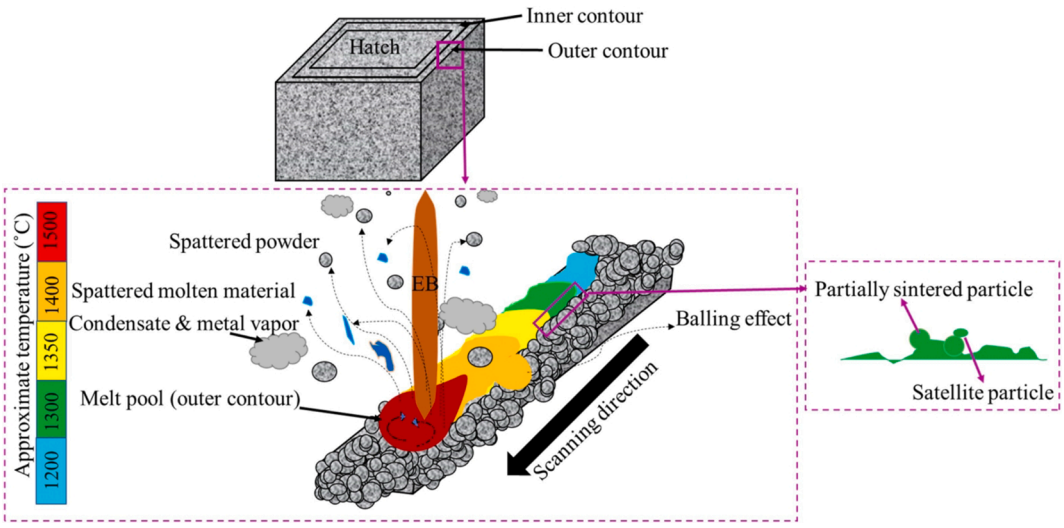

Fig. 64. Schematic view of various competing phenomena occurring during electron beam melting of the contour region resulting in observed surface roughness characteristics on the as-built metal AM surfaces. Reprinted with permission from Ref. [656].

are a multifaceted challenge, still requiring much research and discussion.

Starting materials. Starting powder characteristics are well-known to have a strong effect on surface finish characteristics [659-663]. In particular, powder shape, size, and spreading strongly influence laser absorption characters, and thus influence surface texture. It is deduced that finer powder leads to smoother surfaces; however, spreading of finer powders is more challenging due to powder agglomeration, surface effect of powders, particle–particle and particle-dispensing blade interactions [663]. In contrast, larger powder particles may be easier to spread, but limit the surface finish due to the minimum feature size and minimum layer thickness [663]. Furthermore, the orientation of the AM parts on the build plate to the re-coater blade (e.g. down skin surface roughness) has also been determined to affect surface topography in multiple studies including those in [648,662,664]. Recent work by Kantzos *et al.* [659] discovered that the relevant "hotspot" features on the as-built surface were similar regardless of the powder size for a fine and a coarse Ti-6Al-4V powder. This suggests that surface roughness is indeed more sensitive to build conditions than to variations in particle size and that starting powder characteristics such as powder size may play a small role in the performance of metal AM parts with rough surfaces. This is most likely because near-surface porosity induces localized damage in specific regions at the surface [658] more significantly than surface roughness [659]. The small influence of powder size on fatigue performance was also corroborated in Gockel *et al.* [661]. Here, it was discovered that the average powder particle size in the raw powder would likely highly influence the measured value of roughness parameter S_a but is expected to have little contribution to the fatigue performance. Thus, while powder size may only play a negligible role in fatigue life, this and other starting material characteristics (i.e. spreadability, powder morphology, etc.) still require investigation, particularly in relation to correlation with surface finish in as-built metal AM materials [234].

Processing conditions. As with bulk defects, it is well-known that surface roughness and porosity in as-built metal AM materials is strongly controlled by processing conditions [656,661,665]. Mumtaz and Hopkinson [666] discovered that laser peak power, laser repetition rate, and scan speed impacted both top and side surface roughness. Paria *et al.* [656], Calignano *et al.* [575], and Koutiri *et al.* [665] determined that the formation of rough surfaces was largely due to the selection laser/electron beam power, velocity, and beam profile for E-PBF Alloy 718, L-PBF AlSi10Mg, and L-PBF Alloy 625, respectively. It was shown that additional contour re-melting could enhance surface finish. Similarly, Strano *et al.* [664] discovered that as-built surface topology varies with build orientation angle for L-PBF 316L. Horizontal surfaces were dominated by the ripple effect but as the inclination angle increased, the stair-case effect started to take the key role, showing obvious waves on the surface [660,667-669]. This was potentially due to the effect of gravity that causes melt pools to sag into the un-melted powder bed below, resulting in a much rougher surface on the underside of the component than on the upward-facing surfaces [662]. Differences in upward vs. downward-facing surfaces were characterized by Bacchewar *et al.* [670]. Here, build orientation and layer thickness were found to be significant parameters affecting surface roughness in upward-facing surfaces, whereas for downward-facing surfaces, build orientation, layer thickness, and laser power were also important factors. Solberg *et al.* [671] showed when the angle increased from 0° to 135°, the number of attached particles to the surface increased and in the down skin surfaces (90-135°), the increased surface roughness was significant (see Fig. 65). Furthermore, Triantaphyllou *et al.* investigate the effect of scan strategy producing multidirectional texture underlying lay and laser path changes which the part distortion in certain directions than others leading to surface roughness [662]. Qiu *et al.* [672] found that increasing layer thickness at a constant laser power and scan speed led to the enhanced surface roughness as well as LOF porosity and balling on the surface.

Processing variables selections for the contouring regions have the largest effect on surface roughness characteristics and surface porosity [40,648,660,664,666]. In more detail, the contour parameter sets trace around the outside of the component on each layer in contrast to the bulk parameter sets (the "hatch" parameters) which fill in the internal portion to form solid material [661]. Therefore, the alteration of process variables within the contour regions affecting surface roughness characteristics has been well-characterized such as studies by Karimi *et al.* [656], Chen *et al.* [673], Chua *et al.* [674], Fox *et al.* [675], Mohammadi and Asgari [676], Koutiri *et al.* [665], Whip *et al.* [677], and Mishurova *et al.* [89]. In particular, these studies have focused on process optimization of adjusting contour processing variables to obtain particular surface roughness characteristics. Karimi determined optimized parameters including scanning speed, beam current, focus offset, the number of contour passes, and melting strategies for surface roughness in E-PBF alloy 718 [656]. Mohammadi determined optimal parameters of hatch spacing, laser power, and laser velocity, overlap with core, beam offset, and minimum length leading to different upskin and downskin characteristics for L-PBF AlSi10Mg. This resulted in surface roughness values almost as low as one-fifth of the samples manufactured

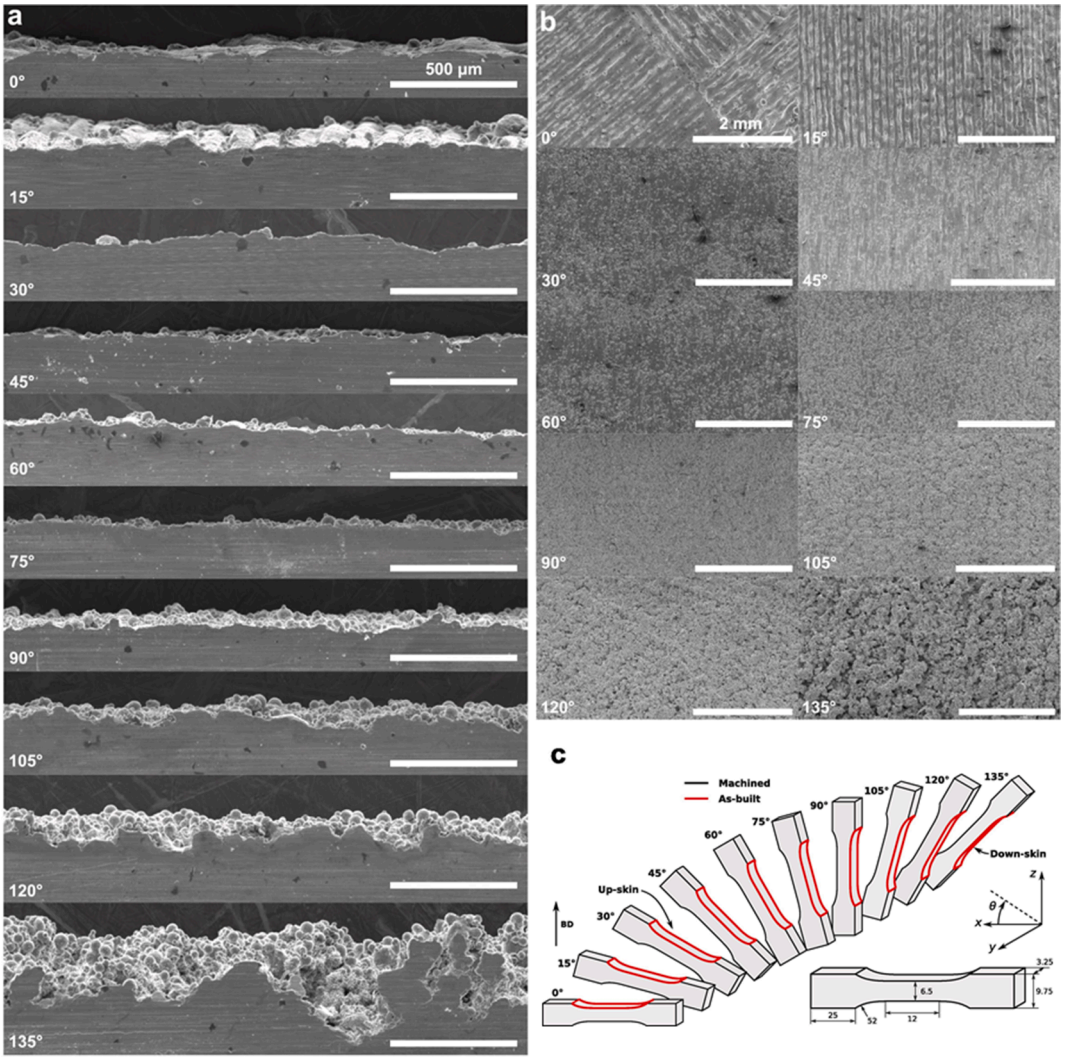

Fig. 65. Microscopy images from (a) side view and (b) top view of LPB maraging steel 300 alloy. (c) Examples indicating specimen orientation based on the build direction. Reprinted with permission from Ref. [671].

using standard process parameters [676]. Importantly, Koutiri determined the importance of proper hatching + contour selections for reduced surface roughness parameter R_a and low porosity for L-PBF alloy 625. However, Koutiri determined that the correlation between surface roughness (in particular R_a) and process parameters was a complex task [665], likely requiring significant trial-and-error type analysis. Qiu *et al.* showed that the surface roughness was increased with increasing layer thickness in which the instability of the melt pool flow was an outcome of the Marangoni force and recoil pressure [672]. In addition, melt pool agitation resulted in spattered powder formation resulted in rougher surface finish by ball formation and surface porosity (Fig. 66). Therefore, analytical modeling and FEA techniques such as those proposed by Yadroitsev *et al.* [560], Michopoulos *et al.* [678], and Meier *et al.* [679] have been employed in order to analyze the effects of process variable alteration on surface roughness characteristics for multiple materials and process methods in metal powder bed AM.

Post-processing. As previously mentioned, metal powder bed AM parts suffer from surface roughness characteristics due to two main causes: (1) the partially melted powder particles and (2) the staircase effect arising from the mismatch between the computer-aided design model and slicing strategy [650]. Therefore, the use of post-processing techniques to reduce surface roughness is typically used for metal AM materials. Largely, the most common surface treatments employed are: (1) surface grinding/machining/polishing e.g. via mechanical, chemical treatments, and/or laser treatment [672,680-686], (2) shot peening [575,687-691], (3) heat treatments [509,692], and (4) coating [693]. It should be mentioned that although Hot Isostatic Pressing (HIP) processes are routinely used post-processing treatments, the HIP processes are only successful at closing internal defects/pores therefore they have negligible effects on surface roughness [680,694]. Masuo *et al.* characterized surface roughness in both L-PBF and E-PBF Ti-6Al-4V, denoting a continued (and large) influence of surface roughness on mechanical behavior after HIP processing. Therefore, HIPed metal AM specimens still possess rough surfaces, which can play a key role in shortening the fatigue lives [694].

Recently, Khan *et al.* published a review article on the effect of post-processing (such as thermal, mechanical, and/or chemical-based) on the surface integrity and properties [695]. Overall, L-PBF processes typically possess smaller layer thicknesses and utilize smaller particle sizes resulting in higher build tolerances, the replication of finer features, and reduced surface roughness as compared to E-PBF techniques [696]. Chan *et al.* [697] showed the mean fatigue life of Ti-6Al-4V decreases with increasing maximum roughness (depth) of the surface features due to stress concentrations at the surface features and L-PBF produces a more fatigue-resistant surface finish than E-PBF, largely due to the reduction of notch-like surface features between individual layers. For E-PBF materials, surface machining can significantly reduce R_a values of ~30–68 um to $R_a < 1$ μm, as shown by Sun *et al.* [650] for Ti-6Al-4V.

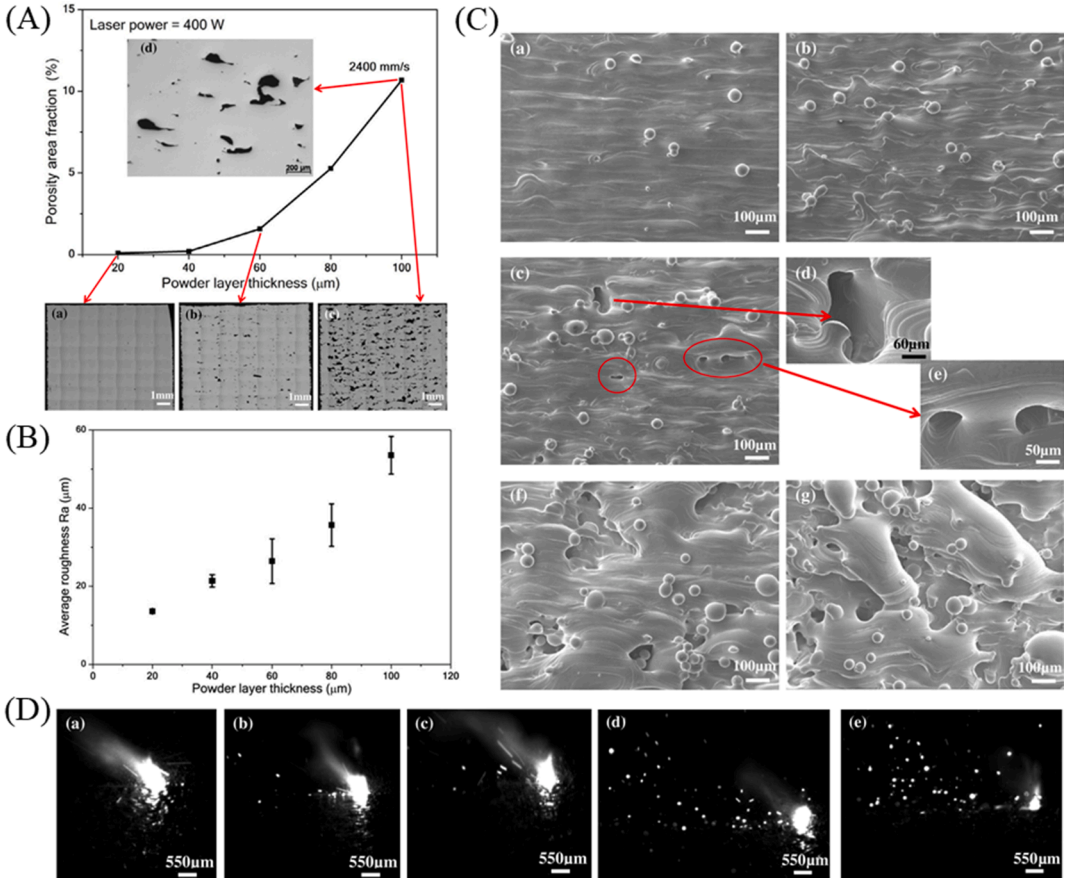

Fig. 66. (A) Porosity area fraction and (B) average surface roughness as a function of powder bed layer thickness. (C) SEM micrographs and (D) high-speed imaging illustrating powder-laser interaction from the surface of L-PBF processed parts with layer thickness varied between 20 and 100 μm. Power and velocity were fixed at 400 W and 2400 mm/s, respectively. Reprinted with permission from Ref. [672].

Similar results have been determined for L-PBF materials, such as the improvement of R_a from 10.0 μm (as-built), 0.4 μm (machined), and 0.1 μm (polished) for L-PBF SS 316L in Spierings *et al.* [698]. Electropolishing has also been shown to greatly reduce surface roughness from approximately from greater than $R_a = 12.04 \pm 1.45$ μm to 3.23 ± 0.22 μm in L-PBF 316L [682]; when combined with mechanical polishing surface roughness can be further reduced to approximately $R_a = 0.13 \pm 0.02$ μm. Shot peening may also result in a reduction of surface roughness in a number of studies, such as Almangour *et al.* [690]. In this study, shot-peened L-PBF SS 17–4 PH possessed R_a values of 1.16 ± 0.13 μm, as compared to the as-built R_a of 4.00 ± 1.37 μm. In addition to improving surface roughness, shot peening also induces high compressive residual stress at the surface, leading to compressive residual stress, and improved fatigue resistance [690]. Recent studies have also shown the beneficial effect of heat treatments on fatigue behavior in L-PBF AlSi10Mg. Heat treatments resulting in surface alterations were discovered in Aboulkhair *et al.* [692]. Here, dimples appearing on the fracture surfaces of the heat-treated samples were not apparent in the as-built specimens, indicating increased ductility. The ductile surface dimples resulted in improved fatigue performance since higher ductility is less susceptible to fatigue crack initiation. Notably, heat treatment resulted in a more substantial improvement in fatigue behavior than surface machining. However, surface roughness values for heat-treated versus machined conditions were not given. Therefore, it is not clear if fatigue behavior was improved by surface condition alone, or as a combination of surface improvement and microstructural effects.

Surface Metrology and Characterization. Although the common measurement method used for AM was stylus-based contact profilometry, as reviewed by Townsend *et al.* [648], the measurement of surface roughness of AM parts using this method demands caution. Dictated by the stylus cone angle and tip radius, the accessibility to deep, hidden, or semi-hidden surface features such as overhangs or reentry points (Fig. 67 for example) can be limited [699]. Because of the three-dimensional character of the AM surfaces, it may be challenging for the tactile profilometry and the two-dimensional, line-scan based surface parameters (R_a, R_t, R_{max}, and R_z, etc.) to capture the surface features that truly affect the mechanical performance (such as the depth, span, and sharpness of surface depressions [659]). In addition to the tactile type profilometry, three major groups of methods have been utilized in the literature [648], namely:

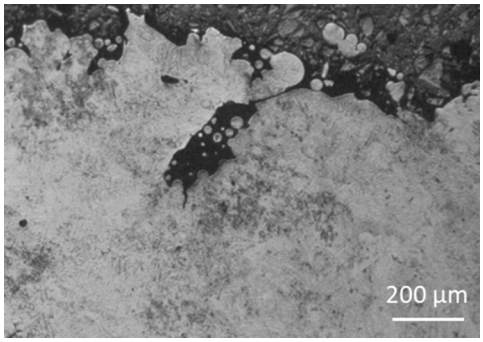

Fig. 67. A notch-like surface defect in an L-PBF Ti-6Al-4V specimen with cross-sectional optical microscopy. Reprinted with permission from Ref. [699].

(1) areal topography: Confocal Microscopy (CM), Focus Variation Microscopy (FVM), and Atomic Force Microscopy (AFM);
(2) optical/electron microscopy: Optical Microscopes (OM) and Scanning Electron Microscopy (SEM);
(3) volumetric methods: such as high-resolution x-ray computed tomography (HR-XCT) [659]. The light source can be a lab-scale x-ray tube or a synchrotron facility.

These methods can be beneficial when applied to AM parts as their irregular surface structures cannot be reliably described by a single line-profile [648]. It has been demonstrated that, for instance, the areal topography measurement by CM can yield a higher statistical significance than the conventional stylus-based one [700,701]. X-ray based volumetric methods, while suitable for characterizing geometric features such as the one depicted in Fig. 67 [659], suffer from the trade-off between the scan resolution and scan time [217].

Determination of appropriate surface measurement techniques and roughness parameters that best describe metal AM surfaces is of extreme importance for standards development and comparison of experimental and modeling results [691]. Typical measurement techniques used to analyze metal AM surfaces include profile topography, areal topography, microscopy (such as optical, confocal, chromatic, and focus variation), and XCT, amongst many others [648]. A large selection of roughness parameters are then used to describe the surface roughness; some of the most common include: average roughness (R_a or S_a) mean roughness depth (R_z or S_z), skewness (R_{sk} or S_{sk}) and kurtosis (R_{ku} or S_{ku}) [648]. However, the determination of a robust and agreed-upon metric for analysis of surface roughness of metal powder bed AM surfaces has not yet been determined to date. As an example, contour parameters affecting surface roughness characteristics are typically optimized based on the R_a (or S_a) surface roughness parameter [648]; however roughness metrics using R_a may be contradictory and unreliable when used to predict roughness characteristics or material behavior as shown in work by Fox *et al.* [675], Gockel *et al.* [661], Kerckhofs [684] and Gulizia *et al.* [650].

Fox *et al.* [675] determined that the analysis of R_{pc}, R_{Sm}, and R_c (peak count, mean width of profile elements, and mean height of profile elements, respectively) can indicate a shift between rough surfaces dominated by partially melted powder particles and surfaces dominated by material from the re-solidified melt track in L-PBF SS 17–4. In comparison, analysis of the effect of process parameters on R_a did not show a significant correlation. Gockel *et al.* [661] discovered that the roughness parameter for maximum surface pit height (S_v) was found to be inversely correlated to the fatigue life in [661]. As S_v increased, the fatigue life decreased. In comparison, the roughness parameter S_a did not show a correlation to fatigue life from either structured light scanning methods or XCT analysis [661]. Fractography showed that high roughness and maximum notch values were the result of the contour pass not adhering to the layer below [661]. However, when proper fusion was achieved, the failure locations were influenced by other factors such as material inclusions, and subsurface porosity [661]. Therefore, the determination of a robust metric for analyzing powder bed metal AM surfaces and the comparison of surface data is of vital importance to the metal AM community. It is unclear if standard profilometry techniques and average values for roughness are sufficient to capture all of the relevant 3D information regarding the metal AM as-built surfaces [659]. Vayssette *et al.* [658] determined that the topology of L-PBF and E-PBF as-built surfaces were better captured by XCT as compared to optical micrography [661,684]. More importantly, it was discovered that the measurements from profilometric analysis failed to predict the fatigue strength of parts obtained by L-PBF since micro notch features on specimen surfaces are not well described using profile measurements. Therefore, the comparison of 3D surface data such as XCT with lineal measurements necessitates further analysis. These needs are anticipated to be addressed in forthcoming standards drawing on current/withdrawn metal AM standards such as ISO/ASTM52900-15, ASTM F2792-12a, and ASTM F42/ISO TC 261, however further research into the comparison of roughness metrics used in powder bed metal AM are essential [702].

Recently, full-field measurement techniques such as XCT and high-fidelity modeling have been used to capture the 3D surface and subsurface features to better aid in the understanding of the effects of processing variables on as-built AM surfaces and mechanical performance [658,659]. Tammas-Williams utilized XCT to quantitatively evaluate the factors (Defect size, location, aspect ratio, and proximity to other pores and the surface) that are important in determining fatigue life. It was discovered that defects nearer to the surface, particularly larger defects were typically associated with shorter fatigue lives in E-PBF Ti-6Al-4V. Vayssette *et al.* [658] utilized finite element simulations to characterize realistic metal powder bed AM surfaces from meshed volumes via surface micrography, surface scans (profilometry), or volume scans (tomography). Kantzos *et al.* [659] utilized XCT with high micron resolution and micromechanical modeling to investigate the effect of as-built metal AM surfaces on the stress concentration under mechanical loading for a fine and coarse powder in L-PBF Ti-6Al-4V. These results indicated that: (1) surface features were more sensitive to build conditions than powder size, (2) adhered powder had little effect as a stress "hotspots" (i.e. stress concentrations), (3) porosity and surface notches showed the largest stress hotspots, and (4) near-surface porosity may be more significant as stress hotspots than surface roughness [659]. Future investigations involving the use of 3D surface analysis to connect processing variables and particular surface characteristics are needed to enable quantification and certification of as-built metal powder bed AM surfaces. In particular, precise and representative descriptions of as-built surfaces are needed in order to correctly take into account stress concentrations due to micro notches and to consider a sufficient number of micro notches for modeling efforts [658]. Further studies that evaluate surface roughness via realistic analysis and modeling techniques have great potential to lead to large advances in the evaluation of process variables affecting surface roughness characteristics [281].

4.9. Metallurgical factors for defect generation

In addition to understanding the steady-state behavior of the vapor depression, which may lead to balling, lack of fusion, and keyhole pores, one needs to consider the influence of the vapor depression in non-steady-state regions. This is quite important because controlling vapor depression is much complicated in non-steady regions, causing location-specific conditions for defect formation.

During powder bed fusion AM processes, microstructural inhomogeneities (columnar grains and segregation), impurities, and loss of alloying elements in powdered materials or built parts may take place. Due to the high temperature of the molten pool, it is most likely that vaporization of alloying elements occurs leading to composition variation and inhomogeneous microstructure in as-built parts. These variations will impact materials properties such as corrosion and mechanical behavior which can be crucial for high-quality products and sensitive industrial applications such as aerospace and nuclear power plant.

Hot Cracking. As mentioned in Section 4.7, cracking in AM could be categorized into solidification cracking, liquation cracking, and strain-aging cracking based on the cracking mechanism. Cracking could also be classified as hot cracking and solid-state cracking based on its occurrence in solidifying or solidified region. According to this criterion, solidification cracking and liquation cracking both belong to hot cracking and strain-aging cracking is solid-state crack. Abundant welding studies have shown that solid-state crack is dominantly dictated by thermal and mechanical related factors, while hot-crack is determined by the interplay of metallurgical-, thermal-, mechanical-factors. Section 4.7 presented the influence of residual stress on each type of cracking. This indicates how thermal–mechanical factors contribute to crack development but does not address the metallurgical factors for hot

cracking formation. Therefore, as a supplement of Section 4.7, here, we focus on the metallurgical factors of hot cracking defects in the context of AM process, to provide a comprehensive overview of AM cracking defects. The phenomenon, characteristics, and criteria for hot cracking could be found in Section 4.7, and thus are not repeated here.

Studies on welding [129,499] have presented that the major metallurgical factors for hot cracking include the freezing range, fraction of liquid at the final solidification stage, eutectic reaction, and precipitation at the interdendritic region and grain structure. They are also important influential factors for AM hot cracking susceptibility due to the analogy of welding and AM solidification. The relation of these four factors with hot cracking in the context of AM process were summarized below:

First, the freezing range directly dictates the dimension scale of the mushy zone. Thus, it is widely accepted that a larger freezing range indicates a higher solidification cracking susceptibility. While it should be noted that for the AM process, the non-equilibrium cooling condition is expected to result in a high degree of micro-segregation. For this reason, the equilibrium freezing range (as usually shown in a phase diagram) is likely to be an unsuitable prediction. Instead, Scheil-calculated freezing range was usually adopted to investigating AM solidification cracking, as exemplified by the study of Tang *et al.* on AM alloy design with Ni-alloy system [703] and the study of Wang *et al.* on AM alloy design with steel system [704]. Both studies adopted Scheil-calculated freezing range as important AM cracking susceptibility criteria to guide AM alloy design. By following the principle that a smaller freezing range leads to a lower cracking susceptibility, new alloys with improved AM cracking resistance were discovered by these studies, which supports the effectiveness of Scheil-calculated freezing range for AM solidification cracking prediction.

Second, the fraction of liquid (f_L) at the terminal solidification stage was the liquid at the intergranular or interdendritic region in the melt pool. Its impact on solidification cracking susceptibility was demonstrated by two classic physical models for solidification cracking, namely the model of Clyne *et al.* [705] and the model of Kou [646]. Both models suggest that a large f_L at the terminal stage of solidification indicates a low crack susceptibility since in this case liquid is sufficient to provide a liquid channel at the interdendritic region, which could help to resist cracking by liquid feeding at the grain boundary. Conversely, with a small f_L at the terminal stage of solidification, the liquid is separated into disconnected interdendritic films, which becomes the vulnerable spot for solidification crack initiation. Clyne *et al.* [705] and Kou [646] proposed two hot cracking susceptibility (HCS) index, which are t_V/t_R and $dT/d(f_S^{1/2})$ at $f_S \rightarrow 1$, respectively, where t_V and t_R are time interval of $0.01 < f_L < 0.1$ and $0.1 < f_L < 0.6$ and f_S is solid fraction. Despite different formality, both HCS indexes are indirect reflections of the magnitude of f_L at the terminal solidification stage: increase in t_V/t_R and $dT/d(f_S^{1/2})$ at $f_S \rightarrow 1$ both indicate a decrease in f_L at the terminal solidification stage and thus a higher cracking susceptibility. Various welding studies [706-710] have validated the two HCS indexes as useful criteria for welding crack susceptibility evaluation. They have also been adopted to aid AM alloy design with Ni alloy [703,711] and AM process optimization of Al alloy [712,713] by providing AM cracking susceptibility assessment. These studies on welding and AM cracking investigation indirectly and directly support f_L at the terminal stage of solidification as a significant influential factor that determines AM cracking susceptibility.

Similar to the freezing range, f_L at the terminal stage of solidification is also dependent on the micro-segregation level. Therefore, considering the rapid solidification in the AM process, a Scheil-calculated solidification path has been adopted to the calculation of the cracking susceptibility index developed by Clyne *et al.* [705] and Kou [646], as exemplified by the studies mentioned above [703,706-712]. However, concerns were reported regarding using the Scheil-Gulliver model for AM solidification micro-segregation prediction [714,715]. This is mainly due to the naïve assumption of no back-diffusion in the Scheil-Gulliver model, which might lead to over-estimation of the micro-segregation level in AM solidification. Therefore, careful consideration is required when using the Scheil-Gulliver model to estimate the magnitude of freeing range and f_L at the terminal stage of solidification for the AM process, especially if the alloy presents interstitial elements [716].

Thirdly, eutectic reaction and precipitation that occurred at the interdendritic region is an important factor for liquation cracking. Generally, the formation of eutectic reaction between grains is beneficial for decreasing crack susceptibility, since the eutectic film presents refined microstructure and eases the movement of grains granular system [706]. However, if the eutectic reaction leads to the formation of a low-melting-point eutectic product or intermetallic eutectic product with high brittleness, then its occurrence at the interdendritic region will result in a noticeable increase in crack susceptibility [717,718]. Similarly, precipitation kinetic in AM-processed alloy is complicated and could sometimes result in low-melting-point carbide, nitride, and borides formation at intergranular or interdendritic regions. For instance, interdendritic MC-type carbide is often reported in AM-processed Alloy alloys [719]. These low-melt precipitates are also important sources for liquation cracking formation. The formation of interdendritic low-melt eutectic and precipitates is a common problem for AM with superalloy alloy: many studies have shown the existence of low melting eutectic γ/γ' phase, Laves eutectic phase, MC-type carbide, M_6C-type carbide at the grain boundary in AM-microstructure of superalloy, including Alloy 718 [203,644,720], Alloy 625 [721,722], Hastelloy-X alloy [723,724], Alloy 738 [719] and CMSX4 [725]. The consensus in the AM literature is to use the terminal solidification stage of the Scheil solidification path to estimate the occurrence of detrimental interdendritic eutectic and precipitates. These interdendritic eutectics and precipitates were usually considered as a major source of large cracks in AM-processed superalloy since they provide cracking initiation locations for liquation cracks due to the high tendency of remelting these low-melting eutectics in the HAZ by successive track and layer deposition. Besides, AM microstructure usually presents large columnar grain with dimension across several layers as a result of epitaxial grain growth. This combination of interdendritic eutectic or precipitates with large grain size creates a beneficial condition for liquation cracks to initiate and propagate to large cracks even penetrating across layers. Therefore, controlling the occurrence of corresponding eutectic and precipitation reactions at the interdendritic region is of significance for enhancing AM hot cracking susceptibility.

Lastly, the grain structure is a critical factor for cracking susceptibility since two important criteria of crack susceptibility, the capability of strain accommodation of granular system and the easiness of liquid feeding between grains, are both strongly dependent on grain structure. Generally, AM solidification condition promotes large columnar grain with high-aspect-ratio geometry to grow across layers due to epitaxial growth nature and high-G thermal condition. With this grain structure, AM-parts often show large cracks penetrating multiple layers with its growth along the grain boundary, as widely observed for AM-processed Ti6Al4V and nickel alloys [691,719,726]. Such large cracks are detrimental to fatigue resistance and could even lead to a failed part build. Conversely, grain structure with equiaxed morphology and refined size is highly desirable, since compared to columnar grains, equiaxed grain morphology can deform more easily to accommodate contraction strains and a refined grain size also facilitate liquid feeding to healing cracks. Therefore, a major research focus in the AM community lies in grain structure modification to promote columnar-to-equiaxed transition (CET) in AM solidification conditions. Extensive experimental evidence has been provided to show the effectiveness of CET promotion on lowering AM crack susceptibility, as further presented in Section 6.7. Advanced microstructure modeling methods, such as phase-field and Cellular-Automata numerical modeling, could be useful tools for predicting grain growth into an equiaxed or columnar structure for the AM process. Analytical models have also been established for CET

prediction. Gäumann *et al.* [727] developed a simple but effective theoretical expression for CET prediction under the rapid solidification process. It determines CET criteria as a function of the temperature gradient, solidification velocity, and alloy properties. The applicability and limitation of the Gäumann model [727] for AM process condition were systematically discussed by the study of Mohammadpour *et al.* [728], which showed the Gäumann model [727] coupled with melt pool heat transfer numerical modeling as an effective tool for CET prediction in the general AM process context. These advanced and analytical CET modeling methods could be considered to integrate with AM cracking susceptibility evaluation.

Columnar-equiaxed transition. It occurs during the welding process based on different mechanisms including (i) heterogeneous nucleation, (ii) dendrite fragmentation, and (iii) grain detachment. The former concern can be achieved by using solid particles (ceramic oxides) that act as nucleation sites during solidifications. The latter two can be stimulated by fluid flow and temperature gradients across the melt pool [729]. The columnar-equiaxed-transition takes place when nucleation of sufficiently numerous equiaxed dendrites occur in the constitutionally undercooled liquid adjacent to the columnar dendritic front [730] and different studies have quantitatively predicted columnar-equiaxed-transition transition for different alloys [239,534,731-736]. Since isotropic properties can be attained in parts with equiaxed grain structures, it is necessary to understand how equiaxed grains can be generated in polycrystalline materials. Planar, cellular, or columnar dendritic substructures are the main characteristics of the columnar grains, while, equiaxed grains have equiaxed dendritic substructures [737]. It is possible to induce the formation of equiaxed grains by promoting the formation of equiaxed dendrites. Mitigation based on promoting the formation of equiaxed grains is presented in Section 6.9.

The large thermal gradient not only imparts severe residual stress but also induces inhomogeneous microstructure. Generally, the nucleation and growth of the crystals are controlled by the preferred orientation of their crystal structure. For instance, for face-centered cubic (FCC) crystals such as Ni, the grains would preferentially orient along the [100] direction due to the highest surface energy on (1 0 0) plane [738]. Therefore, strong texture with [100] direction can be identified in directionally solidified superalloys. Triggered by the large thermal gradient, strong anisotropy is generated after solidification. Furthermore, according to the criterion proposed in [739], the microstructure will be predominately columnar when:

$$\frac{G^n}{V} > C_{st} \tag{5}$$

with

$$C_{st} = a\left(8.6\Delta T_0 \frac{N_0^{1/3}}{n+1}\right)^n \tag{6}$$

Here, ΔT_0 is the equilibrium liquidus-solidus interval, N_0 is the nucleation density, a and n are the alloy constants. It could be seen that an increase in G and decrease in V favors the growth of columnar grains while increasing V and decreasing G favors the growth of more equiaxed grains. Note that the nucleation density is particularly difficult to predict and is generally inferred from experimental data. This trend is also consistent with several models used for predicting the solidification behaviors of other alloys [740-742]. For L-PBF or E-PBF processes, the large thermal gradient guarantees the pronounced columnar grain structure. Both features cause the typical columnar grain structure with a certain preferred orientation within the parts fabricated by powder bed fusion. Simultaneously, since the faster cooling rate generally results in smaller grain size, L-PBF parts present a finer columnar grain structure when compared to that of E-PBF samples. The anisotropic grain structure is commonly observed in PBF parts, in which columnar grains are seen on the cross-section parallel to the build direction while equiaxed and cellular grains are observed on the cross-section perpendicular to the build direction. This inhomogeneous grain structure may lead to the formation of grain boundary crack and induce non-uniform mechanical and corrosion behaviors.

Macro- and micro-segregations. Due to the difference in gravity or solubility of each element in the matrix, macro-segregation or micro-segregation occur during the solidification. This will lead to inhomogeneous thermal expansion or contraction. During the solidification, the rapid cooling rate induced by the PBF process imparts huge stress on the dendritic boundaries, resulting in a large residual strain. One example could be seen in Fig. 68(a), a high density of dislocations was observed to accumulate along the dendritic boundaries [475]. For the alloys with poor ductility, the cracks eventually generate and propagate in order to release the residual stress (Fig. 29). Also, the network of solid restricts the free passage of liquid during the solidification, and hence the liquid is not capable of relative movement between the interlocking dendrites. This would result in the void formation that provides an additional opportunity for crack initiation [743].

Similar to segregation, for some alloys that possess a high tendency to precipitate, the stress concentration may take place on the precipitate/matrix interface as well. additionally, the eutectic phase may form in the interdendritic region due to the segregation of some precipitate-forming elements. When the heat source re-heat this region, those eutectic phases present in heat-affected zone (HAZ) may re-melt and form a liquid layer that will induce the crack formation along the boundaries. Fig. 68(b) presents a typical liquation crack induced by HAZ in superalloy [744]. For Ni-base superalloys, the amount of precipitates directly determines the printability, the less Al and Ti contents, the

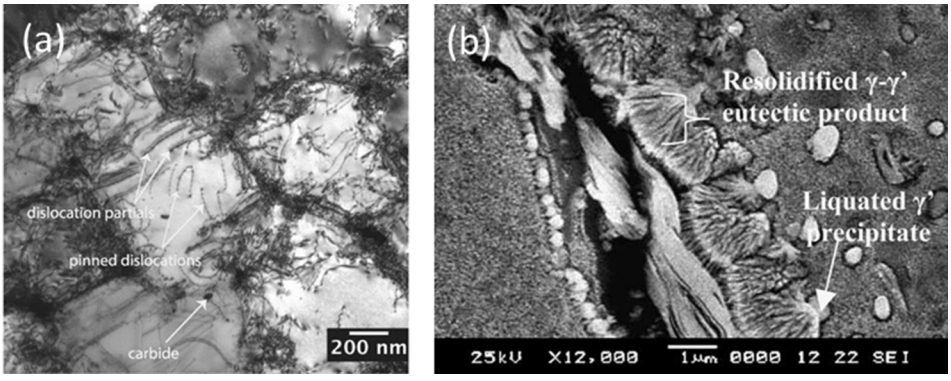

Fig. 68. (a) Selected area bright-field transmission electron microscopy micrograph of a transverse section of the as-built CM247LC processed by L-PBF showing the cell structure. Reprinted with permission from Ref. [475]. (b) Scanning electron micrograph showing the liquation crack present in IN738LC processed by arc welding. Reprinted with permission from Ref. [744].

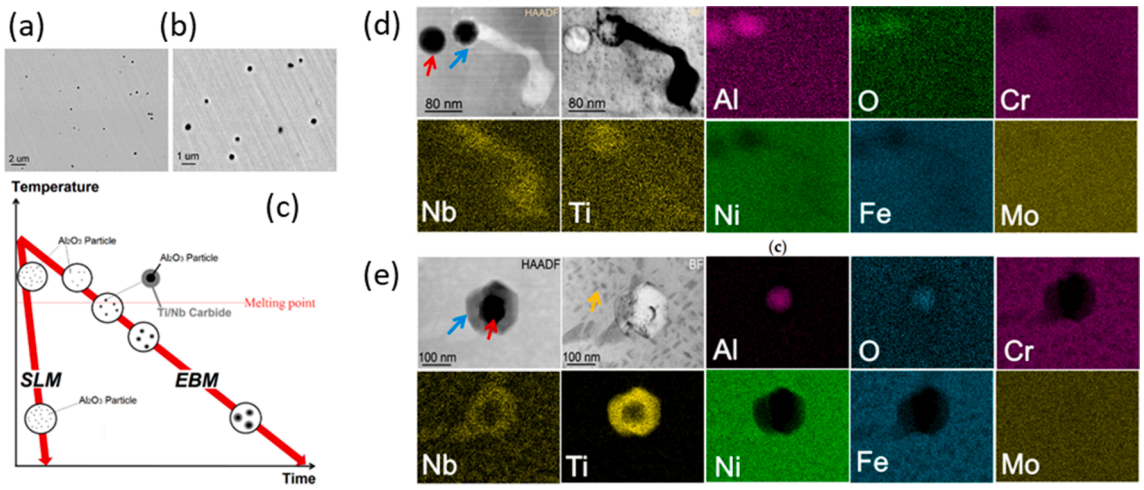

Fig. 69. (a,b) scanning electron micrographs showing the microstructure of alloy 718 processed by L-PBF and E-PBF processes. Note that the black particles are the oxides. (c) Schematic showing cooling rate in L-PBF (aka selective laser melting, SLM) and E-PBF (aka electron beam melting, EBM) processes in which fine aluminum oxides formed in L-PBF parts due to high cooling rate, while coarse alumina particle surrounded by Ti/Nb formed in E-PBF parts. (d,e) TEM micrographs with EDS elemental map of the selected area from alloy 718 processed by L-PBF and E-PBF processes. Reprinted with permission from Ref. [747].

better printability or the weldability (Fig. 29).

Impurities. They include inclusions and un-melted particles. Common inclusions that could be seen in the fabricated parts are oxides and nitrides, which are generated from the oxygen and nitrogen present in the atmosphere or the powders [745,746]. The presence of impurities may cause severe ductility reduction and decrease the fatigue strength. Minor elements in powdered materials may cause the formation of inclusions such as oxides and nitrides. For the alloys containing reactive elements such as Al and Ti, oxygen or nitrogen from the environment or pre-oxidized powder would react with these elements during the processing, resulting in the formation of inclusions. Simultaneously, these inclusions may provide a suitable substrate for other precipitates such as carbide. Thus, a core–shell structure generates around the periphery of the inclusions if the solidification rate is low enough for nucleation. Fig. 69 presents the oxides within alloy 718 processed by L-PBF and E-PBF [747]. Due to the relatively lower solidification rate for E-PBF when compared to L-PBF, it could be seen that larger oxides formed in the E-PBF samples. Moreover, based on the transmission electron micrograph analysis shown in Fig. 69, a Nb/Ti phase was found to nucleate on the surface of oxide particles. With a lower solidification rate in E-PBF samples, the Nb/Ti phase surrounded the entire oxide and formed a core–shell structure consequently.

Some researchers have reported that the alloys that contain minor elements (even lower than 0.2 wt%) such as Zr, Si, and B possess a higher tendency to crack propagation during the L-PBF process of Alloy 738LC [476,747]. Although the mechanism is still not clear, one possible reason can be ascribed to the segregation of these minor elements to grain boundaries. Fig. 70 illustrates the formation mechanism of solidification crack along the grain boundaries. Due to the segregation of minor elements, the high concentration of minor elements at grain boundaries could lower the melting temperature of the alloy. When the heat source passes through and melts the powder, the alloy near the

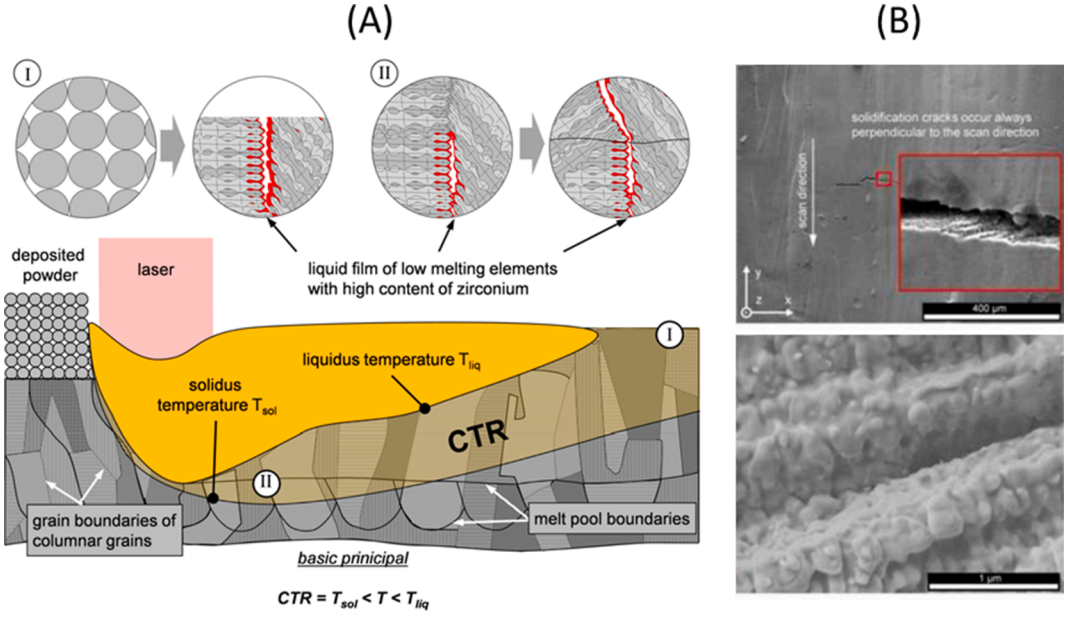

Fig. 70. (A) Schematic illustrating the solidification crack propagating along the grain boundaries. The liquid film with a high concentration of Zr (red area) covers dendrites at the grain boundaries; liquid film cannot absorb solidification shrinkage leading to strain in AM parts; separation of grain boundaries. (B) SEM micrographs showing crack located at the surface of melt polo with dendritic structures at the open surface. Reprinted with permission from Ref. [476].

grain boundaries will remain at the liquid status and generate a thin liquid film. Since this liquid film cannot absorb the solidification shrinkage, the grain boundaries eventually separate and generate a crack in order to compensate for the huge residual stress.

In other cases, Zr and Si have been used extensively to avoid cracking in some high strength Al alloys. Al-Cu-Mg alloy (Al alloy 2xxx) is susceptible to cracking during PBF processes. Zhang *et al.* [748] showed that the addition of 2 wt% Zr to Al-Cu-Mg promoted the formation of Al_3Zr precipitates and resulted in grain refinement, which hindered the formation and propagation of cracks. In another work by Nie *et al.* [749], it was indicated that the grain refinement by the formation of Al_3Zr precipitates plays an important role in hindering the formation and propagation of cracks. In other words, the addition of Zr leads to the occurrence of columnar-equiaxed-transition and the presence of the fine equiaxed grain enhances the grain boundaries, which avoid intergranular cracking. Li *et al.* [750] found that the addition of 1.3 wt% Si to Al-Mg-Sc-Zr could minimize hot cracking during L-PBF due to the formation of coherent Al_3(Sc, Zr) nano-particle and limiting the formation of Al-Mg_2Si interdendritic eutectic in the microstructure.

Loss of alloying elements. During PBF AM processes, the high energy input from laser/electron beam sources will cause vaporization of alloying elements from the surface of the melt pool. When the surface area to volume ratio is high, the vaporization of alloying elements increases. In fusion-based AM processes, melt pool size, temperature profile, and geometry are the key factors in determining the loss of alloying elements. Alloying elements of Mg, Mn, Al, and Ni have a higher tendency to evaporate during the PBF processes [424,751-754]. For instance, a Mn evaporation of 1.1% was reported during the L-PBF of Ni-Mn-Ga magnetic shape memory alloy, causing a different magnetic response in the AM part [755]. Also, the Mn loss was reported in laser-welded stainless steel. Loss of alumina during L-PBF of Al_2O_3 was reported by Liao *et al.* [756] and it was shown when the energy input of laser increased, aluminum acted as a reducing agent leading to the formation of gaseous Al_2O. Barclay [753] laser-processed Ti-6Al-4V powder and found that Al loss occurred for high energy input conditions due to the higher evaporation rate of Al. It was found in [424,425] that the evaporation losses (mainly aluminum and up to 30%) increased with increasing energy input during E-PBF of Ti-6Al-4V, resulting in heterogeneous aluminum content within the material on the scale of the layer thickness. Brice *et al.* [757] additively manufactured aluminum 2139 (Al–Cu–Mg–Ag alloy) and observed Mg evaporation dependent on processing conditions and location within the deposit. When the Mg content became below the threshold, the content of Al_2Cu was significantly decreased leading to lower mechanical properties. Recently, Hojjatzadeh *et al.* [537] observed pore formation along the melting boundary of the melt pool in laser melting of aluminum and its alloys (e.g., pure aluminum and AlSi10Mg) as shown in Fig. 71. They speculated that this type of pore might form because of the vaporization of a volatile impurity substance or expansion of a tiny trapped gas in the material [330,758]. Thus, it was assumed that this pore formation was material dependent.

5. Post-processing-related defects

Post-processing treatments are often sought to alter as-built microstructures, residual stress, and defect distributions in metal powder bed AM materials. Generally, post-processing can be used to modify the size and geometric properties of defects both internally (i.e., LOF, keyhole, gas pores) and externally (e.g., surface roughness); in most cases, this leads to improved mechanical and corrosive behavior [2,691]. For internal defects, both hot isostatic pressing (HIP) treatments [2,154,155,280,546,759] along with heat treatments [81,546,692,760-762] are typically employed. For external defects, surface machining/polishing [672,681-684,763] or shot peening [575,687-691] are typically used. However, while sub-surface defects can often be eliminated via post-processing such as HIP, the resulting microstructural changes and/or coarsening can produce strength reductions [691,764,765]; additionally, subsequent heat treatment may lead to the reappearance of defects [766]. Generally, the HIP equipment and tooling are more complex, the operation is inherently batch rather than continuous, and

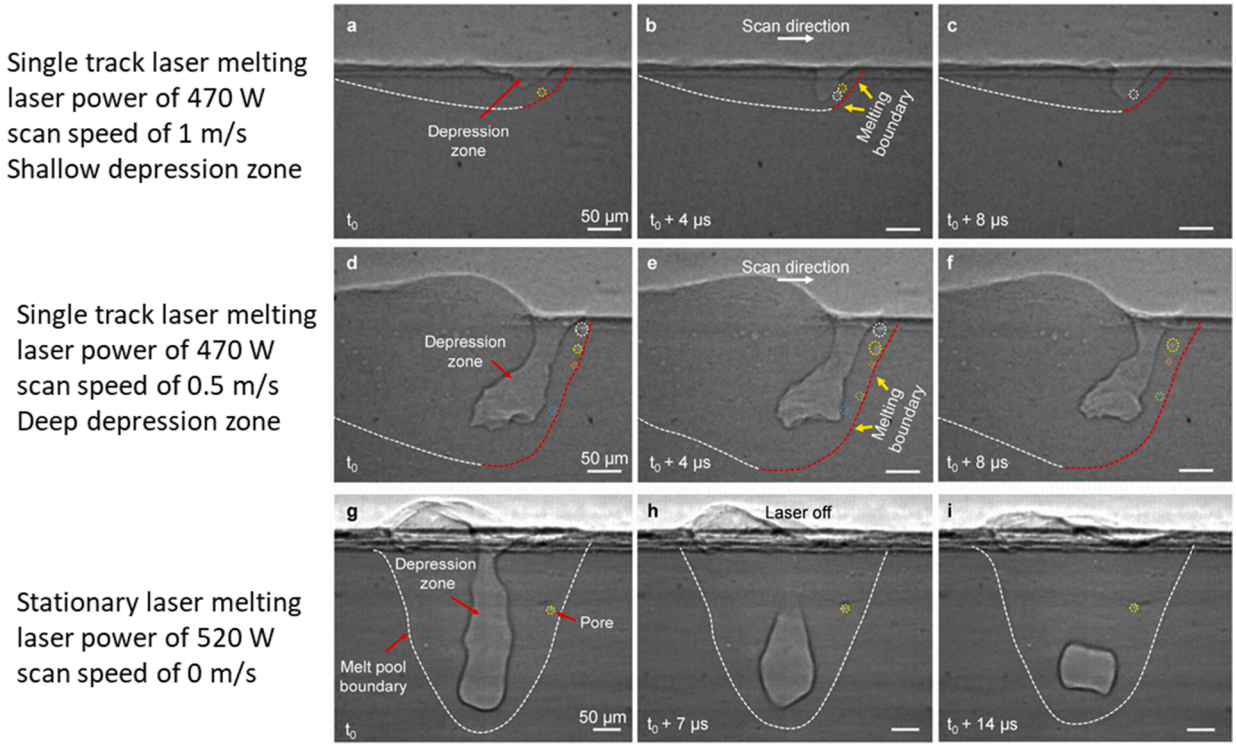

Fig. 71. Pore formation in melt pool boundary during laser melting of aluminum alloys. Pores are displayed by yellow dash circles and melt pool boundaries are shown by red dotted lines. Reprinted with permission from Ref. [537].

the processes overall are expensive and cost more time to finish the parts. Therefore, an understanding of the potential for post-processing related defects is important to take full advantage of their potential benefits.

Internal defects. The combination of HIP and Heat treatment procedures are routinely used in the post-processing of AM parts to reduce the number and severity of internal defects and increase densification [154]. However, Zhang *et al.* [760] recently analyzed the effect of heat treatments and HIP on pore morphology separately for L-PBF Ti-6Al-4V. It was discovered that the pores in HIPed material were slit-shaped with extremely sharp edges (e.g., LOF pores). By contrast, heat treatment alone resulted in a "rounding-off" effect on the LOF porosity within 24 h of treatment. It was also found that continued heat treatments may re-sharpen the pores from the formation of facets of low energy surfaces. However, extended heat treatment time is accompanied by the coarsening of microstructure. Overall, it was determined that heat treatments within 12 h could provide a "pore conditioning effect", while not substantially compromising the microstructure and, consequently, mechanical properties.

HIP treatments typically take place in an inert environment and involve applying high temperature and pressure to shrink the size of internal defects by the reduction of the surface area of the pores. The relatively high temperatures used in HIP effectively lowers the yield strength and enables creep deformation within the material while raising diffusivity to allow for soluble gases to diffuse out of the pores [132,154]. HIP treatments are very effective in reducing porosity and positively affecting mechanical properties in AM parts [81,155,280]. Studies such as [81] and [155] confirm that the HIP process reduced all observed internal porosity below a 5 μm detection limit of μXCT for E-PBF Ti-6Al-4V. Furthermore, Kasperovich *et al.* observed a 6-times reduction in the size of porosity in L-PBF processed Ti-6Al-4V [280]. Zhang *et al.* [760,767] showed that HIP followed by conventional heat treatment on L-PBF processed Ti-6Al-4V could be a good candidate for spheroidizing LOF pores, which reduces stress concentration effects from sharp edges. It was also noted that the HIP processing resulted in considerable microstructural changes in the material due to long times at high temperatures.

However, while the HIP process can be successfully utilized to remove both macro- (e.g., laser-powder interaction porosity) and micro-porosity (e.g., gas porosity), pores containing inert gases may regrow following high-temperature HIP treatments as shown by Fig. 72 [546,759,766-770]. This is referred to as thermally induced porosity (TIP), and can negatively impact mechanical performance [766]. The occurrence of TIP after HIP processing depends on a myriad of factors including grain size, processing medium (i.e., argon, nitrogen, or helium gas), amount of powder (gas) porosity, and the annealing time [766]. The mechanism behind TIP is the result of heating a pressurized pore to temperatures that allow the surrounding material to deform by creep deformation. Recently, Strandh *et al.* [771] revealed that the surface roughness, HIP treatment soaking time and presence of oxide layer on surfaces prior to HIP aggravate the pore growth beneath the surfaces (*aka* argon pick-up).

This is a well-understood process to make porous titanium structures, but the effects of defect regrowth on AM parts have not been well-characterized. Tammas-Williams *et al.* [155] observed TIP in E-PBF Ti-6Al-4V and related this to starting powder and temperature. In this study, spherical gas pores containing argon were found to reappear and grow in proportion to their original as-built size during high-temperature treatments [155]. Tammas-Williams *et al.* demonstrated pore regrowth after heat treatment at 1035 °C of HIPed samples

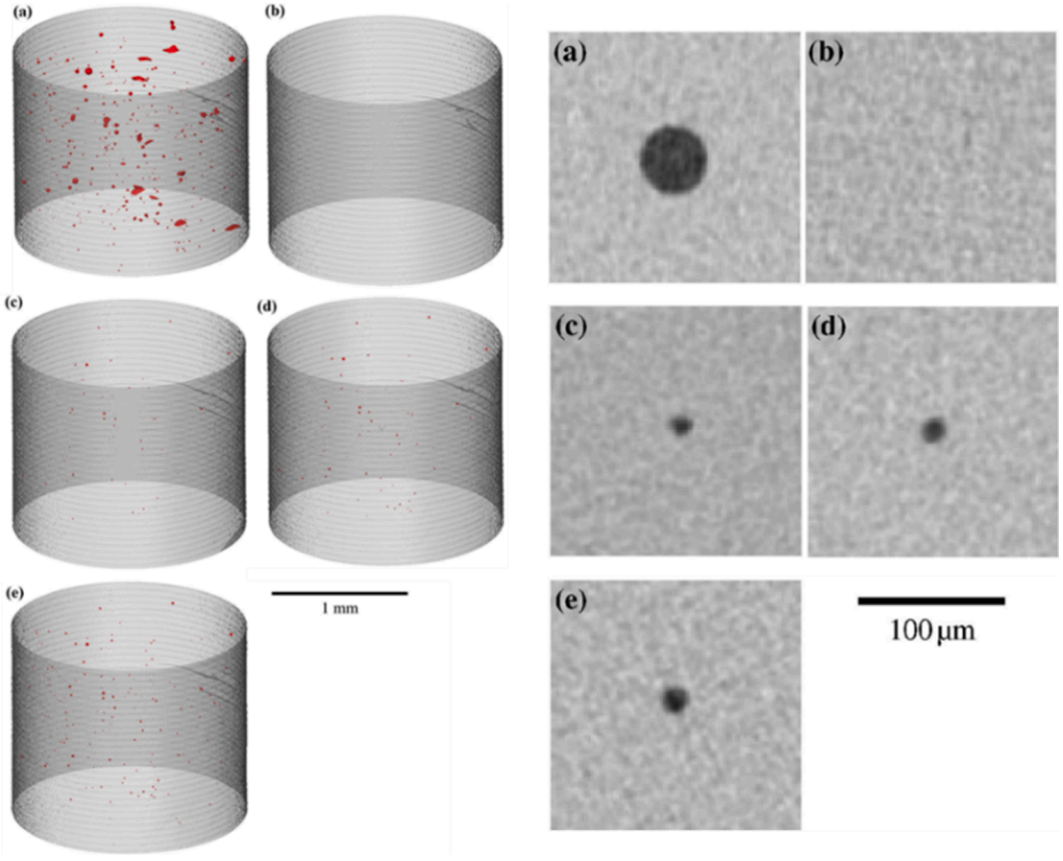

Fig. 72. (Left) 3D and (right) 2D XCT visualization of the porosity (red) in E-PBF Ti-6Al-4V cylindrical samples. (a) As-built, (b) following HIPing, (c) 10 min at 1035 °C, (d) 10 h at 1035 °C, and (e) 10 min at 1200 °C. Note: in 2D CT data, samples were centered on an individual pore (sample location after HIPing) . Reprinted with permission from Ref. [546].

(Fig. 72). Strumza *et al.* reported TIP in L-PBF processed aluminum and titanium alloys [767]. Cunningham *et al.*[132] investigated the tendency for LOF and keyhole defects to experience TIP in plasma atomized and PREP Ti-6Al-4V powder. After HIP processing of 900 °C at 103 MPa in argon, the samples underwent a β-solution heat treatment at 1050 °C for 10 min. While the HIP process greatly reduced LOF and keyhole porosity from the as-built samples, the post HIP heat treatment of the samples resulted in over 200% growth in effective diameter [81]. Interestingly, it was also noticed that the morphology of a pore in the as-built condition may influence its subsequent regrowth behavior at high temperatures. Both starting material and laser-powder interaction defects were observed to coarsen after exposure to temperatures after experiencing temperatures above the β-transus temperature for Ti-6Al-4V (where creep resistance is much reduced) in [132]. This further highlights the importance of using low porosity powders and choosing processing conditions that enable fully dense as-built parts since starting defect size plays an important role in TIP behavior [81]. Shuai *et al.* [767] studied the solubility of Ar in α-Ti during the HIP process in which the radius of Ar-containing pores was found to shrink by 1–2 orders of magnitude. This would lead to an increase in the internal pressure during the HIP process which depends on pore size. The suggested threshold for initial pore is 1 μm, in which a smaller pore will lead to a significant increase in the internal pore pressure (e.g., 10 GPa for a pore with an initial radius of 0.01 μm).

External defects. Although the removal of surface features is generally believed to result in improved surface roughness and enhanced material behavior [691,764] (see Section 4.8), post-processing surface alteration may also result in external (surface) defects [772,773]. An example of this was determined by Edwards and Ramulu [772] for L-PBF Ti-6Al-4V. Here, it was discovered that the effect of surface machining on improving high cycle fatigue (HCF) resistance was more pronounced for horizontally orientated specimens as compared to the vertical orientation. This was likely due to the characteristics of interior voids formed during fabrication [773]. Similar results were observed in Yadallohi and Shamsaei [773] for L-PBF Alloy 718, where the as-built and surface machined conditions performed identically in fully-reversed fatigue loading. Analysis of fatigue fracture surfaces in [773], revealed the presence of large sub-surface un-melted regions (>100 μm). By machining and removing the rough surface, these sub-surface voids (which were formed just beneath the surface due to improper contour parameter, scan strategy, laser power, and velocity) are brought to the surface of the specimens. Therefore, these surface voids can still serve as crack initiation sites and affect the part's fatigue behavior leading to the observed behavior. Additionally, depending on the size and shape, these surface voids may be more detrimental than surface roughness as they can provide a higher stress concentration. Therefore, more analysis is necessary to characterize the effects of surface processing induced defects resultant from sub-surface porosity within the contour regions. However, the use of optimized parameters for contour regions has the potential to reduce this type of defect and thereby improve fatigue life as discussed in Section 4.8.

6. Mitigation of defects

Defect identification and mitigation is an important aspect in metal additive manufacturing to improve part quality and performance. Numerous investigations have been carried out to visualize defect formation mechanisms and remedies were suggested case by case. Here, common mitigation techniques for each kind of defect are discussed.

6.1. Powder porosity and gas pore transfer

Multiple investigations [81,130,134] have shown that typical metal AM starting powders may contain entrapped gas porosity, which motivates a description of preventive measures for the reduction of powder (gas) porosity within finished AM metal parts. Studies by Tammas-Williams *et al.* [774] and Cunningham *et al.* [81] have shown clearly that powder with high porosity results in parts with similarly high defect populations. Furthermore, both static and dynamic mechanical properties are adversely affected by the presence of gas porosity in castings [154]. Accordingly, powder porosity may also have a measurable impact on overall part quality for metal AM components. Currently, one of the most effective and reliable methods to limit the occurrence of gas porosity within as-built parts is the appropriate choice of starting powder feedstock containing the least quantity of retained gas pores such as the PREP powder reported in [350]. Therein, Chen *et al.* characterized gas atomized, PREP, and plasma atomized Ti-6Al-4V powders in order to compare microstructure, porosity, argon gas content, and pore spatial structure within the powder [350]. Notably, it was discovered that gas atomized and plasma atomized powders exhibited significantly higher argon content (0.77 ± 0.06 and 0.70 ± 0.06 μg/g) and porosity (0.20 ± 0.01% and 0.12 ± 0.01%) than PREP powders (0.16 ± 0.06 μg/g and 0.08 ± 0.01% respectively). Larger pore sphericity than PREP powders was also discovered in the atomized powders due to different gas pressures inside of the powders. Overall it was also determined that argon content and porosity increased with increasing powder size for each type of powder. As such, powders such as PREP powders which utilize specific manufacturing techniques to limit entrapped gas within material feedstock should be chosen.

Proper engineering controls on powder feedstock can also have large positive effects on the reduction of gas pore transfer. For example, if a part is to be fabricated with a given supply of powder, then, the first step is drying powder in an oven prior to the AM processing to eliminate surface moisture. In aluminum alloys, moisture in the powder is the main source of hydrogen gas porosity [510]. In addition, alloying elements such as silicon and lithium in aluminum can reduce the solubility of gases AM parts [775]. Additionally, utilizing smaller powder sizes may also lead to less porosity transfer; this is particularly important since porosity size distribution carries over to the as-built part [350]. Proper choice of processing parameters can also significantly reduce gas porosity [81] and may also be a useful method to lower gas porosity when using powders with higher levels of entrapped inert gas (i.e., plasma atomized powders).

Generally, combinations of power, scan speed, and hatch spacing play an important role in the reduction of entrapped gas porosity. Typically, a longer melt pool lifetime affords more time for the formed gas bubbles to escape. The appropriate choice of processing parameters such as the use of low scanning speed to generate increased melt pool sizes may also decrease the amount of gas porosity retained in the part after the laser-powder interaction. Layer re-melting is another method that may enable the escape of trapped gas pores from the melt pool before solidification. However, this may only result in limited success since pores adjacent to the laser scanning path are believed to result in entrapped gas porosity after solidification [132,330,535].

6.2. Balling and bead-up

Balling generally occurs in the high power, high-velocity portions of process space and therefore may practically limit the useable build rates within metal powder bed AM processes [150]. Currently, balling is managed simply by not building parts in the high power, high-velocity regions of the process space. It was also shown by Gu and Shen [562] that low power and low velocity will result in balling, thus, very low power can lead to insufficient heat input and coarsened balls form due to limited liquid formation. Based on the P-R stability hypothesis, any strategy that decreases melt pool length and/or increases width should be beneficial. One such strategy is the increasing of laser spot size, which decreases L/W and reduces the occurrence and severity of balling [85]. Improving the wetting of the substrate may also be beneficial, as was suggested by the results of Gu *et al.* [562]. They showed that adding a trace amount of deoxidant (H_3BO_3 and KBF_4) in the powder largely reduced the balling tendency and improved the surface quality of the

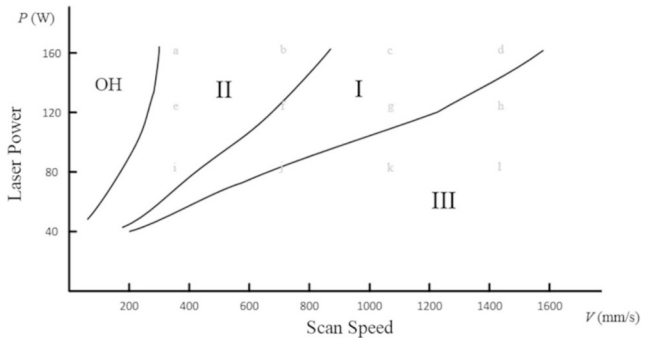

Fig. 73. Processing map. Zone I - fully dense; zone II - subsurface porosity; zone III - insufficient melting; OH - serious surface deformation. Reprinted with permission from Ref. [84].

deposited layer. This was also consistent with gas tungsten arc welding studies [578], where oxygen in the shield gas was detrimental to melt pool stability. In other words, the addition of deoxidants to the powder can assist the generation of a smooth sintering surface and reduce the risk of ball formation by mitigating the formation of an oxide layer on the melt pool. Additionally, beam shaping (elliptical) may help to reprocess areas deposited by circular profiles to reduce surface roughness and potentially balling [776]. More work is necessary to examine how alloy and gas compositions affect the occurrence of balling.

6.3. Lack of fusion

In practice, to prevent laser processing induced lack of fusion porosity, the first choice is to follow the laser power – scanning speed maps [84]. In Fig. 73, zone III corresponds to lack-of-fusion defects like porosity. In addition, the laser spot size, hatch spacing as well as powder bed layer thickness could be adjusted. In general, the smaller the spot size, hatch spacing, and layer thickness, the less tendency there should be for the lack of fusion porosity formation [28,98,777]. However, Tang *et al.* [98] showed that increases in energy density do not necessarily improve part density, and a constant energy density may lead to different porosity. Principally speaking, sufficient penetration of melt pool is required to mitigate or eliminate lack-of-fusion porosity. Therefore, the criteria, $L/D < 1.15$ for Ti-6Al-4V or $L/D < 1.5$ for CoCrMo alloy, proposed by Mukherjee [594], or the one $(H/W)^2 + (L/D)^2 < 1$, proposed by Tang *et al.* [98] could be used, as illustrated in Fig. 45 and Fig. 46, respectively.

On the other hand, to prevent powder induced lack of fusion porosity, unfavorable powder particles should be avoided or mitigated. For example, in the raw feedstock, powder particles with irregular shapes such as elongated shape, or satellites particles, or open or closed porosity, should be removed i.e., by appropriate powder sieving techniques. To mitigate spattering induced larger and irregular clusters [48,602], the approaches described in Section 6.6 could be adopted, such as changing the environmental pressure [325] and introducing a high-velocity laminar flow of protective gas over the powder bed [48,160,778]. Also, preheating of powder bed can mitigate lack-of-fusion porosity because less energy is required for full overlap of melt pools [779,780].

Besides, hot isostatic pressing (HIP) treatment mitigates any kind of (closed) porosity after printing. Synchrotron microtomography in Fig. 74 shows that porosity can be dramatically reduced after HIP [81].

Mechanical performance of AM parts, especially under fatigue, is sensitive to the presence of critical defects [781-784]. Lack of fusion defects, because of their high aspect ratios and sharp edges are often the most critical defect affecting mechanical performance even when other types of defect are present. Cyclic loading whose direction is perpendicular to the lack of fusion defects has been shown to induce more damage than, for instance when the loading direction is parallel to the defects [785]. Utilizing this characteristic and by taking advantage of material anisotropy, a “design for AM” concept may be helpful for the fabrication of AM parts with enhanced fatigue performance. In such an approach, the strongest direction in the material can be aligned with the highest (principal) stress direction at the critical location of the part, based on external loading and part geometry. When the avoidance of these defects is not guaranteed and HIP is not feasible, a critical damage approach—which has shown to be reliable for fatigue life estimations under more realistic multiaxial loading—needs to be adopted for the AM parts [773]. Critical plane approaches for multiaxial fatigue predict the fatigue damage in specific directions based on experimental evidence that fatigue cracks do not form in random directions but respond to the local stress system [786].

6.4. Keyhole porosity

The formation of keyhole porosity is strongly dependent on the choice of laser processing variables (i.e., laser power, laser spot size, laser scan velocity, etc.), material-specific properties (i.e., boiling point, powder particle size and distribution, powder bed thickness, etc.), and choice of the atmosphere [24,26,96,124,136,672,787]. Therefore, mitigation of keyhole porosity is a complex endeavor, and requires both machine and material-specific analysis, particularly with a focus on the influence of processing variables on the melt pool and vapor cavity (keyhole) characteristics. As a general guide, as discussed above, keyholing is expected when the power density is above ~1 MW/cm^2 but the onset of keyhole porosity is a more complex phenomenon that depends on the instability of deep keyholes [48] and must therefore be determined empirically [24]. Given the dependence on power density, mitigation may be achieved via control of beam focus. This is discussed in

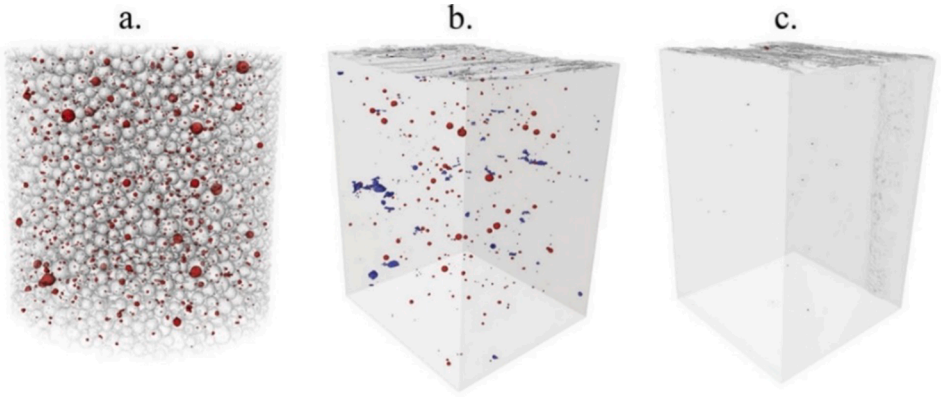

Fig. 74. Synchrotron microtomography results showing that HIP drastically reduces all types of porosity. (a) Raw powder packing. (b) As-built sample. (c) HIP treated sample. Reprinted with permission from Ref. [81].

more detail below.

As with the mitigation of lack of fusion defects, HIPing is also widely used to minimize the keyhole porosity. This treatment, however, cannot guarantee the complete elimination of these pores, which could be eventually responsible for the initiation of fatigue cracks [546,694,760]. The effectiveness of HIP on full closure of keyhole pores in L-PBF processed parts with Ar as shielding gas is low, due to the presence of Ar in the keyhole pores. Owing to the extremely low solubility of Ar in metals, the reduction in defect size is associated with the buildup of internal pressure within the porosity itself, which prevents full closure. Under typical HIP treatment (e.g. for Ti-6Al-4V the typical soaking temperature is 820 °C and the soak time 2 h [694,760]), the size of an Ar containing pore can shrink 1–2 orders of magnitude.

Current research on *operando* experimental methods has led to a greatly increased understanding of the origins of keyhole porosity in metal AM via high-speed synchrotron x-ray imaging [24-26,327,788]. The results are critical to improving physics-based models for the accurate prediction and mitigation of keyhole porosity. Morphological analysis of the keyhole via *operando* experiments have pointed to a specific threshold for keyhole porosity generation as a function of processing variable selections such as laser power and laser velocity (in addition to others) (Fig. 75) [25,788]. L-PBF of Ti-6Al-4V alloy showed that for some laser velocities, which form a keyhole morphology with a front wall angle greater than a specific threshold value (e.g., 77°), keyhole porosity formed in the part [25]. Keyhole pores were discovered to form within the characteristic high power, low scan speed sections of the *P-V* processing space; thus, simple mitigation techniques were suggested including altering laser scan speed or laser power density.

The experiential and modeling results by Bayat *et al.* [788] support the assertion that the "at-risk" keyhole is a function of simple processing variables including laser power. It was shown that exceeding a certain threshold of input power density results in a keyhole due to instability at the bottom of deep keyholes where the pores form. Keyhole porosity then forms within the melt pool due to the occurrence of local cold zones with higher surface tension and insignificant recoil pressure since most of the rays are trapped due to the complex indentation configuration of the melt pool [788]. The abovementioned results suggest that the mitigation of keyhole porosity may be possible through the alteration of key processing variables such as laser focus. Further analyses of other powder bed metal AM materials systems, limited at this time, are greatly needed. However, the recent report by Zhao et al. [24] shows a clear demarcation between stable and unstable keyholes (in terms of porosity generation, Fig. 50), which strongly suggests that it should be possible to avoid keyhole porosity by avoiding the high power-low speed region.

Additionally, spot size adjustments have been utilized to alter laser power density and avoid unwanted keyhole defects as also shown by King *et al.* [96]. This is due to the production of rounded melt pool shapes closer to those generated when operating in conduction mode. In the study by Francis [85], keyhole was produced with narrow beam spot sizes. However, as the spot size increased, keyholing behavior became less pronounced. Increasing spot size eventually leads to conduction mode melting [85]. Mapping of keyhole porosity formation using basic processing variables has great potential to enable the rapid mitigation of keyhole porosity for laser powder bed metal AM processes [24]. This would enable the identification of process variables that lead to keyhole porosity in particular and are to be avoided.

Alternatively, analytical approaches such as enthalpy-based methods covered in Section 4.4 enable rapid analysis of the process, machine, and material characteristics affecting keyhole porosity. Multiple researchers have determined a boundary for keyhole-mode melting using normalized enthalpy for a given set of processing variables and material properties in order to evaluate keyhole porosity for many common metal AM materials [49,88,96,606,787,789-791]. A subset of these results and corresponding studies are summarized in Table 1.

Table 1
Keyhole thresholds for common metals. (values in bold are from experiment, otherwise from theory).

Material	Normalized Enthalpy ($\Delta H/h_s$)	Ref.
SS 316L	6–10 (**30 ± 4**)	[96]
	6	[787]
	3.92–6.34	[88]
	7–8 (Threshold)	[49]
	10–11(Fully developed)	
Ti-6Al-4V	**17 ± 8**	[606]
	10	[789]
Alloy 718	5	[789]
17–4 PH	25	[790]
MA956 steel	19	[791]

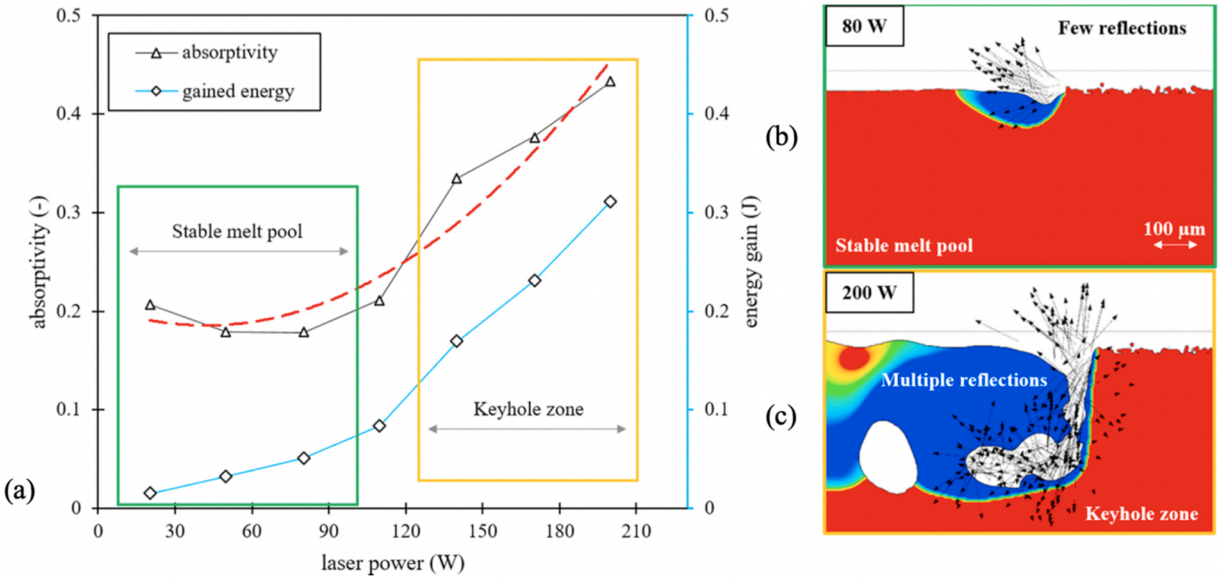

Fig. 75. (a) Keyhole melt pool formation is a function of processing variables, namely laser power (density) for a given laser scan speed in L-PBF Ti-6Al-4V. (b) For laser power values under the keyhole threshold, few reflections of the laser beam occur leading to conduction mode melt pools. (c) For laser power densities above a threshold, a keyhole melt pool is formed leading to multiple laser beam reflections and keyhole porosity. Reprinted with permission from Ref. [788].

Further analyses are greatly warranted to push the understanding of keyhole porosity formation and consequently mitigation. Future work on developing analytical methods that determine a specific threshold for keyhole porosity formation (such as a front wall angle criterion in morphology-based methods) would greatly enable the robust prediction and therefore mitigation of keyhole porosity in powder bed metal AM processes.

6.5. Turnaround and end-of-track porosity

Typically, laser power has the main impact on turnaround or end of track pore formation, whereas scan speed has minimal influence on the melt pool depth or pore dynamics [792]. It was shown that pore formation at the turnaround point could be caused by a momentary increase in energy density [134,232,793,794]. In other words, the combination of the constant laser power and slower laser velocity at the turnaround point resulted in a deep keyhole mode melting. A practical strategy to avoid this pore formation is reducing the laser power near the turning point e.g., through employing "skywriting" scanning techniques [792,795]. Martin *et al.* [327] proposed a pore mitigation strategy based on modulating laser power. As seen in Fig. 76(a,b), a bulge formed at the turnaround region due to overheating and expansion of the melt pool caused by high energy density. Additionally, a few pores were detected 250 μm beneath the surface. In contrast, a modulated laser power showed an improved geometry of the deposited track. As shown in Fig. 76(c,d), a bulge-free high-quality area at the end of the track as well as pore-free structure was achieved. Reduction of laser power can prevent a transition to a deep keyhole vapor depression. Finally, the proposed mitigation technique can improve the geometric tolerance of produced tracks by avoiding overheating.

6.6. Spattering and denudation

As discussed earlier, in laser powder bed fusion additive manufacturing, spatters originate from various sources (1) from the front keyhole rim because of the strong recoil on the keyhole wall [602,618], (2) from the rear keyhole rim because of the intensive flow inside the melt pool and the drag force of the vapor jet from the front keyhole wall [621,622], (3) from both the front and the rear keyhole rims as a result of the bulk explosion of a tongue-like protrusion on the front keyhole wall [48], (4) from the powder bed due to the vapor plume ejection from the keyhole [48,602], and (5) from the powder bed due to the environmental gas flow [66,325]. Regardless of their origins, these spatters tend to have different compositions, microstructures, and morphologies compared to the raw feedstock, and form deleterious defects such as lack of fusion porosity; they also degrade mechanical property such as fatigue life of the end products [330,421,503,601,620]. Hence, to manufacture spatter-free and defect-free parts, effective and efficient mitigation techniques for metal spattering are needed, as summarized below.

Generally, reducing the laser heating intensity by adjusting laser power and scanning speed is a first choice for mitigating metal spatters. When the laser beam advances, most of the incident beam impinges on the front keyhole wall [48,613]. The lower the laser heating intensity, the lower the overheating on the front keyhole wall, the weaker the vapor plume ejection as well as the recoil on the liquid beneath the keyhole wall surface. When the local melt on either the front or the rear keyhole rim does not attain enough momentum from the recoil and/or the vapor plume jet, there will be no spatter ejected directly from the keyhole wall, as shown in Fig. 77(a) [48]. In the presence of metal powder, weaker vapor plume ejection means that fewer spatters will be ejected or denuded from the powder bed, as shown in Fig. 77(b) [66].

A second potential approach to mitigating spatters in laser powder bed fusion is to change the environmental pressure. As described in Fig. 77(c), with an increase in environmental pressure, there is a minimum in the width of the denudation zone, which corresponds well with the peak in the fraction of particles within the denudation zone. Note that this interesting phenomenon is caused by the competition between the drag force on the particles and either the particle collisions by the tangentially vaporizing particles or the metal vapor flow directed by the dynamically undulating melt pool [66]. Besides, the amount of hot spatters, i.e., particles heated up by the laser, vapor, or plasma [61,602], increases with increasing environmental pressure [325].

As illustrated in Fig. 57, the formation of some extremely fast spatters is closely related to the keyhole dynamics and the protrusion structures on the front keyhole wall [48]. To mitigate such spatters, a protective gas stream could be fed to the keyhole at a certain tilt angle (toward the surface of the front wall) to open up and stabilize the keyhole, which was initially adopted by the community to mitigate porosity generation [618], as depicted in Fig. 77(d). We note that such a technique could only be applied to a bare plate or a pre-sintered powder bed. For regular L-PBF, where the powder bed is not pre-sintered, Zhao *et al.* proposed that the laser beam profiles could be modified to suppress the melt flows around the keyhole, which may account for the effects noted for beam shaping [48].

The mitigation techniques mentioned above are all based on the formation mechanisms for metal spattering, and therefore can be called active prevention. Achee *et al.* [796] showed that laser pre-sintering

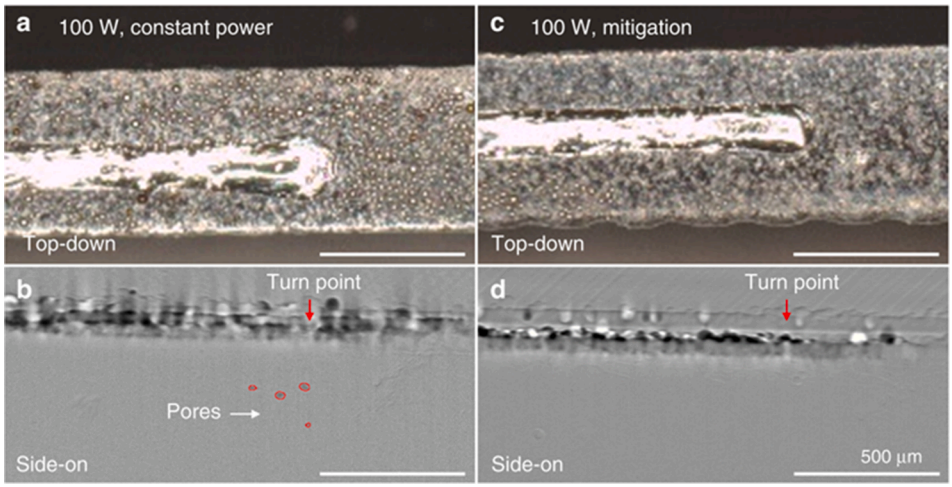

Fig. 76. (a,c) Top view optical micrographs (b,d) side-view *in situ* high-speed x-ray images showing turnaround point area during L-PBF. A track produced using (a,b) a constant power of 100 W resulted in keyhole pores and (c,d) the 100 W peak power with an adjusted laser velocity close to the turnaround area in which pore mitigation occurred. Reprinted with permission from Ref. [327].

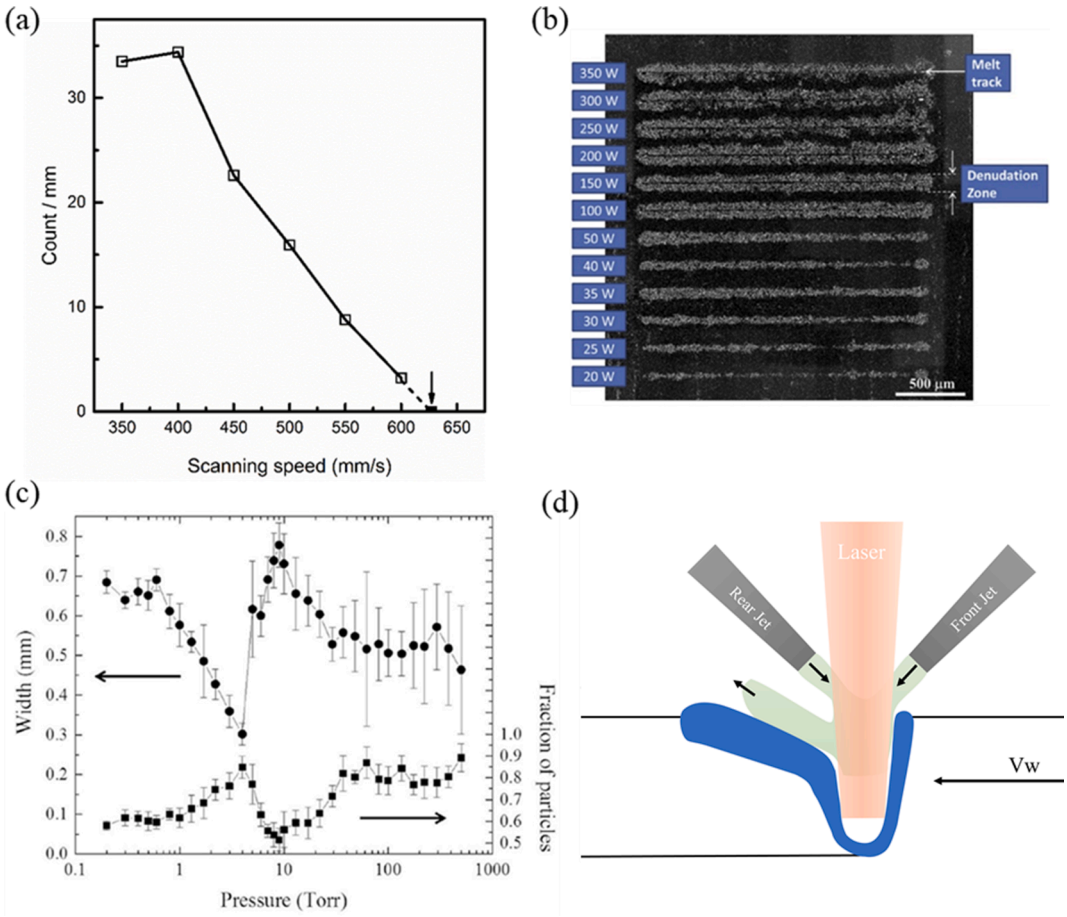

Fig. 77. (a) Occurrence frequency of spatters in a bare metal plate as a function of laser scanning speed. For a given laser beam size and a power, when the scanning speed is higher than a threshold, there will be no spatter ejected directly from the keyhole wall. Reprinted with permission from Ref. [48]. (b) Wide-field image of denudation zones around melt tracks in laser powder bed fusion as a function of laser power. Given a laser beam size and a scanning speed, the denudation zone width tends to reduce with the decrease of laser power. Reprinted with permission from Ref. [66]. (c) Denudation zone width displayed on the left axis and Fraction of detected particles within the denudation zone on the right axis as functions of environmental pressure. Reprinted with permission from Ref. [66]. (d) Feeding a gas jet to open up the keyhole in a bare plate or a pre-sintered powder bed. Reproduced from Ref. [618].

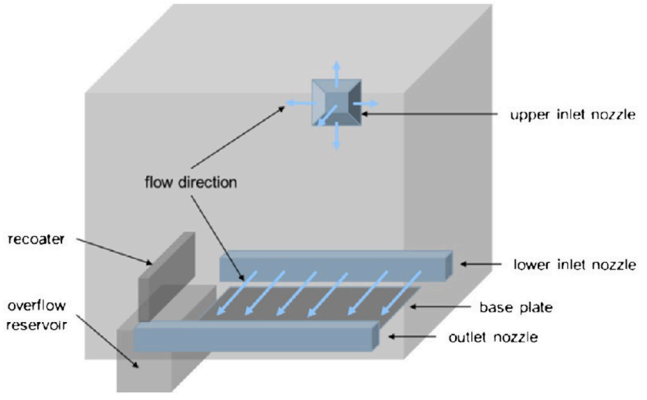

Fig. 78. Schematic representation of the gas laminar flow system in the process chamber. Reprinted with permission from Ref. [778].

could minimize powder spattering and denudation, however, the powder bed is often not pre-sintered in L-PBF, primarily to minimize production cost. As a result, spatters are hard to eliminate with the above approaches. To further mitigate spatter induced defects such as lack of fusion porosity, one solution is to introduce a high-velocity laminar flow of protective gas over the powder bed [48,160,778]. As shown in Fig. 78, the gas flow pattern tends to blow the spatters away from the building area and prevent them from falling back onto the powder bed. This laminar gas flow approach has, however, little influence on the keyhole and melt pool dynamics and is only a remedial measure for the spattering problem.

6.7. *Residual stresses, cracking, and delamination*

Residual stress and its resulting problem including strain-induced cracking and delamination problems are commonly observed in AM-processed ferrous alloys and superalloys (and potentially high strength aluminum and titanium alloys). Mitigation strategies for residual stress in AM and the resulting delamination and cracking defects could be categorized into AM process optimization and post-process treatment. Further discussion on the metallurgical approach for cracking mitigate is provided at the end of this section.

AM process optimization has higher freedom of adjustment and reduced cost compared to post-process treatment. Thus, it is often the primary strategy for consideration. As shown in Section 4.7, residual stress developed in the AM part is largely related to the high-temperature gradient as a result of small-volume melting and fast cooling rate. Noted that the melting-solidification cycle in AM occurs and include melt pool solidification and the partial re-melting during successive track and layer deposition. Therefore, the principle of AM process optimization is to minimize temperature gradient by (1) decreasing the cooling rate of melt pool solidification and cooling rate of

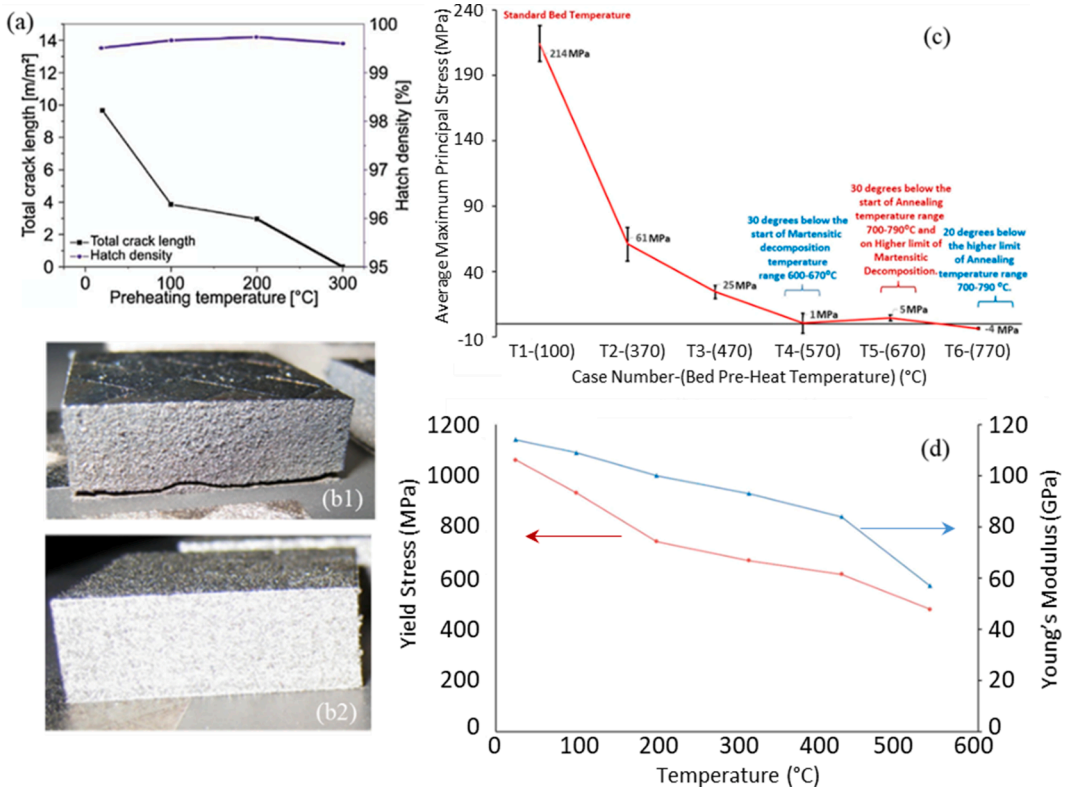

Fig. 79. Influence of preheating temperature on crack density and delamination. (a) H13 steel fabricated by L-PBF processing at various preheat temperature. Reprinted with permission from Ref. [143], and (b1,b2) M2 steel fabricated by L-PBF processing at no preheating illustrated in "b1" and 200 °C preheating shown in "b2" . Reprinted with permission from Ref. [169]. (c, d) Correlation among preheating temperature, residual stress, and mechanical property (yield stress and Youngs Modulus) for L-PBF processing of Ti-6Al-4V. Reprinted with permission from Ref. [817].

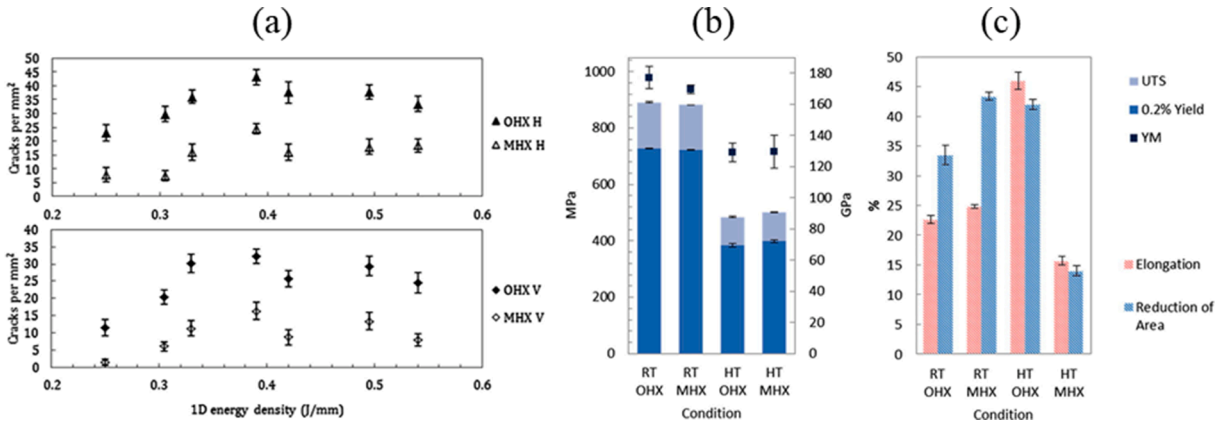

Fig. 80. (a) Comparison of crack density, (b) room-temperature properties, and (c) high-temperature properties for a L-PBF part built with modified composition Hastelloy (MHX) and unmodified Hastelloy (OHX); room-temperature and high-temperature: labeled as RT and HT. Reprinted with permission from Ref. [814].

successive track and layer deposition; (2) altering melt pool volume and partial re-melting volume. The most widely reported approach for AM residual stress mitigation is increasing baseplate preheat temperature since it could decrease the cooling rate throughout the whole part build process. Its effectiveness has been experimentally validated for L-PBF with Ti6Al4V [797], AlSi10Mg [171], Alloy 625 [798], tool steel [170,520], stainless steel [799] and alloy steel [800], as exemplified by Fig. 79 and Fig. 80. For more examples, the reader is directed to the list in Table 2. The correlation among preheat temperature, temperature gradient, and residual stress was also theoretically analyzed by AM thermo-mechanical numerical modeling [801-803]. It should be noted that the effectiveness of increasing baseplate preheat temperature might not be extended to residual stress mitigation for E-PBF process. As mentioned in Section 4.7, residual stress evolution for E-PBF process is different from that of the laser-based AM process mainly due to the inherent E-PBF process characteristic of powder layer preheat, which already results in sufficiently high chamber and powder bed temperatures even reaching the level of 1000 °C. Therefore, other strategies instead of baseplate preheat temperature enhancement should be considered for E-PBF residual stress mitigation.

Besides baseplate preheat temperature, laser power (P) and scan velocity (V) are also important process variables to consider for residual stress mitigation. Energy density is an index that combines the influence of P and V on melt pool volume (and thus HAZ volume) as well as cooling

Table 2
Summary of residual stress, cracking, and delamination defect and mitigation approaches presented in the literature for different alloys and AM systems.

Alloy	AM system	Defect type	Mitigation approach	Ref.
Hastelloy X alloy	L-PBF	Solidification cracking	Modifying the Mn, Si comp.%	[814]
Ni-base superalloy (CM247LC)	L-PBF	Solidification cracking & strain aging cracking	1. Adjusting laser power and scan speed: Increasing energy density to suppress solidification crack; Decreasing energy density to suppress strain aging crack 2. Undergoing HIP post treatment	[470]
Aluminum 6061	L-PBF	Solidification cracking	1. Adopting high preheat temperature 2. Modifying laser power, scan velocity, and layer thickness	[5]
M2 steel	L-PBF	Residual stress & Crack & delamination	1. Adopting high preheat temperature 2. Adopting laser re-melt scan strategy	[170]
Alloy 625	L-PBF	Liquation cracking	Adopting high preheat temperature	[798]
Ni-base alloy (lab-developed)	L-PBF	Cracking & delamination	Adopting a dual-laser scan strategy	[643]
316L stainless steel	L-PBF	Cracking	1. Developing a process window for hatch spacing and laser exposure time 2. Undergoing HIP post treatment	[815]
Alloy 738LC	L-PBF	Solidification cracking or liquation cracking	1. Developing a process window for laser power and scan speed 2. Undergoing HIP post treatment 3. Solid solution post treatment	[637]
Aluminum 6061 Aluminum 7075	L-PBF	Solidification cracking	Modifying the composition by adding Zr nanoparticle	[503]
Ti–45Al–7Nb–0.3 W	E-PBF	Cracking	Adopting beam-reheating scan strategy	[69]
Tungsten carbide-cobalt (83WC-17Co)	L-PBF	Cracking	Adjusting laser power, scan speed & hatch spacing to decrease heat input	[816]
316L SS/ Alloy 718 joining	E-PBF	Strain-aging cracking	Solutionizing treatment for base metal	[516]
Ti-6Al-4V	L-PBF	Solidification cracking	Adopting high preheat temperature	[817]
316L stainless steel	L-PBF	Residual stress & cracking	1. Adopting high preheat temperature 2. Using short scan vectors	[799]
316L stainless steel	L-PBF	Residual stress	Adopting a cheese-board scan pattern	[818]
AlSi10Mg	L-PBF	Residual stress & crack	Adopting high preheat temperature	[171]
H13 steel	L-PBF	Residual stress	Adopting high preheat temperature	[520]

rate, making it a common guiding criterion for residual stress mitigation. Energy density could be expressed as energy input per unit volume ($\frac{P}{Vhd}$), per unit area ($\frac{P}{Vh}$), or per unit length ($\frac{P}{V}$), with h as hatch spacing and d as layer thickness. These three expressions have all been adopted in literature to evaluate the relation between P-V parameter and AM residual stress [800,803-806]. No matter which energy density expression is adopted, these studies all reported the general trend of lower residual stress with higher energy density, which was observed for L-PBF with Alloy 718 [800] and L-PBF with alloy steel [806], stainless steel [804], Ti6Al4V [803] and Alloy 718 [805]. This indicates that residual stress mitigation might be achieved by increasing P at fixed V or decreasing V at fixed P to decrease energy density [807]. However, energy density is by no mean a quantitative index to guide residual stress mitigation since it could not provide comprehensive information for the laser beam and alloy system. Studies have shown that when increasing laser power is combined with decreasing scan velocity [805] (or exposure time for SLM machine [808]) in a manner of keeping a fixed energy density, residual stress could still vary, indicating that energy density becomes useless to evaluate the trend of residual stress if all the involved process variable are allowed to vary. The other two process variables involved in energy density quantity, layer thickness, and hatch spacing, are also important process variables for residual stress control. They directly determine the partial-remelt volume fraction of the previously solidified melt pool during successive track and layer deposition and thus have a profound influence on heat accumulation rate as well as local boundary condition during the part build, in turn influencing residual stress development in the AM part. Studies have shown the general trend of residual stress and distortion decreasing with increasing layer thickness, as observed for L-PBF with Ti-6Al-4V [809] and tool steel [810].

In addition to direct control over the above process variables, altering scan strategies is also an effective process optimization approach for residual stress mitigation [811]. In general, there are two types of scan strategy alteration. One is a double scan of the original pattern. The other is adopting a new scan pattern. For the “double-scan” strategy, the additional scan is assigned with a considerably lower energy density with respect to the default scan. The additional scan could occur prior to or after the default scan deposits the whole layer, to provide a pre-heating effect for powder layer sintering or a re-heating effect for consolidating the current layer respectively [799]. Both numerical modeling [812] and experimental work [799,812] have shown that double-scan in preheating and post-heating deposition order could both effectively decrease residual stress as a result of temperature gradient reduction. This is similar to the thermal effect of the inherent EBM process step of powder layer preheat as mentioned in Section 4.7. For the second type of new scan pattern adoption, one of the most successful cases is adopting the checkerboard or island scanning patterns to replacing the common raster scan pattern. Its effectiveness of residual stress mitigation has been validated by various studies as summarized in Table 2. As exemplified by the checkerboard scan strategy, it could be seen that the key factors of scan pattern optimization are scan vector length and scan vector orientation. The alteration from raster pattern to checkerboard pattern allows substantial shortening in scan vector length and higher freedom to adapt scan vector orientation to the part geometry, both of which are beneficial for reaching a more uniform stress field [813]. This is quantitatively supported by AM thermal–mechanical

numerical modeling [35], which could also be qualitatively shown by the three-bar-frame physical model in Section 4.7.

It should be noted that adopting the presented process-related approach presents the risk of mitigating residual stress at the expense of arousing other process defects. For instance, as mentioned above, residual stress mitigation could be achieved by increasing laser power, decreasing scan velocity, and increasing layer thickness. However, the first two actions present the risk of producing keyholing porosity and the last one might cause lack-of-fusion porosity. Comprehensive consideration is required to determine process-related strategy in an optimal way to mitigate residual stress whilst evaluating the risk of other processing constraints such as porosity.

In terms of post-process treatment, Hot Isostatic Pressing (HIP) is usually adopted to close porosity and cracks in AM as-built components and shot-peening treatment is utilized to alter part residual stress. The effectiveness of HIP to suppress cracking in AM-part was observed for L-PBF processed H13 tool steel [637], nickel superalloy [637,819], and stainless steels [820]. However, HIP could also lead to solid-state microstructure evolution that alters the grain size and phase constituent of the HIP-treated part compared to its original as-built state. Röttger [815] showed that for L-PBF-processed 316L stainless steel, the prior austenite grain coarsened from around 20 μm in the as-built state to 47 μm in the HIP state. Due to grain coarsening, the HIP-treated L-PBF samples showed lower ultimate tensile strength compared to the as-built samples. Therefore, it is necessary to design HIP treatments tailored to the AM processing of each alloy in order to ensure superior properties.

Shot-peening treatments, on the other hand, can alter the residual stress state from tensile to compressive for the near-surface region of AM parts [690]. As mentioned in Section 4.7, the near-surface region usually presents the maximum residual stress magnitude, making it vulnerable for cracking and delamination to occur, which is detrimental to fatigue properties of the AM part. Hence, by altering the residual stress state from tensile to compressive near the surface, shot peening treatment shows the great potential to enhance the fatigue life of AM parts [689].

The above approaches for residual stress mitigation could all be useful strategies for reducing strain-induced cracking and delamination susceptibility of AM part since as demonstrated in Section 4.7, residual stress is a fundamental driver for part cracking and delamination. While as shown in Section 4.9, thermal, mechanical, and metallurgical factors all have a profound influence on the hot cracking susceptibility of AM-part. Approaches for residual stress mitigation could reduce cracking susceptibility by controlling the thermal and mechanical contributor of cracking. While many studies have developed effective cracking mitigation strategies by addressing the metallurgical factors of hot cracking. They are summarized below:

The four major metallurgical factors for AM hot cracking, as demonstrated in Section 4.9, are freezing range, f_L at the final solidification stage, eutectic reaction at interdendritic regions, and grain structure. Based on their relation with cracking susceptibility, the basic principles to reduce AM cracking susceptibility are: (1) reducing freezing range, (2) increasing f_L at the final solidification stage, (3) suppressing detrimental intergranular eutectic reaction and precipitation (4) CET promotion.

Following the principle of freezing range reduction, Tomus *et al.* [821] achieved effective L-PBF cracking reduction by decreasing (Mn + Si) content of Hastelloy X, since lower Mn + Si content could narrow the freezing range as a result of micro-segregation degree modification. Wang *et al.* [704] proposed an alloy design approach to develop new high-strength low-alloy steels for additive manufacturing by evaluating the effect of varying each alloying element on the freezing range through high-throughput CALPHAD calculation. A more common approach is to combine the evaluation of both freezing range and f_L at the final solidification stage as cracking susceptibility criteria for AM alloy design, as exemplified by the studies of Thapliyal et.al. [822,823] and the study of Tang *et al.* [703]. They developed new aluminum alloy, high entropy alloy, and superalloy for additive manufacturing and reported a substantial decrease in crack density or even achieving crack-free AM part. In these studies, CALPHAD calculation with Scheil-Gulliver model was adopted to estimate the freezing range and f_L at the final solidification stage. Moreover, the hot cracking susceptibility (HCS) indexes developed by Clyne *et al.* [705] and Kou [646] were adopted to quantifying f_L at the final solidification stage. The two HCS indexes are introduced earlier in Section 4.9 and thus not repeated here. These studies showed CALPHAD calculation with Scheil-Gulliver model and the HCS index of Clyne *et al.* [705] and Kou [646] as useful alloy design tools to develop low-crack-susceptibility AM alloys, but some limitations need to be noted: first, inappropriate thermodynamic database for CALPHAD calculation could cause error in cracking susceptibility evaluation. Tang *et al.* [703] showed that selecting different thermodynamic databases for CALPHAD calculation resulted in noticeably different freezing ranges for the same alloy composition. Wang *et al.* [704] evaluated the validity of CALPHAD calculation with experimental measurement and found inconsistency for some equilibrium-calculated thermodynamic quantities and their experimental measurements, indicating the inaccuracy of the CALPHAD thermodynamic database. Second, the arbitrary definition of f_L at the final solidification stage could result in inconsistent cracking susceptibility evaluation. For the two HCS indexes of Clyne *et al.* [705] and Kou [646] as mentioned earlier, the interval of f_L at the final solidification stage used for AM and weld cracking susceptibility varies with different studies. For instance, the criteria for f_L at final solidification stage of $0.01 < f_L < 0.2$, $0 < f_L < 0.05$, $0 < f_L < 0.025$ were adopted by the study of Tang *et al.* [703], Thapliyal *et al.* [822], Jiang *et al.*[824] respectively to calculate the HCS index of Kou model[646] for AM-crack susceptibility evaluation. In fact, in the original studies [646,705], f_L at final solidification stage is determined as $0.01 < f_L < 0.1$ and $0.06 < f_s < 0.13$, and they were clarified to be adjustable. This arouses concerns that calculating the HCS index of the same theoretical model but with different definitions of f_L at the final solidification stage leads to inconsistent AM cracking susceptibility evaluation.

The principle of suppressing detrimental intergranular eutectic

Table 3
CET strategies and the corresponding effects on the grain structure and cracking mitigation for AM process.

Alloy	AM process	CET strategy	Effects		Ref.
			Grain structure	Crack	
Alloy 718	E-PBF	Adjust beam deflection speed and line offset	fully E	Not reported	[2]
Al: AA-2024	L-PBF	Adjust Power,Point distance, Exposure time, Apparent velocity	C + E mixed	Not reported	[833]
Al-5 Mg	L-PBF	(Sc + Zr) addition to form Al3(Sc, Zr) particle	C + E mixed;	Not reported	[830]
Al-2 Mg- 6Zn;	L-PBF	(Sc + Zr) addition to form Al3(Sc, Zr) particle	C + E mixed;	Crack-free	[831]
Al-4 Mg-0.2Zr	L-PBF	Sc addition to form Al3(Sc, Zr) particle + adjust power and scan velocity	fully E	Eliminated large crack	[834]
Al 6061; Al-7Si	L-PBF	Sc addition to form Al3(Sc,Zr) particle	fully C; d: reduce 50–80%	Not reported	[832]
Al 6061; Al-7Si	L-PBF	Tibor@ Ti-B nanoparticle addition	fully E; d: reduce 60–80%	Not reported	[832]
Al7075; Al6061	L-PBF	Zr addition to form Al3Zr particle	Fully E	Eliminate hot cracking	[503]
Pure Ti	L-PBF	Cu addition	Fully E; d: reduce 80%	Crack-free	[835]
Ti6Al4V	L-PBF	Adjust part and support geometry, inter-layer time, and layer thickness	C + E	Not reported	[836]

Note: "C" and "E": stands for columnar and equiaxed grain structure respectively.

reaction and precipitation is widely adopted to mitigating cracking for AM-processed Ni-based alloy. This could be achieved by composition adjustment for the involved alloying elements or AM process control to modify microsegregation degree. As mentioned earlier in Section 4.7, a major source of liquation cracking in AM-processed Ni-based superalloy lies in the occurrence of interdendritic Laves eutectic phase, γ/γ' eutectic phase, MC-type and M_6C-type carbide, among which Laves phase control appears to receive the greatest interest in AM community. Laves phase in many Ni-base superalloys presents chemical composition as $(Fe, Ni)_2(Nb, Cr, Mo, Ti)$. Studies showed effective AM crack mitigation based on Laves phase control by Ti% composition adjustment for Alloy 625 [722], adjusting laser wave mode and heat input to modify Nb segregation for Alloy 718 [825826], enhancing baseplate cooling and laser input angle to modify overall segregation degree for Alloy 718 [644,827]. AM-crack mitigation of Ni-based superalloy by control over γ/γ' eutectic phase and carbide was also extensively reported. Similar to Laves phase control, control over γ/γ' eutectic phase and carbide also follow the general principle of micro-segregation degree modification. Some typical examples include Al% adjustment for Alloy 939 [703], carbon composition modification for Hastelloy X alloy [828], adopting scanning laser epitaxy technique to suppress carbide formation of Rene N5 alloy [829], which are all reported to be effectively reduced AM cracking.

Lastly, CET promotion is a major research focus in the AM community. It is not only beneficial for cracking mitigation, but also help to minimize the property anisotropy of the AM part. CET promotion in the AM process could be classified into three categories: introducing nanoparticles to provide heterogeneous nucleation sites; composition modification to promote constitutional supercooling; process control to modify G-R thermal condition. Table 3 summarized the CET strategies adopted for the AM process with various alloy systems and AM techniques. Table 3 also compares their effectiveness on grain structure modification and crack mitigation. In Table 3, the studies that reported cracking characterization all showed a remarkable crack density and dimension reduction as CET is achieved, providing sufficient experimental evidence for CET promotion as an effective AM cracking mitigation approach.

As exemplified by Table 3, introducing nanoparticles appears to be the most widely adopted strategy for CET promotion. There are two approaches to introduce nanoparticles in AM alloy. One is a direct addition of the nanoparticle of selection. Rare earth oxides, TiC, ZrC, and TiB particles are common choices for CET promotion due to their high melting point and remarkable thermal and chemical stability. The other is chemical composition modification to *in situ* grow the nanoparticle of selection, as exemplified by (Sr + Zr) addition on Al-Mg alloy systems [830,831], which allow *in situ* growth of $Al_3(Sr, Zr)$ particles to promote CET in AM process. It should be noted that for the same type of nanoparticle, its CET promotion effect could show remarkable variation when it is coupled with different matrix alloys. This is exemplified by combining the research results from Spierings *et al.* [830], Zhou *et al.* [831] and Carluccio *et al.* [832] in Table 3, which shows that $Al_3(Sc, Zr)$ particle could effectively promote partial CET for Al-5 Mg and Al-2 Mg-6Zn alloy, but it is ineffective for CET promotion of either Al 6061 or Al-7Si, as suggested by their fully columnar AM microstructure with or without $Al_3(Sc, Zr)$ particle [832]. Tibor titanium boride particle, on the other hand, shows remarkable CET promoting effect for Al 6061 and Al-7Si, allowing these two alloys to present fully equiaxed L-PBF microstructure. Therefore, a major challenge is to identify a suitable nanoparticle for the alloy system of interest to achieve the goal of CET promotion in AM microstructure. The outstanding difficulty lies in that trial-and-error experimental work appears to be the only viable approach to resolve this challenge due to the lack of prediction tools to guide nanoparticle selection.

The strategy of process control for CET promotion is more predictable with respect to the strategy of introducing nanoparticles since there are many effective AM modeling tools to guide the AM process design. The common modeling methods to predict CET in AM microstructure include the phase field-finite element (PF-FE) coupling model, cellular automata-finite element (CA-FE) coupling model, and analytical CET model developed by Gaumann *et al.* [727]. As shown in Section 4.9, the Gäumann model [727] is a simple yet effective tool to predict CET promotion, and its applicability to the AM process was supported by the study of Mohammadpour *et al.* [728]. This model could be adopted to construct a solidification microstructure selection (SMS) map for AM processed alloy, which is a great visualization tool for identifying the process window and composition space to promote CET in AM microstructure. This is exemplified by the studies of Mohammadpour *et al.* [721,728], which developed SMS maps for L-PBF-processed Al-Si-10 Mg and high entropy alloy. Compared to the analytical model, the numerical modeling method, including PF-FE and CA-FE methods could provide a more specified simulation scenario and a more comprehensive process-microstructure relation, making it suitable for multi-dimensional process optimization. This is exemplified by the study of Botello *et al.*[833] in Table 3, which conducted multi-dimensional process optimization with four L-PBF process parameters to find the optimal process condition for CET promotion. While analytical model might be insufficient for multi-dimensional process optimization since the involved assumptions might not fully address the interplay among process parameters.

For the strategy of composition modification for constitutional supercooling adjustment, several attempts have been made but the reported effect on CET promotion in AM is usually moderate or negligible, including the attempts of Ti6Al4V modification by (Cr + Mo + Zr)-addition [837] and Si-addition [838] and B-addition [839]. They all failed to promote CET in the AM microstructure of Ti6Al4V. This is because the high-G high-R thermal condition of the AM process results in a sufficiently large nucleation-free zone (NFZ). Such a large NFZ is difficult to be minimized just by the increment of constitutional undercooling from composition modification. Nevertheless, successful cases have been reported, such as the study of Zhang *et al.* [835], which adopted the strategy of Cu addition for Ti to effectively achieve CET in L-PBF microstructure. The effectiveness of Cu addition is owing to the high growth restriction factor (Q) of the Ti-Cu system compared to most other alloying elements. In the study of Zhang *et al.* [835], a normalized Q is adopted to guide the selection of Cu element, defined as $Q = m(k - 1)$. This variable could be considered for future investigations on CET promotion in AM microstructure.

Besides these four categories, AM crack mitigation strategies based on other principles were also reported. Harrison *et al.* [814] proposed an alloy design principle that relies on adding alloy elements with a solid solution strengthening (SSS) effect to the initial alloy to suppress AM cracking susceptibility. With the addition of the SSS element, the modified alloy was likely to form a supersaturated solid solution during AM deposition. That in turn, could achieve higher lattice stress and thus higher thermal shock resistance during AM part build, which in turn leads to higher cracking resistance compared to the initial alloy. Compared to the initial Hastelloy X alloy, the modified Hastelloy X alloy showed about 60% reduction in cracking density and noticeable enhancement in both room-temperature and high-temperature properties, as shown in Fig. 80.

6.8. Surface finish and roughness

The failure of as-built metal AM materials due to surface roughness and porosity is a major cause of concern for fatigue critical metal AM components [652,691]. Particularly detrimental to part performance are deep valleys on the surface which act as preferential sites for mechanical damage and corrosion [653-655]. To remedy these issues, standard practice in metal powder bed AM technologies employs post-processing to alleviate rough surface features through procedures such as heat treatments [692], machining [840], chemical polishing [841,842], laser polishing [686], or electropolishing [843]. However, the use of post-

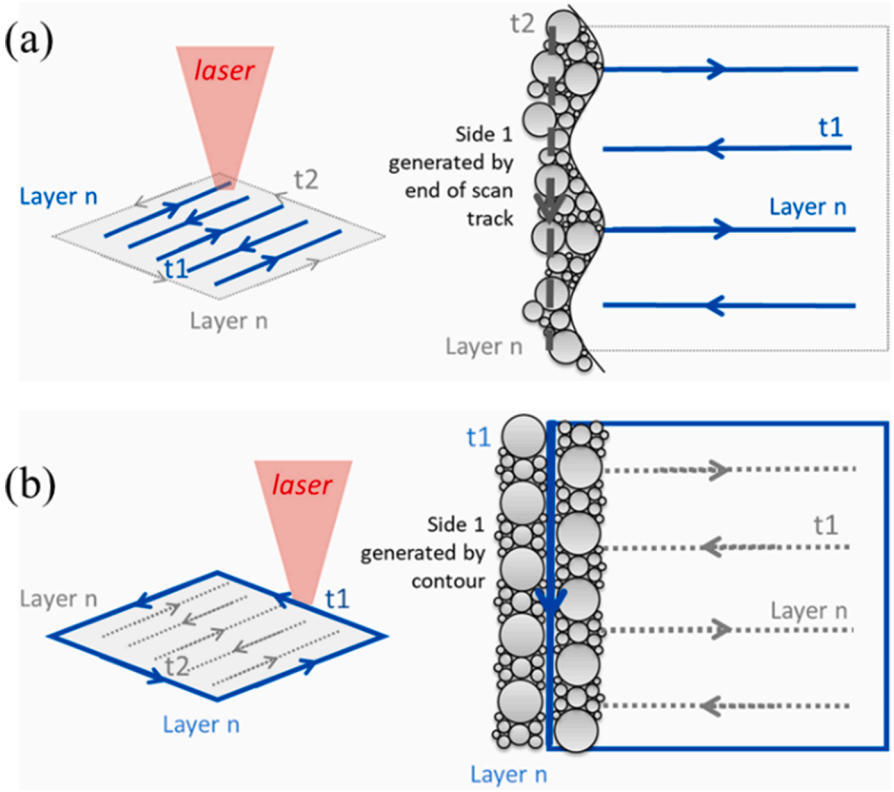

Fig. 81. Two cases of contour settings: (a) Scan then contour and (b) Contour then scan. The later one can be performed to minimize side roughness. Reprinted with permission from Ref. [847].

processing techniques on metal AM parts adds additional manufacturing steps (leading to increased costs) and may undermine the business case for near-net-shape production of metal AM parts [269,672,689,690,842]. Furthermore, surface post-processing may not be possible for certain build geometries such as lattice structures and metamaterials [659]. Therefore, recent work in the metal AM community has focused on the analysis of surface roughness in powder bed metal AM, namely surface metrology, process parameter optimization, and roughness modeling [575,625,647,648,650,652,664,691]. By understanding and reducing the potential for undesirable surface finish and roughness characteristics, improved reliability and durability of metal AM materials is possible [559,575,647,648,652,656,672,691,841,844].

Process variable selection. The relationships between processing variables (particularly in the contour regions) and surface roughness have been confirmed by many studies [84,90,181,255,666,845] and covered in more detail in Section 4.8. Studies such as Calignano *et al.* [575] discovered that the proper choice of process parameters including the reduction of layer thickness, increasing layer re-melting using larger melt pool volumes, and decreasing laser speed was beneficial. Paria *et al.* [656] discovered that for samples possessing a single contour, the scanning speed had the strongest effect on surface roughness parameter S_a (determined by profile analysis). Alternatively, for samples possessing two-contour passes, beam current and focus offset were the most significant parameters affecting surface roughness. Decreasing layer thickness was also discovered to decrease surface roughness since the stair-step effect between layers is reduced [846]. Mumtaz and Hopkinson [666] found that high laser peak power reduced both top and side surface roughness; however, increasing laser repetition rate and reducing scan speed reduced top roughness but increased side roughness. Koutiri *et al.* [562] also discovered a correlation between the roughness parameter S_a was shown to increase with lower scan speeds, to decrease with higher powers, and to increase severely on down-skin sides for large building angles [665]. Recently, Masiagutova et al. showed if the contour is applied prior to the scanning on the heart of samples, the laser crosses a homogeneous powder bed, leading to a fine surface roughness (R_a of 10 μm). In the contrast, when the contouring is carried out after scanning the heart of the samples, the laser crosses an inhomogeneous powder bed, leading to a rougher surface (R_a of 25 μm) (see Fig. 81).

Laser re-melting. Re-melting may also impact surface roughness [143,674,848,849]. In more detail, laser re-melting is a process where a second laser scan is applied to the same slice before spreading a new layer of metal powder [849]. Yu *et al.* [674] determined that R_a decreases on the top surface but increases on the side surface after re-melting. Laser re-melting (outer contour and inner contour parameters) was used in Ibrahim *et al.* [849] to improve the surface quality and improve the density in SLS SS316L. Yasa *et al.* showed that laser re-melting improves the density to almost 100% whereas 90% enhancement is achieved in the surface quality of L-PBF parts after laser re-melting [848]. Although laser re-melting shows promise in improving surface roughness and surface finish, it may also release more keyhole pores at edges and lead to longer production times.

Overall, although improvements in surface roughness are possible using process variable alteration, many investigations utilize trial-and-error type approaches only applicable to single material systems or metal powder bed AM processes. In contrast, studies such as Strano *et al.* [664], Cabanettes *et al.* [850], and Boschetto [851] have great potential to aid in targeted process variable selection and are applicable across multiple metal AM processes and materials by analyzing the stair-step effect and surface roughness in L-PBF. Other analysis techniques such as numerical models [181] and FEA [672] connecting local thermal history and surface roughness may also lead to large advancements in the analysis and prediction of surface roughness characteristics in metal powder bed AM.

6.9. Metallurgical factors

The microstructures of additively manufactured metals have shown to be substantially different from traditionally manufactured counterpart due to the high solidification rate during the AM processes. Therefore, one of the concerns in AM parts is the growth of columnar grains that grow along the build direction which can lead to the growth of cracks discussed in Section 4.7 and anisotropy in the deformation [852]. Therefore, one approach for avoiding columnar grain growth is by varying the process parameters for tailored microstructures. The control of the microstructure is possible by altering the scan strategies and melt themes (e.g., control of the crystallographic orientation of Alloy 718 by altering the electron beam current and scan velocity [853]) or altering the heat input to manipulate the cooling rate and underlying microstructural features [854]. The columnar-to-equiaxed (CTE) transition can be calculated using established methods, but could also be translated into a process map in power-velocity space which allows the selection of the correct combinations of processing parameters to result in tailored microstructure [855]. In a different approach, post-processing heat treatments present a viable option to transition the microstructure from columnar to equiaxed, specifically using recrystallization heat treatments. The material in use undergoes heating at an elevated temperature (close to the material melting temperature) for a period of time long enough to achieve full recrystallization. Some examples of work that has presented recrystallization in AM materials include Alloy 718 [856,857]. However, it is worth noting that the aforementioned mitigation routes may not be practical for all alloys, e.g. Ti-6Al-4V, in which production of equiaxed grains in AM is not feasible and planar growth is dominant [401,858].

To mitigate the loss of alloying element issue, one may measure the composition of feedstock materials and compare it with the AM parts. In a model proposed by Klassen *et al.* [424], a numerical model was developed to measure elemental mass prior to the printing and compare it with the AM part. If the process is carried out in a sealed quartz tube, condensed materials can be collected and analyzed for further measurements of vaporized elements. To compensate for the loss of alloying elements, one may correct the composition of the starting materials [757,859] (e.g., starting with high Al content Ti-6Al-4V powder or wire is essential in E-PBF additive with this alloy because of the loss of Al) or using fluxing during AM process to adjust the composition of the final parts. It is also practical to adjust the power-velocity combination to control power density distribution and heat input. This will assist to have control over microstructural segregation and cracking as well.

7. Prediction of defect and anomalies content

The implicit degradation of part quality due to the presence of defects provides an incentive to predict and mitigate defect formation during powder bed fusion. The design of predictive methodologies and modeling approaches is critical to the long-term success of the AM technology. As such, significant effort has been made in attempting to build these capabilities. Teng *et al.* [860] summarized the modeling of defects in laser material processing techniques, including powder bed fusion processes. Four main defects including (1) balling or bead-up phenomenon (4.2), (2) lack of fusion (4.3), (3) keyhole (4.4), and (4) residual stress (4.7) were modeled in multiple laser material processing techniques. In the following, computational models for the main defects forming in L-PBF are reviewed.

As porosity is generally observed in AM parts, predicting and understanding how its formation occurs has become a serious point of interest in the research community. The major forms of porosity addressed by modeling have been keyhole porosity and lack-of-fusion porosity during builds. Modeling and prediction of these phenomena offer the development of potential mitigation approaches to produce parts with near-full density [542].

7.1. Lack of fusion porosity

As mentioned previously, lack of fusion (LOF) porosity possesses the potential to reduce the quality of the part due to the often-irregular morphology and sharp features characteristic of the defect. The LOF porosity arises when the laser scan strategy selected fails to overlap enough to fully melt all the powder in a fusion region. The work of Tang *et al.* [98] was highlighted in Section 4.3 where a geometry-based model for predicting LOF porosity was developed. Ning *et al.* [861] used a similar approach to Tang *et al.* [98] but extended the approach to include the packing of the powder particles in the powder layer.

The 3DSIM FLEX tool was used to calculate the thermal field for input process parameters. Notably, Teng et al. [862] used the 3DSIM FLEX simulation tool to predict LOF porosity in a similar fashion, focusing on lack of overlap from subsequent melt pool tracks. The thermal solution was then used to predict LOF porosity by simulating a full build and tracking whether the powder was melted at any point throughout the build. The model results showed good agreement with experiments except for a case where excessive balling was believed to have increased the experimentally observed porosity. Yan *et al.* [125] employed a CFD model coupled with a DEM powder bed approach to study LOF porosity in electron beam melting AM. Yan *et al.* noted the potential to form inter-layer voids at the edge of parts and suggest the use of a parallel scan strategy (no rotation) at each layer with a shift to remove LOF porosity. Bayat *et al.* [863] used a multi-physics numerical model to study the evolution of LOF porosity over multi-layers. The LOF pores were observed to have an elongated shape along the scan direction. Bayat *et al.* also observed that the LOF porosity was more common at the bottom of the build as opposed to the top. As layers are added to the AM part, the heat buildup from the deposition of previous layers results in larger melt pools that result in a reduction of the LOF porosity density further away from the build plate.

Bruna-Rosso *et al.* [864] coupled a FEM model used to predict thermal fields during L-PBF processes with high-speed imaging to investigate LOF porosity in single layers of a print. The simulations illustrated that the inter-pass LOF porosity decreased as each subsequent laser scan was made. This is attributed to the increased power density around the first tracks. Mukherjee and DeBroy [777] used a heat transfer and fluid flow model to develop a dimensionless number that consists of all key process parameters corresponding to LOF porosity in AM. The dimensionless number was shown to have a linear relationship with the void fraction observed in experimental parts. The number can be used to directly predict void fraction in parts based on material properties and processing parameters.

Modeling approaches of varying complexity have helped capture the key geometric features that drive the LOF porosity formation in AM parts. Analytical predictions of LOF porosity were developed from the modeling approaches. The criteria developed to address LOF porosity provide solid predictions that can be used to design the build parameters that comfortably avoid the generation of LOF porosity.

7.2. Keyhole porosity

The prevention and mitigation of keyhole porosity have driven the need to predict and model the keyhole porosity in L-PBF, which started with the investigation of a similar phenomenon in welding.

Khairallah *et al.* [63] developed a 3D model that implemented a ray-tracing heat source and considered the Marangoni effect (the effect of temperature-dependent surface tension on the flow in the melt pool), recoil pressure, and evaporative and radiative surface cooling. The randomly packed powder was also included in the simulations. The study highlights the importance of recoil pressure and the Marangoni effect in the determinations of the melt pool and keyhole dynamics in 316L stainless steel. Upon cooling, it was shown that the surface tension can overcome the vapor pressure and cause the keyhole to collapse, trapping vapor within the melt pool and resulting in a pore. Xia *et al.*

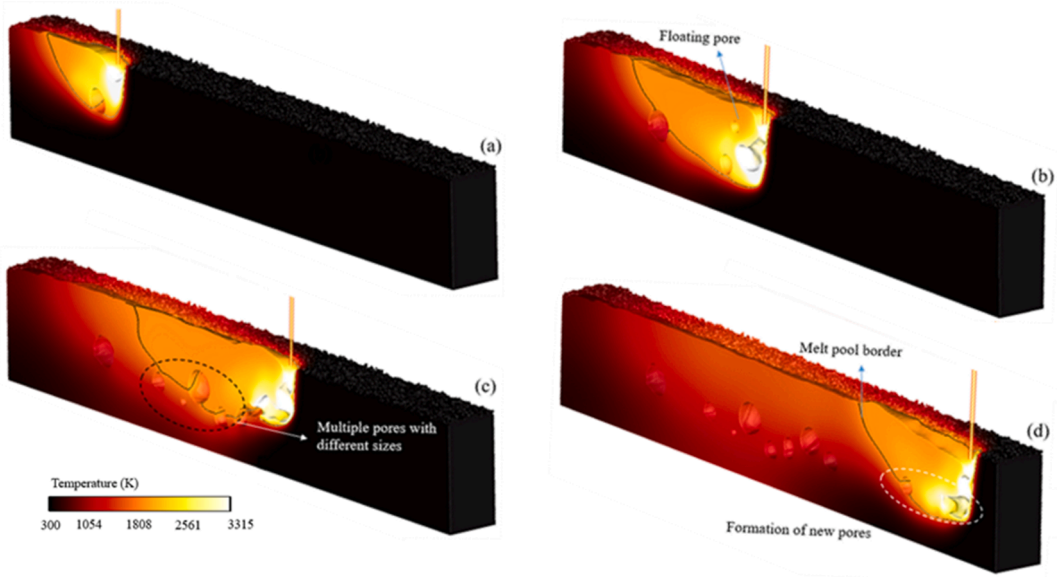

Fig. 82. Evolution of melt as illustrated by simulations published by Bayat. Reprinted with permission from Ref. [788].

[541] studied the fluid flow in the molten pool using the commercial Fluent finite volume method (FVM) package. The results of the simulations suggest that the laser parameters directly influence the nature of the fluid flow within the molten pool. Parameters that altered the linear energy density (LED) were investigated using the model, where LED is calculated as laser power divided by laser scan speed. It was shown that that nonoptimal LED selection, either too high or too low, resulted in increased entrapped porosity. Alternatively, Vastola *et al.* [865] developed a probabilistic, computationally efficient model for the prediction of porosity and showed the ability to reproduce the experimental trend that porosity density increases with increasing energy density.

Tan *et al.* [866] used a physics-based model to study the onset of porosity in AM parts. The model used a volume of fluid (VOF) approach coupled with a DEM model of a randomly paced powder bed. Porosity produced from pinching off of a deep keyhole was again observed, but it was attributed to the high velocity of the molten metal flowing back to fill part of the keyhole. Tang *et al.* [867] used a high-fidelity CFD model to study multiple types of defects. The group used a DEM approach

Table 4
Modeling examples relating to the four major challenges of AM residual stress simulation.

Modeling challenge	Related limitation	Likely consequence	Material	AM system	Major features	Ref.
inclusion of relevant AM physical phenomenon	simplifying near-surface thermal phenomenon	Overpredicting surface residual stress	SS 316L	L-PBF	Layer-scale, Analytical	[873]
	neglecting gas convection	Reducing overall accuracy	Ti-6Al-4V	L-DED	Layer-scale, FEM	[874]
	neglecting pre-placed powder	Large deviation to experiment validation	Alloy 718	L-PBF	track-scale, FEM	[875]
	neglecting metal vaporization	Lacking reliability for high energy density condition	SS 316L	L-PBF	track-scale, FEM	[876]
difference in spatial-time scale between local and global domain	Insufficient mesh refinement	Lacking reliability for small-beam process condition	Ti-6Al-4V	E-PBF	track-scale, FEM	[803]
		Reducing overall accuracy	SS 316L	L-PBF	macro-scale, FEM	[877]
	inappropriate or oversimplified macro scaling method	Underestimating distortion	Fe-based powder	L-PBF	macro-scale, FEM	[878]
		Large deviation to experiment validation	Alloy 718	L-PBF	macro-scale, FEM	[879]
	Inappropriate boundary condition for un-scanned domain	mismatch to experiment validation	Alloy 718	L-PBF	macro-scale, FEM	[873]
non-linear thermal effects and temperature dependence of material properties	neglecting solid-state phase transformation	mismatch to experiment validation	Alloy 718 / Ti-6Al-4V	L-DED	track-scale, FEM-CFD	[880]
	adopting constant thermal properties	mismatch to experiment validation	Alloy 718	L-PBF	macro-scale, FEM	[873]
	adopting constant mechanical properties	mismatch to experiment validation	Alloy 625	L-PBF	macro-scale, FEM	[881]
time-consuming experimental validation	Part warpage leading to unreliable experimental data	Model only qualitatively validated by part geometric feature	Alloy 718	E-PBF	macro-scale, FEM	[167]
	Limited characterization volume of Hole-drilling measurement cannot represent the stress distri- bution on the	insufficient model validation for bottom surface residual stress	Ti-6Al-4V	E-PBF	Layer-scale, FEM	[882]

[868] coupled with a modified version of the OpenFOAM CFD code [869] to study the melt pool behavior. They observed the formation of spherical porosity due to the collapse of the keyhole and the generation of irregularly shaped porosity due to the insufficient applied power density. Furthermore, Bayat *et al.* [788] used a high-fidelity numerical model to investigate porosity formation from keyholing during L-PBF AM processes. The model considered a significant amount of physical phenomena including recoil pressure, evaporation, capillary force, the Marangoni effect, multiple reflections of the laser via a ray-tracing approach, and Fresnel absorption of the laser at the keyhole walls. The modeling results showed good agreement with experimental porosity measurements. Simulation results from Bayat *et al.* are illustrated in Fig. 82. Finally, Martin *et al.* [327] studied keyhole porosity formation by coupling x-ray experiments with multi-physics simulations in the case of a turnaround/end of track case. Using the ALE3D multi-physics software tool [870], the keyhole collapse at turning points in the L-PBF process was both observed experimentally and captured in the model results. More details on turnaround and end of track investigations are detailed above in Section 4.5. Recently, Zhao *et al.* [24] found a well-defined boundary and a novel formation mechanism for the keyhole porosity. These discoveries should prompt more detailed experimental measurements of acoustic waves and more sophisticated multi-physics simulations.

The ability to understand the phenomenon that produces keyhole porosity provides insights into how to mitigate this type of defects during L-PBF builds. The computationally expensive models provide a tremendous amount of understanding about the effect of parameter selection that elucidates certain fields that are not otherwise feasible to measure experimentally, but the computational cost inhibits them from informing parameters for individual builds. The more pragmatic models being developed [788,871,872] offer a more practical approach for the mitigation of porosity during the process of designing builds and selecting parameters.

Due to limited access to high energy synchrotron x-ray beamlines, *in situ* experiments are difficult to achieve and have been performed for a limited number of materials, mostly L-PBF Ti-6Al-4V [25,26,327,606]. Thus, predictive modeling of keyhole porosity via analytical or finite element methods must serve as a principal method for the mitigation of keyhole porosity in diverse metal AM materials. To verify finite element analysis (FEA) of keyhole porosity formation, *in situ* experimental analyses of keyhole porosity have been used for different combinations of processing variables and machine settings. In particular, studies such as Bayat *et al.* [788] compared a high-fidelity FEA model with *in situ* analysis techniques to mitigate keyhole porosity in L-PBF Ti-6Al-4V. Overall the FEA predictions for shape, size, and depth of the keyhole pores were in very good agreement with those found by either XCT or optical images. Comparatively, modeling analysis undertaken by Vastola *et al.* [865], Panwisawas *et al.* [124], Qui *et al.* [672] also show the promise of using FEA as a predictive tool in the mitigation of keyhole porosity in powder bed metal AM processes. However, high-fidelity FEA analysis techniques typically require a substantial amount of computational resources and may not be particularly useful for rapid analysis of keyhole porosity prediction, on the fly, for a given material and machine selection in metal AM. Another potential challenge with using FEA analyses for keyhole porosity prediction is parameter identification for the relevant material properties needed to inform the models.

7.3. Residual stress, distortion, and cracking

As highlighted in Section 4.7, a major concern during the building process of AM parts is the development of large residual stresses that can potentially lead to warping and cracking. Understanding the development of residual stress throughout the build, as well as how to mitigate the development of the stresses to ensure buildability, is key to producing high-quality parts. Efforts in the community have been focused on thermomechanical FE modeling approaches while investigating the effects of processing parameters and improving the efficiency of the simulations.

With continuous efforts, substantial progress can be achieved on AM residual stress modeling, including the improvement of heat source simulation and the development of mesh refinement techniques. However, AM residual stress simulation, especially in macro-scale, is still not fully mature and the above four challenges were often the source of model inefficiency or inaccuracy. Table 4 summarizes some examples that report model limitations relating to one or more of the four challenges above and categorized accordingly. Further details about the resulting consequence, modeling subject (material and AM system) as well as major modeling features are also listed in Table 4. Future research will be needed to remove these barriers to predicting residual stress with improved accuracy and computational efficiency. This could help to develop a more reliable and comprehensive guide to AM process parameter selection and material design. It should be noted that the modeling limitations related to each category were not limited to the ones listed in Table 4, as well as the existing studies in each category. For

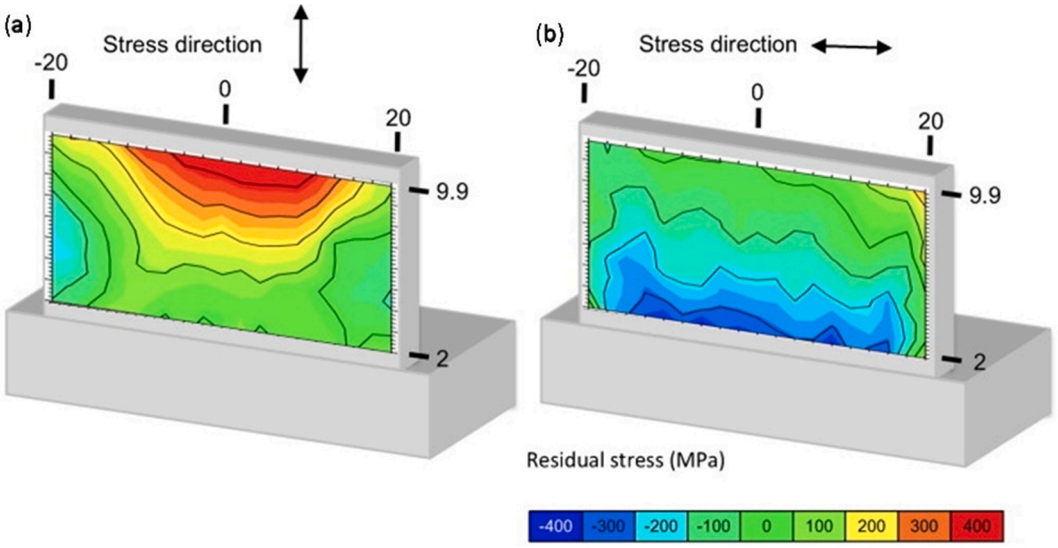

Fig. 83. Computed residual stress distribution for part build with Waspaloy by laser direct metal deposition additive manufacturing. Reprinted with permission from Ref. [883].

instance, the first category in Table 4 regarding AM physical phenomena also includes the limitations of simplifying phenomena such as keyholing and Marangoni flow. These were not included since Table 4 is intended to provide modeling examples for the four major challenge categories, rather than enumerating all relevant previous studies. Further details on AM residual stress modeling are given in Section 7.3.

The result of most AM models combined with their experimental validation present highly anisotropic residual stress distribution in AM parts. Generally, residual stress is higher in the scanning direction than in the perpendicular direction and is higher near the part surface than in the part center or bottom, as shown in Fig. 83 [883]. All the modeling and experimental work suggest that the key influencing factor for temperature gradient have a considerable impact on the magnitude of residual stress in AM parts. Based on that, process variables including support structure placement, power input, scan speed, scan pattern, preheat temperature, hatch spacing, and layer thickness could all play an important role in AM residual stress evolution due to their capability of altering the temperature gradient in a part. The presence of porosity greatly decreases the local material strength. Hence, it should be noted that the presence of porosity in the AM parts could greatly decrease the threshold for residual stress to induce cracking.

It should also be noted that residual stress evolution and the resulting residual stress profile could vary significantly for the same alloy with different AM processing. This is a combined result of different process characteristics for each AM techniques. E-PBF processed parts tend to present lower residual stress magnitude than their counterparts from laser-based AM, since E-PBF allows deeper beam penetration and includes a process step of powder preheating, resulting in a high chamber temperature in the range of 300–1000 °C and an even higher powder bed temperature at the level of 1000 °C [167]. Conversely, the laser-based AM process usually presents a chamber temperature and in the range of 50–400 °C and a similar powder bed temperature. Based on the TGM and three bar-frame model as presented above, this high chamber and powder bed temperature of E-PBF could efficiently lower the temperature gradient, which in turn reduces residual stress. A typical example is provided by the study of Kolbus *et al.* [806], which shows much smaller residual stress in the E-PBF processed Alloy 718 compared to the L-PBF processed counterpart.

Thermomechanical FE approaches have been very popular approaches for the prediction of residual stress and distortion in AM parts. Neugebauer *et al.* [884] used a multi-scale FE model to simulate the printing of cantilever specimens designed to warp when cut from the base plate. The heat flux used to calculate the residual stress build-up was simplified to a cube of constant size to maintain good computational efficiency. The simulations were done in parallel with an experimental study in which the same cantilever design was printed. Two scan strategies were studied with the model, laser scans along the long direction of the cantilever and perpendicular to the long direction of the cantilever. The build with laser scans along the long direction resulted in increased distortion. The model also found increased distortion in the lengthwise scan strategy build but overestimated the distortion. Furthermore, Ganeriwala *et al.* [885] compared the results of a thermomechanical FE model using a lumped layer approach against x-ray synchrotron residual stress measurements. The model showed decent agreement with the simulation approach but did not capture the scan strategy effects due to the layer agglomeration.

The effects of the preheat of the build plate were also noted by many studies. Hodge *et al.* [886,887] used an in-house thermal model coupled with a solid-mechanics model to attempt to capture the residual stress and distortion build-up during L-PBF builds. The results showed good agreement with experimental samples, suggesting that the model is capturing important aspects involved in the development of residual stress. The effect of the selected agglomerated scan path is addressed as a potential source of error for the results. The effect of a heated vs unheated baseplate is also simulated to show the significant decrease in residual stress as a result of including a preheat. Vastola *et al.* [803] investigated the mitigation of residual stress development by looking at single beads in a FE model. It was found that preheat provided the largest quantitative effect on the residual stress development in the single bead passes.

Processing parameters also play an important role in the development of residual stress in AM parts. Fergani *et al.* [873] proposed the use of an analytical model to predict residual stress development during builds. The model couples a point heat source with a set of plain-strain Green's functions to predict residual stress build up in parts. The authors observed that the residual stresses tended to be tensile along the scan direction and that a large heat affected zone was observed to dissipate residual stress. Mukherjee *et al.* [880] used a heat transfer and fluid flow model to calculate thermal field information produced by a laser pass in L-PBF and coupled the results with ABAQUS to investigate the development of residual stress in simulated, tall single pass parts. It was observed that residual stress could be reduced by decreasing the layer thickness when building thin parts like those simulated. Additionally, material effects were investigated. A set of parts with both alloy 718 and Ti-6Al-4V material parameters were simulated. The Ti-6Al-4V parts were observed to develop more residual stress than the alloy 718 parts but also were observed to warp less than the alloy 718 parts. Chen *et al.* [888] investigated the effect of process parameters on residual stress development in thin wall builds using a thermomechanical FE model. The residual stress was found to increase with build height and the residual stress was found to increase with increasing laser power and decrease with an increase in scan speed. Similarly, Ramos *et al.* [36] used a thermomechanical FE model to develop advanced scan strategies to minimize residual stress and distortion. Ramos *et al.* found that residual stress was decreased by melting nonadjacent scan vectors and reducing laser scan length.

With large bulk volume simulations required, the computational efficiency of numerical models is crucial. Williams *et al.* [890] presented a pragmatic approach to FE modeling of the residual stresses and deformations that arise during AM. Again, a thermomechanical FE model was used (ABAQUS) to simulate the residual stress build-up, but instead of considering the melt pool during rastering throughout the part, a simplification was made to deposit large blocks of material in an additive fashion. The large blocks significantly improve computational efficiency and allow for the use of a coarser mesh while still capturing the residual stress and distortion shown by both experiments and modeling approaches that use smaller heat inputs closer to the length scale of melt pools. This work suggests that not every laser pass needs to be modeled to accurately capture the residual stress development in AM parts. More recently, Gouge *et al.* [889] used an adaptive voxel mesh to improve the computation efficiency of a thermomechanical FE model to simulate residual stress build-up in full parts. The full part simulations showed excellent agreement with measured experimental distortion while maintaining acceptable computational efficiency as shown in Fig. 84 which illustrates a result from Gouge *et al.*'s simulation efforts. Chen *et al.* [891] developed an inherent strain-based model for part scale prediction of residual stress development during selective laser melting AM. The approach merges multiple layers to improve computation efficiency and drive down simulation runtime when predicting residual stress development but still demonstrates good agreement to experiments, despite the simplification. Finally, Denlinger *et al.* [892] developed a FE model to predict thermal history and the resulting residual stress and *in situ* distortion in AM parts for a large bulk. They were able to simulate a 91 mm^3 volume using an adaptive coarsening approach to their mesh such that the mesh was allowed to coarsen in the layers below the melt pool, significantly improving computational efficiency. Good agreement was found between the *in situ* distortion measurements and the FE model. The ability to understand the key features that instigate distortion and residual stress in parts produced via powder bed AM, either via L-PBF or E-PBF, allows for designs to be made such that the distortion of parts can be minimized. The modeling approaches currently in use show excellent ability in predicting the development of

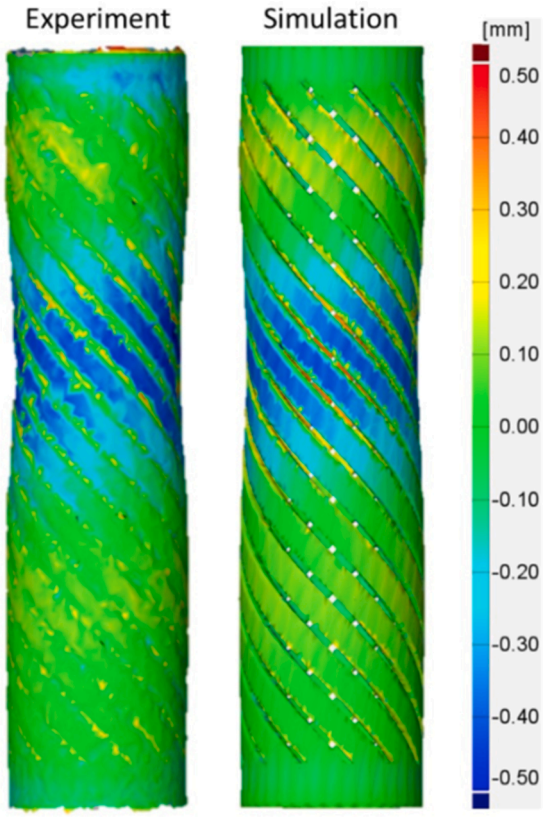

Fig. 84. Comparison of experimental to simulated distortion for a full part. Reprinted with permission from Ref. [889].

residual stress as well as inform decision making when attempting to mitigate the distortion.

Tran *et al.* [186] investigated the prediction of crack formation in a hybrid L-PBF alloy 718 part at the interface between substrate and lattice support in parts manufactured using an EOS machine. The approach taken by Tran *et al.* combined experimental and residual stress simulations to predict cracking, as shown in Fig. 85. The critical geometry for cracking susceptibility at the interface of the hybrid AM parts was first determined experimentally by printing a large number of hybrid structures of different heights. A modified inherent strain method [891,893] was then implemented to simulate the residual stress development in the hybrid parts. From the residual stress simulations, the critical J-integral at the interface between the solid region and lattice support could then be calculated. The ability of the modeling approach to predict cracking by calculation of the J-integral was validated using a separate experimental build, where the model successfully predicted the geometries that would crack as shown in Fig. 85. The results confirm that the use of the J-integral, a nonlinear elastic–plastic fracture parameter, is well suited to the evaluation of crack-susceptibility in AM parts. Additionally, the development of a critical J-value, while validated for limited part geometry and process parameters, is an important step in the evolution of the design of crack-free solid/support interface and eventually AM components. These results also eliminate the uncertainty associated with stress relaxation by heat-treatment and machining after printing.

7.4. Other defects and anomalies

Similar to porosity and residual stress, other process defects may also act as potential sources of premature failure of metal AM parts. Powder spreading, spatter, and ball-up all have the potential to cause builds to fail or produce parts of low quality. Hence, understanding the origins of these defects and predicting their formation allows for minimization of the defect population throughout AM parts and improvement of overall part quality.

Powder spreading. The spreading of each powder layer is a potential source of regularly spaced imperfections in parts. Simulation of powder spreading offers the opportunity to optimize build features to understand and inhibit the formation of these defects. The powder spreading process is most commonly studied using the discrete element method

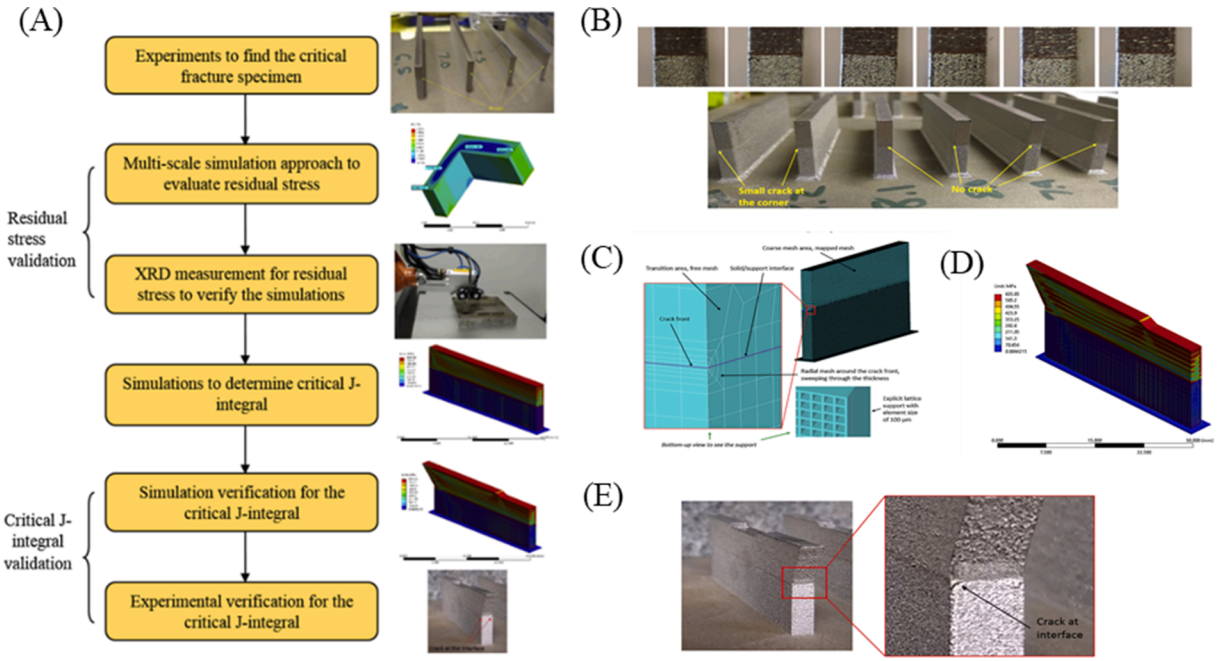

Fig. 85. (A) The combination of experimental and simulation approach taken by Tran *et al.*. (B) Experimental builds performed to determine critical geometries for crack susceptibility at the hybrid (lattice and solid structures) interface for multiple specimen heights and (C) simulations performed to determine the critical J-integral that caused cracking in the printed parts. Prediction of crack susceptibility using (D) simulation of new part design and (E) validation of cracking predicted by the modeling approach observed in the printed part. Reprinted with permission from Ref. [186].

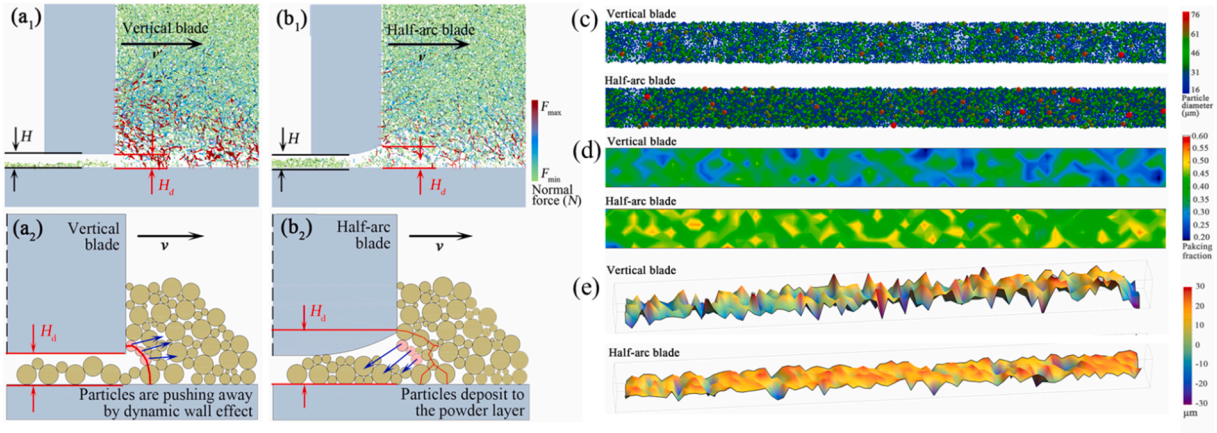

Fig. 86. Proposed mechanism comparing (a_1), (b_1) the intensity of force-arches in front of the vertical blade and the half-arc blade, respectively; and (a_2), (b_2) the particle motions induced by force-arch destruction in front of the tow blades, respectively. Evolution of (c) packing morphology, (d) packing fraction, and (e) surface roughness of dispensed/compacted powder using vertical and half-arc bladed. Reprinted with permission from Ref. [894].

(DEM). DEM is a numerical method to simulate the movement of granular materials through a series of calculations that trace the individual particles constituting the powder material. In a typical powder spreading simulation, the rake or roller is simulated as a rigid body and individual powder particles are tracked as the rake deposits the powder bed.

Recently, Wu *et al.* [894] proposed a new blade design of half-arc blade to maximize powder packing density and minimize surface roughness of the spread powder in each layer (see Fig. 86). The DEM simulation demonstrated that the particle deposition process was improved when the half arc-bottom part (at the front face of the blade) was introduced into the edge of the vertical-blade. It was shown that the dispensed powder particles could be compressed when facing the gradually decreased blade bottom height, leading to and enhanced packing fraction of deposited layer. Authors also demonstrated that the wall effect provided by the straight-bottom part in half-arc blade would maintain the compacted state of particles and gradually remove the contacted forces rather than release it into the particle motion.

Using the numerical simulations, various researchers reported that the packing density of the powder bed increases with decreasing particle

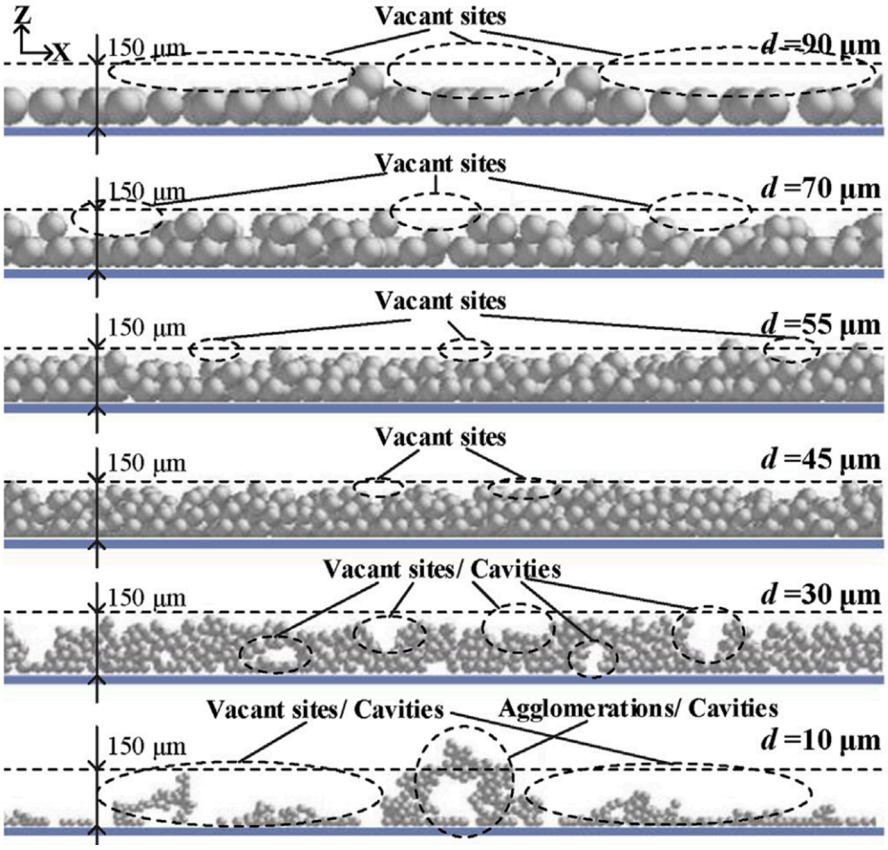

Fig. 87. The deposited powder layer for different powder sizes. Reprinted with permission from Ref. [547].

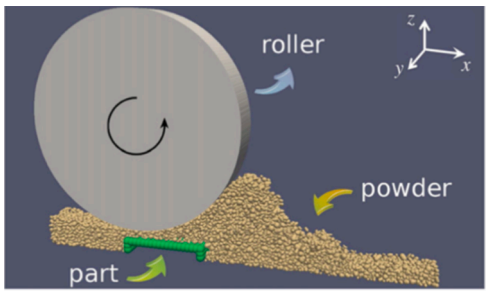

Fig. 88. Powder spreading simulation using DEM powder simulation approach and a simulated roller as performed by Parteli and Pöschel. Reprinted with permission from Ref. [553].

size until the size reaches a critical value after which the density decreases with decreasing particle size [547,550]. Both the cohesion effect and the wall effect contributed to the observed trend. Bimodal or Gaussian particle size distributions were observed to have a weak effect on the packing density for thin powder layers [547,551]. More cohesive powder particles were observed to worsen the continuity and stability of the powder layer [547,557]. Typically, more spherical, unimodal particles were observed to have less internal friction, thus leading to higher layer densities [895]. The defects introduced in the powder bed with changing powder size are visualized in Fig. 87. The number of defects in powder bed tends to first decrease with decreasing powder particle size and then increase below a certain critical particle size. Gu *et al.* [562] and Xia *et al.* [541] showed that the powder size not only affects powder packing density and defect formation during powder spreading, surface finish and surface defects (balling, discontinuous tracks, and porosity) can result from L-PBF of fine or coarse powders.

Ma *et al.* [896] studied the results of a set of FEA single track simulations to understand the influence of a variety of process variables on the temperature profile of single bead passes. The packing density was observed to have a significant effect on the temperature profile in the simulations (>2%). Xiang *et al.* [897] simulated randomly packed powder beds with different size distributions to understand the effect of size distribution and deposition layer thickness on packing density and coordination number of each of the particles. Xiang *et al.* found that increasing the layer thickness improves packing density and coordination number. Parteli and Pöschel [553] simulated powder bed spreading using a DEM approach but included a simulated roller and investigated nonspherical powders as illustrated in the setup shown in Fig. 88. The authors found that the surface roughness of the spread powder layer was increased with increasing roller speed. Additionally, it was observed that the surface roughness of the powder bed was also increased when larger powder size distributions were used due to the agglomeration of smaller particles to the larger powder particles. Zhou *et al.* [898] used a sequential addition packing algorithm to simulate the spreading of a powder bed in powder-bed AM processes. They found that the optimal powder distribution is a bimodal distribution where the small particles outnumber the large particles. Haeri *et al.* [554] also found that increasing the spreader speed increased the surface roughness of the powder bed by using a DEM approach to simulate spreading. Additionally, the authors found that a roller type spreader performed better than a blade type spreader in avoiding spreading defects.

Spattering. On the macroscopic scale, as described in Section 4.6, the spatters are mainly triggered by the vapor plume and the environment gas flow. To predict the gas-driven spatters, it is important to acquire and understand the quantitative information, including the temperature, pressure, and force, during the gas-particle interactions. Since it is rather difficult to experimentally characterize these quantities, multi-physics simulations can serve as an effective approach to study gas-particle interaction in LPBF.

The key to effectively replicate the real physics in L-PBF by the computational models is to couple the physics between the low-speed, condensed, incompressible phases (liquid and solid metal) and the high-speed, gaseous, compressible phase (metallic vapor and

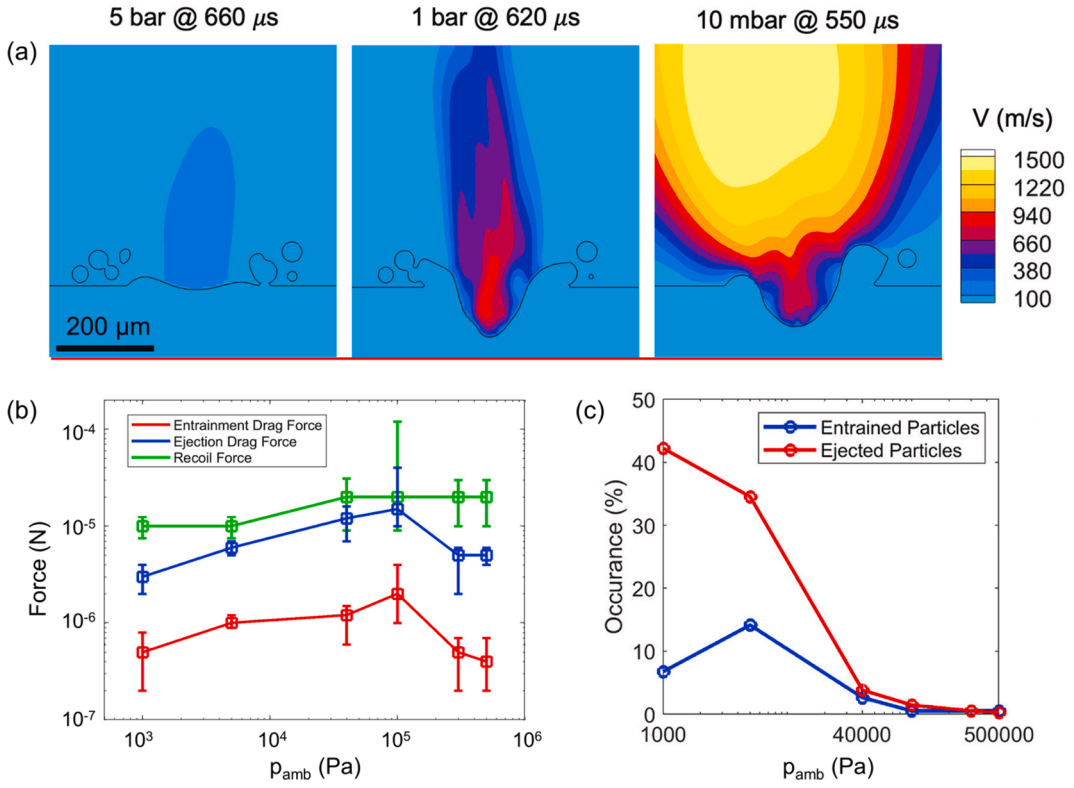

Fig. 89. Multi-physics simulation showing the effect of environment pressure on powder spattering behavior. Reprinted with permission from Ref. [898].

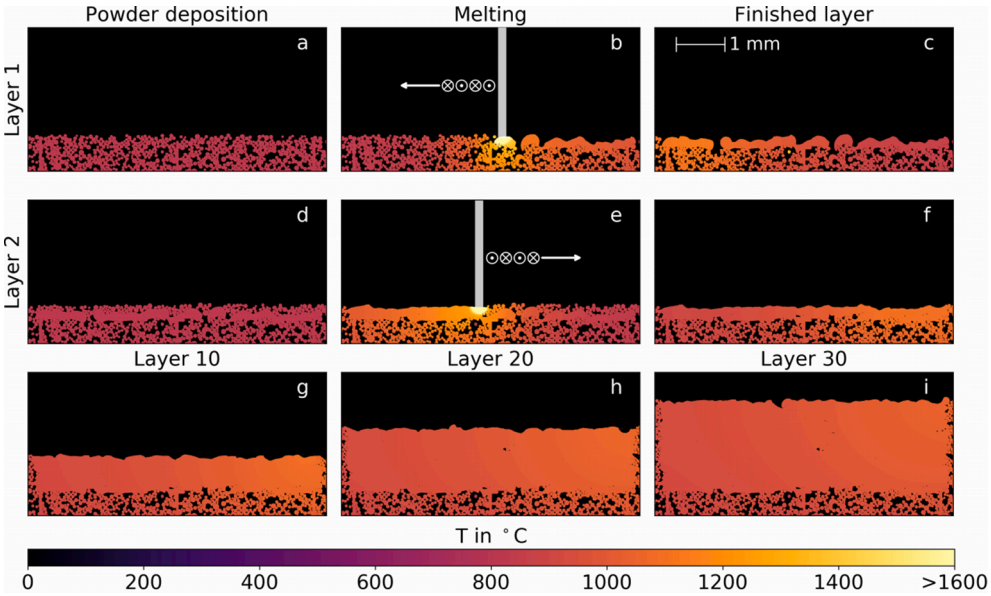

Fig. 90. Temperature field in a 2D, multilayer lattice Boltzmann simulation illustrating porosity evolution over 30 layers. Each layer is randomly laid down and a simulated laser, seen in frames b and e, melt the powder. Note the presence of more pronounced melt track discontinuities in the preliminary layers (frames b and c). Reprinted with permission from Ref. [902].

environment gas). Li et al. [899,900] performed multi-physics modeling works for L-PBF using a unified algorithmic framework [901] to couple the compressible and incompressible flows, in a way that melt pool dynamics, gas flow, and powder motion were considered and simulated within one framework. The model predicted the powder behavior during single-pulse laser illuminations under various environment pressures (10 mbar–5 bar), and was validated by high-speed X-ray imaging experiments under pressures between 10 mbar and 1 bar. The simulation results in Fig. 89(a) show that the metallic vapor velocity and the environment gas flow velocity can be significantly reduced under high environment pressure. As a result, the powder spattering is effectively suppressed during single-pulse laser illumination under high environment pressure (Fig. 89(c)), due to the reduced drag forces from the weakened gas flow (Fig. 89(b)).

During the printing process, spatter possesses the potential to introduce defects into builds. Determining the genesis of the spatter during the build offers routes to minimizing the negative effects the spattering phenomenon has on AM parts as discussed in Section 4.6. Ly *et al.* [602] performed finite element calculations to study micro-droplet ejection and motion to understand the generation of spatter during the AM process. It was found that the generation of these droplets was primarily from the ejection of hot particles entrained in the gas flow, rather than molten material ejected due to recoil pressure. Ly *et al.* found that only 15% of ejected particles were due to recoil pressure. As shown in Fig. 56(a), experimental and simulated results were compared by Ly *et al.* where ejection of the liquid metal from the melt pool is observed in both sets of images.

Balling. The balling phenomenon is one of the major inhibitions when attempting to print at high powers and speeds to improve the build time of projects. A discussion of the ball-up mechanism was presented in Section 4.2. In addition to the mitigation techniques described in Section 6.2, understanding the physics of the balling phenomenon and how it develops throughout single laser passes and full builds provides insight into mitigation techniques and intelligent parameter selection. In stainless steel 316L, Khairallah *et al.* [564] observed balling attributed to the Plateau-Rayleigh instability in their 3D Multiphysics simulations as shown in Fig. 41. Similarly, Lee and Zhang [563] observed the balling phenomenon in their 3D numerical model solutions. The balling phenomenon was observed to worsen with an increased melt pool length. However, a poorly packed powder bed was also observed to cause balling to occur at much shorter melt pool lengths. Khairallah *et al.* [564] included recoil pressure and ray tracing in their multi-physics simulations to comment on the possibility of minimizing the balling phenomenon by controlling the heat content in the melt pool track. Körner *et al.* [62] used a 2D lattice Boltzmann model to study the melting of randomly packed powder particles. Individual powder particles were considered, and each layer of powder was randomly laid down. The packing density was shown to significantly influence the melt pool characteristic. The balling phenomenon was also observed at greater laser scan speeds. Rausch *et al.* [902] expended this 2D lattice Boltzmann simulation technique to multiple layers. The authors noted that the balling effect is more frequently observed when the bulk powder density is low. This is attributed to the presence of regions where substantial gaps between powder particles existed. Li *et al.* [695] developed a thermodynamically consistent phase-field theoretical 2D configuration model and found that the degree of freedom of wetting and fast solidification counter-balance the balling effect, and the Rayleigh–Plateau flow instability plays an important role for cases with relatively low substrate wettability and high scanning rate. Fig. 90 illustrates the expanded 2D lattice Boltzmann method used by Rausch *et al.* to simulate powder bed AM processes. Lu *et al.* [903] used a phase-field model to simulate multiple features of the L-PBF process including the melt pool, powder bed packing effects, and grain structure. They observed the development of a balling void during a multilayer simulation due to the presence of an irregularly large powder particle. And, Liu *et al.* [904] noted the presence of balling defect when using a ray-tracing heat source as opposed to the Gaussian heat source in their CFD mesoscopic simulations. This highlights how the use of more complex inputs and modeling approaches can capture more realistically the balling phenomenon.

Surface roughness. Correlations between surface roughness and process parameters necessitate significant trial-and-error type analyses for diverse materials and metal AM systems. Therefore, analytical and numerical methods have been undertaken to investigate surface roughness characteristics and anticipated material behavior [181,672,850,851]. Notably, Strano [664] extended the classical "stair-step" models to metal powder bed AM since classic models for roughness prediction (based on purely geometrical consideration of the stair-step profile) failed to describe the observed trends of the experimental data. Overall, surface roughness was well-predicted by this model and

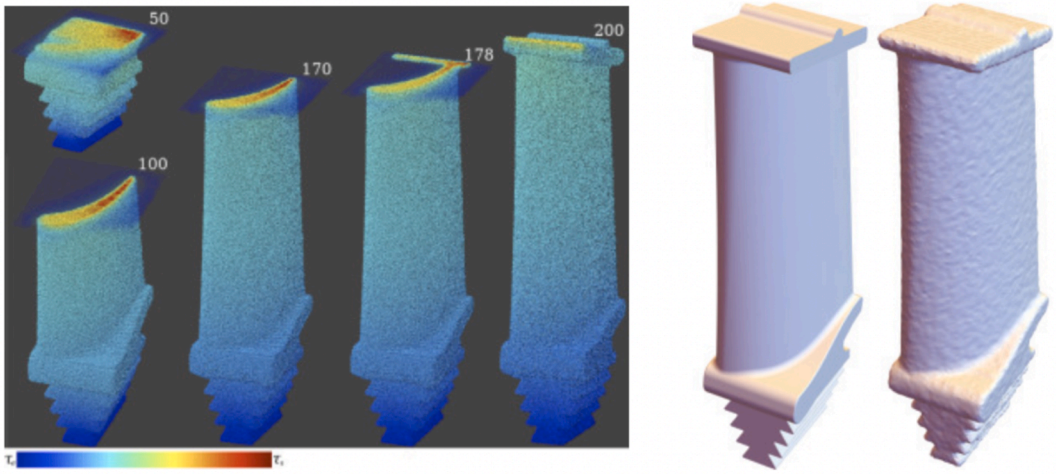

Fig. 91. Modeling techniques employing processing variables and raster + contour scan paths have great potential to verify XCT results of as-built metal AM surfaces. (left images) Discrete Element Method (DEM) simulation output at the 50th, 100th, 170th, and 178th layers, as well as the final output particle system. (right image) Comparison of DEM input model and output model (with roughness). Realistic surface modeling techniques can enable correlation between surface roughness via processing variables for various materials and processed to replace the trial-and-error type analysis currently employed. Reprinted with permission from Ref. [678].

showed good agreement with the experimentally observed roughness values. Additionally, Boschetto [851] developed a model able to predict the roughness as a function of the local part geometry in AlSi10Mg. The model enabled the investigation of the effects of the local stratification angle with a fine resolution. Thermal models have also been developed to investigate the effects of heat accumulation on surface roughness such as the work of Jamshidinia *et al.* [181]. Notably, it was found that the surface quality of E-PBF Ti-6Al-4V thin plates could be controlled not only by process parameters but also by the arrangement of components within the build chamber. Experimental analysis of surface roughness measurement revealed an inverse relationship between the spacing distance and surface roughness in accordance with the numerical results. High-fidelity modeling of as-built metal AM surfaces such as those by Michopoulos *et al.* [678] and Meier *et al.* [679] using DEM show great promise to correlating process variables and surface textures without costly trial and error analyses (Fig. 91). This way, the effect of key processing variables such as laser power, laser velocity, and hatch spacing along with non-steady-state melting effects can be captured for diverse geometries, starting materials, and processing conditions. In this way, optimized process parameter sets can be determined for specific structures and materials in metal powder bed AM.

Simulation techniques elucidate many features of the powder bed AM process that is difficult to capture using experimental techniques. The discoveries made through simulation work offer an insight into the black box of powder bed AM machines. This understanding helps inform the mastery of the technique and set in place operation procedures that aim to ensure high-quality parts from build to build.

8. Properties of defective parts

8.1. Mechanical behavior

The mechanical properties of AM parts are determined by their defects and microstructure, which can be vastly different compared to their wrought counterparts as discussed in the previous sections. Such microstructure/defect variations in AM parts exist not only through the use of various AM systems but also when using the same AM process/system with only slight changes in processing conditions or even part geometry/size [764,905-907]. This wide spectrum of possible microstructural properties may result in a significant scatter in reported mechanical properties of AM parts. In this section, we discuss the most widely reported mechanical properties of four popular AM metallic materials—including Ti-6Al-4V, 17–4 PH stainless steel (SS), alloy 718, and $AlSi_xMg$ {x = 7–12}— available in the open literature. The mechanical properties discussed include yield/ultimate tensile strengths, ductility, high cycle fatigue strength, fracture toughness, and fatigue crack propagation rates. The mechanisms and factors that generally govern mechanical properties are first briefly reviewed, followed by a review of existing data that provides insight on the dependence of mechanical properties on the microscopic features (including both microstructure and defects) of AM alloys. Note that other mechanical properties such as those performed in the high-strain rate regime [231,852,908-911] are less commonly available in the literature and are therefore not the focus of this review.

8.1.1. Tensile

In general, the strength and ductility of all materials manufactured by AM exhibit wide scatter [172,215,432,433,772,912-934]. The AM techniques reviewed include the laser beam and electron beam powder bed fusion techniques (L-PBF and E-PBF, respectively) and the direct energy deposition methods (such as the laser beam direct energy deposition (L-DED)). In the case of Ti-6Al-4V, as shown in Fig. 92, significant variations in data exist in the yield strength (YS), ultimate tensile strength (UTS), and ductility (measured by elongation to failure (EL)). Reference values of a wrought Ti-6Al-4V in these tensile properties, i.e. YS = 930 MPa, UTS = 995 MPa, and EL = 14%, obtained from Ref. [935] were illustrated in Fig. 92. The yield strength (YS, solid markers) and ultimate tensile strength using brown shades. Despite the scatter, the tensile mechanical performance of AM materials can achieve and even surpass that of the wrought material (as indicated by the brown blocks in Fig. 92).

In addition, the scatter seems to be more related to the processing techniques (Fig. 92(c)) and post-processing treatments (Fig. 92(b)), and less related to build orientations (Fig. 92 (a)). Indeed, laser beam powder bed fusion (L-PBF) fabricated specimens tend to have martensitic microstructure (Fig. 92(d)) with high residual stress as a result of faster cooling rates and lower substrate temperatures [919,936,937], leading to parts with higher YS and lower ductility compared to wrought [172,215,432,433,772,913-915,917,919-921] (blue markers in Fig. 92 (c)). On the other hand, E-PBF, green markers in Fig. 92(c), tend to have higher substrate temperatures, which result in essentially stress-free, coarser α + β microstructure (Fig. 92(d)), which correspond to better ductility, and reduced strength relative to those made via L-PBF. On the other hand, the cooling rate of laser beam direct energy deposition (L-

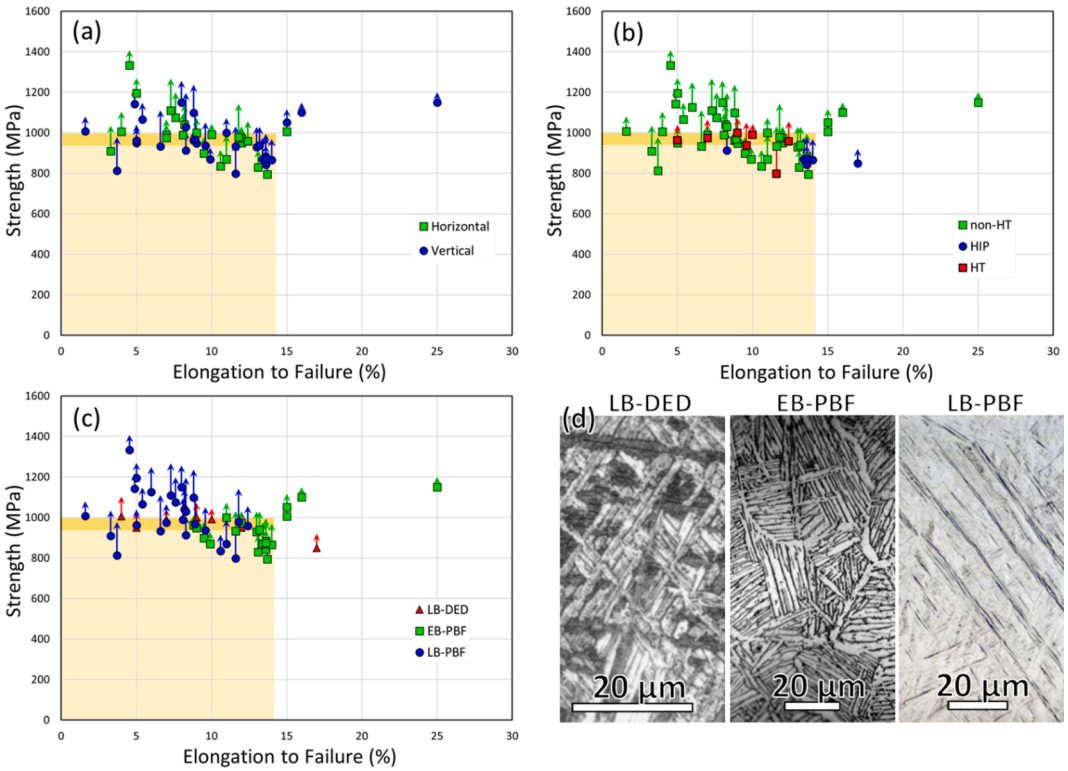

Fig. 92. The yield strength (YS, solid markers) and ultimate tensile strength (UTS, arrows) of Ti-6Al-4V fabricated at (a) different build orientations, (b) with/without post-build treatment, and (c) various AM technologies [172,215,432,433,772,912-921] plotted against elongation. YS and UTS data points from the same specimen have been connected using vertical lines. The reference in YS, UTS and EL have been taken as 930 MPa, 995 MPa, and 14%, respectively, which correspond to those of wrought Ti-6Al-4V [935]. These reference values are visualized by brown shades. The light brown shades are bound by the reference YS and elongation to failure, whereas the dark brown shades extend vertically to the reference UTS. The width of the shades denotes the EL. Typical as-fabricated microstructures produced from L-DED, L-PBF, and E-PBF are shown in (d). Reprinted with permission from Refs. [429,432,913].

DED) is typically between that of the L-PBF and E-PBF. The resulting microstructure is typically Widmanstätten α + β, which generally has a slightly lower strength than the martensitic microstructure produced by L-PBF (Fig. 92(c)) yet higher strength than the lamellar microstructure produced by E-DED. Besides, L-DED specimens appear to be more sensitive to slight changes in processing conditions tend to produce a higher population of lack-of-fusion (LOF) defects embedded in a martensitic microstructure, which leads to inferior ductility compared to both wrought and E-PBF ones[773]. Heat treatments (HT), such as stress relieving, annealing, and solution treatment, regulate the part microstructures, which tend to reduce the scatter in strength. However, the ductility of HT samples is still noticeably lower than that of wrought counterparts. Hot isostatic pressing (HIP), on the other hand, reduces scatter in both ductility and strength (Fig. 92(b)). In comparison, the build orientations do not produce discernable effects in either strength or ductility (Fig. 92(a)). With HIP applied, the YS of the AM Ti-6Al-4V parts approaches the one reported for the wrought material (Fig. 92(b)).

Yielding in metals is often characterized by the long-range motion (slip) of dislocations throughout grains [938,939] which is equivalent to the onset of irreversible deformation. Depending on the microstructure of a material, the obstacles to dislocation motion can be solute atoms, grain boundaries, phase boundaries, or hard/soft (impenetrable/penetrable) particles. In the context of Ti-6Al-4V alloys, due to the coexistence of α and β phases, the relevant interfaces are the α-β interfaces. Plastic flow initiates within the α phase along the $\langle 1\bar{2}10\rangle$ directions on the prismatic $\{10\bar{1}0\}$ planes (prismatic slip) [919,940], or along $\langle 1\bar{2}10\rangle$ directions on the basal {0001} planes (basal slip), where the critical resolved shear stress (CRSS) is the lowest. The CRSS for these slip systems were discovered to be 181 MPa and 209 MPa, respectively, substantially lower than the pyramidal slip mode (474 MPa) [940]. The slip induces dislocation pile-up at the phase interfaces, which upon the application of sufficient remote stress, transmits slips through the β phase and the rest of the alpha colony. The concomitant YS, as suggested by Xu *et al.* [919] using existing data in the literature, obeys the Hall-Petch relation reasonably well (Fig. 93) [941,942], i.e. $\sigma_y = \sigma_o + k/\sqrt{h_\alpha}$ where h_α is the thickness of the alpha laths, σ_0 is the strength of an Ti-6Al-4V alloy with alpha laths that are infinitely thick, k is the Hall-Petch coefficient. However, debate exists in the recent literature on the dominant strengthening mechanisms in this alloy. For instance, Hayes *et al.* [943] suggested that the strength of electron beam directed energy deposited (E-DED) Ti-6Al-4V was controlled primarily by the solid solution strengthening, while the Hall-Petch effect of lath spacing was found to be a minor effect in their study.

Depending on the cooling rate, the microstructure of AM Ti-6Al-4V may be dominated by martensite or fine (α + β) Widmanstätten structure [156]. While the former does not exhibit a well-defined mechanical size effect, a correlation between YS and alpha lath thickness exists in the latter (Fig. 93). Data for α-lath thickness and corresponding YS were obtained from the open literature [432,854,912,914,916,919,944,951,952]. Only data for laser beam-, electron beam-, plasma-based additive manufactured and wrought Ti-6Al-4V were collected. The feedstock for plasma-based additive manufacturing is alloy wire, the technique of which is referred to as plasma-based metal shaped deposition (PB-MSD) in this work [952]. Some references do not specify the thickness; in such cases, an average thickness of α-lath was measured from the provided images of lamellar α-colonies in the same publication. It is seen that not only does the Hall-Petch relation hold for the (α + β) AMed Ti-6Al-4V but also that the data trends are similar to those of wrought alloys (i.e. the constants σ_0 and k). The correlation between the α-lath thickness and the YS also suggests that the presence of porosity does not strongly impact the macroscopic yielding behavior of Ti-6Al-

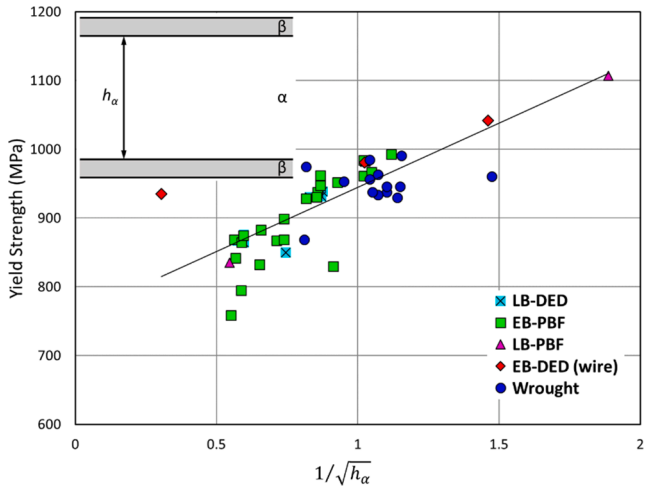

Fig. 93. Dependence of YS on α-lath thickness for lamellar (α + β) Ti-6Al-4V [432,854,912,914,916,919,920,935,944-952].

4V. Xu *et al.* [919] established a similar relationship for AM Ti-6Al-4V, also found in Fig. 93, using references [920,935,945-950,952]. Note that [935] presents a model for yield strength in Ti-6Al-4V that is comprehensive in terms of the variable considered, e.g., composition.

The room temperature strength versus ductility plot for AM alloy 718 is given in Fig. 94(a, b). The work collected in this regard concerns with the laser beam and electron beam processed materials, including L-DED, L-PBF, and E-PBF [459,740,773,953-962]. Coincidentally, the tensile data collected for E-PBF are all HTed with double aging [740,954]. Due to this reason, a comparison of data between E-PBF specimens with L-PBF is not given to prevent bias. Scatter significantly larger than Ti-6Al-4V exists herein. Data points enclosed by the dashed circle correspond to specimens subjected to double aging treatments, which precipitate the strengthening phases of γ' and γ" [963]. The rest of the data points correspond to the specimen in as-built, solution annealed, and HIPed conditions. As discussed in the previous sections, due to the rapid solidification rate in the laser AM process, a dendritic, rather than a multiphase, is usually observed in L-PBF alloy 718 (Fig. 94(c)) [956]. Due to the lack of strengthening phases, the strength of the as-built material is usually rather low (Fig. 94(a)). Due to the significantly higher processing temperature of E-PBF (initial build plate temperature > 1000 °C [954]), the thermal condition during fabrication may resemble that during the solution + aging treatment. As a result, the corresponding as-fabricated microstructure may contain γ'/γ" and δ precipitates (Fig. 94(d)). If double-aging treatment is employed, the harmful δ phase can be dissolved and the strength can be significantly improved. The microstructure produced by the solution annealing and double aging is given in Fig. 94(e), showing the γ'/γ" precipitates. Fig. 94(a) exhibits an increase of yield strength from ~600 MPa to ~1200 MPa—an improvement of a factor of two achieved by double-aging treatment. The data point for non-HTed conditions (including the HTed without aging) still exhibits extreme scatter in both strength and ductility, which is likely due to strong texture induced by directional solidification imposed by the AM process, combined with the presence of the sharp, LOF defects which are typically perpendicular to the build direction [156,773,785]. However, the double aging reduces the ductility in all specimens, while increasing their strengths, which dwarfs the effect of the build orientation (c.f. Fig. 94(a, b)).

Another precipitation hardened alloy of great interest to the AM

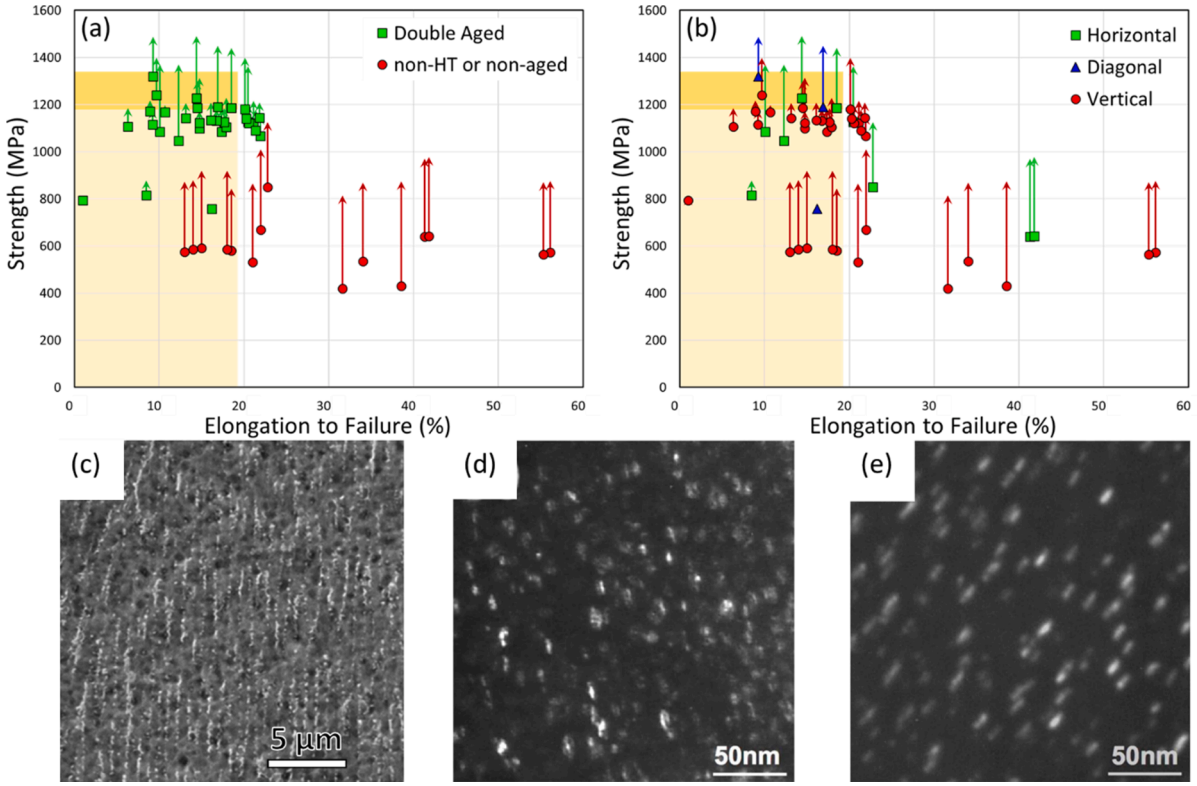

Fig. 94. (a)-(b) Room temperature YS and UTS versus elongation to failure plot for AM alloy 718 [459,773,953,955-962,964]. The brown blocks indicate the YS, UTS, and elongation to failure of a wrought reference material (1185 MPa, 1353 MPa, and 18%) given by Gribbin *et al.* [961], similar to Fig. 92. The solid markers denote the YS, while the arrows bars denote the UTS. YS and UTS data points from the same specimen have been connected using vertical lines. (c), (d), and (e) show the typical as-fabricated microstructure of L-PBF and E-PBF alloy 718 as well as the HTed microstructure of E-PBF alloy 718, respectively. Reprinted with permission from Refs. [740,956].

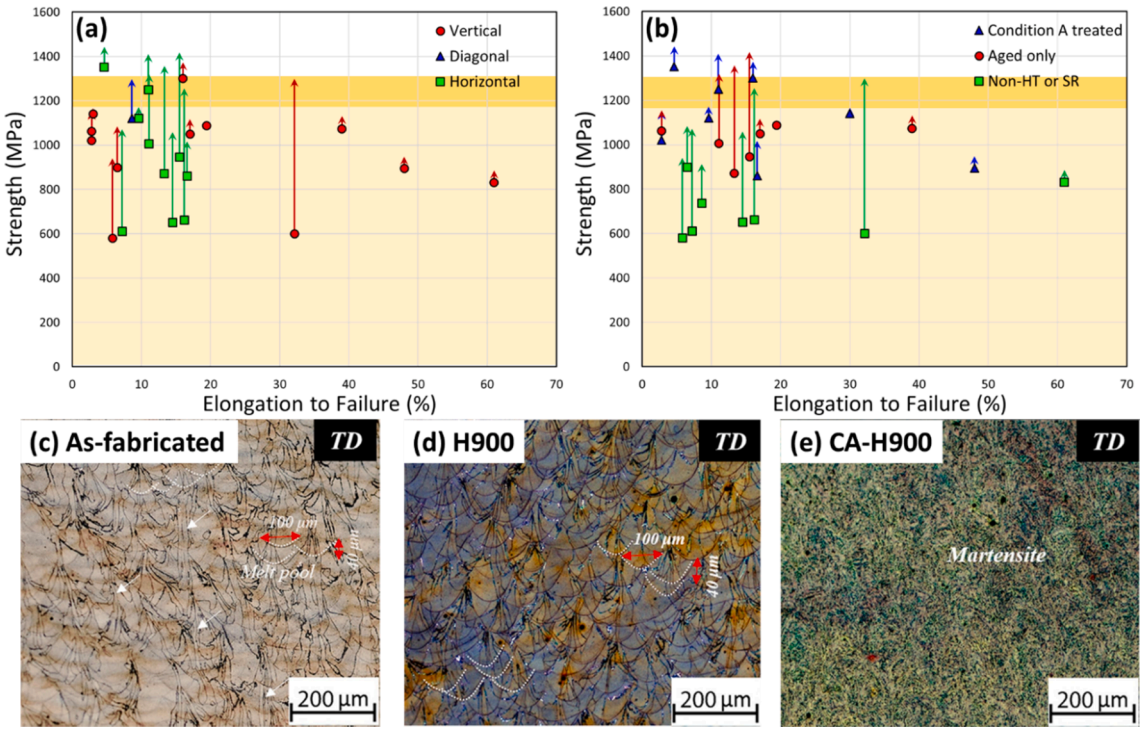

Fig. 95. (a)-(b) YS and UTS versus elongation to failure plots of AM 17–4 PH SS [785,928,965-971]. The brown blocks indicate the yield and ultimate tensile strengths, similar to Fig. 92. The YS and UTS of the wrought material, according to ASTM A693, are 1170 MPa and 1310 MPa, respectively [972]. The ductility is unspecified. Typical microstructure of (c) as-fabricated, (d) directly aged (H900), and (e) Condition A + aged (CA-H900) L-PBF 17–4 PH SS. Reprinted with permission from Ref. [966].

community is the 17–4 PH SS. The strength versus ductility plot for this material fabricated by AM is given in Fig. 95. The data collected in this regard only concern with laser-based AM, including L-DED and L-PBF. A strong orientation effect on the ductility of these materials is visible from Fig. 94(a), although its effect on strength is not discernable. It should be however noted that the origin of the data may have influenced this observation. For instance, most of the data points come from the work by LeBrun *et al.* [965] and Nezhadfar *et al.* [966]. While LeBrun *et al.* exclusively reported the mechanical behavior of horizontally built specimens, Nezhadfar *et al.* exclusively reported that of the vertically

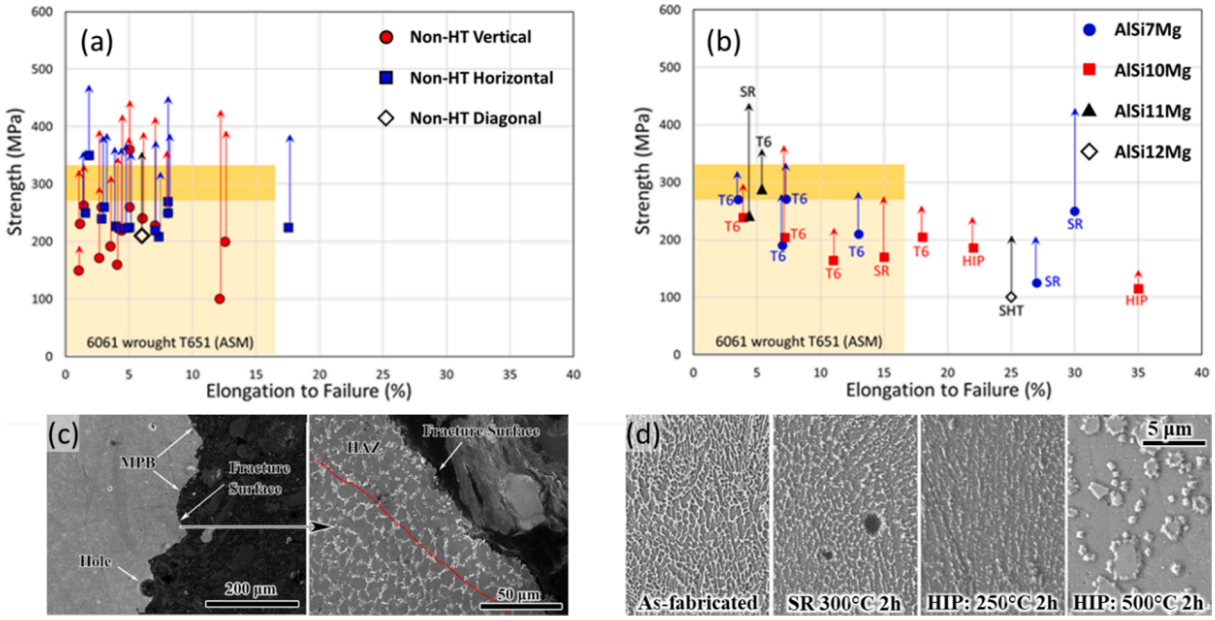

Fig. 96. (a)-(b) YS and UTS versus elongation to failure plots of AM AlSixMg {x = 7–12}. Data shown in (a) only included the non-HT conditions to highlight the effect of build orientation [240,495,503,508,598,762,928,974,976-988], while the ones shown in (b) contained only HT conditions [598,762,977,979-981,989,990]. The brown blocks indicate the yield and ultimate tensile strengths of wrought material, similar to Fig. 92. The reference YS, UTS, and EL of the wrought material (Al alloy 6061T651) used are 275 MPa, 310 MPa, and 17%, respectively [975]. (c) A micrograph on the cross-section perpendicular to the fracture surface showing the melt pool boundary induced fracture. (d) Microstructure as a function of processing conditions.

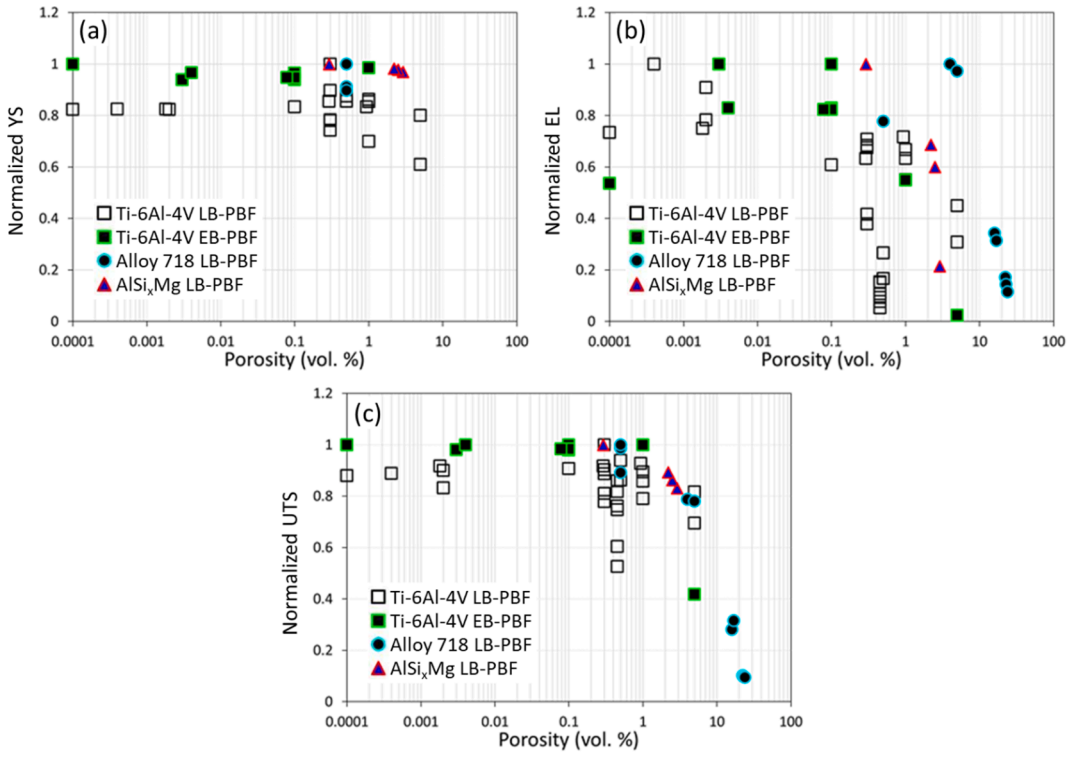

Fig. 97. Plots of normalized (a) YS, (b) Elongation to Failure (EL), and (c) UTS of AM Ti-6Al-4V, Alloy 718, and $AlSi_xMg$ (x = 10 and 12) vs. porosity. Data are collected from Refs. [176,215,984,987,991-996]. The normalization was performed based on the respective maximum values for each material, which are listed in Table 5. Data for both L-PBF and E-PBF processed Ti-6Al-4V are included, while those for only L-PBF Alloy 718 and $AlSi_xMg$ are included. The dependence of tensile properties for AM 17–4 PH SS on porosity is still lacking in the literature to the authors' best knowledge.

built specimens. In this regard, the machine-to-machine (EOS M280 used in Ref. [965] versus EOS M290 used in Ref. [966]) variability may have skewed the observation made in Fig. 95(a) to some extent. Importantly, in a work that has reported the mechanical properties in both orientations, the vertically built specimens were found to have significantly less ductility and lower strength than the horizontally build ones [785]. However, it should be noted that the process parameters used in [785] resulted in significant LOF defects in the material. Therefore, it can be expected that in the presence of excessive LOF defects, not only ductility gets affected, but the strength also may be weakened specifically when the lack of fusion defects are perpendicular to the loading direction.

On the other hand, observation regarding the effect of heat treatment on the tensile properties of 17–4 PH SS is much more conclusive (Fig. 95 (b)). Without heat treatments, the microstructure of this alloy is a mixture of un-strengthened δ ferrite [973], with a yield strength of 600–800 MPa. Because of the absence of strengthening phases or boundaries (Fig. 95(c)), however, the "hardenability" of these materials is generally high (note the large differences between YS and UTS for the as-built specimens in Fig. 95(b)), if aged, Cu-rich second phase particles precipitate within the martensite and significantly strengthen the material. A typical microstructure of the directly aged (H900) microstructure is shown in Fig. 95(d), note that due to their small size, the precipitates are not visible under optical micrographs. After Condition A (CA) treatment, a fine lath martensitic microstructure is formed in addition to the precipitates (Fig. 95(e)), resulting in these specimens exhibiting much higher strength than the ones without Condition A treatment (i.e. specimens that are directly aged). It is noted that similar to the cases of the Ti-6Al-4V and Alloy 718, the tensile mechanical properties of the 17–4 PH SS can surpass those of the wrought counterparts [972].

The effects of build orientation and heat treatment on the tensile properties of $AlSi_xMg$ {x = 7–12} are illustrated in Fig. 96. It is seen from Fig. 96 (a) that the ranges of YS, UTS, and EL of the non-HTed specimens for both build orientations well overlap. However, it is discernable that the YS and EL values for horizontally built specimens are slightly higher on average. This relatively subtle overall trend was echoed in three studies that compared the effect of build orientation, where ~10% higher YS and ~30–60% higher EL were observed for vertically built specimens [508,598,974]. The anisotropy in the tensile properties has been ascribed to the presence of weak regions at the melt pool boundaries where HAZs—characterized by the lack of the dendritic cell structures—exist. It was shown that these weak regions, oriented mostly perpendicular to the build direction, were preferred locations for tensile fracture. Nevertheless, the tensile strengths of the non-HTed $AlSi_xMg$ {x = 7–12} are generally inferior to wrought Al alloys (a comparison is made with the wrought Al alloy 6061 under T651 treatment [975]).

Heat treatment also significantly affects the tensile properties of $AlSi_xMg$ {x = 7–12} (Fig. 96(b)). The as-fabricated dendritic cellular structures, although afforded good strengths, are generally associated with poor ductility due to the strength contrast between the melt pool interiors and the melt pool boundaries [762,974]. This cellular network is metastable and may disintegrate at exposure to temperatures as low as 250 °C [762]. Exposure to higher temperatures at 500 °C eliminates the

Table 5
Reference values used to normalize the data points in Fig. 97 for the four material types considered.

Material	YS (MPa)	EL (%)	UTS (MPa)
Ti-6Al-4V (L-PBF)	1333	12	1407
Ti-6Al-4V (E-PBF)	962	16.4	1012
Alloy 718 (L-PBF)	1329	17.5	1429
$AlSi_xMg$, X = 10 and 12 (L-PBF)	228	7	412

cellular structure and yields a particulate structure akin to the annealed-aged condition [598,989]. Heat treatment substantially reduced the variation in the tensile data, revealing a clear strength-ductility tradeoff.

Although AM defects (including volumetric ones such as porosity, keyhole, and LOF, as well as surface roughness) tend to induce localized plasticity due to the associated stress concentrations, they typically do not affect the overall yield strength of AM materials. Indeed, within the typical tolerable porosity range of AM materials (<1%), the stress-concentrated material volume fraction is vanishingly small and insufficient to induce the early onset of macroscopic plasticity. Indeed, data presented in Fig. 97(a) exhibited clear invariance of YS over a relatively wide porosity range (~0.0003%–3%). On the other hand, the AM defects under tensile loading essentially act as surface/internal notches. The stress concentration is associated with strong stress triaxiality [997] which favors nucleation/growth of void and subsequent cavitation [998,999] leading to early onset of tensile fracture. As a result, the ductility of the AM materials may decrease with the increasing population of defects. As shown in Fig. 97 (b), the EL of all three materials noticeably decreased with increasing porosity. Assuming a constant, positive strain hardening rate for a given material, higher EL generally leads to higher UTS (see data points for $AlSi_xMg$ and Alloy 718 shown in Fig. 97 (c)). E-PBF and L-PBF Ti-6Al-4V are exceptions as these samples exhibited little to no strain hardening. Indeed, in the as-fabricated conditions, the fine lath and lamellar microstructures permitted very small dislocation mean free path, limiting the mutual interaction among dislocations and strain hardening potential. The limited strain hardenability of Ti-6Al-4V is also evident by comparing data presented in Fig. 94 and Fig. 95. Note that higher strain hardening rates can be achieved in E-PBF Ti-6Al-4V via appropriate thermal post-process resulting in a bimodal microstructure comprising lamellar α + β and martensite [1000]. A stronger dependence of UTS on porosity is therefore expected in this case.

8.1.2. Fatigue

The fatigue performance for most of the present AM metal parts is known to be inferior to that of their wrought counterparts, leading to growing concerns toward the applicability of AM parts in safety–critical, load-bearing applications [768,1001-1004]. It is argued that fatigue damage accounts for 50 to 90% of all engineering failures [1005,1006], most of which occurs in the high cycle fatigue (HCF, lives within 10^5–10^7 cycles) or very high cycle fatigue (VHCF, lives longer than 10^7 cycles) regime. Therefore, critical evaluation of the fatigue strength of AM materials in these regimes is vital to assure high levels of durability and to plan around operational life cycles.

A fatigue failure process includes three stages, namely: crack initiation, crack growth, and final fracture. The latter two stages are more relevant for materials under low cycle fatigue (LCF). The crack growth behavior of AM alloys, especially in the Paris regimes, does not exhibit significant difference to their wrought counterparts [1007-1013], although a small dependency on build orientation may exist. For

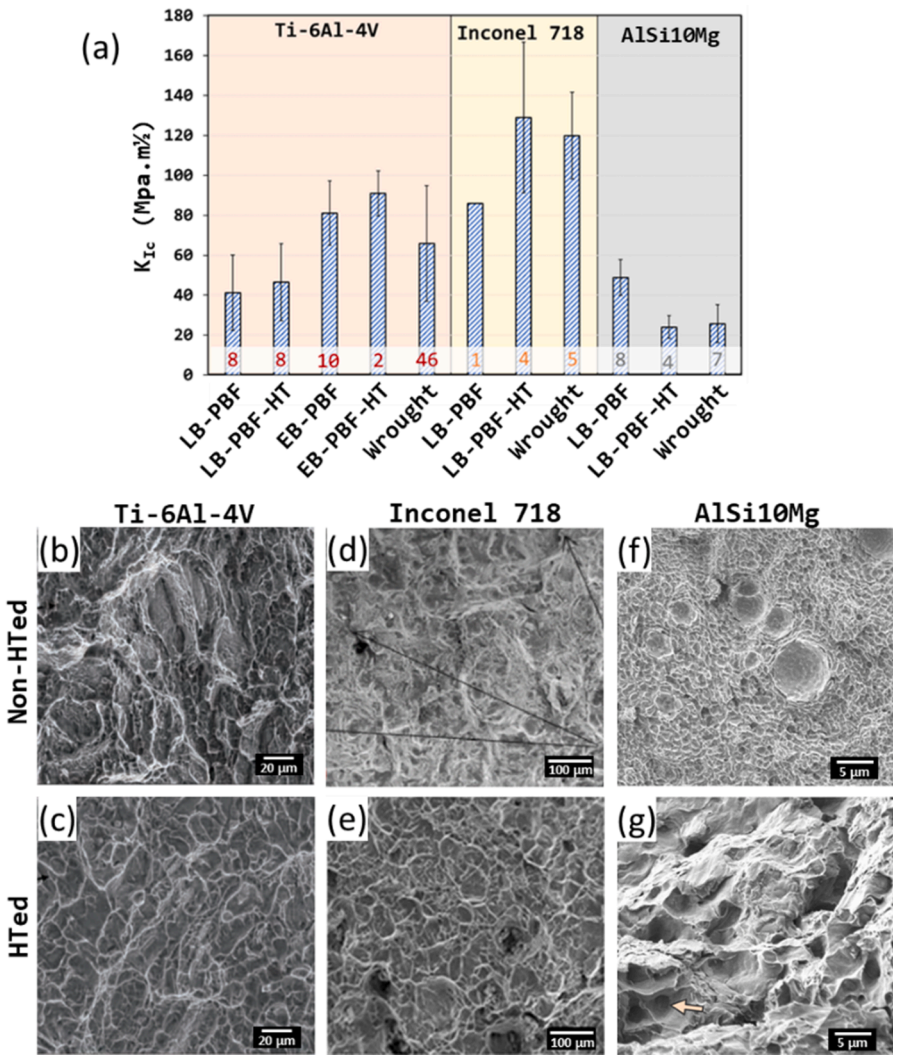

Fig. 98. (a) Summary of plane strain fracture toughness (K_{Ic}) data reported for popular AM and wrought alloys, including Ti-6Al-4V [691,906,1014-1020], Alloy 718 [1021-1023], and AlSi10Mg [762,1024]. Data for 17–4 PH SS is lacking in the literature. Typical fracture surfaces of (b - c) non-HTed and HTed LB-PBF Ti-6Al-4V (reprinted with permission from Ref. [1025]), (d - e) non-HTed (reprinted with permission from Ref. [1022]) and HTed (reprinted with permission from Ref. [1023]) LB-PBF Alloy 718, (f - g) non-HTed an HTed LB-PBF AlSi10Mg (reprinted with permission from Ref. [762]).

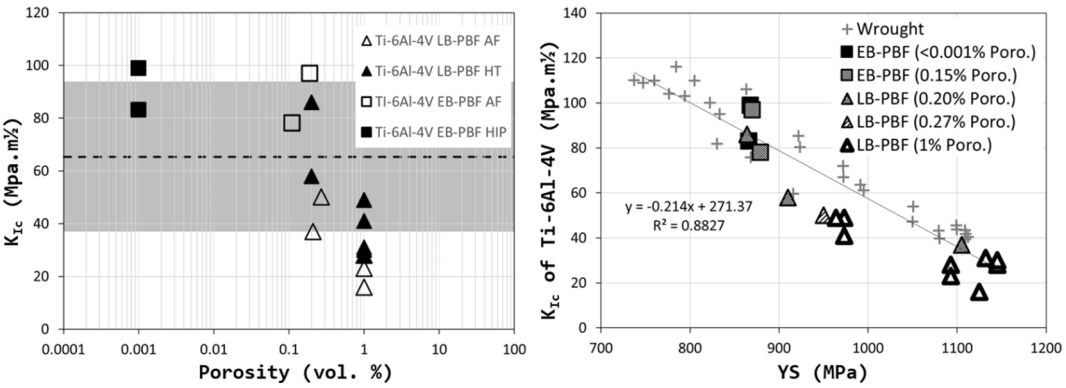

Fig. 99. (a) Plane strain fracture toughness (K_{Ic}) of three types of metals fabricated via L-PBF and E- PBF plotted vs. percent porosity [1014,1019,1020,1022,1024,1028]. (b) K_{Ic} of Ti-6Al-4V plotted as a function of YS. Wrought data are also included [1015,1016].

instance, horizontally built Ti-6Al-4V specimens exhibited lower crack growth rates compared to the ones built in the vertical direction [1007]. Heat treatments tend to eliminate all orientation dependencies on both Ti-6Al-4V [1009] and 17–4 PH SS [1011,1012].In this case, the influencing factors that set the crack growth life of AM materials apart from their wrought counterparts may be the initial and final crack sizes – the latter of which is governed by the plane strain fracture toughness (K_{Ic}) of the material.

Several K_{Ic} data for AM materials, the majority of which being Ti-6Al-4V, are presented in Fig. 98. The significant dependency of K_{Ic} on build orientation, surface condition, and post-processing conditions exists [691]. The anisotropy of fracture toughness was found to partially originate from the presence of LOF defects [691,1014]. Residual stresses, however, are believed to be the most dominant factor controlling the orientation-dependent fracture toughness values. It was shown that, after performing stress relief heat treatment, fracture toughness values under all the specimen orientations are within reasonable agreement [1014]. This also highlights the critical role of residual stresses and subsequent heat treatments in fracture toughness values.

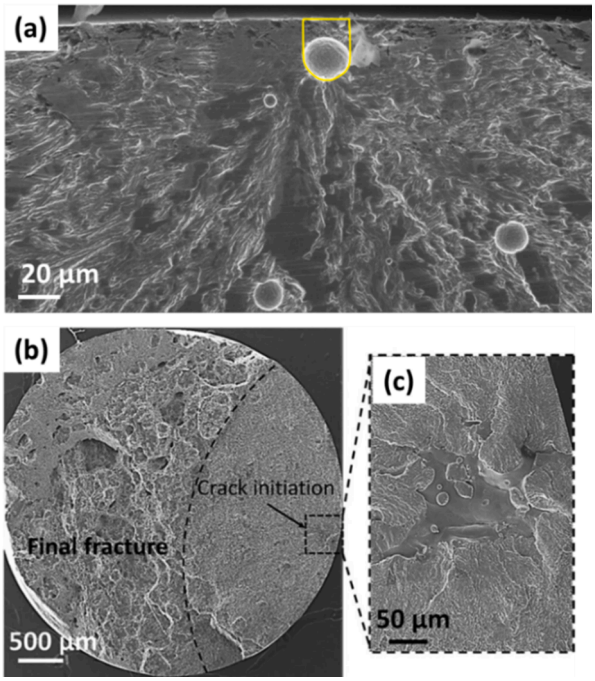

Fig. 100. Typical examples of (a) pores, can be keyholes or gas-entrapped pores, and (b & c) lack-of-fusion on fatigue-induced fracture surfaces. Reprinted with permission from Refs. [783,785].

The data for wrought Ti-6Al-4V is already associated with significant scatter [1015,1016,1026]. The fracture toughness of the AM counterparts, while also vary significantly depending on the fabrication condition and post-fabrication heat treatment, appear to fall in the range of wrought data reasonably well [691,906,1014-1020]. The as-fabricated Ti-6Al-4V microstructure from L-PBF is typically martensitic due to the high cooling rates [156] and lead to more brittle fracture behavior (for instance, Fig. 98(b) shows a quasi-cleavage tensile fracture surface). The lamellar α + β resulted from post-build heat treatment, which can significantly improve the ductility (Fig. 98(c) for a dimpled fracture surface of a HT L-PBF Ti-6Al-4V). HT L-PBF Alloy 718 exhibited fracture toughness superior to the non-HTed condition. This can be ascribed to the removal of the detrimental Laves and δ phases (typical morphology shown in Fig. 94(c)) and the formation of γ“ and γ’ precipitates (shown in Fig. 94(e)). The difference in the fracture toughness in the as-fabricated and HT conditions is echoed by the morphological differences in the fracture surfaces. Fig. 98(d, e) show the typical fracture surfaces of non-HTed and HTed alloy 718 specimens, which shows a quasi-cleavage (more brittle) and dimpled features (more ductile), respectively. The K_{Ic} for Alloy 718 under HT conditions coincides well with their wrought counterparts.

On the contrary, AlSi10Mg appears to have higher fracture toughness in the as-fabricated condition compared to the HT condition as well as similar cast/wrought aluminum alloys in HT conditions [762,1024]. Although the explanation for this anomaly is not readily available in the literature, it is suspected that the as-fabricated cellular structures offered additional toughening via the bridging mechanism noted by Ritchie [1027]. Indeed, the HT microstructure, as well as the HT cast/wrought structure, is essentially relatively large precipitates dispersed in a soft matrix (Fig. 96(d), which is also typical for annealed + aged conditions). Upon fracture, the voids nucleate from the precipitates and grow via rapid cavitation, leading to relatively low toughness. The remnants of these cavities (>5 µm) are visible from the fracture surface (Fig. 98(g)). On the other hand, the cell boundaries in the as-fabricated microstructure appear to have offered substantial resistance to void growth, promoting further void nucleation which leads to toughening. Indeed, the fracture surface of the as-fabricated AlSi10Mg specimens shows very uniform and fine dimples whose length scale is comparable to that of the cells — rapid growth only occurred in very few voids (Fig. 98(f)). The beneficial effects offered by the cellular microstructure are sufficient to overcome any possible detrimental effects of AM defects including porosity.

The abundance of K_{Ic} data for AM Ti-6Al-4V, including L-PBF and E-PBF specimens under both HT (including HIP) and non-HT conditions, permits the assessment of the underlying effect of AM induced defects if any. As presented in Fig. 99(a), K_{Ic} data reported by different sources for

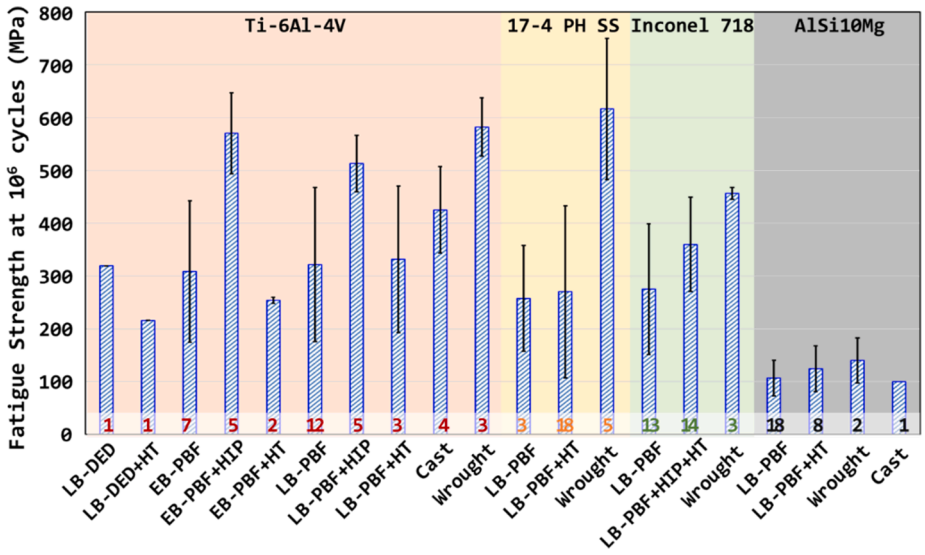

Fig. 101. Summary of fatigue limits of three popular AM alloys; Ti-6Al-4V, 17–4 PH SS, and Alloy 718 from machined specimens with no surface roughness. For practicality, the fatigue limits are acquired as fatigue strength at 10^6 cycles. The color-coded numbers at the base of each bar indicate the number of data points collected. Data are obtained from Refs. [215,280,431,432,509,689,762,772,928,944,976,987,1038-1048].

Ti-6Al-4V (square marker types) appear to suggest that an influence by porosity exist. Among all data points, the reduction of a factor of 5 in fracture toughness can be seen when the porosity of the specimens increases from 0.001% to 1%. This variation, as previously mentioned, appears to fall well within the range of the wrought data (the black horizontal line and the gray band represent the mean and standard deviation of wrought data). However, K_{Ic} is indicative of the energy absorbed per unit area of the fracture surface, related to the plastic strain energy dissipated in the plastic zone before separation, and consequently affected by the strength-ductility characteristics of a material [1029]. Typically, metallic materials are subjected to the strength-ductility tradeoff, which also suggests the existence of a strength-toughness tradeoff [1027]. For instance, the K_{Ic} vs YS for Ti-6Al-4V is plotted in Fig. 99(b), where both wrought and AM data (ones already presented in Fig. 99(a)) are included. It is evident that the strength of wrought Ti-6Al-4V almost linearly decreases with increasing strength. It is also evident that the AM data agrees well with this decreasing trend. A linear fit of both the AM and wrought data yielded goodness of fit $R^2 = 0.88$. Besides, the existence of porosity up to 1% does not appear to have affected the overall strength-toughness tradeoff behavior.

In HCF or VHCF, the fatigue life is often dictated by the initiation and early propagation of microscopically small cracks [938,1030,1031]. Generally, these cracks are initiated by slip. In wrought alloys, stabilization of cyclic stress is due to the collective formation and evolution of dislocation structures (e.g. persistent slip bands in the case of FCC materials, and dislocation cells in the case of BCC materials). Such dislocation structures concentrate the macroscopically-applied deformation into finite deformation bands, which can carry relatively large shear deformation (~1% of shear strain). Such deformation bands form intrusions and extrusions on the surfaces or stress concentrations on the grain boundaries—both of which can then initiate fatigue cracks [1006,1032-1034].

AM materials, especially in HCF and VHCF regimes, contain stress concentrations at and near the volumetric (i.e., pores) or surface defects (surface roughness) may give rise to localized plastic deformation, even if the overall stress–strain response appears linear [907]. Localized plastic deformation then leads to accelerated initiation of fatigue cracks. Defect dominated fatigue crack initiation has been well-documented for AM materials as well as conventionally manufactured materials (such as the cast Ni-superalloys [1035]). Fig. 100(a) and Fig. 100(b) show typical examples of pores and LOF defects identified on fatigue-induced fracture surfaces, respectively. The pores in Fig. 100(a) can be either spherical gas-entrapped pores or keyholes. It is, however, difficult to differentiate between them as both appear circular on fracture surfaces, where the elongated feature of keyholes can be obscured. Nevertheless, the keyholes are generally larger than the gas-entrapped pores [221]. With the presence of surface roughness, such as the one seen in the as-built specimens/parts, fatigue cracks typically initiate from the micro-notches on the rough surface—often surpassing the effect of the volumetric defects [783,966,1036,1037].

The extent of the plastic deformation near the defects depends on multiple factors including the shape, size, and location (i.e. nearest neighbor defect, distance to the free surface) of the defect. For instance, from the perspective of fracture mechanics, the stress intensity factor of a perimeter crack emanating from a flat, LOF defect is expected to be substantially larger than a spherical pore. Also, cracks emanating from a larger flaw would be associated with a higher stress intensity factor than those from a smaller one. For these reasons, the fatigue strength of AM materials is generally much inferior compared to their wrought counterparts, specifically if the AM material contains some lack of fusion defects.

The significant variability in the microstructure, as well as the defects' size and shape, lead to a large scatter in the fatigue data for AM materials. Such variability, which is illustrated in Fig. 101 for AM specimens in the machined surface conditions (i.e., only volumetric defects), maybe caused within a single build, from build to build, from machine to machine, and from AM method to method. Among the three popular alloys in the metal AM community, i.e., Ti-6Al-4V, 17–4 PH SS, Alloy 718, and AlSi10Mg, Ti-6Al-4V is the most extensively studied. All processing techniques produce substantially lower fatigue strengths in the materials in non-HT conditions with significant scatter. The scatter is not alleviated by HT, hinting at the porosity's primary role.

As seen from Fig. 101, HIP both increases the fatigue strength and reduces scatter by reducing the size of the pores and refining the microstructure near the defects [1049]. Although data for HIPed 17–4 PH SS and AlSi10Mg are unavailable, the existing data on the other two materials suggests that HIP can lead to fatigue strengths comparable to wrought materials in machined specimens without surface roughness. AM specimens in as-built surface conditions are reported to have orders of magnitude shorter fatigue lives as compared to the wrought counterparts [783,966,1036]. It has been shown for AM materials with a significant ductility, such as 304L SS and 316L SS, that the fatigue

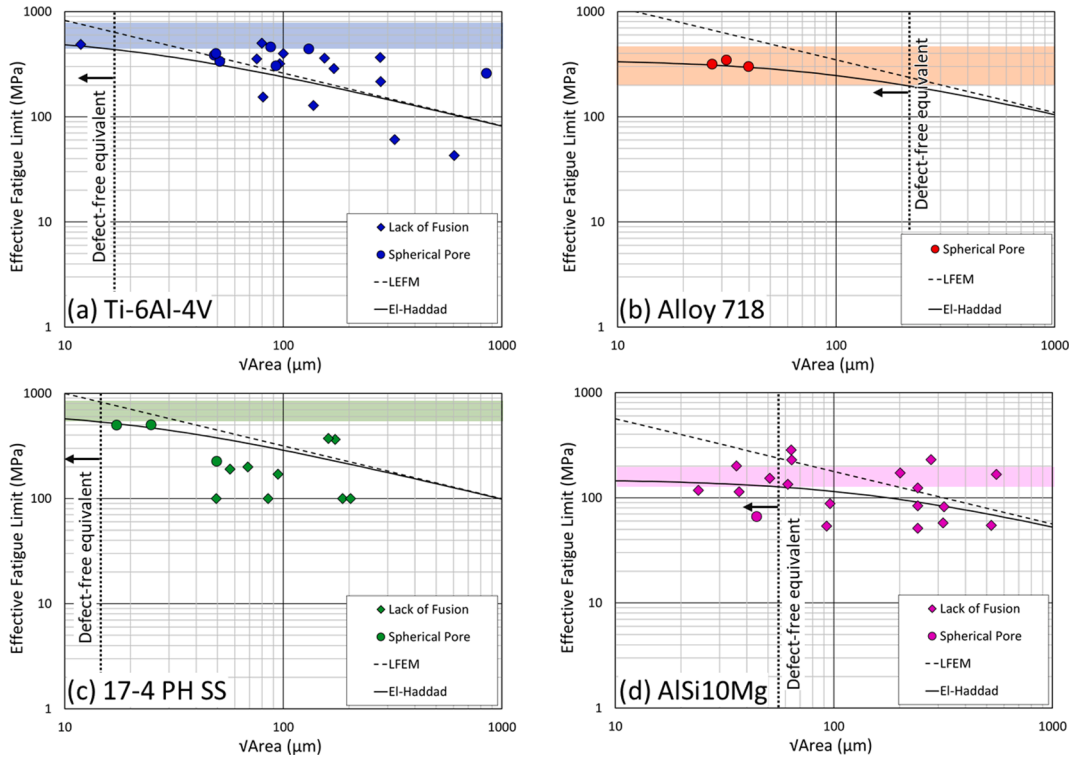

Fig. 102. Kitagawa diagrams showing observed effective fatigue limit vs. $\sqrt{area}$ of the fatigue crack initiating defects for various AM alloys (a) Ti-6Al-4V, (b) Alloy 718, (c) 17–4 PH SS, and (d) AlSi10Mg. The color shades denote the data ranges for HIPed AM specimens in (a) [431,1061,1062] and (b) [953], and the wrought/cast alloys in (c) [785,928,966-968] and (d) [762,989,1038]. The reference data for the wrought/cast Al alloys are A357 and 6061 alloys. Data are obtained from Refs. [215,280,431,432,509,689,762,772,928,944,976,987,1038-1048].

resistance may not be significantly affected by the presence of defects [1036,1050]. The effect of defect size on the fatigue limit of the various AM alloys is shown in Fig. 102. The collected data includes the fatigue properties of Ti-6Al-4V, Alloy 718, 17–4 PH SS and AlSi10Mg specimens fabricated by all AM (i.e., laser beam, electron beam) techniques regardless of the stress ratios [215,280,431,432,509,689,762,772,928,944,976,987,1038-1048].

For practical identification of fatigue limits from S-N curves in the literature, an approach similar to one established by Beretta and Romano [781] and Molaei *et al.* [157], has been adopted here. The fatigue limit, σ_{FL}, is represented by the fatigue strengths (maximum stresses) at the fatigue life of 10^6 cycles from the reported S-N curves with stress ratio $R = -1$. If no data points were available at exactly 10^6 cycles, data points in the HCF regime were fitted to a power law function ($\sigma_{max} = AN_f^{-B}$) and the fatigue strength was estimated based on this fit. This same approach was used for S-N curves with data points not reaching 10^6 cycles. To compensate for different R, the obtained maximum stress was converted to effective stress (σ_{eff}) following the methods of Li *et al.* [1051]:

$$\sigma_{\text{eff}} = \sigma_{\max}\left(\frac{1-R}{2}\right)^n \tag{7}$$

where σ_{eff} represents the effective stress, $\sigma_{\max}$ represents the maximum stress during a load cycle at a given R, and n is a material-dependent exponent. $n = 0.28$ is adopted for Ti-6Al-4V [1051] and $n = 0.5$ is used for alloy 718 according to data presented in [953]. Conversion for the R value for 17–4 PH SS is not necessary as all experiments reported were done at $R = -1$. The effect of R on the fatigue limit of AlSi10Mg is not well known. Therefore, a modified Goodman relation is used to account for the effect of stress, i.e.

$$\frac{\sigma_a^R}{\sigma_{\text{eff}}} + \frac{\sigma_m}{\sigma_{\text{UTS}}} = 1 \tag{8}$$

where σ_a^R is the stress amplitude at the load ratio R, σ_m is the mean stress, and the σ_{UTS} is the UTS. The $\sqrt{area}$ method developed by Murakami *et al.* [654,1052-1055] was utilized to determine the size of each crack initiating defect. If the reported crack initiating defect was not easily identifiable, the data point was ignored.

According to Murakami's approach, the defects were all treated as an irregular crack, with a representative dimension derived from the root of the projected defect area on the loading plane. None of the papers collected in this study directly reported the defect size nor provided fractography of the specimen that failed at exactly 10^6 cycles. We therefore obtained the typical defect size from the corresponding specimen batch. If there were multiple defects with various sizes reported from specimens within a given batch, the largest size was taken. If multiple defect types (namely LOF and spherical pores) were involved, then the size of the most detrimental defect was measured – noting that LOF defects have significantly higher stress concentration than spherical pores.

The collected data of fatigue limit and $\sqrt{area}$ of the fatigue critical defects for four alloys (Ti-6Al-4V, Alloy 718, 17–4 PH SS, and AlSi10Mg)

Table 6
Stress ranges corresponding to fatigue limit ($\Delta\sigma_{w0}$) and long crack threshold stress intensity factor range ($\Delta\mathbf{K}_{th,L}$) used in Eq. (9).

Material	$\Delta\sigma_{w0}$ (MPa)	$\Delta K_{th,L}$ (MPa•√m)	R
Ti-6Al-4V	1200	6 [1059]	−1
AlSi10Mg	300	4.1 [1060]	−1
Alloy 718	700	8 [1058]	0.1
17–4 PH SS	1400	7.27 [783]	−1

are presented as Kitagawa diagrams in Fig. 102. The predictions of fatigue limits by the El-Haddad model [1056] as well as linear elastic fracture mechanics (LEFM) assuming constant long crack threshold stress intensity factor ranges ($\Delta K_{th,L} = Y\Delta\sigma_w\sqrt{\pi\sqrt{area}}$) are also provided on the plots as solid and dashed lines, respectively. The El-Haddad model adopting the $\sqrt{area}$ approach is given as:

$$\Delta\sigma_w = \Delta\sigma_{w0}\sqrt{\frac{\sqrt{area}_0}{\sqrt{area}_0 + \sqrt{area}}} \tag{9a}$$

$$\sqrt{area}_0 = \frac{1}{\pi}\left(\frac{\Delta K_{th,L}}{Y\Delta\sigma_{w0}}\right)^2 \tag{9b}$$

where $\Delta\sigma_w$ and $\Delta\sigma_{w0}$ are the stress ranges corresponding to the fatigue limits (σ_{FL}) with and without the presence of defects, i.e., $\Delta\sigma_w = 2\sigma_{FL}$, Y is a geometrical factor which in this work is assumed to be 0.65 following Ref. [783]. The parameters associated with Eq. 9 for the four alloys are provided in Table 6. Among the data, the $\Delta\sigma_{w0}$ were taken from wrought data with same source as Fig. 101. Whenever possible, $\Delta K_{th,L}$ at R = -1 was used. For Ti-6Al-4V, data at R = -1 appeared to be missing for AM parts, therefore, $\Delta K_{th,L}$ for wrought Ti-6Al-4V was used [1057]. For Alloy 718, $\Delta K_{th,L}$ appeared to be missing for R = -1, regardless of the fabrication technique; therefore, the data for R = 0.1 was used instead [1058]. Due to the less pronounced crack closure effect, the $\Delta K_{th,L}$ at R = 0.1 is expected to be lower than for R = -1.

As presented in Fig. 102(b), the fatigue limit data for non-HIPed AM Alloy 718 (although quite limited) reside well within the data range for the same alloy under HIPed conditions (see brown shaded region). Indeed, the El-Haddad prediction appears to vary very gradually for $\sqrt{area}$<~ 100 μm. In addition, the fatigue limit of AM AlSi10Mg is not only relatively independent of the crack initiating defect size, but it is also comparable to that of the wrought/cast counterparts (Al alloy A357 and 6061 [762,989,1038] see pink shaded region in Fig. 102(d)) when $\sqrt{area}$ <~ 80 μm. This observation appears to be consistent with the prediction from the El-Haddad model, and suggests that the defects in the respective $\sqrt{area}$ ranges of the Alloy 718 and AlSi10Mg (i.e., <~ 100 μm for Alloy 718 and <~ 50 μm for AlSi10Mg) may be microstructurally small and the initiation of fatigue cracks are not substantially accelerated by these defects. In Fig. 102 for all materials, the El-Haddad predictions falling above the lower limit of wrought/HIPed fatigue limit range suggests that fatigue behaviors being roughly equivalent to defect-free conditions. In contrast, the fatigue limits of AM Ti-6Al-4V and 17–4 PH SS appears to be more sensitive to the size of the defects, which is again consistent with the predictions from El-Haddad model. The fatigue limits of AM Ti-6Al-4V and AM 17–4 PH SS for $\sqrt{area}$ >~ 15 μm were seen to decrease noticeably with increasing $\sqrt{area}$ and are inferior to the respective HIPed and wrought conditions. The observations made so far suggest that Ti-6Al-4V and 17–4 PH SS tend to be more defect-sensitive, while the Alloy 718 and AlSi10Mg are less so.

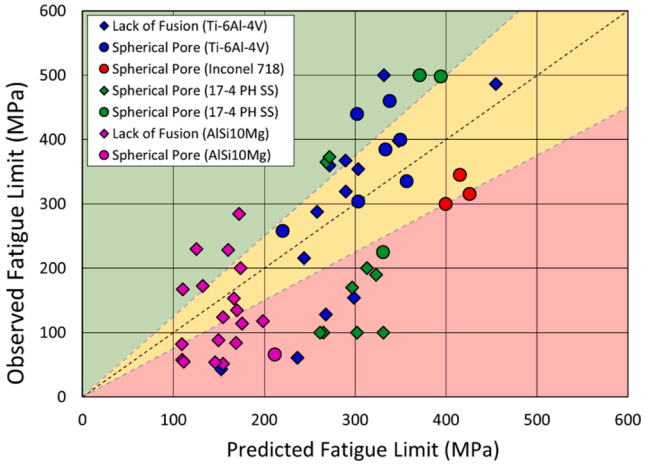

Fig. 103. Observed fatigue limit of various AM alloys vs. the values predicted by the Murakami model. The green region encloses the over-conservative predictions, the brown region encloses the predictions with ± 25% accuracy, and the red region encloses under-predictions. Data are obtained from Refs. [215,280,431,432,509,689,762,772,928,944,976,987,1038-1048].

As shown in Fig. 102, the El-Haddad predictions clearly deviated from the ones made by the LEFM at smaller defect sizes. This is due to the reduction of threshold stress intensity factor range (ΔK_{th}) at smaller defects/crack sizes associated with the under-developed crack closure effect [1063,1064]. When defects/cracks are mechanically or physically short, the increasing trend of ΔK_{th} with increasing defect/crack size are also captured by other defect sensitive fatigue (DSF) models. For instance, Murakami *et al.* observed that, in this regime, the ΔK_{th} was proportional to $\sqrt{area}^{1/3}$ [782]. Following this, they proposed a correlations between fatigue limit (σ_{FL}) and $\sqrt{area}$ [654,781-783], i.e.,

$$\sigma_{FL} = L(HV + 120)/(\sqrt{area})^{1/6} \tag{10}$$

where σ_{FL} is the fatigue limit, L is a location-dependent pre-factor (L = 1.43 for surface/subsurface defects, and 1.56 for internal defects), HV is the Vickers hardness number, $\sqrt{area}$ is the equivalent defect size, and the *area* in this equation is defined as the projected area of the defect on the loading plane.

Detailed derivation and discussion of Eq. (10) are provided elsewhere and are not repeated here [1055,1065,1066]. In what follows, fatigue limit data presented in Fig. 102 has been reorganized and presented in Fig. 103 to further illustrate the effect of defects using Murakami's DSF model. Although the literature abundantly reported the AM materials fatigue performance, the hardness data is not always available for each fatigue data point. To rectify this, a UTS – HV correlation is first obtained for each material based on the existing data, and the missing HV values are filled using the known strength data. When strength is not available either, an average HV for the materials under the specific build and HT conditions are assigned.

Using the defect and fatigue limit data collected for all materials, the observed vs. the predicted fatigue limits are displayed in Fig. 103. The diagonal dashed line represents the perfect match between experimental observation and model prediction. The brown region encloses predictions within ± 25% accuracy of the observed fatigue limits. As shown, although many predictions (31 data points in green and brown regions out of 54 total) were made with acceptable accuracy or conservative, a significant portion of the predictions (23 data points in the red region out of 54 total) significantly underestimated the fatigue limit. It is noted that only 3 out of 14 fatigue limits regarding the spherical pores were significantly underpredicted, which indicates that the Murakami model may be suited for materials containing spherical pores. In the data collected within this study, no LOF defects are noted in alloy 718 specimens, and accordingly, the predictions are very close to experimentally observed endurance limits for this alloy. It is also noted that most of the underpredictions were made when LOF defects are involved, which indicates that the effect of the defects' shape (i.e. spherical vs. flat), in addition to their size and locations may be severely influencing the fatigue limits. Indeed, as discussed earlier, the sharp, LOF defects may increase the higher stress intensity factors of the emanated cracks, and therefore, they can be more detrimental to the fatigue strength. At present, the Murakami model treats all defects as a virtual crack only accounting for the defect's size and location (either internal or surface defects), and may benefit from the additional consideration of defects' shape. Recent work by Sheridan [1067] elaborated a modified El-Haddad model for versatile defect tolerant design and enhanced the legacy model to include finite life behavior and stress ratio effects.

8.2. Corrosion behavior

The unique microstructures and macroscopic defect structures produced in powder bed fusion AM processes can have a strong impact on the degradation behavior of parts in service. This section reviews the literature on the aqueous corrosion and high-temperature oxidation behavior of structural materials (mainly iron-based, aluminum, titanium, and nickel alloys) used in powder bed AM. Since the microstructure of AM parts is different from those produced by casting or metal forming, materials response to the corrosive environment is different. Three review articles containing additional detail on aqueous corrosion behavior have been recently published [1068,1069]. This section focuses on the effects of defect structures, microstructure refinement, and microstructure anisotropy on electrochemical response and high-temperature oxidation behavior of AM parts.

Iron-based Alloys. Corrosion test results have, with a few exceptions, been limited to 17–4 PH and 316L stainless steels. These alloys are widely used in L-PBF AM. Stainless steels obtain their corrosion resistance from a thin layer of chromium and iron oxides called the passive layer. A common corrosion concern for stainless steel is pitting corrosion, where the localized metal loss occurs at locations of passive film breakdown. Pitting is a phenomenon of concern especially when the environment contains chloride anions. Environments that contain chloride ions include seawater (approx. 3.5 wt% NaCl or 0.6 M NaCl) or simulated body fluid (SBF) used in biocompatibility studies. Most corrosion studies of L-PBF material focus on these types of environments and the comparisons of wrought and L-PBF alloys.

Stainless steel 316L produced by L-PBF methods has been reported to have lower pitting resistance compared to wrought material in both $FeCl_3$ [1070] (an aggressive environment used in ASTM standard tests for comparative pitting resistance) and in NaCl solutions [1071-1073]. The higher porosity of L-PBF samples is typically noted as a reason for decreasing corrosion resistance. This was quantified by Sun *et al.* for 316L [1073]. The breakdown potential (E_b, the onset of pitting corrosion) was found to decrease with increasing porosity, indicating decreased resistance to pitting. The decreased repassivation potential (E_r) with porosity shows that pits formed on samples with higher porosity were more difficult to repassivate. Finally, the frequency of metastable pitting was also found to be much higher on the printed samples.

These results were similar to other studies of surface roughness and its effect on pitting corrosion [1074]. Kong *et al.* [1075] examined the effect of varying laser power (other process variables constant) on corrosion resistance of 316L in simulated body fluid (SBF). They found samples built with lower beam power had higher porosity and lower pitting potentials. Samples built with higher beam power performed better than wrought 316L. Recently, Chen *et al.* [686] used laser remelting as a polishing step to reduce the surface roughness of the L-PBF processed 316 alloy. It was indicated that laser polishing could reduce the surface roughness of the as-build part by over 92% (from 4.75 μm to 0.49 μm Sa). Further, microscopy observation close to the top surface showed that the as-build part had columnar grains (hardness of 1.82 GPa) with fine cellular grains (hardness of 2.89 GPa) after laser polishing. Electrochemical studies in 0.4 M HCl with a Hg/Hg_2SO_4 reference electrode confirmed that the laser polished sample had higher corrosion potential and lower corrosion current density (-0.557 V and 0.007 $\mu A/cm^2$) compared to the as-built 316 samples (-0.667 V and 0.280 $\mu A/cm^2$). This led to an increased pitting potential from −0.375 V in the as-build part to −0.258 V in the laser polished part. Enhanced corrosion resistance was associated with removed unmelted powder particles, reduced porosity, reduced surface roughness, and grain refinement.

Sander *et al.* [1072] performed a similar study of pitting on 316L, but with varying porosity <1 vol%, much lower than [1073]. In this work, the pitting potential of the L-PBF samples was much higher than the wrought sample. This was attributed to the refinement of the MnS inclusions at the part surface due to rapid solidification. The frequency of metastable pitting was lower on the L-PBF samples compared to the wrought samples and this frequency was found to increase with porosity. Recently, Lodhi *et al.* [1076] compared the corrosion behavior of L-PBF 316L with wrought alloy in acidic conditions (pH < 3 with different Cl^- content. The enhancement of corrosion resistance was related to the fine sub-granular structure, formation of a stable passive oxide film on the surface, and limited time for MnS inclusion nucleation during AM process [1077]. Another study by Cruz *et al.* [1078] showed that the L-PBF processed 316L had compressive residual stress of 250 MPa and after stress relief treatment at 1100 °C for 5 min, it decreased to −15 MPa. This stress relief treatment had minimal effect on the microstructure, but the corrosion resistance in NaCl was affected. A slight increase in the pitting potential was observed. Their results were analyzed in the context of the point defect model [1079,1080] which links pit initiation to transport of defects through the passive film. The hypothesis in this work was that higher residual stresses led to lower donor densities and point defect concentration in the passive film, which slowed the rate of passive film growth and slightly enhanced the pitting potential.

A detailed study on the porosity of L-PBF parts and its influence on corrosion was conducted by Schaller *et al.* [1081] on 17–4 PH stainless steel, which is a precipitation-hardenable martensitic grade. Like 316L, a major corrosion concern is pitting in chloride-containing environments. The study employed microelectrochemical methods to expose small surface areas to the test solution, meaning they could test pore-free areas and compare them to areas containing pores. Tests were performed in a 0.6 M NaCl solution. The L-PBF samples exhibited lower corrosion potentials, higher corrosion current densities, and lower pitting potentials compared to the wrought condition. An important finding from this study was that larger lack-of-fusion pores much worse for corrosion resistance compared to smaller gas porosity pores. This was illustrated by microelectrochemical testing at specific areas on the sample surface with and without pores. Results are shown in Fig. 104. The irregular shape of LOF pores was suggested to result in more occluded regions than the hemispherical gas pores.

Similar effects of porosity have been observed in 304L stainless steel [1082]. 304L is a common stainless steel grade with a similar composition to 316L, except 316L contains Mo which improves resistance to pitting corrosion. In this study wrought 304L was compared to the L-PBF processed material in the as-built condition. Grit-blast and ground surface finishes were compared. Corrosion resistance was evaluated by weight loss tests in acidic solutions and electrochemical tests in aerated solutions of varying NaCl concentration. In all acidic solutions, the grit-blasted L-PBF sample showed higher corrosion rates than the ground L-PBF or wrought samples. No passive region was evident in the grit-blasted samples anodically polarized in the NaCl solution – severe pitting was observed. Rougher surfaces were suggested to contain more crevice-like regions and the grit-blasted surface was particularly detrimental due to embedded particles. Microelectrochemical test results were similar to those reported above for 17–4 PH. LOF pores showed small passive regions and lower pitting potentials. The passive region was much wider when non-porous regions were tested. Porosity was attacked, with etch pits visible on pore walls. For ground surfaces, L-PBF processed samples were more resistant to corrosion than wrought samples. This attributed to a reduction in oxide inclusion size, as both wrought and AM samples had low S (50 ppm max for L-PBF, <10 ppm for wrought) and few MnS would be expected.

The above-discussed study on 304L also observed no preferential corrosion due to segregation or other microstructural features besides porosity. The microstructure of L-PBF austenitic stainless steel consists of relatively large columnar austenite grains with a cellular substructure and often some δ-ferrite [1083]. Microsegregation of Cr and Mo has been observed in the intercellular regions and these regions also have high dislocation density [1084,1085]. The study from Chao *et al.* [1086] however, found dislocation structures but not evidence of

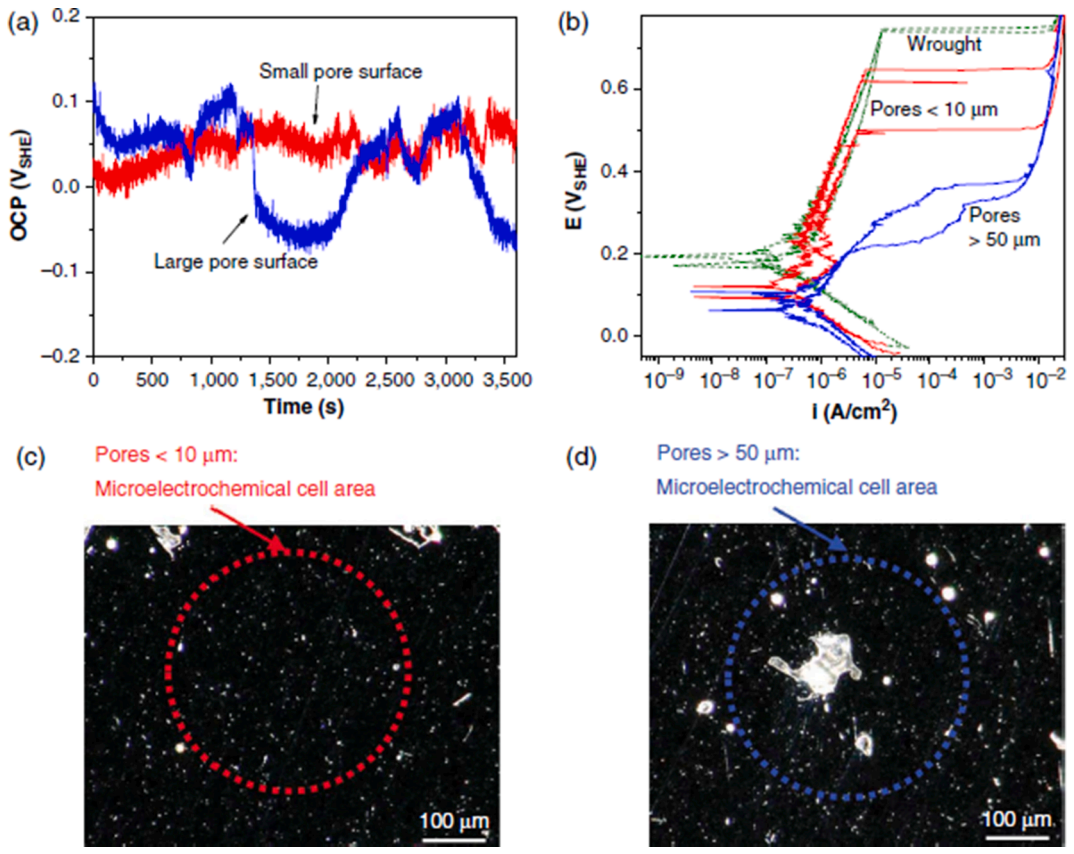

Fig. 104. Results from Schaller *et al.* on 17-4PH stainless steels showing the effects of pore size on polarization behavior. (a) shows the variation in open circuit potential with time, indicating more severe transients on surfaces with large pores. (b) shows potentiodynamic polarization curves that show a lack of a passive region and pitting at large pores. (c) and (d) show the surface areas. Reprinted with permission from Ref. [1081].

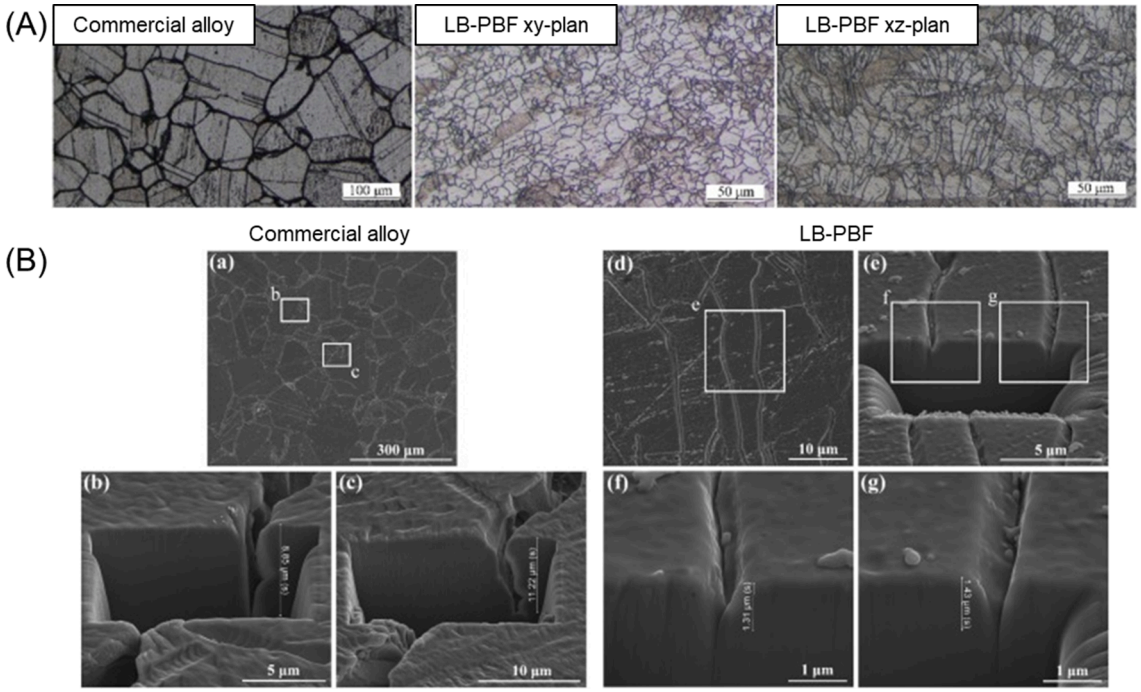

Fig. 105. (A) Optical micrographs after DL-EPR tests (0.5 M H_2SO_4 + 0.01 M KSCN solution at room temperature). (B) Focused ion beam cross-sections from the grain boundaries of specimens to measure the depth of attack. Reprinted with permission from Ref. [1093].

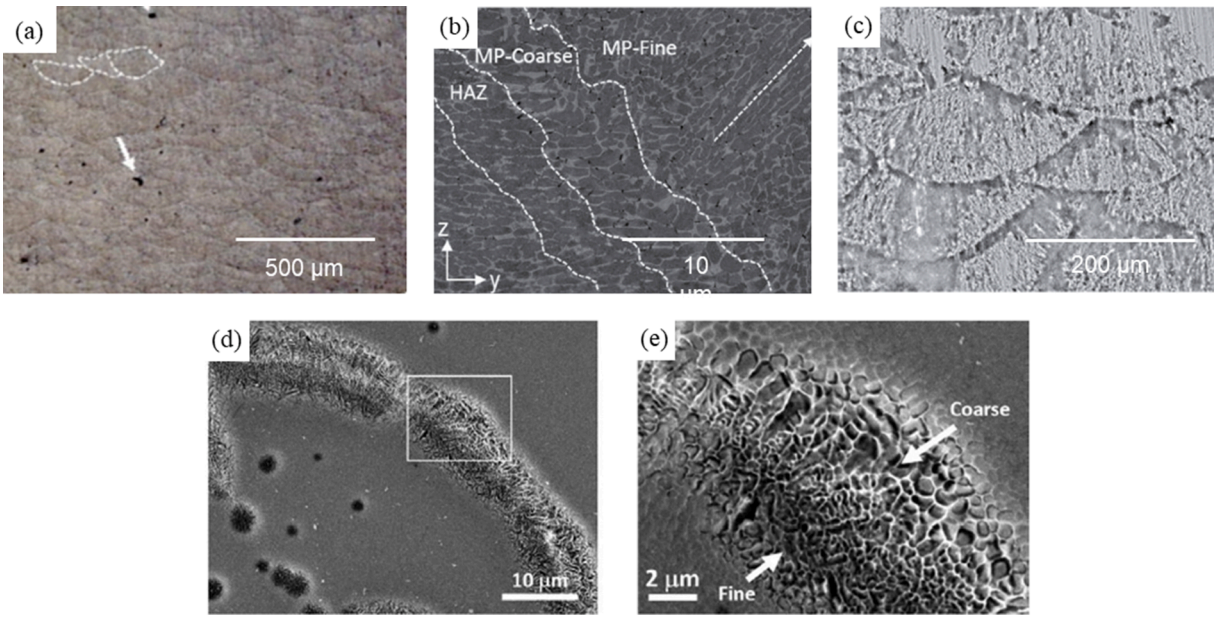

Fig. 106. Example melt pool boundaries (a) and coarsened microstructure at the boundaries (b), images (c-e) show preferential corrosion at melt pool boundaries in L-PBF-processed AlSi10Mg. Reprinted with permission from Refs. [1096,1098].

microsegregation. Improved corrosion resistance compared to wrought material was attributed to refined inclusion size. In 17–4, the refinement in Cu precipitate size has been noted as beneficial [1087]. Barroux *et al.* [1088] evaluated pitting corrosion of solution treated (at 1040 °C for 30 min) and aged (at 480 °C for 1 h) 17–4 PH in 0.5 M NaCl. The post-heat treatment resulted in the formation of recrystallized grains with fine martensite laths and NbCs precipitates, containing more austenite and Cu-rich precipitates. Compared to a wrought alloy, heat-treated L-PBF specimen showed a shift of E_{pit} towards more positive values with very few metastable pits, in agreement with [1089]. Similarly, improved corrosion resistance of maraging steel was suggested to be the result of smaller precipitates [1090]. Trelewicz *et al.* [1091] showed evidence of microsegregation and also reported decreased corrosion resistance of 316L in 0.1 M HCl. The dislocation structure produced by solidification could also influence sensitization behavior and intergranular corrosion with heat treatment times longer than 6 h at 650 °C sensitizing 316L according to double-loop electrochemical potentiokinetic reactivation (DL-EPR) tests [1092]. Laleh *et al.* [1093] reported an unusual intergranular corrosion resistance of L-PBF processed 316L compared to commercial alloy. No Cr-rich precipitates were detected for L-PBF processed 316L after a long-term sensitization heat-treatment (700 °C for 60 h followed by water quenched). Microscopy observations after DL-EPR tests from commercial 316L alloy indicated a continuous network of ditched grain boundaries with grooves extending deeply into the bulk, while, it was less pronounced in the AM specimen. A possible hypothesis for this behavior could be a high frequency of twin boundaries and low-angle grain boundaries along with fine grains in L-PBF processed 316L (Fig. 105). Zhou *et al.* [1094] suggested that subcritical annealing of L-PBF processed 316L at 950 °C for 4 h dissolved melt pool boundary and eliminated high-density dislocation, while, the advantages of inclusion anticrystallization and weak grain boundary segregation during the L-PBF process were retained. This resulted in corrosion resistance enhancement. Laleh *et al.* [1095] also noted when the PBF-processed 316L specimen was heat-treated above 1000 °C, the fine MnS inclusion, which had pitting corrosion resistance improvement, could transform manganese chromite.

In addition to the effects of printed microstructure, the prior processing of powder can also influence corrosion behavior. Pitting of 17–4 was found to be reduced in L-PBF parts compared to wrought material [1089], but the nitrogen level of the powder was much higher than that of the wrought material, and nitrogen is known to improve the pitting resistance of stainless steels. As a result, the direct influence of L-PBF processing was not clear. The gas atomization process (nitrogen vs. argon) could therefore also influence the final material composition and corrosion behavior of printed stainless steels.

L-PBF stainless steels are typically reported to exhibit lower corrosion resistance than wrought alloys of the same grade. However, this finding of lower corrosion resistance is not universal. Nonetheless, the susceptibility of PBF-processed stainless steel alloys to crack initiation and stress corrosion cracking needs more considerations. The corrosion performance of L-PBF-processed iron alloys has been attributed to the following:

1. Increased porosity in L-PBF parts
2. Smaller MnS inclusions (beneficial) and microsegregation (detrimental) due to rapid solidification

Aluminum alloys. Corrosion studies of AM aluminum alloys have focused almost exclusively on AlSi10Mg, the most common Al alloy used in AM applications. The behavior of most interest is pitting corrosion in chloride solutions, typically aqueous NaCl or Harrison's solution ($(NH_4)_2SO_4$ + NaCl). There are generally two classes of studies. The first class focuses on comparisons of L-PBF -processed material to wrought or cast alloys with similar compositions The second class studies AM-related process variables, most commonly surface condition (e.g. orientation, roughness) and post-build heat treatment. A major corrosion concern for aluminum alloys is pitting corrosion in solutions containing chloride ions, consequently, all studies found employed environments of aqueous NaCl or Harrison's solution ($(NH_4)_2SO_4$ + NaCl).

L-PBF-processed material has generally been found to exhibit equivalent or better corrosion resistance compared to conventionally-processed material [1096-1100]. This is attributed to a fine microstructure length scale and the absence of intermetallic particles. The pitting resistance of aluminum alloys and the central role of cathodically active intermetallic precipitates have been well-studied and were reviewed recently [1101,1102]. In general, iron and copper impurities are the main causes of these intermetallics. There are three main influences of intermetallics [1101-1104]: (1) The intermetallics are much more efficient substrates for reduction of dissolved oxygen than the

(A)

The used DMLS process parameters for fabrication of the core of each sample.

Sample	Hatch Distance (mm)	Scan Speed (mm/s)	Laser Power (W)	Stripe Width (mm)	Stripe overlap (mm)	Beam Offset (mm)
(a): Regular	0.19	1300	370	7	0.02	0.02
(b): Surface 1	0.19	1300	370	6	0	0.15
(c): Surface 2	0.19	1300	370	6	0	0.15

The used DMLS process parameters for fabrication of the upskin layers of each sample.

Sample	Hatch Distance (mm)	Scan Speed (mm/s)	Laser Power (W)	Overlap with Core (mm)	Min. Length (mm)	Beam Offset (mm)
(a): Regular	0.21	1000	360	0.02	0.2	0.2
(b): Surface 1	0.13	775	370	0	0.2	0.15
(c): Surface 2	0.12	775	370	0	0.2	0.1

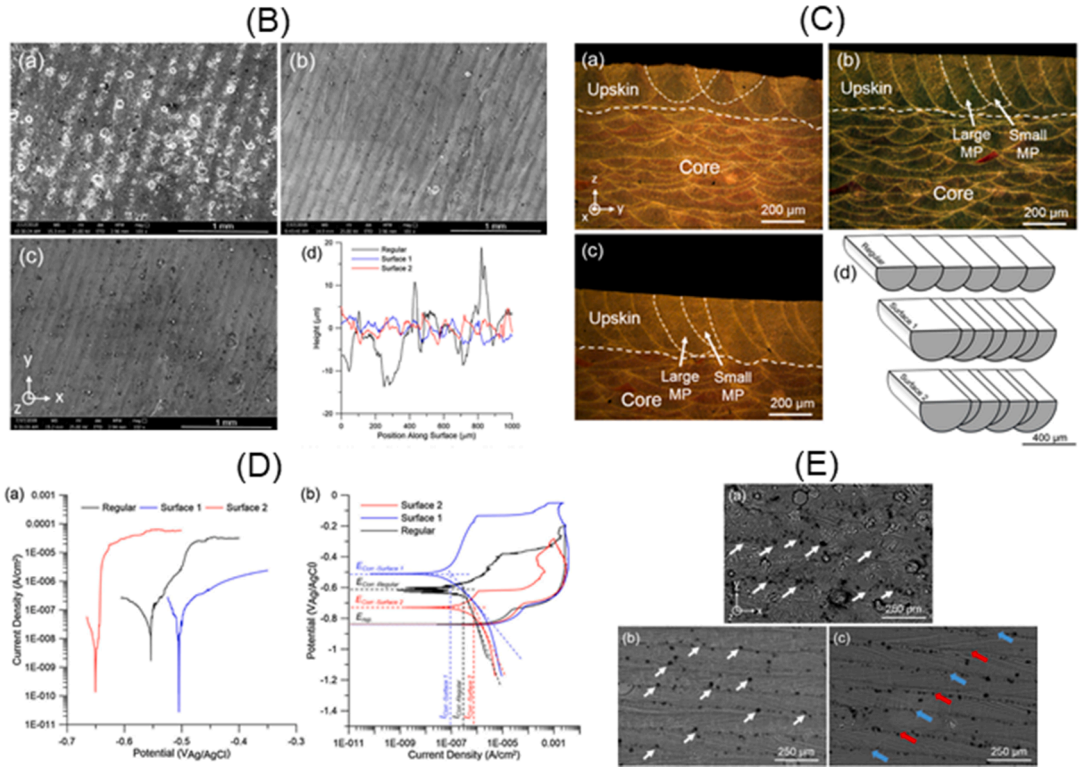

Fig. 107. (A) Process parameters used to fabricate AlSi10Mg parts with different surface roughness. (B) SEM micrographs from the surface of the AM parts showing roughness as a function of the processing condition. (C) Cross-sectional optical micrographs showing melt pool size and morphology. (D) Anodic potentiodynamic polarization curves and cyclic polarization curves taken from the samples' surface immersed in 3.5 wt% NaCl solution. (E) SEM images taken from the top surface (upskin layers) after anodic polarization test illustrating pitting and selective corrosion along with the melt pool boundaries on samples in order of Surface 1 < Regular < Surface 2 samples. Reprinted with permission from Ref. [1111].

oxide-covered aluminum metal surface. The resulting higher cathodic current drives faster pit growth. (2) Because of the high rate of oxygen reduction at the intermetallics, the pH locally increases (the solution becomes more alkaline). This leads to the faster dissolution of aluminum, since aluminum has poor corrosion resistance above a pH of approximately 10, and a trench or incipient pit forms around the intermetallic. (3) The composition of the aluminum matrix next to the intermetallic is different from the average, changing the anodic dissolution behavior. One limitation of the comparative studies mentioned above [1096-1098] is composition control. In all of these studies, the levels of impurities such as Fe, Cu, and Mg were higher in the conventionally processed alloys. The effects of alloy composition, L-PBF processing, and L-PBF post-processing on intermetallic distribution and corrosion resistance require further study.

In addition to the effect on intermetallics, the alloy microstructure is significantly refined after L-PBF processing and this has also been suggested to improve corrosion resistance. The microstructure of L-PBF-processed AlSi10Mg consists of α-aluminum cells with an intercellular network of silicon [605,1105]. The cellular network spacing at the boundaries of adjacent melt pool tracks is generally coarser than in the melt pools. Preferential corrosion at the boundary between melt pool tracks has been frequently observed [1096,1098], as shown in Fig. 106.

As shown in Fig. 106, the aluminum matrix is preferentially attacked where the silicon network is coarser. Revilla *et al.* used scanning Kelvin probe microscopy (SKPM) and found a higher potential difference between Al and Si in the regions where the network was coarser. The galvanic coupling led to enhanced corrosion. A study by Cabrini *et al.* [1106] suggested similar effects and also noted observations of localized corrosion at pores on the surface. Another study from Revilla *et al.* [1107] studied material with 7, 10, and 12 wt% Si. In this work, different energy densities were used for each alloy. The corrosion behavior was similar to that discussed above, with more severe attack at melt pool boundaries. The lower Si samples were found to be more heavily attacked than the 12 wt% Si sample.

The influence of surface condition has been found to affect the corrosion resistance of AlSi10Mg. Most studies have concluded rougher, as-built surfaces are detrimental to corrosion resistance [1108-1110]. The rougher, as-built surfaces have been argued to result in more irregular passive layers [1108] and to result in larger cathodic areas [1110]. Contradictory results were reported by Fathi *et al.* [1098], who

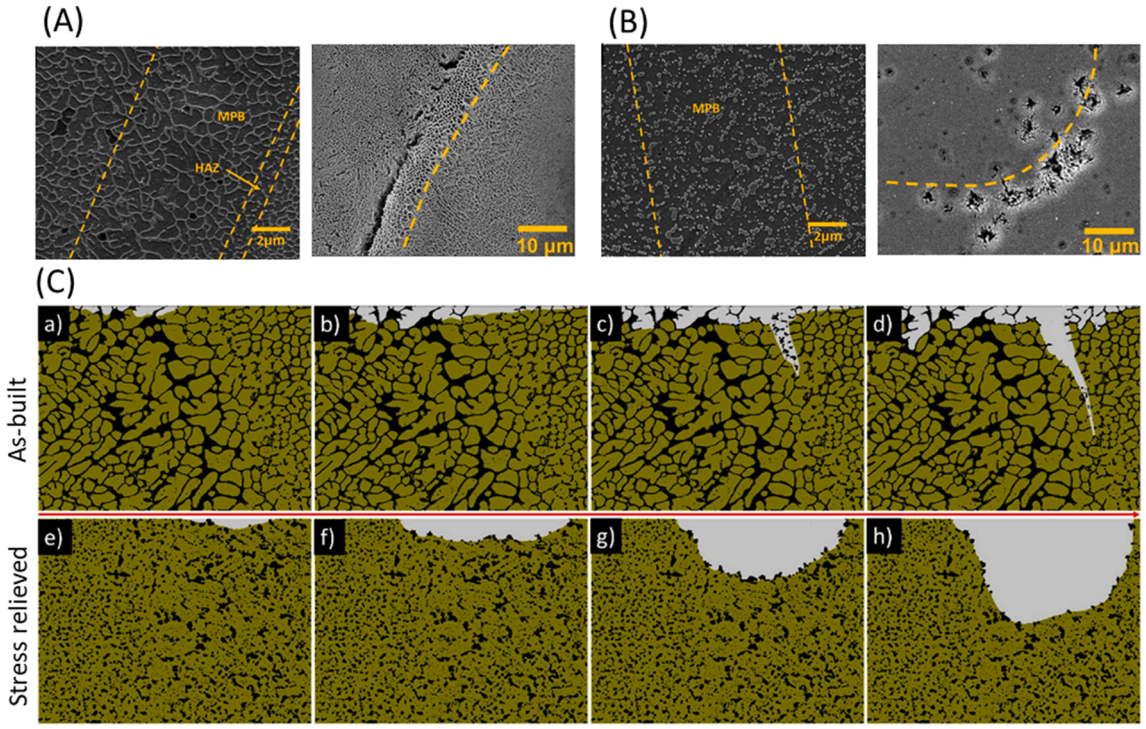

Fig. 108. SEM micrographs from (A-left) as-built L-PBF AlSi10Mg alloy and (B-left) stress-relieved specimen at 300 °C for 2 h. SEM micrographs from samples immersed in a 0.1 M NaCl solution; (A-right) as-built L-PBF AlSi10Mg alloy and (B-right) stress relieved specimen at 300 °C for 2 h. (C) Proposed corrosion mechanism when (a-d) there is a connected silicon network and (e-h) silicon forms separate precipitates (black color represents Si phase). Reprinted with permission from Ref. [1114].

suggested the partially melted and oxidized powder particles led to a more protective passive layer. Fathi *et al.* [1111] studied the effect of surface finish and morphology of the exposed surface to the saline solution (Fig. 107). It was shown that regular processing condition resulted in the surface finish of $Ra = 5.1 \pm 1.5$ μm while reducing hatch spacing reduced roughness to $Ra = 1.4 \pm 0.5$ μm. It was proposed that the faster cooling and solidification rate during AM process of part with smaller hatch spacing of 130 μm (sample labeled as Surafe 1) restricted coarsening of Al dendrites and Si precipitates in the melt pool, thus, a potential difference between silicon and aluminum was reduced leading resulting in a less susceptibility of L-PBF processed AlSi10Mg part to pitting and selective corrosion attack. A study by Cabrini *et al.* [1106] noted a slight effect of surface orientation relative to the build plane, but a later study from the same group concluded differences were not statistically significant [1112].

The effects of post-processing heat treatment have also been examined. A recent study by Cabrini *et al.* found decreasing pitting resistance as post-processing heat treatment temperature increased from 200 °C to 400 °C [1112]. A previous study from the same group found a solution annealing heat treatment at 550 °C led to much lower corrosion resistance compared to the as-built or stress relieved at 300 °C conditions [1108]. Another recent study of post-build heat treatments found that 200–300 °C was an optimum temperature for improved corrosion resistance compared to an as-built case and a 350 °C heat treatment [1113]. Improved corrosion resistance was related to the uniform distribution of the fine Si particles in the microstructure of L-PBF processed AlSi10Mg, which prevented penetrating selective attack along the melt pool boundaries, even though localized corrosion was reported. Contradictory results were presented by Rubben *et al.* [1114] in which stress-relieving treatment at 300 °C for 2 h had a detrimental impact on corrosion resistance. Corrosion attach was dependent on the morphology of the silicon in AM processed AlSi10Mg (Fig. 108). When networks of Si were present in the as-built part, superficial corrosion attack with the formation of microcracks in the heat-affected zone near melt pool borders was observed. However, Si particles in the stress-relieved specimen were broken up into separate coarse precipitates resulted in a more deeply penetrating corrosion attack. It was also reported that the localized Mg-Si precipitates formed in the stress-relieved specimen leading to the reduction of corrosion resistance in aluminum alloys [1115,1116]. Electrochemical testing revealed a larger potential difference between Al and Si phases at the melt pool boundary than within the melt pool, meaning that the larger potential difference gave a larger driving force for galvanic corrosion.

Most of the corrosion-related studies of L-PBF-processed AlSi10Mg have focused on electrochemical behavior and pitting corrosion. Studies from Leon *et al.* [1097,1110], found corrosion fatigue resistance of L-PBF processed specimens was greater than cast counterparts. Zakay *et al.* [1117] evaluated the effect of post-build heat treatment by slow strain rate stress corrosion cracking tests and corrosion fatigue tests. Both tests supported the selection of 200–300 °C as an optimum post-processing temperature.

Titanium alloys. Studies of L-PBF-processed titanium almost exclusively focus on Ti-6Al-4V. Because AM Ti-6Al-4V has many promising applications in biomaterials, common environments are simulated body fluids (SBF), e.g. Hank's solution, Ringer's solution, and phosphate buffered saline (PBS). In the studies, most emphasis is placed on corrosion potential (E_{corr}), corrosion current density (i_{corr}) and the potential at which the passive layer is no longer stable (the breakdown potential, E_b). Lower values of E_{corr} and i_{corr}, along with higher values of E_b imply better corrosion resistance. The desirable state for Ti-6Al-4V in service, especially for biomaterial applications, is the formation of a stable and protective passive layer. Pitting corrosion is generally not observed in Ti-alloys unless they are subjected to very anodic polarization. Generally, the corrosion resistance is dependent on the combined effects of microstructures including type, size, and morphology of constituent phases in titanium alloys.

The microstructure of L-PBF Ti-6Al-4V is mostly α' martensite with small amounts of β due to the rapid solidification. Dai *et al.* [1118]

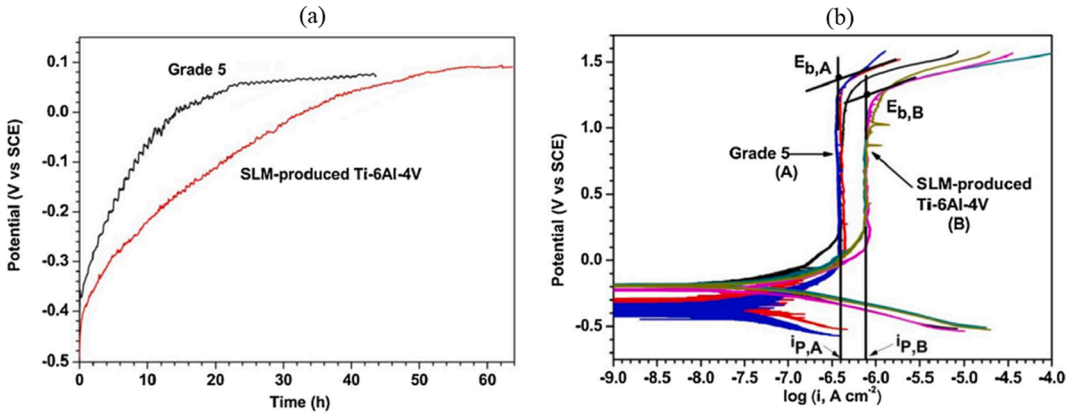

Fig. 109. Comparison of (a) open circuit potential variation and (b) potentiodynamic polarization curves in 3.5 wt% NaCl for L-PBF-processed Ti-6Al-4V and wrought material. The L-PBF-processed material exhibited lower corrosion resistance. Reprinted with permission from Ref. [1118].

observed that corrosion resistance of L-PBF material was worse compared to wrought Ti-6Al-4V. This conclusion was based on results shown in Fig. 109(a, b), a continuously increasing open circuit potential, higher passive current density, and lower breakdown potential. They attributed this to the more rapid dissolution of the metastable martensite phase and the limited presence of β, which may have a more stable TiO_2 passive layer. A separate study in the same environment [1119] found that heat treatments at 500 °C, 850 °C, and 1000 °C coarsened microstructure and led to decreased corrosion resistance. Sharma *et al.* [1120] evaluated the corrosion behavior of L-PBF and cast Ti-6Al-4V alloy. Regardless of the test solution, cast alloy showed higher corrosion resistance compared to the AM processed Ti-6Al-4V part due to the higher β phase fraction in the microstructure. The passivation current increased in the order of NaOH < SBF < NaCl < H_2SO_4, while the pitting potential decreased in those solutions. Hemmasian Ettefagh *et al.* [1121] showed that post heat treatment at 800 °C could enhance the corrosion resistance of L-PBF fabricated Ti-6Al-4V due to the formation of stable β phase in the microstructure. As reported, the as-built Ti-6Al-4V had a corrosion potential of −0.494 VSCE, corrosion current density of 1.82 μA/cm^2, and pitting potential of 1.131 VSCE; with values of −0.337 VSCE, 0.151 μA/cm^2, and 1.318 VSCE for the heat-treated part, suggesting that corrosion resistance enhancement due to post-build heat treatment. Pazhanivel *et al.* [1122] observed corrosion resistance enhancement of L-PBF processed Ti-6Al-4V in NaCl and phosphate buffer electrolytes after heat treatment at 850 °C due to the formation of ultra-fine bimodal α + β microstructure.

Somewhat contradictory comparisons were observed by Yang *et al.* [1123], they observed that corrosion resistance could be improved by heat-treating the L-PBF-processed samples at 750 °C. Such samples possessed fine lamellar $\alpha+\beta$ microstructures and their corrosion resistances were better than the wrought material and the L-PBF samples with coarse lamellar microstructures heat-treated at 1020 °C.

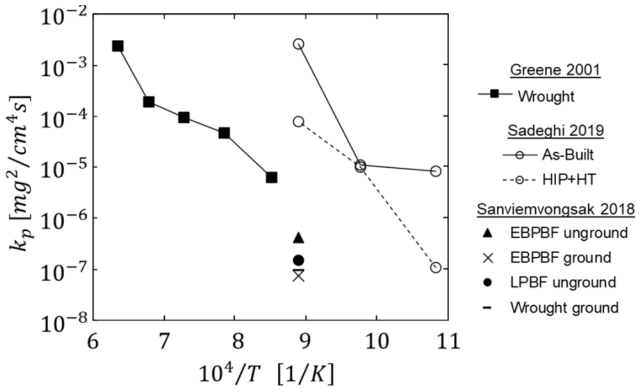

Fig. 110. Parabolic rate constants reported from the oxidation of alloy 718. Green 2001 is from Ref. [1137]. Sadeghi 2019 is from Ref. [1141]. Sanviemvongsak 2018 is from Ref. [1140].

Dai *et al.* [1124] also studied orientation effects, with lower corrosion resistance on surfaces normal to the build direction. They attributed this to a β volume fraction effect, however the β volume fractions were very low and the amounts were only quantified from x-ray diffraction, with no discussion of uncertainties. Relatively few studies have examined effects of the L-PBF process variables. Chiu *et al.* suggested energy density modified the defect structure of the passive film, changing how it reacts with chlorides in the environment [190]. Mahamood *et al.* [1125] observed increasing laser power led to better corrosion resistance, however, this study was conducted for a laser metal deposition (LMD) process. However, E-PBF-processed Ti-6Al-4V showed slightly better corrosion resistance compared to wrought material [1126]. This was attributed to more β phase and a fine-grained $\alpha+\beta$ microstructure. E-PBF requires much higher preheating, consequently melt pool microstructures are very different compared to L-PBF. The increased amount of β was suggested to improve the stability of the passive film.

More attention has been devoted to the effects of surfaces and heat treatment, however, there are a variety of findings. High-temperature heat treatment (850, 950, 1050 °C) was found to result in localized attack at the β phase in a PBS solution [1127]. Martensitic areas were not attached. These results were contradictory to those of Dai [1118]. Another study of heat treatment effects in different environments (1 M H_2SO_4, 1 M HCl, 3.5% NaCl) found the as-built condition exhibited the most severe corrosion compared to heat-treated samples in 1 M H_2SO_4 but the effect of heat treatment was much smaller in the other environments.

Surface modification methods that have been studied include shot peening and anodization. Shot peening could change surface roughness, but all samples exhibited satisfactory corrosion resistance [1128]. Anodized L-PBF Ti-6Al-4V scaffold structures were studied by de Damborena *et al.* [1129]. The anodizing process led to a uniform, nanoporous surface. The L-PBF samples were more uniformly anodized, which was attributed to their fine length-scale microstructures. Anodization led to improved corrosion resistance.

There have been just a few mentions of high-temperature corrosion phenomena related to Ti-alloys. L-PBF-processed Ti-6Al-4V oxidized between 500 and 600 °C was found to exhibit much greater mass gains compared to a rolled + annealed reference [1130]. The extra mass gain was attributed to the oxidation of powders stuck to the surface. It is well-known that titanium can dissolve significant levels of oxygen at high temperatures and this behavior did not seem to be affected by L-PBF processing.

The high-temperature oxidation of a near-α alloy produced by L-PBF

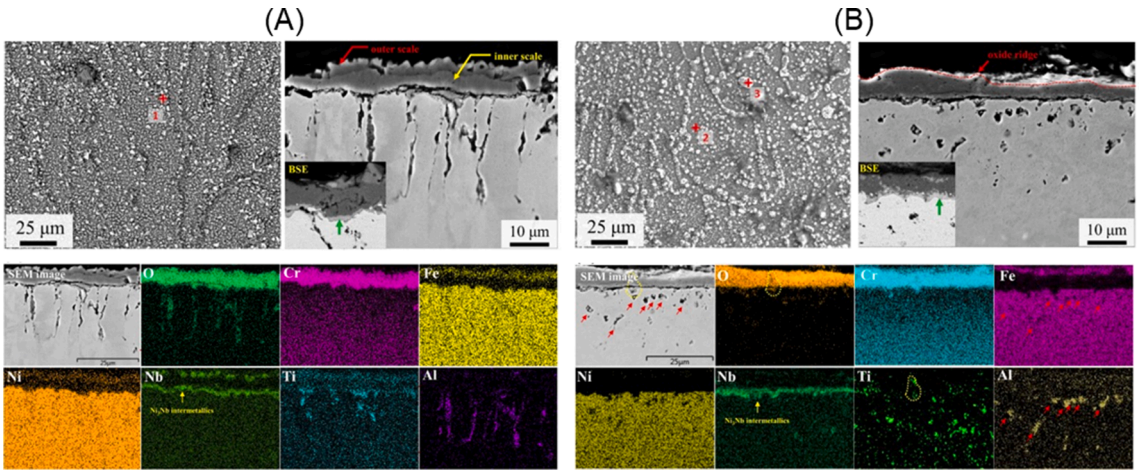

Fig. 111. SEM micrographs taken from the top surface and cross-section of L-PBF alloy 718 followed by post-heat treatment of (A) solution treated + aged and (B) HIPed + aged. Elemental map analysis indicated the distribution of alloying elements after oxidation at 1000 °C in an artificial air atmosphere up to 24 h. Reprinted with permission from Ref. [1142].

has also been reported. For this material, the as-built samples exhibited much lower mass gains compared to as-cast counterparts [1131]. This was attributed to differences in microstructure length scale, but only a relatively brief discussion was made. Cui *et al.* [1132] suggested additional boron to Ti-based alloys could enhance the oxidation resistance of L-PBF processed Ti alloy due to the formation of refined TiB, resulted in reduced evaporation of B_2O_3, thus multiple compact oxidation layers of TiO_2-Al_2O_3 formed on the substrate.

Nickel alloys. There have been few published studies on aqueous corrosion of nickel alloy produced via AM processes. Those found focus on environmental cracking of alloy 625 in aqueous chloride environments [1133,1134]. L-PBF-processed alloy 625 was found to be resistant to environmental fracture under constant displacement tests and it was found to exhibit corrosion fatigue resistance slightly below that of the wrought counterpart material. L-PBF-processed alloy 718 proved that build orientation affected surface defect formation such that vertical printing had the highest corrosion resistance behavior in NaCl solution [1135]. In other words, surface defects (porosity and roughness) became preferential sites for localized corrosion. Recently, Karimi *et al.* [1136] found that build location affects the microstructure and resultant corrosion behavior of E-PBF processed alloy 718. When cubic samples were printed at the center of the build plate, higher Nb-rich phase (~30%), coarser primary dendrite arm spacing (~20–30%), and higher polarization resistance (~40 kΩ.cm^2 compared to ~2 kΩ.cm^2 for exterior printed parts) were attained.

Most of the corrosion studies of nickel alloys produced by powder bed fusion processes have focused on high-temperature phenomena, specifically in alloy 718. At high temperatures, alloy 718 forms a Cr_2O_3 oxide scale that protects it from the surrounding environment [1137,1138]. Jia *et al.* [454] made samples at four P-V combinations and oxidized them in the air at 850 °C. The sample printed with the lowest energy density exhibited the highest mass gains, suggesting the oxide forming on the surface was not as protective. This was further explored in a follow on study by the same group [1139], in which they observed evidence of spalling and more severe internal oxidation in the sample produced with the lowest energy density. Samples processed by both L-PBF and E-PBF oxidized were also oxidized at 850 °C to compare the two processes [1140]. The measured oxidation rates from E-PBF samples were much higher than L-PBF or wrought materials. This was attributed to the sintering of particles on the sample surface and the increased surface roughness. After surface grinding, measured rates from E-PBF samples were much lower and consistent with rates of L-PBF and wrought alloy 718. Oxidation rates in this study were much lower than those found by Jia *et al.* [454], but no conclusive reason for this was identified.

Effects of processing after E-PBF were studied by Sadeghi *et al.* [1141]. That work compared oxidation behavior at 650–850 °C for four conditions:

1. As-built,
2. HT = Solutionizing at 980 °C for 1 h, then water cooling, aging at 720 °C for 8 hr with rapid cooling to 620 °C then holding 8 h and finally air cooling to room temperature
3. HIP = 1185 °C/150 MPa, 4 hr
4. HIP + HT

The lowest oxidation rates for the HIP + HT condition, which formed a compact, adherent, Cr_2O_3 oxide at all temperatures. In the as-built case, the oxide was discontinuous at 850 °C and oxidation rates were much higher than other conditions. A comparison of parabolic rate constants evaluated from these studies (with reference values for the oxidation of wrought alloy 718 from [1137]) is shown in Fig. 110. Recently, Kang *et al.* [1142] showed that HIPed + aged condition had better high-temperature resistance compared to that of solution treated + aged. The microstructure of the as-built specimen was evolved after HIP treatment and melt pool boundary and columnar structures were eliminated. Additionally, δ phase was found at the grain boundary of the solution treated + aged specimen, while, a Ti-rich MC phase was present at the grain boundary of the HIPed + aged specimen. As shown in Fig. 110, a single Cr_2O_3 passive layer was formed on the HIPed + aged sample with minimal internal oxidation, while, the solution treated + aged specimen revealed two oxide layers including an external oxide layer composed of (Ni,Fe,Nb)Cr_2O_4 oxides on top of the Cr_2O_3 passive layer. The authors hypothesized that the presence of TiC at the grain boundary and within grains of the HIPed + aged sample acted as oxide nucleation sites in the early oxidation stage as well as suppression the inner diffusion of oxygen ions (see Fig. 111).

Oxidation of E-PBF alloy 718 has also been studied in wet air environments [1143]. The behavior of alloy 718 differs significantly in wet environments because H_2O in the gas phase leads to the formation of volatile oxyhydroxide species that are rapidly removed into the gas phase. Consequently, the alloy experiences mass loss due to vaporization and mass gain due to oxidation [1144]. Measured overall mass changes are small, but the alloy is still degrading during exposure. E-PBF samples were tested as-built, after HIP (1200 °C, 2 hr) and HIP + HT (similar solutionizing and aging heat treatment described above). Processing differences had little effect on oxidation behavior at 650 °C and 700 °C, with a slight mass loss observed consistent with simultaneous oxidation

and vaporization. At 750 °C the E-PBF samples differed from wrought with thicker oxides containing more Fe-rich oxide nodules observed.

There are still a limited number of studies of the high-temperature oxidation behavior of nickel-base alloys processed by L-PBF or E-PBF. Connections between build parameters, post-processing, underlying microstructure, and oxidation behavior (both external and internal) remain to be developed.

9. Current challenges, gaps, and future trends

Even though significant progress has been achieved in understanding and controlling defects in the PBF of metals, we are still far away from our ultimate goal of printing consistent, reliable, and high-performance metal components by rational design. We identify the following areas as examples of future research directions to close this gap:

Formation and prediction of defects in part scale. Detrimental defects are observed in parts fabricated using parameters optimized for maximizing part density. This poses great challenge for part/process qualification and certification. A deeper understanding of the defect formation on the part scale is critical. The variations of laser beam characteristics (power, beam profile, beam size, focal plane, etc.), thermal condition (temperature distribution, heat accumulation and dissipation on the part), and environmental gas flow (impurity level, flow speed, flow pattern, etc.) over the entire build area might play important roles on defect formation. Significant research efforts are needed to understand the effects of these variations and to incorporate them into predictive models for predicting defects in part scale.

Formation and prediction of atomic/nano-scale defects. Atomic and nanoscale defects (e.g., dislocation, chemical segregation, nanoscale contamination) have been observed in additively manufactured metals. The details as to how these defects form and evolve during rapid cyclic heating and cooling remain unclear. A combination of *in situ* experiments and multi-scale simulation is necessary to understand the formation mechanisms and develop predictive capabilities.

Spatial distribution of all types of defects in part scale. Current research results mainly show the defects in certain areas of a part/build or the distribution of a certain type of defect (e.g., pores) in a part. Significant variations of defect type, defect size and defect amount are expected in a part. Revealing the spatial distribution of all types of defects in part scale is critical for developing more accurate models to predict the mechanical properties of the additively manufactured parts.

Defect mitigation and elimination. Currently, the fatigue life of additively manufactured metals is only about half of their wrought counterparts and exhibits significant variations, which limits the application of additively manufactured metals as load-bearing critical components. Significant efforts are needed to develop novel approaches for mitigating and eliminating detrimental defects in additively manufactured parts. It is expected that the improved understanding of the defect formation mechanisms and the development of novel *in situ* monitoring tools [1145] will accelerate the invention of new approaches to address detrimental defects in metal AM.

Controlled generation of defects. Defects are not always detrimental. Additive manufacturing technology can introduce specific defects in a specific location, which enables the creation of patterned defects in a part. Novel properties may arise from a certain defect pattern in a part. Design, optimization, and controlled generation of defects in additively manufactured metals may lead to unexpected phenomena and novel applications. Little work has been done in this direction. Synergistic collaboration among manufacturing, materials, mechanics, and design communities has the potential to make breakthroughs in this area.

Multi-scale, multi-modal in situ characterization of defect evolution. Individual *in situ* characterization technology (e.g., x-ray imaging/diffraction, visible-light imaging, thermal imaging) has revealed important insights about defect formation and evolution in the past few years. The integration of different *in situ* technologies is critical for getting a wholistic view of defect formation and evolution in different scales, in different areas and under different conditions. Developing multi-scale and multi-modal *in situ* monitoring tools is an ongoing effort and will continue to grow in the future. The multi-scale and multi-modal *in situ* characterization research will make important contributions to reveal new defect formation mechanisms, identify key signals for defect monitoring in commercial machines and establish location-specific processing-microstructure relationships.

Simulation, prediction, and mitigation of spatters. Spatter is a major cause of quality uncertainty in the PBF process. Significant progress has been made in revealing the mechanisms of spatter formation in recent years by advanced *in situ* characterization tools. However, it is still a challenge to predict its formation, size, and landing sites on the powder bed and to quantify its impact on the properties of the part. Great efforts are needed to develop simulation tools that can quantitatively predict spatters and to develop effective approaches to mitigate or even eliminate the most detrimental spatters in the PBF process. Addressing spatter-induced defects is a critical step towards the development of reliable PBF technology.

Probabilistic simulation of defects. Many uncertainties exist in defect formation and evolution in PBF. The deterministic simulations, widely used currently, cannot capture these uncertainties well. Probabilistic simulation, which considers the probabilistic distribution of input parameters and random events, has the potential to address the uncertainty problem in the PBF process. Substantial effort is needed to develop probabilistic models to predict defects in the PBF process. Probabilistic models will provide important information and guidance for processing parameter design and property prediction.

Property prediction. While many efforts have been devoted to developing models to predict the properties of additively manufactured metals, precise prediction of the properties of additively manufactured metals is still a big challenge. With gaining a deeper understanding of defect characteristics, their spatial distribution, and their effects on properties of additively manufactured metals, significant research efforts are necessary to integrate these discoveries into property prediction models to improve the prediction accuracy. The ability to predict the properties of additively manufactured metals is a prerequisite for designing mission-critical components.

Mechanical property assessment. Most standards suggest using specimens with some minimum gage diameter and length to have adequate material at the gauge, thus, enough volume of material (e.g., enough number of grains) is being tested. There are some other considerations for example avoiding buckling in fully reversed fatigue testing as well. However, in metal additive manufacturing, we are often interested in localized properties because of variations in thermal history within the part. Therefore, a lot of work can be found in the literature that have used subsized specimens to generate mechanical properties. The followings are the potential challenges: (1) If the specimens are fabricated separately, they do not represent the properties of the point of interest in the part because of differences in thermal history affected by geometrical and design factors. Therefore, the best practice is to excise specimens from those points of interest. In this case, one part for each specimen is needed which increases the cost/time significantly. (2) The conventional load frames and grips are not suitable for testing these specimens, so specialized load frames and grips will be needed for testing. (3) Due to their small gauge sections, operator cannot connect extensometers and measure strain. Therefore, non-contact extensometers (e.g., video extensometers) will be required to measure strain.

Machine learning. The correlation among processing parameters, defect characteristics, and properties in PBF AM processes is very complex. A huge amount of data has been and is currently being collected. Advanced machine learning tools have great potential to derive the hidden rules from the big data. The application of machine learning in additive manufacturing is an interesting future research direction. Machine learning, especially convolutional neural network, provides a remarkable opportunity for the AM domain to develop algorithms and codes to process *in situ* data collected from real-time

monitoring [301] and obtain information that can be used for process analysis and optimization. However, there are a few challenges, including small datasets, lack of experience in labeling data, lack of knowledge in selecting good features, and the problem of overfitting and underfitting; these may be constraints from using machine learning in the AM industry [1135]. Also, developing algorithms to describe process–structure–property–performance relationship for AM remains a challenge [1146].

Metal additive manufacturing is a very active research area. The topics listed above are just a few examples of future research directions. We expect that many novel research directions will emerge in the future. We anticipate that the collective efforts of the researchers in the community will overcome the challenges that PBF AM technology faces.

Declaration of Competing Interest

The authors declare that they have no known competing financial interests or personal relationships that could have appeared to influence the work reported in this paper.

Acknowledgement

AM acknowledges startup funding from Mechanical, Materials and Aerospace Engineering Department at Illinois Institute of Technology at Chicago, Illinois. Further, AM thanks support from the postdoctoral research fellowship program of the Manufacturing Futures Initiative at Carnegie Mellon University (CMU), and in part by the Pennsylvania Infrastructure Technology Alliance, a partnership of Carnegie Mellon, Lehigh University and the Commonwealth of Pennsylvania's Department of Community and Economic Development (DCED). AM acknowledges the support from the National Science Foundation under grants DMR - 2050916. CZ and BS would like to acknowledge support from the National Natural Science Foundation of China (52175332), the Tsinghua-Imperial Research and Innovation Seed Fund, and the startup fund of Tsinghua University. CZ and BS thank D. Du, B. Chang, F. Lin, L. Ji, P. Mou, P. Wen, and X. Liu at Tsinghua University for the financial support and assistance during the coronavirus disease 2019 (COVID-19) crisis. ADR acknowledges partial support from the NextManufacturing Center at CMU, the National Science Foundation under grant DMR-1905910, the Department of Energy under grants DE-AR0001127 and A19-2112-S001, and the National Aeronautics & Space Administration under grant 80NSSC19M0123. NK acknowledges support from the Department of Defense Office of Economic Adjustment under award no. ST1605-19-03. NS and SS acknowledge the partial support from the National Institute of Standards and Technology (NIST) under Grant Number 70NANB19H170 and National Aeronautics and Space Administration under Grant Number 80MSFC18M0052. This material is partially based upon work supported by the U.S. Department of Energy, Office of Science, Office of Basic Energy Sciences, under Award Number DE-SC0019378. NS and SS also acknowledge graduate students Arun Poudel, Nabeel Ahmad, and Shahrior Ahmed for their assistance in data collection. LC acknowledges the support from the National Science Foundation under grants CMMI - 2011354 and CMMI – 2002840. S.S. acknowledges the help of Shahrior Ahmed for the collection of partial data on Ti-6Al-4V mechanical properties, which was a part of his term project at Louisiana State University.

Disclaimer

References

[1] J. Beuth, J. Fox, J. Gockel, C. Montgomery, R. Yang, H. Qiao, P. Reeseewatt, A. Anvari, S. Narra, N. Klingbeil, Process Mapping for Qualification Across Multiple Direct Metal Additive Manufacturing Processes, in: Solid Free. Fabr. Proc., 2013, pp. 655–665. https://doi.org/10.1007/s13398-014-0173-7.2.

[2] M. Seifi, A. Salem, J. Beuth, O. Harrysson, J.J. Lewandowski, Overview of Materials Qualification Needs for Metal Additive Manufacturing, JOM. 68 (2016) 747–764, https://doi.org/10.1007/s11837-015-1810-0.

[3] R.P. Liu, Z.J. Dong, Y.M. Pan, Solidification crack susceptibility of aluminum alloy weld metals, Trans. Nonferrous Met. Soc. China (English Ed. 16 (2006) 110–116, https://doi.org/10.1016/S1003-6326(06)60019-8.

[4] P. Chiang, R. Jiang, R. Cunningham, N. Parab, C. Zhao, K. Fezzaa, T. Sun, A. D. Rollett, In Situ Characterization of Hot Cracking Using Dynamic X-Ray Radiography, Springer International Publishing, 2019 https://doi.org/10.1007/978-3-030-06143-2.

[5] S.Z. Uddin, L.E. Murr, C.A. Terrazas, P. Morton, D.A. Roberson, R.B. Wicker, Processing and characterization of crack-free aluminum 6061 using high-temperature heating in laser powder bed fusion additive manufacturing, Addit. Manuf. 22 (2018) 405–415, https://doi.org/10.1016/j.addma.2018.05.047.

[6] Z. Snow, A. Nassar, E.W. Reutzel, Review of the Formation and Impact of Flaws in Powder Bed Fusion Additive Manufacturing, Addit. Manuf. (2020), 101457, https://doi.org/10.1016/j.addma.2020.101457.

[7] N. Sanaei, A. Fatemi, Defects in Additive Manufactured Metals and Their Effect on Fatigue Performance: A State-of-the-Art Review, Prog. Mater. Sci. (2020), 100724, https://doi.org/10.1016/j.pmatsci.2020.100724.

[8] M. Borish, B.K. Post, A. Roschli, P.C. Chesser, L.J. Love, K.T. Gaul, Defect Identification and Mitigation Via Visual Inspection in Large-Scale Additive Manufacturing, Jom. 71 (2019) 893–899, https://doi.org/10.1007/s11837-018-3220-6.

[9] H. Taheri, M.R.B.M. Shoaib, L. Koester, T. Bigelow, P.C. Collins, Powder-based additive manufacturing - a review of types of defects, generation mechanisms, detection, property evaluation and metrology, Int. J. Addit. Subtractive Mater. Manuf. 1 (2017) 172–209, https://doi.org/10.1504/ijasmm.2017.088204.

[10] Z.A. Young, Q. Guo, N.D. Parab, C. Zhao, M. Qu, L.I. Escano, K. Fezzaa, W. Everhart, T. Sun, L. Chen, Types of spatter and their features and formation mechanisms in laser powder bed fusion additive manufacturing process, Addit. Manuf. 36 (2020), 101438, https://doi.org/10.1016/j.addma.2020.101438.

[11] G. Repossini, V. Laguzza, M. Grasso, B.M. Colosimo, On the use of spatter signature for in-situ monitoring of Laser Powder Bed Fusion, Addit. Manuf. 16 (2017) 35–48.

[12] H.W. Mindt, O. Desmaison, M. Megahed, A. Peralta, J. Neumann, Modeling of Powder Bed Manufacturing Defects, J. Mater. Eng. Perform. 27 (2018) 32–43, https://doi.org/10.1007/s11665-017-2874-5.

[13] H.L. Wei, T. Mukherjee, W. Zhang, J.S. Zuback, G.L. Knapp, A. De, T. DebRoy, Mechanistic models for additive manufacturing of metallic components, Prog. Mater. Sci. (2020), 100703, https://doi.org/10.1016/j.pmatsci.2020.100703.

[14] C. Gobert, E.W. Reutzel, J. Petrich, A.R. Nassar, S. Phoha, Application of supervised machine learning for defect detection during metallic powder bed fusion additive manufacturing using high resolution imaging, Addit. Manuf. 21 (2018) 517–528, https://doi.org/10.1016/j.addma.2018.04.005.

[15] E.W. Reutzel, A.S. Sakpal, B. Yao, F. Imani, H. Yang, Multifractal Analysis of Image Profiles for the Characterization and Detection of Defects in Additive Manufacturing, J. Manuf. Sci. Eng. 140 (2017), 031014, https://doi.org/10.1115/1.4037891.

[16] Z. Snow, B. Diehl, E.W. Reutzel, A. Nassar, Toward in-situ flaw detection in laser powder bed fusion additive manufacturing through layerwise imagery and machine learning, J. Manuf. Syst. 59 (2021) 12–26, https://doi.org/10.1016/j.jmsy.2021.01.008.

[17] N. Tepylo, X. Huang, P.C. Patnaik, Laser-Based Additive Manufacturing Technologies for Aerospace Applications, Adv. Eng. Mater. 21 (2019) 1–35, https://doi.org/10.1002/adem.201900617.

[18] ASTM International, ISO/ASTM52900-15 Standard Terminology for Additive Manufacturing - General Principles - Terminology, 2015.

[19] J.V. Gordon, S.P. Narra, R.W. Cunningham, H. Liu, H. Chen, R.M. Suter, J. L. Beuth, A.D. Rollett, Defect structure process maps for laser powder bed fusion additive manufacturing, Addit. Manuf. 36 (2020), 101552, https://doi.org/10.1016/j.addma.2020.101552.

[20] C. Yan, L. Hao, A. Hussein, D. Raymont, Evaluations of cellular lattice structures manufactured using selective laser melting, Int. J. Mach. Tools Manuf. 62 (2012) 32–38, https://doi.org/10.1016/j.ijmachtools.2012.06.002.

[21] New manufacturing milestone: 30,000 additive fuel nozzles, n.d.

[22] GM Uses Advanced Software, 3D Printing to Make Kinda Creepy-Looking Lightweight Parts, n.d.

[23] N.T. Aboulkhair, N.M. Everitt, I. Ashcroft, C. Tuck, Reducing porosity in AlSi10Mg parts processed by selective laser melting, Addit. Manuf. 1 (2014) 77–86.
[24] C. Zhao, N.D. Parab, X. Li, K. Fezzaa, W. Tan, A.D. Rollett, T. Sun, Critical instability at moving keyhole tip generates porosity in laser melting, Science (80-.) 1086 (2020) 1080–1086.
[25] R. Cunningham, C. Zhao, N. Parab, C. Kantzos, J. Pauza, K. Fezzaa, T. Sun, A. D. Rollett, Keyhole threshold and morphology in laser melting revealed by ultrahigh-speed x-ray imaging, Science (80-.) 363 (2019) 849–852, https://doi.org/10.1126/science.aav4687.
[26] C. Zhao, K. Fezzaa, R.W. Cunningham, H. Wen, F. De Carlo, L. Chen, A.D. Rollett, T. Sun, Real-time monitoring of laser powder bed fusion process using high-speed X-ray imaging and diffraction, Sci. Rep. 7 (2017) 1–11, https://doi.org/10.1038/s41598-017-03761-2.
[27] I. Yadroitsev, L. Thivillon, P. Bertrand, I. Smurov, Strategy of manufacturing components with designed internal structure by selective laser melting of metallic powder, Appl. Surf. Sci. 254 (2007) 980–983, https://doi.org/10.1016/j.apsusc.2007.08.046.
[28] R. Cunningham, S.P. Narra, C. Montgomery, J. Beuth, A.D. Rollett, Synchrotron-Based X-ray Microtomography Characterization of the Effect of Processing Variables on Porosity Formation in Laser Power-Bed Additive Manufacturing of Ti-6Al-4V, JOM. 69 (2017) 479–484, https://doi.org/10.1007/s11837-016-2234-1.
[29] X. Meng, G. Qin, Z. Zou, Characterization of molten pool behavior and humping formation tendency in high-speed gas tungsten arc welding, Int. J. Heat Mass Transf. 117 (2018) 508–516, https://doi.org/10.1016/J.IJHEATMASSTRANSFER.2017.09.124.
[30] M. Tang, P.C. Pistorius, S. Narra, J.L. Beuth, Rapid Solidification: Selective Laser Melting of AlSi10Mg, Jom. 68 (2016) 960–966, https://doi.org/10.1007/s11837-015-1763-3.
[31] U. Gratzke, P.D. Kapadia, J. Dowden, J. Kroos, G. Simon, Theoretical approach to the humping phenomenon in welding processes, J. Phys. D. Appl. Phys. 25 (1992) 1640–1647, https://doi.org/10.1088/0022-3727/25/11/012.
[32] W.J. Sames, F.A. List, S. Pannala, R.R. Dehoff, S.S. Babu, The metallurgy and processing science of metal additive manufacturing, Int. Mater. Rev. 61 (2016) 315–360, https://doi.org/10.1080/09506608.2015.1116649.
[33] L.N. Carter, C. Martin, P.J. Withers, M.M. Attallah, The influence of the laser scan strategy on grain structure and cracking behaviour in SLM powder-bed fabricated nickel superalloy, J. Alloys Compd. 615 (2014) 338–347.
[34] R. Rashid, S.H. Masood, D. Ruan, S. Palanisamy, R.A. Rahman Rashid, M. Brandt, Effect of scan strategy on density and metallurgical properties of 17–4PH parts printed by Selective Laser Melting (SLM), J. Mater. Process. Technol. 249 (2017) 502–511, https://doi.org/10.1016/J.JMATPROTEC.2017.06.023.
[35] L. Parry, I.A. Ashcroft, R.D. Wildman, Understanding the effect of laser scan strategy on residual stress in selective laser melting through thermo-mechanical simulation, Addit. Manuf. 12 (2016) 1–15, https://doi.org/10.1016/j.addma.2016.05.014.
[36] D. Ramos, F. Belblidia, J. Sienz, New scanning strategy to reduce warpage in additive manufacturing, Addit. Manuf. 28 (2019) 554–564, https://doi.org/10.1016/j.addma.2019.05.016.
[37] J. Robinson, I. Ashton, P. Fox, E. Jones, C. Sutcliffe, Determination of the effect of scan strategy on residual stress in laser powder bed fusion additive manufacturing, Addit. Manuf. 23 (2018) 13–24, https://doi.org/10.1016/j.addma.2018.07.001.
[38] A. Kudzal, B. McWilliams, C. Hofmeister, F. Kellogg, J. Yu, J. Taggart-Scarff, J. Liang, Effect of scan pattern on the microstructure and mechanical properties of Powder Bed Fusion additive manufactured 17–4 stainless steel, Mater. Des. 133 (2017) 205–215, https://doi.org/10.1016/j.matdes.2017.07.047.
[39] X. Zhang, H. Xu, Z. Li, A. Dong, D. Du, L. Lei, G. Zhang, D. Wang, G. Zhu, B. Sun, Effect of the scanning strategy on microstructure and mechanical anisotropy of Hastelloy X superalloy produced by Laser Powder Bed Fusion, Mater. Charact. 173 (2021), 110951, https://doi.org/10.1016/j.matchar.2021.110951.
[40] H. Ali, H. Ghadbeigi, K. Mumtaz, Effect of scanning strategies on residual stress and mechanical properties of Selective Laser Melted Ti6Al4V, Mater. Sci. Eng. A. 712 (2018) 175–187, https://doi.org/10.1016/j.msea.2017.11.103.
[41] S. Catchpole-Smith, N. Aboulkhair, L. Parry, C. Tuck, I.A. Ashcroft, A. Clare, Fractal scan strategies for selective laser melting of 'unweldable' nickel superalloys, Addit. Manuf. 15 (2017) 113–122, https://doi.org/10.1016/j.addma.2017.02.002.
[42] V. Gunenthiram, P. Peyre, M. Schneider, M. Dal, F. Coste, R. Fabbro, Analysis of laser–melt pool–powder bed interaction during the selective laser melting of a stainless steel, J. Laser Appl. 29 (2017), 022303, https://doi.org/10.2351/1.4983259.
[43] C. Lun, A. Leung, S. Marussi, R.C. Atwood, P.D. Lee, M. Towrie, P.J. Withers, In situ X-ray imaging of defect and molten pool dynamics in laser additive manufacturing, Nat. Commun. 9 (2018) 1–9, https://doi.org/10.1038/s41467-018-03734-7.
[44] V. Manvatkar, A. De, T. Debroy, Heat transfer and material flow during laser assisted multi-layer additive manufacturing, J. Appl. Phys. 116 (2014), https://doi.org/10.1063/1.4896751.
[45] M. Bayat, W. Dong, J. Thorborg, A.C. To, J.H. Hattel, A review of multi-scale and multi-physics simulations of metal additive manufacturing processes with focus on modeling strategies, Addit. Manuf. 47 (2021), 102278, https://doi.org/10.1016/j.addma.2021.102278.
[46] W. King, A.T. Anderson, R.M. Ferencz, N.E. Hodge, C. Kamath, S.A. Khairallah, Overview of modelling and simulation of metal powder bed fusion process at Lawrence Livermore National Laboratory, Mater. Sci. Technol. 31 (2014) 957–968, https://doi.org/10.1179/1743284714y.0000000728.
[47] N. Kouraytem, X. Li, R. Cunningham, C. Zhao, N. Parab, T. Sun, A.D. Rollett, A. D. Spear, W. Tan, Effect of Laser-Matter Interaction on Molten Pool Flow and Keyhole Dynamics, Phys. Rev. Appl. 11 (2019), 064054, https://doi.org/10.1103/PhysRevApplied.11.064054.
[48] C. Zhao, Q. Guo, X. Li, N. Parab, K. Fezzaa, W. Tan, L. Chen, T. Sun, Bulk-Explosion-Induced Metal Spattering During Laser Processing, Phys. Rev. X. (2019), https://doi.org/10.1103/physrevx.9.021052.
[49] U. Scipioni Bertoli, G. Guss, S. Wu, M.J. Matthews, J.M. Schoenung, In-situ characterization of laser-powder interaction and cooling rates through high-speed imaging of powder bed fusion additive manufacturing, Mater. Des. 135 (2017) 385–396, https://doi.org/10.1016/j.matdes.2017.09.044.
[50] J. Trapp, A.M. Rubenchik, G. Guss, M.J. Matthews, In situ absorptivity measurements of metallic powders during laser powder-bed fusion additive manufacturing, Appl. Mater. Today. 9 (2017) 341–349, https://doi.org/10.1016/j.apmt.2017.08.006.
[51] T.R. Allen, W. Huang, J.R. Tanner, W. Tan, J.M. Fraser, B.J. Simonds, Energy-Coupling Mechanisms Revealed through Simultaneous Keyhole Depth and Absorptance Measurements during Laser-Metal Processing, Phys. Rev. Appl. 13 (2020) 64070, https://doi.org/10.1103/PhysRevApplied.13.064070.
[52] N.K. Tolochko, Y.V. Khlopkov, S.E. Mozzharov, M.B. Ignatiev, T. Laoui, V.I. Titov, Absorptance of powder materials suitable for laser sintering, Rapid Prototyp. J. 6 (2000) 155–161, https://doi.org/10.1108/13552540010337029.
[53] H. Siva Prasad, F. Brueckner, J. Volpp, A.F.H. Kaplan, Laser metal deposition of copper on diverse metals using green laser sources, Int. J. Adv. Manuf. Technol. (2020) 1559–1568, https://doi.org/10.1007/s00170-020-05117-z.
[54] C.D. Boley, S.C. Mitchell, A.M. Rubenchik, S.S.Q. Wu, Metal powder absorptivity: modeling and experiment, Appl. Opt. 55 (2016) 6496, https://doi.org/10.1364/ao.55.006496.
[55] H. Kügler, Effects of Short-Term Laser Beam Heating on the Absorptivity of Steel Sheets, J. Manuf. Mater. Process. 3 (2019) 41, https://doi.org/10.3390/jmmp3020041.
[56] D. Bergström, The absorption of laser light by rough metal surfaces, Thesis. (2008) 226.
[57] J. Yan, Y. Zhou, R. Gu, X. Zhang, W.M. Quach, M. Yan, A comprehensive study of steel powders (316L, H13, P20 and 18Ni300) for their selective laser melting additive manufacturing, Metals (Basel). 9 (2019), https://doi.org/10.3390/met9010086.
[58] P. Fischer, V. Romano, H.P. Weber, N.P. Karapatis, E. Boillat, R. Glardon, Sintering of commercially pure titanium powder with a Nd:YAG laser source, Acta Mater. 51 (2003) 1651–1662, https://doi.org/10.1016/S1359-6454(02)00567-0.
[59] J. Yin, L.L. Yang, X. Yang, H. Zhu, D. Wang, L. Ke, Z. Wang, G. Wang, X. Zeng, High-power laser-matter interaction during laser powder bed fusion, Addit. Manuf. 29 (2019), 100778, https://doi.org/10.1016/j.addma.2019.100778.
[60] C.L.A. Leung, S. Marussi, M. Towrie, J. del Val Garcia, R.C. Atwood, A.J. Bodey, J. R. Jones, P.J. Withers, P.D. Lee, Laser-matter interactions in additive manufacturing of stainless steel SS316L and 13–93 bioactive glass revealed by in situ X-ray imaging, Addit. Manuf. 24 (2018) 647–657, https://doi.org/10.1016/j.addma.2018.08.025.
[61] P. Bidare, I. Bitharas, R.M. Ward, M.M. Attallah, A.J. Moore, Fluid and particle dynamics in laser powder bed fusion, Acta Mater. 142 (2018) 107–120, https://doi.org/10.1016/j.actamat.2017.09.051.
[62] C. Körner, E. Attar, P. Heinl, Mesoscopic simulation of selective beam melting processes, J. Mater. Process. Technol. 211 (2011) 978–987, https://doi.org/10.1016/j.jmatprotec.2010.12.016.
[63] S.A. Khairallah, A.T. Anderson, A. Rubenchik, W.E. King, Laser powder-bed fusion additive manufacturing: Physics of complex melt flow and formation mechanisms of pores, spatter, and denudation zones, Acta Mater. 108 (2016) 36–45, https://doi.org/10.1016/j.actamat.2016.02.014.
[64] Y. Xiang, S. Zhang, Z. Wei, J. Li, P. Wei, Z. Chen, L. Yang, L. Jiang, Forming and defect analysis for single track scanning in selective laser melting of Ti6Al4V, Appl. Phys. A Mater. Sci. Process. 124 (2018) 1–12, https://doi.org/10.1007/s00339-018-2056-9.
[65] C. Panwisawas, C.L. Qiu, Y. Sovani, J.W. Brooks, M.M. Attallah, H.C. Basoalto, On the role of thermal fluid dynamics into the evolution of porosity during selective laser melting, Scr. Mater. 105 (2015) 14–17, https://doi.org/10.1016/j.scriptamat.2015.04.016.
[66] M.J. Matthews, G. Guss, S.A. Khairallah, A.M. Rubenchik, P.J. Depond, W.E. King, Denudation of metal powder layers in laser powder bed fusion processes, Acta Mater. 114 (2016) 33–42.
[67] G. Fu, D.Z. Zhang, A.N. He, Z. Mao, K. Zhang, Finite element analysis of interaction of laser beam with material in laser metal powder bed fusion process, Materials (Basel). 11 (2018), https://doi.org/10.3390/ma11050765.
[68] C. Guo, F. Lin, C. Guo, F. Lin, W.J. Ge, J. Zhang, Development of Novel EBSM System for High-Tech Material Additive Manufacturing Research Multi-scale multi-physics modeling of Additive Manufacturing Processes View project Inkjet Printing Based on Alternating Viscous-Inertial Force View project Developmen, 2015.
[69] H.P. Tang, G.Y. Yang, W.P. Jia, W.W. He, S.L. Lu, M. Qian, Additive manufacturing of a high niobium-containing titanium aluminide alloy by selective electron beam melting, Mater. Sci. Eng. A. 636 (2015) 103–107, https://doi.org/10.1016/j.msea.2015.03.079.
[70] M. Sigl, S. Lutzmann, M.F. Zaeh, Transient Physical Effects in Electron Beam Sintering, n.d.

[71] C. Körner, Additive manufacturing of metallic components by selective electron beam melting - A review, Int. Mater. Rev. 61 (2016) 361–377, https://doi.org/10.1080/09506608.2016.1176289.
[72] M. Kahnert, S. Lutzmann, M.F. Zaeh, Layer Formations in Electron Beam Sintering, n.d.
[73] S. Biamino, A. Penna, U. Ackelid, S. Sabbadini, O. Tassa, P. Fino, M. Pavese, P. Gennaro, C. Badini, Electron beam melting of Tie48Ale2Cre2Nb alloy: Microstructure and mechanical properties investigation, 2010. https://doi.org/10.1016/j.intermet.2010.11.017.
[74] X. Gong, T. Anderson, K. Chou, Review on powder-based electron beam additive manufacturing Technology, Manuf. Rev. 1 (2014), https://doi.org/10.1051/mfreview/2014001.
[75] D. Cormier, O. Harrysson, H. West, Characterization of H13 steel produced via electron beam melting, Rapid Prototyp. J. (2004) 35–41, https://doi.org/10.1108/13552540410512516.
[76] E. Rodriguez, F. Medina, D. Espalin, C. Terrazas, D. Muse, C. Henry, E. Macdonald, R.B. Wicker, Integration of a Thermal Imaging Feedback Control System in Electron Beam Melting, n.d.
[77] W. He, W. Jia, H. Liu, H. Tang, X. Kang, Y. Huang, Research on preheating of titanium alloy powder in electron beam melting technology, Xiyou Jinshu Cailiao Yu Gongcheng/Rare Met, Mater. Eng. 40 (2011) 2072–2075, https://doi.org/10.1016/s1875-5372(12)60014-9.
[78] M.A. Lodes, R. Guschlbauer, C. Körner, Process development for the manufacturing of 99.94% pure copper via selective electron beam melting, 2014. https://doi.org/10.1016/j.matlet.2014.12.105.
[79] J. Schwerdtfeger, C. Körner, Selective electron beam melting of Tie48Ale2Nbe2Cr: Microstructure and aluminium loss, 2014. https://doi.org/10.1016/j.intermet.2014.01.004.
[80] Y.Y. Sun, S. Gulizia, C.H. Oh, C. Doblin, Y.F. Yang, M. Qian, Manipulation and Characterization of a Novel Titanium Powder Precursor for Additive Manufacturing Applications, JOM. 67 (2015) 564–572, https://doi.org/10.1007/s11837-015-1301-3.
[81] R. Cunningham, A. Nicolas, J. Madsen, E. Fodran, E. Anagnostou, M.D. Sangid, A. D. Rollett, Analyzing the effects of powder and post-processing on porosity and properties of electron beam melted Ti-6Al-4V, Mater. Res. Lett. 5 (2017) 516–525, https://doi.org/10.1080/21663831.2017.1340911.
[82] R. Cunningham, S.P. Narra, T. Ozturk, J. Beuth, A.D. Rollett, Evaluating the Effect of Processing Parameters on Porosity in Electron Beam Melted Ti-6Al-4V via Synchrotron X-ray Microtomography, Jom. 68 (2016) 765–771, https://doi.org/10.1007/s11837-015-1802-0.
[83] H. Gong, H. Gu, K. Zeng, J.J.S. Dilip, D. Pal, B. Stucker, D. Christiansen, J. Beuth, J.J. Lewandowski, Melt pool characterization for selective laser melting of Ti-6Al-4V pre-alloyed powder, Solid Free, Fabr. Proc. (2014) 256–267.
[84] H. Gong, K. Rafi, H. Gu, T. Starr, B. Stucker, Analysis of Defect Generation in Ti-6Al-4V Parts Made using Powder Bed Fusion Additive Manufacturing Processes, Addit. Manuf. 1–4 (2014) 87–98.
[85] Z. Francis, The Effects of Laser and Electron Beam Spot Size in Additive Manufacturing Processes, 2017.
[86] P. Promoppatum, S.C. Yao, P.C. Pistorius, A.D. Rollett, A Comprehensive Comparison of the Analytical and Numerical Prediction of the Thermal History and Solidification Microstructure of Inconel 718 Products Made by Laser Powder-Bed Fusion, Engineering. 3 (2017) 685–694, https://doi.org/10.1016/J.ENG.2017.05.023.
[87] F. Lia, S.-C. Yao, P. Promoppatum, P.C. Pistorius, P.J. Coutts, A.D. Rollett, R. Martukanitz, Numerical modeling and experimental validation of thermal history and microstructure for additive manufacturing of an Inconel 718 product, Prog. Addit. Manuf. 3 (2018) 15–32, https://doi.org/10.1007/s40964-018-0039-1.
[88] J. Metelkova, Y. Kinds, K. Kempen, C. de Formanoir, A. Witvrouw, B. Van Hooreweder, On the influence of laser defocusing in Selective Laser Melting of 316L, Addit. Manuf. 23 (2018) 161–169, https://doi.org/10.1016/j.addma.2018.08.006.
[89] K. Artzt, J. Haubrich, G. Requena, G. Bruno, T. Mishurova, New aspects about the search for the most relevant parameters optimizing SLM materials, Addit. Manuf. 25 (2018) 325–334, https://doi.org/10.1016/j.addma.2018.11.023.
[90] G.E. Bean, D.B. Witkin, T.D. McLouth, D.N. Patel, R.J. Zaldivar, Effect of laser focus shift on surface quality and density of Inconel 718 parts produced via selective laser melting, Addit. Manuf. 22 (2018) 207–215, https://doi.org/10.1016/j.addma.2018.04.024.
[91] H.J. Lee, H.K. Kim, H.U. Hong, B.S. Lee, Influence of the focus offset on the defects, microstructure, and mechanical properties of an Inconel 718 superalloy fabricated by electron beam additive manufacturing, J. Alloys Compd. 781 (2019) 842–856, https://doi.org/10.1016/j.jallcom.2018.12.070.
[92] H. Wang, Y. Zou, Microscale interaction between laser and metal powder in powder-bed additive manufacturing: Conduction mode versus keyhole mode, Int. J. Heat Mass Transf. 142 (2019), 118473, https://doi.org/10.1016/j.ijheatmasstransfer.2019.118473.
[93] J. Yang, J. Han, H. Yu, J. Yin, M. Gao, Z. Wang, X. Zeng, Role of molten pool mode on formability, microstructure and mechanical properties of selective laser melted Ti-6Al-4V alloy, Mater. Des. 110 (2016) 558–570, https://doi.org/10.1016/j.matdes.2016.08.036.
[94] S. Bag, A. Trivedi, A. De, Development of a finite element based heat transfer model for conduction mode laser spot welding process using an adaptive volumetric heat source, Int. J. Therm. Sci. 48 (2009) 1923–1931, https://doi.org/10.1016/j.ijthermalsci.2009.02.010.
[95] A.J. Russo, D.A. Benson, G.R. Hadley, H.C. Peebles, Two-Dimensional Modeling of Conduction-Mode Laser Welding., LIA (Laser Inst, Am. 44 (1985) 8–16, https://doi.org/10.2351/1.5057627.
[96] W.E. King, H.D. Barth, V.M. Castillo, G.F. Gallegos, J.W. Gibbs, D.E. Hahn, C. Kamath, A.M. Rubenchik, Observation of keyhole-mode laser melting in laser powder-bed fusion additive manufacturing, J. Mater. Process. Technol. 214 (2014) 2915–2925.
[97] A. Aggarwal, S. Patel, A. Kumar, Selective Laser Melting of 316L Stainless Steel: Physics of Melting Mode Transition and Its Influence on Microstructural and Mechanical Behavior, Jom. 71 (2019) 1105–1116, https://doi.org/10.1007/s11837-018-3271-8.
[98] M. Tang, P.C. Pistorius, J.L. Beuth, Prediction of lack-of-fusion porosity for powder bed fusion, Addit. Manuf. 14 (2017) 39–48, https://doi.org/10.1016/j.addma.2016.12.001.
[99] T. Qi, H. Zhu, H. Zhang, J. Yin, L. Ke, X. Zeng, Selective laser melting of Al7050 powder: Melting mode transition and comparison of the characteristics between the keyhole and conduction mode, Mater. Des. 135 (2017) 257–266, https://doi.org/10.1016/j.matdes.2017.09.014.
[100] H. Yang, J. Yang, W. Huang, Z. Wang, X. Zeng, The printability, microstructure, crystallographic features and microhardness of selective laser melted Inconel 718 thin wall, Mater. Des. 156 (2018) 407–418, https://doi.org/10.1016/j.matdes.2018.07.007.
[101] I. Eriksson, J. Powell, A.F.H. Kaplan, Melt behavior on the keyhole front during high speed laser welding, Opt. Lasers Eng. 51 (2013) 735–740, https://doi.org/10.1016/j.optlaseng.2013.01.008.
[102] R. Fabbro, S. Slimani, I. Doudet, F. Coste, F. Briand, Experimental study of the dynamical coupling between the induced vapour plume and the melt pool for Nd-Yag CW laser welding, J. Phys. D. Appl. Phys. 39 (2006) 394–400, https://doi.org/10.1088/0022-3727/39/2/023.
[103] Y. Zhang, G. Chen, H. Wei, J. Zhang, A novel "sandwich" method for observation of the keyhole in deep penetration laser welding, Opt. Lasers Eng. 46 (2008) 133–139, https://doi.org/10.1016/j.optlaseng.2007.08.010.
[104] S. Li, G. Chen, M. Zhang, Y. Zhou, Y. Zhang, Dynamic keyhole profile during high-power deep-penetration laser welding, J. Mater. Process. Technol. 214 (2014) 565–570, https://doi.org/10.1016/j.jmatprotec.2013.10.019.
[105] Y. Zhang, Q. Lin, X. Yin, S. Li, J. Deng, Experimental research on the dynamic behaviors of the keyhole and molten pool in laser deep-penetration welding, J. Phys. D. Appl. Phys. 51 (2018), https://doi.org/10.1088/1361-6463/aab2cb.
[106] N. Seto, S. Katayama, A. Matsunawa, High-speed simultaneous observation of plasma and keyhole behavior during high power CO2 laser welding-effect of shielding gas on porosity formation, 187 (2018) E19–E27. https://doi.org/10.2351/1.5059249.
[107] Y. Kawahito, M. Mizutani, S. Katayama, Elucidation of high-power fibre laser welding phenomena of stainless steel and effect of factors on weld geometry, J. Phys. D. Appl. Phys. 40 (2007) 5854–5859, https://doi.org/10.1088/0022-3727/40/19/009.
[108] F. Fetzer, H. Hu, P. Berger, R. Weber, T. Graf, Pores in laser beam welding: generation mechanism and impact on the melt flow, 2018, pp. 12. https://doi.org/10.1117/12.2295798.
[109] Y. Kawahito, N. Matsumoto, Y. Abe, S. Katayama, Relationship of laser absorption to keyhole behavior in high power fiber laser welding of stainless steel and aluminum alloy, J. Mater. Process. Technol. 211 (2011) 1563–1568, https://doi.org/10.1016/j.jmatprotec.2011.04.002.
[110] N.P. Calta, J. Wang, A.M. Kiss, A.A. Martin, P.J. Depond, G.M. Guss, V. Thampy, A.Y. Fong, J.N. Weker, K.H. Stone, C.J. Tassone, M.J. Kramer, M.F. Toney, A. Van Buuren, M.J. Matthews, An instrument for in situ time-resolved X-ray imaging and diffraction of laser powder bed fusion additive manufacturing processes, Rev. Sci. Instrum. 89 (2018), https://doi.org/10.1063/1.5017236.
[111] A. Matsunawa, J.-D. Kim, N. Seto, M. Mizutani, S. Katayama, Dynamics of keyhole and molten pool in laser welding, J. Laser Appl. 10 (2010) 247–254, https://doi.org/10.2351/1.521858.
[112] H. Ki, P.S. Mohanty, J. Mazumder, Multiple reflection and its influence on keyhole evolution, 14 (2001) 933–942. https://doi.org/10.2351/1.5059954.
[113] J.H. Cho, S.J. Na, Implementation of real-time multiple reflection and Fresnel absorption of laser beam in keyhole, J. Phys. D. Appl. Phys. 39 (2006) 5372–5378, https://doi.org/10.1088/0022-3727/39/24/039.
[114] A. Matsunawa, V. Semak, The simulation of front keyhole wall dynamics during laser welding, J. Phys. D. Appl. Phys. 30 (1997) 798–809, https://doi.org/10.1088/0022-3727/30/5/013.
[115] V. Semak, A. Matsunawa, The role of recoil pressure in energy balance during laser materials processing, J. Phys. D. Appl. Phys. 30 (1997) 2541–2552, https://doi.org/10.1088/0022-3727/30/18/008.
[116] A. Kar, T. Rockstroh, J. Mazumder, Two-dimensional model for laser-induced materials damage: Effects of assist gas and multiple reflections inside the cavity, J. Appl. Phys. 71 (1992) 2560–2569, https://doi.org/10.1063/1.351072.
[117] J. Milewski, E. Sklar, Modelling and validation of multiple reflections for enhanced laser welding, Model. Simul. Mater. Sci, Eng, 1996.
[118] P. Solana, G. Negro, A study of the effect of multiple reflections on the shape of the keyhole in the laser processing of materials, J. Phys. D. Appl. Phys. 30 (1997) 3216–3222, https://doi.org/10.1088/0022-3727/30/23/006.
[119] P.S. Wei, C.Y. Ho, Beam focusing characteristics effect on energy reflection and absorption in a drilling or welding cavity of paraboloid of revolution, Int. J. Heat Mass Transf. 41 (1998) 3299–3308, https://doi.org/10.1016/S0017-9310(98)00036-2.

[120] J. Zhou, H.L. Tsai, P.C. Wang, Transfort phenomena and keyhole dynamics during pulsed laser welding, J. Heat Transfer. 128 (2006) 680–690, https://doi.org/10.1115/1.2194043.
[121] S. Pang, L. Chen, J. Zhou, Y. Yin, T. Chen, A three-dimensional sharp interface model for self-consistent keyhole and weld pool dynamics in deep penetration laser welding, J. Phys. D. Appl. Phys. 44 (2011), https://doi.org/10.1088/0022-3727/44/2/025301.
[122] M. Courtois, M. Carin, P. Le Masson, S. Gaied, M. Balabane, A complete model of keyhole and melt pool dynamics to analyze instabilities and collapse during laser welding, J. Laser Appl. 26 (2014), 042001, https://doi.org/10.2351/1.4886835.
[123] Y. Ai, P. Jiang, X. Shao, P. Li, C. Wang, A three-dimensional numerical simulation model for weld characteristics analysis in fiber laser keyhole welding, Int. J. Heat Mass Transf. 108 (2017) 614–626, https://doi.org/10.1016/j.ijheatmasstransfer.2016.12.034.
[124] C. Panwisawas, B. Perumal, R.M. Ward, N. Turner, R.P. Turner, J.W. Brooks, H. C. Basoalto, Keyhole formation and thermal fluid flow-induced porosity during laser fusion welding in titanium alloys: Experimental and modelling, Acta Mater. 126 (2017) 251–263, https://doi.org/10.1016/j.actamat.2016.12.062.
[125] W. Yan, Y. Qian, W. Ge, S. Lin, W.K. Liu, F. Lin, G.J. Wagner, Meso-scale modeling of multiple-layer fabrication process in Selective Electron Beam Melting: Inter-layer/track voids formation, Mater. Des. 141 (2018) 210–219, https://doi.org/10.1016/j.matdes.2017.12.031.
[126] H. Zhao, W. Niu, B. Zhang, Y. Lei, M. Kodama, T. Ishide, Modelling of keyhole dynamics and porosity formation considering the adaptive keyhole shape and three-phase coupling during deep-penetration laser welding, J. Phys. D. Appl. Phys. 44 (2011), https://doi.org/10.1088/0022-3727/44/48/485302.
[127] J.Y. Lee, S.H. Ko, D.F. Farson, C.D. Yoo, Mechanism of keyhole formation and stability in stationary laser welding, J. Phys. D. Appl. Phys. 35 (2002) 1570.
[128] W. Tan, Y.C. Shin, Analysis of multi-phase interaction and its effects on keyhole dynamics with a multi-physics numerical model, J. Phys. D. Appl. Phys. 47 (2014), https://doi.org/10.1088/0022-3727/47/34/345501.
[129] S. Kou, Welding Metallurgy, 2nd Editio, John Wiley & Sons, 2003.
[130] G.K.L. Ng, A.E.W. Jarfors, G. Bi, H.Y. Zheng, Porosity formation and gas bubble retention in laser metal deposition, Appl. Phys. A Mater. Sci. Process. 97 (2009) 641–649, https://doi.org/10.1007/s00339-009-5266-3.
[131] M. Grasso, B.M. Colosimo, Process defects and in situ monitoring methods in metal powder bed fusion: A review, Meas. Sci. Technol. 28 (2017), https://doi.org/10.1088/1361-6501/aa5c4f.
[132] R. Cunningham, Defect Formation Mechanisms in Powder-Bed Metal Additive Manufacturing, Carnegie Mellon University, 2018.
[133] J.A. Slotwinski, E.J. Garboczi, K.M. Hebenstreit, Porosity Measurements and Analysis for Metal Additive Manufacturing Process Control, J. Res. Natl. Inst. Stand. Technol. 119 (2014) 494, https://doi.org/10.6028/jres.119.019.
[134] S. Tammas-Williams, H. Zhao, F. Léonard, F. Derguti, I. Todd, P.B. Prangnell, XCT analysis of the influence of melt strategies on defect population in Ti-6Al-4V components manufactured by Selective Electron Beam Melting, Mater. Charact. 102 (2015) 47–61, https://doi.org/10.1016/j.matchar.2015.02.008.
[135] S.K. Dinda, J.M. Warnett, M.A. Williams, G.G. Roy, P. Srirangam, 3D imaging and quantification of porosity in electron beam welded dissimilar steel to Fe-Al alloy joints by X-ray tomography, Mater. Des. 96 (2016) 224–231, https://doi.org/10.1016/j.matdes.2016.02.010.
[136] J.W. Elmer, J. Vaja, H.D. Carlton, R. Pong, The Effect of Ar and N 2 Shielding Gas on Laser Weld Porosity in Steel, Stainless Steels, and Nickel, Weld. J. 94 (2015) 313–325.
[137] Y. Tian, J.D. Robson, S. Riekehr, N. Kashaev, L. Wang, T. Lowe, A. Karanika, Process Optimization of Dual-Laser Beam Welding of Advanced Al-Li Alloys Through Hot Cracking Susceptibility Modeling, Metall. Mater. Trans. A Phys. Metall. Mater. Sci. 47 (2016) 3533–3544, https://doi.org/10.1007/s11661-016-3509-4.
[138] D. Gu, Y. Shen, Balling phenomena during direct laser sintering of multi-component Cu-based metal powder, J. Alloys Compd. 432 (2007) 163–166, https://doi.org/10.1016/j.jallcom.2006.06.011.
[139] H.J. Niu, I.T.H. Chang, Instability of scan tracks of selective laser sintering of high speed steel powder, Scr. Mater. 41 (1999) 1229–1234, https://doi.org/10.1016/S1359-6462(99)00276-6.
[140] B. Cheng, S. Shrestha, K. Chou, Stress and deformation evaluations of scanning strategy effect in selective laser melting, Addit. Manuf. 12 (2016) 240–251, https://doi.org/10.1016/j.addma.2016.05.007.
[141] L.A. Parry, I.A. Ashcroft, R.D. Wildman, Geometrical effects on residual stress in selective laser melting, Addit. Manuf. 25 (2019) 166–175, https://doi.org/10.1016/j.addma.2018.09.026.
[142] J.P.P. Kruth, L. Froyen, J. Van Vaerenbergh, P. Mercelis, M. Rombouts, B. Lauwers, Selective laser melting of iron-based powder, J. Mater. Process. Technol. 149 (2004) 616–622.
[143] J. Krell, A. Röttger, K. Geenen, W. Theisen, General investigations on processing tool steel X40CrMoV5-1 with selective laser melting, J. Mater. Process. Technol. 255 (2018) 679–688, https://doi.org/10.1016/j.jmatprotec.2018.01.012.
[144] A.N.D. Gasper, B. Szost, X. Wang, D. Johns, S. Sharma, A.T. Clare, I.A. Ashcroft, Spatter and oxide formation in laser powder bed fusion of Inconel 718, Addit. Manuf. 24 (2018) 446–456, https://doi.org/10.1016/j.addma.2018.09.032.
[145] A.F.H. Kaplan, J. Powell, Spatter in laser welding, J. Laser Appl. 23 (2011), 032005, https://doi.org/10.2351/1.3597830.
[146] A. Bin Anwar, Q.C. Pham, Study of the spatter distribution on the powder bed during selective laser melting, Addit. Manuf. 22 (2018) 86–97, https://doi.org/10.1016/j.addma.2018.04.036.
[147] S. Li, G. Chen, S. Katayama, Y. Zhang, Relationship between spatter formation and dynamic molten pool during high-power deep-penetration laser welding, Appl. Surf. Sci. 303 (2014) 481–488, https://doi.org/10.1016/j.apsusc.2014.03.030.
[148] A. Heider, J. Sollinger, F. Abt, M. Boley, R. Weber, T. Graf, High-speed X-ray analysis of spatter formation in laser welding of copper, Phys. Procedia. 41 (2013) 112–118, https://doi.org/10.1016/j.phpro.2013.03.058.
[149] C. Eschey, S. Lutzmann, M.F. Zaeh, Examination of the powder spreading effect in electron beam melting (EBM), Solid Free. Fabr. (2009).
[150] D. Ye, K. Zhu, J.Y.H. Fuh, Y. Zhang, H.G. Soon, The investigation of plume and spatter signatures on melted states in selective laser melting, Opt. Laser Technol. 111 (2019) 395–406, https://doi.org/10.1016/j.optlastec.2018.10.019.
[151] J. Tu, I. Miyamoto, T. Inoue, Characterizing keyhole plasma light emission and plasma plume scattering for monitoring 20 kW class CO2 laser welding processes, J. Laser Appl. 14 (2006) 146–153, https://doi.org/10.2351/1.1493763.
[152] Y. Zhang, G.S. Hong, D. Ye, K. Zhu, J.Y.H. Fuh, Extraction and evaluation of melt pool, plume and spatter information for powder-bed fusion AM process monitoring, Mater. Des. 156 (2018) 458–469, https://doi.org/10.1016/j.matdes.2018.07.002.
[153] M. Grasso, B.M. Colosimo, A statistical learning method for image-based monitoring of the plume signature in laser powder bed fusion, Robot. Comput. Integr. Manuf. 57 (2019) 103–115, https://doi.org/10.1016/j.rcim.2018.11.007.
[154] H.V. Atkinson, S. Davies, Fundamental aspects of hot isostatic pressing: An overview, Metall. Mater. Trans. A Phys. Metall. Mater. Sci. 31 (2000) 2981–3000, https://doi.org/10.1007/s11661-000-0078-2.
[155] S. Tammas-Williams, P.J. Withers, I. Todd, P.B. Prangnell, The Effectiveness of Hot Isostatic Pressing for Closing Porosity in Titanium Parts Manufactured by Selective Electron Beam Melting, Metall. Mater. Trans. A Phys. Metall. Mater. Sci. 47 (2016) 1939–1946, https://doi.org/10.1007/s11661-016-3429-3.
[156] J.W. Pegues, S. Shao, N. Shamsaei, N. Sanaei, A. Fatemi, D.H. Warner, P. Li, N. Phan, Fatigue of additive manufactured Ti-6Al-4V, Part I: The effects of powder feedstock, manufacturing, and post-process conditions on the resulting microstructure and defects, Int. J. Fatigue. 132 (2020), 105358, https://doi.org/10.1016/j.ijfatigue.2019.105358.
[157] R. Molaei, A. Fatemi, N. Sanaei, J. Pegues, N. Shamsaei, S. Shao, P. Li, D. H. Warner, N. Phan, Fatigue of additive manufactured Ti-6Al-4V, Part II: The relationship between microstructure, material cyclic properties, and component performance, Int. J. Fatigue. 132 (2020), 105363, https://doi.org/10.1016/j.ijfatigue.2019.105363.
[158] S.P. Moylan, J. Drescher, M.A. Donmez, Powder bed fusion machine performance testing, in: Proc. 2014 ASPE Spring Top. Meet. Accuracy S, 2014.
[159] B. Foster, E. Reutzel, A. Nassar, B. Hall, S. Brown, C. Dickman, Optical, layerwise monitoring of powder bed fusion, in: Solid Free. Fabr. Symp. Austin, TX, Aug, 2015, pp. 10–12.
[160] B. Ferrar, L. Mullen, E. Jones, R. Stamp, C.J. Sutcliffe, Gas flow effects on selective laser melting (SLM) manufacturing performance, J. Mater. Process. Technol. 212 (2012) 355–364, https://doi.org/10.1016/j.jmatprotec.2011.09.020.
[161] C.Y. Chien, T.N. Le, Z.H. Lin, Y.L. Lo, Numerical and experimental investigation into gas flow field and spattering phenomena in laser powder bed fusion processing of Inconel 718, Mater. Des. 210 (2021), 110107, https://doi.org/10.1016/j.matdes.2021.110107.
[162] C. Schwerz, A. Raza, X. Lei, L. Nyborg, E. Hryha, H. Wirdelius, In-situ detection of redeposited spatter and its influence on the formation of internal flaws in laser powder bed fusion, Addit. Manuf. 47 (2021), 102370, https://doi.org/10.1016/j.addma.2021.102370.
[163] R. Li, J. Liu, Y. Shi, L. Wang, W. Jiang, Balling behavior of stainless steel and nickel powder during selective laser melting process, Int. J. Adv. Manuf. Technol. 59 (2012) 1025–1035, https://doi.org/10.1007/s00170-011-3566-1.
[164] S. Kleszczynski, J. zur Jacobsmühlen, J.T. Sehrt, G. Witt, Error Detection in Laser Beam Melting Systems, FFF Work. (2012) 975–987, https://doi.org/10.1016/j.phpro.2014.08.097.
[165] L. Scime, J. Beuth, Anomaly detection and classification in a laser powder bed additive manufacturing process using a trained computer vision algorithm, Addit. Manuf. 19 (2018) 114–126, https://doi.org/10.1016/J.ADDMA.2017.11.009.
[166] https://www.metal-am.com/articles/from-silicone-and-rubber-to-steel-and-ceramic-the-weird-and-wonderful-world-of-wipers/, n.d.
[167] P. Prabhakar, W.J. Sames, R. Dehoff, S.S. Babu, Computational modeling of residual stress formation during the electron beam melting process for Inconel 718, Addit. Manuf. 7 (2015) 83–91, https://doi.org/10.1016/j.addma.2015.03.003.
[168] K. Zeng, Optimization of support structures for selective laser melting, 2015.
[169] K. Kempen, B. Vrancken, S. Buls, L. Thijs, J. Van Humbeeck, J.P. Kruth, Selective Laser Melting of Crack-Free High Density M2 High Speed Steel Parts by Baseplate Preheating, J. Manuf. Sci. Eng. Trans. ASME. 136 (2014), https://doi.org/10.1115/1.4028513.
[170] L. Kempen, L. Thijs, B. Vrancken, S. Buls, J. Van Humbeeck, J.-P. Kruth, Producing crack-free, high density M2 HSS parts by Selective Laser Melting: Pre-heating the baseplate, in: Proc. 24th Int. Solid Free. Fabr. Symp., 2013, pp. 131–139.
[171] D. Buchbinder, W. Meiners, N. Pirch, K. Wissenbach, J. Schrage, Investigation on reducing distortion by preheating during manufacture of aluminum components using selective laser melting, J. Laser Appl. 26 (2014), 012004, https://doi.org/10.2351/1.4828755.
[172] S. Leuders, M. Thöne, A. Riemer, T. Niendorf, T. Tröster, H.A. Richard, H.J. Maier, On the mechanical behaviour of titanium alloy TiAl6V4 manufactured by

selective laser melting: Fatigue resistance and crack growth performance, Int. J. Fatigue. 48 (2013) 300–307, https://doi.org/10.1016/j.ijfatigue.2012.11.011.
[173] E. Chlebus, B. Kuźnicka, T. Kurzynowski, B. Dybała, Microstructure and mechanical behaviour of Ti-6Al-7Nb alloy produced by selective laser melting, Mater. Charact. 62 (2011) 488–495, https://doi.org/10.1016/j.matchar.2011.03.006.
[174] G. Zió, E. Chlebus, P. Szymczyk, J. Kurzac, Application of X-ray CT method for discontinuity and porosity detection in 316L stainless steel parts produced with SLM technology, Arch. Civ. Mech. Eng. 14 (2014) 608–614, https://doi.org/10.1016/j.acme.2014.02.003.
[175] J. Delgado, J. Ciurana, C.A. Rodríguez, Influence of process parameters on part quality and mechanical properties for DMLS and SLM with iron-based materials, Int. J. Adv. Manuf. Technol. 60 (2012) 601–610.
[176] T. Voisin, N.P. Calta, S.A. Khairallah, J.B. Forien, L. Balogh, R.W. Cunningham, A. D. Rollett, Y.M. Wang, Defects-dictated tensile properties of selective laser melted Ti-6Al-4V, Mater. Des. 158 (2018) 113–126, https://doi.org/10.1016/j.matdes.2018.08.004.
[177] H. Yu, J. Yang, J. Yin, Z. Wang, X. Zeng, Comparison on mechanical anisotropies of selective laser melted Ti-6Al-4V alloy and 304 stainless steel, Mater. Sci. Eng. A. 695 (2017) 92–100, https://doi.org/10.1016/j.msea.2017.04.031.
[178] D. Gu, L. Xi, C. Ma, H. Zhang, M. Xia, H. Zhang, Anisotropic corrosion resistance of TiC reinforced Ni-based composite fabricated by selective laser melting, J. Mater. Sci. Technol. (2018), https://doi.org/10.1016/j.jmst.2018.12.020.
[179] M. Tang, P.C. Pistorius, Anisotropic Mechanical Behavior of AlSi10Mg Parts Produced by Selective Laser Melting, Jom. 69 (2017) 516–522, https://doi.org/10.1007/s11837-016-2230-5.
[180] D. Deng, J. Moverare, R.L. Peng, H. Söderberg, Microstructure and anisotropic mechanical properties of EBM manufactured Inconel 718 and effects of post heat treatments, Mater. Sci. Eng. A. 693 (2017) 151–163, https://doi.org/10.1016/j.msea.2017.03.085.
[181] M. Jamshidinia, R. Kovacevic, The influence of heat accumulation on the surface roughness in powder-bed additive manufacturing, Surf. Topogr. Metrol. Prop. 3 (2015), https://doi.org/10.1088/2051-672X/3/1/014003.
[182] M.J. Holzweissig, A. Taube, F. Brenne, M. Schaper, T. Niendorf, Microstructural Characterization and Mechanical Performance of Hot Work Tool Steel Processed by Selective Laser Melting, Metall. Mater. Trans. B Process Metall. Mater. Process. Sci. 46 (2015) 545–549, https://doi.org/10.1007/s11663-014-0267-9.
[183] X. Liang, W. Dong, S. Hinnebusch, Q. Chen, H.T. Tran, J. Lemon, L. Cheng, Z. Zhou, D. Hayduke, A.C. To, Inherent strain homogenization for fast residual deformation simulation of thin-walled lattice support structures built by laser powder bed fusion additive manufacturing, Addit. Manuf. 32 (2020), 101091, https://doi.org/10.1016/j.addma.2020.101091.
[184] L. Cheng, X. Liang, J. Bai, Q. Chen, J. Lemon, A. To, On utilizing topology optimization to design support structure to prevent residual stress induced build failure in laser powder bed metal additive manufacturing, Addit. Manuf. 27 (2019) 290–304, https://doi.org/10.1016/j.addma.2019.03.001.
[185] D. Herzog, V. Seyda, E. Wycisk, C. Emmelmann, Additive manufacturing of metals, Acta Mater. 117 (2016) 371–392, https://doi.org/10.1016/j.actamat.2016.07.019.
[186] H.T. Tran, Q. Chen, J. Mohan, A.C. To, A new method for predicting cracking at the interface between solid and lattice support during laser powder bed fusion additive manufacturing, Addit. Manuf. 32 (2020), 101050, https://doi.org/10.1016/j.addma.2020.101050.
[187] A. Michalcová, L. Senčekova, G. Rolink, A. Weisheit, J. Pešička, M. Stobik, M. Palm, Laser additive manufacturing of iron aluminides strengthened by ordering, borides or coherent Heusler phase, Mater. Des. 116 (2017) 481–494, https://doi.org/10.1016/j.matdes.2016.12.046.
[188] F.K. Mirzade, R.S. Islamov, A phase field formulation of the coupled effects of defect generation and large strains on microstructure evolution during laser-based additive manufacturing, in: 2019 IEEE 8th Int. Conf. Adv. Optoelectron. Lasers, IEEE, 2019, pp. 342–347. https://doi.org/10.1109/CAOL46282.2019.9019579.
[189] H. Zhang, D. Hobbis, G.S. Nolas, S. LeBlanc, Laser additive manufacturing of powdered bismuth telluride, J. Mater. Res. 33 (2018) 4031–4039, https://doi.org/10.1557/jmr.2018.390.
[190] T.-M. Chiu, M. Mahmoudi, W. Dai, A. Elwany, H. Liang, H. Castaneda, Corrosion assessment of Ti-6Al-4V fabricated using laser powder-bed fusion additive manufacturing, Electrochim. Acta. 279 (2018) 143–151, https://doi.org/10.1016/j.electacta.2018.04.189.
[191] R. Pokharel, L. Balogh, D.W. Brown, B. Clausen, G.T. Gray, V. Livescu, S.C. Vogel, S. Takajo, Signatures of the unique microstructure of additively manufactured steel observed via diffraction, Scr. Mater. 155 (2018) 16–20, https://doi.org/10.1016/j.scriptamat.2018.06.008.
[192] K.M. Bertsch, G. Meric de Bellefon, B. Kuehl, D.J. Thoma, Origin of dislocation structures in an additively manufactured austenitic stainless steel 316L, Acta Mater. 199 (2020) 19–33, https://doi.org/10.1016/j.actamat.2020.07.063.
[193] Y.S.J. Yoo, T.A. Book, M.D. Sangid, J. Kacher, Identifying strain localization and dislocation processes in fatigued Inconel 718 manufactured from selective laser melting, Mater. Sci. Eng. A. 724 (2018) 444–451, https://doi.org/10.1016/j.msea.2018.03.127.
[194] M. Shamsujjoha, S.R. Agnew, J.M. Fitz-Gerald, W.R. Moore, T.A. Newman, High Strength and Ductility of Additively Manufactured 316L Stainless Steel Explained, Metall. Mater. Trans. A. 49 (2018) 3011–3027, https://doi.org/10.1007/s11661-018-4607-2.
[195] M.F. Ashby, The deformation of plastically non-homogeneous materials, Philos. Mag. A J. Theor. Exp. Appl. Phys. 21 (1970) 399–424, https://doi.org/10.1080/14786437008238426.
[196] Y.M. Wang, T. Voisin, J.T. McKeown, J. Ye, N.P. Calta, Z. Li, Z. Zeng, Y. Zhang, W. Chen, T.T. Roehling, R.T. Ott, M.K. Santala, P.J. Depond, M.J. Matthews, A. V. Hamza, T. Zhu, Additively manufactured hierarchical stainless steels with high strength and ductility, Nat. Mater. 17 (2018) 63–70, https://doi.org/10.1038/NMAT5021.
[197] D. Lin, L. Xu, H. Jing, Y. Han, L. Zhao, Y. Zhang, H. Li, A strong, ductile, high-entropy FeCoCrNi alloy with fine grains fabricated via additive manufacturing and a single cold deformation and annealing cycle, Addit. Manuf. 36 (2020), 101591, https://doi.org/10.1016/j.addma.2020.101591.
[198] P. Promoppatum, A.D. Rollett, Influence of material constitutive models on thermomechanical behaviors in the laser powder bed fusion of Ti-6Al-4V, Addit. Manuf. (2020), 101680, https://doi.org/10.1016/j.addma.2020.101680.
[199] S. Guan, D. Wan, K. Solberg, F. Berto, T. Welo, T.M. Yue, K.C. Chan, Additive manufacturing of fine-grained and dislocation-populated CrMnFeCoNi high entropy alloy by laser engineered net shaping, Mater. Sci. Eng. A. 761 (2019), 138056, https://doi.org/10.1016/j.msea.2019.138056.
[200] B. Barkia, P. Aubry, P. Haghi-Ashtiani, T. Auger, L. Gosmain, F. Schuster, H. Maskrot, On the origin of the high tensile strength and ductility of additively manufactured 316L stainless steel: Multiscale investigation, J. Mater. Sci. Technol. 41 (2020) 209–218, https://doi.org/10.1016/j.jmst.2019.09.017.
[201] L. Liu, Q. Ding, Y. Zhong, J. Zou, J. Wu, Y.-L. Chiu, J. Li, Z. Zhang, Q. Yu, Z. Shen, Dislocation network in additive manufactured steel breaks strength–ductility trade-off, Mater. Today. 21 (2018) 354–361, https://doi.org/10.1016/j.mattod.2017.11.004.
[202] S. Gorsse, C. Hutchinson, M. Gouné, R. Banerjee, Additive manufacturing of metals: a brief review of the characteristic microstructures and properties of steels, Ti-6Al-4V and high-entropy alloys, Sci. Technol. Adv. Mater. 18 (2017) 584–610, https://doi.org/10.1080/14686996.2017.1361305.
[203] Y. Chen, K. Zhang, J. Huang, S.R.E. Hosseini, Z. Li, Characterization of heat affected zone liquation cracking in laser additive manufacturing of Inconel 718, Mater. Des. 90 (2016) 586–594, https://doi.org/10.1016/j.matdes.2015.10.155.
[204] G. Bi, A. Gasser, Restoration of Nickel-Base Turbine Blade Knife-Edges with Controlled Laser Aided Additive Manufacturing, Phys. Procedia. 12 (2011) 402–409, https://doi.org/10.1016/j.phpro.2011.03.051.
[205] M. Ni, C. Chen, X. Wang, P. Wang, R. Li, X. Zhang, K. Zhou, Anisotropic tensile behavior of in situ precipitation strengthened Inconel 718 fabricated by additive manufacturing, Mater. Sci. Eng. A. 701 (2017) 344–351, https://doi.org/10.1016/j.msea.2017.06.098.
[206] B. Baufeld, O. Van der Biest, R. Gault, Additive manufacturing of Ti–6Al–4V components by shaped metal deposition: Microstructure and mechanical properties, Mater. Des. 31 (2010) S106–S111, https://doi.org/10.1016/j.matdes.2009.11.032.
[207] Z. Xu, H. Zhang, X. Du, Y. He, H. Luo, G. Song, L. Mao, T. Zhou, L. Wang, Corrosion resistance enhancement of CoCrFeMnNi high-entropy alloy fabricated by additive manufacturing, Corros. Sci. 177 (2020), 108954, https://doi.org/10.1016/j.corsci.2020.108954.
[208] X. Gong, Y. Li, Y. Nie, Z. Huang, F. Liu, L. Huang, L. Jiang, H. Mei, Corrosion behaviour of CoCrMo alloy fabricated by electron beam melting, Corros. Sci. 139 (2018) 68–75, https://doi.org/10.1016/j.corsci.2018.04.033.
[209] C. Huber, H. Sepehri-Amin, M. Goertler, M. Groenefeld, I. Teliban, K. Hono, D. Suess, Coercivity enhancement of selective laser sintered NdFeB magnets by grain boundary infiltration, Acta Mater. 172 (2019) 66–71, https://doi.org/10.1016/j.actamat.2019.04.037.
[210] A.S. Volegov, S.V. Andreev, N.V. Selezneva, I.A. Ryzhikhin, N.V. Kudrevatykh, L. Mädler, I.V. Okulov, Additive manufacturing of heavy rare earth free high-coercivity permanent magnets, Acta Mater. 188 (2020) 733–739, https://doi.org/10.1016/j.actamat.2020.02.058.
[211] I. Bantounas, T.C. Lindley, D. Rugg, D. Dye, Effect of microtexture on fatigue cracking in Ti–6Al–4V, Acta Mater. 55 (2007) 5655–5665, https://doi.org/10.1016/j.actamat.2007.06.034.
[212] T. Zhai, A.J. Wilkinson, J.W. Martin, A crystallographic mechanism for fatigue crack propagation through grain boundaries, Acta Mater. 48 (2000) 4917–4927, https://doi.org/10.1016/S1359-6454(00)00214-7.
[213] K.D. Ralston, N. Birbilis, C.H.J. Davies, Revealing the relationship between grain size and corrosion rate of metals, Scr. Mater. 63 (2010) 1201–1204, https://doi.org/10.1016/j.scriptamat.2010.08.035.
[214] H. Yao, R. Katona, J. Zhou, M.I. Islam, J. Raush, F. Lu, S. Guo, Defects Evaluation of Selective Laser Melting Stainless Steel 316 Parts Using Positron Annihilation Lifetime Measurement, in: Heat Transf. Therm. Eng., vol. 8B, American Society of Mechanical Engineers, 2018. https://doi.org/10.1115/IMECE2018-86729.
[215] H. Gong, K. Rafi, H. Gu, G.D. Janaki Ram, T. Starr, B. Stucker, Influence of defects on mechanical properties of Ti-6Al-4V components produced by selective laser melting and electron beam melting, Mater. Des. 86 (2015) 545–554, https://doi.org/10.1016/j.matdes.2015.07.147.
[216] D.M. Bond, M.A. Zikry, Effects of electron beam manufacturing induced defects on fracture in Inconel 718, Addit. Manuf. 32 (2020), 101059, https://doi.org/10.1016/j.addma.2020.101059.
[217] A. Thompson, I. Maskery, R.K. Leach, X-ray computed tomography for additive manufacturing: A review, Meas. Sci. Technol. 27 (2016), https://doi.org/10.1088/0957-0233/27/7/072001.
[218] S.K. Everton, M. Hirsch, P.I. Stavroulakis, R.K. Leach, A.T. Clare, Review of in-situ process monitoring and in-situ metrology for metal additive manufacturing, Mater. Des. 95 (2016) 431–445, https://doi.org/10.1016/j.matdes.2016.01.099.
[219] S.R. Stock, Recent advances in X-ray microtomography applied to materials, Int. Mater. Rev. 53 (2008) 129–181, https://doi.org/10.1179/174328008X277803.

[220] J. Kastner, B. Harrer, G. Requena, O. Brunke, A comparative study of high resolution cone beam X-ray tomography and synchrotron tomography applied to Fe- and Al-alloys, NDT E Int. 43 (2010) 599–605, https://doi.org/10.1016/j.ndteint.2010.06.004.
[221] R. Snell, S. Tammas-Williams, L. Chechik, A. Lyle, E. Hernández-Nava, C. Boig, G. Panoutsos, I. Todd, Methods for Rapid Pore Classification in Metal Additive Manufacturing, Jom. 72 (2020) 101–109, https://doi.org/10.1007/s11837-019-03761-9.
[222] U. Mueller, R. Förster, M. Hellmig, F.U. Huschmann, A. Kastner, P. Malecki, S. Pühringer, M. Röwer, K. Sparta, M. Steffien, M. Ühlein, P. Wilk, M.S. Weiss, The macromolecular crystallography beamlines at BESSY II of the Helmholtz-Zentrum Berlin: Current status and perspectives, Eur. Phys. J. Plus. 130 (2015), https://doi.org/10.1140/epjp/i2015-15141-2.
[223] M. Montazeri, R. Yavari, P. Rao, P. Boulware, In-Process Monitoring of Material Cross-Contamination Defects in Laser Powder Bed Fusion, J. Manuf. Sci. Eng. 140 (2018), 111001, https://doi.org/10.1115/1.4040543.
[224] M. Grasso, V. Laguzza, Q. Semeraro, B.M. Colosimo, In-Process Monitoring of Selective Laser Melting: Spatial Detection of Defects Via Image Data Analysis, J. Manuf. Sci. Eng. 139 (2016), 051001, https://doi.org/10.1115/1.4034715.
[225] Y. Zhang, J.Y.H. Fuh, D. Ye, G.S. Hong, In-situ monitoring of laser-based PBF via off-axis vision and image processing approaches, Addit. Manuf. 25 (2019) 263–274, https://doi.org/10.1016/j.addma.2018.10.020.
[226] Z.Y. Chua, I.H. Ahn, S.K. Moon, Process monitoring and inspection systems in metal additive manufacturing: Status and applications, Int. J. Precis. Eng. Manuf. - Green Technol. 4 (2017) 235–245, https://doi.org/10.1007/s40684-017-0029-7.
[227] I. Miyamoto, K. Mori, Development of in-process monitoring system for laser welding, ICALEO. 759 (2018) 759–767, https://doi.org/10.2351/1.5058980.
[228] M.R. Gardner, A. Lewis, J. Park, A.B. McElroy, A.D. Estrada, S. Fish, J.J. Beaman, T.E. Milner, In situ process monitoring in selective laser sintering using optical coherence tomography, Opt. Eng. 57 (2018) 1, https://doi.org/10.1117/1.OE.57.4.041407.
[229] B. Zhang, S. Liu, Y.C. Shin, In-Process Monitoring of Porosity During Laser Additive Manufacturing Process, Addit. Manuf. (2019), https://doi.org/10.1016/j.addma.2019.05.030.
[230] F. Imani, A. Gaikwad, M. Montazeri, P. Rao, H. Yang, E. Reutzel, Process Mapping and In-Process Monitoring of Porosity in Laser Powder Bed Fusion Using Layerwise Optical Imaging, J. Manuf. Sci. Eng. 140 (2018), 101009, https://doi.org/10.1115/1.4040615.
[231] N.D. Parab, L. Xiong, Q. Guo, Z. Guo, C. Kirk, Y. Nie, X. Xiao, K. Fezzaa, W. Everheart, W.W. Chen, L. Chen, T. Sun, Investigation of dynamic fracture behavior of additively manufactured Al-10Si-Mg using high-speed synchrotron X-ray imaging, Addit. Manuf. 30 (2019), 100878, https://doi.org/10.1016/J.ADDMA.2019.100878.
[232] H. Choo, K.L. Sham, J. Bohling, A. Ngo, X. Xiao, Y. Ren, P.J. Depond, M. J. Matthews, E. Garlea, Effect of laser power on defect, texture, and microstructure of a laser powder bed fusion processed 316L stainless steel, Mater. Des. 164 (2019), 107534, https://doi.org/10.1016/j.matdes.2018.12.006.
[233] P. Wang, X. Tan, C. He, M.L.S. Nai, R. Huang, S.B. Tor, J. Wei, Scanning optical microscopy for porosity quantification of additively manufactured components, Addit. Manuf. 21 (2018) 350–358, https://doi.org/10.1016/J.ADDMA.2018.03.019.
[234] A.B. Spierings, M. Schneider, R. Eggenberger, Comparison of density measurement techniques for additive manufactured metallic parts, Rapid Prototyp. J. 17 (2011) 380–386.
[235] L. Thijs, F. Verhaeghe, T. Craeghs, J. Van Humbeeck, J.P. Kruth, A study of the microstructural evolution during selective laser melting of Ti-6Al-4V, Acta Mater. 58 (2010) 3303–3312, https://doi.org/10.1016/j.actamat.2010.02.004.
[236] M. Chapman, J.M. Scott, E.J. Schwalbach, M.A. Groeber, S.P. Donegan, M. D. Uchic, Application of Serial Sectioning Microscopy to Additively Manufactured Metallic Samples, Microsc. Microanal. 23 (2017) 318–319, https://doi.org/10.1017/S1431927617002276.
[237] T. Grimm, G. Wiora, G. Witt, Characterization of typical surface effects in additive manufacturing with confocal microscopy, Surf. Topogr. Metrol. Prop. 3 (2015), 014001, https://doi.org/10.1088/2051-672X/3/1/014001.
[238] Z. Tong, X. Ren, J. Jiao, W. Zhou, Y. Ren, Y. Ye, E.A. Larson, J. Gu, Laser additive manufacturing of FeCrCoMnNi high-entropy alloy: Effect of heat treatment on microstructure, residual stress and mechanical property, J. Alloys Compd. 785 (2019) 1144–1159, https://doi.org/10.1016/j.jallcom.2019.01.213.
[239] L.E. Murr, E. Martinez, S.M. Gaytan, D.A. Ramirez, B.I. MacHado, P.W. Shindo, J. L. Martinez, F. Medina, J. Wooten, D. Ciscel, U. Ackelid, R.B. Wicker, Microstructural architecture, microstructures, and mechanical properties for a nickel-base superalloy fabricated by electron beam melting, Metall. Mater. Trans. A Phys. Metall. Mater. Sci. 42 (2011) 3491–3508, https://doi.org/10.1007/s11661-011-0748-2.
[240] M. Fousová, D. Dvorský, A. Michalcová, D. Vojtěch, Changes in the microstructure and mechanical properties of additively manufactured AlSi10Mg alloy after exposure to elevated temperatures, Mater. Charact. 137 (2018) 119–126, https://doi.org/10.1016/j.matchar.2018.01.028.
[241] J.T. McKeown, K. Zweiacker, C. Liu, D.R. Coughlin, A.J. Clarke, J.K. Baldwin, J. W. Gibbs, J.D. Roehling, S.D. Imhoff, P.J. Gibbs, D. Tourret, J.M.K. Wiezorek, G. H. Campbell, Time-Resolved In Situ Measurements During Rapid Alloy Solidification: Experimental Insight for Additive Manufacturing, Jom. 68 (2016) 985–999, https://doi.org/10.1007/s11837-015-1793-x.
[242] V. Bathula, C. Liu, K. Zweiacker, J. McKeown, J.M.K. Wiezorek, Interface velocity dependent solute trapping and phase selection during rapid solidification of laser melted hypo-eutectic Al-11at.%Cu alloy, Acta Mater. 195 (2020) 341–357, https://doi.org/10.1016/j.actamat.2020.04.006.
[243] M.P. Echlin, M. Straw, S. Randolph, J. Filevich, T.M. Pollock, The TriBeam system: Femtosecond laser ablation in situ SEM, Mater. Charact. 100 (2015) 1–12, https://doi.org/10.1016/j.matchar.2014.10.023.
[244] A.T. Polonsky, M.P. Echlin, W.C. Lenthe, R.R. Dehoff, M.M. Kirka, T.M. Pollock, Defects and 3D structural inhomogeneity in electron beam additively manufactured Inconel 718, Mater. Charact. 143 (2018) 171–181, https://doi.org/10.1016/j.matchar.2018.02.020.
[245] A.T. Polonsky, W.C. Lenthe, M.P. Echlin, V. Livescu, G.T. Gray, T.M. Pollock, Solidification-driven Orientation Gradients in Additively Manufactured Stainless Steel, Acta Mater. 183 (2019) 249–260, https://doi.org/10.1016/j.actamat.2019.10.047.
[246] M. Strantza, R.K. Ganeriwala, B. Clausen, T.Q. Phan, L.E. Levine, D. Pagan, W. E. King, N.E. Hodge, D.W. Brown, Coupled experimental and computational study of residual stresses in additively manufactured Ti-6Al-4V components, Mater. Lett. 231 (2018) 221–224, https://doi.org/10.1016/j.matlet.2018.07.141.
[247] G. Zhou, J. Kou, Y. Li, W. Zhu, K. Chen, N. Tamura, Quantitative Scanning Laue Diffraction Microscopy: Application to the Study of 3D Printed Nickel-Based Superalloys, Quantum Beam Sci. 2 (2018) 13, https://doi.org/10.3390/qubs2020013.
[248] M.D. Sangid, T.A. Book, D. Naragani, J. Rotella, P. Ravi, A. Finch, P. Kenesei, J. S. Park, H. Sharma, J. Almer, X. Xiao, Role of heat treatment and build orientation in the microstructure sensitive deformation characteristics of IN718 produced via SLM additive manufacturing, Addit. Manuf. 22 (2018) 479–496, https://doi.org/10.1016/j.addma.2018.04.032.
[249] T.Q. Phan, M. Strantza, M.R. Hill, T.H. Gnaupel-Herold, J. Heigel, C.R. D'Elia, A. T. DeWald, B. Clausen, D.C. Pagan, J.Y. Peter Ko, D.W. Brown, L.E. Levine, Elastic Residual Strain and Stress Measurements and Corresponding Part Deflections of 3D Additive Manufacturing Builds of IN625 AM-Bench Artifacts Using Neutron Diffraction, Synchrotron X-Ray Diffraction, and Contour Method, Integr. Mater. Manuf. Innov. 8 (2019) 318–334, https://doi.org/10.1007/s40192-019-00149-0.
[250] F. Zhang, L.E. Levine, A.J. Allen, M.R. Stoudt, G. Lindwall, E.A. Lass, M. E. Williams, Y. Idell, C.E. Campbell, Effect of heat treatment on the microstructural evolution of a nickel-based superalloy additive-manufactured by laser powder bed fusion, Acta Mater. 152 (2018) 200–214, https://doi.org/10.1016/j.actamat.2018.03.017.
[251] V. Prithivirajan, P. Ravi, D. Naragani, M.D. Sangid, Direct comparison of microstructure-sensitive fatigue crack initiation via crystal plasticity simulations and in situ high-energy X-ray experiments, Mater. Des. 197 (2021), 109216, https://doi.org/10.1016/j.matdes.2020.109216.
[252] J.V. Bernier, R.M. Suter, A.D. Rollett, J. Almer, High Energy Diffraction Microscopy in Materials Science, Annu. Rev. Mater. Res. (2020).
[253] J. Hsieh, Computed tomography principles, design, artifacts, and recent advances, second ed., Wiley, 2009.
[254] A. du Plessis, I. Yadroitsev, I. Yadroitsava, S.G. Le Roux, X-Ray Microcomputed Tomography in Additive Manufacturing: A Review of the Current Technology and Applications, 3D Print, Addit. Manuf. 5 (2018) 227–247, https://doi.org/10.1089/3dp.2018.0060.
[255] J. Damon, S. Dietrich, F. Vollert, J. Gibmeier, V. Schulze, Process dependent porosity and the influence of shot peening on porosity morphology regarding selective laser melted AlSi10Mg parts, Addit. Manuf. 20 (2018) 77–89, https://doi.org/10.1016/j.addma.2018.01.001.
[256] A. du Plessis, S.G. le Roux, J. Waller, P. Sperling, N. Achilles, A. Beerlink, J.-F. Métayer, M. Sinico, G. Probst, W. Dewulf, F. Bittner, H.-J. Endres, M. Willner, Á. Drégelyi-Kiss, T. Zikmund, J. Laznovsky, J. Kaiser, P. Pinter, S. Dietrich, E. Lopez, O. Fitzek, P. Konrad, Laboratory X-ray tomography for metal additive manufacturing: Round robin test, Addit. Manuf. 30 (2019), 100837, https://doi.org/10.1016/J.ADDMA.2019.100837.
[257] A. du Plessis, Effects of process parameters on porosity in laser powder bed fusion revealed by X-ray tomography, Addit. Manuf. 30 (2019), 100871, https://doi.org/10.1016/J.ADDMA.2019.100871.
[258] S. Leuders, M. Vollmer, F. Brenne, T. Tröster, T. Niendorf, Fatigue strength prediction for titanium alloy TiAl6V4 manufactured by selective laser melting, Metall. Mater. Trans. A. 46 (2015) 3816–3823.
[259] E. Chlebus, B. Kuźnicka, R. Dziedzic, T. Kurzynowski, Titanium alloyed with rhenium by selective laser melting, Mater. Sci. Eng. A. 620 (2015) 155–163, https://doi.org/10.1016/J.MSEA.2014.10.021.
[260] H. Attar, L. Löber, A. Funk, M. Calin, L.C. Zhang, K.G. Prashanth, S. Scudino, Y. S. Zhang, J. Eckert, Mechanical behavior of porous commercially pure Ti and Ti–TiB composite materials manufactured by selective laser melting, Mater. Sci. Eng. A. 625 (2015) 350–356, https://doi.org/10.1016/J.MSEA.2014.12.036.
[261] E. Rodriguez, J. Mireles, C.A. Terrazas, D. Espalin, M.A. Perez, R.B. Wicker, Approximation of absolute surface temperature measurements of powder bed fusion additive manufacturing technology using in situ infrared thermography, Addit. Manuf. 5 (2015) 31–39, https://doi.org/10.1016/j.addma.2014.12.001.
[262] X. Cai, A.A. Malcolm, B.S. Wong, Z. Fan, Measurement and characterization of porosity in aluminium selective laser melting parts using X-ray CT, Virtual Phys. Prototyp. 10 (2015) 195–206, https://doi.org/10.1080/17452759.2015.1112412.
[263] I. Maskery, N.T. Aboulkhair, M.R. Corfield, C. Tuck, A.T. Clare, R.K. Leach, R. D. Wildman, I.A. Ashcroft, R.J.M. Hague, Quantification and characterisation of porosity in selectively laser melted Al–Si10–Mg using X-ray computed tomography, Mater. Charact. 111 (2016) 193–204, https://doi.org/10.1016/j.matchar.2015.12.001.

[264] H.D. Carlton, A. Haboub, G.F. Gallegos, D.Y. Parkinson, A.A. MacDowell, Damage evolution and failure mechanisms in additively manufactured stainless steel, Mater. Sci. Eng. A. 651 (2016) 406–414, https://doi.org/10.1016/j.msea.2015.10.073.
[265] F.H. Kim, S.P. Moylan, E.J. Garboczi, J.A. Slotwinski, Investigation of pore structure in cobalt chrome additively manufactured parts using X-ray computed tomography and three-dimensional image analysis, Addit. Manuf. 17 (2017) 23–38, https://doi.org/10.1016/J.ADDMA.2017.06.011.
[266] N.V.Y. Scarlett, P. Tyson, D. Fraser, S. Mayo, A. Maksimenko, Synchrotron X-ray CT characterization of titanium parts fabricated by additive manufacturing. Part II. Defects, J. Synchrotron Radiat. 23 (2016) 1015–1023, https://doi.org/10.1107/S1600577516008018.
[267] S.M. Hojjatzadeh, N.D. Parab, W. Yan, Q. Guo, L. Xiong, C. Zhao, M. Qu, L. I. Escano, X. Xiao, K. Fezzaa, W. Everhart, Pore elimination mechanisms during 3D printing of metals, Nat. Commun. (2019) 1–8, https://doi.org/10.1038/s41467-019-10973-9.
[268] A. Mostafaei, E.T. Hughes, C. Hilla, E.L. Stevens, M. Chmielus, Data on the densification during sintering of binder jet printed samples made from water- and gas-atomized alloy 625 powders, Data Br. 10 (2017) 116–121, https://doi.org/10.1016/j.dib.2016.11.078.
[269] A. du Plessis, P. Sperling, A. Beerlink, O. Kruger, L. Tshabalala, S. Hoosain, S.G. le Roux, Standard method for microCT-based additive manufacturing quality control 3: Surface roughness, MethodsX. 5 (2018) 1111–1116, https://doi.org/10.1016/j.mex.2018.09.004.
[270] P. Hermanek, F. Zanini, S. Carmignato, Traceable porosity measurements in industrial components using X-ray computed tomography, J. Manuf. Sci. Eng. 141 (2019) 1, https://doi.org/10.1115/1.4043192.
[271] T. Zikmund, J. Šalplachta, A. Zatočilová, A. Břínek, L. Pantělejev, R. Štěpánek, D. Koutný, D. Paloušek, J. Kaiser, Computed tomography based procedure for reproducible porosity measurement of additive manufactured samples, NDT E Int. 103 (2019) 111–118, https://doi.org/10.1016/j.ndteint.2019.02.008.
[272] P. Hermanek, S. Carmignato, Establishment of metrological traceability in porosity measurements by x-ray computed tomography, 2017, pp. 22. https://doi.org/10.1117/12.2276942.
[273] A. du Plessis, P. Sperling, A. Beerlink, W.B. du Preez, S.G. le Roux, Standard method for microCT-based additive manufacturing quality control 4: Metal powder analysis, MethodsX. 5 (2018) 1336–1345, https://doi.org/10.1016/j.mex.2018.10.021.
[274] A. du Plessis, P. Sperling, A. Beerlink, W.B. du Preez, S.G. le Roux, Standard method for microCT-based additive manufacturing quality control 1: Porosity analysis, MethodsX. 5 (2018) 1336–1345, https://doi.org/10.1016/j.mex.2018.10.021.
[275] A. du Plessis, P. Sperling, A. Beerlink, L. Tshabalala, S. Hoosain, N. Mathe, S.G. le Roux, Standard method for microCT-based additive manufacturing quality control 2: Density measurement, MethodsX. 5 (2018) 1117–1123, https://doi.org/10.1016/j.mex.2018.09.006.
[276] S. Shrestha, T. Starr, K. Chou, Porosity Analysis in Metal Additive Manufacturing by Micro-CT, in: Proc. ASME 2018, 2019, pp. V002T02A059. https://doi.org/10.1115/imece2018-87897.
[277] R. Chou, J. Milligan, M. Paliwal, M. Brochu, Additive manufacturing of Al-12Si alloy via pulsed selective laser melting, JOM. 67 (2015) 590–596.
[278] J. Mireles, S. Ridwan, P.A. Morton, A. Hinojos, R.B. Wicker, Analysis and correction of defects within parts fabricated using powder bed fusion technology, Surf. Topogr. Metrol. Prop. 3 (2015), 034002, https://doi.org/10.1088/2051-672X/3/3/034002.
[279] S. Siddique, M. Imran, M. Rauer, M. Kaloudis, E. Wycisk, C. Emmelmann, F. Walther, Computed tomography for characterization of fatigue performance of selective laser melted parts, Mater. Des. 83 (2015) 661–669, https://doi.org/10.1016/J.MATDES.2015.06.063.
[280] G. Kasperovich, J. Hausmann, Improvement of fatigue resistance and ductility of TiAl6V4 processed by selective laser melting, J. Mater. Process. Technol. 220 (2015) 202–214, https://doi.org/10.1016/j.jmatprotec.2015.01.025.
[281] S. Tammas-Williams, P.J. Withers, I. Todd, P.B. Prangnell, The Influence of Porosity on Fatigue Crack Initiation in Additively Manufactured Titanium Components, Sci. Rep. 7 (2017) 1–13, https://doi.org/10.1038/s41598-017-06504-5.
[282] Y. Idell, C. Campbell, L. Levine, F. Zhang, G. Olson, D. Snyder, Characterization of Nickel Based Superalloys Processed Through Direct Metal Laser Sintering Technique of Additive Manufacturing, 21 (2015) 465–466.
[283] J.C. Snyder, C.K. Stimpson, K.A. Thole, D.J. Mongillo, Build Direction Effects on Microchannel Tolerance and Surface Roughness, J. Mech. Des. 137 (2015), https://doi.org/10.1115/1.4031071.
[284] S. Berumen, F. Bechmann, S. Lindner, J.P. Kruth, T. Craeghs, Quality control of laser- and powder bed-based Additive Manufacturing (AM) technologies, Phys. Procedia. 5 (2010) 617–622, https://doi.org/10.1016/j.phpro.2010.08.089.
[285] G. Tapia, A. Elwany, A Review on Process Monitoring and Control in Metal-Based Additive Manufacturing, J. Manuf. Sci. Eng. Trans. ASME. 136 (2014), https://doi.org/10.1115/1.4028540.
[286] L. Scime, J. Beuth, Using machine learning to identify in-situ melt pool signatures indicative of flaw formation in a laser powder bed fusion additive manufacturing process, Addit. Manuf. 25 (2019) 151–165, https://doi.org/10.1016/j.addma.2018.11.010.
[287] L. Tan Phuc, M. Seita, A high-resolution and large field-of-view scanner for in-line characterization of powder bed defects during additive manufacturing, Mater. Des. 164 (2019), 107562, https://doi.org/10.1016/j.matdes.2018.107562.
[288] L. Scime, D. Siddel, S. Baird, V. Paquit, Layer-wise anomaly detection and classification for powder bed additive manufacturing processes: A machine-agnostic algorithm for real-time pixel-wise semantic segmentation, Addit. Manuf. (2020), 101453, https://doi.org/10.1016/j.addma.2020.101453.
[289] J.A. Kanko, A.P. Sibley, J.M. Fraser, In situ morphology-based defect detection of selective laser melting through inline coherent imaging, J. Mater. Process. Technol. 231 (2016) 488–500, https://doi.org/10.1016/j.jmatprotec.2015.12.024.
[290] P.J. DePond, G. Guss, S. Ly, N.P. Calta, D. Deane, S. Khairallah, M.J. Matthews, In situ measurements of layer roughness during laser powder bed fusion additive manufacturing using low coherence scanning interferometry, Mater. Des. 154 (2018) 347–359, https://doi.org/10.1016/j.matdes.2018.05.050.
[291] J.L. Bartlett, F.M. Heim, Y.V. Murty, X. Li, In situ defect detection in selective laser melting via full-field infrared thermography, Addit. Manuf. 24 (2018) 595–605, https://doi.org/10.1016/j.addma.2018.10.045.
[292] T. Craeghs, F. Bechmann, S. Berumen, J.P. Kruth, Feedback control of Layerwise Laser Melting using optical sensors, Phys. Procedia. 5 (2010) 505–514, https://doi.org/10.1016/j.phpro.2010.08.078.
[293] T. Craeghs, S. Clijsters, J.P. Kruth, F. Bechmann, M.C. Ebert, Detection of Process Failures in Layerwise Laser Melting with Optical Process Monitoring, Phys. Procedia. 39 (2012) 753–759, https://doi.org/10.1016/j.phpro.2012.10.097.
[294] C.S. Lough, L.I. Escano, M. Qu, C.C. Smith, R.G. Landers, D.A. Bristow, L. Chen, E. C. Kinzel, In-situ optical emission spectroscopy of selective laser melting, J. Manuf. Process. 53 (2020) 336–341, https://doi.org/10.1016/j.jmapro.2020.02.016.
[295] P.A. Hooper, Melt pool temperature and cooling rates in laser powder bed fusion, Addit. Manuf. 22 (2018) 548–559, https://doi.org/10.1016/j.addma.2018.05.032.
[296] D. You, X. Gao, S. Katayama, WPD-PCA-based laser welding process monitoring and defects diagnosis by using FNN and SVM, IEEE Trans. Ind. Electron. 62 (2015) 628–636, https://doi.org/10.1109/TIE.2014.2319216.
[297] B. Yuan, B. Giera, G. Guss, I. Matthews, S. Mcmains, Semi-Supervised Convolutional Neural Networks for In-Situ Video Monitoring of Selective Laser Melting, 2019, pp. 744–753. https://doi.org/10.1109/wacv.2019.00084.
[298] T.G. Fleming, S.G.L. Nestor, T.R. Allen, M.A.B. Smith, N.J. Oukhaled, J.M. Fraser, Tracking and Controlling the Morphology Evolution of 3D Powder-Bed Fusion in situ using Inline Coherent Imaging, ADDMA 100978, Addit. Manuf. (2020), https://doi.org/10.1016/j.addma.2019.100978.
[299] S. Coeck, M. Bisht, J. Plas, F. Verbist, Prediction of lack of fusion porosity in selective laser melting based on melt pool monitoring data, Addit. Manuf. 25 (2019) 347–356, https://doi.org/10.1016/j.addma.2018.11.015.
[300] P. Lott, H. Schleifenbaum, W. Meiners, K. Wissenbach, C. Hinke, J. Bültmann, Design of an optical system for the in situ process monitoring of Selective Laser Melting (SLM), Phys. Procedia. 12 (2011) 683–690, https://doi.org/10.1016/j.phpro.2011.03.085.
[301] B. Yuan, G.M. Guss, A.C. Wilson, S.P. Hau-Riege, P.J. DePond, S. McMains, M. J. Matthews, B. Giera, Machine-Learning-Based Monitoring of Laser Powder Bed Fusion, Adv. Mater. Technol. 3 (2018) 1–6, https://doi.org/10.1002/admt.201800136.
[302] Y.S. Lee, M.M. Kirka, J. Ferguson, V.C. Paquit, Correlations of cracking with scan strategy and build geometry in electron beam powder bed additive manufacturing, Addit. Manuf. 32 (2020), 101031, https://doi.org/10.1016/j.addma.2019.101031.
[303] L. Scime, J. Beuth, A multi-scale convolutional neural network for autonomous anomaly detection and classification in a laser powder bed fusion additive manufacturing process, Addit. Manuf. 24 (2018) 273–286, https://doi.org/10.1016/j.addma.2018.09.034.
[304] S.M. Peyghambarzadeh, A. Hatami, A. Ebrahimi, S.A.A. Fazel, Scientific Paper Photographic Study of Bubble Departure Diameter in Saturated Pool Boiling To, 20 (2012) 1–23. https://doi.org/10.2298/CICEQ120707120P.
[305] E. Uhlmann, R.P. Pontes, A. Laghmouchi, A. Bergmann, Intelligent Pattern Recognition of a SLM Machine Process and Sensor Data, Procedia CIRP. 62 (2017) 464–469, https://doi.org/10.1016/j.procir.2016.06.060.
[306] M. Khanzadeh, S. Chowdhury, M. Marufuzzaman, M.A. Tschopp, Porosity prediction : Supervised-learning of thermal history for direct laser deposition, J. Manuf. Syst. 47 (2018) 69–82, https://doi.org/10.1016/j.jmsy.2018.04.001.
[307] I.A. Okaro, S. Jayasinghe, C. Sutcliffe, K. Black, P. Paoletti, P.L. Green, Automatic fault detection for laser powder-bed fusion using semi-supervised machine learning, Addit. Manuf. 27 (2019) 42–53, https://doi.org/10.1016/j.addma.2019.01.006.
[308] R. Jafari-Marandi, M. Khanzadeh, W. Tian, B. Smith, L. Bian, From in-situ monitoring toward high-throughput process control: cost-driven decision-making framework for laser-based additive manufacturing, J. Manuf. Syst. 51 (2019) 29–41, https://doi.org/10.1016/j.jmsy.2019.02.005.
[309] S. Everton, P. Dickens, C. Tuck, B. Dutton, Using Laser Ultrasound to Detect Subsurface Defects in Metal Laser Powder Bed Fusion Components, Jom. 70 (2018) 378–383, https://doi.org/10.1007/s11837-017-2661-7.
[310] D. You, X. Gao, S. Katayama, Monitoring of high-power laser welding using high-speed photographing and image processing, Mech. Syst. Signal Process. 49 (2014) 39–52.
[311] M. Tehrani-Andani, R. Dehghani, M.R. Karamooz-Ravari, R. Mirzaeifar, J. Ni, Spatter formation in selective laser melting process using multi-laser technology, Mater. Des. 131 (2017) 460–469.
[312] S. Kleszczynski, J. Zur Jacobsmühlen, J.T. Sehrt, G. Witt, Error detection in laser beam melting systems by high resolution imaging, in: 23rd Annu. Int. Solid Free. Fabr. Symp. - An Addit. Manuf. Conf. SFF 2012, 2012, pp. 975–987.

[313] S.J. Foster, K. Carver, R.B. Dinwiddie, F. List, K.A. Unocic, A. Chaudhary, S. S. Babu, Process-Defect-Structure-Property Correlations During Laser Powder Bed Fusion of Alloy 718: Role of In Situ and Ex Situ Characterizations, Metall. Mater. Trans. A Phys. Metall. Mater. Sci. 49 (2018) 5775–5798, https://doi.org/10.1007/s11661-018-4870-2.
[314] P. Fischer, M. Locher, V. Romano, H.P. Weber, S. Kolossov, R. Glardon, Temperature measurements during selective laser sintering of titanium powder, Int. J. Mach. Tools Manuf. 44 (2004) 1293–1296, https://doi.org/10.1016/j.ijmachtools.2004.04.019.
[315] Y. Chivel, I. Smurov, On-line temperature monitoring in selective laser sintering/melting, Phys. Procedia. 5 (2010) 515–521, https://doi.org/10.1016/j.phpro.2010.08.079.
[316] M. Islam, T. Purtonen, H. Piili, A. Salminen, O. Nyrhilä, Temperature profile and imaging analysis of laser additive manufacturing of stainless steel, Phys. Procedia. 41 (2013) 835–842, https://doi.org/10.1016/j.phpro.2013.03.156.
[317] N. Boone, C. Zhu, C. Smith, I. Todd, J.R. Willmott, Thermal near infrared monitoring system for electron beam melting with emissivity tracking, Addit. Manuf. 22 (2018) 601–605, https://doi.org/10.1016/j.addma.2018.06.004.
[318] B. Cheng, S. Price, J. Lydon, K. Cooper, K. Chou, On Process Temperature in Powder-Bed Electron Beam Additive Manufacturing: Model Development and Validation, J. Manuf. Sci. Eng. Trans. ASME. 136 (2014) 1–12, https://doi.org/10.1115/1.4028484.
[319] J. Raplee, A. Plotkowski, M.M. Kirka, R. Dinwiddie, A. Okello, R.R. Dehoff, S. S. Babu, Thermographic Microstructure Monitoring in Electron Beam Additive Manufacturing, Sci. Rep. 7 (2017) 1–16, https://doi.org/10.1038/srep43554.
[320] J.L. McNeil, K. Sisco, C. Frederick, M. Massey, K. Carver, F.L. Iii, C. Qiu, M. Mader, S. Sundarraj, S.S. Babu, In-Situ Monitoring for Defect Identification in Nickel Alloy Complex Geometries Fabricated by L-PBF Additive Manufacturing, Metall. Mater. Trans. A. (2020), https://doi.org/10.1007/s11661-020-06036-0.
[321] N.D. Parab, C. Zhao, R. Cunningham, L.I. Escano, K. Fezzaa, W. Everhart, A. D. Rollett, L. Chen, T. Sun, Ultrafast X-ray imaging of laser–metal additive manufacturing processes, J. Synchrotron Radiat. 25 (2018) 1467–1477, https://doi.org/10.1107/S1600577518009554.
[322] N.D. Parab, J.E. Barnes, C. Zhao, R.W. Cunningham, A.D. Rollett, T. Sun, Real time observation of binder jetting printing process using high-speed X-ray imaging, Sci. Rep. (2019) 28–30.
[323] S.J. Wolff, H. Wu, N. Parab, C. Zhao, K.F. Ehmann, T. Sun, J. Cao, In-situ high-speed X-ray imaging of piezo-driven directed energy deposition additive manufacturing, Sci. Rep. 9 (2019) 1–14, https://doi.org/10.1038/s41598-018-36678-5.
[324] B. Gould, S. Wolff, N. Parab, C. Zhao, M.C. Lorenzo-Martin, K. Fezzaa, A. Greco, T. Sun, In Situ Analysis of Laser Powder Bed Fusion Using Simultaneous High-Speed Infrared and X-ray Imaging, JOM. (2020), https://doi.org/10.1007/s11837-020-04291-5.
[325] Q. Guo, C. Zhao, L.I. Escano, Z. Young, L. Xiong, K. Fezzaa, W. Everhart, B. Brown, T. Sun, L. Chen, Transient dynamics of powder spattering in laser powder bed fusion additive manufacturing process revealed by in-situ high-speed high-energy x-ray imaging, Acta Mater. 151 (2018) 169–180, https://doi.org/10.1016/j.actamat.2018.03.036.
[326] A.A. Martin, N.P. Calta, J.A. Hammons, S.A. Khairallah, M.H. Nielsen, R. M. Shuttlesworth, N. Sinclair, M.J. Matthews, J.R. Jeffries, T.M. Willey, J.R.I. Lee, Ultrafast dynamics of laser-metal interactions in additive manufacturing alloys captured by in situ X-ray imaging, Mater. Today Adv. 1 (2019), 100002, https://doi.org/10.1016/j.mtadv.2019.01.001.
[327] A.A. Martin, N.P. Calta, S.A. Khairallah, J. Wang, P.J. Depond, A.Y. Fong, V. Thampy, G.M. Guss, A.M. Kiss, K.H. Stone, C.J. Tassone, J.N. Weker, M. F. Toney, T. Van Buuren, M.J. Matthews, Dynamics of pore formation during laser powder bed fusion additive manufacturing bed fusion additive manufacturing, Nat. Commun. 10 (2019) 1–10, https://doi.org/10.1038/s41467-019-10009-2.
[328] V. Thampy, A.Y. Fong, N.P. Calta, J. Wang, A.A. Martin, P.J. Depond, A.M. Kiss, G. Guss, Q. Xing, R.T. Ott, A. van Buuren, M.F. Toney, J.N. Weker, M.J. Kramer, M.J. Matthews, C.J. Tassone, K.H. Stone, Subsurface Cooling Rates and Microstructural Response during Laser Based Metal Additive Manufacturing, Sci. Rep. 10 (2020) 1981, https://doi.org/10.1038/s41598-020-58598-z.
[329] S.A. Khairallah, A.A. Martin, J.R.I. Lee, G. Guss, N.P. Calta, J.A. Hammons, M. H. Nielsen, K. Chaput, E. Schwalbach, M.N. Shah, M.G. Chapman, T.M. Willey, A. M. Rubenchik, A.T. Anderson, Y.M. Wang, M.J. Matthews, W.E. King, Controlling interdependent meso-nanosecond dynamics and defect generation in metal 3D printing, Science (80-.) 368 (2020) 660 LP–665 LP, https://doi.org/10.1126/science.aay7830.
[330] C.L.A. Leung, S. Marussi, M. Towrie, R.C. Atwood, P.J. Withers, P.D. Lee, The effect of powder oxidation on defect formation in laser additive manufacturing, Acta Mater. 166 (2019) 294–305, https://doi.org/10.1016/j.actamat.2018.12.027.
[331] P. Lhuissier, X. Bataillon, C. Maestre, J. Sijobert, E. Cabrol, P. Bertrand, E. Boller, A. Rack, J.J. Blandin, L. Salvo, G. Martin, In situ 3D X-ray microtomography of laser-based powder-bed fusion (L-PBF)—A feasibility study, Addit. Manuf. 34 (2020), 101271, https://doi.org/10.1016/j.addma.2020.101271.
[332] C. Kenel, D. Grolimund, X. Li, E. Panepucci, V.A. Samson, D.F. Sanchez, F. Marone, C. Leinenbach, In situ investigation of phase transformations in Ti-6Al-4V under additive manufacturing conditions combining laser melting and high-speed micro-X-ray diffraction, Sci. Rep. 7 (2017) 1–10, https://doi.org/10.1038/s41598-017-16760-0.
[333] N.P. Calta, V. Thampy, D.R.C. Lee, A.A. Martin, R. Ganeriwala, J. Wang, P. J. Depond, T.T. Roehling, A.Y. Fong, A.M. Kiss, C.J. Tassone, K.H. Stone, J. Nelson Weker, M.F. Toney, A.W. Van Buuren, M.J. Matthews, Cooling dynamics of two titanium alloys during laser powder bed fusion probed with in situ X-ray imaging and diffraction, Mater. Des. 195 (2020), 108987, https://doi.org/10.1016/j.matdes.2020.108987.
[334] D.W. Brown, A. Losko, J.S. Carpenter, J.C. Cooley, B. Clausen, J. Dahal, P. Kenesei, J.S. Park, Microstructure Development of 308L Stainless Steel During Additive Manufacturing, Metall. Mater. Trans. A Phys. Metall. Mater. Sci. 50 (2019) 2538–2553, https://doi.org/10.1007/s11661-019-05169-1.
[335] S. Hocine, H. Van Swygenhoven, S. Van Petegem, C. Sin, T. Chang, T. Maimaitiyili, G. Tinti, D.F. Sanchez, D. Grolimund, N. Casati, Operando X-ray diffraction during laser 3D printing, Mater. Today. xxx (2019) 1–12, https://doi.org/10.1016/j.mattod.2019.10.001.
[336] J.T. Norris, C.V. Robino, Development of a time resolved energy absorption measurement technique for laser beam spot welds, Int. Congr. Appl. Lasers Electro-Optics. 2008 (2008) P149, https://doi.org/10.2351/1.5061443.
[337] B.J. Simonds, J. Sowards, J. Hadler, E. Pfeif, B. Wilthan, J. Tanner, C. Harris, P. Williams, J. Lehman, Time-Resolved Absorptance and Melt Pool Dynamics during Intense Laser Irradiation of a Metal, Phys. Rev. Appl. 10 (2018) 44061, https://doi.org/10.1103/PhysRevApplied.10.044061.
[338] B.J. Simonds, J. Tanner, A. Artusio-Glimpse, P.A. Williams, N. Parab, C. Zhao, T. Sun, Simultaneous high-speed x-ray transmission imaging and absolute dynamic absorptance measurements during high-power laser-metal processing, Procedia CIRP. 94 (2020) 775–779, https://doi.org/10.1016/j.procir.2020.09.135.
[339] C.M. Kube, Y. Shu, A. Lew, D. Galles, Real-Time Characterization of Laser-Generated Melt Pools using Ultrasound, Mater. Eval. 76 (2018) 525–534.
[340] S.A. Shevchik, C. Kenel, C. Leinenbach, K. Wasmer, Acoustic emission for in situ quality monitoring in additive manufacturing using spectral convolutional neural networks, Addit. Manuf. 21 (2018) 598–604, https://doi.org/10.1016/j.addma.2017.11.012.
[341] S. Shevchik, T. Le-Quang, B. Meylan, F.V. Farahani, M.P. Olbinado, A. Rack, G. Masinelli, C. Leinenbach, K. Wasmer, Supervised deep learning for real-time quality monitoring of laser welding with X-ray radiographic guidance, Sci. Rep. 10 (2020) 3389, https://doi.org/10.1038/s41598-020-60294-x.
[342] S. Singh, S. Ramakrishna, R. Singh, Material issues in additive manufacturing : A review, J. Manuf. Process. 25 (2017) 185–200, https://doi.org/10.1016/j.jmapro.2016.11.006.
[343] C. Pleass, S. Jothi, Influence of powder characteristics and additive manufacturing process parameters on the microstructure and mechanical behaviour of Inconel 625 fabricated by Selective Laser Melting, Addit. Manuf. 24 (2018) 419–431, https://doi.org/10.1016/j.addma.2018.09.023.
[344] J.H. Tan, W.L.E. Wong, K.W. Dalgarno, An overview of powder granulometry on feedstock and part performance in the selective laser melting process, Addit. Manuf. 18 (2017) 228–255, https://doi.org/10.1016/j.addma.2017.10.011.
[345] M.J. Matthews, G. Guss, S.A. Khairallah, A.M. Rubenchik, P.J. Depond, W.E. King, Denudation of metal powder layers in laser powder-bed fusion processes, Acta Mater. 114 (2016) 33–42, https://doi.org/10.1201/9781315119106.
[346] S. Vock, B. Klöden, A. Kirchner, T. Weißgärber, B. Kieback, Powders for powder bed fusion: a review, Prog. Addit. Manuf. 4 (2019) 383–397, https://doi.org/10.1007/s40964-019-00078-6.
[347] Metal Powder Additive Manufacturing, in: Igor Shishkovsky (Ed.), Anatoliy Popovich Vadim Sufiiarov. Met. Powder Addit. Manuf. New Trends 3D Printing, InTech., 2016.
[348] J. Dawes, R. Bowerman, R. Trepleton, Introduction to the additive manufacturing powder metallurgy supply chain, Johnson Matthey, Technol. Rev. 59 (2015) 243–256, https://doi.org/10.1595/205651315X688686.
[349] N. Kouraytem, E.Q. Li, S.T. Thoroddsen, Formation of microbeads during vapor explosions of Field's metal in water, Phys. Rev. E. 93 (2016) 4–9, https://doi.org/10.1103/PhysRevE.93.063108.
[350] G. Chen, S.Y. Zhao, P. Tan, J. Wang, C.S. Xiang, H.P. Tang, A comparative study of Ti-6Al-4V powders for additive manufacturing by gas atomization, plasma rotating electrode process and plasma atomization, Powder Technol. 333 (2018) 38–46, https://doi.org/10.1016/j.powtec.2018.04.013.
[351] B.H. Rabin, G.R. Smolik, G.E. Korth, Characterization of entrapped gases in rapidly solidified powders, Mater. Sci. Eng. A. 124 (1990) 1–7, https://doi.org/10.1016/0921-5093(90)90328-Z.
[352] H. Bissett, I.J. Van Der Walt, J.L. Havenga, J.T. Nel, Titanium and zirconium metal powder spheroidization by thermal plasma processes, J. South. African Inst. Min. Metall. 115 (2015) 937–942. https://doi.org/10.17159/2411-9717/2015/v115n10a6.
[353] S.P. Narra, Z. Wu, J. Capone, M. Paliwal, A.D. Rollett, Use of Non-Spherical Hydride-DeHydride (HDH) Powders in Powder Bed Fusion Additive Manufacturing, Addit. Manuf. 34 (2020), 101188, https://doi.org/10.1016/j.addma.2020.101188.
[354] Z. Wu, M. Asherloo, R. Jiang, M.H. Delpazir, N. Sivakumar, M. Paliwal, J. Capone, B. Gould, A. Rollett, A. Mostafaei, Study of Printability and Porosity Formation in Laser Powder Bed Fusion Built Hydride-Dehydride (HDH) Ti-6Al-4V, Addit. Manuf. (2021).
[355] M.J. Heiden, L.A. Deibler, J.M. Rodelas, J.R. Koepke, D.J. Tung, D.J. Saiz, B. H. Jared, Evolution of 316L stainless steel feedstock due to laser powder bed fusion process, Addit. Manuf. 25 (2019) 84–103, https://doi.org/10.1016/j.addma.2018.10.019.
[356] Y.F. Ternovoi, A.G. Tsipunov, S.B. Kuratchenko, O.M. Kuimova, K. V. Kondakova, 9, 1985 Accepted:, Poroshkovaya Metall. 265 (1985) 10–14.
[357] U. Fritsching, V. Uhlenwinkel, Hybrid Gas Atomization for Powder Production, Powder Metall. (2012), https://doi.org/10.5772/35807.

[358] J. Zegzulka, D. Gelnar, L. Jezerska, A. Ramirez-Gomez, J. Necas, J. Rozbroj, Internal friction angle of metal powders, Metals (Basel). 8 (2018) 1–12, https://doi.org/10.3390/met8040255.
[359] G. Yablokova, M. Speirs, J. Van Humbeeck, J.P. Kruth, J. Schrooten, R. Cloots, F. Boschini, G. Lumay, J. Luyten, Rheological behavior of β-Ti and NiTi powders produced by atomization for SLM production of open porous orthopedic implants, Powder Technol. (2015), https://doi.org/10.1016/j.powtec.2015.05.015.
[360] K. Amado, A. Schmid, M. Wegener, Advances in SLS powder characterization, 11 (2011) 10–14. https://doi.org/10.16194/j.cnki.31-1059/g4.2011.07.016.
[361] U. Fritsching, Hybrid Gas Atomization for Powder Production, 2012, pp. 13. https://doi.org/10.5772/57353.
[362] N. O, Atomization and granulation, Handbook of non-ferrous metal powders, Elsevier, 2009.
[363] N. Kouraytem, S.T. Thoroddsen, J.O. Marston, Penetration in bimodal, polydisperse granular material, Phys. Rev. E. 94 (2016) 1–8, https://doi.org/10.1103/PhysRevE.94.052902.
[364] H.H. Zhu, J.Y.H. Fuh, L. Lu, The influence of powder apparent density on the density in direct laser-sintered metallic parts, Int. J. Mach. Tools Manuf. 47 (2007) 294–298.
[365] R.M. German, Prediction of sintered density for bimodal powder mixtures, Metall. Trans. A. 23 (1992) 1455–1465.
[366] G. Egger, P.E. Gygax, R. Glardon, N.P. Karapatis, Optimization of powder layer density in selective laser sintering, 10th Solid Free, Fabr. Symp. (1999) 255–263.
[367] R.K. McGEARY, Mechanical Packing of Spherical Particles, J. Am. Ceram. Soc. 44 (1961) 513–522.
[368] R. Streubel, M.B. Wilms, C. Doñate-Buendía, A. Weisheit, S. Barcikowski, J. H. Schleifenbaum, B. Gökce, Depositing laser-generated nanoparticles on powders for additive manufacturing of oxide dispersed strengthened alloy parts via laser metal deposition, Jpn. J. Appl. Phys. 57 (2018), https://doi.org/10.7567/JJAP.57.040310.
[369] M.C.H. Karg, A. Munk, B. Ahuja, M.V. Backer, J.P. Schmitt, C. Stengel, S. V. Kuryntsev, M. Schmidt, Expanding particle size distribution and morphology of aluminium-silicon powders for Laser Beam Melting by dry coating with silica nanoparticles, J. Mater. Process. Technol. 264 (2019) 155–171, https://doi.org/10.1016/j.jmatprotec.2018.08.045.
[370] G. Jacob, C. Brown, A. Donmez, S. Watson, Effects of powder recycling on stainless steel powder and built material properties in metal powder bed fusion processes, NIST Adv. Manuf. Ser. Series 100 (2017) 59.
[371] D. Powell, A.E.W. Rennie, L. Geekie, N. Burns, Understanding powder degradation in metal additive manufacturing to allow the upcycling of recycled powders, J. Clean. Prod. 268 (2020), 122077, https://doi.org/10.1016/j.jclepro.2020.122077.
[372] L.C. Ardila, F. Garciandia, J.B. González-Díaz, P. Álvarez, A. Echeverria, M. M. Petite, R. Deffley, J. Ochoa, Effect of IN718 recycled powder reuse on properties of parts manufactured by means of Selective Laser Melting, Phys. Procedia. 56 (2014) 99–107, https://doi.org/10.1016/j.phpro.2014.08.152.
[373] H. Asgari, C. Baxter, K. Hosseinkhani, M. Mohammadi, On microstructure and mechanical properties of additively manufactured AlSi10Mg_200C using recycled powder, Mater. Sci. Eng. A. 707 (2017) 148–158, https://doi.org/10.1016/j.msea.2017.09.041.
[374] L. Cordova, M. Campos, T. Tinga, Revealing the Effects of Powder Reuse for Selective Laser Melting by Powder Characterization, Jom. 71 (2019) 1062–1072, https://doi.org/10.1007/s11837-018-3305-2.
[375] M. Rafieazad, A. Chatterjee, A.M. Nasiri, Effects of Recycled Powder on Solidification Defects, Microstructure, and Corrosion Properties of DMLS Fabricated AlSi10Mg, Jom. 71 (2019) 3241–3252, https://doi.org/10.1007/s11837-019-03552-2.
[376] M. Taheri Andani, R. Dehghani, M.R. Karamooz-Ravari, R. Mirzaeifar, J. Ni, A study on the effect of energy input on spatter particles creation during selective laser melting process, Addit. Manuf. 20 (2018) 33–43, https://doi.org/10.1016/j.addma.2017.12.009.
[377] Y. Liu, Y. Yang, S. Mai, D. Wang, C. Song, Investigation into spatter behavior during selective laser melting of AISI 316L stainless steel powder, Mater. Des. 87 (2015) 797–806, https://doi.org/10.1016/j.matdes.2015.08.086.
[378] S. Pal, G. Lojen, N. Gubeljak, V. Kokol, I. Drstvensek, Melting, fusion and solidification behaviors of Ti-6Al-4V alloy in selective laser melting at different scanning speeds, Rapid Prototyp. J. 26 (2020) 1209–1215, https://doi.org/10.1108/RPJ-07-2019-0206.
[379] R. German, Powder metallurgy and particulate materials processing: the processes, materials, products, properties, and applications, 2005.
[380] B.L. DeCost, H. Jain, A.D. Rollett, E.A. Holm, Computer vision and machine learning for autonomous characterization of AM powder feedstocks, JOM. 69 (2017) 456–465.
[381] R. Harrison, E.A. Holm, M. De Graef, On the use of 2D moment invariants in the classification of additive manufacturing powder feedstock, Mater. Charact. 149 (2019) 255–263, https://doi.org/10.1016/j.matchar.2019.01.019.
[382] B.M. Morrow, T.J. Lienert, C.M. Knapp, J.O. Sutton, M.J. Brand, R.M. Pacheco, V. Livescu, J.S. Carpenter, G.T. Gray, Impact of Defects in Powder Feedstock Materials on Microstructure of 304L and 316L Stainless Steel Produced by Additive Manufacturing, Metall. Mater. Trans. A Phys. Metall. Mater. Sci. 49 (2018) 3637–3650, https://doi.org/10.1007/s11661-018-4661-9.
[383] A.B. Spierings, N. Herres, G. Levy, Influence of the particle size distribution on surface quality and mechanical properties in AM steel parts, Rapid Prototyp. J. 17 (2011) 195–202, https://doi.org/10.1108/13552541111124770.
[384] H. Irrinki, M. Dexter, B. Barmore, R. Enneti, S. Pasebani, S. Badwe, J. Stitzel, R. Malhotra, S.V. Atre, Effects of Powder Attributes and Laser Powder Bed Fusion (L-PBF) Process Conditions on the Densification and Mechanical Properties of 17–4 PH Stainless Steel, Jom. 68 (2016) 860–868, https://doi.org/10.1007/s11837-015-1770-4.
[385] I.E. Anderson, E.M.H. White, R. Dehoff, Feedstock powder processing research needs for additive manufacturing development, Curr. Opin. Solid State Mater. Sci. 1–8 (2018).
[386] E.A. Périgo, J. Jacimovic, F. García Ferré, L.M. Scherf, Additive manufacturing of magnetic materials, Addit. Manuf. 30 (2019), 100870, https://doi.org/10.1016/j.addma.2019.100870.
[387] V. Chaudhary, S.A. Mantri, R.V. Ramanujan, R. Banerjee, Additive manufacturing of magnetic materials, Prog. Mater. Sci. 114 (2020), 100688, https://doi.org/10.1016/j.pmatsci.2020.100688.
[388] C. Teng, H. Gong, A. Szabo, J.J.S. Dilip, K. Ashby, S. Zhang, N. Patil, D. Pal, B. Stucker, Simulating Melt Pool Shape and Lack of Fusion Porosity for Selective Laser Melting of Cobalt Chromium Components, J. Manuf. Sci. Eng. 139 (2016), 011009, https://doi.org/10.1115/1.4034137.
[389] B. Richter, N. Blanke, C. Werner, N.D. Parab, T. Sun, F. Vollertsen, F. E. Pfefferkorn, High-speed X-ray investigation of melt dynamics during continuous-wave laser remelting of selective laser melted Co-Cr alloy, CIRP Ann. (2019), https://doi.org/10.1016/j.cirp.2019.04.110.
[390] A. Iveković, N. Omidvari, B. Vrancken, K. Lietaert, L. Thijs, K. Vanmeensel, J. Vleugels, J.P. Kruth, Selective laser melting of tungsten and tungsten alloys, Int. J. Refract. Met. Hard Mater. 72 (2018) 27–32.
[391] R.K. Enneti, R. Morgan, S.V. Atre, Effect of process parameters on the Selective Laser Melting (SLM) of tungsten, Int. J. Refract. Met. Hard Mater. 71 (2018) 315–319.
[392] X. Zhou, X. Liu, D. Zhang, Z. Shen, W. Liu, Balling phenomena in selective laser melted tungsten, J. Mater. Process. Technol. 222 (2015) 33–42, https://doi.org/10.1016/j.jmatprotec.2015.02.032.
[393] P. Vora, K. Mumtaz, I. Todd, N. Hopkinson, AlSi12 in-situ alloy formation and residual stress reduction using anchorless selective laser melting, Addit. Manuf. 7 (2015) 12–19, https://doi.org/10.1016/j.addma.2015.06.003.
[394] V.V. Popov, A. Katz-Demyanetz, A. Koptyug, M. Bamberger, Selective electron beam melting of Al0.5CrMoNbTa0.5 high entropy alloys using elemental powder blend, Heliyon. 5 (2019), e01188, https://doi.org/10.1016/j.heliyon.2019.e01188.
[395] C. Galy, E. Le Guen, E. Lacoste, C. Arvieu, Main defects observed in aluminum alloy parts produced by SLM: From causes to consequences, Addit. Manuf. 22 (2018) 165–175, https://doi.org/10.1016/j.addma.2018.05.005.
[396] I.A. Radulov, V.V. Popov, A. Koptyug, F. Maccari, A. Kovalevsky, S. Essel, J. Gassmann, K.P. Skokov, M. Bamberger, Production of net-shape Mn-Al permanent magnets by electron beam melting, Addit. Manuf. 30 (2019), 100787, https://doi.org/10.1016/j.addma.2019.100787.
[397] A. Koptyug, V.V. Popov, C.A. Botero Vega, E. Jiménez-Piqué, A. Katz-Demyanetz, L.E. Rännar, M. Bäckström, Compositionally-tailored steel-based materials manufactured by electron beam melting using blended pre-alloyed powders, Mater. Sci. Eng. A. 771 (2020), https://doi.org/10.1016/j.msea.2019.138587.
[398] M. Fischer, D. Joguet, G. Robin, L. Peltier, P. Laheurte, In situ elaboration of a binary Ti-26Nb alloy by selective laser melting of elemental titanium and niobium mixed powders, Mater. Sci. Eng. C. 62 (2016) 852–859, https://doi.org/10.1016/j.msec.2016.02.033.
[399] L. Yan, X. Chen, W. Li, J. Newkirk, F. Liou, Direct laser deposition of Ti-6Al-4V from elemental powder blends, Rapid Prototyp. J. 22 (2016) 810–816, https://doi.org/10.1108/RPJ-10-2015-0140.
[400] R.M. Clayton, The use of elemental powder mixes in laser-based additive manufacturing, Masters Theses. (2013). http://scholarsmine.mst.edu/masters_theses/7194.
[401] B. Vrancken, L. Thijs, J.P. Kruth, J. Van Humbeeck, Microstructure and mechanical properties of a novel β titanium metallic composite by selective laser melting, Acta Mater. 68 (2014) 150–158, https://doi.org/10.1016/j.actamat.2014.01.018.
[402] A. Uriondo, M. Esperon-Miguez, S. Perinpanayagam, The present and future of additive manufacturing in the aerospace sector: A review of important aspects, Proc. Inst. Mech. Eng. Part G J. Aerosp. Eng. 229 (2015) 2132–2147, https://doi.org/10.1177/0954410014568797.
[403] M. Abdel-Hady Gepreel, M. Niinomi, Biocompatibility of Ti-alloys for long-term implantation, J. Mech. Behav. Biomed. Mater. 20 (2013) 407–415, https://doi.org/10.1016/j.jmbbm.2012.11.014.
[404] F. Wang, Direct laser fabrication of Ti-25V-15Cr-2Al-0.2C (wt pct) burn-resistant titanium alloy, Metall. Mater. Trans. A Phys. Metall. Mater. Sci. 43 (2012) 677–686, https://doi.org/10.1007/s11661-011-0883-9.
[405] H. Schwab, F. Palm, U. Kühn, J. Eckert, Microstructure and mechanical properties of the near-beta titanium alloy Ti-5553 processed by selective laser melting, Mater. Des. 105 (2016) 75–80, https://doi.org/10.1016/j.matdes.2016.04.103.
[406] Y. Zhu, X. Tian, J. Li, H. Wang, The anisotropy of laser melting deposition additive manufacturing Ti-6.5Al-3.5Mo-1.5Zr-0.3Si titanium alloy, Mater. Des. 67 (2015) 538–542, https://doi.org/10.1016/j.matdes.2014.11.001.
[407] J. Hernandez, S.J. Li, E. Martinez, L.E. Murr, X.M. Pan, K.N. Amato, X.Y. Cheng, F. Yang, C.A. Terrazas, S.M. Gaytan, Y.L. Hao, R. Yang, F. Medina, R.B. Wicker, Microstructures and hardness properties for β-phase Ti-24Nb-4Zr-7.9Sn alloy fabricated by electron beam melting, J. Mater. Sci. Technol. 29 (2013) 1011–1017, https://doi.org/10.1016/j.jmst.2013.08.023.
[408] C.Y.-P. in aerospace and defense technologies, undefined 1990, Gas atomized titanium and titanium aluminide alloys, n.d.

[409] A.J. Heidloff, J.R. Rieken, I.E. Anderson, D. Byrd, J. Sears, M. Glynn, R.M. Ward, Advanced gas atomization processing for Ti and Ti alloy powder manufacturing, JOM. 62 (2010) 35–41, https://doi.org/10.1007/s11837-010-0075-x.
[410] S. Pleier, W. Goy, B. Schaub, M. Hohmann, et al., undefined 2004, EIGA–an innovative production method for metal powder from reactive and refractory alloys, n.d.
[411] P. Loewenstein, Specialty powders by the rotating electrode process, Prog. Powder Metall. (1981) 9–21.
[412] P. Roberts, J. Airey, J. Blout, 824,478 JJ Airey - US Patent 4, undefined 1989, Method and apparatus for producing fine metal powder, Google Patents, n.d.
[413] M.I. Boulos, New frontiers in thermal plasmas from space to nanomaterials, Nucl. Eng. Technol. 44 (2012) 1–8, https://doi.org/10.5516/NET.77.2012.001.
[414] Y. Seki, S. Okamoto, H. Takigawa, N. Kawai, Effect of atomization variables on powder characteristics in the high-pressured water atomization process, Met. Powder Rep. 45 (1990) 38–40, https://doi.org/10.1016/S0026-0657(10)80014-1.
[415] F.H. Froes, O.N. Senkov, J.I. Qazi, Hydrogen as a temporary alloying element in titanium alloys: thermohydrogen processing, 2013. https://doi.org/10.1179/095066004225010550.
[416] I. Mellor, L. Grainger, K. Rao, J. Deane, M. Conti, G. Doughty, D. Vaughan, Titanium powder production via the Metalysis process, in: Titan. Powder Metall. Sci. Technol. Appl., Elsevier Inc., 2015, pp. 51–67. https://doi.org/10.1016/B978-0-12-800054-0.00004-6.
[417] M. Qian, F. Froes, Titanium powder metallurgy: science, technology and applications, 2015.
[418] M. Qian, F.H. Sam Froes, Titanium powder metallurgy: Science, technology and applications, Elsevier Inc., 2015. https://doi.org/10.1016/C2013-0-13619-7.
[419] S. Ghods, E. Schultz, C. Wisdom, R. Schur, R. Pahuja, A. Montelione, D. Arola, M. Ramulu, Electron beam additive manufacturing of Ti6Al4V: Evolution of powder morphology and part microstructure with powder reuse, Materialia. 9 (2020), 100631, https://doi.org/10.1016/j.mtla.2020.100631.
[420] A.S.-A.I.W. Conshohocken, undefined PA, undefined USA, undefined 2014, Specification for Additive Manufacturing Titanium-6 Aluminum-4 Vanadium with Powder Bed Fusion, n.d.
[421] M. Simonelli, C. Tuck, N.T. Aboulkhair, I. Maskery, I. Ashcroft, R.D. Wildman, R. Hague, A study on the laser spatter and the oxidation reactions during selective laser melting of 316L stainless steel, Al-Si10-Mg, and Ti-6Al-4V, Metall. Mater. Trans. A. 46 (2015) 3842–3851.
[422] H.P. Tang, M. Qian, N. Liu, X.Z. Zhang, G.Y. Yang, J. Wang, Effect of Powder Reuse Times on Additive Manufacturing of Ti-6Al-4V by Selective Electron Beam Melting, Jom. 67 (2015) 555–563, https://doi.org/10.1007/s11837-015-1300-4.
[423] V. Juechter, T. Scharowsky, R.F. Singer, C. Körner, Processing window and evaporation phenomena for Ti-6Al-4V produced by selective electron beam melting, Acta Mater. 76 (2014) 252–258, https://doi.org/10.1016/j.actamat.2014.05.037.
[424] A. Klassen, T. Scharowsky, C. Körner, Evaporation model for beam based additive manufacturing using free surface lattice Boltzmann methods, J. Phys. D. Appl. Phys. 47 (2014), https://doi.org/10.1088/0022-3727/47/27/275303.
[425] S.L. Semiatin, V.G. Ivanchenko, S.V. Akhonin, O.M. Ivasishin, Diffusion models for evaporation losses during electron-beam melting of alpha/beta-titanium alloys, Metall. Mater. Trans. B Process Metall. Mater. Process. Sci. 35 (2004) 235–245, https://doi.org/10.1007/s11663-004-0025-5.
[426] C. Leyens, M. Peters, Titanium and Titanium Alloys, 2003.
[427] M. Yan, Microstructural characterization of as-sintered titanium and titanium alloys, in: Titan. Powder Metall. Sci. Technol. Appl., Elsevier Inc., 2015, pp. 555–578. https://doi.org/10.1016/B978-0-12-800054-0.00029-0.
[428] R. Ding, Z.X. Guo, A. Wilson, Microstructural evolution of a Ti-6Al-4V alloy during thermomechanical processing, Mater. Sci. Eng. A. 327 (2002) 233–245, https://doi.org/10.1016/S0921-5093(01)01531-3.
[429] S.M. Kelly, S.L. Kampe, Microstructural Evolution in Laser-Deposited Multilayer Ti-6Al-4V Builds: Part II. Thermal Modeling, n.d.
[430] T. Ahmed, H.J. Rack, Phase transformations during cooling in α + β titanium alloys, Mater. Sci. Eng. A. 243 (1998) 206–211, https://doi.org/10.1016/s0921-5093(97)00802-2.
[431] X. Zhao, S. Li, M. Zhang, Y. Liu, T.B. Sercombe, S. Wang, Y. Hao, R. Yang, L. E. Murr, Comparison of the microstructures and mechanical properties of Ti-6Al-4V fabricated by selective laser melting and electron beam melting, Mater. Des. 95 (2016) 21–31, https://doi.org/10.1016/j.matdes.2015.12.135.
[432] H.K. Rafi, N.V. Karthik, H. Gong, T.L. Starr, B.E. Stucker, Microstructures and mechanical properties of Ti6Al4V parts fabricated by selective laser melting and electron beam melting, J. Mater. Eng. Perform. 22 (2013) 3872–3883, https://doi.org/10.1007/s11665-013-0658-0.
[433] B. Vrancken, L. Thijs, J.P. Kruth, J. Van Humbeeck, Heat treatment of Ti6Al4V produced by Selective Laser Melting: Microstructure and mechanical properties, J. Alloys Compd. 541 (2012) 177–185, https://doi.org/10.1016/j.jallcom.2012.07.022.
[434] L.E. Murr, E.V. Esquivel, S.A. Quinones, S.M. Gaytan, M.I. Lopez, E.Y. Martinez, F. Medina, D.H. Hernandez, E. Martinez, J.L. Martinez, S.W. Stafford, D.K. Brown, T. Hoppe, W. Meyers, U. Lindhe, R.B. Wicker, Microstructures and mechanical properties of electron beam-rapid manufactured Ti-6Al-4V biomedical prototypes compared to wrought Ti-6Al-4V, Mater. Charact. 60 (2009) 96–105, https://doi.org/10.1016/j.matchar.2008.07.006.
[435] K. Puebla, L.E. Murr, S.M. Gaytan, E. Martinez, F. Medina, R.B. Wicker, Effect of Melt Scan Rate on Microstructure and Macrostructure for Electron Beam Melting of Ti-6Al-4V, Mater. Sci. Appl. 3 (2012) 259–264, https://doi.org/10.4236/msa.2012.35038.
[436] P.A. Kobryn, S.L. Semiatin, Microstructure and texture evolution during solidification processing of Ti-6A1-4V, J. Mater. Process. Technol. 135 (2003) 330–339, https://doi.org/10.1016/S0924-0136(02)00865-8.
[437] S.P. Narra, R. Cunningham, J. Beuth, A.D. Rollett, Location specific solidification microstructure control in electron beam melting of Ti-6Al-4V, Addit. Manuf. 19 (2018) 160–166, https://doi.org/10.1016/j.addma.2017.10.003.
[438] A. Sengupta, S.K. Putatunda, L. Bartosiewicz, J. Hangas, P.J. Nailos, M. Peputapeck, F.E. Alberts, Tensile behavior of a new single-crystal nickel-based superalloy (CMSX-4) at room and elevated temperatures, J. Mater. Eng. Perform. 3 (1994) 73–81, https://doi.org/10.1007/BF02654502.
[439] W.S. Walston, A. Cetel, R. Mackay, K. Ohara, D. Duhl, R. Dreshfield, Joint Development of a Fourth Generation Single Crystal Superalloy, Superalloys 2004, TMS, 2004, pp. 15–24.
[440] J.F. Barker, E.W. Ross, J.F. Radavich, Long Time Stability Of Inconel 718, JOM. 22 (1970) 31–41, https://doi.org/10.1007/BF03355624.
[441] T.M. Pollock, S. Tin, Nickel-Based Superalloys for Advanced Turbine Engines: Chemistry, Microstructure and Properties, J. Propuls. Power. 22 (2006) 361–374, https://doi.org/10.2514/1.18239.
[442] D. Furrer, H. Fecht, Ni-based superalloys for turbine discs, JOM. 51 (1999) 14–17, https://doi.org/10.1007/s11837-999-0005-y.
[443] G.P. Sabol, R. Stickler, Microstructure of Nickel-Based Superalloys, Phys. Status Solidi. 35 (1969) 11–52.
[444] S. Sanchez, P. Smith, Z. Xu, G. Gaspard, C.J. Hyde, W.W. Wits, I.A. Ashcroft, H. Chen, A.T. Clare, Powder Bed Fusion of nickel-based superalloys: A review, Int. J. Mach. Tools Manuf. 165 (2021), https://doi.org/10.1016/j.ijmachtools.2021.103729.
[445] H.J. Wagner, A.M. Hall, Physical Metallurgy of Alloy 718, Columbus, OH, 1965.
[446] J.M. Oblak, D.F. Paulonis, D.S. Duvall, Coherency strengthening in Ni base alloys hardened by DO22 γ' precipitates, Metall. Trans. 5 (1974) 143, https://doi.org/10.1007/BF02642938.
[447] S.H. Reichman, J.W. Smythe, New Developments in Superalloy Powders, in: H. H. Hausner (Ed.), Mod, Dev. Powder Metall, Springer, US, Boston, MA, 1971, pp. 73–84.
[448] G. He, F. Liu, L. Huang, Z. Huang, L. Jiang, Microstructure evolutions and nucleation mechanisms of dynamic recrystallization of a powder metallurgy Ni-based superalloy during hot compression, Mater. Sci. Eng. A. 677 (2016) 496–504, https://doi.org/10.1016/j.msea.2016.09.083.
[449] G.A. Rao, K.S. Prasad, M. Kumar, M. Srinivas, D.S. Sarma, Characterisation of hot isostatically pressed nickel base superalloy Inconel* 718, Mater. Sci. Technol. 19 (2003) 313–321, https://doi.org/10.1179/026708303225010605.
[450] L. Chang, W. Sun, Y. Cui, F. Zhang, R. Yang, Effect of heat treatment on microstructure and mechanical properties of the hot-isostatic-pressed Inconel 718 powder compact, J. Alloys Compd. 590 (2014) 227–232, https://doi.org/10.1016/j.jallcom.2013.12.107.
[451] V.D. Barth, E.T. Hall, J.G. Kura, H. Mc Curdy, H.O. Mc Intire, W.H. Safranek, The making of nickel and nickel-alloy shapes by casting, powder metallurgy, electroforming, chemical vapor deposition, and metal spraying, 1965.
[452] C. Zhong, J. Chen, S. Linnenbrink, A. Gasser, S. Sui, R. Poprawe, A comparative study of Inconel 718 formed by High Deposition Rate Laser Metal Deposition with GA powder and PREP powder, Mater. Des. 107 (2016) 386–392, https://doi.org/10.1016/j.matdes.2016.06.037.
[453] M. Ramsperger, R.F. Singer, C. Körner, Microstructure of the Nickel-Base Superalloy CMSX-4 Fabricated by Selective Electron Beam Melting, Metall. Mater. Trans. A Phys. Metall. Mater. Sci. 47 (2016) 1469–1480, https://doi.org/10.1007/s11661-015-3300-y.
[454] Q. Jia, D. Gu, Selective laser melting additive manufacturing of Inconel 718 superalloy parts: Densification, microstructure and properties, J. Alloys Compd. 585 (2014) 713–721, https://doi.org/10.1016/j.jallcom.2013.09.171.
[455] M.B. Henderson, D. Arrell, R. Larsson, M. Heobel, G. Marchant, Nickel based superalloy welding practices for industrial gas turbine applications, Sci. Technol. Weld. Join. 9 (2004) 13.
[456] C. Kantzos, J. Pauza, R. Cunningham, S.P. Narra, J. Beuth, A. Rollett, An Investigation of Process Parameter Modifications on Additively Manufactured Inconel 718 Parts, J. Mater. Eng. Perform. (2018), https://doi.org/10.1007/s11665-018-3612-3.
[457] V.A. Popovich, E.V. Borisov, A.A. Popovich, V.S. Sufiiarov, D.V. Masaylo, L. Alzina, Functionally graded Inconel 718 processed by additive manufacturing : Crystallographic texture, anisotropy of microstructure and mechanical properties Functionally graded Inconel 718 processed by additive manufacturing : Crystallographic texture, anisot, JMADE. 114 (2016) 441–449, https://doi.org/10.1016/j.matdes.2016.10.075.
[458] H.E. Helmer, C. Körner, R.F. Singer, Additive manufacturing of nickel-based superalloy Inconel 718 by selective electron beam melting: Processing window and microstructure, J. Mater. Res. 29 (2014) 1987–1996, https://doi.org/10.1557/jmr.2014.192.
[459] T. Trosch, J. Strößner, R. Völkl, U. Glatzel, Microstructure and mechanical properties of selective laser melted Inconel 718 compared to forging and casting, Mater. Lett. 164 (2016) 428–431, https://doi.org/10.1016/j.matlet.2015.10.136.
[460] Z. Wang, E. Denlinger, P. Michaleris, A.D. Stoica, D. Ma, A.M. Beese, Residual stress mapping in Inconel 625 fabricated through additive manufacturing: Method for neutron diffraction measurements to validate thermomechanical model predictions, Mater. Des. 113 (2017) 169–177, https://doi.org/10.1016/j.matdes.2016.10.003.
[461] E.A. Lass, M.R. Stoudt, M.E. Williams, M.B. Katz, L.E. Levine, T.Q. Phan, T. H. Gnaeupel-Herold, D.S. Ng, Formation of the Ni3Nb δ-Phase in Stress-Relieved Inconel 625 Produced via Laser Powder-Bed Fusion Additive Manufacturing,

Metall. Mater. Trans. A Phys. Metall. Mater. Sci. 48 (2017) 5547–5558, https://doi.org/10.1007/s11661-017-4304-6.
[462] J.A. Muñiz-Lerma, Y. Tian, X. Wang, R. Gauvin, M. Brochu, Microstructure evolution of Inconel 738 fabricated by pulsed laser powder bed fusion, Prog. Addit. Manuf. 4 (2019) 97–107, https://doi.org/10.1007/s40964-018-0062-2.
[463] L.E. Murr, E. Martinez, X.M. Pan, S.M. Gaytan, J.A. Castro, C.A. Terrazas, F. Medina, R.B. Wicker, D.H. Abbott, Microstructures of Rene 142 nickel-based superalloy fabricated by electron beam melting, Acta Mater. 61 (2013) 4289–4296, https://doi.org/10.1016/j.actamat.2013.04.002.
[464] Y. Tian, D. Tomus, P. Rometsch, X. Wu, Influences of processing parameters on surface roughness of Hastelloy X produced by selective laser melting, Addit. Manuf. 13 (2017) 103–112, https://doi.org/10.1016/j.addma.2016.10.010.
[465] R. Esmaeilizadeh, U. Ali, A. Keshavarzkermani, Y. Mahmoodkhani, E. Marzbanrad, E. Toyserkani, On the effect of spatter particles distribution on the quality of Hastelloy X parts made by laser powder-bed fusion additive manufacturing, J. Manuf. Process. 37 (2019) 11–20, https://doi.org/10.1016/j.jmapro.2018.11.012.
[466] T. Bauer, K. Dawson, A.B. Spierings, K. Wegener, Microstructure and mechanical characterisation of SLM processed Haynes® 230®, in: Proc. 26th Annu. Int. Solid Free. Fabr. Symp., 2015, pp. 813–822.
[467] Y. Ahn, B. Yoon, H. Kim, C. Lee, Effect of dilution on the behavior of solidification cracking in PTAW overlay deposit on Ni-Base superalloys, Met. Mater. Int. 8 (2002) 469–477, https://doi.org/10.1007/BF03027245.
[468] J.M. Kilnowski, Weldability of a Nickel-based Superalloy, 1994.
[469] E. Chauvet, P. Kontis, E.A. Jägle, B. Gault, D. Raabe, C. Tassin, J.-J. Blandin, R. Dendievel, B. Vayre, S. Abed, G. Martin, Hot cracking mechanism affecting a non-weldable Ni-based superalloy produced by selective electron Beam Melting, Acta Mater. 142 (2018) 82–94, https://doi.org/10.1016/j.actamat.2017.09.047.
[470] L.N. Carter, M.M. Attallah, R.C. Reed, Laser powder bed fabrication of nickel-base superalloys: influence of parameters; characterisation, quantification and mitigation of cracking, Superalloys 2012 (2012) 577–586.
[471] G. Çam, M. Koçak, Progress in joining of advanced materials, Int. Mater. Rev. 43 (1998) 1–44, https://doi.org/10.1179/imr.1998.43.1.1.
[472] A. Sato, Y.-L. Chiu, R.C. Reed, Oxidation of nickel-based single-crystal superalloys for industrial gas turbine applications, Acta Mater. 59 (2011) 225–240, https://doi.org/10.1016/j.actamat.2010.09.027.
[473] A.G. Evans, M.Y. He, A. Suzuki, M. Gigliotti, B. Hazel, T.M. Pollock, A mechanism governing oxidation-assisted low-cycle fatigue of superalloys, Acta Mater. 57 (2009) 2969–2983, https://doi.org/10.1016/j.actamat.2009.02.047.
[474] Y.N. Zhang, X. Cao, P. Wanjara, M. Medraj, Oxide films in laser additive manufactured Inconel 718, Acta Mater. 61 (2013) 6562–6576, https://doi.org/10.1016/j.actamat.2013.07.039.
[475] V.D. Divya, R. Muñoz-Moreno, O.M.D.M. Messé, J.S. Barnard, S. Baker, T. Illston, H.J. Stone, Microstructure of selective laser melted CM247LC nickel-based superalloy and its evolution through heat treatment, Mater. Charact. 114 (2016) 62–74, https://doi.org/10.1016/j.matchar.2016.02.004.
[476] M. Cloots, P.J. Uggowitzer, K. Wegener, Investigations on the microstructure and crack formation of IN738LC samples processed by selective laser melting using Gaussian and doughnut profiles, Mater. Des. 89 (2016) 770–784, https://doi.org/10.1016/j.matdes.2015.10.027.
[477] S. Huang, C. Ye, H. Zhao, Z. Fan, Additive Manufacturing of Thin Alumina Ceramic Cores Using Binder-Jetting, Addit. Manuf. 29 (2019), 100802, https://doi.org/10.1016/j.addma.2019.100802.
[478] M. Wong, S. Tsopanos, C.J. Sutcliffe, I. Owen, Selective laser melting of heat transfer devices, Rapid Prototyp. J. 13 (2007) 291–297, https://doi.org/10.1108/13552540710824797.
[479] E.O. Olakanmi, R.F. Cochrane, K.W. Dalgarno, A review on selective laser sintering/melting (SLS/SLM) of aluminium alloy powders: Processing, microstructure, and properties, Prog. Mater. Sci. 74 (2015) 401–477, https://doi.org/10.1016/j.pmatsci.2015.03.002.
[480] V.G. Gopienko, Production of Aluminum Powders, in: Handb. Non-Ferrous Met. Powders, Elsevier, 2019, pp. 459–480. https://doi.org/10.1016/b978-0-08-100543-9.00015-4.
[481] S.H. Huo, M. Qian, G.B. Schaffer, E. Crossin, Aluminium powder metallurgy, in: Fundam. Alum. Metall. Prod. Process. Appl., Elsevier Ltd., 2010, pp. 655–701. https://doi.org/10.1533/9780857090256.3.655.
[482] O.D. Neikov, G.I. Vasilieva, A.V. Sameljuk, A.V. Krajnikov, Water atomised aluminium alloy powders, Mater. Sci. Eng. A. 383 (2004) 7–13, https://doi.org/10.1016/j.msea.2004.02.030.
[483] O.N.-P. of 2000 P.M.W. Congress, undefined 2000, Water atomized powder technologies for advanced aluminum alloy production, n.d.
[484] O.D. Neikov, Production of Aluminum Alloy Powders, in: Handb. Non-Ferrous Met. Powders, Elsevier, 2019, pp. 481–531. https://doi.org/10.1016/b978-0-08-100543-9.00016-6.
[485] M.L. Montero Sistiaga, R. Mertens, B. Vrancken, X. Wang, B. Van Hooreweder, J. P. Kruth, J., Van Humbeeck, Changing the alloy composition of Al7075 for better processability by selective laser melting, J. Mater. Process. Technol. 238 (2016) 437–445, https://doi.org/10.1016/j.jmatprotec.2016.08.003.
[486] N. Kaufmann, M. Imran, T.M. Wischeropp, C. Emmelmann, S. Siddique, F. Walther, Influence of process parameters on the quality of aluminium alloy en AW 7075 using Selective Laser Melting (SLM), in: Phys. Procedia, Elsevier B.V., 2016, pp. 918–926, https://doi.org/10.1016/j.phpro.2016.08.096.
[487] H. Zhao, D.R. White, T. Debroy, Current issues and problems in laser welding of automotive aluminium alloys, 2013. https://doi.org/10.1179/095066099101528298.
[488] X. Cao, W. Wallace, J.P. Immarigeon, C. Poon, Research and progress in laser welding of wrought aluminum alloys. II. Metallurgical microstructures, defects, and mechanical properties, Mater. Manuf. Process. 18 (2003) 23–49, https://doi.org/10.1081/AMP-120017587.
[489] E.O. Olakanmi, R. Cochrane, K. Dalgarno, E.O. Olakanmi, R.F. Cochrane, K.W. Dalgarno, Spheroidisation and oxide disruption phenomena in direct selective laser melting (SLM) of pre-alloyed Al-Mg and Al-Si powders, 2009.
[490] E. Louvis, P. Fox, C.J. Sutcliffe, Selective laser melting of aluminium components, J. Mater. Process. Technol. 211 (2011) 275–284, https://doi.org/10.1016/j.jmatprotec.2010.09.019.
[491] N.T. Aboulkhair, C. Tuck, I. Ashcroft, I. Maskery, N.M. Everitt, On the Precipitation Hardening of Selective Laser Melted AlSi10Mg, Metall. Mater. Trans. A Phys. Metall. Mater. Sci. 46 (2015) 3337–3341, https://doi.org/10.1007/s11661-015-2980-7.
[492] U. Tradowsky, J. White, R.M. Ward, N. Read, W. Reimers, M.M. Attallah, Selective laser melting of AlSi10Mg: Influence of post-processing on the microstructural and tensile properties development, Mater. Des. 105 (2016) 212–222.
[493] K. Kempen, L. Thijs, J. Van Humbeeck, J.-P. Kruth, Mechanical Properties of AlSi10Mg Produced by Selective Laser Melting, Phys. Procedia. 39 (2012) 439–446.
[494] M. Tang, P.C. Pistorius, Oxides, porosity and fatigue performance of AlSi10Mg parts produced by selective laser melting, Int. J. Fatigue. 94 (2017) 192–201, https://doi.org/10.1016/j.ijfatigue.2016.06.002.
[495] K.G. Prashanth, S. Scudino, H.J. Klauss, K.B. Surreddi, L. Löber, Z. Wang, A. K. Chaubey, U. Kühn, J. Eckert, Microstructure and mechanical properties of Al-12Si produced by selective laser melting: Effect of heat treatment, Mater. Sci. Eng. A. 590 (2014) 153–160, https://doi.org/10.1016/j.msea.2013.10.023.
[496] H. Zhang, H. Zhu, T. Qi, Z. Hu, X. Zeng, Selective laser melting of high strength Al-Cu-Mg alloys: Processing, microstructure and mechanical properties, Mater. Sci. Eng. A. 656 (2016) 47–54, https://doi.org/10.1016/j.msea.2015.12.101.
[497] M. Ameli, B. Agnew, P.S. Leung, B. Ng, C.J. Sutcliffe, J. Singh, R. McGlen, A novel method for manufacturing sintered aluminium heat pipes (SAHP), Appl. Therm. Eng. 52 (2013) 498–504, https://doi.org/10.1016/j.applthermaleng.2012.12.011.
[498] H.R. Kotadia, G. Gibbons, A. Das, P.D. Howes, A review of Laser Powder Bed Fusion Additive Manufacturing of aluminium alloys: Microstructure and properties, Addit. Manuf. 46 (2021), 102155, https://doi.org/10.1016/j.addma.2021.102155.
[499] S. Kou, Solidification and liquation cracking issues in welding, Jom. 55 (2003) 37–42, https://doi.org/10.1007/s11837-003-0137-4.
[500] F.M. Ghaini, M. Sheikhi, M.J. Torkamany, J. Sabbaghzadeh, The relation between liquation and solidification cracks in pulsed laser welding of 2024 aluminium alloy, Mater. Sci. Eng. A. 519 (2009) 167–171, https://doi.org/10.1016/j.msea.2009.04.056.
[501] J.H.-M. Park, undefined OH, undefined 1984, Aluminium: Properties and Physical Metallurgy, by ASM, n.d.
[502] G. Levi, W.D. Kaplan, Oxygen induced interfacial phenomena during wetting of alumina by liquid aluminium, Acta Mater. 50 (2002) 75–88, https://doi.org/10.1016/S1359-6454(01)00333-0.
[503] J.H. Martin, B.D. Yahata, J.M. Hundley, J.A. Mayer, T.A. Schaedler, T.M. Pollock, 3D printing of high-strength aluminium alloys, Nature. 549 (2017) 365–369, https://doi.org/10.1038/nature23894.
[504] V. Laurent, D. Chatain, C. Chatillon, N. Eustathopoulos, Wettability of monocrystalline alumina by aluminium between its melting point and 1273 K, Acta Metall. 36 (1988) 1797–1803, https://doi.org/10.1016/0001-6160(88)90248-9.
[505] H. John, H. Hausner, Wetting of Aluminum Oxide by Liquid Aluminum (1986).
[506] F. Abe, K. Osakada, M. Shiomi, K. Uematsu, M. Matsumoto, The manufacturing of hard tools from metallic powders by selective laser melting, n.d.
[507] D.R. Gaskell, D.R. Gaskell, Introduction to the thermodynamics of materials, Taylor & Francis, 1995.
[508] N. Read, W. Wang, K. Essa, M.M. Attallah, Selective laser melting of AlSi10Mg alloy: Process optimisation and mechanical properties development, Mater. Des. 65 (2015) 417–424, https://doi.org/10.1016/j.matdes.2014.09.044.
[509] E. Brandl, U. Heckenberger, V. Holzinger, D. Buchbinder, Additive manufactured AlSi10Mg samples using Selective Laser Melting (SLM): Microstructure, high cycle fatigue, and fracture behavior, Mater. Des. 34 (2012) 159–169.
[510] C. Weingarten, D. Buchbinder, N. Pirch, W. Meiners, K. Wissenbach, R. Poprawe, Formation and reduction of hydrogen porosity during selective laser melting of AlSi10Mg, J. Mater. Process. Technol. 221 (2015) 112–120, https://doi.org/10.1016/j.jmatprotec.2015.02.013.
[511] A. Zadi-Maad, R. Rohib, A. Irawan, Additive manufacturing for steels: A review, IOP Conf. Ser. Mater. Sci. Eng. 285 (2018).
[512] K.D. Fuchs, Hot-work steels with improved properties for diecasting applications, Foundry Trade J. 183 (2009) 219–221.
[513] G.L. Winters, M.J. Nutt, Stainless Steels for Medical and Surgical Applications, Stainl. Steels Med. Surg. Appl. (2003), https://doi.org/10.1520/stp1438-eb.
[514] A.M. Bayer, B.A. Becherer, T. Vasco, Bulletin: High Speed Tool Steels, Latrobe Spec. Steel Co. 16 (n.d.) 10–11.
[515] Z. Gan, G. Yu, X. He, S. Li, Surface-active element transport and its e ff ect on liquid metal fl ow in laser- assisted additive manufacturing, Int. Commun. Heat Mass Transf. 86 (2017) 206–214, https://doi.org/10.1016/j.icheatmasstransfer.2017.06.007.
[516] A. Hinojos, J. Mireles, A. Reichardt, P. Frigola, P. Hosemann, L.E. Murr, R. B. Wicker, Joining of Inconel 718 and 316 Stainless Steel using electron beam

melting additive manufacturing technology, Mater. Des. 94 (2016) 17–27, https://doi.org/10.1016/j.matdes.2016.01.041.
[517] H. Chen, D. Gu, D. Dai, C. Ma, M. Xia, Microstructure and composition homogeneity, tensile property, and underlying thermal physical mechanism of selective laser melting tool steel parts, Mater. Sci. Eng. A. 682 (2017) 279–289, https://doi.org/10.1016/j.msea.2016.11.047.
[518] L.M.S. Santos, J.A.M. Ferreira, J.S. Jesus, J.M. Costa, C. Capela, Fatigue behaviour of selective laser melting steel components, Theor. Appl. Fract. Mech. 85 (2016) 9–15, https://doi.org/10.1016/j.tafmec.2016.08.011.
[519] E. Liverani, S. Toschi, L. Ceschini, A. Fortunato, Effect of selective laser melting (SLM) process parameters on microstructure and mechanical properties of 316L austenitic stainless steel, J. Mater. Process. Technol. 249 (2017) 255–263, https://doi.org/10.1016/j.jmatprotec.2017.05.042.
[520] R. Mertens, B. Vrancken, N. Holmstock, Y. Kinds, J.P. Kruth, J. Van Humbeeck, Influence of powder bed preheating on microstructure and mechanical properties of H13 tool steel SLM parts, Phys. Procedia. 83 (2016) 882–890, https://doi.org/10.1016/j.phpro.2016.08.092.
[521] B. AlMangour, D. Grzesiak, J.M. Yang, Nanocrystalline TiC-reinforced H13 steel matrix nanocomposites fabricated by selective laser melting, Mater. Des. 96 (2016) 150–161, https://doi.org/10.1016/j.matdes.2016.02.022.
[522] R. Cottam, J. Wang, V. Luzin, Characterization of microstructure and residual stress in a 3D H13 tool steel component produced by additive manufacturing, J. Mater. Res. 29 (2014) 1978–1986, https://doi.org/10.1557/jmr.2014.190.
[523] G. Miranda, S. Faria, F. Bartolomeu, E. Pinto, S. Madeira, A. Mateus, P. Carreira, N. Alves, F.S. Silva, O. Carvalho, Predictive models for physical and mechanical properties of 316L stainless steel produced by selective laser melting, Mater. Sci. Eng. A. 657 (2016) 43–56, https://doi.org/10.1016/j.msea.2016.01.028.
[524] B. Song, Z. Wang, Q. Yan, Y. Zhang, J. Zhang, C. Cai, Q. Wei, Y. Shi, Integral method of preparation and fabrication of metal matrix composite: Selective laser melting of in-situ nano/submicro-sized carbides reinforced iron matrix composites, Mater. Sci. Eng. A. 707 (2017) 478–487, https://doi.org/10.1016/j.msea.2017.09.092.
[525] X. Yan, C. Huang, C. Chen, R. Bolot, L. Dembinski, R. Huang, W. Ma, H. Liao, M. Liu, Additive manufacturing of WC reinforced maraging steel 300 composites by cold spraying and selective laser melting, Surf. Coatings Technol. 371 (2019) 161–171, https://doi.org/10.1016/j.surfcoat.2018.03.072.
[526] D. Galicki, F. List, S.S. Babu, A. Plotkowski, H.M. Meyer, R. Seals, C. Hayes, Localized Changes of Stainless Steel Powder Characteristics During Selective Laser Melting Additive Manufacturing, Metall. Mater. Trans. A Phys. Metall. Mater. Sci. 50 (2019) 1582–1605, https://doi.org/10.1007/s11661-018-5072-7.
[527] L. Hitzler, C. Janousch, J. Schanz, M. Merkel, B. Heine, F. Mack, W. Hall, A. Öchsner, Direction and location dependency of selective laser melted AlSi10Mg specimens, J. Mater. Process. Technol. 243 (2017) 48–61, https://doi.org/10.1016/j.jmatprotec.2016.11.029.
[528] T. Fedina, J. Sundqvist, J. Powell, A.F.H. Kaplan, A comparative study of water and gas atomizedlow alloy steel powders for additive manufacturing, Addit. Manuf. (2020), 101675, https://doi.org/10.1016/j.addma.2020.101675.
[529] C.L.A. Leung, S. Marussi, M. Towrie, J. del Val Garcia, R.C. Atwood, A.J. Bodey, J. R. Jones, P.J. Withers, P.D. Lee, C. Lun, A. Leung, S. Marussi, M. Towrie, V. Garcia, R.C. Atwood, A.J. Bodey, J.R. Jones, P.J. Withers, P.D. Lee, C.L. A. Leung, S. Marussi, M. Towrie, J. del Val Garcia, R.C. Atwood, A.J. Bodey, J. R. Jones, P.J. Withers, P.D. Lee, Laser-matter interactions in additive manufacturing of stainless steel SS316L and 13–93 bioactive glass revealed by in situ X-ray imaging, Addit. Manuf. 24 (2018) 647–657, https://doi.org/10.1016/j.addma.2018.08.025.
[530] A. Sharan, A.W. Cramb, Surface Tension and Wettability Studies of Liquid Fe-Ni-O Alloys, 28 (1997) 465–472.
[531] C.X. Zhao, C. Kwakernaak, Y. Pan, I.M. Richardson, Z. Saldi, S. Kenjeres, The effect of oxygen on transitional Marangoni flow in laser spot welding, Acta Mater. 58 (2010) 6345–6357, https://doi.org/10.1016/j.actamat.2010.07.056.
[532] S.N. Neikov, D. Oleg, N.V. Yefimov, Handbook of non-ferrous metal powders: technologies and applications, Elsevier (2009).
[533] P. Sun, Z.Z. Fang, Y. Zhang, Y. Xia, Review of the Methods for Production of Spherical Ti and Ti Alloy Powder, Jom. 69 (2017) 1853–1860, https://doi.org/10.1007/s11837-017-2513-5.
[534] L.E. Murr, S.M. Gaytan, A. Ceylan, E. Martinez, J.L. Martinez, D.H. Hernandez, B. I. Machado, D.A. Ramirez, F. Medina, S. Collins, R.B. Wicker, Characterization of titanium aluminide alloy components fabricated by additive manufacturing using electron beam melting, Acta Mater. 58 (2010) 1887–1894, https://doi.org/10.1016/j.actamat.2009.11.032.
[535] S.A. Khairallah, A.T. Anderson, A. Rubenchik, W.E. King, Laser powder-bed fusion additive manufacturing: Physics of complex melt flow and formation mechanisms of pores, spatter, and denudation zones Saad, Acta Mater. 108 (n.d.) 36–45. https://doi.org/10.1016/j.actamat.2016.02.014.
[536] M. Iebba, A. Astarita, D. Mistretta, I. Colonna, M. Liberini, F. Scherillo, C. Pirozzi, R. Borrelli, S. Franchitti, A. Squillace, Influence of Powder Characteristics on Formation of Porosity in Additive Manufacturing of Ti-6Al-4V Components, J. Mater. Eng. Perform. 26 (2017) 4138–4147, https://doi.org/10.1007/s11665-017-2796-2.
[537] S.M.H. Hojjatzadeh, N.D. Parab, Q. Guo, M. Qu, L. Xiong, C. Zhao, L.I. Escano, K. Fezzaa, W. Everhart, T. Sun, Direct observation of pore formation mechanisms during LPBF additive manufacturing process and high energy density laser welding, Int. J. Mach. Tools Manuf. (2020), 103555, https://doi.org/10.1016/j.ijmachtools.2020.103555.
[538] C.R. Heiple, J.R. Rope, R.T. Stagner, R.J. Aden, Surface Active Element Effects on the Shape of Gta, Laser, and Electron Beam Welds, Weld. J. (Miami, Fla). 62 (1983) 72–77.
[539] T. Debroy, S.A. David, Physical processes in fusion welding, Rev. Mod. Phys. 67 (1995) 85–112, https://doi.org/10.1103/RevModPhys.67.85.
[540] K.V. Yang, P. Rometsch, T. Jarvis, J. Rao, S. Cao, C. Davies, X. Wu, Porosity formation mechanisms and fatigue response in Al-Si-Mg alloys made by selective laser melting, Mater. Sci. Eng. A. 712 (2018) 166–174, https://doi.org/10.1016/j.msea.2017.11.078.
[541] M. Xia, D. Gu, G. Yu, D. Dai, H. Chen, Q. Shi, Porosity evolution and its thermodynamic mechanism of randomly packed powder-bed during selective laser melting of Inconel 718 alloy, Int. J. Mach. Tools Manuf. 116 (2017) 96–106, https://doi.org/10.1016/j.ijmachtools.2017.01.005.
[542] G. Tapia, A.H. Elwany, H. Sang, Prediction of porosity in metal-based additive manufacturing using spatial Gaussian process models, Addit. Manuf. 12 (2016) 282–290, https://doi.org/10.1016/j.addma.2016.05.009.
[543] G. Kasperovich, J. Haubrich, J. Gussone, G. Requena, Correlation between porosity and processing parameters in TiAl6V4 produced by selective laser melting, Mater. Des. 105 (2016) 160–170, https://doi.org/10.1016/j.matdes.2016.05.070.
[544] R. Rai, J.W. Elmer, T.A. Palmer, T. Debroy, Heat transfer and fluid flow during keyhole mode laser welding of tantalum, Ti-6Al-4V, 304L stainless steel and vanadium, J. Phys. D. Appl. Phys. 40 (2007) 5753–5766, https://doi.org/10.1088/0022-3727/40/18/037.
[545] J.L. Huang, N. Warnken, J.C. Gebelin, M. Strangwood, R.C. Reed, On the mechanism of porosity formation during welding of titanium alloys, Acta Mater. 60 (2012) 3215–3225, https://doi.org/10.1016/j.actamat.2012.02.035.
[546] S. Tammas-Williams, P.J. Withers, I. Todd, P.B. Prangnell, Porosity regrowth during heat treatment of hot isostatically pressed additively manufactured titanium components, Scr. Mater. 122 (2016) 72–76, https://doi.org/10.1016/j.scriptamat.2016.05.002.
[547] H. Chen, Q. Wei, Y. Zhang, F. Chen, Y. Shi, W. Yan, Powder-spreading mechanisms in powder-bed-based additive manufacturing: Experiments and computational modeling, Acta Mater. 179 (2019) 158–171, https://doi.org/10.1016/j.actamat.2019.08.030.
[548] S. Ziegelmeier, P. Christou, F. Wöllecke, C. Tuck, R. Goodridge, R. Hague, E. Krampe, E. Wintermantel, An experimental study into the effects of bulk and flow behaviour of laser sintering polymer powders on resulting part properties, J. Mater. Process. Technol. 215 (2015) 239–250, https://doi.org/10.1016/j.jmatprotec.2014.07.029.
[549] O.O. Eyitayo, Laser sintering of blended Al-Si powders, Rapid Prototyp. J. 18 (2012) 109–119, https://doi.org/10.1108/13552541211212096.
[550] H. Chen, Q. Wei, S. Wen, Z. Li, Y. Shi, Flow behavior of powder particles in layering process of selective laser melting: Numerical modeling and experimental verification based on discrete element method, Int. J. Mach. Tools Manuf. 123 (2017) 146–159.
[551] Y.S. Lee, P. Nandwana, W. Zhang, Dynamic simulation of powder packing structure for powder bed additive manufacturing, Int. J. Adv. Manuf. Technol. 96 (2018) 1507–1520, https://doi.org/10.1007/s00170-018-1697-3.
[552] W. Nan, M. Ghadiri, Numerical simulation of powder flow during spreading in additive manufacturing, Powder Technol. 342 (2019) 801–807, https://doi.org/10.1016/J.POWTEC.2018.10.056.
[553] E.J.R. Parteli, T. Pöschel, Particle-based simulation of powder application in additive manufacturing, Powder Technol. 288 (2016) 96–102.
[554] S. Haeri, Y. Wang, O. Ghita, J. Sun, Discrete element simulation and experimental study of powder spreading process in additive manufacturing, Powder Technol. 306 (2017) 45–54, https://doi.org/10.1016/j.powtec.2016.11.002.
[555] Q. Han, H. Gu, R. Setchi, Discrete element simulation of powder layer thickness in laser additive manufacturing, Powder Technol. 352 (2019) 91–102, https://doi.org/10.1016/J.POWTEC.2019.04.057.
[556] W. Nan, M. Pasha, T. Bonakdar, A. Lopez, U. Zafar, S. Nadimi, M. Ghadiri, Jamming during particle spreading in additive manufacturing, Powder Technol. 338 (2018) 253–262, https://doi.org/10.1016/J.POWTEC.2018.07.030.
[557] C. Meier, R. Weissbach, J. Weinberg, W.A. Wall, A.J. Hart, Critical influences of particle size and adhesion on the powder layer uniformity in metal additive manufacturing, J. Mater. Process. Technol. 266 (2019) 484–501, https://doi.org/10.1016/j.jmatprotec.2018.10.037.
[558] L.I. Escano, N.D. Parab, L. Xiong, Q. Guo, C. Zhao, K. Fezzaa, W. Everhart, T. Sun, L. Chen, Revealing particle-scale powder spreading dynamics in powder-bed-based additive manufacturing process by high-speed x-ray imaging, Sci. Rep. 8 (2018) 15079.
[559] J.P. Kruth, G. Levy, F. Klocke, T.H.C. Childs, Consolidation phenomena in laser and powder-bed based layered manufacturing, CIRP Ann. - Manuf. Technol. 56 (2007) 730–759, https://doi.org/10.1016/j.cirp.2007.10.004.
[560] I. Yadroitsev, A. Gusarov, I. Yadroitsava, I. Smurov, Single track formation in selective laser melting of metal powders, J. Mater. Process. Technol. 210 (2010) 1624–1631, https://doi.org/10.1016/j.jmatprotec.2010.05.010.
[561] N.K. Tolochko, S.E. Mozzharov, I.A. Yadroitsev, T. Laoui, L. Froyen, V.I. Titov, M. B. Ignatiev, Balling processes during selective laser treatment of powders, Rapid Prototyp. J. 10 (2004) 78–87, https://doi.org/10.1108/13552540410526953.
[562] D. Gu, Y. Shen, Balling phenomena in direct laser sintering of stainless steel powder: Metallurgical mechanisms and control methods, Mater. Des. 30 (2009) 2903–2910, https://doi.org/10.1016/j.matdes.2009.01.013.
[563] Y.S. Lee, W. Zhang, Mesoscopic simulation of heat transfer and fluid flow in laser powder bed additive manufacturing, in: Solid Free. Fabr. Proc., 2015, pp. 1154–1165.

[564] S.A. Khairallah, A. Anderson, Mesoscopic simulation model of selective laser melting of stainless steel powder, J. Mater. Process. Technol. 214 (2014) 2627–2636, https://doi.org/10.1016/j.jmatprotec.2014.06.001.
[565] I. Yadroitsev, I. Smurov, Selective laser melting technology: From the single laser melted track stability to 3D parts of complex shape, Phys. Procedia. 5 (2010) 551–560, https://doi.org/10.1016/j.phpro.2010.08.083.
[566] D. Wang, Y. Yang, X. Su, Y. Chen, Study on energy input and its influences on single-track, multi-track, and multi-layer in SLM, Int. J. Adv. Manuf. Technol. 58 (2012) 1189–1199, https://doi.org/10.1007/s00170-011-3443-y.
[567] A.V. Gusarov, I. Yadroitsev, P. Bertrand, I. Smurov, Model of Radiation and Heat Transfer in Laser-Powder Interaction Zone at Selective Laser Melting, J. Heat Transfer. 131 (2009), 072101, https://doi.org/10.1115/1.3109245.
[568] N.T. Aboulkhair, I. Maskery, C. Tuck, I. Ashcroft, N.M. Everitt, On the formation of AlSi10Mg single tracks and layers in selective laser melting: Microstructure and nano-mechanical properties, J. Mater. Process. Technol. 230 (2016) 88–98.
[569] X. Nie, H. Zhang, H. Zhu, Z. Hu, L. Ke, X. Zeng, Analysis of processing parameters and characteristics of selective laser melted high strength Al-Cu-Mg alloys: From single tracks to cubic samples, J. Mater. Process. Technol. 256 (2018) 69–77, https://doi.org/10.1016/j.jmatprotec.2018.01.030.
[570] Y. He, C. Montgomery, J. Beuth, B. Webler, Melt pool geometry and microstructure of Ti6Al4V with B additions processed by selective laser melting additive manufacturing, Mater. Des. 183 (2019), 108126, https://doi.org/10.1016/j.matdes.2019.108126.
[571] J.H. Lee, J.H. Jang, B.D. Joo, H.S. Yim, Y.H. Moon, Application of direct laser metal tooling for AISI H13 tool steel, Trans. Nonferrous Met. Soc. China (English Ed. 19 (2009) s284–s287, https://doi.org/10.1016/S1003-6326(10)60286-5.
[572] F. Klocke, C. Wagner, F. Klocke, Coalescence Behaviour of Two Metallic Particles as Base Mechanism of Selective Laser Sintering, CIRP Ann. 52 (2003) 177–180, https://doi.org/10.1016/S0007-8506(07)60559-9.
[573] S. Chandrasekhar, Hydrodynamic and Hydromagnetic Stability, first ed., Oxford University Press, London, 1961.
[574] R. Li, Y. Shi, Z. Wang, L. Wang, J. Liu, W. Jiang, Densification behavior of gas and water atomized 316L stainless steel powder during selective laser melting, Appl. Surf. Sci. 256 (2010) 4350–4356.
[575] F. Calignano, D. Manfredi, E.P. Ambrosio, L. Iuliano, P. Fino, Influence of process parameters on surface roughness of aluminum parts produced by DMLS, Int. J. Adv. Manuf. Technol. 67 (2013) 2743–2751, https://doi.org/10.1007/s00170-012-4688-9.
[576] W. Morgan, R. Sutcliffe, C.J. O'Neill, Experimental investigation of nanosecond pulsed Nd YAG laser re-melted pre-placed powder beds.pdf, Rapid Prototyp. J. 7 (2001) 159–172.
[577] E. Yasa, K. Kempen, J.-P. Kruth, Microstructure and mechanical properties of maraging steel 300 after selective laser melting, Solid Free. Fabr. Symp. Proc. (2010) 383–396.
[578] B.J. Bradstreet, Effect of surface tension and metal flow on weld bead formation, Weld. J. 47 (1968) 314s–322s.
[579] C. Thomy, T. Seefeld, F. Vollertsen, Humping Effect in Welding of Steel with Single-Mode Fibre Laser, Weld. World. 52 (2008) 9–18, https://doi.org/10.1007/BF03266636.
[580] K.C. Mills, B.J. Keene, Factors affecting variable weld penetration, Int. Mater. Rev. 35 (1990) 185–216, https://doi.org/10.1179/095066090790323966.
[581] W.F. Savage, E.P. Nippes, K. Agusa, Effect of arc force on defect formation in GTA welding, Weld. Journal1. 58 (1979).
[582] P.F. Mendez, T.W. Eagar, Penetration and defect formation in high-current arc welding, Weld. J. 82 (2003) 296s–306s.
[583] T.C. Nguyen, D.C. Weckman, D.A. Johnson, H.W. Kerr, The humping phenomenon during high speed gas metal arc welding, Sci. Technol. Weld. Join. 10 (2005) 447–459, https://doi.org/10.1179/174329305X44134.
[584] A. Kumar, T. DebRoy, Toward a Unified Model to Prevent Humping Defects in Gas Tungsten Arc Welding, Weld. J. 85 (2006) 292s–304s.
[585] E. Kannatey-Asibu, Principles of Laser Materials Processing, first ed., John Wiley & Sons Inc, Hoboken, New Jersey, 2009.
[586] A. Otto, A. Patschger, M. Seiler, Numerical and Experimental Investigations of Humping Phenomena in Laser Micro Welding, Phys. Procedia. 83 (2016) 1415–1423, https://doi.org/10.1016/J.PHPRO.2016.09.004.
[587] A. Otto, R.G. Vázquez, Fluid dynamical simulation of high speed micro welding, J. Laser Appl. 30 (2018), 032411, https://doi.org/10.2351/1.5040652.
[588] M. Seiler, A. Patschger, L. Tianis, C. Rochholz, J. Bliedtner, Experimental determination of influencing factors on the humping phenomenon during laser micro welding of thin metal sheets, J. Laser Appl. 29 (2017), 022413, https://doi.org/10.2351/1.4983506.
[589] M. Seiler, A. Patschger, J. Bliedtner, Investigations of welding instabilities and weld seam formation during laser microwelding of ultrathin metal sheets, J. Laser Appl. 28 (2016), 022417, https://doi.org/10.2351/1.4944446.
[590] M. Beck, P. Berger, F. Dausinger, H. Huegel, Aspects of keyhole/melt interaction in high-speed laser welding, in: 8th Intl Symp Gas Flow Chem. Lasers, 1991, pp. 769–774. https://doi.org/10.1117/12.25985.
[591] P. Berger, H. Hügel, A. Hess, R. Weber, T. Graf, Understanding of Humping Based on Conservation of Volume Flow, Phys. Procedia. 12 (2011) 232–240, https://doi.org/10.1016/J.PHPRO.2011.03.030.
[592] T. DebRoy, H.L. Wei, J.S. Zuback, T. Mukherjee, J.W. Elmer, J.O. Milewski, A. M. Beese, A. Wilson-Heid, A. De, W. Zhang, Additive manufacturing of metallic components – Process, structure and properties, Prog. Mater. Sci. 92 (2018) 112–224.
[593] H.E. Sabzi, P.E.J. Rivera-Díaz-del-Castillo, Defect Prevention in Selective Laser Melting Components: Compositional and Process Effects, Materials (Basel). 12 (2019) 3791.
[594] T. Mukherjee, J.S. Zuback, A. De, T. DebRoy, Printability of alloys for additive manufacturing, Sci. Rep. 6 (2016) 1–8, https://doi.org/10.1038/srep19717.
[595] L. Scime, J. Beuth, Melt pool geometry and morphology variability for the Inconel 718 alloy in a laser powder bed fusion additive manufacturing process, Addit. Manuf. 29 (2019), 100830, https://doi.org/10.1016/j.addma.2019.100830.
[596] K. Darvish, Z.W. Chen, T. Pasang, Reducing lack of fusion during selective laser melting of CoCrMo alloy: Effect of laser power on geometrical features of tracks, Mater. Des. 112 (2016) 357–366.
[597] W.E. King, A.T. Anderson, R.M. Ferencz, N.E. Hodge, C. Kamath, S.A. Khairallah, A.M. Rubenchik, Laser powder bed fusion additive manufacturing of metals; physics, computational, and materials challenges, Appl. Phys. Rev. 2 (2015) 41304.
[598] T. Kimura, T. Nakamoto, Microstructures and mechanical properties of A356 (AlSi7Mg0. 3) aluminum alloy fabricated by selective laser melting, Mater. Des. 89 (2016) 1294–1301.
[599] H. Gu, H. Gong, D. Pal, K. Rafi, T. Starr, B. Stucker, Influences of energy density on porosity and microstructure of selective laser melted 17-4PH stainless steel, in: 2013 Solid Free. Fabr. Symp., 2013.
[600] C. Tenbrock, T. Kelliger, N. Praetzsch, M. Ronge, L. Jauer, J.H. Schleifenbaum, Effect of laser-plume interaction on part quality in multi-scanner Laser Powder Bed Fusion, Addit. Manuf. 38 (2021), 101810, https://doi.org/10.1016/j.addma.2020.101810.
[601] J.A. Slotwinski, E.J. Garboczi, P.E. Stutzman, C.F. Ferraris, S.S. Watson, M. A. Peltz, Characterization of Metal Powders Used for Additive Manufacturing, J. Res. Natl. Inst. Stand. Technol. 119 (2014) 460–493, https://doi.org/10.6028/jres.119.018.
[602] S. Ly, A.M. Rubenchik, S.A. Khairallah, G. Guss, M.J. Matthews, Metal vapor micro-jet controls material redistribution in laser powder bed fusion additive manufacturing, Sci. Rep. 7 (2017) 1–12, https://doi.org/10.1038/s41598-017-04237-z.
[603] A. Bobel, L.G. Hector, I. Chelladurai, A.K. Sachdev, T. Brown, W.A. Poling, R. Kubic, B. Gould, C. Zhao, N. Parab, A. Greco, T. Sun, In situ synchrotron X-ray imaging of 4140 steel laser powder bed fusion, Materialia. 6 (2019), https://doi.org/10.1016/j.mtla.2019.100306.
[604] F. Verhaeghe, T. Craeghs, J. Heulens, L. Pandelaers, A pragmatic model for selective laser melting with evaporation, Acta Mater. 57 (2009) 6006–6012, https://doi.org/10.1016/j.actamat.2009.08.027.
[605] L. Thijs, K. Kempen, J.P. Kruth, J. Van Humbeeck, Fine-structured aluminium products with controllable texture by selective laser melting of pre-alloyed AlSi10Mg powder, Acta Mater. 61 (2013) 1809–1819, https://doi.org/10.1016/j.actamat.2012.11.052.
[606] A.M. Kiss, A.Y. Fong, N.P. Calta, V. Thampy, A.A. Martin, P.J. Depond, J. Wang, M.J. Matthews, R.T. Ott, C.J. Tassone, K.H. Stone, M.J. Kramer, A. van Buuren, M. F. Toney, J. Nelson Weker, Laser-Induced Keyhole Defect Dynamics during Metal Additive Manufacturing, Adv. Eng. Mater. 21 (2019) 1–7, https://doi.org/10.1002/adem.201900455.
[607] D.B. Hann, J. Iammi, J. Folkes, A simple methodology for predicting laser-weld properties from material and laser parameters, J. Phys. D. Appl. Phys. 44 (2011), https://doi.org/10.1088/0022-3727/44/44/445401.
[608] D. Wu, X. Hua, L. Huang, F. Li, Y. Cai, Elucidation of keyhole induced bubble formation mechanism in fiber laser welding of low carbon steel, Int. J. Heat Mass Transf. 127 (2018) 1077–1086, https://doi.org/10.1016/j.ijheatmasstransfer.2018.07.107.
[609] D. Zhang, M. Wang, C. Shu, Y. Zhang, D. Wu, Y. Ye, Dynamic keyhole behavior and keyhole instability in high power fiber laser welding of stainless steel, Opt. Laser Technol. 114 (2019) 1–9, https://doi.org/10.1016/j.optlastec.2019.01.018.
[610] M. Miyagi, H. Wang, R. Yoshida, Y. Kawahito, H. Kawakami, T. Shoubu, Effect of alloy element on weld pool dynamics in laser welding of aluminum alloys, Sci. Rep. 8 (2018) 1–10, https://doi.org/10.1038/s41598-018-31350-4.
[611] X. He, J.T. Norris, P.W. Fuerschbach, T. Debroy, Liquid metal expulsion during laser spot welding of 304 stainless steel, J. Phys. D. Appl. Phys. 39 (2006) 525–534, https://doi.org/10.1088/0022-3727/39/3/016.
[612] R. Fabbro, K. Chouf, Keyhole modeling during laser welding, J. Appl. Phys. 87 (2000) 4075–4083, https://doi.org/10.1063/1.373033.
[613] A. Kaplan, A model of deep penetration laser welding based on calculation of the keyhole profile, J. Phys. D. Appl. Phys. 27 (1994) 1805.
[614] X. Jin, P. Berger, T. Graf, Multiple reflections and Fresnel absorption in an actual 3D keyhole during, J. Appl. Phys. (2006), https://doi.org/10.1088/0022-3727/39/21/030.
[615] M. Jiang, X. Chen, Y. Chen, W. Tao, Increasing keyhole stability of fiber laser welding under reduced ambient pressure, J. Mater. Process. Technol. 268 (2019) 213–222, https://doi.org/10.1016/j.jmatprotec.2019.01.026.
[616] M.A. Groeber, E. Schwalbach, S. Donegan, K. Chaput, T. Butler, J. Miller, Application of characterization, modelling, and analytics towards understanding process-structure linkages in metallic 3D printing, IOP Conf. Ser. Mater. Sci. Eng. 219 (2017), https://doi.org/10.1088/1757-899X/219/1/012002.
[617] L. Sinclair, C.L.A. Leung, A. Marussi, A.J. Clark, Y. Chen, M.P. Olbinado, A. Rack, J. Gardy, G.J. Baxter, P.D. Lee, In situ radiographic and ex situ tomographic analysis of pore interactions during multilayer builds in laser powder bed fusion, Addit. Manuf. 36 (2020), 101512.
[618] R. Fabbro, Melt pool and keyhole behaviour analysis for deep penetration laser welding, J. Phys. D. Appl. Phys. 43 (2010), 445501.

[619] A.R. Nassar, M.A. Gundermann, E.W. Reutzel, P. Guerrier, M.H. Krane, M. J. Weldon, Formation processes for large ejecta and interactions with melt pool formation in powder bed fusion additive manufacturing, Sci. Rep. 9 (2019) 5038, https://doi.org/10.1038/s41598-019-41415-7.
[620] A. Bauereiß, T. Scharowsky, C. Körner, Defect generation and propagation mechanism during additive manufacturing by selective beam melting, J. Mater. Process. Technol. 214 (2014) 2522–2528, https://doi.org/10.1016/j.jmatprotec.2014.05.002.
[621] D.K.Y. Low, L. Li, P.J. Byrd, Spatter prevention during the laser drilling of selected aerospace materials, J. Mater. Process. Technol. 139 (2003) 71–76.
[622] M.J. Zhang, G.Y. Chen, Y. Zhou, S.C. Li, H. Deng, Observation of spatter formation mechanisms in high-power fiber laser welding of thick plate, Appl. Surf. Sci. 280 (2013) 868–875, https://doi.org/10.1016/j.apsusc.2013.05.081.
[623] M. Lutter-Günther, M. Bröker, T. Mayer, S. Lizak, C. Seidel, G. Reinhart, Spatter formation during laser beam melting of AlSi10Mg and effects on powder quality, Procedia CIRP. 74 (2018) 33–38, https://doi.org/10.1016/j.procir.2018.08.008.
[624] U. Ali, R. Esmaeilizadeh, F. Ahmed, D. Sarker, W. Muhammad, A. Keshavarzkermani, Y. Mahmoodkhani, E. Marzbanrad, E. Toyserkani, Identification and characterization of spatter particles and their effect on surface roughness, density and mechanical response of 17–4 PH stainless steel laser powder-bed fusion parts, Mater. Sci. Eng. A. (2019), https://doi.org/10.1016/j.msea.2019.04.026.
[625] D. Greitemeier, C. Dalle Donne, F. Syassen, J. Eufinger, T. Melz, Effect of surface roughness on the fatigue life of laser additive manufactured Effect of surface roughness on fatigue performance of additive manufactured Ti–6Al–4V alloy, Mater. Sci. Technol. 32 (2016) 629–634, https://doi.org/10.1179/1743284715Y.0000000053.
[626] R. Cottam, J. Wang, Characterization of microstructure and residual stress in a 3D H13 tool steel component produced by additive manufacturing Characterization of microstructure and residual stress in a 3D H13 tool steel component produced by additive manufacturing, 2014. https://doi.org/10.1557/jmr.2014.190.
[627] P. Mercelis, J.P. Kruth, Residual stresses in selective laser sintering and selective laser melting, Rapid Prototyp. J. 12 (2006) 254–265, https://doi.org/10.1108/13552540610707013.
[628] K. Masubuchi, Analysis of welded structures Residual Stresses, Distortion, and their Consequences, 1980. https://doi.org/10.1016/0026-0800(82)90012-X.
[629] R. Acevedo, P. Sedlak, R. Kolman, M. Fredel, Residual stress analysis of additive manufacturing of metallic parts using ultrasonic waves: State of the art review, J. Mater. Res. Technol. 9 (2020) 9457–9477, https://doi.org/10.1016/j.jmrt.2020.05.092.
[630] S. Edition, Metallurgy Second Edition Welding Metallurgy, 2003. https://doi.org/10.1016/j.theochem.2007.07.017.
[631] K. Masubuchi, Analysis of welded structures: residual stresses, distortion, and their consequences, 2013.
[632] Z. Yan, W. Liu, Z. Tang, X. Liu, N. Zhang, M. Li, H. Zhang, Review on thermal analysis in laser-based additive manufacturing, Opt. Laser Technol. 106 (2018) 427–441, https://doi.org/10.1016/j.optlastec.2018.04.034.
[633] L. Bertini, F. Bucchi, F. Frendo, M. Moda, B.D. Monelli, Residual stress prediction in selective laser melting A critical review of simulation strategies Leonardo: A critical review of simulation, Int. J. Adv. Manuf. Technol. 105 (2019) 609–636.
[634] P. Michaleris, Modeling metal deposition in heat transfer analyses of additive manufacturing processes, Finite Elem. Anal. Des. 86 (2014) 51–60, https://doi.org/10.1016/j.finel.2014.04.003.
[635] L.E. Criales, M. Ar, Sensitivity analysis of material and process parameters in finite element modeling of selective laser melting of Inconel, 625 (2016) 2653–2666. https://doi.org/10.1007/s00170-015-8329-y.
[636] M. Zhong, H. Sun, W. Liu, X. Zhu, J. He, Boundary liquation and interface cracking characterization in laser deposition of Inconel 738 on directionally solidified Ni-based superalloy, 53 (2005) 159–164. https://doi.org/10.1016/j.scriptamat.2005.03.047.
[637] H. Wang, X. Zhang, G.B. Wang, J. Shen, G.Q. Zhang, Y.P. Li, M. Yan, Selective laser melting of the hard-to-weld IN738LC superalloy: Efforts to mitigate defects and the resultant microstructural and mechanical properties, J. Alloys Compd. 807 (2019), https://doi.org/10.1016/j.jallcom.2019.151662.
[638] C. Huang, S. Kou, Liquation Cracking in Full-Penetration Al-Cu Welds, n.d.
[639] C. Huang, S. Kou, Liquation Cracking in Full-Penetration Al-Mg-Si Welds A higher fraction solid in the weld metal than in the partially melted zone during terminal sofidification is a necessary condition for cracking to occur, n.d.
[640] J.E. Franklin, W.F. Savage, Stress Relaxation and Strain-Age Cracking in Rene 41 Weldments, in: 55th AWS Annu. Meet., Houston, 1974, pp. 380-s.
[641] B. Onuike, A. Bandyopadhyay, Additive manufacturing of Inconel 718 – Ti6Al4V bimetallic structures, Addit. Manuf. 22 (2018) 844–851, https://doi.org/10.1016/j.addma.2018.06.025.
[642] M. Alimardani, E. Toyserkani, J.P. Huissoon, C.P. Paul, On the delamination and crack formation in a thin wall fabricated using laser solid freeform fabrication process: An experimental-numerical investigation, Opt. Lasers Eng. 47 (2009) 1160–1168, https://doi.org/10.1016/j.optlaseng.2009.06.010.
[643] F. Abe, K. Osakada, M. Shiomi, K. Uematsu, M. Matsumoto, The manufacturing of hard tools from metallic powders by selective laser melting, J. Mater. Process. Technol. 111 (2001) 210–213, https://doi.org/10.1016/S0924-0136(01)00522-2.
[644] Y. Chen, F. Lu, K. Zhang, P. Nie, S.R. Elmi Hosseini, K. Feng, Z. Li, Dendritic microstructure and hot cracking of laser additive manufactured Inconel 718 under improved base cooling, J. Alloys Compd. 670 (2016) 312–321, https://doi.org/10.1016/j.jallcom.2016.01.250.
[645] N. Coniglio, C.E. Cross, Mechanisms for Solidification Crack Initiation and Growth in Aluminum Welding, 2009. https://doi.org/10.1007/s11661-009-9964-4.
[646] S. Kou, A criterion for cracking during solidification, Acta Mater. 88 (2015) 366–374, https://doi.org/10.1016/j.actamat.2015.01.034.
[647] M. Gharbi, P. Peyre, C. Gorny, M. Carin, S. Morville, P. Le Masson, D. Carron, R. Fabbro, Influence of a pulsed laser regime on surface finish induced by the direct metal deposition process on a Ti64 alloy, J. Mater. Process. Technol. 213 (2013) 791–800, https://doi.org/10.1016/j.jmatprotec.2013.10.004.
[648] A. Townsend, N. Senin, L. Blunt, R.K. Leach, J.S. Taylor, Surface texture metrology for metal additive manufacturing: a review, Precis. Eng. 46 (2016) 34–47, https://doi.org/10.1016/j.precisioneng.2016.06.001.
[649] J. Vaithilingam, R.D. Goodridge, S.D. Christie, S. Edmondson, R.J.M. Hague, Surface modification of selective laser melted structures using self-assembled monolayers for biomedical applications, in: 23rd Annu. Int. Solid Free. Fabr. Symp. - An Addit. Manuf. Conf. SFF 2012, 2012, pp. 316–325. https://doi.org/10.1016/j.jct.2017.08.006.
[650] Y.Y. Sun, S. Gulizia, C.H. Oh, D. Fraser, M. Leary, Y.F. Yang, M. Qian, The Influence of As-Built Surface Conditions on Mechanical Properties of Ti-6Al-4V Additively Manufactured by Selective Electron Beam Melting, JOM. 68 (2016) 791–798, https://doi.org/10.1007/s11837-015-1768-y.
[651] K.S. Chan, Characterization and analysis of surface notches on Ti-alloy plates fabricated by additive manufacturing techniques, Surf. Topogr. Metrol. Prop. 3 (2015), 044006, https://doi.org/10.1088/2051-672X/3/4/044006.
[652] B. Torries, A. Imandoust, S. Beretta, S. Shao, N. Shamsaei, Overview on Microstructure- and Defect-Sensitive Fatigue Modeling of Additively Manufactured Materials, Jom. 70 (2018) 1853–1862, https://doi.org/10.1007/s11837-018-2987-9.
[653] D.L. Mcdowell, F.P.E. Dunne, Microstructure-sensitive computational modeling of fatigue crack formation, Int. J. Fatigue. 32 (2010) 1521–1542, https://doi.org/10.1016/j.ijfatigue.2010.01.003.
[654] M. Murakami, Y. Endo, Effects of defects, inclusions and inhomogeneities on fatigue strength, Int. J. Fatigue. 16 (1994) 163–182, https://doi.org/10.1016/0142-1123(94)90001-9.
[655] C. Ni, Y. Shi, J. Liu, Effects of inclination angle on surface roughness and corrosion properties of selective laser melted 316L stainless steel, Mater. Res. Express. 6 (2019), https://doi.org/10.1088/2053-1591/aaf2d3.
[656] P. Karimi, C. Schnur, E. Sadeghi, J. Andersson, Contour design to improve topographical and microstructuralcharacteristics of Alloy 718 manufactured using electron beam-powderbed fusion, Addit. Manuf. (2019), https://doi.org/10.1016/j.pharmthera.2019.107402.
[657] M. Gharbi, P. Peyre, C. Gorny, M. Carin, S. Morville, P. Le Masson, D. Carron, R. Fabbro, Influence of various process conditions on surface finishes induced by the direct metal deposition laser technique on a Ti-6Al-4V alloy, J. Mater. Process. Technol. 213 (2013) 791–800, https://doi.org/10.1016/j.jmatprotec.2012.11.015.
[658] B. Vayssette, N. Saintier, C. Brugger, M. El May, E. Pessard, Numerical modelling of surface roughness effect on the fatigue behavior of Ti-6Al-4V obtained by additive manufacturing, Int. J. Fatigue. 123 (2019) 180–195, https://doi.org/10.1016/j.ijfatigue.2019.02.014.
[659] C.A. Kantzos, R.W. Cunningham, V. Tari, A.D. Rollett, Characterization of metal additive manufacturing surfaces using synchrotron X-ray CT and micromechanical modeling, Comput. Mech. 61 (2018) 575–580, https://doi.org/10.1007/s00466-017-1531-z.
[660] S. Lou, X. Jiang, W. Sun, W. Zeng, L. Pagani, P.J. Scott, Characterisation methods for powder bed fusion processed surface topography, Precis. Eng. 57 (2019) 1–15, https://doi.org/10.1016/j.precisioneng.2018.09.007.
[661] J. Gockel, L. Sheridan, B. Koerper, B. Whip, The influence of additive manufacturing processing parameters on surface roughness and fatigue life, Int. J. Fatigue. 124 (2019) 380–388, https://doi.org/10.1016/j.ijfatigue.2019.03.025.
[662] A. Triantaphyllou, C.L. Giusca, G.D. Macaulay, F. Roerig, M. Hoebel, R.K. Leach, B. Tomita, K.A. Milne, Surface texture measurement for additive manufacturing, Surf. Topogr. Metrol. Prop. 3 (2015), https://doi.org/10.1088/2051-672X/3/2/024002.
[663] J. Karlsson, A. Snis, H. Engqvist, J. Lausmaa, Characterization and comparison of materials produced by Electron Beam Melting (EBM) of two different Ti-6Al-4V powder fractions, J. Mater. Process. Technol. 213 (2013) 2109–2118, https://doi.org/10.1016/j.jmatprotec.2013.06.010.
[664] G. Strano, L. Hao, R.M. Everson, K.E. Evans, Surface roughness analysis, modelling and prediction in selective laser melting, J. Mater. Process. Technol. 213 (2013) 589–597.
[665] I. Koutiri, E. Pessard, P. Peyre, O. Amlou, T. De Terris, Influence of SLM process parameters on the surface finish, porosity rate and fatigue behavior of as-built Inconel 625 parts, J. Mater. Process. Technol. 255 (2018) 536–546, https://doi.org/10.1016/j.jmatprotec.2017.12.043.
[666] K. Mumtaz, N. Hopkinson, Top surface and side roughness of Inconel 625 parts processed using selective laser melting, Rapid Prototyp. J. 15 (2009) 96–103, https://doi.org/10.1108/13552540910943397.
[667] M. Mele, A. Bergmann, G. Campana, T. Pilz, Experimental investigation into the effect of supports and overhangs on accuracy and roughness in laser powder bed fusion, Opt. Laser Technol. 140 (2021), https://doi.org/10.1016/j.optlastec.2021.107024.
[668] A. Jones, M. Leary, S. Bateman, M. Easton, Effect of surface geometry on laser powder bed fusion defects, J. Mater. Process. Technol. 296 (2021), 117179, https://doi.org/10.1016/j.jmatprotec.2021.117179.

[669] A. Charles, A. Elkaseer, U. Paggi, L. Thijs, V. Hagenmeyer, S. Scholz, Down-facing surfaces in laser powder bed fusion of Ti6Al4V: Effect of dross formation on dimensional accuracy and surface texture, Addit. Manuf. 46 (2021), 102148, https://doi.org/10.1016/j.addma.2021.102148.
[670] P.B. Bacchewar, S.K. Singhal, P.M. Pandey, Statistical modelling and optimization of surface roughness in the selective laser sintering process, Proc. Inst. Mech. Eng. Part B J. Eng. Manuf. 221 (2007) 35–52, https://doi.org/10.1243/09544054JEM670.
[671] K. Solberg, E.W. Hovig, K. Sørby, F. Berto, Directional fatigue behaviour of maraging steel grade 300 produced by laser powder bed fusion, Int. J. Fatigue. 149 (2021), https://doi.org/10.1016/j.ijfatigue.2021.106229.
[672] C. Qiu, C. Panwisawas, M. Ward, H.C. Basoalto, J.W. Brooks, M.M. Attallah, On the role of melt flow into the surface structure and porosity development during selective laser melting, Acta Mater. 96 (2015) 72–79, https://doi.org/10.1016/j.actamat.2015.06.004.
[673] Z. Chen, X. Wu, D. Tomus, C.H.J. Davies, Surface roughness of Selective Laser Melted Ti-6Al-4V alloy components, Addit. Manuf. 21 (2018) 91–103, https://doi.org/10.1016/j.addma.2018.02.009.
[674] W. Yu, S.L. Sing, C.K. Chua, X. Tian, Influence of re-melting on surface roughness and porosity of AlSi10Mg parts fabricated by selective laser melting, J. Alloys Compd. 792 (2019) 574–581, https://doi.org/10.1016/j.jallcom.2019.04.017.
[675] J.C. Fox, S.P. Moylan, B.M. Lane, Effect of Process Parameters on the Surface Roughness of Overhanging Structures in Laser Powder Bed Fusion Additive Manufacturing, Procedia CIRP. 45 (2016) 131–134, https://doi.org/10.1016/j.procir.2016.02.347.
[676] M. Mohammadi, H. Asgari, Achieving low surface roughness AlSi10Mg_200C parts using direct metal laser sintering, Addit. Manuf. 20 (2018) 23–32, https://doi.org/10.1016/j.addma.2017.12.012.
[677] B. Whip, L. Sheridan, J. Gockel, The effect of primary processing parameters on surface roughness in laser powder bed additive manufacturing, Int. J. Adv. Manuf. Technol. 103 (2019) 4411–4422, https://doi.org/10.1007/s00170-019-03716-z.
[678] J.C. Steuben, A.P. Iliopoulos, J.G. Michopoulos, Discrete element modeling of particle-based additive manufacturing processes, Comput. Methods Appl. Mech. Eng. 305 (2016) 537–561, https://doi.org/10.1016/j.cma.2016.02.023.
[679] C. Meier, R. Weissbach, J. Weinberg, W.A. Wall, A., John Hart, Modeling and characterization of cohesion in fine metal powders with a focus on additive manufacturing process simulations, Powder Technol. 343 (2019) 855–866, https://doi.org/10.1016/j.powtec.2018.11.072.
[680] H. Masuo, Y. Tanaka, S. Morokoshi, H. Yagura, T. Uchida, Y. Yamamoto, Y. Murakami, Effects of Defects, Surface Roughness and HIP on Fatigue Strength of Ti-6Al-4V manufactured by Additive Manufacturing, in: Procedia Struct. Integr., Lecco, Italy, 2017, pp. 19–26.
[681] K.A. Mumtaz, N. Hopkinson, Selective Laser Melting of thin wall parts using pulse shaping, J. Mater. Process. Technol. 210 (2010) 279–287, https://doi.org/10.1016/j.jmatprotec.2009.09.011.
[682] E. Lyczkowska-Widlak, P. Lochynski, G. Nawrat, E. Chlebus, Comparison of electropolished 316L steel samples manufactured by SLM and traditional technology, Rapid Prototyp. J. 25 (2019) 566–580, https://doi.org/10.1108/RPJ-03-2018-0060.
[683] J. Pegues, M. Roach, R. Scott Williamson, N. Shamsaei, Surface roughness effects on the fatigue strength of additively manufactured Ti-6Al-4V, Int. J. Fatigue. 116 (2018) 543–552, https://doi.org/10.1016/j.ijfatigue.2018.07.013.
[684] G. Kerckhofs, G. Pyka, M. Moesen, S. Van Bael, J. Schrooten, M. Wevers, High-resolution microfocus X-ray computed tomography for 3d surface roughness measurements of additive manufactured porous materials, Adv. Eng. Mater. 15 (2013) 153–158, https://doi.org/10.1002/adem.201200156.
[685] M. Kahlin, H. Ansell, D. Basu, A. Kerwin, L. Newton, B. Smith, J.J. Moverare, Improved fatigue strength of additively manufactured Ti6Al4V by surface post processing, Int. J. Fatigue. 134 (2020), 105497, https://doi.org/10.1016/j.ijfatigue.2020.105497.
[686] L. Chen, B. Richter, X. Zhang, X. Ren, F.E. Pfefferkorn, Modification of surface characteristics and electrochemical corrosion behavior of laser powder bed fused stainless-steel 316L after laser polishing, Addit. Manuf. 32 (2020), 101013, https://doi.org/10.1016/j.addma.2019.101013.
[687] A. Maamoun, M. Elbestawi, S. Veldhuis, Influence of Shot Peening on AlSi10Mg Parts Fabricated by Additive Manufacturing, J. Manuf. Mater. Process. 2 (2018) 40, https://doi.org/10.3390/jmmp2030040.
[688] M. Sugavaneswaran, A.V. Jebaraj, M.D.B. Kumar, K. Lokesh, A.J. Rajan, Enhancement of surface characteristics of direct metal laser sintered stainless steel 316L by shot peening, Surf. Interf. 12 (2018) 31–40, https://doi.org/10.1016/j.surfin.2018.04.010.
[689] N.E. Uzan, S. Ramati, R. Shneck, N. Frage, O. Yeheskel, On the effect of shot-peening on fatigue resistance of AlSi10Mg specimens fabricated by additive manufacturing using selective laser melting (AM-SLM), Addit. Manuf. 21 (2018) 458–464, https://doi.org/10.1016/j.addma.2018.03.030.
[690] B. AlMangour, J.M. Yang, Improving the surface quality and mechanical properties by shot-peening of 17–4 stainless steel fabricated by additive manufacturing, Mater. Des. 110 (2016) 914–924, https://doi.org/10.1016/j.matdes.2016.08.037.
[691] J.J. Lewandowski, M. Seifi, Metal Additive Manufacturing: A Review of Mechanical Properties, Annu. Rev. Mater. Res. 46 (2016) 151–186.
[692] N.T. Aboulkhair, I. Maskery, C. Tuck, I. Ashcroft, N.M. Everitt, Improving the fatigue behaviour of a selectively laser melted aluminium alloy: Influence of heat treatment and surface quality, Mater. Des. 104 (2016) 174–182, https://doi.org/10.1016/j.matdes.2016.05.041.
[693] K.T. Yang, M.K. Kim, D. Kim, J. Suhr, Investigation of laser powder bed fusion manufacturing and post-processing for surface quality of as-built 17–4PH stainless steel, Surf. Coatings Technol. 422 (2021), 127492, https://doi.org/10.1016/j.surfcoat.2021.127492.
[694] R. Molaei, A. Fatemi, N. Phan, Significance of hot isostatic pressing (HIP) on multiaxial deformation and fatigue behaviors of additive manufactured Ti-6Al-4V including build orientation and surface roughness effects, Int. J. Fatigue. 117 (2018) 352–370, https://doi.org/10.1016/j.ijfatigue.2018.07.035.
[695] H.M. Khan, Y. Karabulut, O. Kitay, Y. Kaynak, I.S. Jawahir, Influence of the post-processing operations on surface integrity of metal components produced by laser powder bed fusion additive manufacturing: a review, Mach. Sci. Technol. 25 (2020) 118–176, https://doi.org/10.1080/10910344.2020.1855649.
[696] R. Molaei, A. Fatemi, Crack Paths in Additive Manufactured Metallic Materials Subjected to Multiaxial Cyclic Loads Including Surface Roughness, HIP, and Notch Effects, Int. J. Fatigue. (2019), https://doi.org/10.1016/j.ijfatigue.2019.03.007.
[697] K.S. Chan, M. Koike, R.L. Mason, T. Okabe, Fatigue life of titanium alloys fabricated by additive layer manufacturing techniques for dental implants, Metall. Mater. Trans. A Phys. Metall. Mater. Sci. 44 (2013) 1010–1022, https://doi.org/10.1007/s11661-012-1470-4.
[698] A.B. Spierings, T.L. Starr, K. Wegener, Fatigue performance of additive manufactured metallic parts, Rapid Prototyp. J. 19 (2013) 88–94, https://doi.org/10.1108/13552541311302932.
[699] P. Li, D.H. Warner, J.W. Pegues, M.D. Roach, N. Shamsaei, N. Phan, Towards predicting differences in fatigue performance of laser powder bed fused Ti-6Al-4V coupons from the same build, Int. J. Fatigue. (2019), https://doi.org/10.1016/j.ijfatigue.2019.05.004.
[700] B. Bhushan, Surface roughness analysis and measurement techniques, Mod. Tribol. Handb. Vol. One Princ. Tribol. (2000) 49–119, https://doi.org/10.1201/9780849377877-10.
[701] L. Newton, N. Senin, C. Gomez, R. Danzl, F. Helmli, L. Blunt, R. Leach, Areal topography measurement of metal additive surfaces using focus variation microscopy, Addit. Manuf. 25 (2019) 365–389, https://doi.org/10.1016/j.addma.2018.11.013.
[702] R.K. Leach, D. Bourell, S. Carmignato, A. Donmez, N. Senin, W. Dewulf, Geometrical metrology for metal additive manufacturing, CIRP Ann. 68 (2019) 677–700, https://doi.org/10.1016/j.cirp.2019.05.004.
[703] Y.T. Tang, C. Panwisawas, J.N. Ghoussoub, Y. Gong, J. Clark, A. Németh, D. G. McCartney, R.C. Reed, Alloys-By-Design: Application to New Superalloys for Additive Manufacturing, Acta Mater. (2020), https://doi.org/10.1016/j.actamat.2020.09.023.
[704] X. Wang, S. Sridar, W. Xiong, Thermodynamic Investigation of New High-Strength Low-Alloy Steels with Heusler Phase Strengthening for Welding and Additive Manufacturing: High-Throughput CALPHAD Calculations and Key Experiments for Database Verification, J. Phase Equilibria Diffus. (2020), https://doi.org/10.1007/s11669-020-00828-y.
[705] Clyne and Davis_2.pdf, n.d.
[706] T. Pabel, S. Bozorgi, C. Kneissi, K. Faerber, P. Schumacher, Hot cracking susceptibility of AlSi7MgCu alloys and effects of alloying elements magnesium and copper, China Foundry. 10 (2013) 248–253.
[707] T. Hashimoto, H. Terasaki, Y.I. Komizo, Solidification cracking susceptibility of alloy tool steel under rapid solidification, Yosetsu Gakkai Ronbunshu/Quarterly, J. Japan Weld. Soc. 27 (2009) 126–129, https://doi.org/10.2207/qjjws.27.126s.
[708] J. Liu, S. Kou, Susceptibility of ternary aluminum alloys to cracking during solidification, Acta Mater. 125 (2017) 513–523, https://doi.org/10.1016/j.actamat.2016.12.028.
[709] T. Soysal, S. Kou, A simple test for assessing solidification cracking susceptibility and checking validity of susceptibility prediction, Acta Mater. 143 (2018) 181–197, https://doi.org/10.1016/j.actamat.2017.09.065.
[710] K. Liu, S. Kou, Susceptibility of magnesium alloys to solidification cracking, Sci. Technol. Weld. Join. 25 (2020) 251–257, https://doi.org/10.1080/13621718.2019.1681160.
[711] L.S.B.A. & Wolfman, Superalloys 2020, Springer International Publishing, 2020. https://doi.org/10.1007/978-3-030-51834-9.
[712] W. Stopyra, K. Gruber, I. Smolina, T. Kurzynowski, B. Kuźnicka, Laser powder bed fusion of AA7075 alloy: Influence of process parameters on porosity and hot cracking, Addit. Manuf. 35 (2020), https://doi.org/10.1016/j.addma.2020.101270.
[713] A. Sonawane, G. Roux, J.J. Blandin, A. Despres, G. Martin, Cracking mechanism and its sensitivity to processing conditions during laser powder bed fusion of a structural aluminum alloy, Materialia. 15 (2021), 100976, https://doi.org/10.1016/j.mtla.2020.100976.
[714] T. Keller, G. Lindwall, S. Ghosh, L. Ma, B.M. Lane, F. Zhang, U.R. Kattner, E. A. Lass, J.C. Heigel, Y. Idell, M.E. Williams, A.J. Allen, J.E. Guyer, L.E. Levine, Application of finite element, phase-field, and CALPHAD-based methods to additive manufacturing of Ni-based superalloys, Acta Mater. 139 (2017) 244–253, https://doi.org/10.1016/j.actamat.2017.05.003.
[715] K. Karayagiz, L. Johnson, R. Seede, V. Attari, B. Zhang, X. Huang, S. Ghosh, T. Duong, I. Karaman, A. Elwany, R. Arróyave, Finite interface dissipation phase field modeling of Ni–Nb under additive manufacturing conditions, Acta Mater. 185 (2020) 320–339, https://doi.org/10.1016/j.actamat.2019.11.057.
[716] Q. Chen, B. Sundman, Computation of Partial Equilibrium Solidification with Complete Interstitial and Negligible Substitutional Solute Back Diffusion, Mater. Trans. 43 (2002) 551–559, https://doi.org/10.2320/matertrans.43.551.

[717] J. Liu, B. Yin, Z. Sun, P. Wen, Y. Zheng, Y. Tian, Hot cracking in ZK60 magnesium alloy produced by laser powder bed fusion process, Mater. Lett. 301 (2021), 130283, https://doi.org/10.1016/j.matlet.2021.130283.
[718] M. Mohsin Raza, Y.L. Lo, Experimental investigation into microstructure, mechanical properties, and cracking mechanism of IN713LC processed by laser powder bed fusion, Mater. Sci. Eng. A. 819 (2021), 141527, https://doi.org/10.1016/j.msea.2021.141527.
[719] X. Zhang, H. Chen, L. Xu, J. Xu, X. Ren, X. Chen, Cracking mechanism and susceptibility of laser melting deposited Inconel 738 superalloy, Mater. Des. 183 (2019), 108105, https://doi.org/10.1016/j.matdes.2019.108105.
[720] W.J. Sames, K.A. Unocic, R.R. Dehoff, T. Lolla, S.S. Babu, Thermal effects on microstructural heterogeneity of Inconel 718 materials fabricated by electron beam melting, J. Mater. Res. 29 (2014) 1920–1930, https://doi.org/10.1557/jmr.2014.140.
[721] P. Mohammadpour, A.B. Phillion, Solidification microstructure selection maps for laser powder bed fusion of multicomponent alloys, IOP Conf. Ser. Mater. Sci. Eng. 861 (2020), https://doi.org/10.1088/1757-899X/861/1/012005.
[722] Y.L. Hu, X. Lin, X.B. Yu, J.J. Xu, M. Lei, W.D. Huang, Effect of Ti addition on cracking and microhardness of Inconel 625 during the laser solid forming processing, J. Alloys Compd. 711 (2017) 267–277, https://doi.org/10.1016/j.jallcom.2017.03.355.
[723] D. Tomus, P.A. Rometsch, M. Heilmaier, X. Wu, Effect of minor alloying elements on crack-formation characteristics of Hastelloy-X manufactured by selective laser melting, Addit. Manuf. 16 (2017) 65–72, https://doi.org/10.1016/j.addma.2017.05.006.
[724] O. Sanchez-Mata, X. Wang, J.A. Muñiz-Lerma, M.A. Shandiz, R. Gauvin, M. Brochu, Fabrication of crack-free nickel-based superalloy considered non-weldable during laser powder bed fusion, Materials (Basel). 11 (2018) 1–9, https://doi.org/10.3390/ma11081288.
[725] C. Körner, M. Ramsperger, C. Meid, D. Bürger, P. Wollgramm, M. Bartsch, G. Eggeler, Microstructure and Mechanical Properties of CMSX-4 Single Crystals Prepared by Additive Manufacturing, Metall. Mater. Trans. A Phys. Metall. Mater. Sci. 49 (2018) 3781–3792, https://doi.org/10.1007/s11661-018-4762-5.
[726] K. Li, D. Wang, L. Xing, Y. Wang, C. Yu, J. Chen, T. Zhang, J. Ma, W. Liu, Z. Shen, Crack suppression in additively manufactured tungsten by introducing secondary-phase nanoparticles into the matrix, Int. J. Refract. Met. Hard Mater. 79 (2019) 158–163, https://doi.org/10.1016/j.ijrmhm.2018.11.013.
[727] M. Gäumann, R. Trivedi, W. Kurz, Nucleation ahead of the advancing interface in directional solidification, Mater. Sci. Eng. A. 226–228 (1997) 763–769, https://doi.org/10.1016/s0921-5093(97)80081-0.
[728] P. Mohammadpour, A. Plotkowski, A.B. Phillion, Revisiting solidification microstructure selection maps in the frame of additive manufacturing, Addit. Manuf. 31 (2020), 100936, https://doi.org/10.1016/j.addma.2019.100936.
[729] J.P. Oliveira, T.G. Santos, R.M. Miranda, Revisiting fundamental welding concepts to improve additive manufacturing: From theory to practice, Prog. Mater. Sci. (2019), 100590, https://doi.org/10.1016/j.pmatsci.2019.100590.
[730] T. DebRoy, H.L. Wei, J.S. Zuback, T. Mukherjee, J.W. Elmer, J.O. Milewski, A. M. Beese, A. Wilson-Heid, A. De, W. Zhang, Additive manufacturing of metallic components–process, structure and properties, Prog. Mater. Sci. 92 (2018) 112–224.
[731] Q. Zhang, J. Chen, X. Lin, H. Tan, W.D. Huang, Grain morphology control and texture characterization of laser solid formed Ti6Al2Sn2Zr3Mo1.5Cr2Nb titanium alloy, J. Mater. Process. Technol. 238 (2016) 202–211, https://doi.org/10.1016/j.jmatprotec.2016.07.011.
[732] H. Helmer, A. Bauereiß, R.F. Singer, C. Körner, Grain structure evolution in Inconel 718 during selective electron beam melting, Mater. Sci. Eng. A. 668 (2016) 180–187, https://doi.org/10.1016/j.msea.2016.05.046.
[733] L. Wang, N. Wang, Effect of substrate orientation on the formation of equiaxed stray grains in laser surface remelted single crystal superalloys: Experimental investigation, Acta Mater. 104 (2016) 250–258, https://doi.org/10.1016/j.actamat.2015.11.018.
[734] W. Liu, J.N. Dupont, Effects of substrate crystallographic orientations on crystal growth and microstructure development in laser surface-melted superalloy single crystals. Mathematical modeling of single-crystal growth in a melt pool (Part II), Acta Mater. 53 (2005) 1545–1558, https://doi.org/10.1016/j.actamat.2004.12.007.
[735] W. Liu, J.N. DuPont, Effects of melt-pool geometry on crystal growth and microstructure development in laser surface-melted superalloy single crystals. Mathematical modeling of single-crystal growth in a melt pool (part I), Acta Mater. 52 (2004) 4833–4847, https://doi.org/10.1016/j.actamat.2004.06.041.
[736] L. Wang, N. Wang, W.J. Yao, Y.P. Zheng, Effect of substrate orientation on the columnar-to-equiaxed transition in laser surface remelted single crystal superalloys, Acta Mater. 88 (2015) 283–292, https://doi.org/10.1016/j.actamat.2015.01.063.
[737] H.L. Wei, J.W. Elmer, T. Debroy, Origin of grain orientation during solidification of an aluminum alloy, Acta Mater. 115 (2016) 123–131, https://doi.org/10.1016/j.actamat.2016.05.057.
[738] J.M. Zhang, F. Ma, K.W. Xu, Calculation of the surface energy of FCC metals with modified embedded-atom method, Appl. Surf. Sci. 229 (2004) 34–42, https://doi.org/10.1016/j.apsusc.2003.09.050.
[739] M. Gäumann, C. Bezençon, P. Canalis, W. Kurz, Single-crystal laser deposition of superalloys: processing–microstructure maps, Acta Mater. 49 (2001) 1051–1062.
[740] S.H. Sun, Y. Koizumi, T. Saito, K. Yamanaka, Y.P. Li, Y. Cui, A. Chiba, Electron beam additive manufacturing of Inconel 718 alloy rods: Impact of build direction on microstructure and high-temperature tensile properties, Addit. Manuf. 23 (2018) 457–470, https://doi.org/10.1016/j.addma.2018.08.017.
[741] W. Kurz, C. Bezençon, M. Gäumann, Columnar to equiaxed transition in solidification processing, Sci. Technol. Adv. Mater. 2 (2001) 185–191, https://doi.org/10.1016/S1468-6996(01)00047-X.
[742] J.A. Spittle, Columnar to equiaxed grain transition in as solidified alloys, Int. Mater. Rev. 51 (2006) 247–269, https://doi.org/10.1179/174328006X102493.
[743] L.N. Carter, M.M. Attallah, R.C. Reed, Laser powder bed fabrication of nickel-base superalloys: Influence of parameters; characterisation, quantification and mitigation of cracking, Proc. Int. Symp. Superalloys. (2012) 577–586, https://doi.org/10.7449/2012/superalloys_2012_577_586.
[744] O.A. Ojo, N.L. Richards, M.C. Chaturvedi, Contribution of constitutional liquation of gamma prime precipitate to weld HAZ cracking of cast Inconel 738 superalloy, Scr. Mater. 50 (2004) 641–646, https://doi.org/10.1016/j.scriptamat.2003.11.025.
[745] R. Casati, J. Lemke, M. Vedani, Microstructure and Fracture Behavior of 316L Austenitic Stainless Steel Produced by Selective Laser Melting, J. Mater. Sci. Technol. 32 (2016) 738–744, https://doi.org/10.1016/j.jmst.2016.06.016.
[746] C. Pauzon, A. Markström, S.D. Le Goff, E. Hryha, Effect of the process atmosphere composition on alloy 718 produced by laser powder bed fusion, Metals (Basel). 11 (2021), https://doi.org/10.3390/met11081254.
[747] R. Engeli, T. Etter, F. Geiger, A. Stankowski, K. Wegener, Effect of Si on the SLM processability of IN738LC R., Solid Free, Fabr. Symp. (2015) 823–831.
[748] H. Zhang, H. Zhu, X. Nie, J. Yin, Z. Hu, X. Zeng, Effect of Zirconium addition on crack, microstructure and mechanical behavior of selective laser melted Al-Cu-Mg alloy, Scr. Mater. 134 (2017) 6–10, https://doi.org/10.1016/j.scriptamat.2017.02.036.
[749] X. Nie, H. Zhang, H. Zhu, Z. Hu, L. Ke, X. Zeng, Effect of Zr content on formability, microstructure and mechanical properties of selective laser melted Zr modified Al-4.24Cu-1.97Mg-0.56Mn alloys, J. Alloys Compd. 764 (2018) 977–986, https://doi.org/10.1016/j.jallcom.2018.06.032.
[750] R. Li, M. Wang, Z. Li, P. Cao, T. Yuan, H. Zhu, Developing a high-strength Al-Mg-Si-Sc-Zr alloy for selective laser melting: Crack-inhibiting and multiple strengthening mechanisms, Acta Mater. 193 (2020) 83–98, https://doi.org/10.1016/j.actamat.2020.03.060.
[751] X. He, T. DebRoy, P.W. Fuerschbach, Composition change of stainless steel during mlcrojoinlng with short laser pulse, J. Appl. Phys. 96 (2004) 4547–4555, https://doi.org/10.1063/1.1785868.
[752] K. Mundra, T. Debroy, Calculation of weld metal composition change in high-power conduction mode carbon dioxide laser-welded stainless steels, Metall. Trans. B. 24 (1993) 145–155, https://doi.org/10.1007/BF02657881.
[753] R. Barclay, Parameter optimization for controlling aluminum loss when laser depositing Ti-6Al-4V, Masters Theses. (2013). http://scholarsmine.mst.edu/masters_theses/5370.
[754] H. Zhao, T. Debroy, Weld metal composition change during conduction mode laser welding of aluminum alloy 5182, Metall. Mater. Trans. B Process Metall. Mater. Process. Sci. 32 (2001) 163–172, https://doi.org/10.1007/s11663-001-0018-6.
[755] V. Laitinen, A. Sozinov, A. Saren, A. Salminen, K. Ullakko, Laser powder bed fusion of Ni-Mn-Ga magnetic shape memory alloy, Addit. Manuf. 30 (2019), 100891, https://doi.org/10.1016/j.addma.2019.100891.
[756] H. Liao, H. Zhu, G. Xue, X. Zeng, Alumina loss mechanism of Al2O3-AlSi10 Mg composites during selective laser melting, J. Alloys Compd. 785 (2019) 286–295, https://doi.org/10.1016/j.jallcom.2019.01.116.
[757] C. Brice, R. Shenoy, M. Kral, K. Buchannan, Precipitation behavior of aluminum alloy 2139 fabricated using additive manufacturing, Mater. Sci. Eng. A. 648 (2015) 9–14, https://doi.org/10.1016/j.msea.2015.08.088.
[758] M. Simonelli, C. Tuck, N.T. Aboulkhair, I. Maskery, I. Ashcroft, R.D. Wildman, R. Hague, A Study on the Laser Spatter and the Oxidation Reactions During Selective Laser Melting of 316L Stainless Steel, Al-Si10-Mg, and Ti-6Al-4V, Metall. Mater. Trans. A Phys. Metall. Mater. Sci. (2015).
[759] D. Eylon, S.W. Schwenker, F.H. Froes, Thermally induced porosity in Ti-6Al-4V prealloyed powder compacts, Metall. Trans. A. 16 (1985) 1526–1531, https://doi.org/10.1007/BF02658686.
[760] B. Zhang, W.J. Meng, S. Shao, N. Phan, N. Shamsaei, Effect of heat treatments on pore morphology and microstructure of laser additive manufactured parts, Mater. Des. Process. Commun. 1 (2019), e29, https://doi.org/10.1002/mdp2.29.
[761] V.A. Popovich, E.V. Borisov, A.A. Popovich, V.S. Sufiiarov, D.V. Masaylo, L. Alzina, Impact of heat treatment on mechanical behaviour of Inconel 718 processed with tailored microstructure by selective laser melting, Mater. Des. 131 (2017) 12–22, https://doi.org/10.1016/j.matdes.2017.05.065.
[762] N.E. Uzan, R. Shneck, O. Yeheskel, N. Frage, Fatigue of AlSi10Mg specimens fabricated by additive manufacturing selective laser melting (AM-SLM), Mater. Sci. Eng. A. 704 (2017) 229–237, https://doi.org/10.1016/j.msea.2017.08.027.
[763] H. Masuo, Y. Tanaka, S. Morokoshi, H. Yagura, T. Uchida, Y. Yamamoto, Y. Murakami, Influence of defects, surface roughness and HIP on the fatigue strength of Ti-6Al-4V manufactured by additive manufacturing, Int. J. Fatigue. 117 (2018) 163–179, https://doi.org/10.1016/j.ijfatigue.2018.07.020.
[764] M. Seifi, M. Gorelik, J. Waller, N. Hrabe, N. Shamsaei, S. Daniewicz, J. J. Lewandowski, Progress Towards Metal Additive Manufacturing Standardization to Support Qualification and Certification, Jom. 69 (2017) 439–455, https://doi.org/10.1007/s11837-017-2265-2.
[765] A.M. Beese, B.E. Carroll, Review of Mechanical Properties of Ti-6Al-4V Made by Laser-Based Additive Manufacturing Using Powder Feedstock, Jom. 68 (2016) 724–734, https://doi.org/10.1007/s11837-015-1759-z.
[766] R.V. Dreshfield, R.L. Miner, Effects of thermally induced porosity on an as-hip powder metallurgy superalloy, in: Annu. Meet. Am. Inst. Min. Metall. Pet. Eng., 1980, https://doi.org/10.1111/add.14038.

[767] E. Strumza, S. Hayun, S. Barzilai, Y. Finkelstein, R. Ben David, O. Yeheskel, In situ detection of thermally induced porosity in additively manufactured and sintered objects, J. Mater. Sci. 54 (2019) 8665–8674, https://doi.org/10.1007/s10853-019-03452-5.
[768] S. Shao, M.J. Mahtabi, N. Shamsaei, S.M. Thompson, Solubility of argon in laser additive manufactured α-titanium under hot isostatic pressing condition, Comput. Mater. Sci. 131 (2017) 209–219, https://doi.org/10.1016/j.commatsci.2017.01.040.
[769] G. Wegmann, R. Gerling, F.P. Schimansky, Temperature induced porosity in hot isostatically pressed gamma titanium aluminide alloy powders, Acta Mater. 51 (2003) 741–752, https://doi.org/10.1016/S1359-6454(02)00465-2.
[770] D.B. Menasche, P.A. Shade, J. Lind, S.F. Li, J.V. Bernier, P. Kenesei, J.C. Schuren, R.M. Suter, Correlation of Thermally Induced Pores with Microstructural Features Using High Energy X-rays, Metall. Mater. Trans. A Phys. Metall. Mater. Sci. 47 (2016) 5580–5588, https://doi.org/10.1007/s11661-016-3712-3.
[771] E. Strandh, P. Mellin, S.-D.-L. Goff, J. Gårdstam, M. Ahlfors, A. Strondl, Surface pick-up of argon during hot isostatic pressing of material built by laser powder bed fusion, Addit. Manuf. (2020), 101763, https://doi.org/10.1016/j.addma.2020.101763.
[772] P. Edwards, M. Ramulu, Fatigue performance evaluation of selective laser melted Ti-6Al-4V, Mater. Sci. Eng. A. 598 (2014) 327–337.
[773] A. Yadollahi, N. Shamsaei, Additive manufacturing of fatigue resistant materials: Challenges and opportunities, Int. J. Fatigue. 98 (2017) 14–31, https://doi.org/10.1016/j.ijfatigue.2017.01.001.
[774] S. Tammas-Williams, H. Zhao, F. Léonard, F. Derguti, I. Todd, P.B. Prangnell, XCT analysis of the influence of melt strategies on defect population in Ti–6Al–4V components manufactured by Selective Electron Beam Melting, Mater. Charact. 102 (2015) 47–61, https://doi.org/10.1016/j.matchar.2015.02.008.
[775] S. Kou, Welding Metallurgy, Wiley, Second, 1987.
[776] T.T. Roehling, S.S.Q. Wu, S.A. Khairallah, J.D. Roehling, S.S. Soezeri, M.F. Crumb, M.J. Matthews, Modulating laser intensity profile ellipticity for microstructural control during metal additive manufacturing, Acta Mater. 128 (2017) 197–206.
[777] T. Mukherjee, T. DebRoy, Mitigation of lack of fusion defects in powder bed fusion additive manufacturing, J. Manuf. Process. 36 (2018) 442–449, https://doi.org/10.1016/j.jmapro.2018.10.028.
[778] A. Ladewig, G. Schlick, M. Fisser, V. Schulze, U. Glatzel, Influence of the shielding gas flow on the removal of process by-products in the selective laser melting process, Addit. Manuf. 10 (2016) 1–9.
[779] P.A. Kobryn, E.H. Moore, S.L. Semiatin, The effect of laser power and traverse speed on microstructure, porosity, and build height in laser-deposited Ti-6Al-4V, Scr. Mater. 4 (2000) 299–305.
[780] A.G. Demir, B. Previtali, Investigation of remelting and preheating in SLM of 18Ni300 maraging steel as corrective and preventive measures for porosity reduction, Int. J. Adv. Manuf. Technol. 93 (2017) 2697–2709.
[781] S. Beretta, S. Romano, A comparison of fatigue strength sensitivity to defects for materials manufactured by AM or traditional processes, Int. J. Fatigue. 94 (2017) 178–191, https://doi.org/10.1016/j.ijfatigue.2016.06.020.
[782] Y. Murakami, S. Beretta, Small Defects and Inhomogeneities in Fatigue Strength: Experiments, Models and Statistical Implications, Extremes. 2 (1999) 123–147, https://doi.org/10.1023/A:1009976418553.
[783] S. Romano, P.D. Nezhadfar, N. Shamsaei, M. Seifi, S. Beretta, High cycle fatigue behavior and life prediction for additively manufactured 17–4 PH stainless steel: Effect of sub-surface porosity and surface roughness, Theor. Appl. Fract. Mech. 106 (2020), 102477, https://doi.org/10.1016/j.tafmec.2020.102477.
[784] S. Romano, A. Abel, J. Gumpinger, A.D. Brandão, S. Beretta, Quality control of AlSi10Mg produced by SLM: Metallography versus CT scans for critical defect size assessment, Addit. Manuf. 28 (2019) 394–405, https://doi.org/10.1016/j.addma.2019.05.017.
[785] A. Yadollahi, N. Shamsaei, S.M. Thompson, A. Elwany, L. Bian, Effects of building orientation and heat treatment on fatigue behavior of selective laser melted 17–4 PH stainless steel, Int. J. Fatigue. 94 (2017) 218–235, https://doi.org/10.1016/j.ijfatigue.2016.03.014.
[786] A. Fatemi, N. Shamsaei, Multiaxial fatigue: An overview and some approximation models for life estimation, Int. J. Fatigue. 33 (2011) 948–958, https://doi.org/10.1016/j.ijfatigue.2011.01.003.
[787] U. Scipioni, A.J. Wolfer, M.J. Matthews, J.R. Delplanque, J.M. Schoenung, On the limitations of Volumetric Energy Density as a design parameter for Selective Laser Melting, JMADE. 113 (2017) 331–340, https://doi.org/10.1016/j.matdes.2016.10.037.
[788] M. Bayat, A. Thanki, S. Mohanty, A. Witvrouw, S. Yang, J. Thorborg, N. Skat, J. Henri, Keyhole-induced porosities in Laser-based Powder Bed Fusion (L-PBF) of Ti6Al4V : High-fidelity modelling and experimental validation, Addit. Manuf. 30 (2019), 100835, https://doi.org/10.1016/j.addma.2019.100835.
[789] P. Promoppatum, S. Yao, Analytical evaluation of defect generation for selective laser melting of metals, 2019, pp. 1185–1198.
[790] L. Meng, J. Zhang, Process Design of Laser Powder Bed Fusion of Stainless Steel Using a Gaussian Process-Based Machine Learning Model, JOM. (2019), https://doi.org/10.1007/s11837-019-03792-2.
[791] R.M. Hunt, K.J. Kramer, B. El-dasher, Selective laser sintering of MA956 oxide dispersion strengthened steel, J. Nucl. Mater. 464 (2015) 80–85, https://doi.org/10.1016/j.jnucmat.2015.04.011.
[792] N. Calta, P. Collins, A. Martin, M. Matthews, J.N. Weker, R. Ott, K. Stone, C. Tassone, In-situ Data Acquisition and Tool Development for Additive Manufacturing Metal Powder Systems, 2019.
[793] D. Manfredi, F. Calignano, M. Krishnan, R. Canali, E. Paola, S. Biamino, D. Ugues, M. Pavese, P. Fino, Additive Manufacturing of Al Alloys and Aluminium Matrix Composites (AMCs), Light Met. Alloy. Appl, InTech, 2014. https://doi.org/10.5772/58534. https://doi.org/10.5772/57353.
[794] B. Wysocki, P. Maj, A. Krawczyńska, K. Rożniatowski, J. Zdunek, K. J. Kurzydłowski, W. Święszkowski, Microstructure and mechanical properties investigation of CP titanium processed by selective laser melting (SLM), J. Mater. Process. Technol. 241 (2017) 13–23, https://doi.org/10.1016/j.jmatprotec.2016.10.022.
[795] S.A. Khairallah, A.T. Anderson, A.M. Rubenchik, W.E. King, Laser powder-bed fusion additive manufacturing: Physics of complex melt flow and formation mechanisms of pores, spatter, and denudation zones, Addit. Manuf. Handb. Prod. Dev. Def. Ind. 108 (2017) 613–628, https://doi.org/10.1201/9781315119106.
[796] T. Achee, G. Guss, A. Elwany, M. Matthews, Laser pre-sintering for denudation reduction in the laser powder bed fusion additive manufacturing of Ti-6Al-4V alloy, Addit. Manuf. 42 (2021), 101985, https://doi.org/10.1016/j.addma.2021.101985.
[797] S. Le Roux, M. Salem, A. Hor, Improvement of the bridge curvature method to assess residual stresses in selective laser melting, Addit. Manuf. 22 (2018) 320–329, https://doi.org/10.1016/j.addma.2018.05.025.
[798] L. Shuai, Q. Wei, Y. Shi, J. Zhang, L. Wei, Micro-Crack Formation and Controlling of Inconel625 Parts Fabricated by Selective Laser Melting, Solid Free, in: Fabr. Symp. – An Addit. Manuf. Conf., 2016, pp. 520–529.
[799] J.P. Kruth, J. Deckers, E. Yasa, R. Wauthlé, Assessing and comparing influencing factors of residual stresses in selective laser melting using a novel analysis method, Proc. Inst. Mech. Eng. Part B J. Eng. Manuf. 226 (2012) 980–991, https://doi.org/10.1177/0954405412437085.
[800] M. Shiomi, K. Osakada, K. Nakamura, T. Yamashita, F. Abe, Residual stress within metallic model made by selective laser melting process, CIRP Ann. - Manuf. Technol. 53 (2004) 195–198, https://doi.org/10.1016/S0007-8506(07)60677-5.
[801] N.W. Klingbeil, J.L. Beuth, R.K. Chin, C.H. Amon, Residual stress-induced warping in direct metal solid freeform fabrication, Int. J. Mech. Sci. 44 (2002) 57–77, https://doi.org/10.1016/S0020-7403(01)00084-4.
[802] A.V. Gusarov, M. Pavlov, I. Smurov, Residual stresses at laser surface remelting and additive manufacturing, Phys. Procedia. 12 (2011) 248–254, https://doi.org/10.1016/j.phpro.2011.03.032.
[803] G. Vastola, G. Zhang, Q.X. Pei, Y.W. Zhang, Controlling of residual stress in additive manufacturing of Ti6Al4V by finite element modeling, Addit. Manuf. 12 (2016) 231–239, https://doi.org/10.1016/j.addma.2016.05.010.
[804] T. Simson, A. Emmel, A. Dwars, J. Böhm, Residual stress measurements on AISI 316L samples manufactured by selective laser melting, Addit. Manuf. 17 (2017) 183–189, https://doi.org/10.1016/j.addma.2017.07.007.
[805] T. Mukherjee, V. Manvatkar, A. De, T. DebRoy, Mitigation of thermal distortion during additive manufacturing, Scr. Mater. 127 (2017) 79–83, https://doi.org/10.1016/j.scriptamat.2016.09.001.
[806] L.M. Sochalski-Kolbus, E.A. Payzant, P.A. Cornwell, T.R. Watkins, S.S. Babu, R. R. Dehoff, M. Lorenz, O. Ovchinnikova, C. Duty, Comparison of Residual Stresses in Inconel 718 Simple Parts Made by Electron Beam Melting and Direct Laser Metal Sintering, Metall. Mater. Trans. A Phys. Metall. Mater. Sci. 46 (2015) 1419–1432, https://doi.org/10.1007/s11661-014-2722-2.
[807] Y. Cao, H.L. Wei, T. Yang, T.T. Liu, W.H. Liao, Printability assessment with porosity and solidification cracking susceptibilities for a high strength aluminum alloy during laser powder bed fusion, Addit. Manuf. 46 (2021), 102103, https://doi.org/10.1016/j.addma.2021.102103.
[808] H. Ali, H. Ghadbeigi, K. Mumtaz, Residual stress development in selective laser-melted Ti6Al4V: a parametric thermal modelling approach, Int. J. Adv. Manuf. Technol. 97 (2018) 2621–2633, https://doi.org/10.1007/s00170-018-2104-9.
[809] L.S. Anderson, A.M. Venter, B. Vrancken, D. Marais, J. Van Humbeeck, Investigating the Residual Stress Distribution in Selective Laser Melting Produced Ti-6Al-4V using Neutron Diffraction, Mech. Stress Eval. by Neutron Synchrotron Radiat. 4 (2018) 73–78. https://doi.org/10.21741/9781945291678-11.
[810] M.F. Zaeh, G. Branner, Investigations on residual stresses and deformations in selective laser melting, Prod. Eng. 4 (2010) 35–45, https://doi.org/10.1007/s11740-009-0192-y.
[811] N. Nadammal, T. Mishurova, T. Fritsch, I. Serrano-Munoz, A. Kromm, C. Haberland, P.D. Portella, G. Bruno, Critical role of scan strategies on the development of microstructure, texture, and residual stresses during laser powder bed fusion additive manufacturing, Addit. Manuf. 38 (2021), 101792, https://doi.org/10.1016/j.addma.2020.101792.
[812] P. Aggarangsi, J.L. Beuth, Localized preheating approaches for reducing residual stress in additive manufacturing, in: 17th Solid Free. Fabr. Symp. SFF 2006, 2006, pp. 709–720.
[813] Q. Chen, H. Taylor, A. Takezawa, X. Liang, X. Jimenez, R. Wicker, A.C. To, Island scanning pattern optimization for residual deformation mitigation in laser powder bed fusion via sequential inherent strain method and sensitivity analysis, Addit. Manuf. 46 (2021), 102116, https://doi.org/10.1016/j.addma.2021.102116.
[814] N.J. Harrison, I. Todd, K. Mumtaz, Reduction of micro-cracking in nickel superalloys processed by Selective Laser Melting: A fundamental alloy design approach, Acta Mater. 94 (2015) 59–68, https://doi.org/10.1016/j.actamat.2015.04.035.
[815] A. Röttger, K. Geenen, M. Windmann, F. Binner, W. Theisen, Comparison of microstructure and mechanical properties of 316 L austenitic steel processed by selective laser melting with hot-isostatic pressed and cast material, Mater. Sci. Eng. A. 678 (2016) 365–376, https://doi.org/10.1016/j.msea.2016.10.012.
[816] E. Uhlmann, A. Bergmann, W. Gridin, Investigation on Additive Manufacturing of tungsten carbide-cobalt by Selective Laser Melting, Procedia CIRP. 35 (2015) 8–15.

[817] H. Ali, L. Ma, H. Ghadbeigi, K. Mumtaz, In-situ residual stress reduction, martensitic decomposition and mechanical properties enhancement through high temperature powder bed pre-heating of Selective Laser Melted Ti6Al4V, Mater. Sci. Eng. A. 695 (2017) 211–220, https://doi.org/10.1016/j.msea.2017.04.033.
[818] A.S. Wu, D.W. Brown, M. Kumar, G.F. Gallegos, W.E. King, An Experimental Investigation into Additive Manufacturing-Induced Residual Stresses in 316L Stainless Steel, Metall. Mater. Trans. A Phys. Metall. Mater. Sci. 45 (2014) 6260–6270, https://doi.org/10.1007/s11661-014-2549-x.
[819] H. Wang, L. Chen, B. Dovgyy, W. Xu, A. Sha, X. Li, H. Tang, Y. Liu, H. Wu, M. S. Pham, Micro-cracking, microstructure and mechanical properties of Hastelloy-X alloy printed by laser powder bed fusion: As-built, annealed and hot-isostatic pressed, Addit. Manuf. 39 (2021), 101853, https://doi.org/10.1016/j.addma.2021.101853.
[820] B. AlMangour, D. Grzesiak, J.M. Yang, Selective laser melting of TiB2/H13 steel nanocomposites: Influence of hot isostatic pressing post-treatment, J. Mater. Process. Technol. 244 (2017) 344–353, https://doi.org/10.1016/j.jmatprotec.2017.01.019.
[821] D. Tomus, T. Jarvis, X. Wu, J. Mei, P. Rometsch, E. Herny, J.F. Rideau, S. Vaillant, Controlling the microstructure of Hastelloy-X components manufactured by Selective Laser Melting, Phys. Procedia. 41 (2013) 823–827, https://doi.org/10.1016/j.phpro.2013.03.154.
[822] S. Thapliyal, M. Komarasamy, S. Shukla, L. Zhou, H. Hyer, S. Park, Y. Sohn, R. S. Mishra, An integrated computational materials engineering-anchored closed-loop method for design of aluminum alloys for additive manufacturing, Materialia. 9 (2020), 100574, https://doi.org/10.1016/j.mtla.2019.100574.
[823] S. Thapliyal, S.S. Nene, P. Agrawal, T. Wang, C. Morphew, R.S. Mishra, B. A. McWilliams, K.C. Cho, Damage-tolerant, corrosion-resistant high entropy alloy with high strength and ductility by laser powder bed fusion additive manufacturing, Addit. Manuf. 36 (2020), 101455, https://doi.org/10.1016/j.addma.2020.101455.
[824] P. Jiang, S. Geng, X. Shao, G. Mi, C. Wang, H. Wu, C. Han, S. Gao, Fine Grains Reduce Cracking Susceptibility During Solidification: Insights from Phase-Field Simulations, Jom. 71 (2019) 3223–3229, https://doi.org/10.1007/s11837-019-03342-w.
[825] H. Xiao, S. Li, X. Han, J. Mazumder, L. Song, Laves phase control of Inconel 718 alloy using quasi-continuous-wave laser additive manufacturing, Mater. Des. 122 (2017) 330–339, https://doi.org/10.1016/j.matdes.2017.03.004.
[826] T. Artaza, T. Bhujangrao, A. Suárez, F. Veiga, A. Lamikiz, Influence of heat input on the formation of laves phases and hot cracking in plasma arc welding (PAW) additive manufacturing of inconel 718, Metals (Basel). 10 (2020) 1–17, https://doi.org/10.3390/met10060771.
[827] Y. Chen, F. Lu, K. Zhang, P. Nie, S.R. Elmi Hosseini, K. Feng, Z. Li, P.K. Chu, Investigation of dendritic growth and liquation cracking in laser melting deposited Inconel 718 at different laser input angles, Mater. Des. 105 (2016) 133–141, https://doi.org/10.1016/j.matdes.2016.05.034.
[828] Q. Han, Y. Gu, S. Soe, F. Lacan, R. Setchi, Effect of hot cracking on the mechanical properties of Hastelloy X superalloy fabricated by laser powder bed fusion additive manufacturing, Opt. Laser Technol. 124 (2020), 105984, https://doi.org/10.1016/j.optlastec.2019.105984.
[829] A. Basak, S. Das, Additive Manufacturing of Nickel-Base Superalloy René N5 through Scanning Laser Epitaxy (SLE) – Material Processing, Microstructures, and Microhardness Properties, Adv. Eng. Mater. 19 (2017) 1–10.
[830] A.B. Spierings, K. Dawson, T. Heeling, P.J. Uggowitzer, R. Schäublin, F. Palm, K. Wegener, Microstructural features of Sc- and Zr-modified Al-Mg alloys processed by selective laser melting, Mater. Des. 115 (2017) 52–63, https://doi.org/10.1016/j.matdes.2016.11.040.
[831] L. Zhou, H. Pan, H. Hyer, S. Park, Y. Bai, B. McWilliams, K. Cho, Y. Sohn, Microstructure and tensile property of a novel AlZnMgScZr alloy additively manufactured by gas atomization and laser powder bed fusion, Scr. Mater. 158 (2019) 24–28, https://doi.org/10.1016/j.scriptamat.2018.08.025.
[832] D. Carluccio, M.J. Bermingham, Y. Zhang, D.H. StJohn, K. Yang, P.A. Rometsch, X. Wu, M.S. Dargusch, Grain refinement of laser remelted Al-7Si and 6061 aluminium alloys with Tibor® and scandium additions, J. Manuf. Process. 35 (2018) 715–720, https://doi.org/10.1016/j.jmapro.2018.08.030.
[833] O. Lopez-Botello, U. Martinez-Hernandez, J. Ramírez, C. Pinna, K. Mumtaz, Two-dimensional simulation of grain structure growth within selective laser melted AA-2024, Mater. Des. 113 (2017) 369–376, https://doi.org/10.1016/j.matdes.2016.10.031.
[834] K.V. Yang, Y. Shi, F. Palm, X. Wu, P. Rometsch, Columnar to equiaxed transition in Al-Mg(-Sc)-Zr alloys produced by selective laser melting, Scr. Mater. 145 (2018) 113–117, https://doi.org/10.1016/j.scriptamat.2017.10.021.
[835] D. Zhang, D. Qiu, M.A. Gibson, Y. Zheng, H.L. Fraser, D.H. StJohn, M.A. Easton, Additive manufacturing of ultrafine-grained high-strength titanium alloys, Nature. 576 (2019) 91–95, https://doi.org/10.1038/s41586-019-1783-1.
[836] W. Xu, E.W. Lui, A. Pateras, M. Qian, M. Brandt, In situ tailoring microstructure in additively manufactured Ti-6Al-4V for superior mechanical performance, Acta Mater. 125 (2017) 390–400, https://doi.org/10.1016/j.actamat.2016.12.027.
[837] M.J. Bermingham, D.H. StJohn, J. Krynen, S. Tedman-Jones, M.S. Dargusch, Promoting the columnar to equiaxed transition and grain refinement of titanium alloys during additive manufacturing, Acta Mater. 168 (2019) 261–274, https://doi.org/10.1016/j.actamat.2019.02.020.
[838] S. Mereddy, M.J. Bermingham, D.H. StJohn, M.S. Dargusch, Grain refinement of wire arc additively manufactured titanium by the addition of silicon, J. Alloys Compd. 695 (2017) 2097–2103, https://doi.org/10.1016/j.jallcom.2016.11.049.
[839] M.J. Bermingham, D. Kent, H. Zhan, D.H. Stjohn, M.S. Dargusch, Controlling the microstructure and properties of wire arc additive manufactured Ti-6Al-4V with trace boron additions, Acta Mater. 91 (2015) 289–303, https://doi.org/10.1016/j.actamat.2015.03.035.
[840] D.T. Ardi, Y. Gli, K.H.K. Chan, L. Blunt, M.R. Bache, Surface topography and the impact on fatigue performance, Surf. Topogr. Metrol. Prop. 3 (2015), https://doi.org/10.1088/2051-672X/3/1/015007.
[841] E. Lyczkowska, P. Szymczyk, B. Dybała, E. Chlebus, Chemical polishing of scaffolds made of Ti-6Al-7Nb alloy by additive manufacturing, Arch. Civ. Mech. Eng. 14 (2014) 586–594, https://doi.org/10.1016/j.acme.2014.03.001.
[842] F. Scherillo, Chemical surface finishing of AlSi10Mg components made by additive manufacturing, Manuf. Lett. 19 (2019) 5–9, https://doi.org/10.1016/j.mfglet.2018.12.002.
[843] L. Yang, Y. Wu, A. Lassell, B. Zhou, Electropolishing of Ti6Al4V Parts Fabricated by Electron Beam Melting, Solid Free. Fabr. Proc. (2016) 1333–1344.
[844] S. Rahmati, E. Vahabli, Evaluation of analytical modeling for improvement of surface roughness of FDM test part using measurement results, Int. J. Adv. Manuf. Technol. 79 (2015) 823–829, https://doi.org/10.1007/s00170-015-6879-7.
[845] A.H. Maamoun, Y.F. Xue, M.A. Elbestawi, S.C. Veldhuis, Effect of selective laser melting process parameters on the quality of al alloy parts: Powder characterization, density, surface roughness, and dimensional accuracy, Materials (Basel). 11 (2018), https://doi.org/10.3390/ma11122343.
[846] A. Ghanekar, R. Crawford, D. Watson, Optimization of SLS Process Parameters using D-Optimality, Solid Free, Fabr. Proc. (2003) 348–362.
[847] E. Masiagutova, F. Cabanettes, A. Sova, M. Cici, G. Bidron, P. Bertrand, Side surface topography generation during laser powder bed fusion of AlSi10Mg, Addit. Manuf. 47 (2021), 102230, https://doi.org/10.1016/j.addma.2021.102230.
[848] E. Yasa, J. Deckers, J.-P. Kruth, The investigation of the influence of laser re-melting on density, surface quality and microstructure of selective laser melting parts, Rapid Prototyp. J. 17 (2011) 312–327.
[849] K.A. Ibrahim, B. Wu, N.P. Brandon, Electrical conductivity and porosity in stainless steel 316L scaffolds for electrochemical devices fabricated using selective laser sintering, Mater. Des. 106 (2016) 51–59, https://doi.org/10.1016/j.matdes.2016.05.096.
[850] F. Cabanettes, A. Joubert, G. Chardon, V. Dumas, J. Rech, C. Grosjean, Z. Dimkovski, Topography of as built surfaces generated in metal additive manufacturing: A multi scale analysis from form to roughness, Precis. Eng. 52 (2018) 249–265, https://doi.org/10.1016/j.precisioneng.2018.01.002.
[851] A. Boschetto, L. Bottini, F. Veniali, Roughness modeling of AlSi10Mg parts fabricated by selective laser melting, J. Mater. Process. Technol. 241 (2017) 154–163, https://doi.org/10.1016/j.jmatprotec.2016.11.013.
[852] N. Kouraytem, R.A. Chanut, D.S. Watring, T. Loveless, J. Varga, A.D. Spear, O. T. Kingstedt, Dynamic-loading behavior and anisotropic deformation of pre- and post-heat-treated IN718 fabricated by selective laser melting, Addit. Manuf. 33 (2020), 101083, https://doi.org/10.1016/j.addma.2020.101083.
[853] R.R. Dehoff, M. Kirka, W.J. Sames, H. Bilheux, A.S. Tremsin, L.E. Lowe, S.S. Babu, Site specific control of crystallographic grain orientation through electron beam additive manufacturing, Mater. Sci. Technol. (United Kingdom) 31 (2015) 931–938, https://doi.org/10.1179/1743284714Y.0000000734.
[854] N. Hrabe, T. Quinn, Effects of processing on microstructure and mechanical properties of a titanium alloy (Ti-6Al-4V) fabricated using electron beam melting (EBM), Part 2: Energy input, orientation, and location, Mater. Sci. Eng. A. 573 (2013) 271–277, https://doi.org/10.1016/j.msea.2013.02.065.
[855] J. Gockel, J. Beuth, Understanding Ti-6Al-4V microstructure control in additive manufacturing via process maps, in: 24th Int. SFF Symp. - An Addit. Manuf. Conf. SFF 2013, 2013, pp. 666–674.
[856] W.M. Tucho, P. Cuvillier, A. Sjolyst-Kverneland, V. Hansen, Microstructure and hardness studies of Inconel 718 manufactured by selective laser melting before and after solution heat treatment, Mater. Sci. Eng. A. 689 (2017) 220–232, https://doi.org/10.1016/j.msea.2017.02.062.
[857] E. Chlebus, K. Gruber, B. Kuźnicka, J. Kurzac, T. Kurzynowski, Effect of heat treatment on the microstructure and mechanical properties of Inconel 718 processed by selective laser melting, Mater. Sci. Eng. A. 639 (2015) 647–655, https://doi.org/10.1016/j.msea.2015.05.035.
[858] M.J. Bermingham, S.D. McDonald, M.S. Dargusch, D.H. St. John, Grain-refinement mechanisms in titanium alloys, J. Mater. Res. 23 (2008) 97–104, https://doi.org/10.1557/jmr.2008.0002.
[859] C.A. Brice, B.T. Rosenberger, S.N. Sankaran, K.M. Taminger, B. Woods, R. Nasserrafi, Chemistry Control in Electron Beam Deposited Titanium Alloys, Mater. Sci. Forum. 618–619 (2009) 155–158, https://doi.org/10.4028/www.scientific.net/msf.618-619.155.
[860] C. Teng, D. Pal, H. Gong, K. Zeng, K. Briggs, N. Patil, B. Stucker, A review of defect modeling in laser material processing, Addit. Manuf. 14 (2017) 137–147, https://doi.org/10.1016/j.addma.2016.10.009.
[861] J. Ning, W. Wang, B. Zamorano, S.Y. Liang, Analytical modeling of lack-of-fusion porosity in metal additive manufacturing, Appl. Phys. A. 125 (2019) 797, https://doi.org/10.1007/s00339-019-3092-9.
[862] C. Teng, H. Gong, A. Szabo, J. Dilip, K. Ashby, S. Zhang, N. Patil, D. Pal, B. Stucker, Simulating Melt Pool Shape and Lack of Fusion Porosity for Selective Laser Melting of Cobalt Chromium Components, 2016. https://doi.org/10.1115/1.4034137.
[863] M. Bayat, S. Mohanty, J.H. Hattel, Multiphysics modelling of lack-of-fusion voids formation and evolution in IN718 made by multi-track/multi-layer L-PBF, Int. J. Heat Mass Transf. 139 (2019) 95–114, https://doi.org/10.1016/j.ijheatmasstransfer.2019.05.003.
[864] C. Bruna-Rosso, A.G. Demir, B. Previtali, Selective laser melting finite element modeling: Validation with high-speed imaging and lack of fusion defects

prediction, Mater. Des. 156 (2018) 143–153, https://doi.org/10.1016/j.matdes.2018.06.037.
[865] G. Vastola, Q.X. Pei, Y.W. Zhang, Predictive model for porosity in powder-bed fusion additive manufacturing at high beam energy regime, Addit. Manuf. 22 (2018) 817–822, https://doi.org/10.1016/j.addma.2018.05.042.
[866] J.L. Tan, C. Tang, C.H. Wong, A Computational Study on Porosity Evolution in Parts Produced by Selective Laser Melting, Metall. Mater. Trans. A Phys. Metall. Mater. Sci. 49 (2018) 3663–3673, https://doi.org/10.1007/s11661-018-4697-x.
[867] C. Tang, J.L. Tan, C.H. Wong, A numerical investigation on the physical mechanisms of single track defects in selective laser melting, Int. J. Heat Mass Transf. 126 (2018) 957–968, https://doi.org/10.1016/j.ijheatmasstransfer.2018.06.073.
[868] C. Kloss, C. Goniva, LIGGGHTS – Open Source Discrete Element Simulations of Granular Materials Based on Lammps, in: Suppl. Proc., John Wiley & Sons, Ltd, 2011, pp. 781–788. https://doi.org/10.1002/9781118062142.ch94.
[869] H. Jaska, A. Jemcov, Z. Tukovic, OpenFOAM: A C++ library for complex physics simulationsNo Title, Int. Work. Coupled Methods Numer. Dyn. 1000 (2007) 1–20.
[870] A.M. Rubenchik, W.E. King, S.S. Wu, Scaling laws for the additive manufacturing, J. Mater. Process. Technol. 257 (2018) 234–243, https://doi.org/10.1016/j.jmatprotec.2018.02.034.
[871] J. Ye, S.A. Khairallah, A.M. Rubenchik, M.F. Crumb, G. Guss, J. Belak, M. J. Matthews, Energy Coupling Mechanisms and Scaling Behavior Associated with Laser Powder Bed Fusion Additive Manufacturing, Adv. Eng. Mater. 21 (2019) 1900185, https://doi.org/10.1002/adem.201900185.
[872] A.M. Philo, S. Mehraban, M. Holmes, S. Sillars, C.J. Sutcliffe, J. Sienz, S.G. R. Brown, N.P. Lavery, A pragmatic continuum level model for the prediction of the onset of keyholing in laser powder bed fusion, Int. J. Adv. Manuf. Technol. 101 (2019) 697–714, https://doi.org/10.1007/s00170-018-2770-7.
[873] O. Fergani, F. Berto, T. Welo, S.Y. Liang, Analytical modelling of residual stress in additive manufacturing, Fatigue Fract. Eng. Mater. Struct. 40 (2017) 971–978, https://doi.org/10.1111/ffe.12560.
[874] J.C. Heigel, P. Michaleris, E.W. Reutzel, Thermo-mechanical model development and validation of directed energy deposition additive manufacturing of Ti-6Al-4V, Addit. Manuf. 5 (2015) 9–19, https://doi.org/10.1016/j.addma.2014.10.003.
[875] E.R. Denlinger, V. Jagdale, G.V. Srinivasan, T. El-Wardany, P. Michaleris, Thermal modeling of Inconel 718 processed with powder bed fusion and experimental validation using in situ measurements, Addit. Manuf. 11 (2016) 7–15, https://doi.org/10.1016/j.addma.2016.03.003.
[876] L. Parry, I. Ashcroft, D. Bracket, R.D. Wildman, Investigation of residual stresses in selective laser melting, Key Eng. Mater. 627 (2015) 129–132, https://doi.org/10.4028/www.scientific.net/KEM.627.129.
[877] S. Jayanath, A. Achuthan, A Computationally Efficient Finite Element Framework to Simulate Additive Manufacturing Processes, J. Manuf. Sci. Eng. Trans. ASME. 140 (2018) 1–13, https://doi.org/10.1115/1.4039092.
[878] C. Li, J.F. Liu, Y.B. Guo, Prediction of Residual Stress and Part Distortion in Selective Laser Melting, in: Procedia CIRP, Elsevier B.V., 2016, pp. 171–174, https://doi.org/10.1016/j.procir.2016.02.058.
[879] L. Papadakis, A. Loizou, J. Risse, J. Schrage, Numerical computation of component shape distortion manufactured by Selective Laser Melting, Procedia CIRP. 18 (2014) 90–95, https://doi.org/10.1016/j.procir.2014.06.113.
[880] T. Mukherjee, W. Zhang, T. DebRoy, An improved prediction of residual stresses and distortion in additive manufacturing, Comput. Mater. Sci. 126 (2017) 360–372, https://doi.org/10.1016/j.commatsci.2016.10.003.
[881] A. Olleak, Z. Xi, Efficient LPBF process simulation using finite element modeling with adaptive remeshing for distortions and residual stresses prediction, Manuf. Lett. 24 (2020) 140–144, https://doi.org/10.1016/j.mfglet.2020.05.002.
[882] J. Cao, M.A. Gharghouri, P. Nash, Finite-element analysis and experimental validation of thermal residual stress and distortion in electron beam additive manufactured Ti-6Al-4V build plates, J. Mater. Process. Technol. 237 (2016) 409–419, https://doi.org/10.1016/j.jmatprotec.2016.06.032.
[883] R.J. Moat, A.J. Pinkerton, L. Li, P.J. Withers, M. Preuss, Residual stresses in laser direct metal deposited Waspaloy, Mater. Sci. Eng. A. 528 (2011) 2288–2298, https://doi.org/10.1016/j.msea.2010.12.010.
[884] F. Neugebauer, N. Keller, A.W. Gmbh, V. Ploshikhin, F. Feuerhahn, B. Gmbh, Multi Scale FEM Simulation for Distortion Calculation in Additive Manufacturing of Hardening Stainless Steel Multi Scale FEM Simulation for Distortion Calculation in Additive Manufacturing of Hardening Stainless Steel, 2014.
[885] R.K. Ganeriwala, M. Strantza, W.E. King, B. Clausen, T.Q. Phan, L.E. Levine, D. W. Brown, N.E. Hodge, Evaluation of a thermomechanical model for prediction of residual stress during laser powder bed fusion of Ti-6Al-4V, Addit. Manuf. 27 (2019) 489–502, https://doi.org/10.1016/j.addma.2019.03.034.
[886] N.E. Hodge, R.M. Ferencz, J.M. Solberg, Implementation of a thermomechanical model for the simulation of selective laser melting, Comput. Mech. 54 (2014) 33–51, https://doi.org/10.1007/s00466-014-1024-2.
[887] N.E. Hodge, R.M. Ferencz, R.M. Vignes, Experimental comparison of residual stresses for a thermomechanical model for the simulation of selective laser melting, Addit. Manuf. 12 (2016) 159–168, https://doi.org/10.1016/j.addma.2016.05.011.
[888] C. Chen, G. Wang, L. Ke, The effect of process parameters on the residual stress of selective laser melted Inconel 718 thin-walled part, 8 (2019) 1359–1369. https://doi.org/10.1108/RPJ-09-2018-0249.
[889] M. Gouge, E. Denlinger, J. Irwin, C. Li, P. Michaleris, Experimental validation of thermo-mechanical part-scale modeling for laser powder bed fusion processes, Addit. Manuf. 29 (2019), 100771, https://doi.org/10.1016/j.addma.2019.06.022.
[890] R.J. Williams, C.M. Davies, P.A. Hooper, A pragmatic part scale model for residual stress and distortion prediction in powder bed fusion, Addit. Manuf. 22 (2018) 416–425, https://doi.org/10.1016/j.addma.2018.05.038.
[891] Q. Chen, X. Liang, D. Hayduke, J. Liu, L. Cheng, J. Oskin, R. Whitmore, A.C. To, An inherent strain based multiscale modeling framework for simulating part-scale residual deformation for direct metal laser sintering, Addit. Manuf. 28 (2019) 406–418, https://doi.org/10.1016/j.addma.2019.05.021.
[892] E.R. Denlinger, M. Gouge, J. Irwin, P. Michaleris, Thermomechanical model development and in situ experimental validation of the Laser Powder-Bed Fusion process, Addit. Manuf. 16 (2017) 73–80, https://doi.org/10.1016/j.addma.2017.05.001.
[893] X. Liang, Q. Chen, L. Cheng, D. Hayduke, A.C. To, Modified inherent strain method for efficient prediction of residual deformation in direct metal laser sintered components, Comput. Mech. 64 (2019) 1719–1733, https://doi.org/10.1007/s00466-019-01748-6.
[894] Q. Wu, C. Qiao, J. Wang, D. Yao, Y. Wu, W. Fan, M. Li, X. An, Adaptability investigations on bottom modified blade in powder spreading process of additive manufacturing, Addit. Manuf. (2021), 102477, https://doi.org/10.1016/j.addma.2021.102477.
[895] A.T. Sutton, C.S. Kriewall, M.C. Leu, J.W. Newkirk, Powder characterisation techniques and effects of powder characteristics on part properties in powder-bed fusion processes, Virtual Phys. Prototyp. 12 (2017) 3–29, https://doi.org/10.1080/17452759.2016.1250605.
[896] L. Ma, J. Fong, B. Lane, S. Moylan, J. Filliben, A. Heckert, L. Levine, Using Design of Experiments in Finite Element Modeling To Identify Critical Variables for Laser Powder Bed Fusion, Proc. Solid Free. Fabr. Symp. (2015) 219–228.
[897] Z. Xiang, M. Yin, Z. Deng, X. Mei, G. Yin, Simulation of Forming Process of Powder Bed for Additive Manufacturing, 2016. https://doi.org/10.1115/1.4032970.
[898] J. Zhou, Y. Zhang, J.K. Chen, Numerical Simulation of Random Packing of Spherical Particles for Powder-Based Additive Manufacturing, J. Manuf. Sci. Eng. 131 (2009), https://doi.org/10.1115/1.3123324.
[899] X. Li, C. Zhao, T. Sun, W. Tan, Revealing transient powder-gas interaction in laser powder bed fusion process through multi-physics modeling and high-speed synchrotron X-ray imaging, Addit. Manuf. (2020).
[900] X. Li, Q. Guo, L. Chen, W. Tan, Quantitative investigation of gas flow, powder-gas interaction, and powder behavior under different ambient pressure levels in laser powder bed fusion, Int. J. Mach. Tools Manuf. 170 (2021), 103797, https://doi.org/10.1016/j.ijmachtools.2021.103797.
[901] D. Li, C.L. Merkle, A unified framework for incompressible and compressible fluid flows, J. Hydrodyn. 18 (2006) 111–117, https://doi.org/10.1007/BF03400433.
[902] A.M. Rausch, V.E. Küng, C. Pobel, M. Markl, C. Körner, Predictive Simulation of Process Windows for Powder Bed Fusion Additive Manufacturing : Influence of the Powder Bulk Density, 2017. https://doi.org/10.3390/ma10101117.
[903] L.-X. Lu, N. Sridhar, Y.-W. Zhang, Phase field simulation of powder bed-based additive manufacturing, Acta Mater. 144 (2018) 801–809, https://doi.org/10.1016/j.actamat.2017.11.033.
[904] B. Liu, G. Fang, L. Lei, W. Liu, A new ray tracing heat source model for mesoscale CFD simulation of selective laser melting (SLM), Appl. Math. Model. 79 (2020) 506–520, https://doi.org/10.1016/j.apm.2019.10.049.
[905] R. Shrestha, N. Shamsaei, M. Seifi, N. Phan, An investigation into specimen property to part performance relationships for laser beam powder bed fusion additive manufacturing, Addit. Manuf. (2019), https://doi.org/10.1016/j.addma.2019.100807.
[906] M. Seifi, M. Dahar, R. Aman, O. Harrysson, J. Beuth, J.J. Lewandowski, Evaluation of Orientation Dependence of Fracture Toughness and Fatigue Crack Propagation Behavior of As-Deposited ARCAM EBM Ti-6Al-4V, JOM. 67 (2015) 597–607, https://doi.org/10.1007/s11837-015-1298-7.
[907] A. Yadollahi, N. Shamsaei, S.M. Thompson, D.W. Seely, Effects of process time interval and heat treatment on the mechanical and microstructural properties of direct laser deposited 316L stainless steel, Mater. Sci. Eng. A. 644 (2015) 171–183, https://doi.org/10.1016/j.msea.2015.07.056.
[908] O.G. Rivera, P.G. Allison, J.B. Jordon, O.L. Rodriguez, L.N. Brewer, Z. McClelland, W.R. Whittington, D. Francis, J. Su, R.L. Martens, N. Hardwick, Microstructures and mechanical behavior of Inconel 625 fabricated by solid-state additive manufacturing, Mater. Sci. Eng. A. 694 (2017) 1–9, https://doi.org/10.1016/j.msea.2017.03.105.
[909] G. Asala, J. Andersson, O.A. Ojo, Rapid #: -16037513 CROSS REF ID, LENDER (2020).
[910] A. Mostafa, D. Shahriari, I.P. Rubio, V. Brailovski, M. Jahazi, M. Medraj, Hot compression behavior and microstructure of selectively laser-melted IN718 alloy, Int. J. Adv. Manuf. Technol. 96 (2018) 371–385, https://doi.org/10.1007/s00170-017-1522-4.
[911] A. Mohammadhosseini, S.H. Masood, D. Fraser, M. Jahedi, Dynamic compressive behaviour of Ti-6Al-4V alloy processed by electron beam melting under high strain rate loading, Adv. Manuf. 3 (2015) 232–243, https://doi.org/10.1007/s40436-015-0119-0.
[912] L. Facchini, E. Magalini, P. Robotti, A. Molinari, Microstructure and mechanical properties of Ti-6Al-4V produced by electron beam melting of pre-alloyed powders, Rapid Prototyp. J. 15 (2009) 171–178, https://doi.org/10.1108/13552540910960262.
[913] L. Facchini, E. Magalini, P. Robotti, A. Molinari, S. Höges, K. Wissenbach, Ductility of a Ti-6Al-4V alloy produced by selective laser melting of prealloyed powders, Rapid Prototyp. J. 16 (2010) 450–459, https://doi.org/10.1108/13552541011083371.

[914] C. Qiu, G.A. Ravi, C. Dance, A. Ranson, S. Dilworth, M.M. Attallah, Fabrication of large Ti-6Al-4V structures by direct laser deposition, J. Alloys Compd. 629 (2015) 351–361, https://doi.org/10.1016/j.jallcom.2014.12.234.
[915] M. Simonelli, Y.Y. Tse, C. Tuck, Effect of the build orientation on the mechanical properties and fracture modes of SLM Ti-6Al-4V, Mater. Sci. Eng. A. 616 (2014) 1–11, https://doi.org/10.1016/j.msea.2014.07.086.
[916] S.S. Al-Bermani, M.L. Blackmore, W. Zhang, I. Todd, The Origin of Microstructural Diversity, Texture, and Mechanical Properties in Electron Beam Melted Ti-6Al-4V, Metall. Mater. Trans. A. 41 (2010) 3422–3434, https://doi.org/10.1007/s11661-010-0397-x.
[917] Y. Zhai, H. Galarraga, D.A. Lados, Microstructure Evolution, Tensile Properties, and Fatigue Damage Mechanisms in Ti-6Al-4V Alloys Fabricated by Two Additive Manufacturing Techniques, Procedia Eng. 114 (2015) 658–666, https://doi.org/10.1016/j.proeng.2015.08.007.
[918] L.E. Murr, E.V. Esquivez, S.A. Quinones, S.M. Gaytan, M.I. Lopez, E.Y. Martinez, F. Medina, D.H. Hernandez, E. Martinez, J.L. Martinez, S.W. Stafford, D.K. Brown, T. Hoppe, W. Meyers, U. Lindhe, R.B. Wicker, Microstructures and mechanical properties of electron beam- rapid manifactured Ti-6Al-4V biomedical prototypes compared to wrought Ti-6Al-4V, Mater. Charact. 60 (2009) 96–105, https://doi.org/10.1016/j.matchar.2008.07.
[919] W. Xu, M. Brandt, S. Sun, J. Elambasseril, Q. Liu, K. Latham, K. Xia, M. Qian, Additive manufacturing of strong and ductile Ti-6Al-4V by selective laser melting via in situ martensite decomposition, Acta Mater. 85 (2015) 74–84, https://doi.org/10.1016/j.actamat.2014.11.028.
[920] L.E. Murr, S.A. Quinones, S.M. Gaytan, M.I. Lopez, A. Rodela, E.Y. Martinez, D. H. Hernandez, E. Martinez, F. Medina, R.B. Wicker, Microstructure and mechanical behavior of Ti-6Al-4V produced by rapid-layer manufacturing, for biomedical applications, J. Mech. Behav. Biomed. Mater. 2 (2009) 20–32, https://doi.org/10.1016/j.jmbbm.2008.05.004.
[921] B. Vandenbroucke, J. Kruth, Selective laser melting of biocompatible metals for rapid manufacturing of medical parts, Rapid Prototyp. J. 13 (2007) 196–203, https://doi.org/10.1108/13552540710776142.
[922] S.R. Ch, A. Raja, P. Nadig, R. Jayaganthan, N.J. Vasa, Influence of working environment and built orientation on the tensile properties of selective laser melted AlSi10Mg alloy, Mater. Sci. Eng. A. 750 (2019) 141–151, https://doi.org/10.1016/j.msea.2019.01.103.
[923] W. Xiong, L. Hao, Y. Li, D. Tang, Q. Cui, Z. Feng, C. Yan, Effect of selective laser melting parameters on morphology, microstructure, densification and mechanical properties of supersaturated silver alloy, Mater. Des. 170 (2019), 107697, https://doi.org/10.1016/j.matdes.2019.107697.
[924] P. Wang, H. Lei, X. Zhu, H. Chen, D. Fang, Influence of manufacturing geometric defects on the mechanical properties of AlSi10Mg alloy fabricated by selective laser melting, J. Alloys Compd. 789 (2019) 852–859, https://doi.org/10.1016/j.jallcom.2019.03.135.
[925] J.L. Bartlett, X. Li, An overview of residual stresses in metal powder bed fusion, Addit. Manuf. 27 (2019) 131–149, https://doi.org/10.1016/j.addma.2019.02.020.
[926] S. Liu, Y.C. Shin, Additive manufacturing of Ti6Al4V alloy: A review, Mater. Des. 164 (2019), 107552, https://doi.org/10.1016/j.matdes.2018.107552.
[927] R. Rashid, S.H. Masood, D. Ruan, S. Palanisamy, R.A. Rahman Rashid, J. Elambasseril, M. Brandt, Effect of energy per layer on the anisotropy of selective laser melted AlSi12 aluminium alloy, Addit. Manuf. 22 (2018) 426–439, https://doi.org/10.1016/j.addma.2018.05.040.
[928] T.M. Mower, M.J. Long, Mechanical behavior of additive manufactured, powder-bed laser-fused materials, Mater. Sci. Eng. A. 651 (2016) 198–213, https://doi.org/10.1016/j.msea.2015.10.068.
[929] A. Kopp, T. Derra, M. Müther, L. Jauer, J.H. Schleifenbaum, M. Voshage, O. Jung, R. Smeets, N. Kröger, Influence of design and postprocessing parameters on the degradation behavior and mechanical properties of additively manufactured magnesium scaffolds, Acta Biomater. (2019), https://doi.org/10.1016/j.actbio.2019.04.012.
[930] Z. Wang, Z. Xiao, Y. Tse, C. Huang, W. Zhang, Optimization of processing parameters and establishment of a relationship between microstructure and mechanical properties of SLM titanium alloy, Opt. Laser Technol. 112 (2019) 159–167, https://doi.org/10.1016/j.optlastec.2018.11.014.
[931] D.H. Smith, J. Bicknell, L. Jorgensen, B.M. Patterson, N.L. Cordes, I. Tsukrov, M. Knezevic, Microstructure and mechanical behavior of direct metal laser sintered Inconel alloy 718, Mater. Charact. 113 (2016) 1–9.
[932] A. Bin Anwar, Q.C. Pham, Selective laser melting of AlSi10Mg: Effects of scan direction, part placement and inert gas flow velocity on tensile strength, J. Mater. Process. Technol. 240 (2017) 388–396, https://doi.org/10.1016/j.jmatprotec.2016.10.015.
[933] Y.J. Liu, S.J. Li, H.L. Wang, W.T. Hou, Y.L. Hao, R. Yang, T.B. Sercombe, L. C. Zhang, Microstructure, defects and mechanical behavior of beta-type titanium porous structures manufactured by electron beam melting and selective laser melting, Acta Mater. 113 (2016) 56–67, https://doi.org/10.1016/j.actamat.2016.04.029.
[934] P.H. Li, W.G. Guo, K.B. Yuan, Y. Su, J.J. Wang, X. Lin, Y.P. Li, Effects of processing defects on the dynamic tensile mechanical behavior of laser-solid-formed Ti-6Al-4 V, Mater. Charact. 140 (2018) 15–29, https://doi.org/10.1016/j.matchar.2018.03.032.
[935] T. Vilaro, C. Colin, J.D. Bartout, As-fabricated and heat-treated microstructures of the Ti-6Al-4V alloy processed by selective laser melting, Metall. Mater. Trans. A Phys. Metall. Mater. Sci. 42 (2011) 3190–3199, https://doi.org/10.1007/s11661-011-0731-y.
[936] B. Baufeld, E. Brandl, O. van der Biest, Wire based additive layer manufacturing: Comparison of microstructure and mechanical properties of Ti–6Al–4V components fabricated by laser-beam deposition and shaped metal deposition, J. Mater. Process. Technol. 211 (2011) 1146–1158, https://doi.org/10.1016/j.jmatprotec.2011.01.018.
[937] D.K. Do, P. Li, The effect of laser energy input on the microstructure, physical and mechanical properties of Ti-6Al-4V alloys by selective laser melting, Virtual Phys. Prototyp. 11 (2016) 41–47, https://doi.org/10.1080/17452759.2016.1142215.
[938] M.A. Meyers, K.K. Chawla, Mechanical Behavior of Materials, second ed., Cambridge University Press, Cambridge, 2009.
[939] J. Wang, Q. Zhou, S. Shao, A. Misra, Strength and plasticity of nanolaminated materials, Mater. Res. Lett. 5 (2017), https://doi.org/10.1080/21663831.2016.1225321.
[940] J. Gong, A.J. Wilkinson, Anisotropy in the plastic flow properties of single-crystal α titanium determined from micro-cantilever beams, Acta Mater. 57 (2009) 5693–5705, https://doi.org/10.1016/j.actamat.2009.07.064.
[941] E.O. Hall, The deformation and aging of mild steel. III: Discussion of results, Proc. Phys. Soc. Lond. B. 64 (1951) 747–753.
[942] N.J. Petch, The cleavage strength of polycrystals, J. Iron Steel Inst. 174 (1953) 25–28.
[943] B.J. Hayes, B.W. Martin, B. Welk, S.J. Kuhr, T.K. Ales, D.A. Brice, I. Ghamarian, A. H. Baker, C.V. Haden, D.G. Harlow, H.L. Fraser, P.C. Collins, Predicting tensile properties of Ti-6Al-4V produced via directed energy deposition, Acta Mater. 133 (2017) 120–133, https://doi.org/10.1016/j.actamat.2017.05.025.
[944] R.K. Nalla, B.L. Boyce, J.P. Campbell, J.O. Peters, R.O. Ritchie, Influence of microstructure on high-cycle fatigue of Ti-6Al-4V: Bimodal vs. lamellar structures, Metall. Mater. Trans. A. 33 (2002) 899–918, https://doi.org/10.1007/s11661-002-1023-3.
[945] R.Z. Valiev, I.V. Alexandrov, Y.T. Zhu, T.C. Lowe, Paradox of Strength and Ductility in Metals Processed Bysevere Plastic Deformation, J. Mater. Res. 17 (2002) 5–8, https://doi.org/10.1557/JMR.2002.0002.
[946] L.E. Murr, S.M. Gaytan, D.A. Ramirez, E. Martinez, J. Hernandez, K.N. Amato, P. W. Shindo, F.R. Medina, R.B. Wicker, Metal Fabrication by Additive Manufacturing Using Laser and Electron Beam Melting Technologies, J. Mater. Sci. Technol. 28 (2012) 1–14, https://doi.org/10.1016/S1005-0302(12)60016-4.
[947] S. Nag, R. Banerjee, Laser deposition and deformation behavior of Ti-Nb-Zr-Ta alloys for orthopedic implan, J. Mech. Behav. Biomed. Mater. 16 (2012) 21–28, https://doi.org/10.1016/j.jmbbm.2012.08.014.
[948] M. Williams, J. Blackburn, A comparison of phase transformations in three commercial titanium alloys, ASM Trans. 60 (1967).
[949] A.S.M. Handbook, Heat Treating, vol. 4, ASM International, Materials Park, OH, 1995.
[950] P.J. Fopiano, M.B. Bever, B.L. Averbach, Phase transformations and strengthening mechanicsms in the alloy Ti-6Al-4V, ASM Trans. Q. 62 (1969) 324.
[951] K. Puebla, L.E. Murr, S.M. Gaytan, E. Martinez, F. Medina, R.B. Wicker, L.E. Murr, S.M. Gaytan, E. Martinez, F. Medina, R.B. Wicker, Effect of Melt Scan Rate on Microstructure and Macrostructure for Electron Beam Melting of Ti-6Al-4V, Mater. Sci. Appl. (2012) 259–264, https://doi.org/10.4236/msa.2012.35038.
[952] B. Baufeld, O. Van Der Biest, S. Dillien, Texture and crystal orientation in Ti-6Al-4V builds fabricated by shaped metal deposition, Metall. Mater. Trans. A Phys. Metall. Mater. Sci. 41 (2010) 1917–1927, https://doi.org/10.1007/s11661-010-0255-x.
[953] D.B. Witkin, D. Patel, T.V. Albright, G.E. Bean, T. McLouth, Influence of surface conditions and specimen orientation on high cycle fatigue properties of Inconel 718 prepared by laser powder bed fusion, Int. J. Fatigue. 132 (2020), 105392, https://doi.org/10.1016/j.ijfatigue.2019.105392.
[954] X. Ding, Y. Koizumi, K. Aoyagi, T. Kii, N. Sasaki, Y. Hayasaka, K. Yamanaka, A. Chiba, Microstructural control of alloy 718 fabricated by electron beam melting with expanded processing window by adaptive offset method, Mater. Sci. Eng. A. 764 (2019), 138058, https://doi.org/10.1016/j.msea.2019.138058.
[955] A.S. Johnson, S. Shao, N. Shamsaei, S.M. Thompson, L. Bian, Microstructure, Fatigue Behavior, and Failure Mechanisms of Direct Laser-Deposited Inconel 718, JOM. 69 (2017) 597–603, https://doi.org/10.1007/s11837-016-2225-2.
[956] D. Zhang, W. Niu, X. Cao, Z. Liu, Effect of standard heat treatment on the microstructure and mechanical properties of selective laser melting manufactured Inconel 718 superalloy, Mater. Sci. Eng. A. 644 (2015) 32–40, https://doi.org/10.1016/j.msea.2015.06.021.
[957] P.F. Kelley, A. Saigal, J.K. Vlahakis, A. Carter, Tensile and Fatigue Behavior of Direct Metal Laser Sintered (DMLS) Inconel 718, in: Adv. Manuf., vol. 2A, American Society of Mechanical Engineers, 2015. https://doi.org/10.1115/IMECE2015-50937.
[958] M.E. Aydinöz, F. Brenne, M. Schaper, C. Schaak, W. Tillmann, J. Nellesen, T. Niendorf, On the microstructural and mechanical properties of post-treated additively manufactured Inconel 718 superalloy under quasi-static and cyclic loading, Mater. Sci. Eng. A. 669 (2016) 246–258.
[959] D. Wells, Overview of Fatigue and Damage Tolerance Performance of Powder Bed Fusion Alloy N07718, in: ASTM Comm. E08 / NIST Work. Mech. Behav. Addit. Manuf. Components, San Antonio, TX, 2016, pp. 49.
[960] V.A. Popovich, E.V. Borisov, A.A. Popovich, V.S. Sufiiarov, D.V. Masaylo, L. Alzina, Functionally graded Inconel 718 processed by additive manufacturing: Crystallographic texture, anisotropy of microstructure and mechanical properties, Mater. Des. 114 (2017) 441–449, https://doi.org/10.1016/j.matdes.2016.10.075.
[961] S. Gribbin, J. Bicknell, L. Jorgensen, I. Tsukrov, M. Knezevic, Low cycle fatigue behavior of direct metal laser sintered Inconel alloy, Int. J. Fatigue. 93 (2016) 156–167.

[962] K. Solberg, F. Berto, Notch-defect interaction in additively manufactured Inconel 718, Int. J. Fatigue. 122 (2019) 35–45, https://doi.org/10.1016/j.ijfatigue.2018.12.021.
[963] T.G. Gallmeyer, S. Moorthy, B.B. Kappes, M.J. Mills, B. Amin-Ahmadi, A. P. Stebner, Knowledge of process-structure-property relationships to engineer better heat treatments for laser powder bed fusion additive manufactured Inconel 718, Addit. Manuf. 31 (2020), 100977, https://doi.org/10.1016/j.addma.2019.100977.
[964] R. Konečná, G. Nicoletto, L. Kunz, A. Bača, Microstructure and directional fatigue behavior of Inconel 718 produced by selective laser melting, Procedia Struct. Integr. 2 (2016) 2381–2388, https://doi.org/10.1016/j.prostr.2016.06.298.
[965] T. LeBrun, T. Nakamoto, K. Horikawa, H. Kobayashi, Effect of retained austenite on subsequent thermal processing and resultant mechanical properties of selective laser melted 17–4 PH stainless steel, Mater. Des. 81 (2015) 44–53, https://doi.org/10.1016/j.matdes.2015.05.026.
[966] P.D. Nezhadfar, R. Shrestha, N. Phan, N. Shamsaei, Fatigue behavior of additively manufactured 17–4 PH stainless steel: Synergistic effects of surface roughness and heat treatment, Int. J. Fatigue. 124 (2019) 188–204, https://doi.org/10.1016/j.ijfatigue.2019.02.039.
[967] A. Yadollahi, N. Shamsaei, S.M.S.M. Thompson, A. Elwany, L. Bian, M. Mahmoudi, Fatigue Behavior of Selective Laser Melted 17–4 PH Stainless Steel, Solid Free Fabr Proc. (2015) 721.
[968] L. Carneiro, B. Jalalahmadi, A. Ashtekar, Y. Jiang, Cyclic deformation and fatigue behavior of additively manufactured 17–4 PH stainless steel, Int. J. Fatigue. 123 (2019) 22–30, https://doi.org/10.1016/j.ijfatigue.2019.02.006.
[969] L. Facchini, N. Vicente, I. Lonardelli, E. Magalini, P. Robotti, A. Molinari, Metastable Austenite in 17–4 Precipitation-Hardening Stainless Steel Produced by Selective Laser Melting, Adv. Eng. Mater. 12 (2010) 184–188, https://doi.org/10.1002/adem.200900259.
[970] M. Mahmoudi, A. Elwany, A. Yadollahi, S.M. Thompson, L. Bian, N. Shamsaei, Mechanical properties and microstructural characterization of selective laser melted 17–4 PH stainless steel, Rapid Prototyp. J. 23 (2017) 280–294, https://doi.org/10.1108/RPJ-12-2015-0192.
[971] S. Cheruvathur, E.A. Lass, C.E. Campbell, Additive Manufacturing of 17–4 PH Stainless Steel: Post-processing Heat Treatment to Achieve Uniform Reproducible Microstructure, JOM. 68 (2016) 930–942, https://doi.org/10.1007/s11837-015-1754-4.
[972] ASTM International, ASTM A693: Standard Specification for Precipitation-Hardening Stainless and Heat- Resisting Steel Plate, Sheet, and Strip, 2016.
[973] M. Alnajjar, F. Christien, K. Wolski, C. Bosch, Evidence of austenite by-passing in a stainless steel obtained from laser melting additive manufacturing, Addit. Manuf. 25 (2019) 187–195, https://doi.org/10.1016/j.addma.2018.11.004.
[974] Z.H. Xiong, S.L. Liu, S.F. Li, Y. Shi, Y.F. Yang, R.D.K. Misra, Role of melt pool boundary condition in determining the mechanical properties of selective laser melting AlSi10Mg alloy, Mater. Sci. Eng. A. (2019), https://doi.org/10.1016/j.msea.2018.10.083.
[975] K. Anderson, J. Weritz, J.G. Kaufman (Eds.), ASM Handbook, vol. 2A, Aluminum Science and Technology, 2018.
[976] G. Nicoletto, Influence of rough as-built surfaces on smooth and notched fatigue behavior of L-PBF AlSi10Mg, Addit. Manuf. 34 (2020), 101251, https://doi.org/10.1016/j.addma.2020.101251.
[977] N.T. Aboulkhair, I. Maskery, C. Tuck, I. Ashcroft, N.M. Everitt, The microstructure and mechanical properties of selectively laser melted AlSi10Mg: The effect of a conventional T6-like heat treatment, Mater. Sci. Eng. A. 667 (2016) 139–146, https://doi.org/10.1016/j.msea.2016.04.092.
[978] M. Awd, J. Tenkamp, M. Hirtler, S. Siddique, M. Bambach, F. Walther, Comparison of Microstructure and Mechanical Properties of Scalmalloy® Produced by Selective Laser Melting and Laser Metal Deposition, Materials (Basel). 11 (2017) 17, https://doi.org/10.3390/ma11010017.
[979] L. Zhuo, Z. Wang, H. Zhang, E. Yin, Y. Wang, T. Xu, C. Li, Effect of post-process heat treatment on microstructure and properties of selective laser melted AlSi10Mg alloy, Mater. Lett. 234 (2019) 196–200, https://doi.org/10.1016/j.matlet.2018.09.109.
[980] A.V. Pozdniakov, A.Y. Churyumov, I.S. Loginova, D.K. Daubarayte, D.K. Ryabov, V.A. Korolev, Microstructure and properties of novel AlSi11CuMn alloy manufactured by selective laser melting, Mater. Lett. 225 (2018) 33–36, https://doi.org/10.1016/j.matlet.2018.04.077.
[981] X.P.P. Li, X.J.J. Wang, M. Saunders, A. Suvorova, L.C.C. Zhang, Y.J.J. Liu, M.H. H. Fang, Z.H.H. Huang, T.B.B. Sercombe, A selective laser melting and solution heat treatment refined Al–12Si alloy with a controllable ultrafine eutectic microstructure and 25% tensile ductility, Acta Mater. 95 (2015) 74–82, https://doi.org/10.1016/j.actamat.2015.05.017.
[982] K. Gokuldoss Prashanth, S. Scudino, J. Eckert, Tensile Properties of Al-12Si Fabricated via Selective Laser Melting (SLM) at Different Temperatures, Technologies. 4 (2016) 38, https://doi.org/10.3390/technologies4040038.
[983] A.S. Fefelov, A.G. Merkushev, O.A. Chikova, Microstructure and mechanical properties of Al-12Si produced by selective laser melting, IOP Conf. Ser. Earth Environ. Sci. 87 (2017), 092011, https://doi.org/10.1088/1755-1315/87/9/092011.
[984] X.J. Wang, L.C. Zhang, M.H. Fang, T.B. Sercombe, The effect of atmosphere on the structure and properties of a selective laser melted Al–12Si alloy, Mater. Sci. Eng. A. 597 (2014) 370–375, https://doi.org/10.1016/j.msea.2014.01.012.
[985] S. Siddique, M. Imran, E. Wycisk, C. Emmelmann, F. Walther, Influence of process-induced microstructure and imperfections on mechanical properties of AlSi12 processed by selective laser melting, J. Mater. Process. Technol. 221 (2015) 205–213, https://doi.org/10.1016/j.jmatprotec.2015.02.023.
[986] K. Prashanth, S. Scudino, R. Chatterjee, O. Salman, J. Eckert, Additive Manufacturing: Reproducibility of Metallic Parts, Technologies. 5 (2017) 8, https://doi.org/10.3390/technologies5010008.
[987] M. Hamidi Nasab, A. Giussani, D. Gastaldi, V. Tirelli, M. Vedani, Effect of Surface and Subsurface Defects on Fatigue Behavior of AlSi10Mg Alloy Processed by Laser Powder Bed Fusion (L-PBF), Metals (Basel) 9 (2019) 1063, https://doi.org/10.3390/met9101063.
[988] E. Bassoli, L. Denti, A. Comin, A. Sola, E. Tognoli, Fatigue Behavior of As-Built L-PBF A357.0 Parts, Metals (Basel) 8 (2018) 634, https://doi.org/10.3390/met8080634.
[989] J.H. Rao, Y. Zhang, A. Huang, X. Wu, K. Zhang, Improving fatigue performances of selective laser melted Al-7Si-0.6Mg alloy via defects control, Int. J. Fatigue. 129 (2019), 105215, https://doi.org/10.1016/j.ijfatigue.2019.105215.
[990] N.E. Uzan, R. Shneck, O. Yeheskel, N. Frage, High-temperature mechanical properties of AlSi10Mg specimens fabricated by additive manufacturing using selective laser melting technologies (AM-SLM), Addit. Manuf. 24 (2018) 257–263, https://doi.org/10.1016/j.addma.2018.09.033.
[991] E. Hosseini, V.A. Popovich, A review of mechanical properties of additively manufactured Inconel 718, Addit. Manuf. (2019), https://doi.org/10.1016/j.addma.2019.100877.
[992] P. Krakhmalev, G. Fredriksson, I. Yadroitsava, N. Kazantseva, A. du Plessis, I. Yadroitsev, Deformation Behavior and Microstructure of Ti6Al4V Manufactured by SLM, Phys. Procedia. 83 (2016) 778–788, https://doi.org/10.1016/j.phpro.2016.08.080.
[993] J. Stef, A. Poulon-quintin, A. Redjaimia, J. Ghanbaja, O. Ferry, M. De Sousa, M. Gouné, Mechanism of porosity formation and influence on mechanical properties in selective laser melting of Ti-6Al-4V parts, Mater. Des. 156 (2018) 480–493, https://doi.org/10.1016/j.matdes.2018.06.049.
[994] J. Elambasseril, S.L. Lu, Y.P. Ning, N. Liu, J. Wang, M. Brandt, H.P. Tang, M. Qian, 3D characterization of defects in deep-powder-bed manufactured Ti–6Al–4V and their influence on tensile properties, Mater. Sci. Eng. A. (2019), 138031, https://doi.org/10.1016/j.msea.2019.138031.
[995] A. du Plessis, I. Yadroitsava, S.G. le Roux, I. Yadroitsev, J. Fieres, C. Reinhart, P. Rossouw, Prediction of mechanical performance of Ti6Al4V cast alloy based on microCT-based load simulation, J. Alloys Compd. 724 (2017) 267–274, https://doi.org/10.1016/j.jallcom.2017.06.320.
[996] C. Pei, D. Shi, H. Yuan, H. Li, Assessment of mechanical properties and fatigue performance of a selective laser melted nickel-base superalloy Inconel 718, Mater. Sci. Eng. A. 759 (2019) 278–287, https://doi.org/10.1016/j.msea.2019.05.007.
[997] K. Decamp, L. Bauvineau, J. Besson, A. Pineau, Size and geometry effects on ductile rupture of notched bars in a C-Mn steel: experiments and modelling, Int. J. Fract. 88 (1997) 1–18, https://doi.org/10.1023/A:1007369510442.
[998] V. Tvergaard, Material Failure by Void Growth to Coalescence, in (1989:) 83–151, https://doi.org/10.1016/S0065-2156(08)70195-9.
[999] Y. Huang, J.W.W. Hutchinson, V. Tvergaard, Cavitation instabilities in elastic-plastic solids, J. Mech. Phys. Solids. 39 (1991) 223–241, https://doi.org/10.1016/0022-5096(91)90004-8.
[1000] K. Sofinowski, M. Šmíd, I. Kuběna, S. Vivès, N. Casati, S. Godet, H. Van Swygenhoven, In situ characterization of a high work hardening Ti-6Al-4V prepared by electron beam melting, Acta Mater. 179 (2019) 224–236, https://doi.org/10.1016/j.actamat.2019.08.037.
[1001] B. Torries, A.J. Sterling, N. Shamsaei, S.M. Thompson, S.R. Daniewicz, Utilization of a Microstructure Sensitive Fatigue Model for Additively Manufactured Ti-6Al-4V, Rapid Prototyp. 22 (2016) 817–825.
[1002] A.S. Johnson, S. Shuai, N. Shamsaei, S.M. Thompson, L. Bian, Fatigue behavior and failure mechanisms of direct laser deposited inconel 718, in: Proc. 26th Annu. Int. Solid Free. Fabr. Symp. – An Addit. Manuf. Conf., Austin, 2016, pp. 499–511.
[1003] N. Shamsaei, A. Yadollahi, L. Bian, S.M. Thompson, An overview of Direct Laser Deposition for additive manufacturing; Part II: Mechanical behavior, process parameter optimization and control, Addit. Manuf. 8 (2015) 12–35, https://doi.org/10.1016/j.addma.2015.07.002.
[1004] S.M. Thompson, L. Bian, N. Shamsaei, A. Yadollahi, An overview of Direct Laser Deposition for additive manufacturing; Part I: Transport phenomena, modeling and diagnostics, Addit. Manuf. 8 (2015) 36–62.
[1005] G.E. Dieter, Mechanical Metallurgy, third ed., McGraw-Hill, Boston, MA, MA, 1986.
[1006] R.R.I. Stephens, A. Fatemi, R.R.I. Stephens, H.O. Fuchs, Metal Fatigue in Engineering, second ed., John Wiley & Sons, 2000.
[1007] A.K. Syed, B. Ahmad, H. Guo, T. Machry, D. Eatock, J. Meyer, M.E. Fitzpatrick, X. Zhang, An experimental study of residual stress and direction-dependence of fatigue crack growth behaviour in as-built and stress-relieved selective-laser-

melted Ti6Al4V, Mater. Sci. Eng. A. (2019), https://doi.org/10.1016/j.msea.2019.04.023.
[1008] H. Zhang, D. Dong, S. Su, A. Chen, Experimental study of effect of post processing on fracture toughness and fatigue crack growth performance of selective laser melting Ti-6Al-4V, Chinese J. Aeronaut. 32 (2019) 2383–2393, https://doi.org/10.1016/j.cja.2018.12.007.
[1009] S. Leuders, M. Thöne, A. Riemer, T. Niendorf, T. Tröster, H.A. Richard, H. J. Maier, On the Mechanical Behaviour of Titanium Alloy Ti6Al4V Manufactured by Selective Laser Melting: Fatigue Resisitance and Crack Growth Performance, Int. J. Fatigue. 48 (2013) 300–307.
[1010] Y. Zhai, D.A. Lados, E.J. Brown, G.N. Vigilante, Fatigue crack growth behavior and microstructural mechanisms in Ti-6Al-4V manufactured by laser engineered net shaping, Int. J. Fatigue. (2016), https://doi.org/10.1016/j.ijfatigue.2016.08.009.
[1011] P.D. Nezhadfar, E. Burford, K. Anderson-Wedge, B. Zhang, S. Shao, S. R. Daniewicz, N. Shamsaei, Fatigue crack growth behavior of additively manufactured 17–4 PH stainless steel: Effects of build orientation and microstructure, Int. J. Fatigue. 123 (2019) 168–179, https://doi.org/10.1016/j.ijfatigue.2019.02.015.
[1012] A. Yadollahi, M. Mahmoudi, A. Elwany, H. Doude, L. Bian, J.C. Newman, Effects of crack orientation and heat treatment on fatigue-crack-growth behavior of AM 17–4 PH stainless steel, Eng. Fract. Mech. 226 (2020), 106874, https://doi.org/10.1016/j.engfracmech.2020.106874.
[1013] R. Konečná, L. Kunz, G. Nicoletto, A. Bača, Long fatigue crack growth in Inconel 718 produced by selective laser melting, Int. J. Fatigue. 92 (2016) 499–506, https://doi.org/10.1016/j.ijfatigue.2016.03.012.
[1014] V. Cain, L. Thijs, J. Van Humbeeck, B. Van Hooreweder, R. Knutsen, Crack propagation and fracture toughness of Ti6Al4V alloy produced by selective laser melting, Addit. Manuf. 5 (2015) 68–76, https://doi.org/10.1016/j.addma.2014.12.006.
[1015] T. Kishi, H.S. Park, R. Horiuchi, T. Kakimi, M. Nakanose, T. Tanabe, Fracture toughness of Ti-6Al-4V alloys determined by ASTM standard and AE method, in: H. Kimura, O. Izumi (Eds.), Proc. Fourth Int. Conf. Titan., Kyoto, Japan, 1980.
[1016] Y.J. Ma, D.C. Wang, H.W. Wang, J.F. Lei, J. Wang, Y.Y. Liu, Q. Gao, R. Yang, Factors influencing fracture toughness of TC4 ELI alloy, Chin J Nonferr Met. 20 (2010) s415–s418.
[1017] M. Seifi, D. Christiansen, J. Beuth, O. Harrysson, J.J. Lewandowski, Process Mapping, Fracture and Fatigue Behavior of Ti-6Al-4V Produced by Ebm Additive Manufacturing, in: Proc. 13th World Conf. Titan., John Wiley & Sons, Inc., Hoboken, NJ, USA, 2016, pp. 1373–1377. https://doi.org/10.1002/9781119296126.ch232.
[1018] P. Edwards, A. O'Conner, M. Ramulu, Electron Beam Additive Manufacturing of Titanium Components: Properties and Performance, J. Manuf. Sci. Eng. 135 (2013), 061016, https://doi.org/10.1115/1.4025773.
[1019] B. Van Hooreweder, D. Moens, R. Boonen, J.-P. Kruth, P. Sas, Analysis of Fracture Toughness and Crack Propagation of Ti6Al4V Produced by Selective Laser Melting, Adv. Eng. Mater. 14 (2012) 92–97, https://doi.org/10.1002/adem.201100233.
[1020] T.H. Becker, M. Beck, C. Scheffer, Microstructure and mechanical properties of direct metal laser sintered TI-6AL-4V, South African J. Ind. Eng. 26 (2015) 1, https://doi.org/10.7166/26-1-1022.
[1021] X. Yu, X. Lin, F. Liu, L. Wang, Y. Tang, J. Li, S. Zhang, W. Huang, Influence of post-heat-treatment on the microstructure and fracture toughness properties of Inconel 718 fabricated with laser directed energy deposition additive manufacturing, Mater. Sci. Eng. A. 798 (2020), 140092, https://doi.org/10.1016/j.msea.2020.140092.
[1022] B. Vieille, C. Keller, M. Mokhtari, H. Briatta, T. Breteau, J. Nguejio, F. Barbe, M. Ben Azzouna, E. Baustert, Investigations on the fracture behavior of Inconel 718 superalloys obtained from cast and additive manufacturing processes, Mater. Sci. Eng. A. (2020), https://doi.org/10.1016/j.msea.2020.139666.
[1023] R. Firoz, S.K. Basantia, N. Khutia, H.N. Bar, S. Sivaprasad, G.V.S. Murthy, Effect of microstructural constituents on mechanical properties and fracture toughness of Inconel 718 with anomalous deformation behavior at 650 °C, J. Alloys Compd. 845 (2020), 156276, https://doi.org/10.1016/j.jallcom.2020.156276.
[1024] L. Hitzler, J. Hirsch, J. Schanz, B. Heine, M. Merkel, W. Hall, A. Öchsner, Fracture toughness of selective laser melted AlSi10Mg, Proc. Inst. Mech. Eng. Part L J. Mater. Des. Appl. (2019), https://doi.org/10.1177/1464420716687337.
[1025] P. Tao, H. Li, B. Huang, Q. Hu, S. Gong, Q. Xu, Tensile behavior of Ti-6Al-4V alloy fabricated by selective laser melting: effects of microstructures and as-built surface quality, China Foundry. 15 (2018) 243–252, https://doi.org/10.1007/s41230-018-8064-8.
[1026] F. Chen, Y. Gu, G. Xu, Y. Cui, H. Chang, L. Zhou, Improved fracture toughness by microalloying of Fe in Ti-6Al-4V, Mater. Des. 185 (2020), 108251, https://doi.org/10.1016/j.matdes.2019.108251.
[1027] R.O. Ritchie, The conflicts between strength and toughness, Nat. Mater. 10 (2011) 817–822, https://doi.org/10.1038/nmat3115.
[1028] M. Svensson, U. Ackelid, Titanium alloys manufactured with electron beam melting mechanical and chemical properties, in: Med. Device Mater. V - Proc. Mater. Process. Med. Devices Conf., ASM International, 2010, pp. 6.
[1029] R.O. Ritchie, A.W. Thompson, On macroscopic and microscopic analyses for crack initiation and crack growth toughness in ductile alloys, Metall. Trans. A. (1985), https://doi.org/10.1007/BF02815305.
[1030] M. Waqas Tofique, J. Bergström, C. Burman, Very high cycle fatigue crack initiation mechanisms in different engineering alloys, Procedia Struct. Integr. 2 (2016) 1181–1190, https://doi.org/10.1016/j.prostr.2016.06.151.
[1031] V. Kazymyrovych, J. Bergström, C. Burman, The Significance of Crack Initiation Stage in Very High Cycle Fatigue of Steels, Steel Res. Int. 81 (2010) 308–314, https://doi.org/10.1002/srin.200900139.
[1032] M.D. Sangid, The physics of fatigue crack initiation, Int. J. Fatigue. 57 (2013) 58–72, https://doi.org/10.1016/j.ijfatigue.2012.10.009.
[1033] J. Hall, Fatigue crack initiation in alpha-beta titanium alloys, Int. J. Fatigue. 19 (1997) 23–37, https://doi.org/10.1016/S0142-1123(97)00047-9.
[1034] F. Bridier, P. Villechaise, J. Mendez, Slip and fatigue crack formation processes in an α/β titanium alloy in relation to crystallographic texture on different scales, Acta Mater. 56 (2008) 3951–3962, https://doi.org/10.1016/j.actamat.2008.04.036.
[1035] R. Jiang, D.J. Bull, A. Evangelou, A. Harte, F. Pierron, I. Sinclair, M. Preuss, X. T. Hu, P.A.S. Reed, Strain accumulation and fatigue crack initiation at pores and carbides in a SX superalloy at room temperature, Int. J. Fatigue. 114 (2018) 22–33, https://doi.org/10.1016/j.ijfatigue.2018.05.003.
[1036] R. Shrestha, J. Simsiriwong, N. Shamsaei, Fatigue behavior of additive manufactured 316L stainless steel parts: Effects of layer orientation and surface roughness, Addit. Manuf. 28 (2019) 23–38, https://doi.org/10.1016/j.addma.2019.04.011.
[1037] D.S. Watring, K.C. Carter, D. Crouse, B. Raeymaekers, A.D. Spear, Mechanisms driving high-cycle fatigue life of as-built Inconel 718 processed by laser powder bed fusion, Mater. Sci. Eng. A. (2019), https://doi.org/10.1016/j.msea.2019.06.003.
[1038] G. Nicoletto, L. Gallina, E. Riva, Influence of as-built surfaces on the fatigue behavior of AlSi10Mg parts obtained by laser powder bed fusion, Procedia Struct. Integr. (2019), https://doi.org/10.1016/j.prostr.2020.02.035.
[1039] A. du Plessis, S. Beretta, Killer notches: The effect of as-built surface roughness on fatigue failure in AlSi10Mg produced by laser powder bed fusion, Addit. Manuf. 35 (2020), 101424, https://doi.org/10.1016/j.addma.2020.101424.
[1040] J. Günther, D. Krewerth, T. Lippmann, S. Leuders, T. Tröster, A. Weidner, H. Biermann, T. Niendorf, Fatigue life of additively manufactured Ti–6Al–4V in the very high cycle fatigue regime, Int. J. Fatigue. 94 (2017) 236–245, https://doi.org/10.1016/j.ijfatigue.2016.05.018.
[1041] E. Wycisk, C. Emmelmann, S. Siddique, F. Walther, High Cycle Fatigue (HCF) Performance of Ti-6Al-4V Alloy Processed by Selective Laser Melting, Adv. Mater. Res. 816–817 (2013) 134–139, https://doi.org/10.4028/www.scientific.net/AMR.816-817.134.
[1042] J.H. Zuo, Z.G. Wang, E.H. Han, Effect of microstructure on ultra-high cycle fatigue behavior of Ti-6Al-4V, Mater. Sci. Eng. A. 473 (2008) 147–152, https://doi.org/10.1016/j.msea.2007.04.062.
[1043] H. Gong, K. Rafi, T. Starr, B. Stucker, The Effects of Processing Parameters on Defect Regularity in Ti-6Al-4V Parts Fabricated By Selective Laser Melting and Electron Beam Melting, 24th Annu, Solid Free. Fabr. Symp. (2013) 424–439, https://doi.org/10.1007/s11665-013-0658-0.
[1044] C.W. Lin, C.P. Ju, J.H. Chern Lin, A comparison of the fatigue behavior of cast Ti-7.5Mo with c.p. titanium, Ti-6Al-4V and Ti-13Nb-13Zr alloys, Biomaterials. 26 (2005) 2899–2907, https://doi.org/10.1016/j.biomaterials.2004.09.007.
[1045] D. Greitemeier, F. Palm, F. Syassen, T. Melz, Fatigue performance of additive manufactured TiAl6V4 using electron and laser beam melting, Int. J. Fatigue. 94 (2017) 211–217, https://doi.org/10.1016/j.ijfatigue.2016.05.001.
[1046] V. Crupi, G. Epasto, E. Guglielmino, A. Squillace, Influence of microstructure [alpha+beta and beta] on very high cycle fatigue behaviour of Ti-6Al-4V alloy, Int. J. Fatigue. 95 (2017) 64–75, https://doi.org/10.1016/j.ijfatigue.2016.10.002.
[1047] J. Oh, J.G. Lee, N.J. Kim, S. Lee, E.W. Lee, Effects of thickness on fatigue properties of investment cast Ti-6Al-4V alloy plates, J. Mater. Sci. 39 (2004) 587–591, https://doi.org/10.1023/B:JMSC.0000011515.84569.ec.
[1048] A.J. Sterling, B. Torries, N. Shamsaei, S.M. Thompson, D.W. Seely, Fatigue behavior and failure mechanisms of direct laser deposited Ti-6Al-4V, Mater. Sci. Eng. A. 655 (2016) 100–112, https://doi.org/10.1016/j.msea.2015.12.026.
[1049] P. Li, D.H. Warner, J.W. Pegues, M.D. Roach, N. Shamsaei, N. Phan, Investigation of the mechanisms by which hot isostatic pressing improves the fatigue performance of powder bed fused Ti-6Al-4V, Int. J. Fatigue. 120 (2019) 342–352, https://doi.org/10.1016/j.ijfatigue.2018.10.015.
[1050] J.W. Pegues, M.D. Roach, N. Shamsaei, Additive manufacturing of fatigue resistant austenitic stainless steels by understanding process-structure–property relationships, Mater. Res. Lett. 8 (2020) 8–15, https://doi.org/10.1080/21663831.2019.1678202.
[1051] P. Li, D.H. Warner, A. Fatemi, N. Phan, Critical assessment of the fatigue performance of additively manufactured Ti-6Al-4V and perspective for future research, Int. J. Fatigue. 85 (2016) 130–143, https://doi.org/10.1016/j.ijfatigue.2015.12.003.
[1052] Y. Murakami, M. Endo, Effects of hardness and crack geometry on.DELTA.Kth of small cracks, J. Soc. Mater. Sci. Japan. 35 (1986) 911–917, https://doi.org/10.2472/jsms.35.911.
[1053] Y. Murakami, Material Defects as the Basis of Fatigue Design, Int. J. Fatigue. 41 (2012) 2–10.
[1054] B.M. Schöbauer, H. Mayer, K. Yanase, M. Endo, Influence of Small Defects on the Uniaxial and Torsional Fatigue Strength of 17-4PH Stainless Steel, in: Procedia Struct. Integr., Lecco, Italy, 2017, pp. 492–496.
[1055] Y. Murakami, M. Endo, Quantitative evaluation of fatigue strength of metals containing various small defects or cracks, Eng. Fract. Mech. 17 (1983) 1–15, https://doi.org/10.1016/0013-7944(83)90018-8.
[1056] M.H.E. Haddad, T.H. Topper, K.N. Smith, Development of multi-purpose wheelchair, Eng. Fract. Mech. 111 (1979) 573–584.

[1057] N. Sanaei, A. Fatemi, Defect-based fatigue life prediction of L-PBF additive manufactured metals, Eng. Fract. Mech. 244 (2021), 107541, https://doi.org/10.1016/j.engfracmech.2021.107541.
[1058] D. Wells, Overview of Fatigue and Damage Tolerance Performance of Powder Bed Fusion Alloy N07718, 2016. https://core.ac.uk/download/pdf/42695108.pdf.
[1059] K. Wang, F. Wang, W. Cui, T. Hayat, B. Ahmad, Prediction of short fatigue crack growth of Ti-6Al-4V, Fatigue Fract. Eng. Mater. Struct. 37 (2014) 1075–1086, https://doi.org/10.1111/ffe.12177.
[1060] S. Romano, A. Brückner-Foit, A. Brandão, J. Gumpinger, T. Ghidini, S. Beretta, Fatigue properties of AlSi10Mg obtained by additive manufacturing: Defect-based modelling and prediction of fatigue strength, Eng. Fract. Mech. 187 (2018) 165–189, https://doi.org/10.1016/j.engfracmech.2017.11.002.
[1061] N. Hrabe, T. Gnäupel-Herold, T. Quinn, Fatigue properties of a titanium alloy (Ti–6Al–4V) fabricated via electron beam melting (EBM): Effects of internal defects and residual stress, Int. J. Fatigue. 94 (2017) 202–210, https://doi.org/10.1016/j.ijfatigue.2016.04.022.
[1062] V. Popov, A. Katz-Demyanetz, A. Garkun, G. Muller, E. Strokin, H. Rosenson, Effect of Hot Isostatic Pressure treatment on the Electron-Beam Melted Ti-6Al-4V specimens, Procedia Manuf. 21 (2018) 125–132, https://doi.org/10.1016/j.promfg.2018.02.102.
[1063] U. Zerbst, G. Bruno, J.Y. Buffière, T. Wegener, T. Niendorf, T. Wu, X. Zhang, N. Kashaev, G. Meneghetti, N. Hrabe, M. Madia, T. Werner, K. Hilgenberg, M. Koukolíková, R. Procházka, J. Džugan, B. Möller, S. Beretta, A. Evans, R. Wagener, K. Schnabel, Damage tolerant design of additively manufactured metallic components subjected to cyclic loading: State of the art and challenges, Prog. Mater. Sci. 121 (2021) 1–73, https://doi.org/10.1016/j.pmatsci.2021.100786.
[1064] U. Zerbst, M. Madia, B. Schork, J. Hensel, P. Kucharczyk, D. Ngoula, D. Tchuindjang, J. Bernhard, C. Beckmann, Fatigue and Fracture of Weldments. the IBESS approach for the determination of the fatigue life and strength of weldments by fracture mechanics analysis, 2019.
[1065] Y. Murakami, H. Usuki, Quantitative evaluation of effects of non-metallic inclusions on fatigue strength of high strength steels. II: Fatigue limit evaluation based on statistics for extreme values of inclusion size, Int. J. Fatigue. (1989), https://doi.org/10.1016/0142-1123(89)90055-8.
[1066] Y. Murakami, S. Kodama, S. Konuma, Quantitative evaluation of effects of non-metallic inclusions on fatigue strength of high strength steels. I: Basic fatigue mechanism and evaluation of correlation between the fatigue fracture stress and the size and location of non-metallic inclusions, Int. J. Fatigue. (1989), https://doi.org/10.1016/0142-1123(89)90054-6.
[1067] L. Sheridan, A modified El-Haddad model for versatile defect tolerant design, Int. J. Fatigue. 145 (2021), 106062, https://doi.org/10.1016/j.ijfatigue.2020.106062.
[1068] G. Sander, J. Tan, P. Balan, O. Gharbi, D.R. Feenstra, L. Singer, S. Thomas, R. G. Kelly, J.R. Scully, N. Birbilis, Corrosion of additively manufactured alloys: A review, Corrosion. 74 (2018) 1318–1350, https://doi.org/10.5006/2926.
[1069] D. Kong, C. Dong, X. Ni, X. Li, Corrosion of metallic materials fabricated by selective laser melting, Npj Mater. Degrad. 3 (2019) 24, https://doi.org/10.1038/s41529-019-0086-1.
[1070] C. Prieto, M. Singer, T. Cyders, D. Young, Investigation of Pitting Corrosion Initiation and Propagation of a Type 316L Stainless Steel Manufactured by the Direct Metal Laser Sintering Process, CORROSION. 75 (2019) 140–143, https://doi.org/10.5006/3075.
[1071] K. Geenen, A. Röttger, W. Theisen, Corrosion behavior of 316L austenitic steel processed by selective laser melting, hot-isostatic pressing, and casting, Mater. Corros. 68 (2017) 764–775, https://doi.org/10.1002/maco.201609210.
[1072] G. Sander, S. Thomas, V. Cruz, M. Jurg, N. Birbilis, X. Gao, M. Brameld, C. R. Hutchinson, On The Corrosion and Metastable Pitting Characteristics of 316L Stainless Steel Produced by Selective Laser Melting, J. Electrochem. Soc. 164 (2017) C250–C257, https://doi.org/10.1149/2.0551706jes.
[1073] Y. Sun, A. Moroz, K. Alrbaey, Sliding Wear Characteristics and Corrosion Behaviour of Selective Laser Melted 316L Stainless Steel, J. Mater. Eng. Perform. 23 (2014) 518–526, https://doi.org/10.1007/s11665-013-0784-8.
[1074] K. Sasaki, G.T. Burstein, The generation of surface roughness during slurry erosion-corrosion and its effect on the pitting potential, Corros. Sci. 38 (1996) 2111–2120, https://doi.org/10.1016/S0010-938X(96)00066-2.
[1075] D. Kong, X. Ni, C. Dong, X. Lei, L. Zhang, C. Man, J. Yao, X. Cheng, X. Li, Bio-functional and anti-corrosive 3D printing 316L stainless steel fabricated by selective laser melting, Mater. Des. 152 (2018) 88–101, https://doi.org/10.1016/J.MATDES.2018.04.058.
[1076] I.A. Segura, L.E. Murr, C.A. Terrazas, D. Bermudez, J. Mireles, V.S.V. Injeti, K. Li, B. Yu, R.D.K. Misra, R.B. Wicker, Grain boundary and microstructure engineering of Inconel 690 cladding on stainless-steel 316L using electron-beam powder bed fusion additive manufacturing, J. Mater. Sci. Technol. 35 (2019) 351–367, https://doi.org/10.1016/j.jmst.2018.09.059.
[1077] N.S. Al-Mamun, K.M. Deen, W. Haider, E. Asselin, I. Shabib, Corrosion behavior biocompatibility of additively manufactured 316L stainless steel in a physiological environment: the effect of citrate ions, Addit. Manuf. (2020), 101237, https://doi.org/10.1016/j.addma.2020.101237.
[1078] V. Cruz, Q. Chao, N. Birbilis, D. Fabijanic, P.D. Hodgson, S. Thomas, Electrochemical studies on the effect of residual stress on the corrosion of 316L manufactured by selective laser melting, Corros. Sci. 164 (2020), 108314, https://doi.org/10.1016/j.corsci.2019.108314.
[1079] C.Y. Chao, L.F. Lin, D.D. Macdonald, A Point Defect Model for Anodic Passive Films - I. Film Growth Kinetics, J. Electrochem. Soc. 128 (1981) 1187, https://doi.org/10.1149/1.2127591.
[1080] L.F. Lin, C.Y. Chao, D.D. Macdonald, A Point Defect Model for Anodic Passive Films - II. Chemical Breakdown and Pit Initiation, J. Electrochem. Soc. 128 (1981) 1194, https://doi.org/10.1149/1.2127592.
[1081] R.F. Schaller, J.M. Taylor, J. Rodelas, E.J. Schindelholz, Corrosion Properties of Powder Bed Fusion Additively Manufactured 17–4 PH Stainless Steel, Corrosion. 73 (2017) 796–807, https://doi.org/10.5006/2365.
[1082] R.F. Schaller, A. Mishra, J.M. Rodelas, J.M. Taylor, E.J. Schindelholz, The Role of Microstructure and Surface Finish on the Corrosion of Selective Laser Melted 304L, J. Electrochem. Soc. 165 (2018) C234–C242, https://doi.org/10.1149/2.0431805jes.
[1083] T. Kurzynowski, K. Gruber, W. Stopyra, B. Kuźnicka, E. Chlebus, Correlation between process parameters, microstructure and properties of 316 L stainless steel processed by selective laser melting, Mater. Sci. Eng. A. 718 (2018) 64–73, https://doi.org/10.1016/J.MSEA.2018.01.103.
[1084] K. Saeidi, X. Gao, Y. Zhong, Z.J. Shen, Hardened austenite steel with columnar sub-grain structure formed by laser melting, Mater. Sci. Eng. A. 625 (2015) 221–229, https://doi.org/10.1016/J.MSEA.2014.12.018.
[1085] Z. Sun, X. Tan, S. Tor, W.Y. Yeong, Selective laser melting of stainless steel 316L with low porosity and high build rates, JMADE. 104 (2016) 197–204, https://doi.org/10.1016/j.matdes.2016.05.035.
[1086] Q. Chao, V. Cruz, S. Thomas, N. Birbilis, P. Collins, A. Taylor, P.D. Hodgson, D. Fabijanic, On the enhanced corrosion resistance of a selective laser melted austenitic stainless steel, Scr. Mater. 141 (2017) 94–98, https://doi.org/10.1016/J.SCRIPTAMAT.2017.07.037.
[1087] Z. Cheng, C.T. Kwok, K.H. Lo, Laser surface melting of 17-4 PH precipitation-hardenable stainless steel, in: Pacific Int. Conf. Appl. Lasers Opt., Laser Institute of America, 2010, pp. 1203. https://doi.org/10.2351/1.5057183.
[1088] A. Barroux, N. Ducommun, E. Nivet, L. Laffont, C. Blanc, Pitting corrosion of 17–4PH stainless steel manufactured by laser beam melting, Corros. Sci. (2020), https://doi.org/10.1016/j.corsci.2020.108594.
[1089] M.R. Stoudt, R.E. Ricker, E.A. Lass, L.E. Levine, Influence of Postbuild Microstructure on the Electrochemical Behavior of Additively Manufactured 17–4 PH Stainless Steel, JOM. 69 (2017) 506–515, https://doi.org/10.1007/s11837-016-2237-y.
[1090] C. Tan, K. Zhou, M. Kuang, W. Ma, T. Kuang, Microstructural characterization and properties of selective laser melted maraging steel with different build directions, Sci. Technol. Adv. Mater. 19 (2018) 746–758, https://doi.org/10.1080/14686996.2018.1527645.
[1091] J.R. Trelewicz, G.P. Halada, O.K. Donaldson, G. Manogharan, Microstructure and Corrosion Resistance of Laser Additively Manufactured 316L Stainless Steel, Jom. 68 (2016) 850–859.
[1092] C. Man, Z. Duan, Z. Cui, C. Dong, D. Kong, T. Liu, S. Chen, X. Wang, The effect of sub-grain structure on intergranular corrosion of 316L stainless steel fabricated via selective laser melting, Mater. Lett. 243 (2019) 157–160, https://doi.org/10.1016/J.MATLET.2019.02.047.
[1093] M. Laleh, A.E. Hughes, W. Xu, N. Haghdadi, K. Wang, P. Cizek, I. Gibson, M. Y. Tan, On the unusual intergranular corrosion resistance of 316L stainless steel additively manufactured by selective laser melting, Corros. Sci. 161 (2019), 108189, https://doi.org/10.1016/j.corsci.2019.108189.
[1094] C. Zhou, S. Hu, Q. Shi, H. Tao, Y. Song, J. Zheng, P. Xu, L. Zhang, Improvement of corrosion resistance of SS316L manufactured by selective laser melting through subcritical annealing, Corros. Sci. 164 (2020), 108353, https://doi.org/10.1016/j.corsci.2019.108353.
[1095] M. Laleh, A.E. Hughes, W. Xu, P. Cizek, M.Y. Tan, Unanticipated drastic decline in pitting corrosion resistance of additively manufactured 316L stainless steel after high-temperature post-processing, Corros. Sci. 165 (2020), 108412, https://doi.org/10.1016/j.corsci.2019.108412.
[1096] R.I. Revilla, J. Liang, S. Godet, I. De Graeve, Local Corrosion Behavior of Additive Manufactured AlSiMg Alloy Assessed by SEM and SKPFM, J. Electrochem. Soc. 164 (2017) C27–C35, https://doi.org/10.1149/2.0461702jes.
[1097] A. Leon, A. Shirizly, E. Aghion, Corrosion Behavior of AlSi10Mg Alloy Produced by Additive Manufacturing (AM) vs, Its Counterpart Gravity Cast Alloy, Metals (Basel) 6 (2016) 148.
[1098] P. Fathi, M. Mohammadi, X. Duan, A.M. Nasiri, A comparative study on corrosion and microstructure of direct metal laser sintered AlSi10Mg_200C and die cast A360.1 aluminum, J. Mater. Process. Technol. 259 (2018) 1–14, https://doi.org/10.1016/J.JMATPROTEC.2018.04.013.
[1099] O. Gharbi, D. Jiang, D.R. Feenstra, S.K. Kairy, Y. Wu, C.R. Hutchinson, N. Birbilis, On the corrosion of additively manufactured aluminium alloy AA2024 prepared by selective laser melting, Corros. Sci. 143 (2018) 93–106, https://doi.org/10.1016/j.corsci.2018.08.019.

[1100] H. Chen, C. Zhang, D. Jia, D. Wellmann, W. Liu, Corrosion behaviors of selective laser melted aluminum alloys: A review, Metals (Basel). 10 (2020), https://doi.org/10.3390/met10010102.
[1101] G.S. Frankel, 2015 W.R. Whitney Award Lecture: The Effects of Microstructure and Composition on Al Alloy Corrosion, Corrosion. 71 (2015) 1308–1320, https://doi.org/10.5006/1887.
[1102] J. Li, J. Dang, A Summary of Corrosion Properties of Al-Rich Solid Solution and Secondary Phase Particles in Al Alloys, Metals (Basel). 7 (2017) 84, https://doi.org/10.3390/met7030084.
[1103] J. Li, B. Hurley, R. Buchheit, Effect of Temperature on the Localized Corrosion of AA2024-T3 and the Electrochemistry of Intermetallic Compounds During Exposure to a Dilute NaCl Solution, CORROSION. 72 (2016) 1281–1291, https://doi.org/10.5006/2136.
[1104] H. Kakinuma, I. Muto, Y. Oya, Y. Kyo, Y. Sugawara, N. Hara, Mechanism for the Morphological Change from Trenching to Pitting around Intermetallic Particles in AA1050 Aluminum, J. Electrochem. Soc. 166 (2019) C19–C32, https://doi.org/10.1149/2.0331902jes.
[1105] J. Wu, X.Q. Wang, W. Wang, M.M. Attallah, M.H. Loretto, Microstructure and strength of selectively laser melted AlSi10Mg, Acta Mater. 117 (2016) 311–320.
[1106] M. Cabrini, S. Lorenzi, T. Pastore, S. Pellegrini, M. Pavese, P. Fino, E. P. Ambrosio, F. Calignano, D. Manfredi, Corrosion resistance of direct metal laser sintering AlSiMg alloy, Surf. Interface Anal. 48 (2016) 818–826.
[1107] R.I. Revilla, I. De Graeve, Influence of Si Content on the Microstructure and Corrosion Behavior of Additive Manufactured Al-Si Alloys, J. Electrochem. Soc. 165 (2018) C926–C932, https://doi.org/10.1149/2.0101814jes.
[1108] M. Cabrini, S. Lorenzi, T. Pastore, S. Pellegrini, E.P. Ambrosio, F. Calignano, D. Manfredi, M. Pavese, P. Fino, Effect of heat treatment on corrosion resistance of DMLS AlSi10Mg alloy, Electrochim. Acta. 206 (2016) 346–355.
[1109] M. Cabrini, S. Lorenzi, T. Astore, S. Pellegrini, D. Manfredi, P. Fino, S. Biamino, C. Badini, Evaluation of corrosion resistance of Al-10Si-Mg alloy obtained by means of Direct Metal Laser Sintering, J. Mater. Process. Technol. 231 (2016) 326–335.
[1110] A. Leon, E. Aghion, Effect of surface roughness on corrosion fatigue performance of AlSi10Mg alloy produced by Selective Laser Melting (SLM), Mater. Charact. (2017), https://doi.org/10.1016/j.matchar.2017.06.029.
[1111] P. Fathi, M. Rafieazad, X. Duan, M. Mohammadi, A.M. Nasiri, On microstructure and corrosion behaviour of AlSi10Mg alloy with low surface roughness fabricated by direct metal laser sintering, Corros. Sci. 157 (2019) 126–145, https://doi.org/10.1016/j.corsci.2019.05.032.
[1112] M. Cabrini, S. Lorenzi, C. Testa, T. Pastore, D. Manfredi, M. Lorusso, F. Calignano, P. Fino, Statistical approach for electrochemical evaluation of the effect of heat treatments on the corrosion resistance of AlSi10Mg alloy by laser powder bed fusion, Electrochim. Acta. 305 (2019) 459–466, https://doi.org/10.1016/j.electacta.2019.03.103.
[1113] M. Rafieazad, M. Mohammadi, A.M. Nasiri, On microstructure and early stage corrosion performance of heat treated direct metal laser sintered AlSi10Mg, Addit. Manuf. 28 (2019) 107–119, https://doi.org/10.1016/j.addma.2019.04.023.
[1114] T. Rubben, R.I. Revilla, I. De Graeve, Influence of heat treatments on the corrosion mechanism of additive manufactured AlSi10Mg, Corros. Sci. 147 (2019) 406–415, https://doi.org/10.1016/j.corsci.2018.11.038.
[1115] H. Ahlatci, Production and corrosion behaviours of the Al-12Si-XMg alloys containing in situ Mg2Si particles, J. Alloys Compd. 503 (2010) 122–126, https://doi.org/10.1016/j.jallcom.2010.04.214.
[1116] F.L. Zeng, Z.L. Wei, J.F. Li, C.X. Li, X. Tan, Z. Zhang, Z.Q. Zheng, Corrosion mechanism associated with Mg 2Si and Si particles in Al-Mg-Si alloys, Trans. Nonferrous Met. Soc. China (English Ed. 21 (2011) 2559–2567, https://doi.org/10.1016/S1003-6326(11)61092-3.
[1117] A. Zakay, E. Aghion, Effect of Post-heat Treatment on the Corrosion Behavior of AlSi10Mg Alloy Produced by Additive Manufacturing, Jom. 71 (2019) 1150–1157, https://doi.org/10.1007/s11837-018-3298-x.
[1118] N. Dai, L.-C. Zhang, J. Zhang, Q. Chen, M. Wu, Corrosion behavior of selective laser melted Ti-6Al-4V alloy in NaCl solution, Corros. Sci. 102 (2016) 484–489, https://doi.org/10.1016/j.corsci.2015.10.041.
[1119] N. Dai, J. Zhang, Y. Chen, L.-C. Zhang, Heat Treatment Degrading the Corrosion Resistance of Selective Laser Melted Ti-6Al-4V Alloy, J. Electrochem. Soc. 164 (2017) C428–C434, https://doi.org/10.1149/2.1481707jes.
[1120] A. Sharma, M.C. Oh, J. Kim, A.K. Srivastava, B. Ahn, Investigation of electrochemical corrosion behavior of additive manufactured Ti–6Al–4V alloy for medical implants in different electrolytes, Elsevier B.V. (2020), https://doi.org/10.1016/j.jallcom.2020.154620.
[1121] A. Hemmasian Ettefagh, C. Zeng, S. Guo, J. Raush, Corrosion behavior of additively manufactured Ti-6Al-4V parts and the e ff ect of post annealing, Addit. Manuf. 28 (2019) 252–258, https://doi.org/10.1016/j.addma.2019.05.011.
[1122] B. Pazhanivel, P. Sathiya, G. Sozhan, Ultra-fine bimodal (α + β) microstructure induced mechanical strength and corrosion resistance of Ti-6Al-4V alloy produced via laser powder bed fusion process, Opt. Laser Technol. 125 (2020), 106017, https://doi.org/10.1016/j.optlastec.2019.106017.
[1123] J. Yang, H. Yang, H. Yu, Z. Wang, X. Zeng, Corrosion Behavior of Additive Manufactured Ti-6Al-4V Alloy in NaCl Solution, Metall. Mater. Trans. A. 48 (2017) 1–11, https://doi.org/10.1007/s11661-017-4087-9.
[1124] N. Dai, L.-C.-C. Zhang, J. Zhang, X. Zhang, Q. Ni, Y. Chen, M. Wu, C. Yang, Distinction in corrosion resistance of selective laser melted Ti-6Al-4V alloy on different planes, Corros. Sci. 111 (2016) 703–710, https://doi.org/10.1016/j.corsci.2016.06.009.
[1125] R.M. Mahamood, E.T. Akinlabi, Corrosion behavior of laser additive manufactured titanium alloy, Int. J. Adv. Manuf. Technol. 99 (2018) 1545–1552, https://doi.org/10.1007/s00170-018-2537-1.
[1126] Y. Bai, X. Gai, S. Li, L.-C. Zhang, Y. Liu, Y. Hao, X. Zhang, R. Yang, Y. Gao, Improved corrosion behaviour of electron beam melted Ti-6Al–4 V alloy in phosphate buffered saline, Corros. Sci. (2017), https://doi.org/10.1016/j.corsci.2017.05.003.
[1127] G.A. Longhitano, M.A. Arenas, A. Conde, M.A. Larosa, A.L. Jardini, C.A.D. C. Zavaglia, J.J. Damborenea, Heat treatments effects on functionalization and corrosion behavior of Ti-6Al-4V ELI alloy made by additive manufacturing, J. Alloys Compd. 765 (2018) 961–968, https://doi.org/10.1016/j.jallcom.2018.06.319.
[1128] R. Żebrowski, M. Walczak, The effect of shot peening on the corrosion behaviour of Ti-6Al-4V alloy made by DMLS, Adv. Mater. Sci. 18 (2018) 43–54, https://doi.org/10.1515/adms-2017-0040.
[1129] J.J. de Damborenea, M.A. Larosa, M.A. Arenas, J.M. Hernández-López, A. L. Jardini, M.C.F. Ierardi, C.A.C. Zavaglia, R.M. Filho, A. Conde, Functionalization of Ti6Al4V scaffolds produced by direct metal laser for biomedical applications, Mater. Des. 83 (2015) 6–13.
[1130] A. Casadebaigt, J. Hugues, D. Monceau, Influence of Microstructure and Surface Roughness on Oxidation Kinetics at 500–600 °C of Ti–6Al–4V Alloy Fabricated by Additive Manufacturing, Oxid. Met. 90 (2018) 633–648, https://doi.org/10.1007/s11085-018-9859-0.
[1131] Y. Zhou, S.F. Wen, B. Song, X. Zhou, Q. Teng, Q.S. Wei, Y.S. Shi, A novel titanium alloy manufactured by selective laser melting: Microstructure, high temperature oxidation resistance, Mater. Des. 89 (2016) 1199–1204, https://doi.org/10.1016/J.MATDES.2015.10.092.
[1132] Y. Cui, K. Aoyagi, Y. Koizumi, T. Fujieda, A. Chiba, Enhanced oxidation resistance of a titanium–based alloy by the addition of boron and the application of electron beam melting, Addit. Manuf. 31 (2020), 100971, https://doi.org/10.1016/j.addma.2019.100971.
[1133] H. Hack, S. Olig, E. Knudsen, R. Link, A. Beckwith, A. Arcari, Fatigue and Corrosion Fatigue Properties of Additive-Manufactured Nickel Alloy 625 and Ti-6Al-4V, Mater. Perform. Charact. 7 (2018) 20170150, https://doi.org/10.1520/MPC20170150.
[1134] H. Hack, R. Link, E. Knudsen, B. Baker, S. Olig, Mechanical properties of additive manufactured nickel alloy 625, Addit. Manuf. 14 (2017) 105–115.
[1135] H.S. Klapper, N. Molodtsov, M. Burns, C. Wangenheim, Critical factors affecting the pitting corrosion resistance of additively manufactured nickel alloy in chloride containing environments, NACE - Int. Corros. Conf. Ser. 2 (2017) 1205–1212.
[1136] P. Karimi, E. Sadeghi, J. Ålgårdh, P. Harlin, J. Andersson, Effect of build location on microstructural characteristics and corrosion behavior of EB-PBF built Alloy 718, Int. J. Adv. Manuf. Technol. 106 (2020) 3597–3607, https://doi.org/10.1007/s00170-019-04859-9.
[1137] G.A. Greene, C.C. Finfrock, Oxidation of Inconel 718 in Air at High Temperatures, Oxid. Met. 55 (2001) 505–521, https://doi.org/10.1023/A:1010359815550.
[1138] C. Juillet, A. Oudriss, J. Balmain, X. Feaugas, F. Pedraza, Characterization and oxidation resistance of additive manufactured and forged IN718 Ni-based superalloys, Corros. Sci. 142 (2018) 266–276, https://doi.org/10.1016/j.corsci.2018.07.032.
[1139] Q. Jia, D. Gu, Selective laser melting additive manufactured Inconel 718 superalloy parts: High-temperature oxidation property and its mechanisms, Opt. Laser Technol. 62 (2014) 161–171.
[1140] T. Sanviemvongsak, D. Monceau, B. Macquaire, High temperature oxidation of IN 718 manufactured by laser beam melting and electron beam melting: Effect of surface topography, Corros. Sci. 141 (2018) 127–145, https://doi.org/10.1016/J.CORSCI.2018.07.005.
[1141] E. Sadeghi, P. Karimi, S. Momeni, M. Seifi, A. Eklund, J. Andersson, Influence of thermal post treatments on microstructure and oxidation behavior of EB-PBF manufactured Alloy 718, Mater. Charact. 150 (2019) 236–251, https://doi.org/10.1016/J.MATCHAR.2019.02.016.
[1142] Y.J. Kang, S. Yang, Y.K. Kim, B. AlMangour, K.A. Lee, Effect of post-treatment on the microstructure and high-temperature oxidation behaviour of additively manufactured inconel 718 alloy, Corros. Sci. 158 (2019), 108082, https://doi.org/10.1016/j.corsci.2019.06.030.

[1143] K.A. Unocic, L.M. Kolbus, R.R. Dehoff, S.N. Dryepondt, B.A. Pint, High-Temperature Performance of UNS N07718 Processed by Additive Manufacturing, in: Corros. 2014, 2014, p. 4478.
[1144] D. Young, High Temperature Oxidation and Corrosion of Metals, second ed., Elsevier, 2016.
[1145] R. McCann, M.A. Obeidi, C. Hughes, É. McCarthy, D.S. Egan, R. K. Vijayaraghavan, A.M. Joshi, V. Acinas Garzon, D.P. Dowling, P.J. McNally, D. Brabazon, In-situ sensing, process monitoring and machine control in Laser Powder Bed Fusion: A review, Addit. Manuf. 45 (2021), https://doi.org/10.1016/j.addma.2021.102058.
[1146] N.S. Johnson, P.S. Vulimiri, A.C. To, X. Zhang, C.A. Brice, B.B. Kappes, A.P. Stebner, Machine Learning for Materials Developments in Metals Additive Manufacturing, 2020. http://arxiv.org/abs/2005.05235.

Dr. Amir Mostafaei is currently an Assistant Professor in the Department of Materials, Mechanical and Aerospace Engineering at the Illinois Institute of Technology, Chicago, since January 2020, with a Ph.D. in Materials Science and Engineering from the University of Pittsburgh, PA, USA, a post-doc research fellow at the Manufacturing Futures Initiatives (MFI) Center at Carnegie Mellon University between September 2018 and December 2019 and an M.Sc. degree in Corrosion and Materials Protection (Sahand University of Technology, Iran). His Ph.D. research was primary on binder jet 3D printing of structural, bio-compatible, metal matrix composites and magnetic shape memory alloys. Effects of print processing optimization during binder jetting as well as post-processing development including sintering and surface treatment of the 3D printed parts were investigated on the microstructural evolution, phase formation, and resulting properties of binder jetted parts. Additionally, he has been working on laser powder bed fusion of metallic materials and evaluation of the processing parameters on the microstructure, porosity distribution, mechanical properties, and corrosion behavior of various additive manufactured parts from aluminum, stainless steel, and nickel-based alloys. Dr. Mostafaei has published literature in high temperature corrosion and failure analysis of stainless steels and nickel-based superalloys used in petroleum and nuclear power plants, multifunctional organic coatings, welding metallurgy, and nanomaterials fabrication. Finally, Dr. Mostafaei's research mainly focuses on applying fundamental aspects of materials science and engineering to address the demands of various manufacturing industries via additive manufacturing.

Dr. Cang Zhao is currently an assistant professor in the Department of Mechanical Engineering at Tsinghua University. He received his Ph.D. degree in Structural Engineering from the University of California, San Diego in 2015, his master's degree in Condensed Matter Physics from the University of Science and Technology of China in 2011, and his bachelor's degree in Materials Science and Engineering from the University of Science and Technology Beijing in 2009. Prior to his current position, Cang worked as a postdoctoral researcher at the Advanced Photon Source of Argonne National Laboratory from 2016 to 2019. A few keywords could be used to summarize his research: metal additive manufacturing, cellular solids, and multiscale mechanics. He has published more than twenty peer-reviewed papers in journals such as *Science* and *Physical Review X*, and has achieved the Outstanding Postdoctoral Performance Award in Applied Science from Argonne National Laboratory and the President Award of the Chinese Academy of Sciences.

Yining He was a Ph.D. student in Prof. Bryan Webler's research group at Materials Science and Engineering department of Carnegie Mellon University. She received a B.S. from Shandong University in China and M.S. from Carnegie Mellon University, both in materials science and engineering. Her research work was with NextManufacturing Center at Carnegie Mellon, focus on selective laser melting (SLM)-type additive manufacturing with tool steel (H13, M2, D2 and P20 grades), in specific studying their melt pool geometrical and microstructural evolution across SLM P-V space to understand P-V selection for SLM-tool steel part cracking control. In addition, she worked on L-PBF new alloy development of boron-modified Ti6Al4V-xB material system and high entropy alloy (HEA) class, by integrating melt pool scale experimental observation with machine learning-accelerated property predictions by CALPHAD and DFT calculation in a Bayesian Global Optimization (BGO) design-of-experiments framework. Her master research work was with Center for Iron and Steelmaking Research (CISR) in Professor Chris Pistorius's research group at Carnegie Mellon, studying decarburization of direct reduced iron (DRI) in electric arc furnace (EAF) slag-steel system.

Dr. Reza Ghiaasiaan is currently with the Department of Mechanical Engineering at Auburn University, as Assistant Research Professor working at the National Center for Additive Manufacturing Excellence. NCAME is a NASA and NIST funded research center focused on advancing the additive manufacturing (AM) technology. NCAME is also one of the two U.S.-based founding partners of the ASTM International Additive Manufacturing Center of Excellence (AM CoE). Prior to his appointment at NCAME, Dr. Ghiaasiaan has obtained a wealth of engineering experience through many years in industry, including leadership and R&D engineering positions, specializing in thermofluid, solidification/casting and physical/mechanical metallurgy of metallic alloying systems. Dr. Ghiaasiaan then took his skillset to McMaster University, where he received his Ph.D. in 2015 in Mechanical Engineering focused on microscopic characterization and materials properties using various processing methodologies such as innovative casting and additive manufacturing processes. The focus of his research was on the physical metallurgy and various processing methods of metallic alloying systems including additive manufacturing, which is his continued primary area of interest at Auburn University. Dr. Ghiaasiaan received his Professional Engineer (P.Eng.) licensure in 2018 as he obtained his full membership to the *Professional Engineering Ontario* (*PEO*) Association, designated as P.Eng. in Canada.

Bo Shi is a research assistant under the supervision of Dr. Cang Zhao in the Department of Mechanical Engineering at Tsinghua University. His research interest is in understanding and controlling microstructural defects in metal additive manufacturing. Through the effort of combing experimental observation, theoretical modeling, and machine learning, he is tackling the underlying causes for various defects like porosity and cracking. Also, he is developing new tools to monitor the metal additive manufacturing processes.

Dr. Shuai Shao is currently an associate professor of Mechanical Engineering at Auburn University. He has published over 50 peer reviewed journal articles and book chapters and has given 20+ invited/regular presentations. His expertise is multiscale materials modeling, materials characterization, and fatigue applied to additively manufactured materials. Dr. Shao has served as PI/Co-PI in multiple research projects from federal agencies, including the Department of Energy, the National Aeronautics and Space Administration, and the National Institute of Standards and Technology. Dr. Shao is serving as referee for prestigious journals as well as organizing symposia in prominent international conferences. He has also received numerous awards, including the "2019 LSU Mechanical Engineering Outstanding Teacher Award", "2019 LSU Alumni Association Rising Faculty Research Award", "2018 LSU Summer Research Stipend", and "2015 TMS Hysitron Presentation Silver Medal Award". One of his research articles made the cover of the Jan 2016 issue of JOM.

Dr. Nima Shamsaei is currently the Philpott-WestPoint Stevens Distinguished Associate Professor in the Department of Mechanical Engineering at Auburn University (AU), where he is also the founding director of the National Center for Additive Manufacturing Excellence (NCAME). Prior to joining academia, Dr. Shamsaei spent many years in industry, including leadership positions, specializing in fatigue analysis and durability development. The focus of his research in academia is on the structural integrity of AM metals, which has resulted so far in publishing over 170 peer-reviewed journal articles and conference proceedings as well as 50+ technical presentations including 30+ invited talks or keynote/plenary speeches in the areas of fatigue, fracture, mechanics of materials, and AM part qualification and certification. He is the recipient of multiple awards including AU's College of Engineering Research Award (2019), ASTM International Emerging Professional Award (2016), Schillig Teaching Award (2015), and SAE International's Henry O. Fuchs Fatigue Award (2010).

Ziheng Wu (Dino) was a Ph.D. student, working under Professor Anthony Rollett's supervision in the Materials Science and Engineering department at Carnegie Mellon University. He was an active member of CMU's NextManufacturing Center for Additive Manufacturing (AM) Research. His research focused on exploring the capabilities of powder-bed metal additive manufacturing (AM), studying the porosity formation mechanism in AM and using modeling techniques to understand the thermal history and the microstructure evolution in AM parts. He also has experience on AM fabrication using non-spherical powder, e.g., Hydride-DeHydride (HDH) Ti-6Al-4V materials. He earned his bachelor's degree in Materials Science and Engineering from Purdue University in 2015 and master's degree in Materials Science and Engineering from Carnegie Mellon in 2017. His master thesis is about development of medium carbon secondary hardening steel for the application of aircraft landing gear under Professor Warren Garrison's guidance.

Dr. Nadia Kouraytem is currently an Assistant Professor at the Mechanical and Aerospace Engineering Department at Utah State University. Kouraytem focuses on advancing additive manufacturing for structural applications in defense, energy, and aerospace. Kouraytem's research interests are in the broad area of the characterization of the process-structure-property relationships in laser-based metal additive manufacturing for structural applications using advanced experimental techniques and *in situ* measurements. Prior to joining Utah State University, she was a Post-doctoral Research Associate at the Mechanical Engineering Department at the University of Utah where she studied the influence of additive manufacturing parameters on location-specific microstructure and mechanical response of structural metals and spent a semester visiting the Department of Materials Science and Engineering at Carnegie Mellon University. Kouraytem received her BE in Mechanical Engineering from the American University of Beirut, and her M.Sc. and Ph.D. in Mechanical Engineering from KAUST working at the High-Speed Fluids Imaging Laboratory.

Dr. Tao Sun is an Associate Professor at the Department of Materials Science and Engineering of University of Virginia. Sun obtained his Bachelor and Master degrees in Materials Science and Engineering (MSE) from Tsinghua University, and his Ph.D. in MSE from Northwestern University. Sun's doctoral research at Northwestern was focused on fabrication and characterization of nanostructured oxides. In 2010, Sun joined the X-ray Science Division at Argonne National Laboratory as a postdoc. During this period, Sun developed correlograph electron analysis technique for characterizing the atomic structures of amorphous materials, and coherent x-ray surface scattering imaging technique for resolving sample surface structures with high spatial resolution. Sun became an Assistant Physicist in 2012, and was promoted to Physicist in 2017 at Argonne. In Sep 2019, Sun started his academic career as an Associate Professor at UVA. Sun's team currently studies additive manufacturing processes and materials using synchrotron x-ray and other *in situ/ex situ* structure characterization tools. The research focuses on developing advanced alloy/composite systems and building innovative architectures using laser-based additive manufacturing techniques, as well as understanding the physics underlying the laser-material interaction and non-equilibrium material structural evolution.

Joseph Pauza (Joe) was a PhD student in Professor Anthony Rollett's lab at Carnegie Mellon University. Joe completed his undergraduate degree in mechanical engineering at Colorado School of Mines where he spent time in Dr. Aaron Stebner's lab. At Mines, he worked on characterization of both laser powder-bed fusion (L-PBF) additively manufactured parts and shape memory alloys. Joe's research was heavily focused on modeling of microstructure development during the fabrication of L-PBF additively manufactured parts. Specifically, using Monte Carlo Potts models to understand grain structure evolution during L-PBF additive manufacturing builds. Additionally, Joe has spent time studying in situ laser melt pool behavior using dynamic x-ray radiography, part performance of L-PBF parts, as well as NiTiHf and CuAlMn shape memory alloys.

Dr. Jerard Vincent Gordon is currently an Assistant Professor in the Mechanical Engineering Department at University of Michigan. He was a President's Postdoctoral Fellow jointly with the NextManufacturing Center and Mechanical Engineering Department at Carnegie Mellon University, working with Professor Anthony Rollett, on developing a multiscale modeling and experimental framework to optimize mechanical performance within wire and powder-based metal AM parts. In particularly, he is interested in the effect of complex processing histories on the static and cyclic material performance of AM materials using experimental techniques and high fidelity spectral and self-consistent crystal plasticity modeling methods. For his doctoral research, Jerard studied the fatigue behavior of directed energy deposition (DED) metastable austenitic stainless-steel. His other research experience includes experimental analysis and constitutive modeling of wire + arc AM materials, AM steels, materials characterization, optimization of cellular materials for thermal protection system, and analytical limit state analysis (shakedown). He was awarded a Ph.D. in mechanical engineering from Lehigh University in May 2018.

Dr. Bryan Webler is currently an Associate Professor in the Materials Science and Engineering Department at Carnegie Mellon University, affiliated with the Center for Iron and Steelmaking Research (CISR) and the NextManufacturing Center. He received a BS in Engineering Physics from the University of Pittsburgh in 2005 and an MS (2007) and PhD (2008) in Materials Science and Engineering from Carnegie Mellon. His PhD work at Carnegie Mellon was with CISR, studying high temperature oxidation and copper-induced hot shortness of steel. From 2008 to 2013, he was a Senior Engineer in the Materials Technology Department of the Bettis Atomic Power Laboratory, studying corrosion resistance and mechanical behavior of stainless steels and nickel-base alloys. Dr. Webler joined the Carnegie Mellon faculty in 2013. His research interests are in the reactions between metals and their environment, both during processing and in-service. In addition to the work above, Dr. Webler has projects studying microstructure development during casting of steels for automotive applications, high temperature oxidation and deformation processing of multi-phase alloys, additive manufacturing of steels, and corrosion of stainless steels. He also teaches classes on phase diagrams and phase transformations, computational thermodynamics, and corrosion/oxidation of metals.

Dr. Niranjan D. Parab is a post-doctoral appointee working at the advanced photon source in Argonne National Laboratory. He obtained his bachelors and Ph.D. in aerospace engineering from Indian Institute of Technology Bombay and Purdue University, respectively. His research interests are in the broad areas of dynamic behavior of materials and additive manufacturing. During his graduate and post-doctoral work, he has developed various experimental setups using the high-speed synchrotron X-ray imaging and diffraction techniques. His current research is focused on improving the fundamental understanding of various additive manufacturing processes.

Mohammadreza Asherloo is a Ph.D. student, working under Professor Amir Mostafaei's supervision in Advanced Manufacturing and Innovation Research Lab (AMIR Lab) at the Mechanical, Materials and Aerospace Engineering department at Illinois Institute of Technology. His research focuses on exploring the capabilities of laser-beam powder-bed fusion of metallic materials, developing processing map and studying the process-structure-property-performance relationship in additive manufactured parts. He is currently investigating printability of non-spherical Ti-6Al-4V powder produced by Hydride-DeHydride process. He earned his bachelor's degree in Materials Science and Engineering from K.N. Toosi University of Technology, Tehran, Iran in 2019.

Qilin Guo is a Ph.D. candidate in Prof. Lianyi Chen's research group at Mechanical Engineering Department of University of Wisconsin-Madison. He received his master's degree in Materials Science from Harbin Institute of Technology, China in 2015, and his bachelor's degree in Materials Science and Engineering from Harbin Institute of Technology, China in 2013. Qilin's research interest lies at the intersection of materials science and metal additive manufacturing. His current research is focusing on the in-situ characterization of process dynamics (melt pool, melt flow, phase transformation, etc.) during laser powder bed fusion process with high-speed synchrotron X-ray imaging/diffraction.

Dr. Lianyi Chen is an assistant professor in the Department of Mechanical Engineering and Department of Materials Science and Engineering at University of Wisconsin-Madison. Dr. Chen received his Ph.D. degree in Materials Science and Engineering from Zhejiang University in 2009. He worked in the Department of Mechanical Engineering and Materials Science Program at the University of Wisconsin-Madison as a Research Associate from 2010 to 2013. He was a postdoctoral scholar in the Department of Mechanical and Aerospace Engineering at UCLA from 2013-2014. He worked in Missouri University of Science and Technology as an assistant professor from 2015-2019 before joining UW-Madison. His research activities and interests are at the intersection of materials science, advanced manufacturing, nanotechnology, and advanced in-situ/in-operando characterization. His research goal is to drive performance and manufacturing of metals to a new level by integrating materials design and manufacturing. His research program includes four highly interrelated research areas: metal additive manufacturing, metals design based on nanoelements, smart metal manufacturing, and in-situ/in-operando characterization. Dr. Chen has published more than 70 peer-reviewed journal papers. He is also an inventor with 7 patents (2 licensed).

Professor Anthony D. Rollett has been a Professor of Materials Science & Engineering at Carnegie Mellon University since 1995 and before that was with the Los Alamos National Laboratory. His most recent honor was the award of US Steel Professor of Metallurgical Engineering & Materials Science in 2017. He is the co-Director of CMU's NextManufacturing Center that is dedicated to advancing manufacturing especially through 3D printing. He has over 200 peer-reviewed publications. Rollett's research focuses on microstructural evolution and microstructure-property relationships in 3D, using both experiments and simulations. Interests include 3D printing of metals, materials for energy conversion systems, strength of materials, constitutive relations, microstructure, texture, anisotropy, grain growth, recrystallization, formability, extreme value statistics and stereology. Relevant techniques highlight spectral methods in micro-mechanics, Dynamic X-ray Radiography and High Energy Diffraction Microscopy. Important recent results include definition of process windows in 3D printing through characterization of porosity, 3D comparisons of experiment and simulation for plastic deformation in metals, the appearance of new grains during grain growth, and grain size stabilization.